

ANSYS

SVS FEM

Your partner in computing

Proceedings of

20th SVSFEM ANSYS Users' Group Meeting and Conference 2012
17th – 19th of October 2012, Hotel Jana in Přerov, Czech
Republic

Sponsors:



© SVS FEM s.r.o.

ISBN: 978-80-260-2722-5

Content

SPOJENÍ ANSYS CLASSIC S AUTODESK MOLDFLOW	6
Matěj Bartecký	
CRACK GROWTH SIMULATION IN THE COURSE OF INDUSTRIAL EQUIPMENT LIFE EXTENSION	13
Jiří Běhal, Kirill Solodyankin	
STRESS ANALYSIS OF VALVES FOR NUCLEAR POWER PLANTS.....	22
Lina Bryukhova*, Jiří Táborský	
ELECTROHYDRODYNAMICS AND RELATIVISTIC THEORY IN ACCURATE NUMERICAL MODELING.....	30
Pavel Fiala	
NMR DIAGNOSTICS AND BRAIN CANCER TREATMENT, NUMERICAL MODEL.....	47
Pavel fiala, Karel Bartusek, Michael Hanzelka	
NUMERICAL MODELING, SENSORS AND EXPERIMENTAL MODEL DEVELOPMENT FOR PARTIAL DISCHARGE LOCALIZATION IN HIGH VOLTAGE TRANSFORMERS	57
Petr Drexler, Pavel Fiala, Zoltan Szabo, Michael Hanzelka	
NUMERICAL MODEL OF A SOLAR ELEMENT WITH CONTROLLED EFFICIENCY	71
Pavel Fiala, Dusan Nesor, Michael Hanzelka	
STOCHASTIC NUMERICAL MODEL OF ELECTRODYNAMICS, TESTS.....	82
Pavel Fiala, Michael Hanzelka	
INCREASING THE RESISTANCE TO INTERNAL EXPLOSION OF THE STRUCTURE OF A BROWN COAL TRAY	92
Petr Horyl, Petr Jahn	
BALLISTIC RESISTANCE OF THE TRANSPORT AIRPLANE FUSELAGE TO IMPACT OF 9 MM ACTION 5 PISTOL BULLET	103
Juraj Hub ¹ , Jan Komenda ²	
MODEL OF RADIATION HEATING OF SLUSH MOULDING TECHNOLOGY	122
Martin Hušek	
MODAL ANALYSIS OF THE ROTOR SYSTEM.....	129
Tomáš Jamrůz, Karel Patočka, Vladimír Dániel, Tomáš Horáček	
ANALÝZA VRSTEVNATEJ DOSKY	138
Norbert Jendželovský	
A RSM Method for Nonlinear Analysis of Fire Resistance of Technology Support Structures in Accordance with Eurocode	147
Juraj Králik	

COMPARISON OF PROBABILISTIC METHODS TO ANALYSE PROBABILITY OF STRUCTURAL FAILURE USING ANSYS.....	162
Juraj Králik, Juraj Králik,jr.	
CFD ANALYSIS OF COOLANT HOMOGENIZATION IN NUCLEAR REACTOR VVER440.....	177
Emil Mojto ^A , Vladimír Kutiš ^A , Juraj Paulech ^A	
FEM ANALYSIS OF MEMS PIEZOELECTRIC PRESSURE SENSOR	184
Vladimír Kutiš ^a , Jaroslav Dzuba ^b , Juraj Paulech ^a , Viktor Královič ^A , Justín Murín ^a , Tibor Lalinský ^B	
AERODYNAMIC CHARACTERISTICS OF A DOUBLE SKIN FAÇADE	193
Milan Palko	
POSITION THE WINDOW IN THE WALL OF PASSIVE HOUSE	199
Milan Palko	
WATER VAPOR IN THE FUNCTIONAL GAP OF WINDOW	206
Milan Palko	
NUMERICKÝ MODEL TESTOVÁNÍ FIXACE SEGMENTÁLNÍHO DEFEKTU PRASEČÍHO FEMURU S 4,5 MM LCP Z CP-Ti GRADE 4	219
Jan Pěnčík ¹ , Lucie Urbanová ² , Robert Srnec ² , Petra Fedorová ² , Alois Nečas ²	
PARAMETRICKÁ STUDIE PRŮBĚHU RYCHLOSTI PROUDĚNÍ V PULTOVÉ DVOUPLÁŠŤOVÉ PROVĚTRÁVANÉ STŘEŠE NA VSTUPNÍ RYCHLOSTI.....	228
Tomáš Bartoš, Jan Pěnčík	
THE NON-LINEAR STATIC ANALYSIS OF THE TEXTILE BAG	234
Jiří Podešva, Zdeněk Poruba, Ondřej František	
MODELOVANIE KONTAKTU PILOTA – ZEMNÝ MASÍV.....	242
Prekop Ľubomír	
A STUDY OF THE CENTRIFUGAL COMPRESSOR DISCHARGE PIPELINE CONSTRAINED OSCILLATION	248
Kirill Solodyankin*, Jiří Běhal	
PARAMETRIZACE DYNAMICKÉHO ZATÍŽENÍ OBĚŽNÝCH KOL RADIÁLNÍCH KOMPRESORŮ	261
Oto Štěpaník*, Kirill Solodyankin, Jiří Běhal	
ANALYSIS OF 3-D LATTICE PLATE USING FEM.....	274
Martin Štiglic, Katarína Tvrdá	
A NEW SOFTWARE TOOL FOR PARALLEL COMPUTING WITH ANSYS	279
Jindřich Sušeň, Jaroslav Šindler, Matěj Sulitka	
VÝPOČET NÍZKOCYKLOVÉ ÚNAVY JADERNÉ ARMATURY DLE NORMY NTD A.S.I. SEKCE III.....	291
Jiří Táborský*, Lina Bryukhova	
COMPARATIVE ANALYSIS OF DIFFERENT APPROACHS TO MODEL TRABECULAR AND COMPACT BONE IN LONG BONES	300

Petr Vosynek, David Nečas, Tomáš Návrat

ANALÝZA SMYKOVÉHO PORUŠENÍ ŽELEZOBETONOVÉ STĚNY..... 309

Lubomír Jurášek¹, Petr Hradil¹, Petr Vymlátíl²

SPOJENÍ ANSYS CLASSIC S AUTODESK MOLDFLOW

MATĚJ BARTECKÝ

Continetal automotive systems s.r.o.

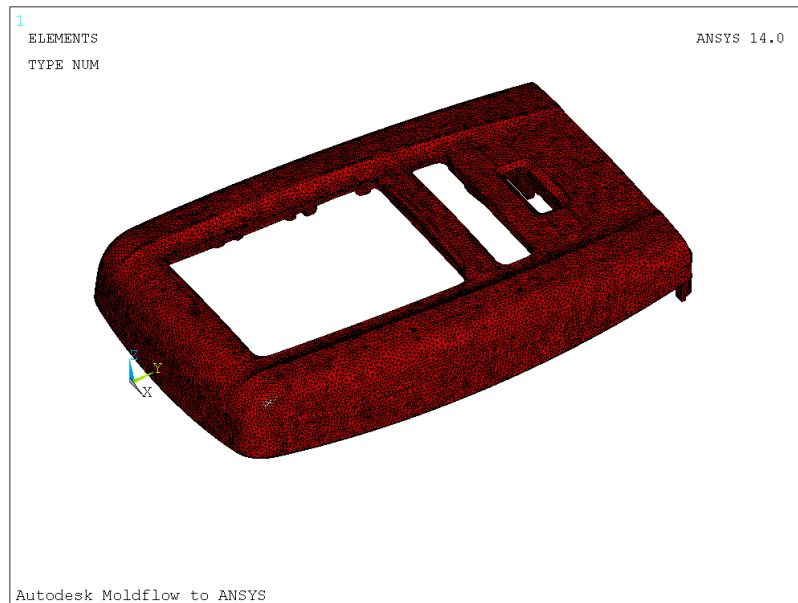
Abstract:

The paper solves base simulation of mechanical loading on exported data from numerical simulation of Moldflow. Inputs were finite element mesh include approximately 9 million decrease of freedom and 1,5 million definition of material parameters with residual stresses. The inputs were made by AUTODESK Moldflow.

Keywords: Ansys, autodesk moldflow, drop test,

1 Úvod

Jednou velkou nejistotou v oblasti kalkulací plastových dílců je vždy materiál. V mnoha případech se uvažuje isotropní elastický model, který mnohdy s realitou nemá nic společného. Za těchto a mnoha dalších důvodů je vhodné nejprve provést kalkulaci zatékání plastové hmoty ve formě a její následné chladnutí, která odhalí slabá místa jako jsou lunkry, studené spoje, orientaci a distribuci skelných vláken. Následně lze optimalizovat jak tvar součásti, tak i parametry vstřikovacího procesu, které značně ovlivňují mechanickou odolnost dílce. Níže blíže specifikovaný případ je celý založen na exportovaných datech z AUTODESK Moldflow. Kompletní model je diskretizován přibližně 1,5 milionem lineárních elementů s 6 stupni volnosti v každém uzlu s obecnou definicí materiálu pro každý z nich. Dále je použito přibližně 15 000 kontaktních elementů zajišťujících interakci mezi jednotlivým tělesy. Numerickým modelem je řešen případ nárazu na pevnou překážku popsanou skořepinovými prvky shell181.



Obrázek 1 – importovaná síť konečných prvků

2 Materiál metodika

Exportem z moldflow vzniknou soubory:

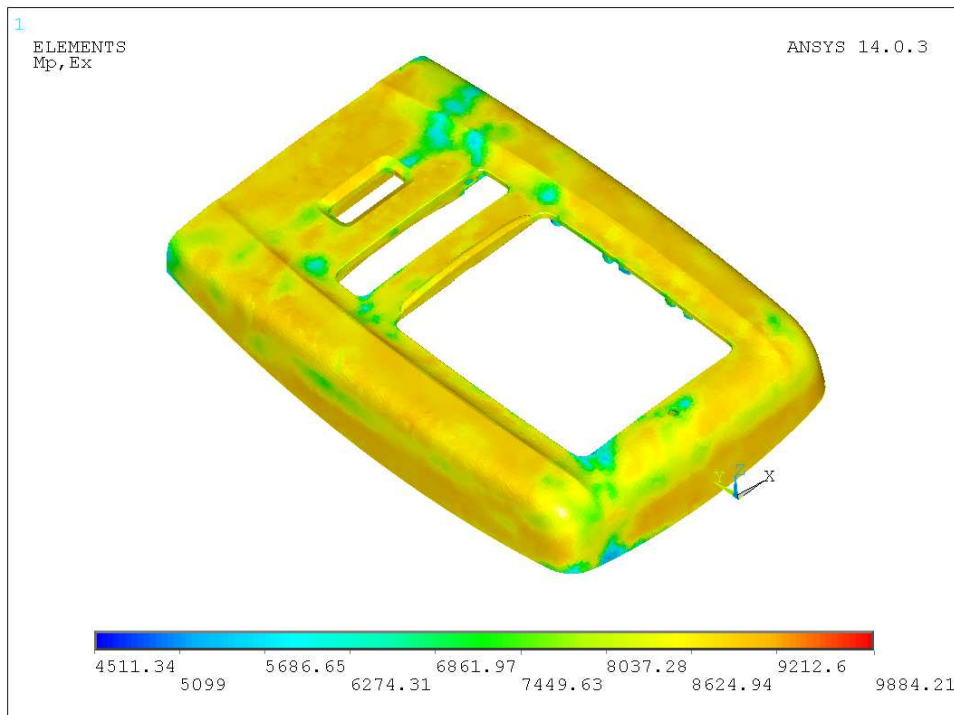
- .cdb
- .mts
- .ist
- .db

Input.cdb obsahuje informace:

- Pozice uzlů, elementů
- Typ použitých prvků
- Přiřazení materiálového čísla k elementům
- Přiřazení lokálních souřadných systémů elementům

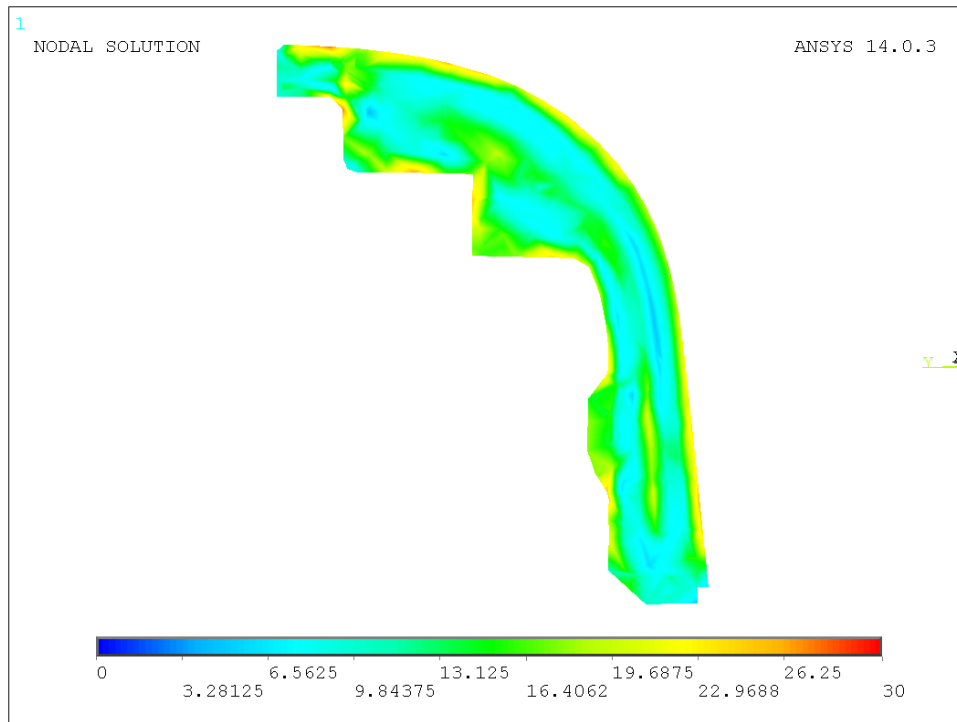
Zajímavý může být například dnes již nepodporovaný lineární element solid72, který má v uzlových bodech kromě standardních stupňů volnosti v posunutí také i rotace. Tento element se ale v průběhu načítání skriptu změní na standardní solid187 a následně jsou i přidány mezi-uzly. Nicméně po pár jednoduchých testech bylo zvaženo, zda-li je vůbec nutná tato změna. V případě dostatečného dělení je možno založit numerickou analýzu i na těchto lineárních elementech bez výrazné ztráty přesnosti. Ziskem je mnohem rychlejší běh výpočtu, naopak nevýhodou je chybějící dokumentace. Neméně důležité jsou lokální souřadné systémy elementů, které definují směry pro anisotropní materiálový model tedy počet materiálových modelů se musí rovnat počtu souřadných systémů.

Input.mts obsahuje informace o materiálu. V průběhu scriptu jsou načteny anisotropní parametry pro každý element sítě a stočeny dle příslušného lokálního souřadného systému.



Obrázek 2 – rozložení materiálových vlastností E_x

Input.ist následně přiřadí zbytková napětí do integračních bodů elementů a z nich jsou následně zkopírovány do uzlů.



Obrázek 3 – residuální napětí řez stěnou - HMH

Posledním krokem je výpočet, tím zapsání zbytkových napětí do databáze.

3 Výsledky

Tyto vstupní informace byly doplněny o další díly, které mohou výrazně ovlivnit výsledky analyzovaného dílce a celý model je záměrně natočen tak, aby zatížení bylo koncentrováno na nejslabší místo produktu. Pro druhý díly jsou nastaveny standardní podmínky a to lineární isotropní materiál, popsany solid185 elementy.

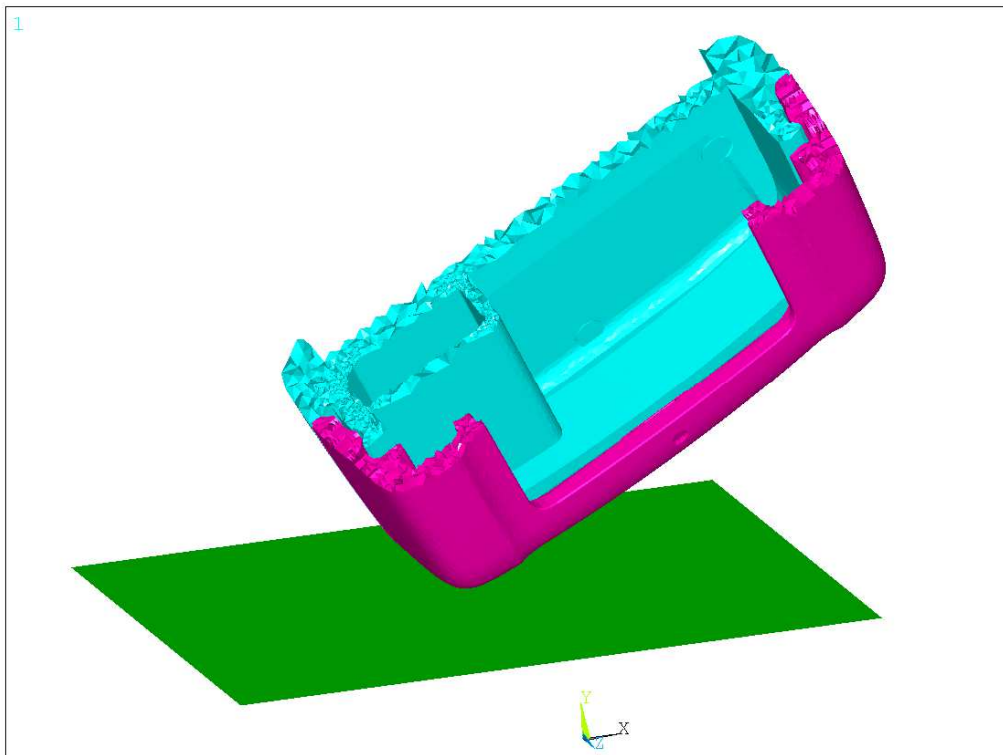
Kontakt mezi tělesy je proveden pomocí conta173 elementů využívajících pure penalty algoritmus s detekcí na gaussových bodech. Tuhost těchto kontaktů byla postupně zpřesňována na finální hodnotu penetrace 5e-3. Kde se již výrazně neměnily hodnoty napětí a kontaktních tlaků.

Oda dílce jsou ve své horní části drženy okrajovou podmínkou, která posouvá kompletní sestavu do nárazu na betonovou podlahu. Ta je uvažována jako dokonale tuhá a je diskretizována pomocí lineárních skořepinových elementů shell181 založených na mindlinově teorii. Konečné zatížení je zvoleno podle výpočtu podobného dílce zpracovaného již v minulosti v ANSYS explicit a potvrzeno jednoduchým analytickým výpočtem založeným na momentu hybnosti a impulzu síly.

$$m \cdot \Delta v = F \cdot t \quad (1)$$

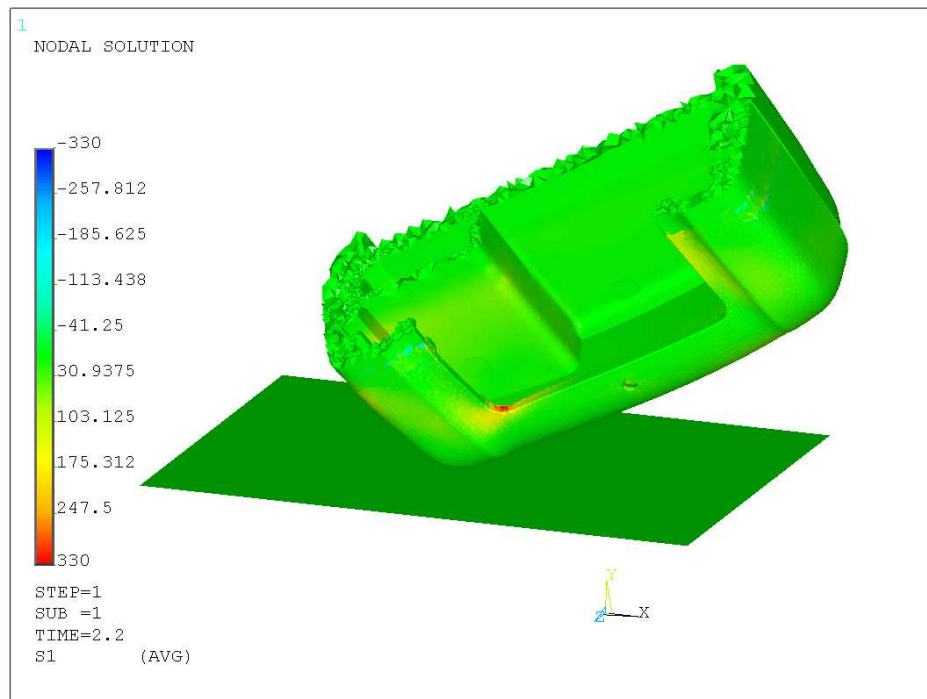
Pro výpočet byl použit distribuovaný přímý řešič SPARSE společně s Newton – raphsonovou iterační procedurou. Criteria pro iterační proces byla ponechána původní. Celé

řešení probíhalo na 14 jádrech a ve špičce potřebovalo okolo 53Gb RAM. Doba řešení jednoho substepu a záloven loadstepu byla přibližně 15min.

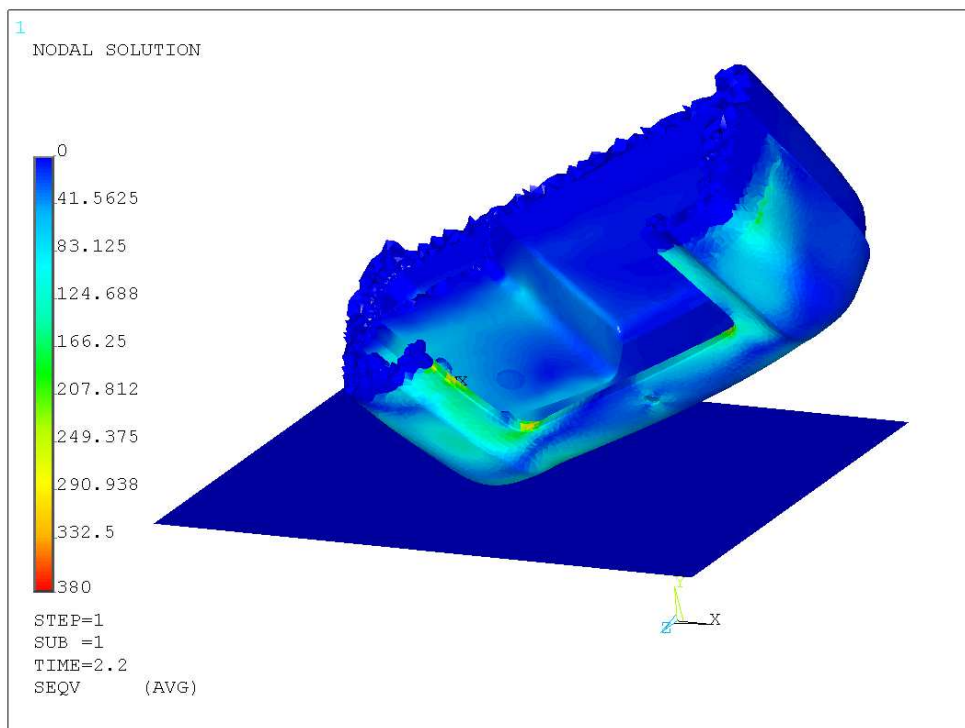


Obrázek 4 – model pro výpočet

Na analyzovaných dílcích je sledováno poměrně mnoho veličin zejména však velikosti složek napětí na kritickém místě silně nepříznivě ovlivněném výrobním procesem. Pro toto místo byly v laboratoři naměřeny hodnoty kritické při kterých dojde k porušení. Nejdůležitější z nich je deformační chování během nárazu, kde lze snadno pozorovat, které oblasti během testu došly do kontaktu a kde naopak k dotykům vůbec nedošlo, a tedy je nutné je dále optimalizovat.



Obrázek 5 – první hlavní napětí



Obrázek 6 – ekvivalentní napětí

4 Závěr

Značným ziskem tohoto spojení je velmi přesný materiálový popis produktu, který respektuje rozložení a směr skelných vláken spolu s uvažováním vměstků a studených spojů viz. Obrázek 2. Všechny tyto defekty jsou zahrnuty v konečných hodnotách modulů pružnosti a poissonových konstant v jednotlivých směrech. Během řešení tohoto případu se autor setkal s značnými potížemi, ohledně nemožnosti načíst spočtený výsledkový soubor, požadavek na velikost paměti RAM byl mnohonásobně vyšší než limit použité stanice HP Z820 s 128GB RAM. Z tohoto důvodu byly nastaveny podmínky výpočtu tak že loadstep = substep a při každém loadstepu byla vytvořena separátní databáze, která obsahovala ony výsledky.

Na základě výše uvedených dat bylo možné rozhodnout zda-li produkt vyhoví specifikaci s možností snadno a lehce model virtuálně modifikovat.

Poděkování

Zejména Ing. Laszlo Ivánovi, Ph.D a Doc. Petru Koňasovi, Ph.D z firmy SVSFEM s.r.o. za podporu při práci na tomto projektu.

Literatura:

ANSYS release 14 documentation

Kontakt:

Kopanská 1713;74401;Frenštát pod Radhoštěm

CRACK GROWTH SIMULATION IN THE COURSE OF INDUSTRIAL EQUIPMENT LIFE EXTENSION

JIŘÍ BĚHAL, KIRILL SOLODYANKIN
ČKD Kompresory, a.s., Klečákova 347, Prague, Czech Republic

Abstract: Fatigue crack growth is simulated. For general 3-D object, a stress intensity factor for given crack-tip position is determined by a finite element method in the ANSYS system. Calculated parameters for samples of simple geometry are compared to published empirical values. After appropriate methodology development, a fatigue life of reciprocate compressor could be extended.

Keywords: Finite Element Method, Stress Intensity Factor, J-integral, Fatigue Crack Growth, Damage Tolerance Approach, Operation Mechanical Reliability

1 Introduction

Mechanical structures had been used to design as “safe life” in the history. It means that during operation period there is no danger of fatigue cracking of structural parts. However, it leads to termination of a machine operation relatively early because of an uncertainty of crack initiation.

Advanced concepts, such as a damage tolerance approach, took place in modern design. A common feature of these efforts is to allow fatigue degradation as an inherent feature of material, but it shall be detected till the critical configuration is reached. It is obvious that a crack growth period should be known very well for a reliability demonstration. The crack growth rate is described for a lot of standard objects, such as plates or rods. For general 3-D objects, the critical point as well as crack growth itself may be investigated experimentally or by a finite element method (FEM).

A specific task is to extend a service life of an old design structure by scheduling of periodical inspections (NDT - nondestructive testing). It allows operating the specific structure further using its real value. The final life may be usually a multiple of the original one. However, costs for inspections or health monitoring should not exceed economical benefits.

A failure of operated reciprocating compressor occurred after 40 years of full service. Others compressors, Fig. 1, also exceeding design life, were shut-down immediately till safety operation is proven. A question of a life extension had been raised as there is no replacement for multiple machines in technology available immediately.



Fig. 1 – Reciprocating compressors operated in chemical industry facility

2 Fracture Mechanics

For simulation of fatigue crack growth, Fig. 2, following knowledge is demanded:

data	source
load cycle / load sequence	operation / design
stress intensity factor on the crack tip	analytical / FEM simulation
fatigue crack growth curve (C , m , K_{th} , K_{IC})	experiment / reference

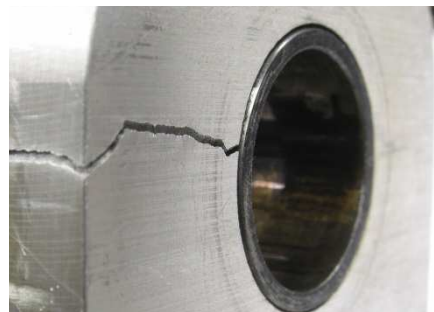


Fig. 2 - Example of fatigue crack in cyclically loaded lug, bushing is still in place

According to the theory of a linear fracture mechanics, a stress intensity factor (K) on the crack tip can be expressed by nominal load (σ) and a crack length (a):

$$K = \sigma \cdot \sqrt{\pi \cdot a} \left[\text{MPa} \cdot \text{m}^{0.5} \right]. \quad (1)$$

The finite dimension of the object and cross-section shape is introduced by a corrective function (Y):

$$K = \sigma \cdot \sqrt{\pi \cdot a} \cdot Y. \quad (2)$$

For standard geometries, the Y functions are published. For direct calculation of K values, especially in general objects, several local approaches have been developed, e.g. so called J-integral or the energy release rate (G). The J-integral is based on a closed loop independent of the path. Thus the

singular point on a sharp crack tip can be excluded and a numerical solution is very suitable for FEM implementation. The J-integral value correlates with K value, e.g. for plane strain:

$$J = \frac{1}{E} \cdot \left[(1-\nu^2) \cdot (K_I^2 + K_{II}^2) + (1+\nu) \cdot K_{III}^2 \right], \quad (3)$$

where E and ν are material constants and I to III refer to fracture modes, Fig. 3.

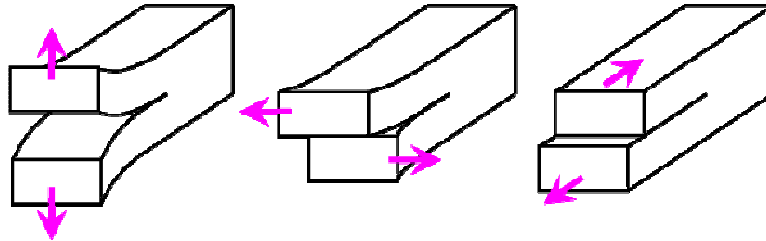


Fig. 3 – Unified modes of crack loading results in specific direction of crack propagation

3 Numerical Simulation

When K value along the crack tip is known, crack growth rate can be calculated based on material characteristics. There is no necessity to consider a crack length itself or shape of tip front anymore. Each $\Delta\sigma$ load cycle produces ΔK on a crack tip. It is used to consider a load sequence, cycle asymmetry etc. If simple Paris' law is supposed:

$$\frac{da}{dN} = C(\Delta K)^n, \quad (4)$$

a simple linear curve in log-log transformation is obtained, Fig. 4. For small cracks, the situation is more complex and it is hard to predict crack behaviour. Fortunately, this region is usually related to undetectable crack sizes and it is not necessary to study it for the purpose of an inspection interval definition. On the other hand, the growth rate curve is more progressive close to a failure. The crack growth rate is usually relatively fast here and it means a short time-period of the investigated interval. For the purpose of this study, the curve is approximated by Paris' law in a whole range with respect to the K_{IC} critical value. This K_{IC} value is usually available from material proof testing.

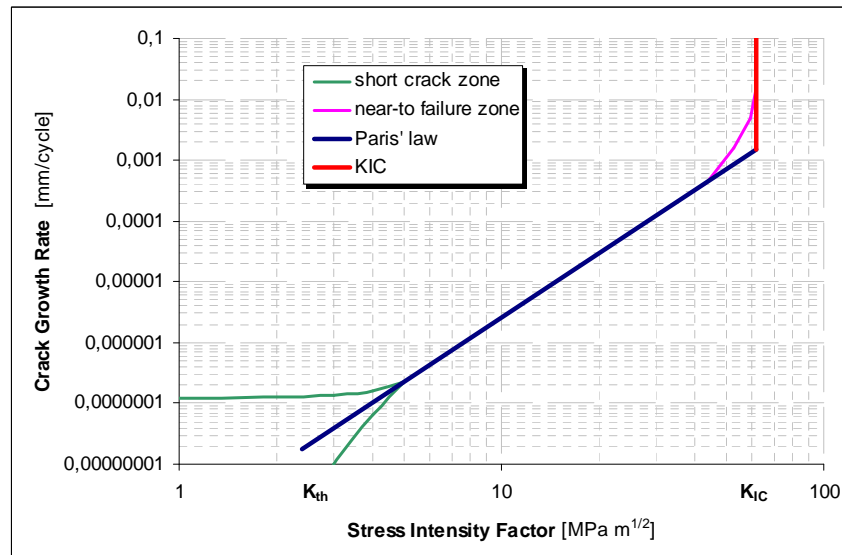


Fig. 4 – Crack Growth Curve

More complex formulas have been developed for experimental data regression, such as modified Forman equation [1]:

$$\frac{da}{dN} = \frac{C(\Delta K)^n \cdot (\Delta K - \Delta K_{th})^p}{((1-R) \cdot K_{cf} - \Delta K)^q} \quad (5)$$

The crack growth rate for a single cycle is very small. It is useful to evaluate increases in a block of cycles for given ΔK value, or consider a simplified increasing of the rate with increased crack size (an equivalent crack size should be estimated here).

If a crack shape and sizes are available e.g. coming from already failed structure, considering any detail information about "milestones", in the means of both crack size and shape, significantly improves result of simulation. Calculated crack parameters can be corrected when a known parameter value is reached improving confidence level.

4 ANSYS Contribution

4.1 Fracture Mechanic Parameters

Assessment of the K value for given crack tip position is much more complicated because of mixing physical models of material and mathematical behaviour of elements. A special "crack" element type, popular in the history, has been replaced by J-integral calculation over regular elements. A potential of X-FEM approach, where general mesh is cut by crack surface and supplemental virtual nodes are generated allowing a crack opening under load application, is also interesting.

In the ANSYS system, there are 3 ways to calculate the K values implemented today:

method	physics	switch of CINT command
K	stress intensity factor	SIFS - K1, K2 or K3
J	J-integral	JINT
G	energy release rate	VCCT

The ANSYS official examples are freely available, see [2] or [3].

The J-integral value can be calculated via ANSYS for each node on selected crack-tip. The linear analysis of a loaded object is required for input of stress distribution around a crack tip. The J-integral value can be easily calculated based on stress-strain distribution in the crack-tip region, see Fig. 5:

$$J = \int_{\Gamma} \frac{dU}{dV} dy + \left(T_x \frac{\partial u}{\partial x} + T_y \frac{\partial v}{\partial x} + T_z \frac{\partial w}{\partial x} \right) ds, \quad (6)$$

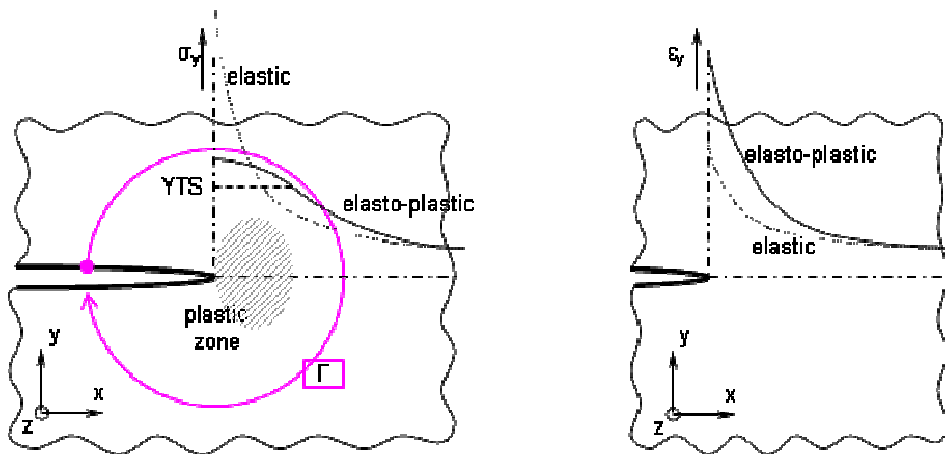


Fig. 5 – Stress and strain field on the crack tip and integration path of “J” method

4.2 Static Analysis

A fatigue crack initiation is expected in the high tension areas for common industrial structures under cyclic loading. Investigation of these areas as well as static analysis of the object is a routine application of strength modules of FEM systems and it is not discussed here.

4.3 Methodology Development on Samples

A flat tension samples with central or edge crack were simulated. An empirical calculation using corrective function, partially validated by experiments, has been considered as a reference. A multi-parameter study was performed in the means of:

- circle pattern diameter (related to plastic zone size)
- circle pattern division
- outside element type (hexa- vs. tetrahedron)
- outside element size

A well-known circular pattern [5], Fig. 6, has been kept. The results were analysed externally in spread-sheet, Fig. 7.

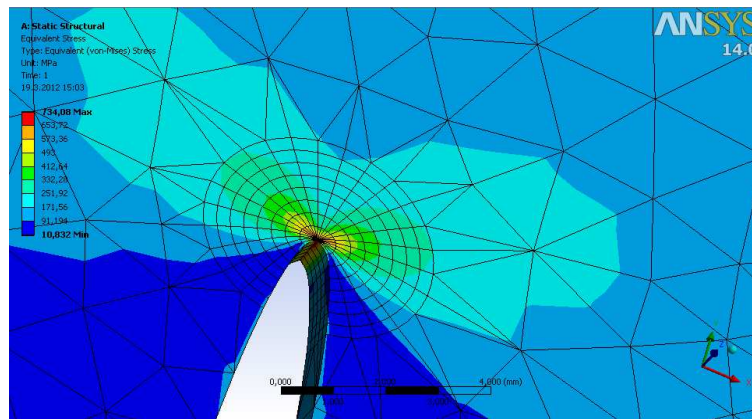


Fig. 6 – Investigation of stress map in the crack tip region

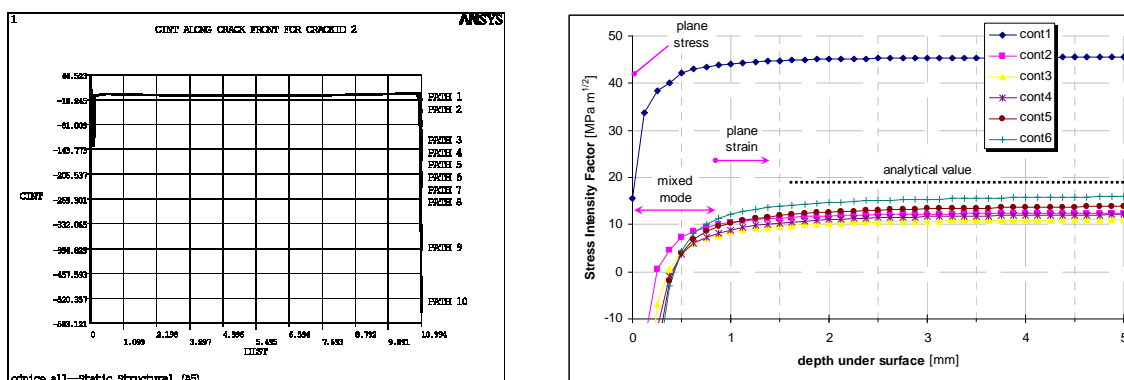


Fig. 7 – Stress Intensity Factor value investigated along the crack-tip

```

cint,new,1
cint,ctnc,Selection
cint,type,jint
cint,normal,12,1
cint,ncon,12

cint,new,2
cint,ctnc,Selection
cint,type,sifs
cint,normal,12,1
cint,ncon,12

outr,cint,all
csys,12
nlist,Selection,,,Coord,,,

```

Fig. 8 –Commands for calculation of „J“ and „K“ methods, result output and identification

4.4 Evaluation

The "K" method is apparently the most flexible because of direct evaluation of each fracture mode separately. Unfortunately, results calculated by ANSYS are not easy to interpret because of strong dependence on a contour order. Although some trends of correlation between FEM and empirical solutions are obvious, an appropriate data correction in general application is not revealed.

The "J" method calculation seems to be much more robust as expected. Even the first contour misses the desired value completely, every other fits very well. Out of structured mesh with circular pattern (when path order exceeds a pattern division), a divergence appears. The calculated results are almost independent of mesh pattern diameter and number of divisions as well as of the type and size of elements outside.

The values calculated on samples were compared with analytical solution, see Fig. 9 and Fig. 10. When a contour order exceeds circular pattern of the mesh, the result seems to be chaotic. A result of "K" method strongly depends on contour order, or element size respectively. Superior stability of the "J" method is obvious. In some cases, the "J" method

provided acceptable values even on tetrahedrons, e.g. Fig. 10. The “G” method behaviour has not been evaluated.

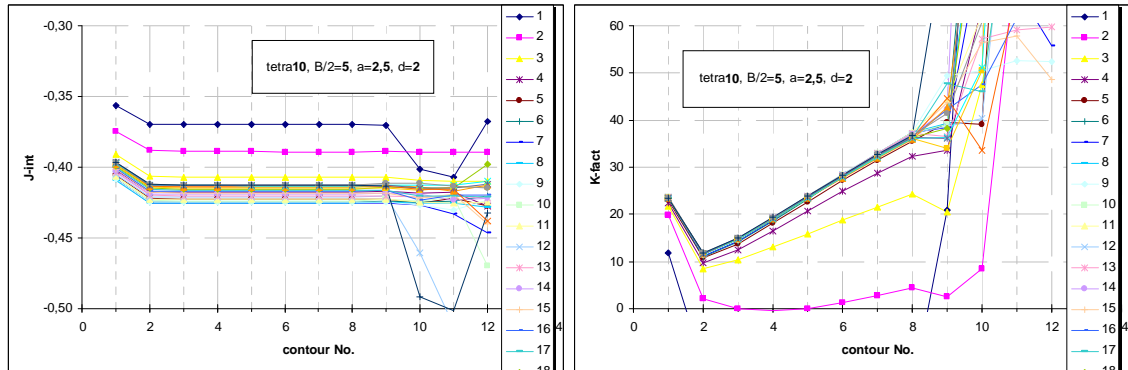


Fig. 9 - Fracture mechanic parameters calculated for small crack growth rate

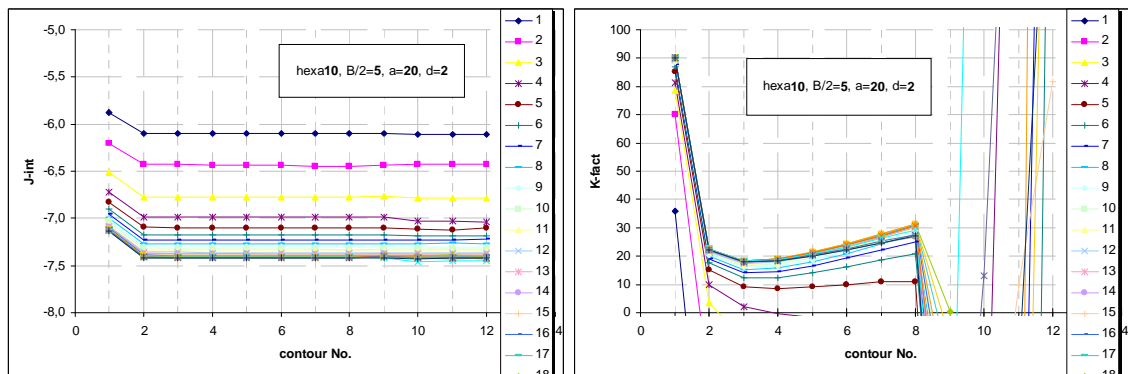


Fig. 10 – Fracture mechanic parameters calculated for large crack growth rate

5 Application

A fatigue crack in a lug of connection rod was identified as the cause of in-service failure. The crack origin is situated on an inner surface and it grows through one side of the lug and nearly a half of opposite one. Because of time pressure, a brief estimation of crack growth period had been done with a standard solution of cracking lug using empirical formulas [6]. The object was simplified to the 2-D body and crack symmetry in the means of critical cross-section was supposed. Almost eight thousand service hours were calculated for the time period between a detectable crack size and the critical one. However, a large safety factor shall be used because of rough simplification of the geometrical situation and a stress map.

A FEM simulation of crack growth in 3-D object was performed consequently, Fig. 11, for the purpose of a reduction of safety factor value. Even the estimated crack-growth period slightly decreases, Fig. 12, the period of NDT inspections was set to acceptable couple of months after a confidence level improvement.

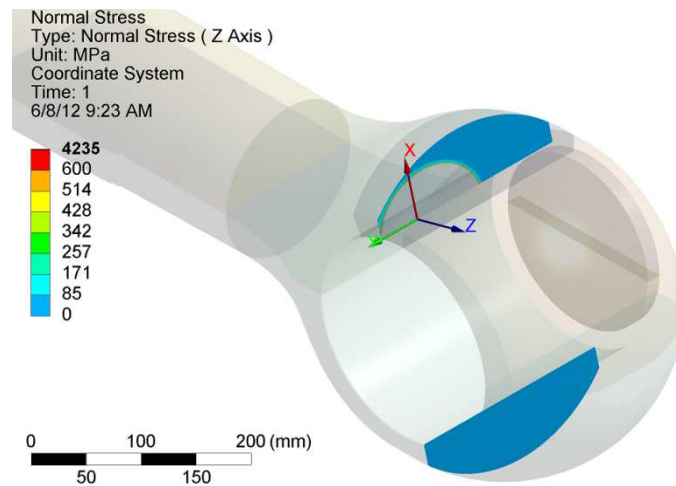


Fig. 11 – Fatigue crack propagating through a lug of connection rod

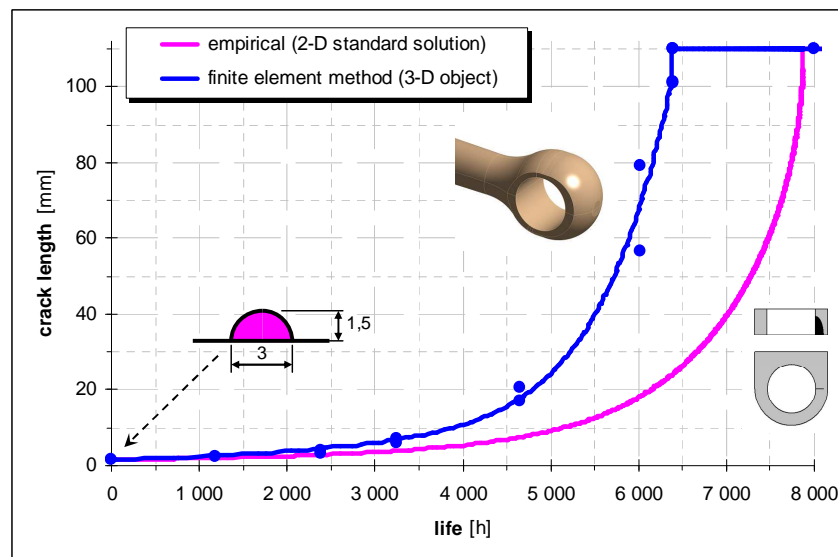


Fig. 12 – Simulated crack growth curves

6 Discussion

6.1 Experience

In the course of damage tolerance approach, a FEM application provides us with answers to 2 fundamental questions:

- critical area location;
- stress intensity factor value along given crack tip.

The ANSYS system seems to be a very strong tool for solution of traditional as well as emerging tasks. Basic functions for crack growth simulations are already available in an actual Release (r13 or r14 respectively). However, the calculated results should be interpreted carefully as a large and systematic error may be produced.

The WorkBench shell is easy to use for simple operations. The meshing of at least topologically recognised shapes is impressive. However, the traditional tools such a node merging control (both joining and doubling) are not available anymore. Large automation of routine steps leads to reduction of flexibility in special tasks. A lot of time has been spent by "how to define" steps instead of reasonable "how to calculate" here.

For the CIF command, the crack-plane normal or at least a direction of crack propagation shall be defined. Definition of a crack-plane normal can be difficult in the case of a general 3D shape, however it is task of geometry modelling. A crack propagation direction cannot be supposed a-priory, as it depends on mixing of load modes. Unfortunately, the "J" method doesn't distinguish propagation direction. For direction estimation in general application, a direction should be investigated via "K" or "G" methods.

6.2 Future Development

Basic tools, such as several methods of fracture mechanics parameters on crack tip, are available now. For future improvement of a methodology, implemented physics should be extended in the means of:

- shear mode near to object surface (plain stress vs. plain strain)
- all 3 fracture modes calculated together (3-D propagation)
- cycle-by-cycle sequence internal processing (load sequence or randomised spectrum)
- crack growth rate curve of general shape including small crack region deviations (real dimension of the body)
- availability of another criteria for fracture mechanics study or an experimental validation, e.g. a crack tip opening displacement

Discarding of special crack element allows mass usage of crack growth simulations. However, when a circle pattern on crack tip, see KSCON and KCALC commands in [7], should be defined in every case, some kind of automated tool or mesh-processor function seems to be appropriate for general 3D object especially in popular WorkBench shell. The commands of K values calculation should be supplemented by user defined quantities in an open library allowing a crack increment calculation using advanced material characteristics and physical models.

7 Conclusion

The ANSYS system simulation has been tested on known samples. Fracture mechanic parameters calculated by some methods correlate with expected values based on empirical solution very well. The crack growth itself was simulated in an external spread sheet processor because of data processing and post-processing flexibility.

Developed methodology has been applied on a structural item of a real machine consequently. A linear model of material is sufficient in presented approaches. A multibody part, their assembly, free contact between them even an overlap, Fig. 13, can be simulated and calculated using ANSYS in the course of crack growth rate investigation.

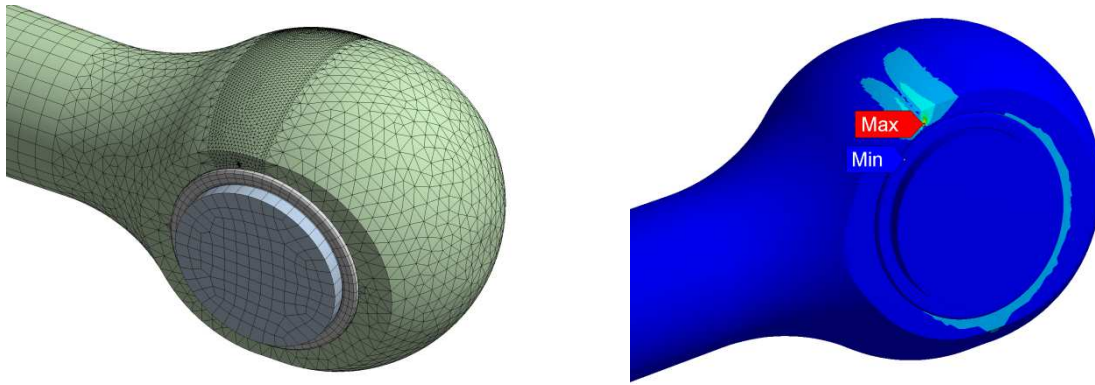


Fig. 13 – Assembly of multibody parts including contacts, both free and overlap

Acknowledgement

This study has been supported by the Ministry of Industry and Trade, Czech Republic, project No. FR-TI2/206.

The ANSYS implementation of fracture mechanics and cracked body definition was consulted on SVS-FEM hot-line.

References

- [1] Kunz, J.: Základy lomové mechaniky, ČVUT 2000
- [2] Imaoka, S.: Penny3D, example published for ANSYS Workbench 12.0, available at "<http://ansys.net/input/penny3d.zip>"
- [3] Imaoka, S.: VM256, example published for ANSYS Workbench 12.0, available at "<http://ansys.net/input/vm256.zip>"
- [4] ANSYS Help, Structural Analysis Guide, chap.11 - Fracture Mechanics
- [5] Bist, S., Kannusamy, R.: Predicting 3-D Fatigue Cracks without a Crystal Ball. ANSYS Advantage Vol.III, Iss.1, 2009
- [6] Brooks, C., Honeycutt, K., Domasky, S.P.: Implementing Models and Libraries. Report No.AFRL-VA-WP-TR-2006-3043, AP/ES Inc., 2006
- [7] Fatigue Crack Propagation Analysis in ANSYS. CAE Associates 2011

STRESS ANALYSIS OF VALVES FOR NUCLEAR POWER PLANTS

LINA BRYUKHOVA*, JIŘÍ TÁBORSKÝ

KRÁLOVOPOLSKÁ STRESS ANALYSIS GROUP, s.r.o.

Abstract: Valves are very important pieces of equipment on nuclear power plants. Their detailed stress and tightness analyses have to be carried out for the valve manufacturer to

be granted a permission to install valves on power plants. The article describes the procedure of stress and tightness analyses performed using ANSYS Workbench v.14.0.

Keywords: valve, gasket pressure, fatigue assessment

5 Introduction

As piping valves are widely used to control all thermal processes on nuclear power plants, they are very important and accountable pieces of nuclear power plants equipment. Valve failure may lead to the nuclear power plant or its systems shutdown, that is why valves' reliability contributes significantly to the reliability of the whole plant. The valves have to fulfill major requirements to their strength, tightness, failure-free performance and service lifetime.

6 Valve description

Check valves normally allow medium to flow only in one direction. A lift-check valve is a check valve in which the disc, sometimes called a lift, can be lifted up off its seat by higher pressure of inlet or upstream fluid to allow flow to the outlet or downstream side. A guide keeps motion of the disc on a vertical line, so the valve can later reseat properly. When the pressure is no longer higher, gravity or higher downstream pressure will cause the disc to lower onto its seat, shutting the valve to stop reverse flow. All horizontal check valves for nuclear application are welded to the piping, while vertical check valves are connected to piping by flange joints.

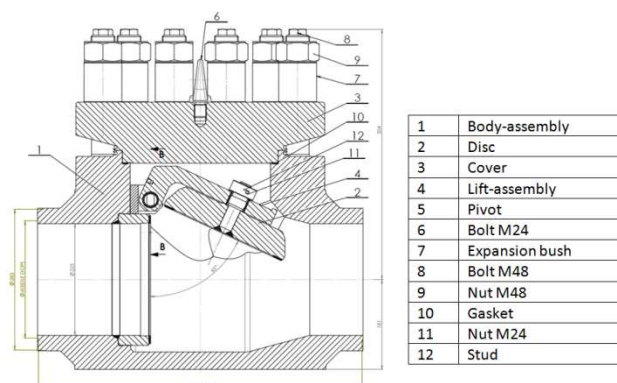


Image 2 - Analyzed check valve

For the valves to be used in nuclear power plants their strength, tightness and lifetimes assessment have to be done according to relevant standards and corresponding reports supporting the results have to be presented. Hence, it was necessary to elaborate reports clearly demonstrating strength reliability of the valve elements (body, cover, bolts, etc.), tightness of the body-cover flange joint at all operating regimes and sufficient lifetime including all the operating, test and emergency conditions in the numbers required. Detailed requirements towards valves are given in the Technical conditions [[1]. In order to meet these requirements the calculations were carried out according to NTD A.S.I. Section III [[2] standard using ANSYS Workbench v.14.0 software.

This article gives a description of the check valve analysis shown in the [3]. Body and cover material is austenitic stainless steel, bolts are of low-alloyed steel. The body-cover flange joint is sealed by a spiral wound gasket.

7 The procedure of analysis

Firstly, the initial *.iges model was adopted in ANSYS Design Modeller in such a way that small, unnecessary and otherwise not influencing results elements were either deleted or simplified.

Next, materials characteristics were input in Engineering data. It is worth noting that ANSYS Workbench v.14.0 does not support transient-thermal analysis with gasket characteristics data input through Engineering data. In order to overcome this, measured gasket compression curve and unloading curves were input through Commands in Mechanical Simulation, which is quite an inconvenience since doing so demands certain knowledge of commands which is often not mastered by users acquainted with ANSYS Workbench only and unfamiliar with ANSYS APDL. The process of gasket characteristics data input is shown in the Image 3.

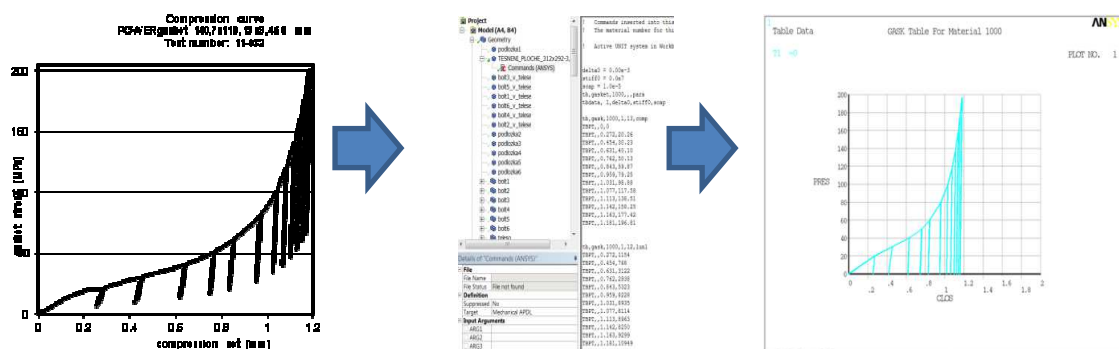


Image 3 - Gasket characteristics input

The model was then meshed as shown in the Image 4.

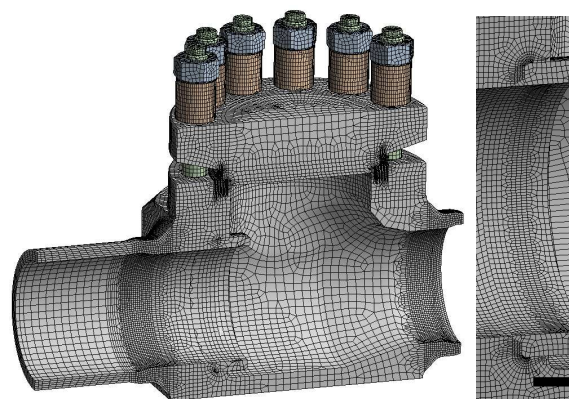


Image 4 - Meshed valve model

The thermal transient analysis was carried out to determine thermal fields distribution during thermal shocks. Medium flowing rates were taken from the Technical Conditions [[1]. Based on these rates heat transfer coefficients were determined as according to [[3]. Having input heat transfer coefficients and temperatures of flowing medium, non-uniform thermal fields distributions were determined. The distributions were non-uniform both along the body of the valve and through its thickness. The resultant thermal fields distributions are shown in the Image 6.

The boundary conditions and loads were applied as shown in the Image 5. The forces and moments on the nozzles were taken from the Technical Conditions [[1] based on the nominal diameter of the valve, pressure in the valve body and material of connected piping. It was necessary to determine such tightening forces that from one side the flange joint would be tight and from another side bolts could still bear applied forced. To do this, an iterative approach had to be used.

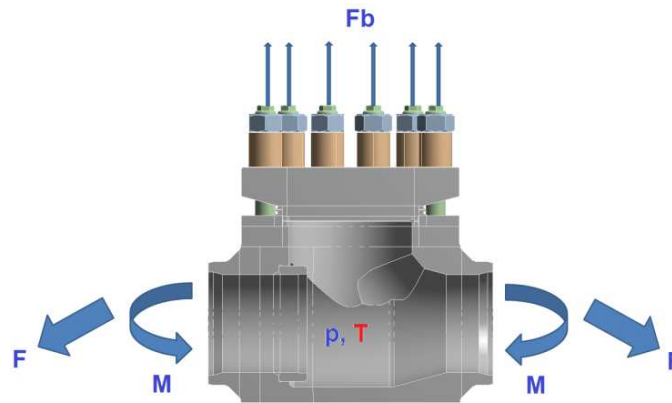


Image 5 - The loads applied to the valve model

Nonlinear contacts between the cover, the gasket and the body were considered. Contacts stiffness had to be chosen carefully since too low a stiffness allowing for better convergence influenced gasket pressure results significantly. Though more desired, higher contact stiffness on the other hand caused worse convergence.

8 Results assessment

Temperature fields distribution is shown in the Image 6.

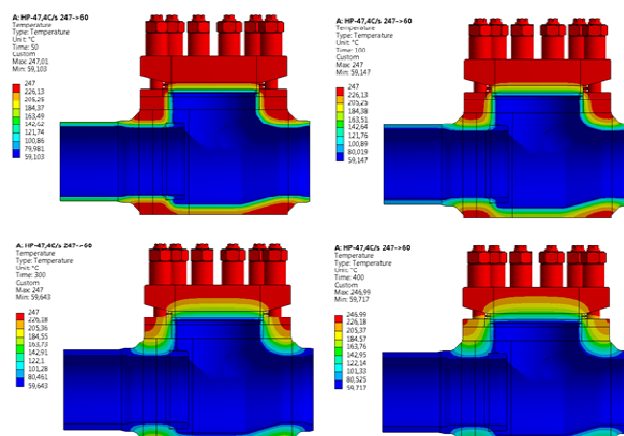


Image 6 - Thermal fields distribution during the thermal shock at emergency conditions

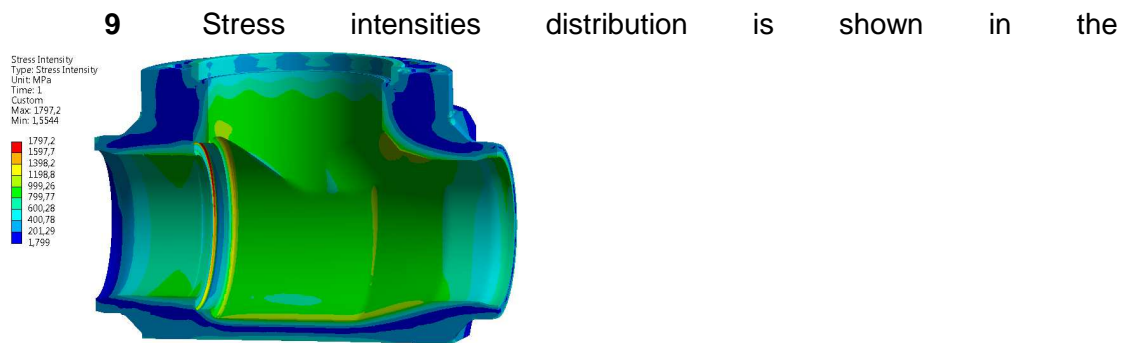


Image 7. The results for the model as shown in the Image 5 showed that even with maximum tightening forces that bolts could still bear the body-cover flange joint would not be tight. This happened due to “opening” of the flange joint under non-uniform thermal fields. During the thermal shock the body and the cover deform in such a way that the gasket ceases to be compressed along its internal diameter and is compressed only slightly along its external diameter. Thus, required minimum gasket pressure is not achieved. Since gasket elements were used in the calculation, direct output of values of gasket pressure was possible for these elements. Application of heavy duty disc springs proved to help in this case.

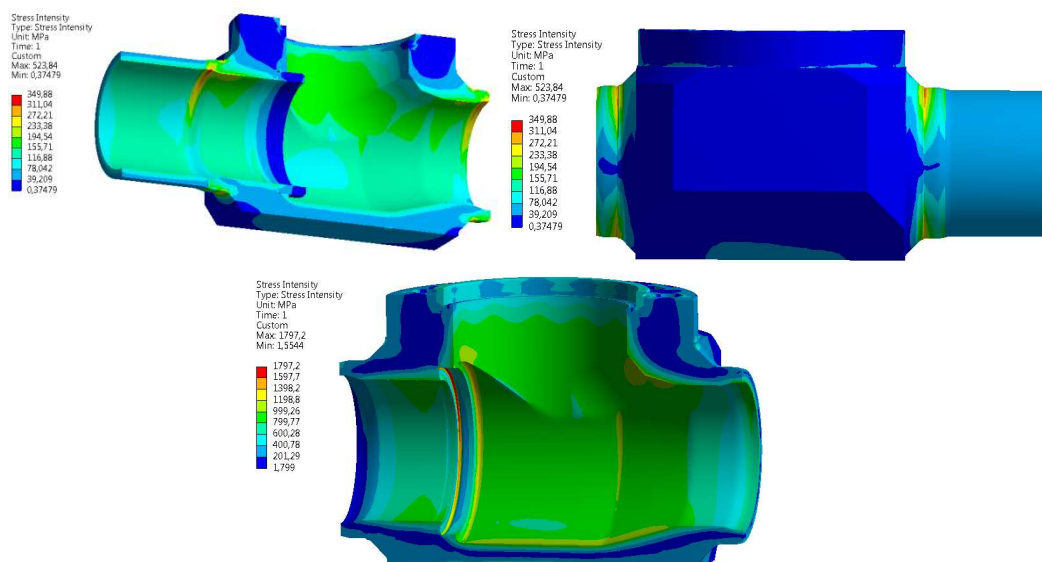
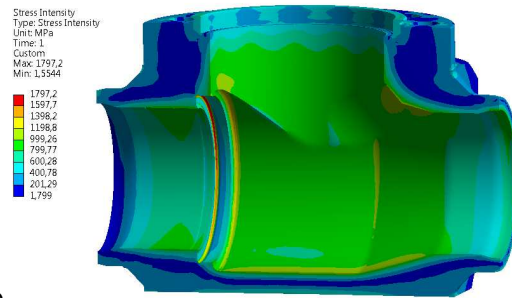


Image 7 - Stress intensities distribution in the valve body

10 Stresses in the valve were assessed by stress categorization method according to NTD A.S.I. Section III [[2]] and fatigue assessment was carried out. Low-cycle fatigue assessment was done according to [[2]]. The results of fatigue

assessment showed that too high an accumulation is in the groove under the saddle



as is seen in the

Image 7. It was not only the non-uniform field distribution through the thickness of the body that caused these stresses, but the presence of shape discontinuity in a form of the groove contributed to the high stresses significantly. Such high stresses in calculation considering only elastic behavior of material were not acceptable.

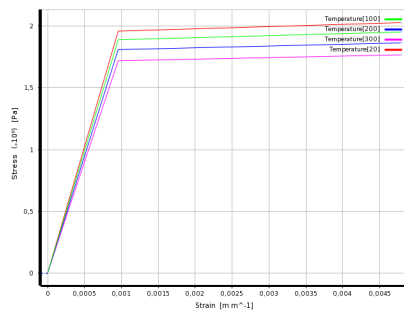
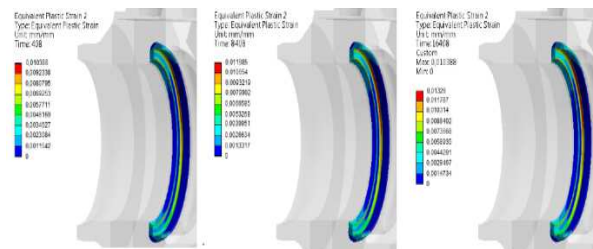


Image 8 - Bilinear material characteristics with hardening

Using elastic model of material behaviour from the one hand decreases time of the calculation, but on the other hand has proved to be too conservative and unacceptable. NTD A.S.I. Section III, chapter 8.5.6 allows for application of elastic-plastic behavior of material in the calculation. Hence, more precise calculation accounting for elastic-plastic behavior of material was used. Material characteristics considered in the calculation are shown in the Image 9. The values of equivalent plastic strain are shown in the Image 9. The highest contribution towards accumulation of the plastic strain was in the first load cycle, further load cycles contributed to that accumulation less significantly. Ideally all load cycles should have been calculated. But since the calculation using elastic-plastic behaviour of material is highly time demanding, it was decided that 3 cycles were sufficient to describe the nature of plastic strain accumulation.



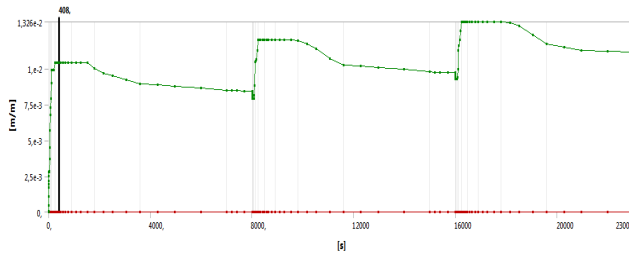


Image 9 - Equivalent plastic strain during 3 steps of analysis

11 Modifications adopted

Certain changes had to be adopted since required gasket pressure could not be achieved. Disc springs help significantly in preserving tightening forces in the bolts and sufficient gasket pressure during thermal shocks. Thickness of disc springs, their number and combination (parallel or in series) was chosen so that sufficient gasket pressure would still be present during thermal shocks. Location of the disc springs is shown in the Image 10. The disc springs were substituted by springs in the analysis with longitudinal stiffness of the disc spring shown in the Image 11. It is generally advised that disc springs are used in the area of linear stiffness behavior which corresponds to a half of maximum flattening value.

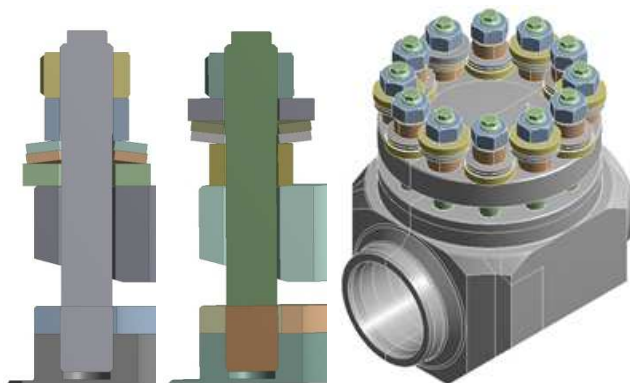


Image 10 - Disc springs location

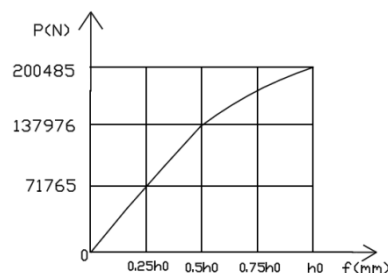


Image 11 - Axial stiffness characteristics of a disc spring

12 Conclusion

The procedure described above allows to design valves meeting the requirements to the valves for nuclear power plants. Design of the valves can be improved and modified based on the results of the calculations in such a way that the valve is satisfactory from

stress and strain state point of view. Tightening forces can be chosen based on the results of the gasket pressure achieved during the calculation. Although less demanding in time, purely elastic behaviour of material may turn out to be too conservative and more detailed and at the same time demanding elastic-plastic behaviour of material is to be considered.

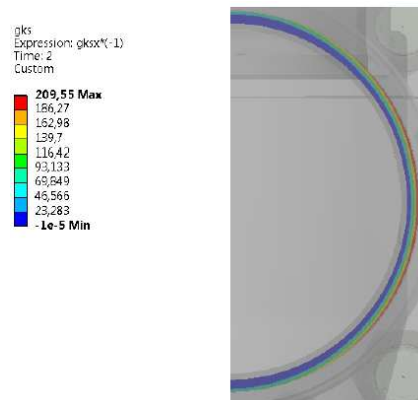


Image 11 - Gasket pressure distribution after adopted modifications to the design

References

- [1] FEDERÁLNÍ SLUŽBA PRO EKOLOGICKÝ, TECHNOLOGICKÝ A JADERNÝ DOZOR, 2005. *Potrubní armatury pro jaderné elektrárny. Všeobecné technické podmínky*. Moskva:92 p.
- [2] ASOCIACE STROJNÍCH INŽENÝRŮ, 2007. *Normativně technická dokumentace A.S.I. Hodnocení pevnosti zařízení a potrubí jaderných elektráren typu VVER Sekce III*. Praha, Brno: 169 p.
- [3] ENEKL V., HLOUŠEK J., 1983. *Thermomechanics*. Brno.

Contact address:
Ing. Lina Bryukhova
KRÁLOVOPOLSKÁ STRESS ANALYSIS GROUP, s.r.o.
Okružní 19a, 638 00 Brno

ELECTROHYDRODYNAMICS AND RELATIVISTIC THEORY IN ACCURATE NUMERICAL MODELING

PAVEL FIALA

Brno university of technology, Faculty of electrical engineering and communication,
Department of theoretical and experimental electrical engineering, Czech Republic

Abstract: The author investigates the problem of utilizing a magnetic field coupled model and analyzes conductive area motion in a magnetic field. The analysis shows that, for exact evaluation of the influence of all effects, it is necessary to consider the phenomena related to the movement of one system relatively to the other. It is shown that related distinctive effects affect the resultant electromagnetic field distribution from the relative velocity of $v_0 = 1 \text{ m} \cdot \text{s}^{-1}$. This paper examines the problem of utilisation of the coupled magnetic field model and the subject of the conductive/dielectric area motion in a magnetic field. The model is dealt with *per partes*: The first aspect solved is a stationary model of a magnetic field, the following aspect consists in a quasi-stationary model for the assumed motion of elements of the task, and the last part constitutes a model respecting the relativistic principle in electromagnetic field modelling Stratton J.A., 1985.

Keywords: numerical model, accuracy, relative, moving object, moving system, magnetic field, electromagnetic field, wave propagation.

1 Introduction

From the first moments of its application Maxwell J.C., 1873, Dědek L., Dědková J., 2000, Stratton J.A., 1985, Haňka L., 1971, electromagnetic theory has included the static, quasi-static and non-stationary parts of description of the electromagnetic field, in addition to electrodynamics and relativistics. Sources describing the theoretical part of applied electrodynamics and relativistics are exemplified by Stratton J.A., 1985, Haňka L., 1971, Kikuchi H., 2001.

At present, the modeling and simulation of technical systems constitutes a substantial part of the entire network of modeled problems. Among the currently modeled tasks there are various problems related to fields with the fastest pace of both the development and the application of modeling, namely to energetics, mechanical engineering, metallurgy, electrical engineering, space and nuclear technologies Kuneš J., Vavroch O., Franta O., 1989, Ansys, 1994-2012. This paper examines the problem of utilization of the coupled hybrid magnetic field model and the subject of conductive area motion in a magnetic field. The model is dealt with *per partes*: the first aspect solved is a stationary model of a magnetic field, the following aspect consists in a quasi-stationary model for the assumed motion of elements of the problem, and the last part constitutes a model respecting the relativistic principle in electromagnetic field modeling Stratton J.A., 1985. Let us consider an example of conductor movement in a stationary or non-stationary magnetic field. This appears to be a trivial

problem with a straightforward solution; however, for an exact evaluation of the influence of all effects, the phenomena related to the movement of one system relatively to the other must not be neglected. As shown in Haňka L., 1971, this distinctive effect affects the resultant electromagnetic field distribution from the relative velocity of $\mathbf{v}_0 = 1 \text{ m}\cdot\text{s}^{-1}$.

2 Description of the Model

The physical model is based on the solution of the reduced Maxwell equations Stratton J.A., 1985; the stationary magnetic/electric field can be described as

$$\text{rot } \mathbf{H} = \mathbf{J}, \quad (1)$$

$$\text{rot } \mathbf{E} = \mathbf{0}, \quad (2)$$

$$\text{div } \mathbf{B} = 0, \quad (3)$$

$$\text{div } \mathbf{J} = 0, \quad (4)$$

$$\text{div } \mathbf{D} = 0, \quad (5)$$

where \mathbf{H} , \mathbf{J} , \mathbf{E} , \mathbf{D} , \mathbf{B} are the vectors of magnetic field intensity, current density, electric field intensity, electric flux density, magnetic flux density, respectively. The material relations are represented by the expressions

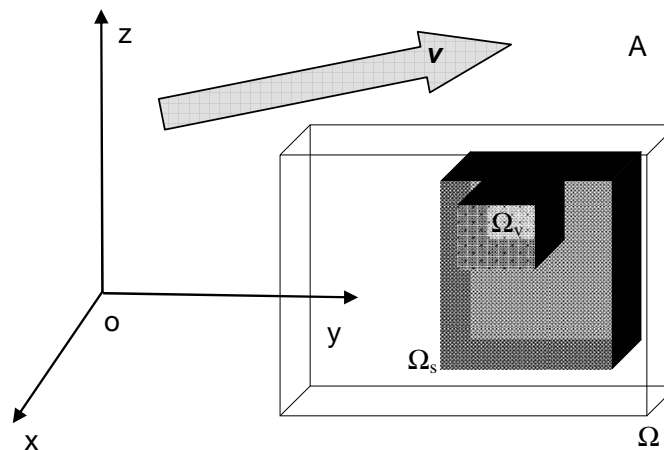


Figure 1. Basic model of the \mathbf{A} system in the Cartesian coordinate system, motion of the area part at velocity \mathbf{v} .

$$\mathbf{B} = \mu_0 \mu_r \mathbf{H}, \quad (6)$$

$$\mathbf{J}_v = \gamma \mathbf{E}, \quad (7)$$

$$\mathbf{D} = \varepsilon_0 \varepsilon_r \mathbf{E}. \quad (8)$$

where ε , μ , γ are the permittivity, permeability, conductivity of the environment. Vector functions of the electric and the magnetic fields \mathbf{E} , \mathbf{B} are expressed by the help of the scalar electric potential ϕ_e and the vector magnetic potential \mathbf{A} ; for the stationary, quasi-static, quasi-stationary, non-stationary task, figure1, in the relation for the electric field intensity, the time derivation of the vector magnetic potential is zero

$$\mathbf{E} = -\text{grad } \phi_e - \frac{\partial \mathbf{A}}{\partial t}, \quad (9)$$

$$\mathbf{B} = \text{rot } \mathbf{A}. \quad (10)$$

The resulting current density \mathbf{J} from relation (4) is formed by the exciting current density $\mathbf{J}_s = \rho \mathbf{v}$ with the specific density of electric charge ρ and the current density caused by eddy currents

$$\mathbf{J}_v = \frac{\partial \rho}{\partial t} d\mathbf{l}. \quad (11)$$

where $d\mathbf{l}$ is the element of length of the trajectory on which the eddy currents close. Motion effect for the instantaneous velocity vector \mathbf{v} is respected in the model by current density

$$\mathbf{J}_m = \gamma(\mathbf{v} \times \mathbf{B}). \quad (12)$$

Then, in respecting eddy currents (11),

$$\mathbf{J} = \mathbf{J}_v + \mathbf{J}_s + \mathbf{J}_m. \quad (13)$$

The electromagnetic field distribution is formulated using expressions (1) to (13).

$$\text{rot } \mathbf{H} = \mathbf{J} \text{ in the entire region of model } \Omega. \quad (14)$$

$$\text{rot } \mathbf{E} = -\frac{\partial \mathbf{B}}{\partial t}. \quad (15)$$

For the individual parts of model Ω there holds $\Omega \subset \Omega_v \cup \Omega_s$, where Ω_v is the area with dominant eddy currents which behave according to relation (7), and Ω_s is the area with the known distribution of current density \mathbf{J}_s . In the assumed model there holds

$$\Omega_s \subset \Omega_v. \quad (16)$$

These basic relations were complemented with boundary and initial conditions and, using the finite element method, the physical model was transferred to the mathematical. The mathematical model is a system of non-linear, time-variable equations; reference Fiala P., 1999 provides a complete derivation of the model. The finite element method (FEM) Ansys, 1994-2012 program system enabled us to perform a complete analysis; the FEM program was modified using suitably selected boundary conditions in order to respect the model characteristics described in relations (11) to (13), Fiala P., 1999.

According to reference Haňka L., 1971, in any investigation into electro-dynamic systems it is necessary to respect the relativistic approach to electrodynamics. The entire problem begins at the moment when the vector of intensities of both the electric and the magnetic fields of the moving system is **relative**.

3 Relativity effect in the model

In the example provided by reference Haňka L., 1971, current density in the A system is $\mathbf{J} = \rho \mathbf{v}$, for mutually moving A-A' systems in the component form

$$\mathbf{J}_{\square} = J'_x \mathbf{u}_x + J'_y \mathbf{u}_y + J'_z \mathbf{u}_z + jc \rho' \mathbf{u}_t. \quad (17)$$

The continuity equation can be formulated as

$$\text{div } \mathbf{J}_{\square} = 0. \quad (18)$$

After applying the Lorentz transformation for the simplicity of the moving systems in the direction of x , current density (17) can be written in the form

$$\mathbf{J}_{\square} = \underbrace{\frac{J'_x + j \frac{v_x}{c} J'_t}{\sqrt{1 - \left(\frac{\|\mathbf{v}\|}{c}\right)^2}} \mathbf{u}_x + J'_y \mathbf{u}_y + J'_z \mathbf{u}_z}_{\text{C}} + j \underbrace{\frac{c\rho' - \frac{v_x}{c} J'_x}{\sqrt{1 - \left(\frac{\|\mathbf{v}\|}{c}\right)^2}} \mathbf{u}_t}_{\text{D}}. \quad (19)$$

From expression (19), for the instantaneous velocity of the moving system A' in relation to observer A (Figure 1), at $v \ll c$, the component part C is negligible; then, the simplification of relations (21) and (22) can be written as

$$\mathbf{J}_{\square} = \underbrace{\frac{J'_x}{\sqrt{1 - \left(\frac{\|\mathbf{v}\|}{c}\right)^2}} \mathbf{u}_x + J'_y \mathbf{u}_y + J'_z \mathbf{u}_z}_{\text{C}} + j \underbrace{\frac{c\rho' - \frac{v_x}{c} J'_x}{\sqrt{1 - \left(\frac{\|\mathbf{v}\|}{c}\right)^2}} \mathbf{u}_t}_{\text{D}}. \quad (20)$$

This relation, or component C from expression (20), is well-known from electromagnetodynamics in respecting the ratio of velocities v/c . However, the second part, or component D in expression (19), is nonnegligible and has a character relative with respect to systems $A-A'$, component D in expression (20). The first part of the relation, C, from expression (20) is based on electrostatics at $v \ll c$ conventional current. The second relation, or D, (20) is for the magnitude of electric charge density $\rho' \neq 0$ unknown in electrostatics and is typical of the relativistic description of behavior of two mutually moving systems. Then, we can easily formulate

$$\rho = \frac{v}{c^2} J'_x \quad (21)$$

In the non-dynamic system, the model is shown in relations (1) and (8). In order to eliminate possible errors, it is suitable to include in relation (14) the term which respects Faraday's law of induction

$$\text{rot } \mathbf{E} = -\frac{\partial \mathbf{B}}{\partial t} + \text{rot}(\mathbf{v} \times \mathbf{B}). \quad (22)$$

and for the magnetic field relation (13)

$$\text{rot } \mathbf{H} = \mathbf{J}_s + \mathbf{J}_m + \frac{\partial \mathbf{D}}{\partial t} + \text{rot}(\mathbf{v} \times \mathbf{D}). \quad (23)$$

where ρ is the volume density of electric charge. The complete Maxwell equations are covariant in all the systems; therefore, it is not important to specify the system within which the observer moves, because the described relations always hold true. After the derivation of the four-vector and respecting the Lorentz transformation, Kikuchi H., 2001, for the moving electric charge with density ρ from the viewpoint of two individual systems relatively moving at the velocity of \mathbf{v} A and A' , the source current density is written in the form

$$\mathbf{J}_{s\square} = \rho \frac{\partial s}{\partial t} + jc\rho \mathbf{u}_t. \quad (24)$$

and where \mathbf{s} is the position vector of a material point in the coordinate system. Then, the interface between the dielectric with electric permittivity ε and the conductive material having conductivity γ (22), (23)

$$\text{rot} \left(\mathbf{E} + \frac{(\mathbf{J}_s + jc\rho\mathbf{u}_t)}{\gamma} \right) = -\frac{\partial \mathbf{B}}{\partial t} + \text{rot}(\mathbf{v} \times \mathbf{B}). \quad (25)$$

$$\text{rot} \mathbf{H} = \mathbf{J}_s + \mathbf{J}_m + jc\rho\mathbf{u}_t + \frac{\partial \mathbf{D}}{\partial t} + \text{rot}(\mathbf{v} \times \mathbf{D}). \quad (26)$$

$$\text{rot} \mathbf{E} = -\frac{\partial \mathbf{B}}{\partial t} + \text{rot}(\mathbf{v} \times \mathbf{B}) - \frac{1}{\gamma} \text{rot}(\rho\mathbf{v} + jc\rho\mathbf{u}_t). \quad (27)$$

$$\text{rot} \mathbf{H} = \rho\mathbf{v} + \gamma(\mathbf{v} \times \mathbf{B}) + jc\rho\mathbf{u}_t + \frac{\partial \mathbf{D}}{\partial t} + \text{rot}(\mathbf{v} \times \mathbf{D}). \quad (28)$$

where j is the symbol of the imaginary component of the quantity complex shape, c is the velocity of light module in the vacuum, \mathbf{s} is the position vector of the relative system and the system, Figure 1., of the moving electric charge in axis x of the Cartesian coordinate system with electric charge density ρ . For the continuity equation (4) there holds

$$\text{div}(\mathbf{J}_{\square}) = 0. \quad (29)$$

In order to facilitate simplification, if we assume the motion of one reference system as $()'$ (for example, in the x axis of the Cartesian coordinate system), Figure 2, the four-vector of current density can be written, after application of the Lorentz transformation, in the (invariant) form (19) and the electric charge volume density in the reference system is, after transformation, written as

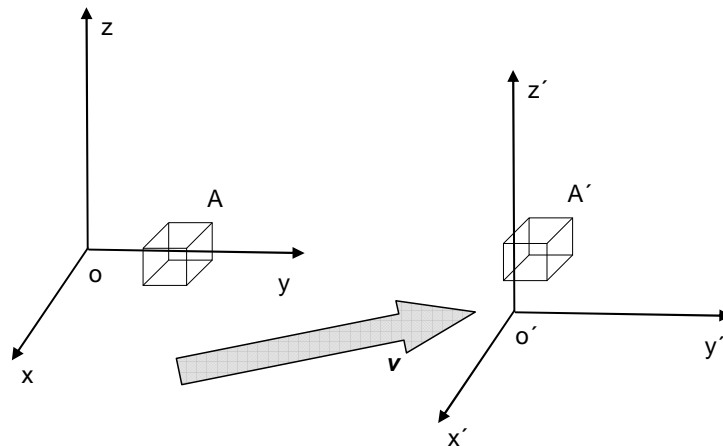


Figure 2. Relation of two moving systems with the object A and A' , moving mutually at velocity \mathbf{v} .

$$\rho = \frac{\rho' - \frac{v_x}{c^2} J'_x}{\sqrt{1 - \left(\frac{\|\mathbf{v}\|}{c}\right)^2}}, \quad \rho' = \frac{\rho - \frac{v_x}{c^2} J_x}{\sqrt{1 - \left(\frac{\|\mathbf{v}\|}{c}\right)^2}}. \quad (30)$$

Applying Maxwell's equation for the electric charge presence in the modeled area, Figure 2.

$$\rho = \text{div} \mathbf{D} \quad (31)$$

the expression for the current density \mathbf{J} can be written in the form for the interface between the dielectric and the conductive layer.

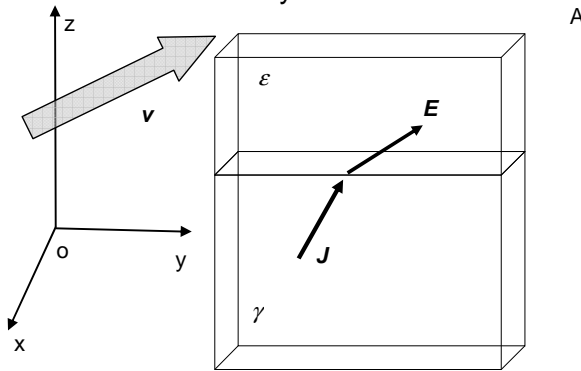


Figure 3. Approximation of conditions on the dielectric/metal interface for the relativistic approach in the model.

$$\mathbf{J}_{\square} = \frac{J'_x - v_x \operatorname{div} \left(\frac{\epsilon'}{\gamma'} \mathbf{J}'_{\Delta} \right)}{\sqrt{1 - \left(\frac{\|\mathbf{v}\|}{c} \right)^2}} \mathbf{u}_x + J'_y \mathbf{u}_y + J'_z \mathbf{u}_z + j \frac{c \operatorname{div} \left(\frac{\epsilon'}{\gamma'} \mathbf{J}'_{\Delta} \right) - \frac{v_x}{c} J'_x}{\sqrt{1 - \left(\frac{\|\mathbf{v}\|}{c} \right)^2}} \mathbf{u}_t. \quad (32)$$

$$\mathbf{J}_{\square} = \frac{J_x - v_x \operatorname{div} \left(\frac{\epsilon'}{\gamma'} (J'_x \mathbf{u}_x + J'_y \mathbf{u}_y + J'_z \mathbf{u}_z) \right)}{\sqrt{1 - \left(\frac{\|\mathbf{v}\|}{c} \right)^2}} \mathbf{u}_x + J'_y \mathbf{u}_y + J'_z \mathbf{u}_z + j \frac{c \operatorname{div} \left(\frac{\epsilon'}{\gamma'} (J'_x \mathbf{u}_x + J'_y \mathbf{u}_y + J'_z \mathbf{u}_z) \right) - \frac{v_x}{c} J'_x}{\sqrt{1 - \left(\frac{\|\mathbf{v}\|}{c} \right)^2}} \mathbf{u}_t. \quad (33)$$

Then for the unabbreviated expression, respecting the motion at velocity \mathbf{v} in all directions, current density in relation to the moving system A-A' can be written as

$$\mathbf{J}_{\square} = \frac{J'_x - v_x \operatorname{div} \left(\frac{\epsilon'}{\gamma'} \mathbf{J}'_{\Delta} \right)}{\sqrt{1 - \left(\frac{\|\mathbf{v}\|}{c} \right)^2}} \mathbf{u}_x + \frac{J'_y - v_y \operatorname{div} \left(\frac{\epsilon'}{\gamma'} \mathbf{J}'_{\Delta} \right)}{\sqrt{1 - \left(\frac{\|\mathbf{v}\|}{c} \right)^2}} \mathbf{u}_y + \frac{J'_z - v_z \operatorname{div} \left(\frac{\epsilon'}{\gamma'} \mathbf{J}'_{\Delta} \right)}{\sqrt{1 - \left(\frac{\|\mathbf{v}\|}{c} \right)^2}} \mathbf{u}_z + j \frac{c \operatorname{div} \left(\frac{\epsilon'}{\gamma'} \mathbf{J}'_{\Delta} \right) - \frac{v_x}{c} J'_x - \frac{v_y}{c} J'_y - \frac{v_z}{c} J'_z}{\sqrt{1 - \left(\frac{\|\mathbf{v}\|}{c} \right)^2}} \mathbf{u}_t. \quad (34)$$

The expression for current density in the area of conductive material with conductivity γ can be written from relation (21) in the form assuming zero value of electric charge ρ in the electrically conductive material (metal)

$$\mathbf{J}_{\square} = \frac{J'_x}{\sqrt{1 - \left(\frac{\|\mathbf{v}\|}{c} \right)^2}} \mathbf{u}_x + J'_y \mathbf{u}_y + J'_z \mathbf{u}_z + j \frac{-\frac{v_x}{c} J'_x}{\sqrt{1 - \left(\frac{\|\mathbf{v}\|}{c} \right)^2}} \mathbf{u}_t. \quad (35)$$

$$\mathbf{J}_{\square} = \frac{J'_x}{\sqrt{1 - \left(\frac{\|\mathbf{v}\|}{c}\right)^2}} \mathbf{u}_x + \frac{J'_y}{\sqrt{1 - \left(\frac{\|\mathbf{v}\|}{c}\right)^2}} \mathbf{u}_y + \frac{J'_z}{\sqrt{1 - \left(\frac{\|\mathbf{v}\|}{c}\right)^2}} \mathbf{u}_z + j \frac{-\frac{v_x}{c} J'_x - \frac{v_y}{c} J'_y - \frac{v_z}{c} J'_z}{\sqrt{1 - \left(\frac{\|\mathbf{v}\|}{c}\right)^2}} \mathbf{u}_t \quad (36)$$

$$\mathbf{J}_{\square} = \frac{\mathbf{J}'_{\Delta} + j\mathbf{v}\rho'}{\sqrt{1 - \left(\frac{\|\mathbf{v}\|}{c}\right)^2}} \quad (37)$$

$$\rho = \frac{\rho' - \frac{\mathbf{v}}{c^2} \mathbf{J}'_{\Delta}}{\sqrt{1 - \left(\frac{\|\mathbf{v}\|}{c}\right)^2}} \quad (38)$$

For the relationship within one system A the relations are known and written in the form

$$\text{rot } \mathbf{H}_{\Delta} = \mathbf{J}_{\Delta} + \frac{\partial \mathbf{D}_{\Delta}}{\partial t} + \text{rot}(\mathbf{v}_{\Delta} \times \mathbf{D}_{\Delta}). \quad (39)$$

$$\text{rot } \mathbf{E}_{\Delta} = -\frac{\partial \mathbf{B}_{\Delta}}{\partial t} + \text{rot}(\mathbf{v}_{\Delta} \times \mathbf{B}_{\Delta}). \quad (40)$$

and the expression of current density \mathbf{J} within two mutually moving systems A-A' is

$$\mathbf{J}_{\square} = \begin{pmatrix} 0 & \frac{\partial H_3}{\partial x_2} & \frac{\partial H_3}{\partial x_3} & -jc \frac{\partial D_1}{\partial x_4} \\ -\frac{\partial H_3}{\partial x_1} & 0 & \frac{\partial H_1}{\partial x_3} & -jc \frac{\partial D_2}{\partial x_4} \\ \frac{\partial H_2}{\partial x_1} & -\frac{\partial H_1}{\partial x_2} & 0 & -jc \frac{\partial D_3}{\partial x_4} \\ jc \frac{\partial D_1}{\partial x_1} & jc \frac{\partial D_2}{\partial x_2} & jc \frac{\partial D_3}{\partial x_3} & 0 \end{pmatrix} \quad (41)$$

There is no problem obtaining, by means of reversal in the sign of velocity, transformed quantities of the opposite system (which is moving) for the above-expressed transformed quantities. Let us have a simple geometric task, Figure 4.

4 Example of the relativity effect on the simply model

The author of Haňka⁸ has shown that a simple model can be used to demonstrate the critical velocity at which the relativistic effect described in the current density \mathbf{J}_{\square} relation (34) will appear. The model, whose scheme is presented in fig. 4, is a magnetic circuit composed of pole extensions and an exciting coil. A very long ("infinite") conductive strip of finite thickness passes through an air gap in the magnetic circuit; in relation to the circuit, this strip moves at an instantaneous velocity with the component in the x-axis of the Cartesian coordinate system, $v_x = 1 \text{ ms}^{-1}$. It is evident from both source Haňka L., 1971 and the example according to Figure 4 that there only figures the normal component of the electric field intensity E_n in the boundary of conductor/air in the magnetic circuit air gap. For the first approximation, the component is perpendicular to the velocity vector \mathbf{v}_x of the

moving conductive strip. According to Ohm's law, flowlines on the surface of the conductive strip ought to be perpendicular to the velocity vector, which is inconsistent with both the experiment and the model. The resulting form of the flow lines is shaped by, among other aspects, electric charge density ρ in relation (19). Even though, at first sight, the electric charge density ρ may appear as a very small value, it will induce the excitation of electric intensity and current density, which in superposition with the exciting value of electric intensity and current density create a deformed magnetic field. However, there remains the question of the value of instantaneous velocity \mathbf{v} at which the effect will show itself.

The problem can be described as follows: For the formation of current density, $J = 1 \text{ A mm}^{-2}$, therefore $J = 1 \cdot 10^6 \text{ A} \cdot \text{m}^{-2}$; with the electrical conductivity of $\gamma = 100 \text{ MS m}^{-1}$, the electric field intensity is $E = J\gamma^{-1}$, $E = 0.01 \text{ V} \cdot \text{m}^{-1}$. Let us assume a plane unlimited problem and therefore the electric field intensity function depending on the distance from the plate $E_x = k \cdot x$; then, for simplicity, we may write relation (31) as

$$\rho = \text{div}(\epsilon E) \quad (42)$$

then

$$\text{div}(E) = \frac{\rho}{\epsilon} \quad (43)$$

$$\text{div}(E) \cong \frac{dE_x}{dx} \quad (44)$$

In the comparison of (43) with (44) there holds

$$\frac{dE_x}{dx} = \frac{\rho}{\epsilon} \quad (45)$$

and, therefore, for approximation $\epsilon = 8.8 \cdot 10^{-12} \text{ F} \cdot \text{m}^{-1}$ the electric charge volume density is in the distance of $x = 10^{-1} \text{ m}$

$$\rho = \epsilon \frac{dE_x}{dx} \quad (46)$$

$$\rho = 8.8 \cdot 10^{-12} \frac{10^{-2}}{10^{-1}} \text{ C} \cdot \text{m}^{-3}$$

From expression (30) we can obtain the relation for the value of instantaneous velocity in moving systems A-A' respecting the relativistic effect of the system electrodynamics

$$\rho = \frac{\rho' - \frac{v_x}{c^2} J'_x}{\sqrt{1 - \left(\frac{\|\mathbf{v}\|}{c}\right)^2}}, \text{ which for the assumed problem and the low value of instantaneous}$$

velocity module from relation (21) is

$$v_x = \frac{\rho' c^2}{J'} \quad (47)$$

$$\text{For the above-quoted problem} \quad v_x = \frac{\rho' c^2}{J'} = \frac{8.8 \cdot 10^{-11} (3 \cdot 10^8)^2}{1 \cdot 10^6} \cong 0.79 \text{ m} \cdot \text{s}^{-1}.$$

Now, with respect to the relation (47), for the non-moving system A, in which the instantaneous velocity value without accepting the relativistic effect (11), we can calculate different value

$$v = \frac{10^6}{8.8 \cdot 10^{-13}} \cong 1.13 \cdot 10^{19} \text{ m.s}^{-1}. \quad (48)$$

Thus, in relations (47) and (48) can be traced the diametral difference of results with comparable values of electric field intensity and at instantaneous motion velocity value of the moving strip.

There follows an example of the representation of changes in the electromagnetic field distribution for the given model of problem (Figure 4); for simplicity, the velocity of the moving strip is assumed to be $v_x = 1 \text{ m.s}^{-1}$.

In the numerical analysis, the simple model in Figure 4, is used for the demonstration of influence of the relativistic approach on the model (34), (36) creation on the analysis results. The physical model is based on the solution of the reduced Maxwell equations Stratton J.A., 1985, Fiala P., 2010. The resulting current density \mathbf{J} is formed by the exciting current density $\mathbf{J}_s = \rho \mathbf{v}$ with the specific density of electric charge ρ and the current density caused by eddy currents \mathbf{J}_e . Motion effect for the instantaneous velocity vector \mathbf{v} is respected in the model by current density \mathbf{J}_m . The Finite element method (FEM) program was modified using suitably selected boundary conditions in order to respect the model characteristics described in Fiala P., 1999, Fiala P., 2010. The entire problem begins at the moment when the vector of intensities of both the electric and the magnetic fields of the moving system is **relative**. The complete Maxwell equations are covariant in all the systems; therefore, it is not important to specify the system within which the observer moves as the described relations always hold true. After the derivation of the four-vector and respecting the Lorentz transformation, the current density is written in the form (41).

There is no problem in obtaining, by means of reversal in the sign of velocity, transformed quantities of the opposite system (which is moving) for the above-expressed transformed quantities. Let us have a simple geometric task, figure 4. The model example consists of a conductive strip in the air gap which is a part of the magnetic circuit. The distribution of magnetic field in the system is evaluated for a different case of the strip movement and for the non-relativistic and relativistic approaches.

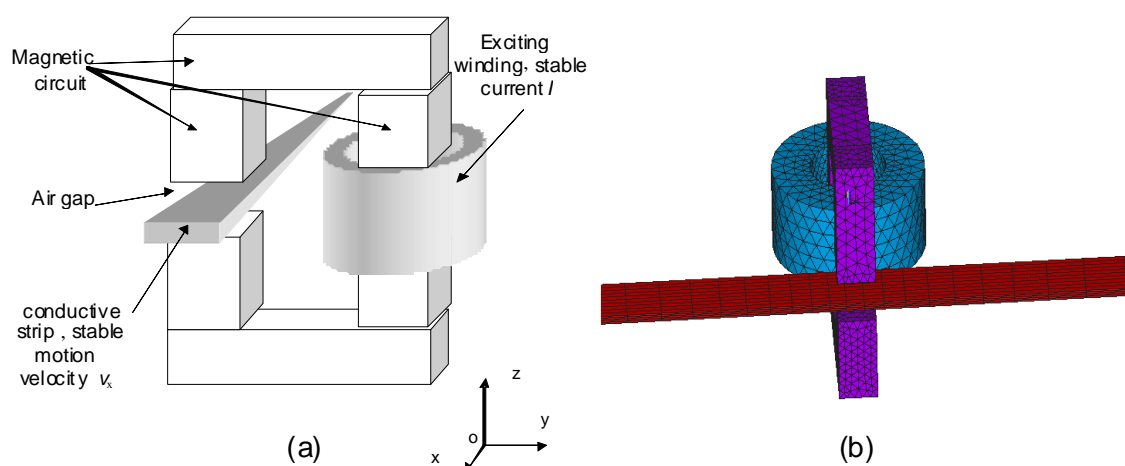


Figure 4. A simple geometry for the verification of the relativistic approach of electrodynamics (a) and its numerical model (b).

Numerical analysis of the above-mentioned example provided by the author of Haňka L., 1971 is realized for the assumption of linear material environment by means of the

superposition method. In this context, several consecutive operations within the electromagnetic field analysis are carried out.

Generally, the first step consists in an elementary analysis of the magnetic field without the moving strip, relations (1) to (5), the second step embodies an analysis of the magnetic field with steady motion of the conductive strip and the effect of eddy currents (21), and the third action involves the evaluation of current density in the moving strip with electrodynamic and relativistic effects according to relations (34) to (41).

These analyses were performed using the program providing FEM analysis with magnetic vector potential, and the related verification was realized through an analysis of the model with magnetic scalar potential Ansys, 1994-2012 (program in the APDL language for ANSYS).

In the case of the above-mentioned first step, the results of the realized evaluation of magnetic induction B module distribution correspond in both models to the assumed theoretical results for the stationary magnetic field, Figures. 5 and 6.

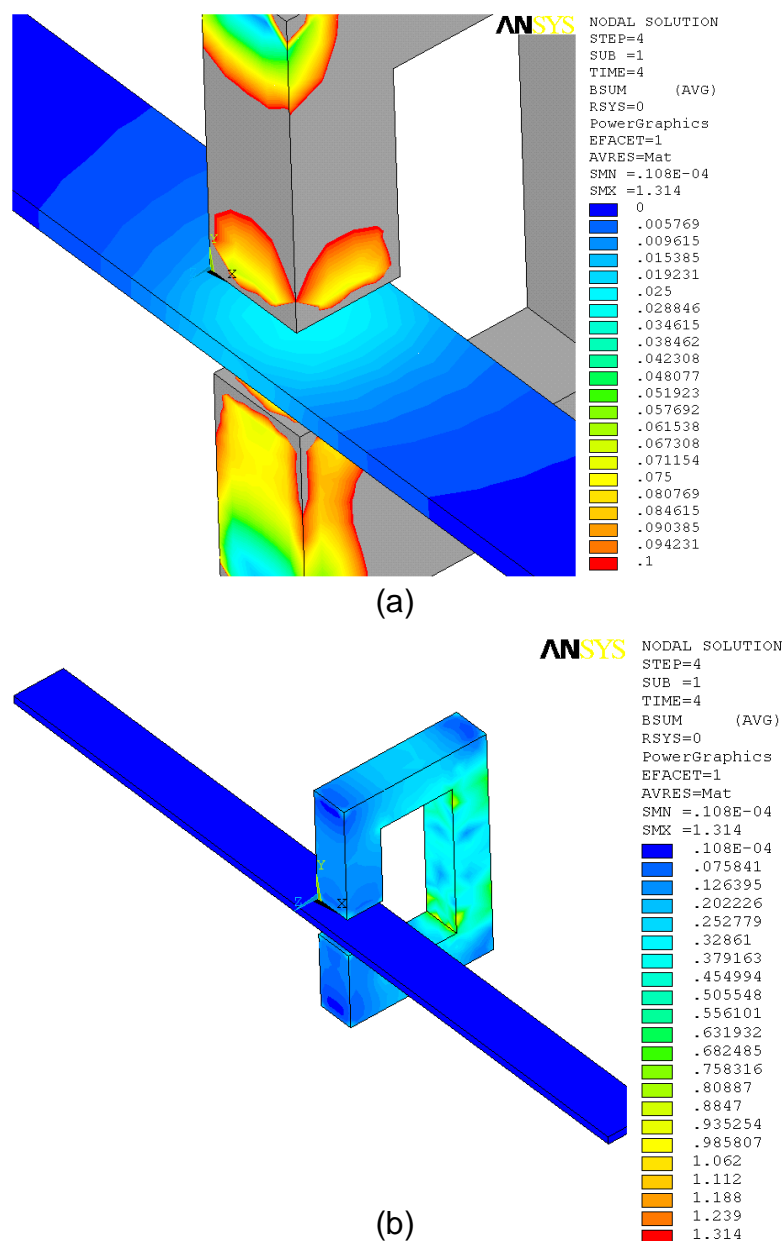


Figure 5. Magnetostatic problem analysis: Distribution of the magnetic flux density B vector module (a), magnetic circuit evaluation (b).

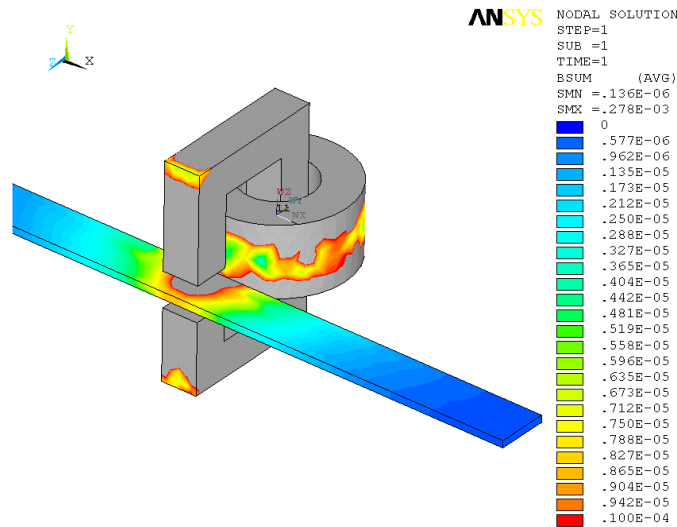


Figure 6. Magnetostatic problem analysis: Distribution of the magnetic flux density B vector module, analysed through a vector magnetic potential formulation.

The second step is analyzed in Figure 7. Here, the description shows the evaluated module of current density vector in a quasi-stationary model of the problem; the conductor moves in the direction of axis x at the velocity of $v=1\text{m}\cdot\text{s}^{-1}$. The reactionary magnetic field with the distribution of the magnetic flux density B vector module B_r is described in Figure 8. This result is then inserted in the model from the first step (the magnetostatic part) and complemented with an analysis of the superposed magnetic field, Figure 9. This figure demonstrates the fact that the influence upon the basic magnetic field with magnetic flux density B is of a lower order when we perform the analysis excluding the effect of relativistic electrodynamics.

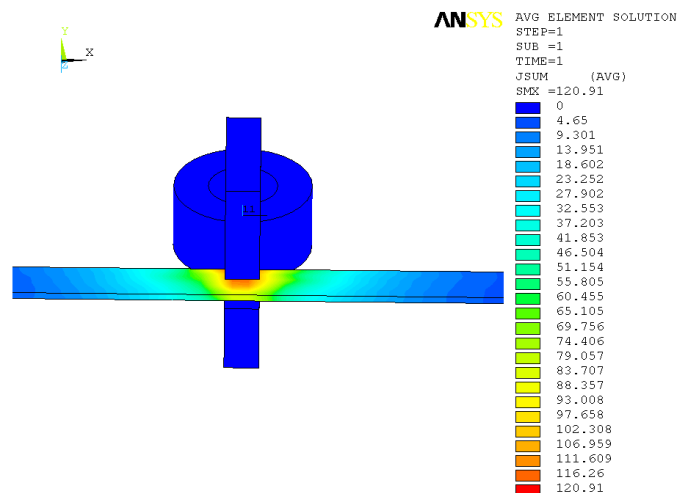


Figure 7. Magnetostatic problem analysis: Distribution of the current density J vector module.

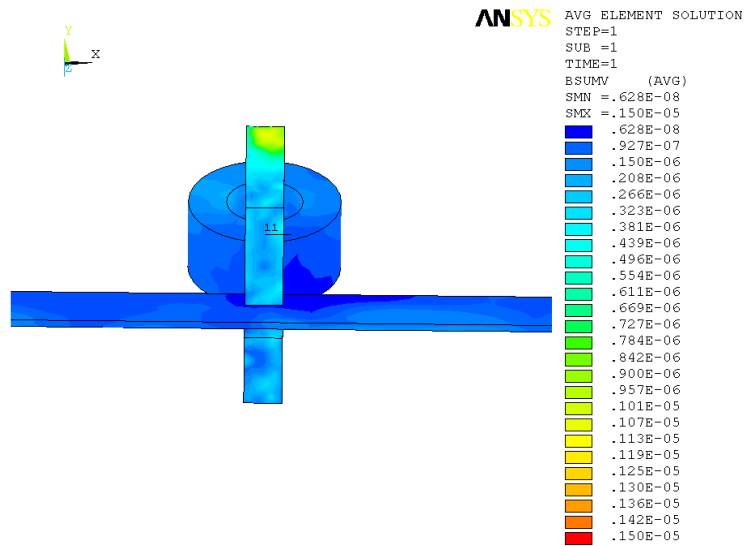


Figure 8. Analysis of the quasi-stationary magnetic field: Distribution of the reaction magnetic flux density B_r vector module, vector magnetic potential.

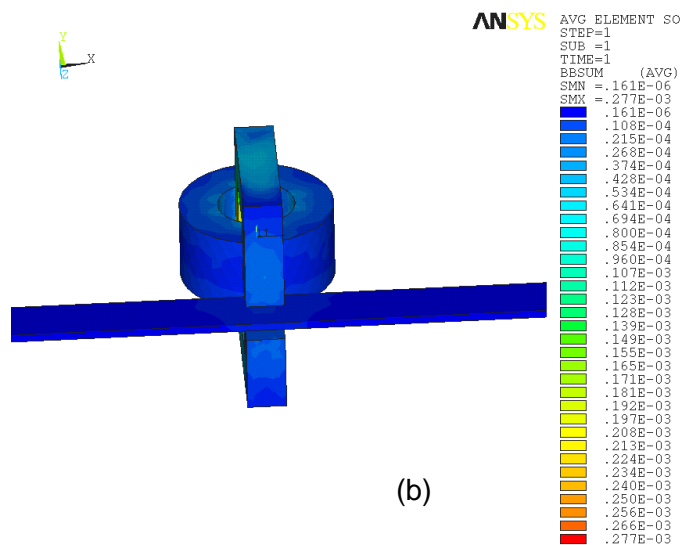
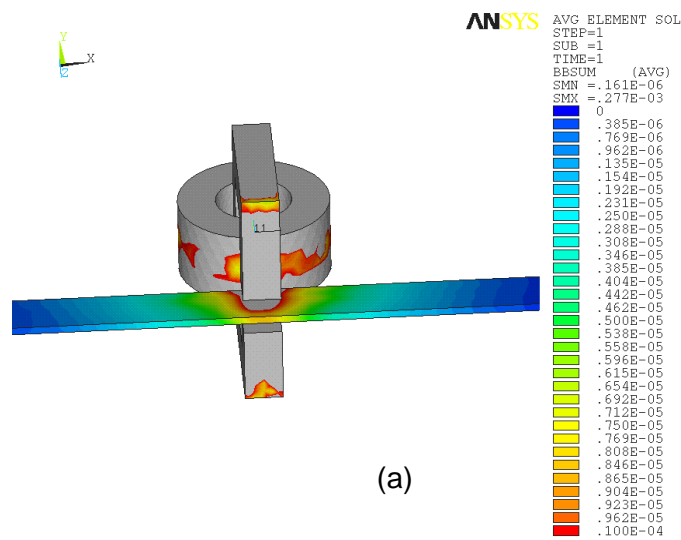


Figure 9. Analysis of the quasi-stationary magnetic field: Distribution of the superposed magnetic flux density \mathbf{B}_s vector module (a), (b).

According to relations (34) and (36) within the third step, we evaluated the vector of current density \mathbf{J}_{re} , \mathbf{J}_{ima} in both the real and the imaginary component (Figure 10.). This value was superposed in relation to the elementary component of current density \mathbf{J} , and an analysis of the magnetic field was carried out for the set conditions (respecting the motion and its dynamic and relativistic character).

The magnetic field excitation for this simple problem and its approximation was executed only by the real component of the resulting current density \mathbf{J}_{re} . The resulting distribution of the magnetic field and the real component module of the magnetic induction B_{re} vector are shown in Figure 11; naturally, it is possible to perform the analysis also for the imaginary part of current density component \mathbf{J}_{ima} .

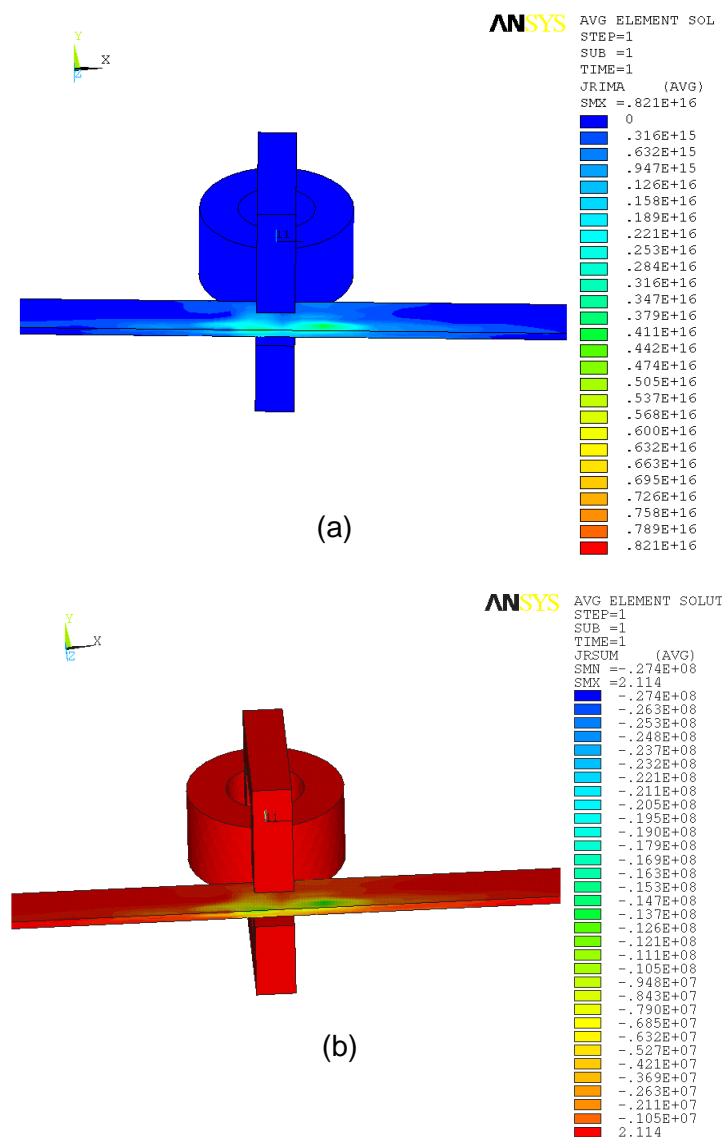


Figure 10. Distribution of imaginary component of the current density \mathbf{J}_{ima} (a) and real component of the current density \mathbf{J}_{re} (b).

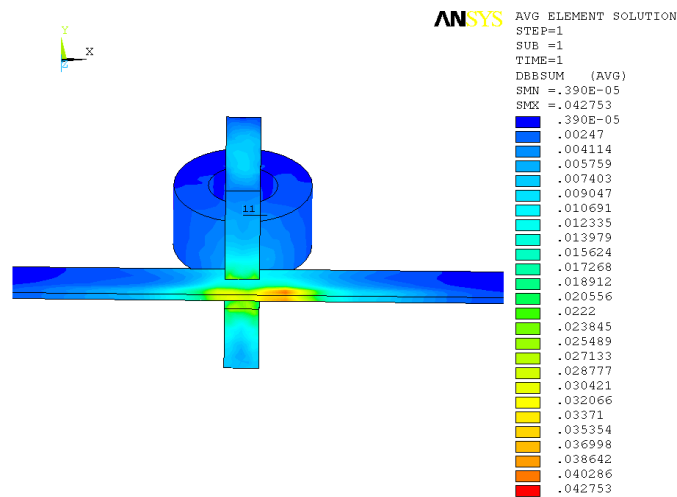


Figure 11. Analysis of the relativistic field: Distribution of the superposed magnetic flux density B_r

5 Example of the relativity effect on the experimental model

The numerical model of ballistic projectile velocity measurement is shown in Figure 12. There are electric coils for excitation of basic magnetic flux density B , Figure 13. The secondary magnetic flux density are dependent on the effects on move projectile on the its surface. The effects depend on eddy currents and relativistic theory. The final vector magnetic flux density is measured with classical sensors, Figure 14a. It can be shown real and imaginary components of current density module, Figure 14b, and results of relativistic contribution of magnetic flux density modul, B_{re} , B_{im} , Figure 15.

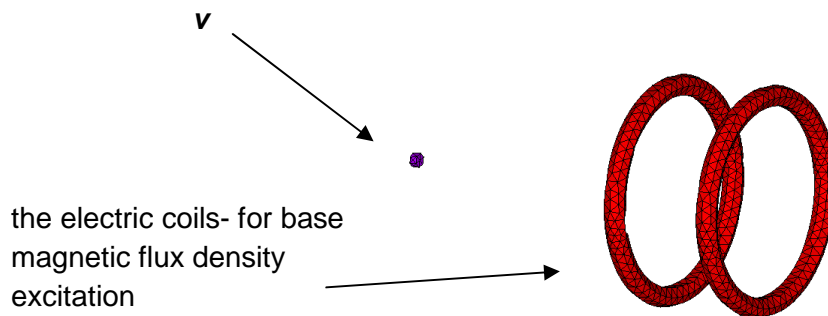


Figure 12. The electrodynamic magnetic field analysis: model of simple ballistic projectile velocity measurement

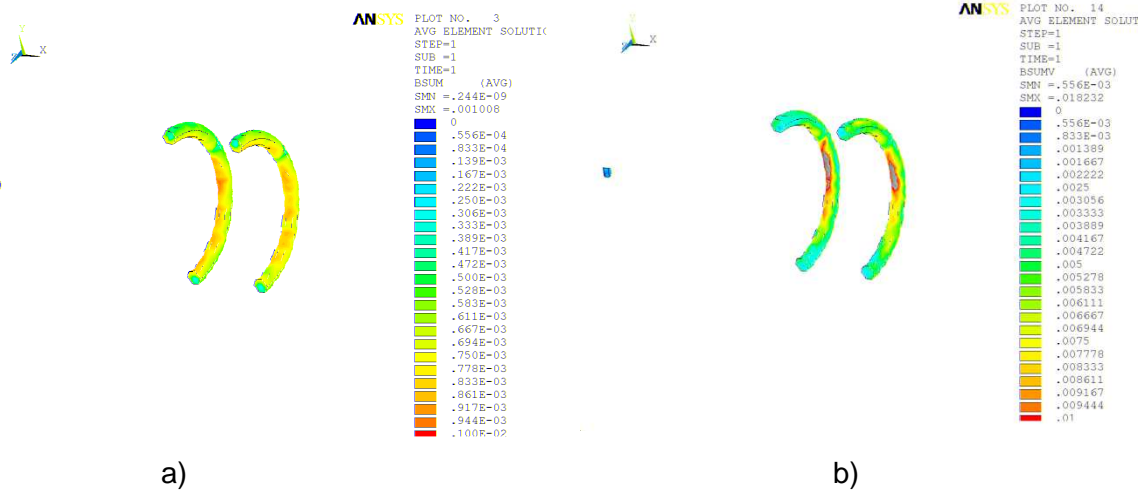


Figure 13. The electrodynamic magnetic field analysis: a) the basic magnetic flux density vector module B distribution, b) the final magnetic flux density vector module B distribution

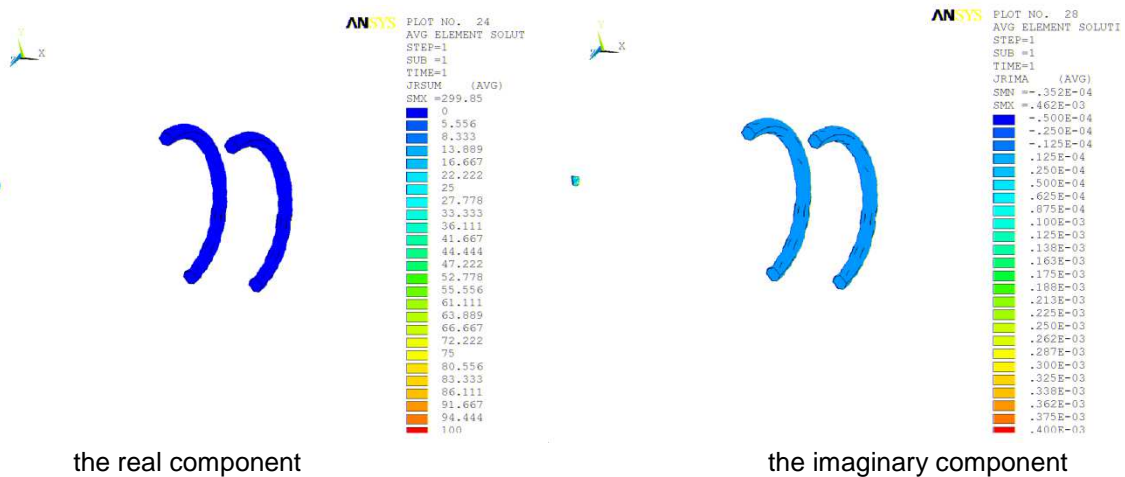


Figure 14. The electrodynamic magnetic field analysis: the real component current density J_{re} vector module distribution, the imaginary component current density J_{im} vector module distribution

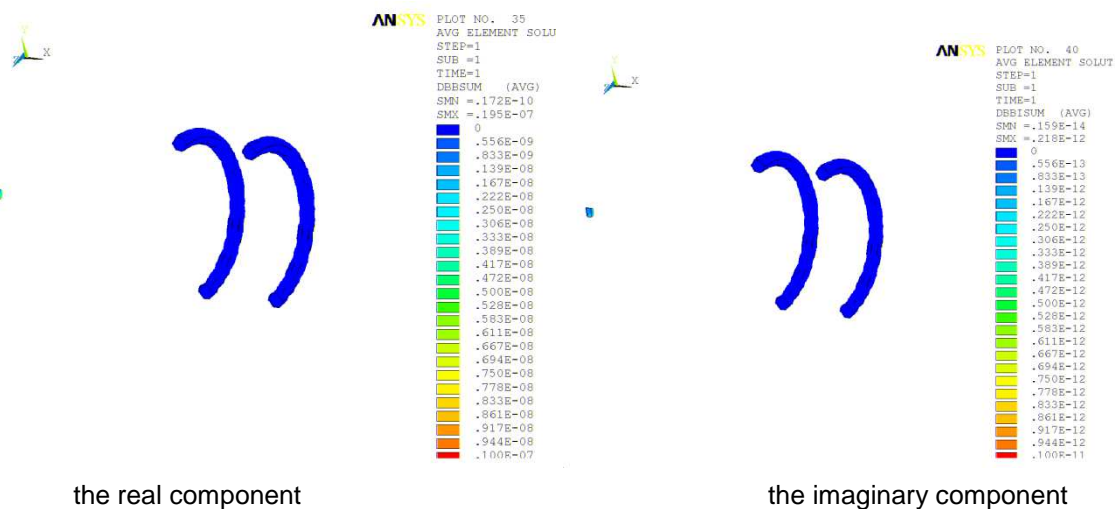


Figure 15. The electrodynamic magnetic field analysis: the real component of magnetic flux density B_{re} , the imaginary component of magnetic flux density B_{im} .

6 Conclusion

The model makes apparent the distinction by order of the individual phenomena. It is evident that the relativistic electro-magneto-dynamic principle is indispensable and introduces substantial changes into the original non-dynamic conception of this type of simple task analysis. The effect is apparent of motion on the magnetic field imbalance. A higher value of an elementary magnetic field combines with a decrease in relative magnitude of the electro-magneto-dynamic field influence.

Between the numerical values we may point to $B_{\max}=0.277 \cdot 10^{-3}\text{T}$ for quasi-stationary task and $B_{\maxre}=0.427 \cdot 10^{-1}\text{T}$ for electrodynamic model. Relations (32) to (38) ought to be considered and respected in the process of designing dynamic and electromechanical systems such as rotary electrical machines; in the same manner, the relations should be utilized in electromagnetic and electromechanical systems with moving elements designed for velocity in the order of 1 ms^{-1} . It can be assumed that, due to the disrespect of results flowing from this interpretation of the electromagnetic field of dynamic systems, inaccuracies occur within the modeling and simulation that supports the actual design and realization of the systems.

Acknowledgements: The research described in the paper was financially supported by a grant from the Ministry of Industry and Trade of the Czech Republic (MPO No. FR-TI1/368), GAČR 102/09/0314, BUT Grant Agency FEKT-S-10-13.

References

- ³ Ansys, 1994-2012, Inc. *Ansys Theory Reference Manual*, Program Ansys supplement
- ⁴ Dědek L., Dědková J., 2000, *Elektromagnetismus* (VUTIUM, Brno, Czech Republic)
- ⁶ Fiala P., 1999, *Secondary winding model of current transformer- switchable variant* (Research report, Laboratory of modeling and optimization field in electromagnetic systems, FEI VUT and ABB EJV a.s. Brno no.1/99, 21.1.1999, Brno, Czech Republic, 1999)
- ⁹ Fiala P., 2010, *EMHD model used for linear moving objects analysis* (Progress in electromagnetic research, Boston, USA, 5.-8.7.2010) **ISSN 1559-9450**.
- ⁷ Fiala P., 1999, *Transformer partial discharge modeling, minimal breakdown value set in critical parts of transformer design* (Research report, Laboratory of modeling and optimization field in electromagnetic systems, FEI VUT and ABB EJV a.s. Brno no.2/99, 18.3.1999, Brno, Czech Republic, 1999)
- ⁸ Haňka L., 1971, *Teorie elektromagnetického pole* (SNTL, Praha, Czech Republic, 1971), p. 578.
- ² Kuneš J., Vavroch O., Franta O., 1989, *Základy modelování* (SNTL, Praha, Czech Republic, 1989, ISBN 80-03-00147-1), p. 264 2000), p. 234.
- ¹⁰ Kikuchi H., 2001, *Electrohydrodynamics in dusty and dirty plasmas, gravito-electrohydrodynamics and EHD* (Kluwer Academic Publishers, 2001, ISBN 0-7923-6822-3), p. 228.
- ¹ Maxwell J.C., 1873, *A treatise on electricity and magnetism* (London Macmillan and co., Publishers to the University of Oxford, 1873), p. 532.
- ⁵ Stratton J.A., 1985, *Teorie elektromagnetického pole* (SNTL, Praha, Czech Republic, 1985), p. 51-60.

Contact address:

assoc.prof. Ing.Pavel Fiala, Ph.D.,

Brno university of technology, Faculty of electrical engineering and communication, Department of theoretical and experimental electrical engineering Kolejní 2906/4, 612 00 Brno, Czech Republic
fialap@feec.vutbr.cz

NMR DIAGNOSTICS AND BRAIN CANCER TREATMENT, NUMERICAL MODEL

PAVEL FIALA, KAREL BARTUSEK, MICHAEL HANZELKA

Brno university of technology, Faculty of electrical engineering and communication,
Department of theoretical and experimental electrical engineering, Czech Republic

Abstract: Brain cancer can be treated by several therapies. One of the methods available is the elimination of cancer cells in the tumor targeted volume through the influence of heat. In the case of this technique, it is necessary to know the location and distribution of the tumor volume in the surrounding tissue. Correct and precise tumor localization is one of the crucial parts of the brain tumor local hyperthermia, which is necessary for the corresponding adjustment of the local hyperthermia system. This method of cancer treatment requires the observance of temperature distribution in the treated tissue. In this article, the authors focus on local hyperthermia for local increase of the tumor tissue temperature and on the minimization of the treatment influence on the healthy tissue. The paper includes simulations of the tumor tissue heating method based on the utilization of the complex permeability and complex permittivity of the heated tissue. The authors also discuss the adjustment of the local hyperthermia system, mainly the time of exposition needed to achieve the required temperature distribution in the tumor volume.

Keywords: Nuclear magnetic resonance, tumor, head, numerical modeling, hyperthermia, treatment, tissue, exposition.

1 Introduction

This article analyzes the possibilities of use of local hyperthermia as a method of cancer treatment. Local hyperthermia is used together with other methods of cancer treatment. This technique is based on the effect of temperatures up to 42°C, which cause elimination of the cells in the targeted volume Wust P, Hildebrandt B, et al. ,2002. Effect of the heat is also shown in radiation therapy and chemotherapeutic drugs Bull JMC. ,1984, Urano M, Kuroda M, Nishimura Y. ,1999.

Systems for local hyperthermia of non-surface tumors are based on arrays of antennas emitting microwaves or radiowaves delivering the required power density in W/kg. Commercially used antennas are designed with regard to the size of the heated area. These antennas could be designed as a whole body, regional or local, in dependence on the size of the heated area and the required therapeutic depth. All hyperthermia system also require a system for the heated area temperature monitoring.

1.1 Whole body hyperthermia

This method is used in the case of metastatic malignant tumors where the use of local or regional hyperthermia is not feasible because of a higher number of tumors in different areas of the body. The whole body hyperthermia utilizes lower temperatures (less than 42°C) to prevent any damage to the healthy tissue.

1.2 Regional hyperthermia

The method of regional hyperthermia is used for deep localized tumors or in the case of a higher number of tumors in the same area. This method requires a sophisticated system for the planning of the heating process. Three-dimensional antenna systems are used for the controlling of power distribution in the heated area.

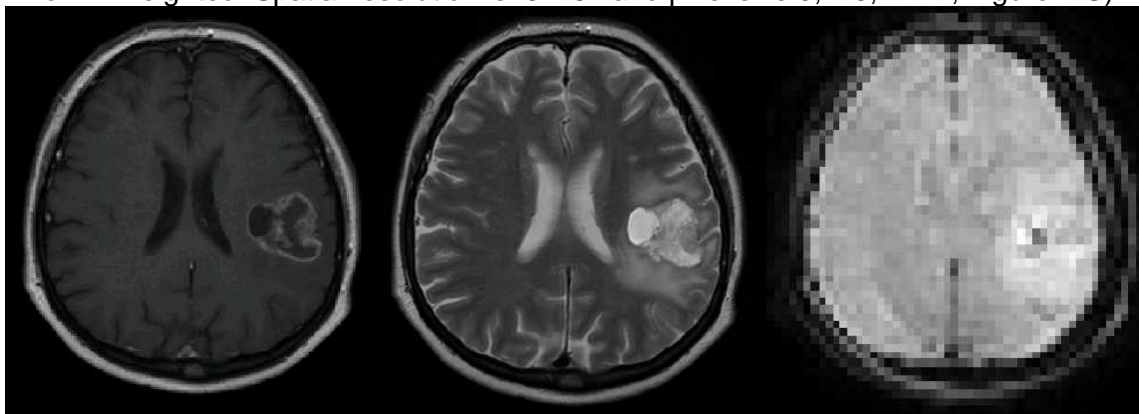
1.3 Local hyperthermia

If the tumor is close to the body surface, it is possible to use the local hyperthermia system. In this way, the adjustment of the local hyperthermia system is crucial for achieving a high temperature only in the tumor volume.

2 MR Methods of brain cancer localization

MRI is a constantly developing field of medicine suitable for the study of soft tissues, KUBÁSEK R., BARTUŠEK K., FIALA P.,2010. The current methodologies for obtaining images weighted by relaxation times provide us not only with information about the distribution of soft tissues, but also with an image insight into the function of the tissue. The localization of brain cancer is a necessary precondition for further treatment. In the case of radiation therapy, precise localization of the tumor and the surrounding tissues constitutes a crucial element.

Many MR sequences are used for imaging the tumor and the peritumoral region area with the aim to achieve an image with a higher contrast. Figure 1 shows an example of the T1 weighted (T1W), T2 weighted (T2W), and perfusion weighted (PWI) images. The T1W and T2W images show anatomical information about the tissue in the slice volume. These images are acquired in a higher spatial resolution, such as 512x512, pixel size 0,4x0,4 mm. PWI images are used for investigation into the function of the tissue. A PWI image could be a T1 or T2 weighted. Spatial resolution is 64x64 and pixel size 3,4x3,4 mm, Figure1. C).



A) B) C)
Figure 1. Imaging examples: Tumor and the peritumoral region area

3 Optimum Mode of the Hyperthermic Method

Optimal progress of the hyperthermic process depends on the method of heating the target material group, Wust P, Hildebrandt B, et al. ,2002. In this paper, the authors describe the method of tissue heating by the help of an antenna and tissue temperature monitoring, Figure 2. According to the applied source, a patient can participate in magnetic resonance

(MR) tomography diagnostics, MIKULKA J., GESCHIEDTOVÁ E., BARTUŠEK K.,2011, while the therapy is in progress. Here, the proposed method of electromagnetic heating can be affected by problems related to the stability and accuracy of an MR tomograph (MRT) as a diagnostic instrument for the monitoring of tissue heating. The frequency of an electromagnetic wave excitation ranges within 100-150 MHz. As a rule, there occurs the heating of surrounding tissue that is not being/not to be subject to therapy; in this tissue, contrariwise, non-reversible damage may be incurred MARCOŇ P., BARTUŠEK K., BURDKOVÁ M., DOKOUPIL Z.,2011. Using the MRT, we can nevertheless arrive at another progressive solution. Viewed from macroscopic description of the electromagnetic field, the tissue of carcinomes shows peculiar characteristics, which holds true even in respect of the dependence on temperature and frequency. In the case of the described model of heating by means of an electromagnetic wave, it is possible to formulate the electromagnetic wave in this environment using the diffusion equation for function u and parameters C Kadlec R., Kroutilova E., Nesporek D. and Fiala P., 2011, Drexler P., Jirku T., Szabo Z. et al.,2007.

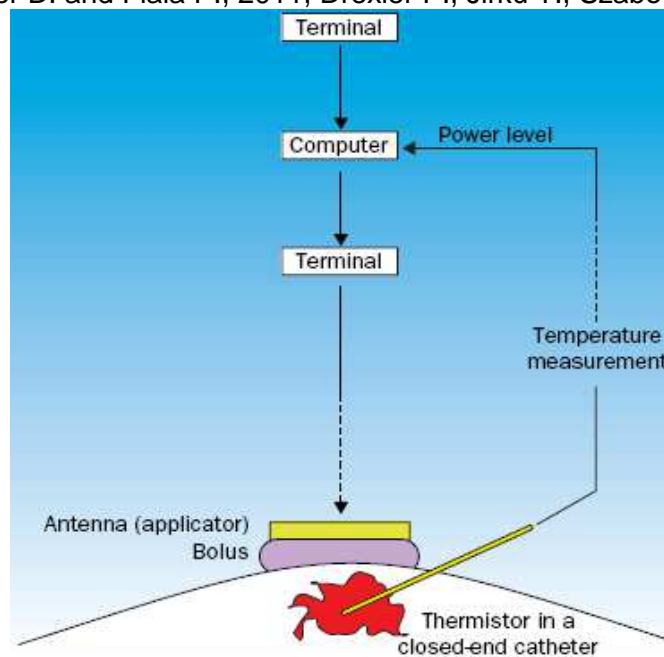


Figure 2. Scheme of a system for local hyperthermia. The applicator position and power output may vary until a clinically satisfactory adjustment is achieved Wust P, Hildebrandt B, et al. ,2002

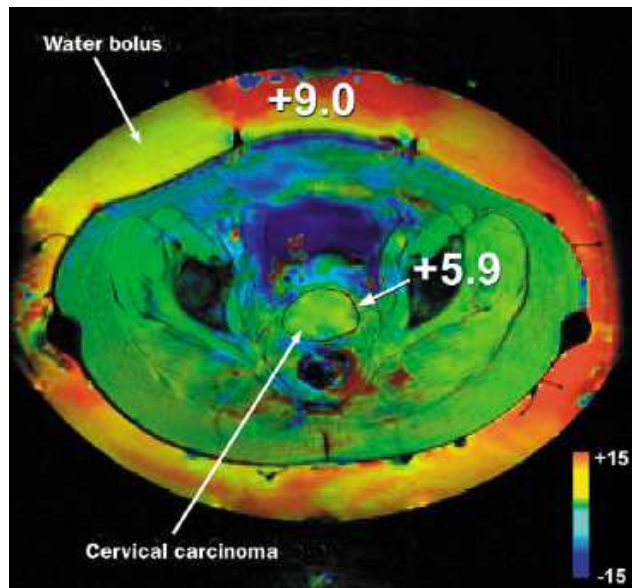


Figure 3. Non-invasive measurement of temperature distribution in the hybrid hyperthermia applicator Wust P, Hildebrandt B, et al. ,2002.

$$\Delta u = C_{t0} \frac{\partial^2 u}{\partial t^2} + C_{t1} \frac{\partial u}{\partial t} + C_{t2} u + C_{t3} . \quad (1)$$

(1): The electric component incident wave, according to Figure 4, is according to formula

$$\mathbf{E}_i = \mathbf{E}_0 e^{-jk_1 \mathbf{u}_{n0} \cdot \mathbf{r}}, \quad (2)$$

where \mathbf{k} is the complex wave number

$$\mathbf{k} = \sqrt{j\omega\mu \cdot (\gamma + j\omega\varepsilon)}, \quad (3)$$

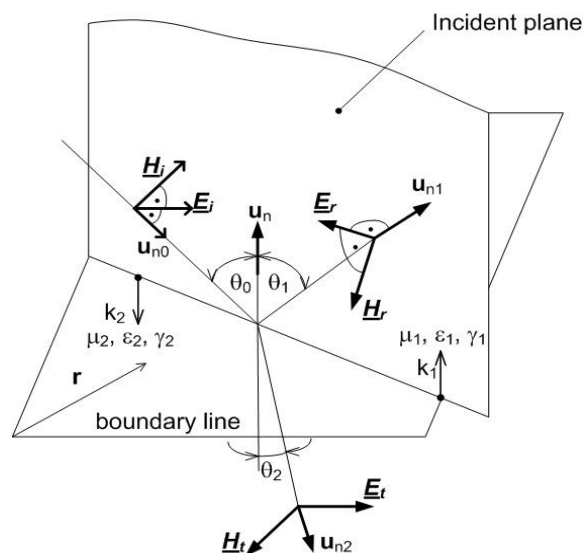


Figure 4: The reflection and refraction of light [9]

where γ is the conductivity, ε the permittivity and μ the permeability. Relation (1) is defining for the boundary line between the dielectrics medium. Generally, \mathbf{k}_1 and \mathbf{k}_2 is

complex; then angle θ_2 is complex. The propagation of the electromagnetic wave is understood as the propagation of electric field strength and magnetic field strength.

$$\mathbf{E}_r = \mathbf{E}_1 e^{-jk_1 u_{n1} \cdot r}, \quad \mathbf{E}_t = \mathbf{E}_2 e^{-jk_2 u_{n2} \cdot r}, \quad (4)$$

where \mathbf{E}_0 is the amplitude of electric field strength on the boundary line, \mathbf{r} is the positional vector and \mathbf{u}_{n0} is the unit vector of the direction of propagation. For numerical modelling, there is a suitable relation in the form of

$$\mathbf{E}_r = \frac{\mu_2 k_1 \cos \theta_0 - \mu_1 \sqrt{k_2^2 - k_1^2 \sin^2 \theta_0}}{\mu_2 k_1 \cos \theta_0 + \mu_1 \sqrt{k_2^2 - k_1^2 \sin^2 \theta_0}} \mathbf{E}_0 \cdot e^{-jk_1 u_{n1} \cdot r},$$

$$\mathbf{E}_t = \frac{2\mu_2 k_1 \cos \theta_0}{\mu_2 k_1 \cos \theta_0 + \mu_1 \sqrt{k_2^2 - k_1^2 \sin^2 \theta_0}} \mathbf{E}_0 \cdot e^{-jk_2 u_{n2} \cdot r}. \quad (5)$$

In view of the given problem, it is important to remain within the model of electromagnetic wave propagation (5) respecting the complex character of magnetic permeability μ and electric permittivity ϵ . However, these material parameters of the environment are the functions of temperature and frequency MARCOŇ P., BARTUŠEK K., BURDKOVÁ M., DOKOUPIL Z.,2011, MARCOŇ P., BARTUŠEK K., ČÁP M.,2011, KUBÁSEK R., BARTUŠEK K., FIALA P.,2010.

$$\epsilon = \epsilon(T, f), \quad \mu = \mu(T, f) . \quad (6)$$

In respect of these forms of material characteristics, an optimum heating method can be proposed for a small increase in temperature as already applied in the field of hyperthermic therapy. These characteristics were respected in the emulsion microwave heating with a phase change of materials Drexler P., Jirku T., Szabo Z. et al.,2007.

4 Heating Test in the Numerical Model

The described model (1) having the given characteristics (6) was tested in the numerical model using the finite element method. The geometrical model was simplified to a phantom according to Figure 5.

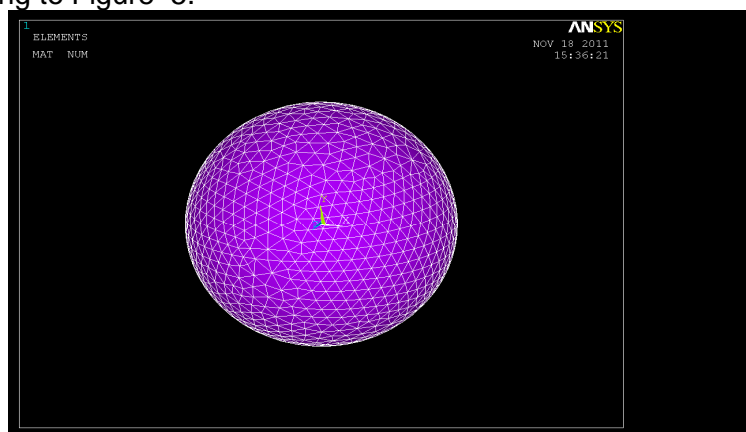


Figure 5: A phantom of the human head- numerical model

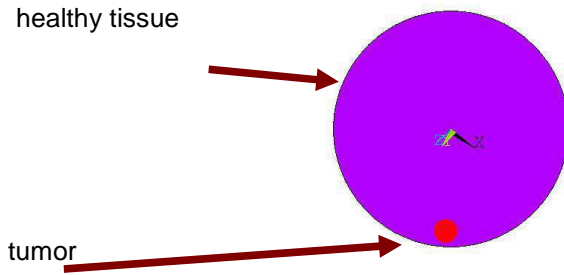


Figure 6. A phantom of the human head – the non-homogeneity position

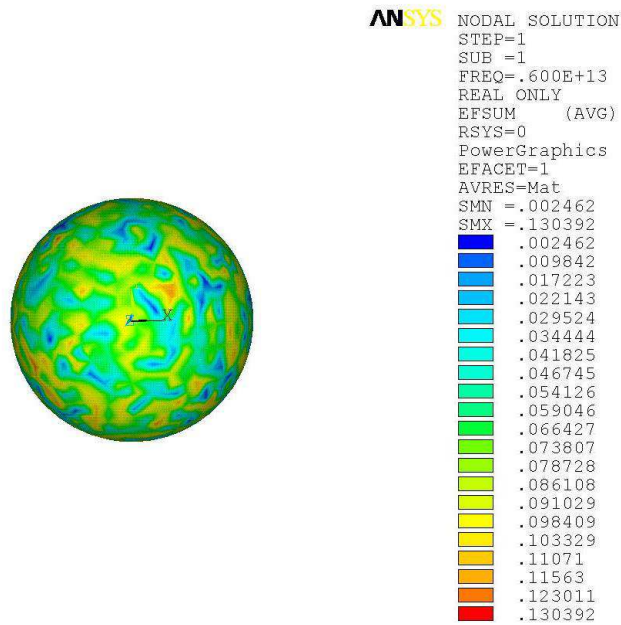


Figure 7. A phantom of the human head – result , distribution of the electric intensity E module , max=6THz

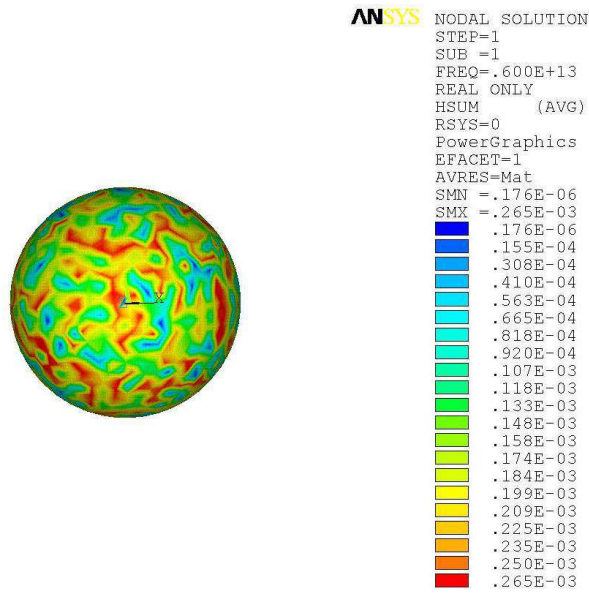


Figure 8. A phantom of the human head – result , distribution of the magnetic intensity H module , max=6THz

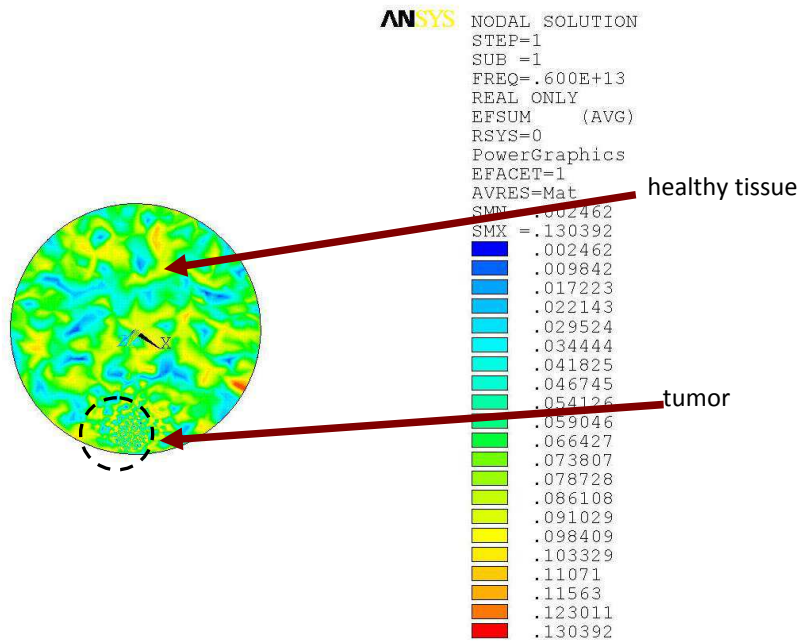


Figure 9. A phantom of the human head – result , distribution of the electric intensity E module , max=6THz

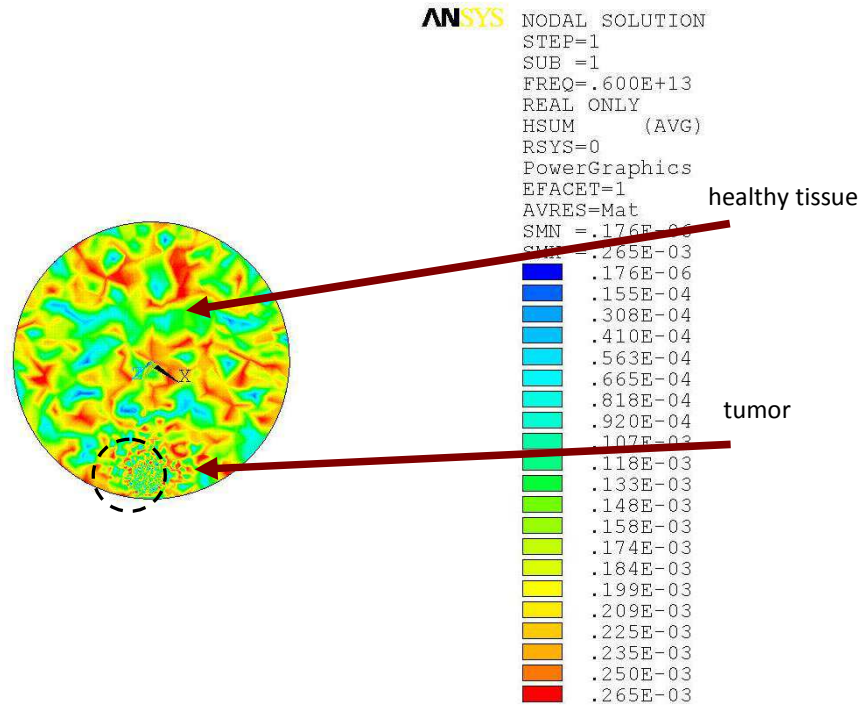


Figure 10. A phantom of the human head – result , distribution of the magnetic intensity H module , max=6THz

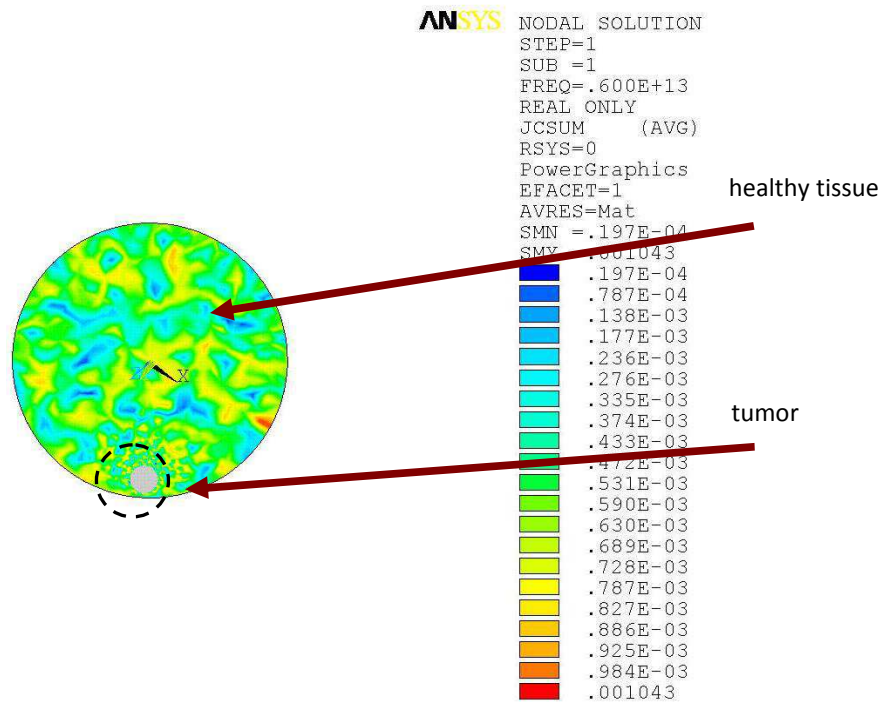


Figure 11. A phantom of the human head – result , distribution of the current density J module , max=6THz

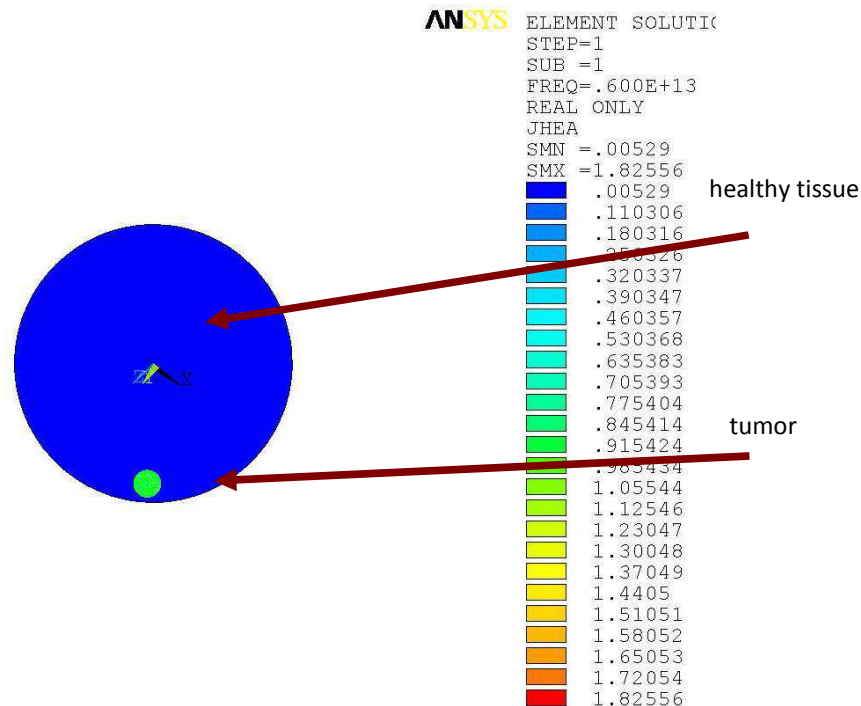


Figure 12. A phantom of the human head – result , distribution of the joule heat generation J_{he} module , max=6THz

The analysis of numerical modeling, results evaluation of field distribution are shown in Figures 7 -12.

5 Conclusion

Using the inversion problem method, the numerical model reconstructs such signal and electromagnetic pulse shape that will only provide for local heating of the carcinoma tissue, with the surrounding tissue not subject to heating by the source of the electromagnetic wave. This shape of the electromagnetic field can be applied, without any spurious effects resulting from hyperthermia, to specific conditions of individual tissue disorder cases.

Acknowledgement- The research described in the paper was financially supported by a grant of the Czech Science Foundation GACR 102/09/0314, a project of the BUT Foundation Agency FEKT-S-10-13 and EC and MEYS CR, project No. CZ.1.05/2.1.00/01.0017.

REFERENCES

Bull JMC. ,1984, *An update on the anticancer effects of a combination of chemotherapy and hyperthermia.* Cancer Res 1984; 44 (suppl): 4853–56, <http://www.ncbi.nlm.nih.gov/pubmed/6205752>

Drexler P., Jirku T., Szabo Z. et al.,2007, [Model of a reactor chamber with microwave heating](#),Kong J.A. Conference: **Progress in Electromagnetics Research Symposium (PIERS 2007)** , Beijing, PEOPLES R. CHINA ,MAR 26-30, 2007, Electromagnet Acad Source: Piers 2007 Beijing: Progress in Electromagnetics Research Symposium, Pts I and II, Proceedings , Pages: **399-402** , ISSN 1931-7360.

Kadlec R., Kroutilova E., Nesor D. and Fiala P., 2011, *EM Wave Propagation in Layered Heterogeneous Medium*, Kong J.A. Conference: **Progress in Electromagnetics Research Symposium (PIERS 2011), Marakesh ,MAR 26-30, 2011, Electromagnet Acad** Source: Piers 2011, Progress in Electromagnetics Research Symposium, ISSN 1931-7360.

KUBÁSEK R., BARTUŠEK K., FIALA P.,2010, *Determination of pre- emphasis constants for eddy current reduction*. Measurement Science and Technology, vol. 2010, no. 21, s. 1-9. ISSN: 0957- 0233.

MARCOŇ P., BARTUŠEK K., BURDKOVÁ M., DOKOUPIL Z.,2011, *Magnetic susceptibility measurement using 2D magnetic resonance imaging*. Measurement Science and Technology, vol. 2011, no. 22, pg. 1-8. ISSN: 0957- 0233.

MARCOŇ P., BARTUŠEK K., ČÁP M.,2011, *Modeling and Measuring of the Changes of the Magnetic Field Next to Non- Ferromagnetic Substances for Magnetic Susceptibility Calculation*. In Measurement 2011. Bratislava: Institute of Measurement Sciences, 2011. s. 213-216. ISBN: 978-80-969672-4- 7.

MIKULKA J., GESCHIEDTOVÁ E., BARTUŠEK K.,2011, *Interpolation of 3D Magnetic Resonance Data*. PIERS ONLINE, 2011, roč. 7, č. 1, s. 31-34. ISSN: 1931- 7360.

Urano M, Kuroda M, Nishimura Y. ,1999, *For the clinical application of thermochemotherapy given at mild temperatures*. Int J Hyperthermia, vo.15, pg. 79–107, <http://www.ncbi.nlm.nih.gov/pubmed/10323618>.

Wust P, Hildebrandt B, et al. ,2002, [Hyperthermia in combined treatment of cancer](#). Lancet Oncol. 2002 Aug;3(8):487-97. Review.THE LANCET Oncology Vol 3 August 2002, <http://oncology.thelancet.com>, Pages 487-497, ISSN 1470-2045, 10.1016/S1470-2045(02)00818-5. (<http://www.sciencedirect.com/science/article/pii/S1470204502008185>)

Contact address:

assoc.prof. Ing.Pavel Fiala, Ph.D.,
prof. Ing. Karel Bartusek, DrSc.,
Ing. Michael Hanzelka, MBA

Brno university of technology, Faculty of electrical engineering and communication, Department of theoretical and experimental electrical engineering Kolejní 2906/4, 612 00 Brno, Czech Republic
fialap@feec.vutbr.cz, bar@feec.vutbr.cz, michael.hanzelka@daccee.eu

NUMERICAL MODELING, SENSORS AND EXPERIMENTAL MODEL DEVELOPMENT FOR PARTIAL DISCHARGE LOCALIZATION IN HIGH VOLTAGE TRANSFORMERS

PETR DREXLER, PAVEL FIALA, ZOLTAN SZABO, MICHAEL HANZELKA

Brno university of technology, Faculty of electrical engineering and communication,
Department of theoretical and experimental electrical engineering, Czech Republic

Abstract: The aim of this paper is to present an antenna-based sensors which have been designed numerical analysed and built for partial discharge (PD) detection. PD is characterized by the electromagnetic wave radiation in ultra high frequency (UHF) band. The sensors have been designed to meet the frequency requirements for PD detection and the frequency dependence of SWR is presented for three types of sensor. For the experimental verification of localization method a model setup has been built. The model setup is equipped with antenna sensors, RF amplifiers and data acquisition unit. The model setup is described in the paper as a following step of the research. The result of the measurement which has been performed up to the present are presented also.

Keywords: Numerical modelling, noise, non-linear, permittivity, oil, dielectric, electric discharge, electromagnetic field, signal, impulse, wave.

1 INTRODUCTION

One of the problematic phenomena in the field of high-voltage technology, is the occurrence of partial discharge (PD). Several other effects have combined with this notion over time Fiala P.,1999. In consequence of these effects there emerge short electromagnetic pulses with a defined and measurable spectrum in the characteristic frequency band Sarathi R., Reid A.J., Judd M.D.,2008.. The group of end products attributable to the emergence of interfering signals involves, for example, displacement current in a dielectric, pulse current on the interface between dielectrics, or the dielectric/metal interface owing to high electric field intensity and structure of the dielectric.

In HV and VHV transformers the dielectric is mineral or synthetic oil. Due to the increase in PD activity in transformer oil free atoms of carbon, hydrogen and oxygen develop from hydrocarbons, and there also generates a certain percentage of water and other organic compounds. All of these elements decrease the quality of the dielectric. In addition to that, rapid increase in pulse activity may cause the formation of a hazardous explosive compound of oxygen and hydrogen. Then, this situation may result in explosion and damage to the device.

In order to prevent the transformer failure the observation of pulse activity is necessary. The occurrence of discharge with substantial charge transport level can be localized in critical areas of the transformers. Having a possibility to localize the increased discharge activity in some of the critical areas allows us to undertake precautions in order to avoid the critical transformer failure. The discharge activity localization can be determined on

the basis of processing of signals from suitable installed sensors. The evaluation of the discharge location utilizes the model of wave propagation inside the transformer, which has been presented in early work Fiala P., Drexler P., Jirku T.,2010.

2 NUMERICAL MODEL

The results of research in the field of PD activity detection are presented in this paper as subsequent steps in the PD detection concept development. In the previous work the analysis of electromagnetic field inside the transformers dielectric parts has been performed Fiala P., Jirku T., Drexler P., 2009. For the analysis purposes the finite element method (FEM) has been used. The geometric model of high voltage power transformer was built and the FEM representation of the model is shown in Figure 1.

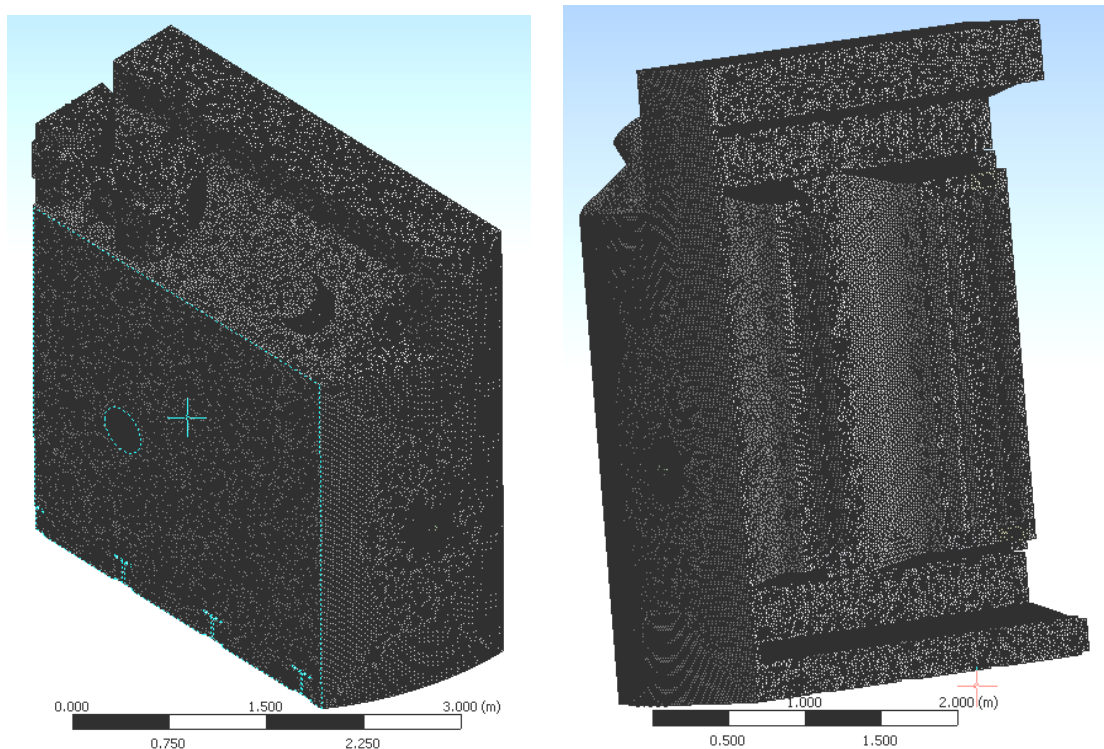


Figure 1. The geometrical/FEM model of the transformer

The critical increase in the PD activity can be evaluated as minimum required signal level on selected discrete frequencies in the output signal spectrum. For the detection of PD activity in the UHF band suitable sensors has to be chosen. The frequency characteristic of sensors should be accordant with radiated PD signal spectrum.

3 UHF SENSING

The sensors of electromagnetic field which can be used for PD detection has been described in report Fiala P., Jirku T., Drexler P., 2009. According to their properties and according to required frequency range suitable sensors have been chosen for verification on experimental setup. The general experimental setup is shown in Figure 2. This setup has been used by Kaneiwa H., Suzuoki Y. and Mizutan T., 2001 or Sarathi R., Reid A.J., Judd M.D.,2008.

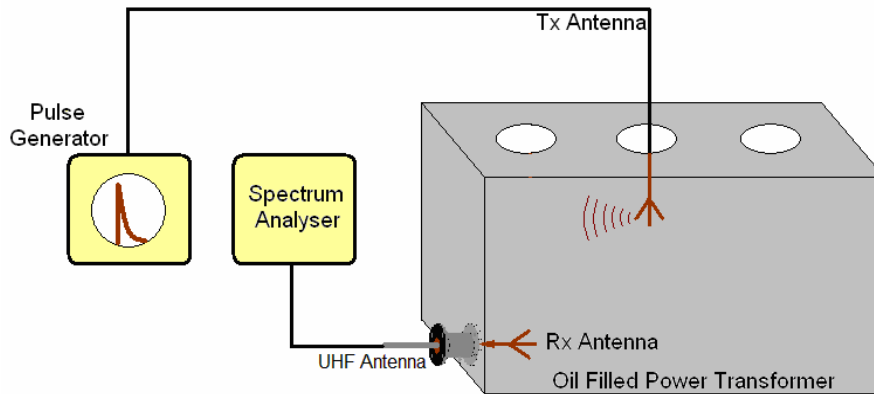


Figure 2. The experimental setup for sensor verification in PD detection system.

4 MATHEMATICAL MODEL

It is possible to carry out an analysis of an MG model as a numerical solution by means of the Finite element method (FEM). The electromagnetic part of the model is based on the solution of full Maxwell's equations. The results of the FEM analysis of the transformers ,Fiala P., Jirku T., Drexler P., 2009, have been utilized for the verification of sensors emplacement convenience. Suggested sensors emplacement is shown in Figure 3 and example of numerical model analysis electric intensity attenuation, results and its interpretation are shown in Figure 4- Figure 13.

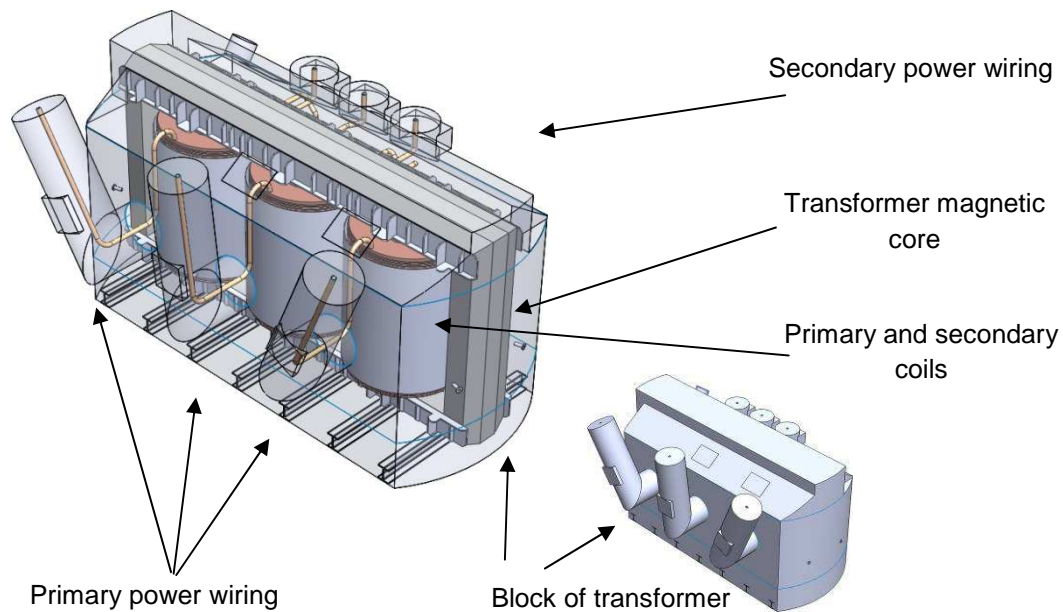


Figure 3. The geometrical transformer model

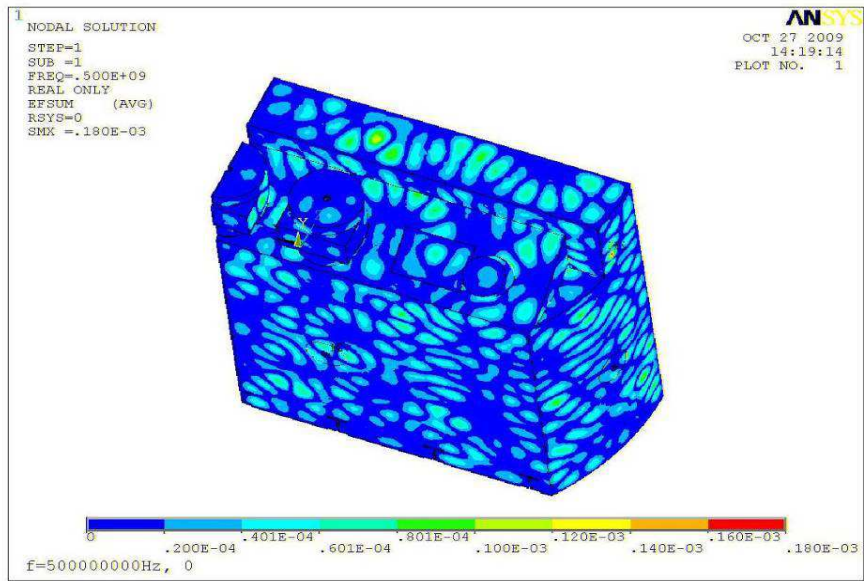


Figure 4. The electric intensity module E distribution. $E_{db} \in <-38.6;0>dB$

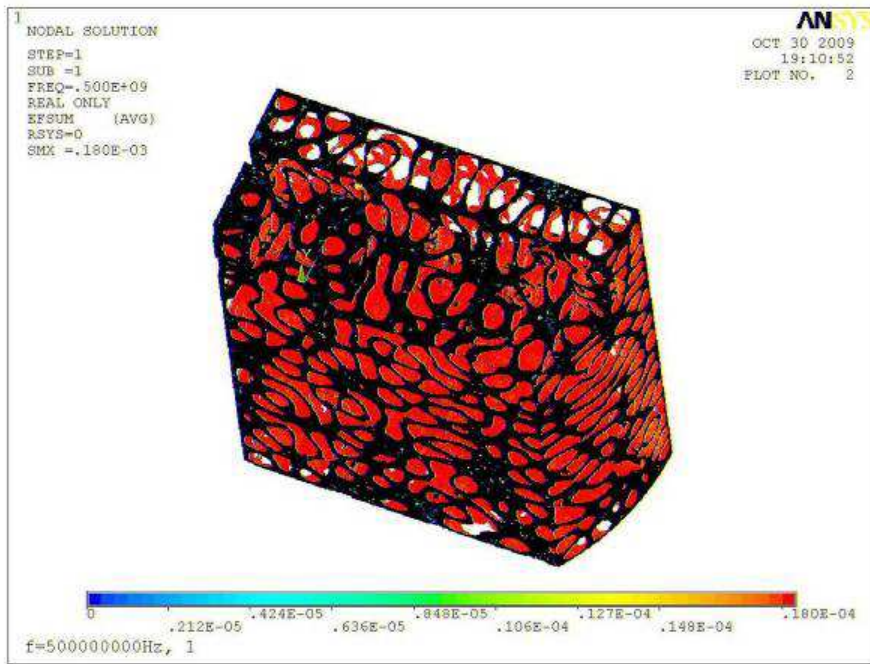


Figure 5. The electric intensity module E distribution. $E_{db} \in <-58.6;-20>dB$

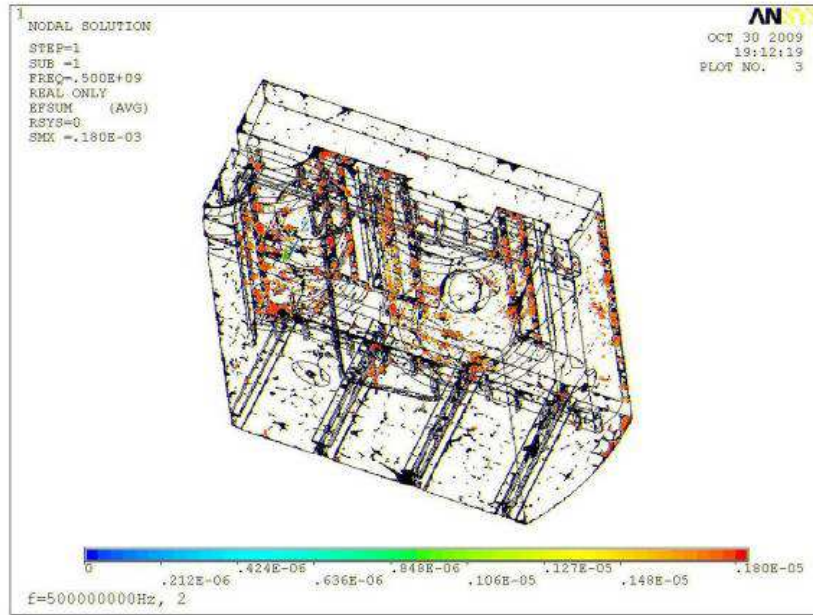


Figure 6. The electric intensity module E distribution. $E_{db} \in \langle -78.6; -40 \rangle dB$

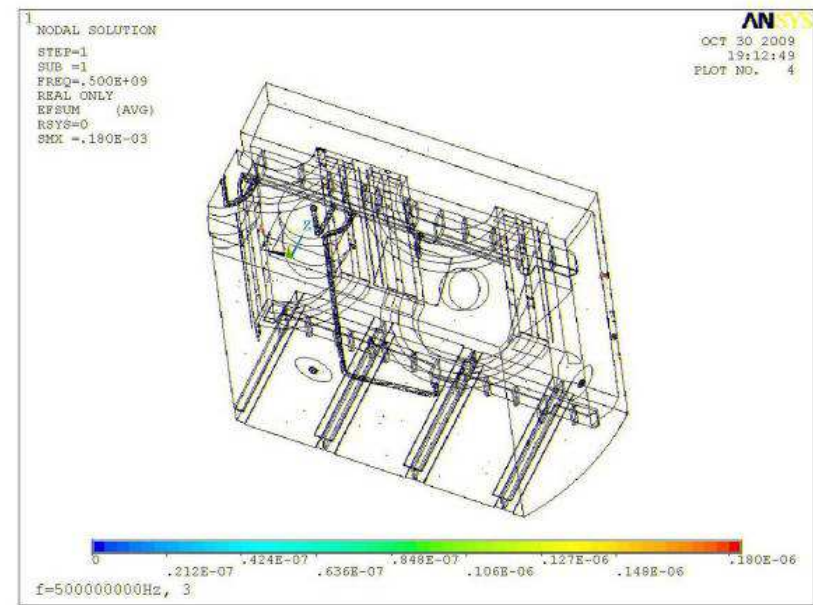


Figure 7. The electric intensity module E distribution. $E_{db} \in \langle -98.6; -60 \rangle dB$

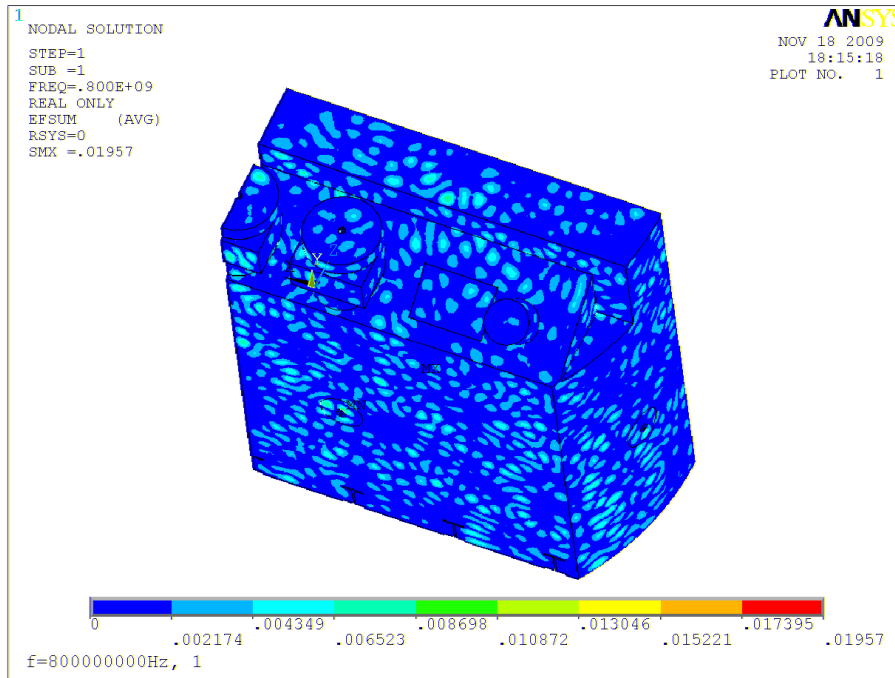


Figure 9. The electric intensity module E distribution. $E_{db} \in <-38.6;0>dB$, $f=800MHz$

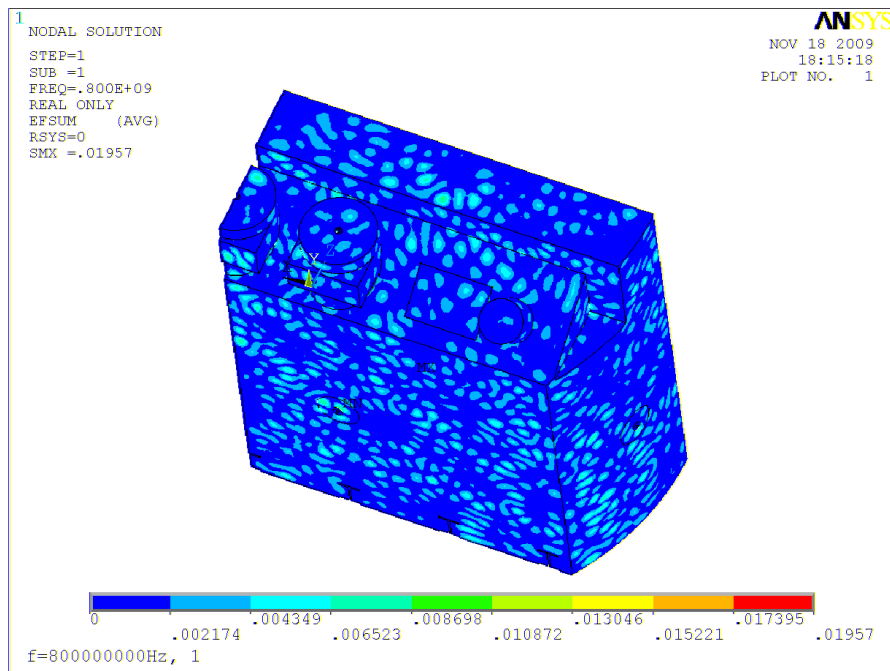


Figure 10. The electric intensity module E distribution. $E_{db} \in <-38.6;0>dB$, $f=1000MHz$

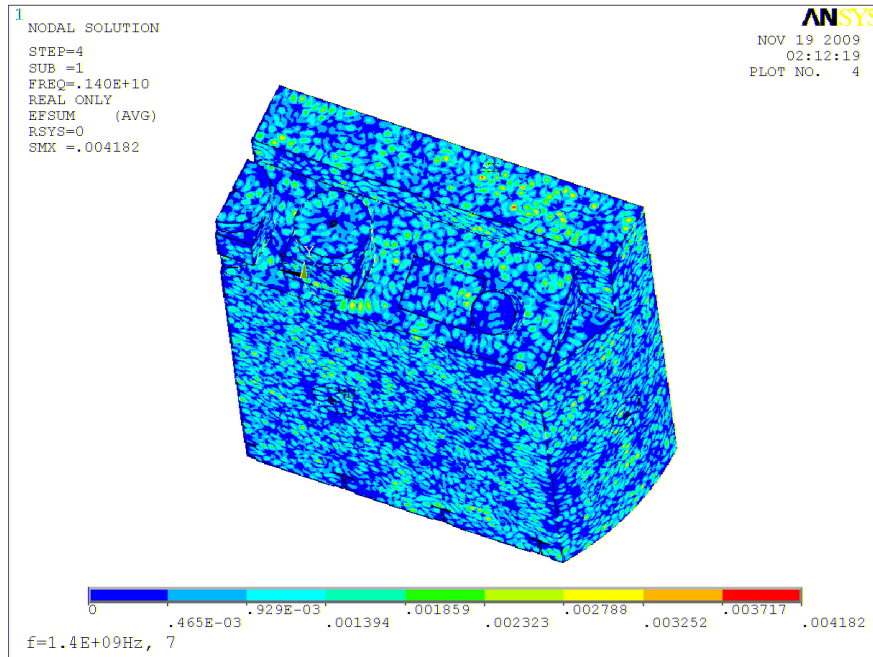


Figure 11. The electric intensity module E distribution. $E_{db} \in <-38.6;0>dB$, $f=1400MHz$

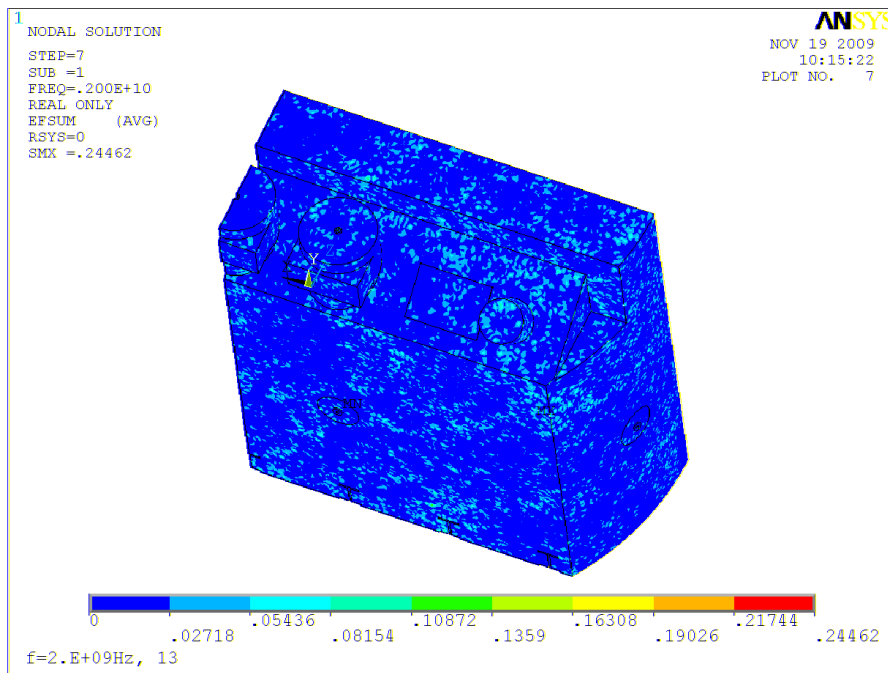


Figure 12. The electric intensity module E distribution. $E_{db} \in <-38.6;0>dB$, $f=2000MHz$

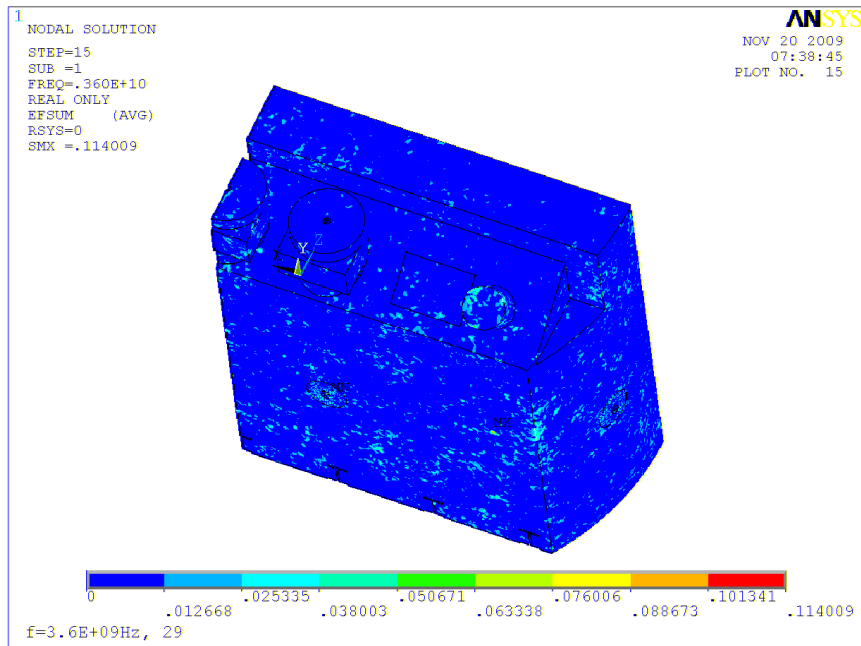


Figure 13. The electric intensity module E distribution. $E_{db} \in <-38.6;0>dB$, $f=3600MHz$

5 MEASUREMENT MODEL SETUP

For the evaluation of PD detection and localization the measurement model has been designed and built. The model is based on the oil filled metal tank which is box-shaped. The tests tank contains 230 l of transformer oil. Four inserts are assembled on the wall of the tank. The inserts are in the form of cylinder cavity and they allows to put the antennas inside in order to be able to collect PD radiated RF energy. The oil tank is shown in the left of the Figure 14. In the uper of Figure 14 the antennas positions in the tests tank with their labels are shown also. The tank is equipped with the metal cover which can be removed to insert additional objects with specified material properties $\epsilon_{r,n}$, $\mu_{r,n}$ and $\gamma_{r,n}$ inside the tank. The insertion of additional objects allows to observe changes in signal time relations which are caused by the additional reflections on the walls and different propagation velocities in the objects and at their boundaries.

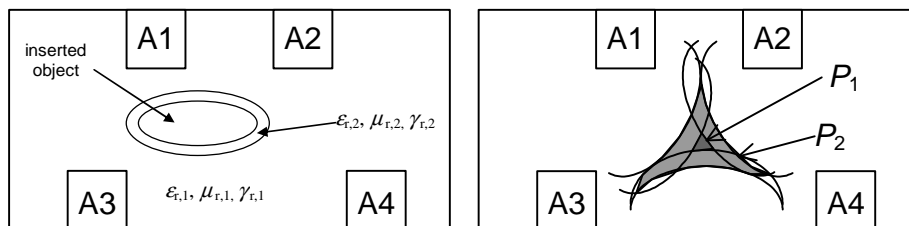


Figure 14. Tank with inserts for antennas (up), position of antennas with labels (left), PD occurrence areas (right).

The presence of objects with properties different to the oil environment (left of Figure 14) causes the propagation of waves with different wave numbers \bar{k}_n in compare to the primary wave number \bar{k}_1

$$\bar{k}_1 = \sqrt{-j\omega_1\mu_1(\gamma + j\omega_1\epsilon_1)}; \bar{k}_n = \sqrt{-j\omega_n\mu_n(\gamma + j\omega_n\epsilon_n)}. \quad (1)$$

Considering the known configuration of the model (or the HV transformer) there is a possibility to determine the probability areas of PD occurrence by means of the numerical model evaluation. The example of probabilities P_1, \dots, P_n areas are shown in the right part of Figure 14 for P_1 and P_2 .

The basic properties of proposed antenna sensors have been presented in [3]. From these sensors the cone-type antenna and the Vivaldi-type antenna has been chosen for further experiments in oil tank. In order to get an idea about the wave propagation inside the oil filled tank with regard to spectral characteristic of this model the measurement of insertion loss has been performed. The measurement has been performed for various positions of transmitting (TX) antenna and the receiving (RX) antenna in the inserts. For example, the TX antenna was placed in insert A1 and the insertion loss has been measured for the position of RX antenna in insert A2, A3 and A4. In the next step the TX antenna has been moved into the insert A2 etc. Special attention was given to the Vivaldi antenna. The Vivaldi-type antenna belongs to linear polarization antennas. Hence a various mutual positions of antennas polarization planes were examined. The polarization planes have been placing to horizontal and to vertical positions during the experiment. The results of this measurement show that there is no distinctive effect of the TX and RX antennas position, eventually the mutual polarizations orientation, on spectral characteristic of the tank oil environment insertion loss. The character of the results is probably caused by the presence of multiple wave reflections on the tank walls. The example of the insertion loss frequency characteristic for the TX cone-type antenna in position A1 and the RX cone-type antenna in position A4 is shown in Figure 15. It should be noted that the insertion loss characteristic contains the frequency characteristics of both antennas also.

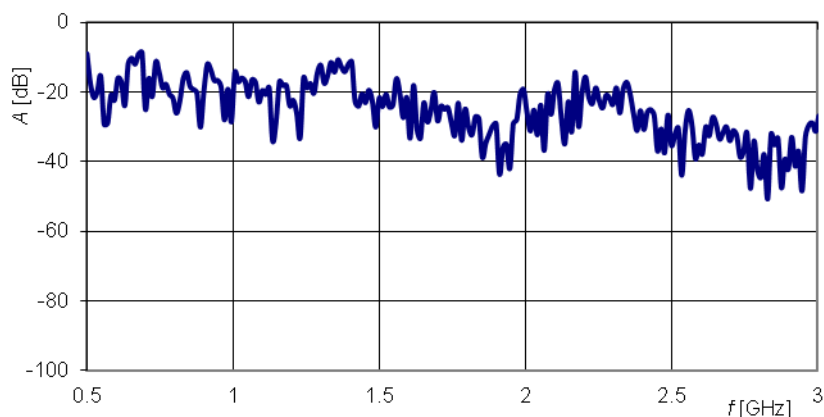


Figure 15. The example of insertion loss frequency characteristic of the measurement model.

6 TIME DOMAIN MEASUREMENT

We can localize the area of the PD activity by evaluating the time relation of the signal received on antennas. The verification of the time-of-arrival difference in different receiving channels has been made by means of short testing pulse. The testing pulse was

applied on the TX antenna and the signals on the remaining RX antennas were captured. The positions of the antennas in the measurement model have been designed in the way that the distances of three RX antennas to the TX antenna are mutually different. TX antenna has been placed in the position A1. RX antennas have occupied positions A2, A3 and A4 in Figure 14. A negative short pulse of electrical voltage with the peak level of approx. -6 V was fed in TX antenna in position A1. The pulse was supplied by the pulse generator based on the avalanche effect in the RF transistor in the transition from saturation into the off-state. The pulse fall time is $t_f = 370$ ps, rise time is $t_r = 880$ ps and the pulse width is $t_w = 650$ ps. The pulse waveform is shown in the left part of Figure 3. In order to preserve the time-of-arrival differences the cables between the RX antennas and the acquiring device were of the same length. The signals on the receiving antennas were captured by the digital storage oscilloscope with the sampling rate 2 GSa/s and with the analog bandwidth of 1 GHz. The captured waveforms are shown in the right part of Figure 16.

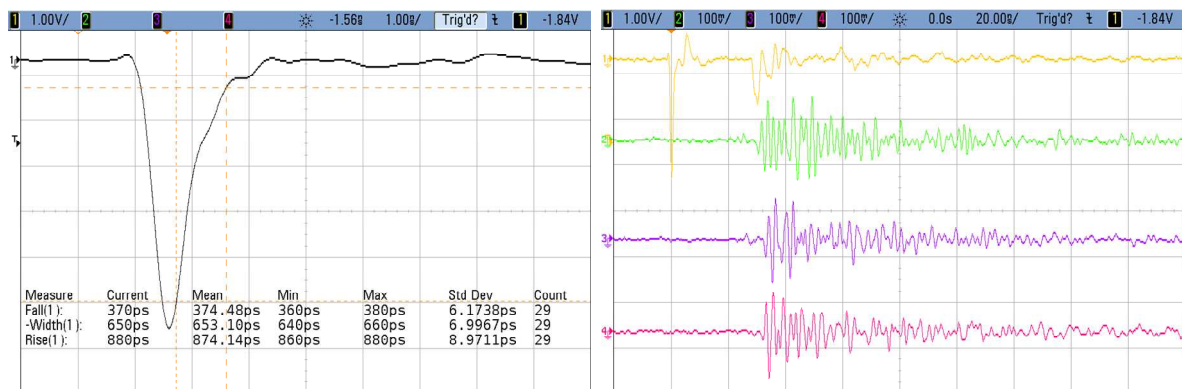


Figure 16. The pulse waveform for the time-of-arrival difference verification (left) and captured waveforms of signals at the RX antennas (right).

In channel 1 (the top waveform) a waveform of excitation pulse is shown. The output signals of RX antennas are shown in the rest of the channels. Due to the propagation in cavity with conducting walls a considerable amount of multiple reflections can be observed in the RX channels. However, for the signals time relations evaluation the occurrence of the first remarkable transient has to be watched. The details of the front-end transients in the RX channels are shown in Figure 17. The received pulse signal is represented by the negative going transients, whose time of occurrence difference is in order of nanoseconds. The time difference is a function of the propagation velocity which can be calculated for the oil environment with defined dielectric constant. The sequence of the front-end transients is in agreement with the distances between the TX antenna and RX antennas.

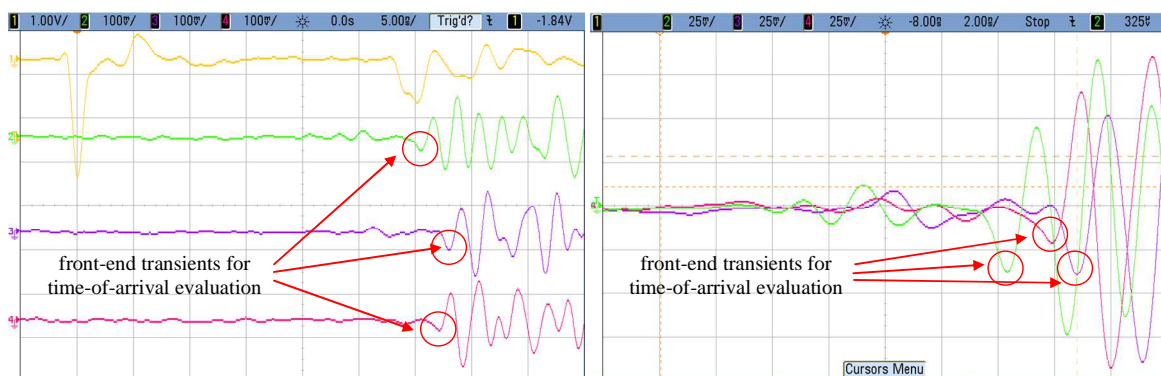


Figure 17. Detail of front-end transients for time-of-arrival evaluation.

It should be noted the even in the case of a small dimensions of the measurement model the time differences between the signals are measurable. In the target application the

dimensions of the transformer to be watched are much greater which results in greater time differences also. A substantial is the fact the in the real application the direct visibility between the area of PD occurrence and the receiving point is not guaranteed. This fundamental issue causes that remarkable transient can be received after a number of reflections. This can introduce a several delay even if the PD occurrence area is close to the receiving antenna. The solution of the PD occurrence location can be evaluated by means of the numerical model which has been presented in previous work [3]. This effect can be modeled by inserting of additional walls into the oil tank which is the goal of further research.

7 MEASUREMENT OF SIMULATED PARTIAL DISCHARGE

In order to test the designed detection system in the measurement model a need for suitable discharge source occurs. A spark-gap with low breakdown voltage has been proposed. Due to the low level of charge transport during the PD activity in order of 10^{-10} C the low breakdown voltage is required in order to get the similar charge transport level. The spark-gap consists in two tungsten electrodes of sharp-tip shape to maximize the field intensity in the gap. The gap distance, Figure 18., has been set to 0,1 mm.

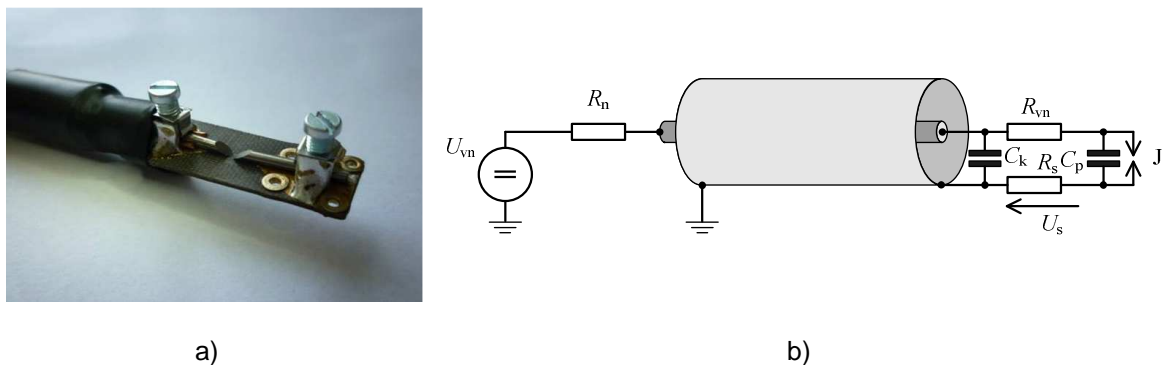


Figure 18. a) Spark-gap construction and b) schematic diagram of spark-gap

The spark-gap has been placed in the oil tank and the electromagnetic radiation of the discharge has been captured by means of four antenna sensors. The waveform and the spectrum of the spark-gap discharge should approximate the characteristic of the partial discharge. The waveform and the spectrum of the PD radiation is shown in Figure 19. The signal has been obtained by measurement on real high voltage transformer during the PD.

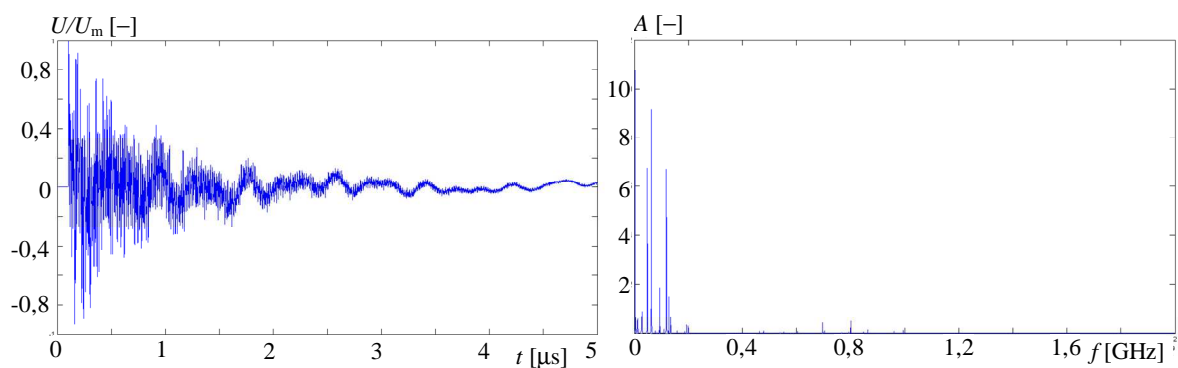


Figure 19. Waveform (left) and spectrum (right) of the PD radiated signal.

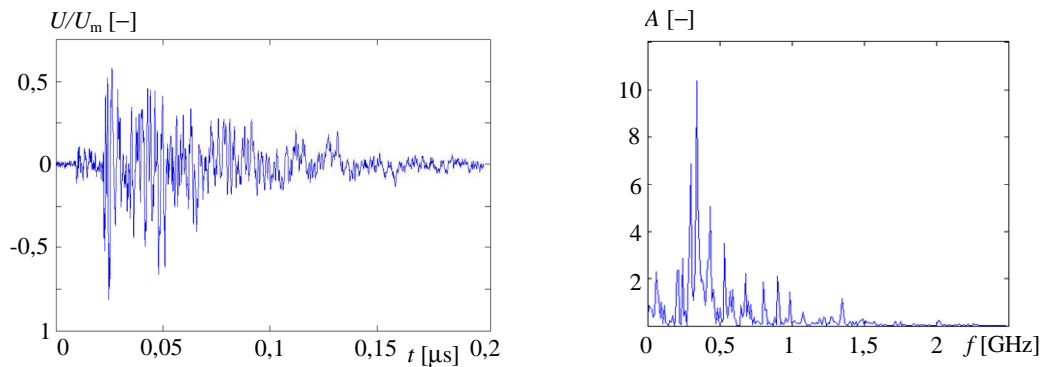


Figure 20. Waveform (left) and spectrum (right) of the spark-gap discharge radiated signal.

The characteristics obtained by measurement of the spark-gap discharge in the oil tank are shown in Figure 20. The differences in the characteristics in Figure 19 and Figure 20 are obvious. The PD waveform has longer time duration in compare to spark-gap discharge waveform. The next difference is the content of harmonic components. The most of the power is carried by the harmonic components on frequencies in range 10 – 200 MHz. While the waveform of the spark-gap discharge has shorter time duration and the frequency content is also different. The most of the signal power is carried by frequencies of hundreds of MHz. Components with frequencies up to 2 GHz are present also.

8 EXPERIMENTAL TIME DOMAIN MEASUREMENT

We can localize the area of the PD activity by evaluating the time relation of the signal received on antennas inside a transformer. The measuring was realized in nuclear power plant Czech Republic, as can be seen on Figure. 21.



Figure 21 Measuring setup in nuclear power plant

A negative short pulse of electrical voltage with the peak level of approx. -6 V was fed in TX antenna. The pulse fall time is $t_f = 370$ ps, rise time is $t_r = 880$ ps and the pulse width is $t_w = 650$ ps. The captured waveforms are shown in the right part of Figure 22.

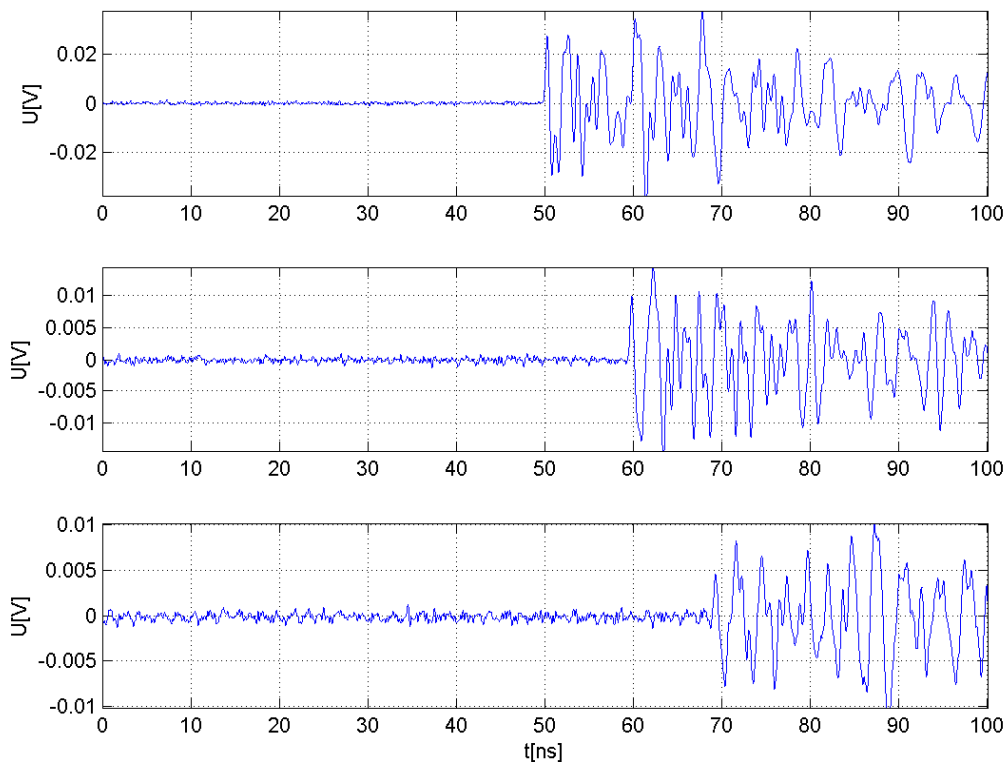


Figure 22. The captured waveforms from RX antennas

The ground of scanning channels was connected to the body of transformer. Due to the propagation in cavity with conducting walls a considerable amount of multiple reflections can be observed in the RX channels. However, for the signals time relations evaluation the occurrence of the first remarkable transient has to be watched.

The solution of the PD occurrence location can be evaluated by means of the numerical model which has been presented in previous work Fiala P., Drexler P., Jirku T., 2010. This effect can be modeled by inserting of additional walls into the oil tank which is the goal of further research.

9 CONCLUSIONS

The description of the numerical analysis and measurement model for PD detection and localization method evaluation is presented in the paper. The spectral transmission characteristic of the model equipped with antenna sensor is shown further. In order to demonstrate the ability of transients time-of-arrival resolving the time domain measurement has been performed. Simulated discharge is compared to the real PD acquisition. Regarding to differences another discharge source should be intended which is a part of further research. The designed circuitry for RF signal processing is a point of subsequent publication.

ACKNOWLEDGEMENT

The research described in the paper was supported by grant of Czech ministry of industry and trade no. FR-T11/001 and project of the BUT Grant Agency FEKT-S-10-13.

REFERENCES

Fiala P.,1999, *Transformer partial discharge modeling, minimal breakdown value set in a critical parts of transformer design*, Research report, Laboratory of modeling and optimization fields in electromagnetic systems, FEI VUT and ABB EJV a.s. Brno no.2/99, 18.3.1999, Brno, Czech Republic.

Fiala P., Drexler P., Jirku T.,2010, *Detection of partial discharge inside of hv transformer, modeling, sensors and measurement*. In Proceedings of Progress In Electromagnetics Research Symposium PIERS 2010, pp. 909-912, USA: Cambridge, **ISSN 1559-9450**.

Fiala P., Jirku T., Drexler P., 2009, *Discharge activities detection inside of power transformer oil: Detection method*, Numerical model analysis, design. Research report, DTEEE FEEC BUT, Laboratory of modeling and optimization fields in electromagnetic systems, FEI VUT and ABB EJV a.s. , Czech Republic.

Kaneiwa H., Suzuoki Y. and Mizutan T., 2001, *Characteristics of Partial Discharges, Artificial Simulated Tree Channels During in Tree Propagation*, IEEE Transactions on Dielectrics and Electrical Insulation, vol. 8, no. 1, ISSN 1070-9878

Sarathi R., Reid A.J., Judd M.D.,2008, *Partial discharge study in transformer oil due to particle movement under DC voltage using the UHF technique*, Electric Power Systems Research 78 , pp. 1819-1825, Elsevier, ISSN 0378-7796.

Contact address:

assoc.prof. Ing.Petr Drexler, Ph.D.,
assoc.prof. Ing.Pavel Fiala, Ph.D.,
Ing. Zoltan Szabo
Ing. Michael Hanzelka, MBA

Brno university of technology, Faculty of electrical engineering and communication, Department of theoretical and experimental electrical engineering Kolejní 2906/4, 612 00 Brno, Czech Republic
fialap@feec.vutbr.cz, drexler@feec.vutbr.cz, szabo@feec.vutbr.cz, michael.hanzelka@daccee.eu

NUMERICAL MODEL OF A SOLAR ELEMENT WITH CONTROLLED EFFICIENCY

PAVEL FIALA, DUSAN NESPOR, MICHAEL HANZELKA

Brno university of technology, Faculty of electrical engineering and communication,
Department of theoretical and experimental electrical engineering ,Czech Republic

Abstract: The authors propose an analysis of a model solar element based on the principle of a resonance system facilitating the transformation of the external form of impinging energy into electric energy. A similar principle provides the basis for harvesters designed to operate at lower frequencies Jirků T., Fiala P. and Kluge M.,2010, Wen J.L., Wen Z., Wong P.K., 2000 in these harvesters, the efficiency of the energy form transformation can be controlled from the frequency spectrum of an external source.)

Keywords: Solar, element, harvester, energy, tuned, periodical structure, controlled efficiency.

1 INTRODUCTION

Initial research studies in the field of mini- and microgenerators conceived as harvesters ,Stratton J.A. , 1961, mainly examined the problem of exploiting a form of energy from the mechanical motion of a system, with special regard paid to possible utilization of the energy for feeding the electronic components of the moving system.

The central issue in the part of the research related to this paper and chiefly solved in the WISE project (6-FP EU) was to develop an independent energy source for a temperature sensor (or other sensor types). The sensor has been applied in an NH-90 helicopter EUROCOPTER. From all the investigated solutions, the Vibration Micro-Generator (MG) was chosen as the independent energy source for the sensor. The MG can provide energy proportionally to the helicopter vibration on a specific resonant frequency Jirků T., Fiala P. and Kluge M.,2010, Wen J.L., Wen Z., Wong P.K., 2000.

2 TUNED STRUCTURES: The active part of a generator

Tuned structures were partially analyzed and developed in research study Jirků T., Fiala P. and Kluge M.,2010. Utilizing the semiconductor technology, the authors designed a resonant element (Fig. 1), Fiala P. and Jirku T., 2008, which satisfied the basic requirements for resonance (Fig. 2) on the wavelength of the impinging electromagnetic wave. Further conditions for function Jirků T., Fiala P. and Kluge M.,2010, Patent ,2006, no. PV-2006-571, Patent ,2006, no. PUV-2006-18391, Patent ,2007, no. PV 2007-331, Patent ,2011, no. PCT/CZ2011/000076 can be formulated as follows: In the course of impingement of an externally generated electromagnetic wave there must not emerge a stationary electromagnetic wave. The elementary resonator (Fig. 3) must pass into a resonant state and reach a multiple amplitude in desired parts of the resonant circuit: the transforming element, Fig. 3. The criterion must be met of the spectrum bandwidth of the impinging electromagnetic wave in order for the structure to be kept in the resonant state under the desired multiple of the impinging amplitude. The principle of the resonant circuit (Fig. 4) as a

method of converting electromagnetic field components to a processible level was already tested Fiala P. and Jirku T., 2008.

The principle of a resonance generator (RG) operation is based on the utilization of external vibrations. The basic conception of energy transformation can be described by means of Faraday's law Kikuchir H., 2001, Stratton J.A. , 1961, Patent ,2006, no. PV-2006-571, Patent ,2006, no. PUV-2006-18391, Patent ,2007, no. PV 2007-331, Patent ,2011, no. PCT/CZ2011/000076. The required output power depends on the type of output load, namely on the used impedance. The basic arrangement of the RG is provided in Fig. 4. The generator was conceived on the basis of magnetic field variations owing to mechanical vibrations, and the non-stationary electromagnetic field was excited through the variation of magnetic field in the preset magnetic circuit. The vibrational generator (VG) body is tightly connected with the vibration source; for us, for example in an airplane fuselage and in association with the oscillation of the whole system, the VG core starts moving with respect to the fuselage activity. The mechanical part of the VG is designed in such a manner that the VG core driven by external vibrations performs non-damped oscillations. The design of the VG enables the oscillations of the VG core to fit within a comparatively wide spectrum of external oscillation frequencies. The operation of the VG is based on Faraday's law. The core, which contains ferromagnetic parts and permanent magnets (with a high density of the stored energy, e.g. FeNdB, SmCo), moves with respect to the winding connected to the shell and induces a voltage in it. In relation to this, the connected external current starts carrying a core-braking current. Both the induced voltage and the current in the external circuit are generally complex functions of time.

3 THE STRUCTURE MODEL

The basic model was built in a system based on the finite element method, namely in the ANSYS system, in order to facilitate the retrieval of the basic resonant circuit with maximum efficiency. As the elementary structure basis, the type according to Fig. 1, Fig.2 was chosen and solved as the model Fiala P. and Jirku T., 2008. There occur several points in the design and solution of the model. The first of these points consists in the solution of impedance matching of the structure and in the possibility of emergence of reflected electromagnetic waves, another one lies in the state of propagation and damping of electromagnetic waves in the space behind the mask, and still another one is the designing of the basic geometry with respect to the required utilization of both the electric and the magnetic components of the electromagnetic wave. In Fig. 2 the design is presented of the basic elementary structure as a resonant circuit with the aim to obtain the maximum component of electric field on the detector electrodes.

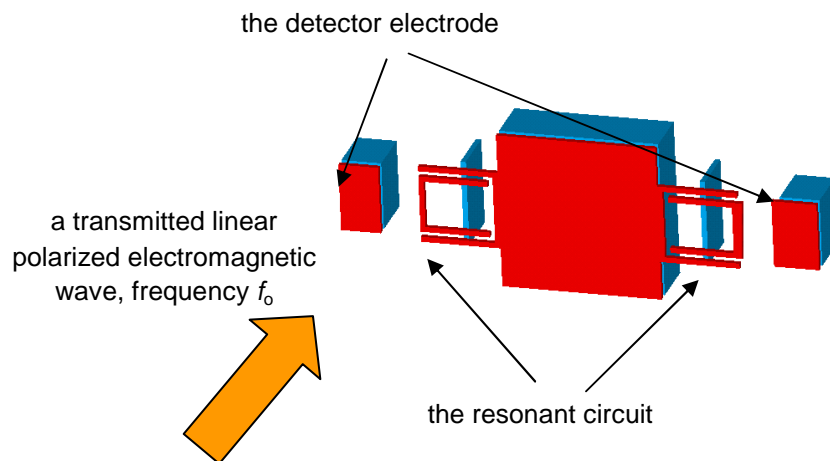


Figure 1. Instances of the basic elements of resonator

Figure 3, figure 5 presents schematically the arrangement of the periodic structure of resonators with their connectivity. The numerical model was analyzed in such a manner that we reached the above-described input conditions of the RG function. Figure 6, 7 and 8 shows the distribution of the module of the electric intensity E and magnetic intensity components. The model in Figures. 2, 3, 5 was designed for the frequency of 100 THz. The dimension is $x = 9 \mu\text{m}$. The intensity module of an electromagnetic wave impinging on the structure is $E_{\text{in}}=0.1 \text{ V/m}$, the wave orientation is in the direction of the y axis, and the wave was modeled as linearly polarized. It follows from the analysis that, within the range of excited frequencies, there may occur even a 21-fold amplification of the signal. However, this signal is already processible by means of currently available technologies.

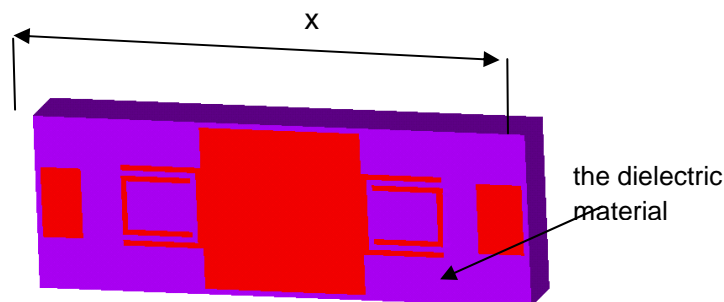


Figure 2. A geometrical model of the resonant circuit basic element

In Fig. 4, a basic schematic expression is provided of a modelled RG including components for shaping the utilizable form of energy. In order to enable correct functioning of the generator, electric and magnetic field analysis in figure 6, 7, 8 we have to embed controlling electronics, Fiala P. and Drexler P., 2011, between the electrical load and the junction components of the RG. The electronics will ensure that, at any condition on the output of the device, the VG generator is loaded with constant impedance Z in the junction points. This type of connection can be realized, for example, according to the diagram in Figure 9 (power management circuit); in practice, it was already tested on the mini- and microharvesters, and the simulated behaviour from Figure 10 corresponds to the measured

values. These tests, which were easily measurable and realizable using the generators, enabled us to produce the basic power management circuit design for the RG.

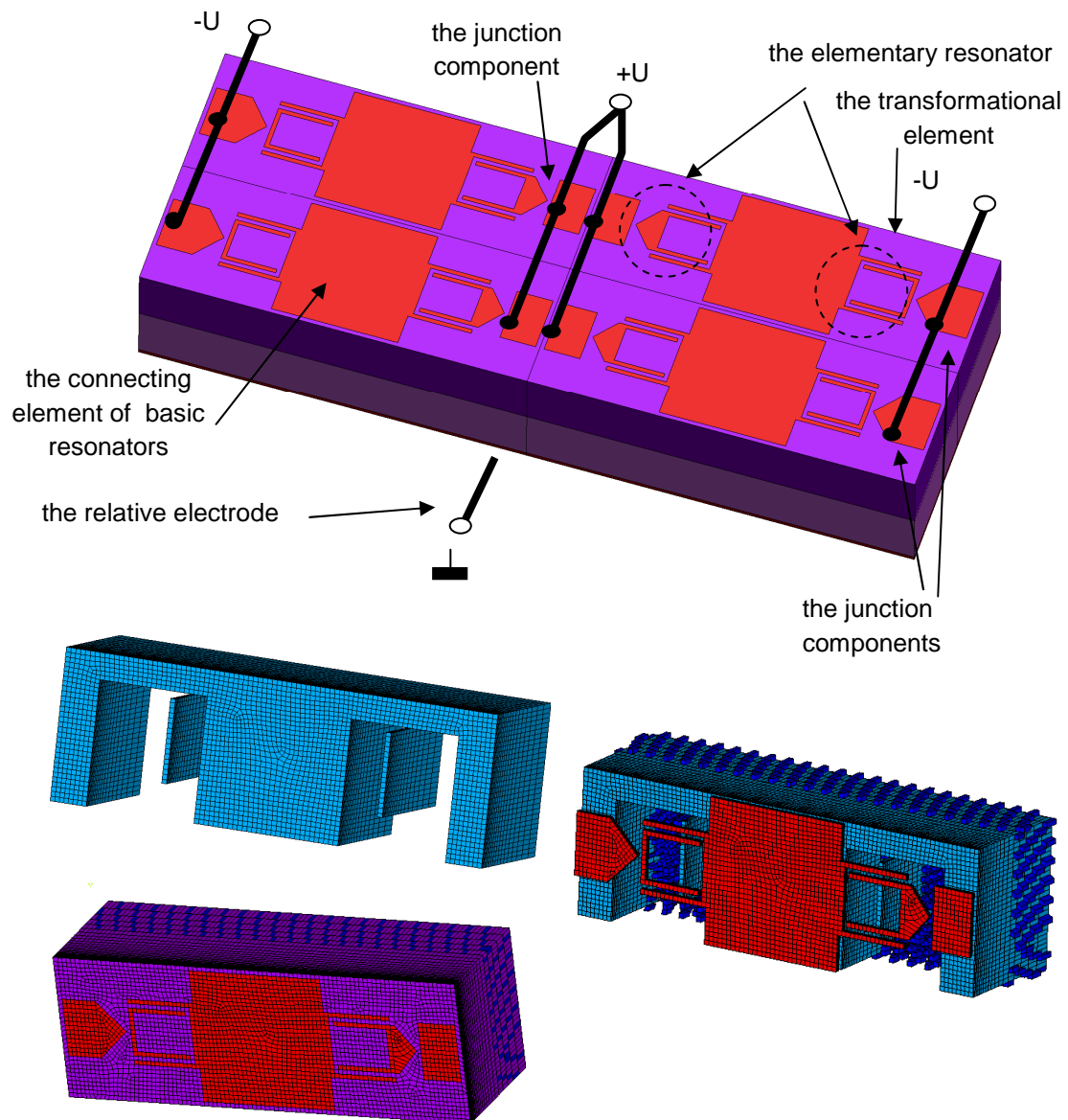


Figure 3. A geometrical model of the resonant circuit structure

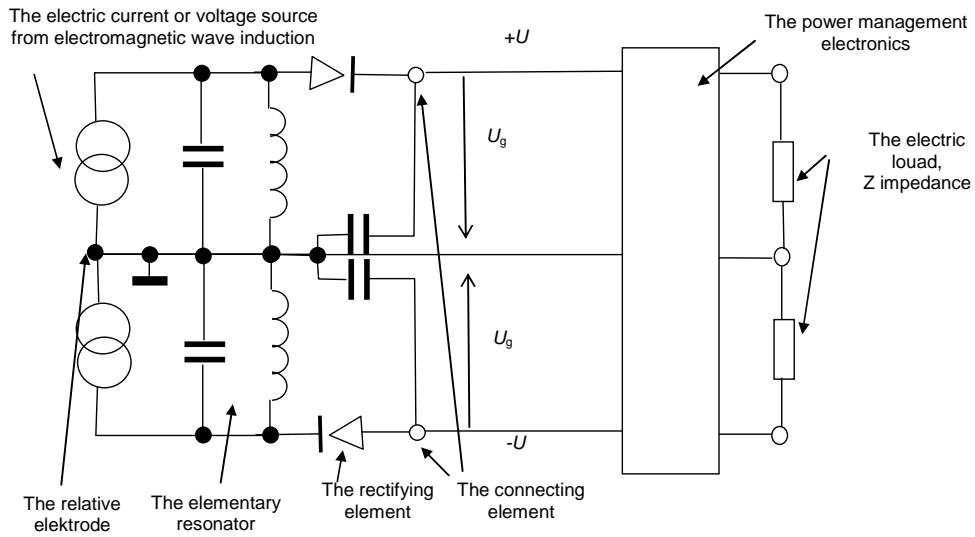


Figure 4. The resonance circuit structure of the generator

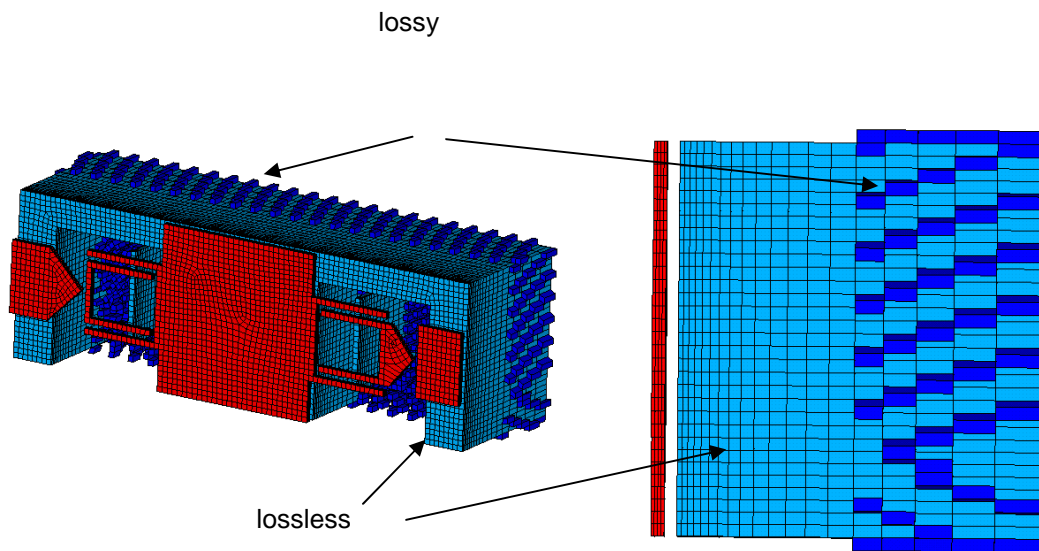


Figure 5. The geometrical model- structure of the resonant circuit basic element, changed characteristics region

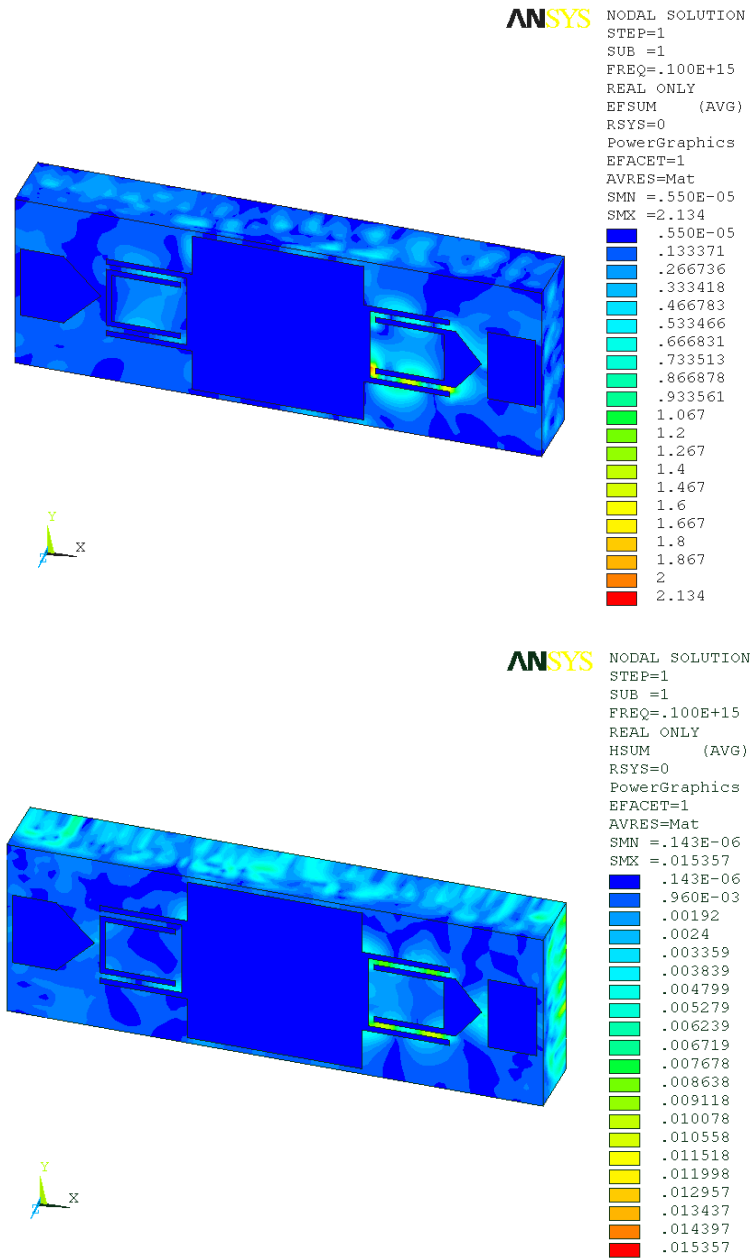


Figure 6. The interpretation of solution of the resonant circuit basic element model, the electric and magnetic field intensity components

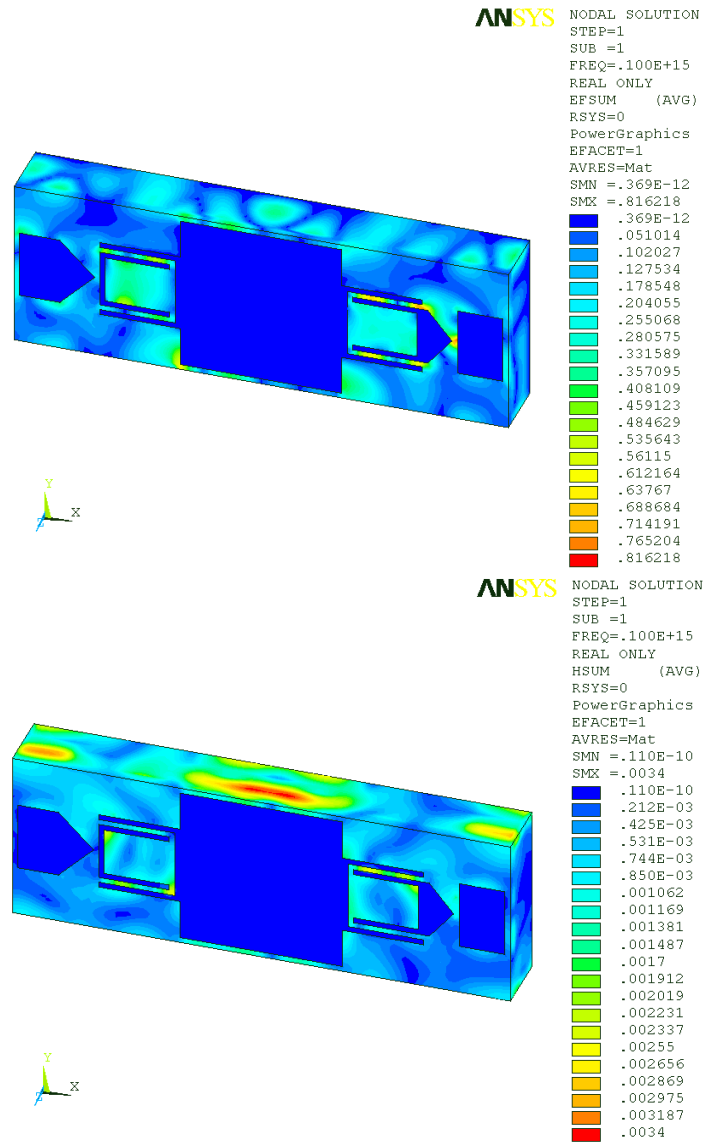
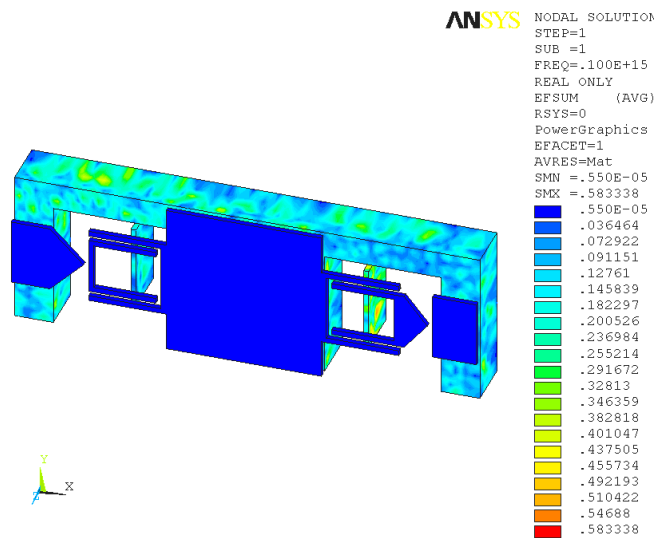


Figure 7. The interpretation of solution of the resonant circuit basic element model, the electric and magnetic field intensity components of wrong material designed model



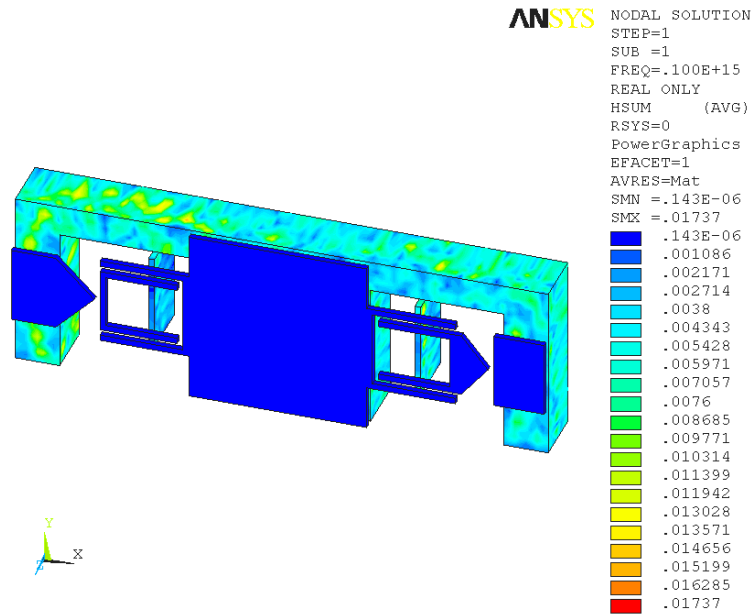


Figure 8. The interpretation of solution of the resonant circuit inside structure basic element model, the electric and magnetic field intensity

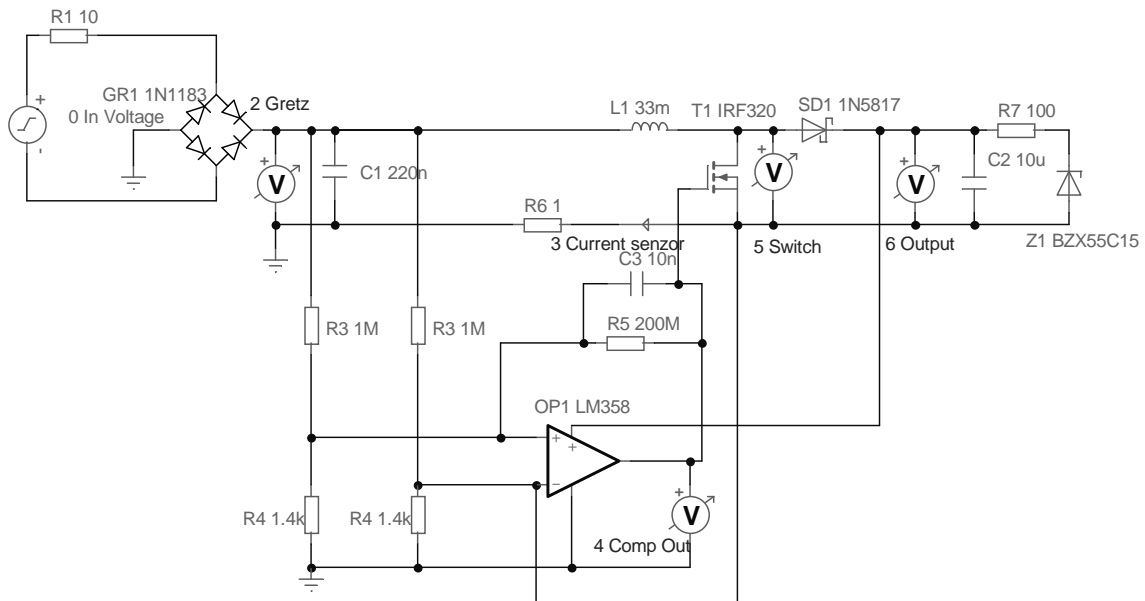


Figure 9. The simulation diagram for power management circuit -PFC.

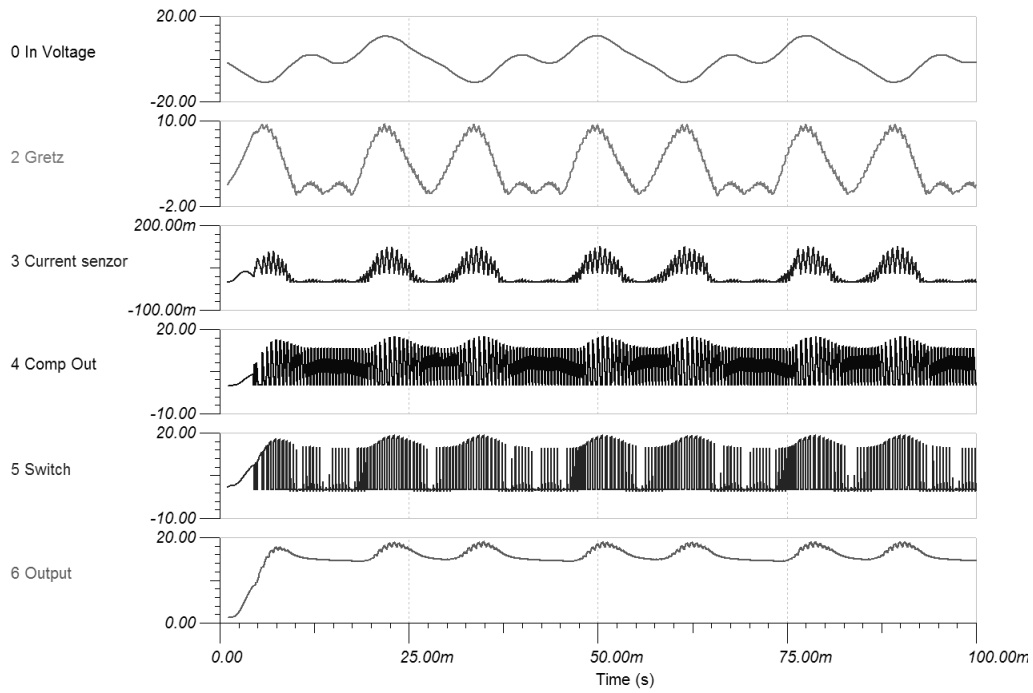


Figure 10. Simulated waveforms for the PFC power management circuit.

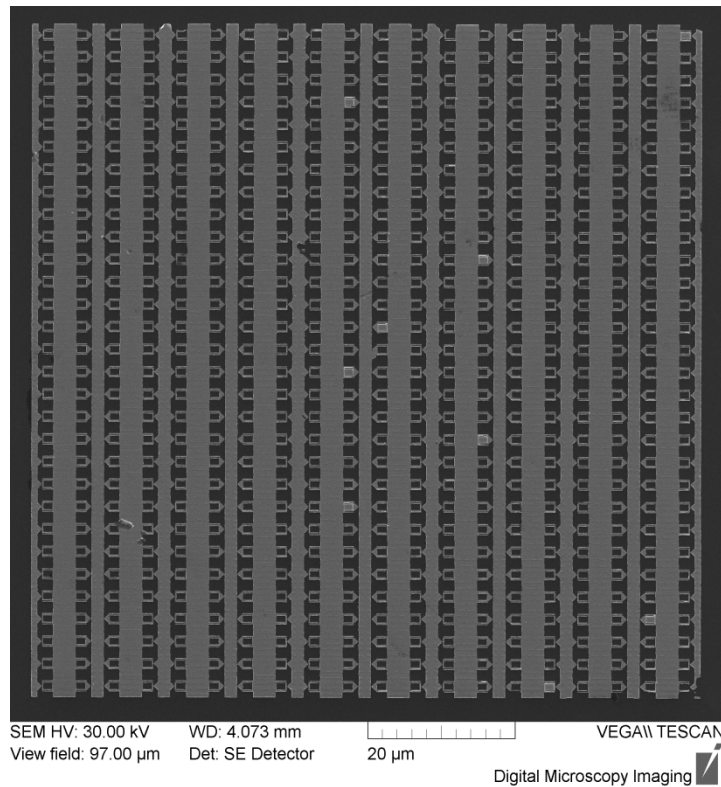


Figure 11. Experimental structure of harvester.

4 CONCLUSION

The experimental VG on a solar element is currently in the process of testing. The applied research of the numerical model periodical structures has brought a considerable sum of experience in the resonant mode modeling; the results of the related analysis are utilized for the manufacturing technology, fig.11 proposals concerning the RGs and their experimental operation.

Acknowledgements, The research described in the paper was financially supported by the grant provided by the BUT Grant Agency FEKT-S-10-13.

References

- Fiala P. and Drexler P., 2011, *Power supply sources based on resonant energy harvesting*, Microsystem Technologies, Volume 18, Numbers 7-8 (2012), 1181-1192, From the issue entitled "Special issue of the conference 'Smart Sensors, Actuators and MEMS' within the SPIE EUROPE Symposium 'MICROTECHNOLOGIES' Prague, Czech Republic, 18-20 April 2011" , DOI: 1007/s00542-012-1474-4
- Fiala P. and Jirku T., 2008, *Analysis and design of minigenerator* , *Progress In Electromagnetics Research Symposium 2008*, PIERS Online, vol.4, no.7, Boston, USA, ISSN 1559-9450.
- Jirků T., Fiala P. and Kluge M., 2010, *Magnetic resonant harvesters and power management circuit for magnetic resonant harvesters*, Microsystem Technologies, Volume 16, Number 5, 677-690, DOI 10.1007/s00542-010-1045-5
- Kikuchi H., 2001, *Electrohydrodynamics in dusty and dirty plasmas, gravito-electrodynamics and EHD*, Kluwer academic publishers, Dordrecht/Boston/London, ISBN 0792368223, 9780792368229
- Patent ,2006, no. PV-2006-571, Czech Republic.
- Patent ,2006, no. PUV-2006-18391, Czech Republic.
- Patent ,2007, no. PV 2007-331, Czech Republic.
- Patent ,2011, no. PCT/CZ2011/000076, Czech Republic
- Polivka J., Fiala P., and Machac J. , 2011, *Microwave Noise Field Behaves Like White Light*, *Progress In Electromagnetics Research*, PIER 111, 311-330. doi:10.2528/PIER10041304
- Stratton J.A. , 1961, *Theory of electromagnetic field*. SNTL Praha , In Czech.
- Wen J.L., Wen Z., Wong P.K., 2000, *A micromachined vibration induced power generator for low power sensors of robotic systems*. World Automation Congress, Maui, Hawaii, 11.-16. July 2000.

Contact address:

assoc.prof. Ing.Pavel Fiala, Ph.D.,
Ing. Dusan Nesor,
Ing. Michael Hanzelka, MBA

Brno university of technology, Faculty of electrical engineering and communication, Department of theoretical and experimental electrical engineering Kolejní 2906/4, 612 00 Brno, Czech Republic
fialap@feec.vutbr.cz, nespor@feec.vutbr.cz, michael.hanzelka@daccee.eu

STOCHASTIC NUMERICAL MODEL OF ELECTRODYNAMICS, TESTS

PAVEL FIALA, MICHAEL HANZELKA

Brno university of technology, Faculty of electrical engineering and communication,
Department of theoretical and experimental electrical engineering, Czech Republic

Abstract: The article presents the transient task numerical modelling of the electrodynamic process in gas with a pulsed electric field. Within the numerical model, non-linear electric properties of gas are respected and, by the help of a non-deterministic stochastic model, the possibility of an electric charge generation is analyzed. The authors examine the problem of electric charge probability evaluation on 3-D spark gap model; on the basis of testing the tip-tip disposition, a comparison of individual instances of the probability function evaluation is provided.

Keywords: Numerical modelling, stochastic, non-linear, material, discharge, electric field, probabilistic function.

1 INTRODUCTION

The origins of research in the field of single-shot processes modelling date back deep into the past century. Then, the related problems were solved through the use of experimental methods as applied by Nikola Tesla, the Nestor of electrical engineering [www¹](#), [www²](#). For the solution of the pulse process in an electromagnetic field, models based on the conversion of a physical model into a mathematical one can be classified as stochastic. From the perspective of a macroscopic physical model, the concerned tasks mostly involve a high number of relations of the system elements, with the possibility of description comprising only several external parameters and functions of the system. The models can be further solved as stochastic or deterministic. For numerical models based on finitary methods, it is easier to utilize the stochastic approach Enokizono M., Tsutsumi H., 1994 in the first approximation. This article uses the example of a 2-D model to present the algorithm and parameters of a stochastic model of a discharge generation in an air spark gap, Figure 1.



Figure 1. A simple electrical spark gap, 3-D model

2 The numerical model

As it was already discussed in study Enokizono M., Tsutsumi H.,1994, the model is formulated for a quasi-stationary electric field from reduced Maxwell's equations Stratton J.A. , 1961,

$$\operatorname{div} \varepsilon \mathbf{E} = q, \operatorname{div} \mathbf{J} = -\frac{\partial q}{\partial t} \quad (1)$$

$$\operatorname{div}(\gamma \mathbf{E}) = -\frac{\partial q}{\partial t} \quad (2)$$

where \mathbf{E} is the electric field intensity, \mathbf{J} is the current density vector, ε is the permittivity, γ the conductivity, and q the electric charge. After modification, the equations from (1) become

$$\operatorname{div} \left(\gamma \mathbf{E} + \frac{\partial(\varepsilon \mathbf{E})}{\partial t} \right) = 0 \quad (3)$$

If the formulation of electric intensity vector by the help of potential φ is respected,

$$\mathbf{E} = -\operatorname{grad} \varphi \quad (4)$$

then the model according to expression (3) can be written as

$$\operatorname{div} \left(\gamma \operatorname{grad} \varphi + \frac{\partial(\varepsilon \operatorname{grad} \varphi)}{\partial t} \right) = 0 \quad (5)$$

In expression (5), the partial derivative includes the formulation $\varepsilon \operatorname{grad} \varphi$. If we assume time independence of the environment macroscopic characteristic – permittivity ε , the form can be written in a manner consistent with paper Enokizono M., Tsutsumi H.,1994

$$\operatorname{div} \left(\gamma \operatorname{grad} \varphi + \varepsilon \operatorname{grad} \frac{\partial \varphi}{\partial t} \right) = 0 \quad (6)$$

This form, in the dynamical modelling of an electric field shock wave, does not include the effect of permittivity variation. Conversely, conductivity γ or electrical resistivity ρ as its reversed value, is shown in Figure 2.

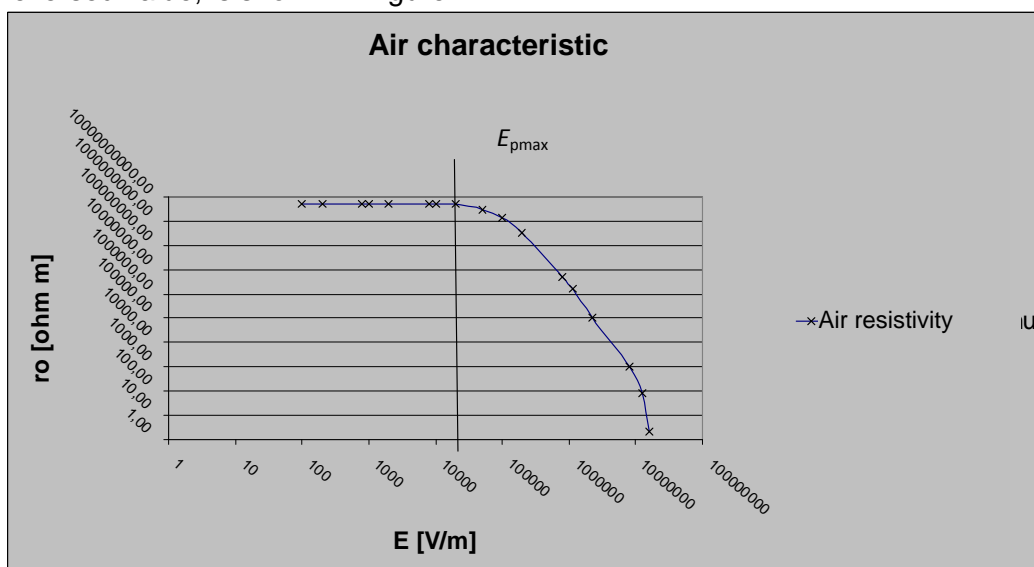


Figure 2. Characteristics of the electrical resistivity dependence on electric field intensity

If we assumed the dependence of electrical permittivity ε on time variation and the module of electric intensity \mathbf{E} , model (5) could be employed to describe more exactly the processes related to an electric discharge. The time behaviour of electric potential variation was preset with parameters of 0.1/50 μs , Figure 3.

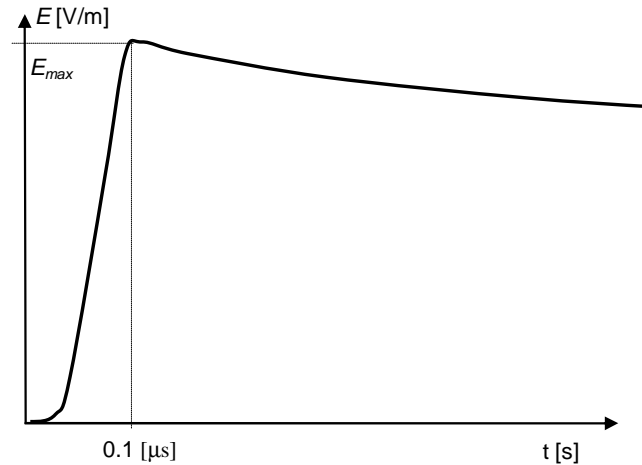


Figure 3. The electric potential time behaviour in model (5)

3 A comparison of the 2-D and 3-D models

If we apply the probabilistic function for the 2-D stochastic model based on relation (6)

$$P_{i,j} = \left(\frac{E_{i,j}}{E_{\max}} \right)^\eta \quad (7)$$

where E_{ij} is the electric intensity module of the numerical model element solved by means of the finite element method (FEM), η relates the growth probability with the local electric field. The time behaviour of electric potential φ according to Figure 2, in which we tested the model behaviour for $E_{\max}=3\text{kV/cm}$, 100 kV/cm , is shown in Figure 3.

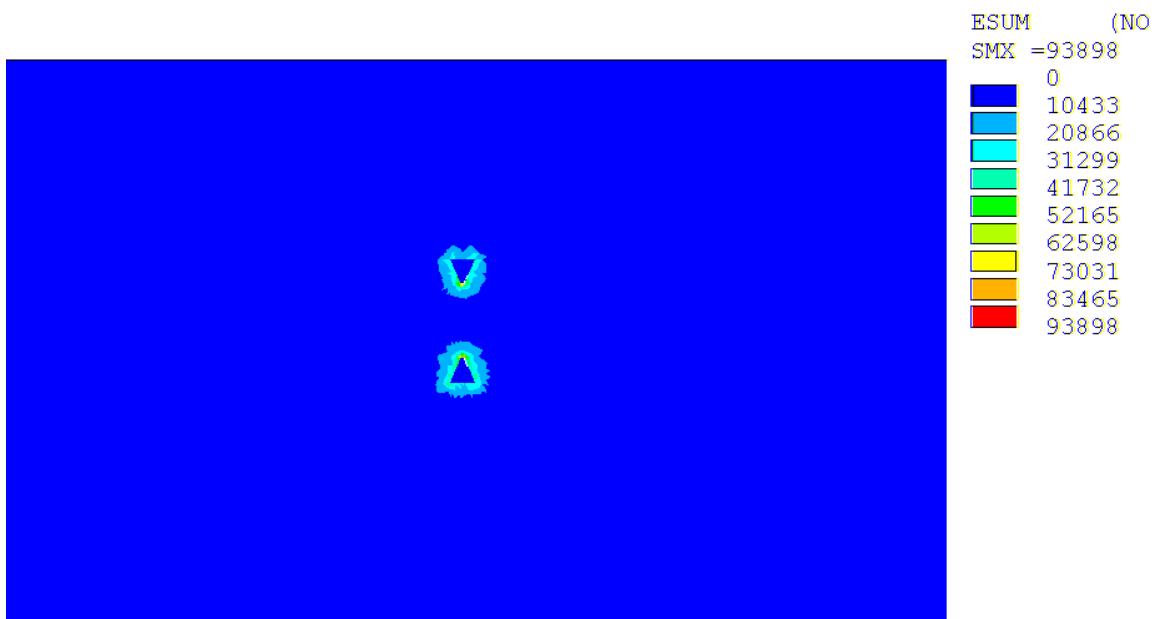


Figure 4. The module distribution of electric intensity E , $t=0.4\mu\text{s}$

For example, for entering the waveform of intensity of electric field E (electric potential φ) P. Fiala, 2003, P. Fiala, 2007, from the behaviour described in Figure 3 $E_{\max}=3\text{kV/cm}$, the distribution of electric field E for the non-uniform mesh of the 3-D model elements is shown in Figure 4. However, for the process described in paper Enokizono M.; Tsutsumi H.,1994 and the evaluation of probabilistic function (7), probability distribution P in the quasi-stationary 3-D model (6) is shown in Figure 5. Figure 6 describes, based on the transient process modelling, the distribution of changed characteristics of conductivity γ in the 3-D stochastic model. Figure 7 shows conductivity γ distribution in the model as a function of electric field E intensity according to the characteristics from Figure 5. Thus, the entire transient process was modelled according to the time behaviour of the exciting quantity from Figure 3. Also, it was determined that the described probabilistic function from Enokizono M.; Tsutsumi H.,1994 has certain drawbacks for the 3-D numerical model; therefore, we used (for example) the Laplace probabilistic function, double Gauss probabilistic function, Figure 9. and brought it under testing, from Figure 10 to 20.

$$L_{i,j} = \frac{p}{2B} e^{\left(\frac{-|E_{i,j}-E_{med}|}{B}\right)} + \frac{1-p}{2C} e^{\left(\frac{-|E_{i,j}-E_{med}|}{C}\right)} \quad (8)$$

where $p \in \langle 0,1 \rangle$, $B, C > 0$.

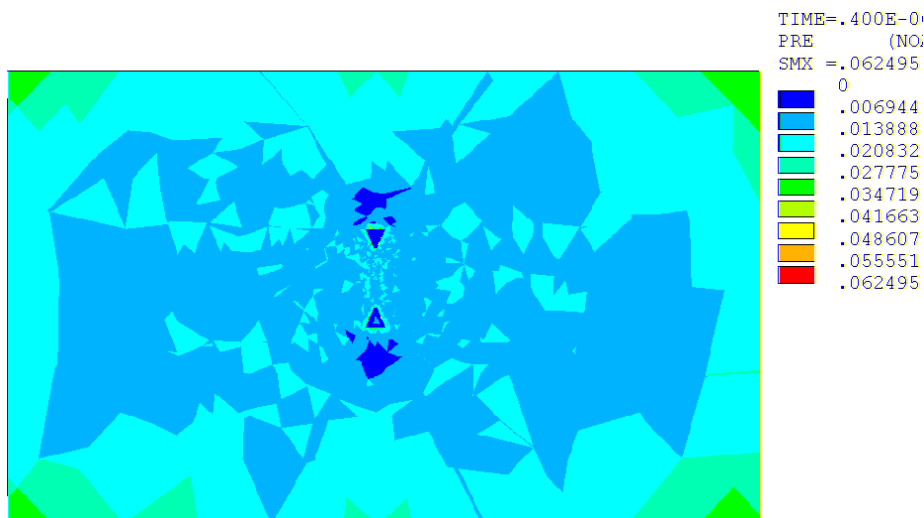
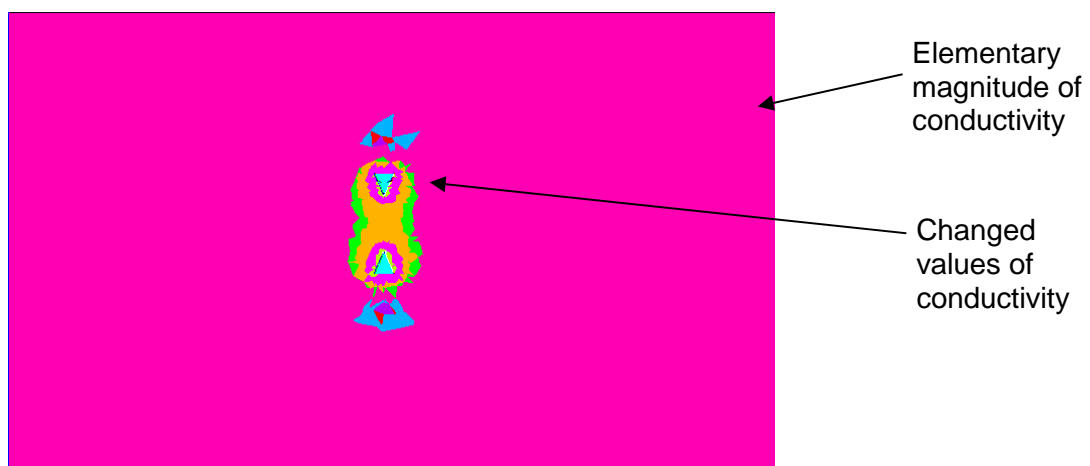
Figure 5. The distribution of probability P , $t=0.4\mu\text{s}$ 

Figure 6. The distribution of the electric conductivity changed characteristics γ , $t=0.4\mu s$



Figure 7. The distribution of electric conductivity γ , $t=0.4\mu s$

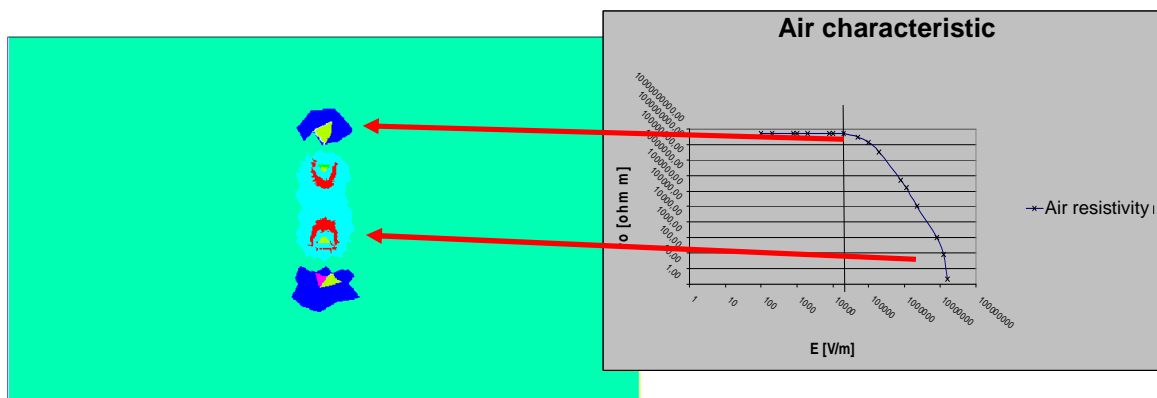


Figure 8. The distribution of changed material properties, electric conductivity γ dependence on electric field intensity, $t=0.4\mu s$

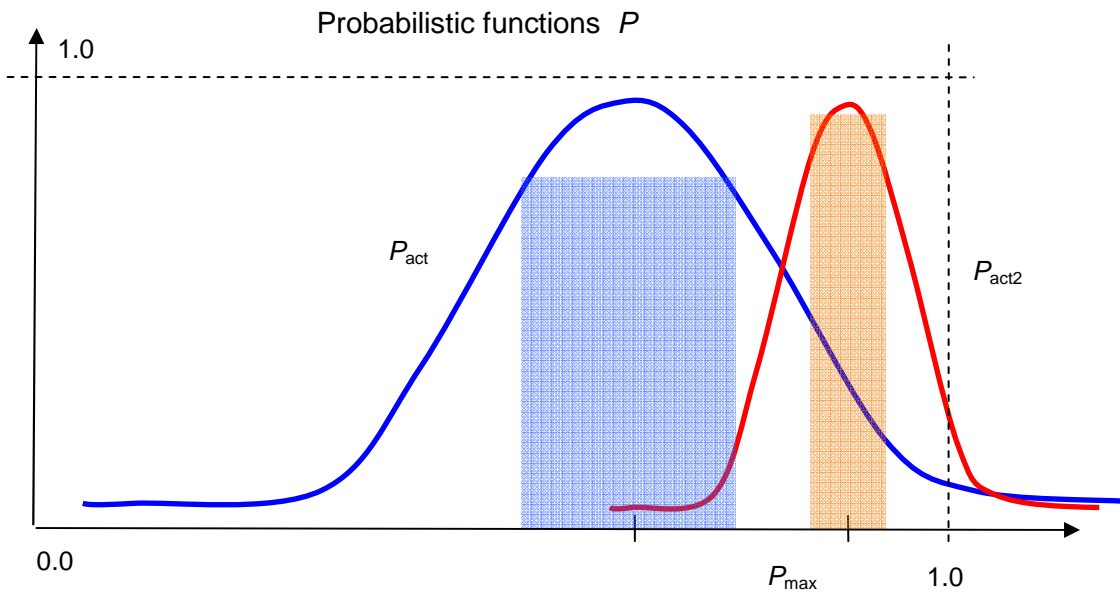


Figure 9. Used a double Gauss probabilistic function, P_{act} , P_{act2}



Figure 10. The module distribution of electric intensity E , $t = 0.4 \mu s$

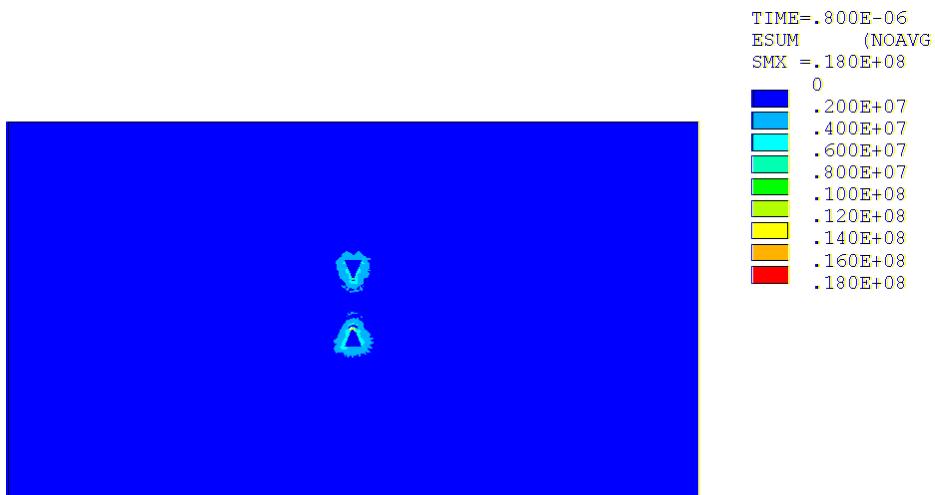


Figure 11. The module distribution of electric intensity E , $t = 0.8\mu s$

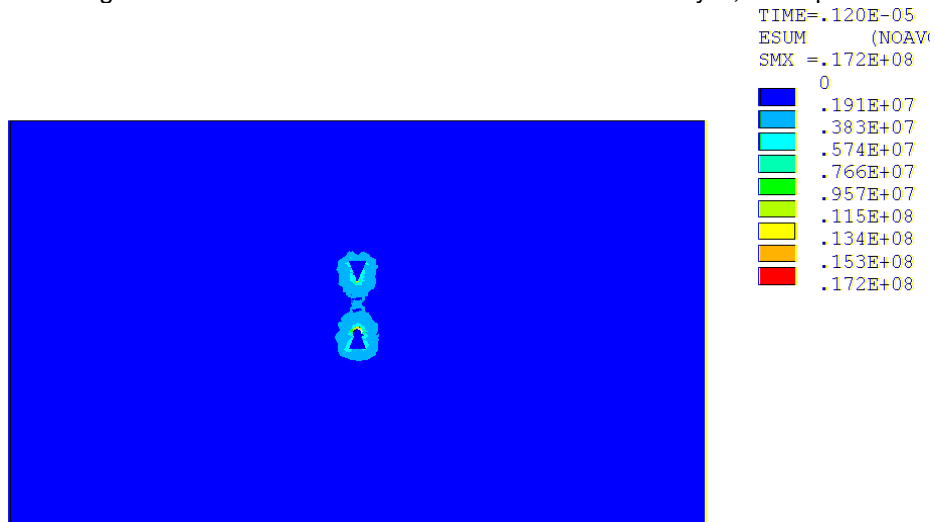


Figure 12. The module distribution of electric intensity E , $t = 1.2\mu s$

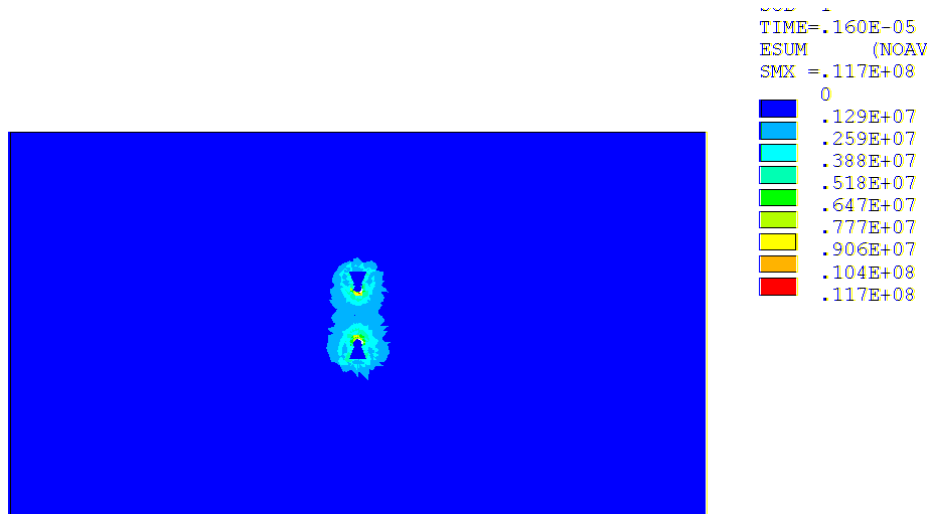


Figure 13. The module distribution of electric intensity E , $t = 1.6\mu s$

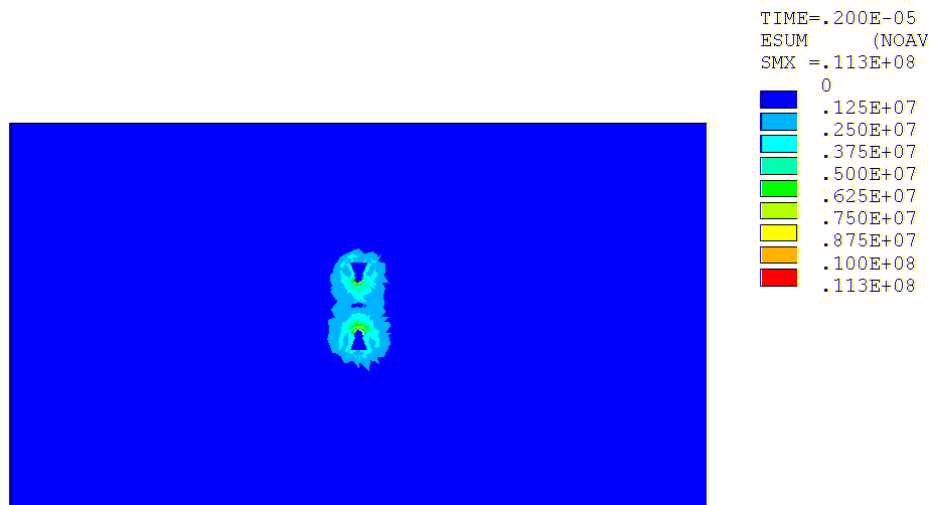


Figure 14. The module distribution of electric intensity E , $t = 2.0\mu s$

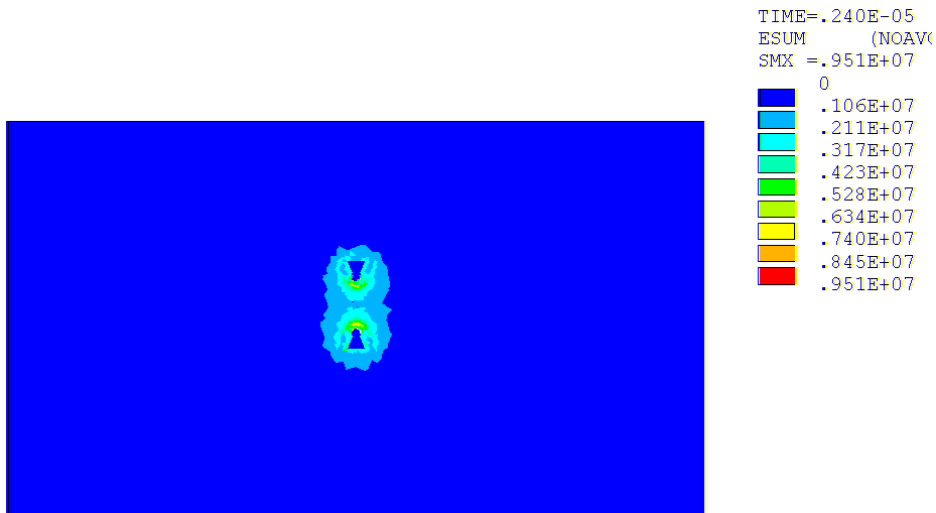


Figure 15. The module distribution of electric intensity E , $t=2.4\mu\text{s}$

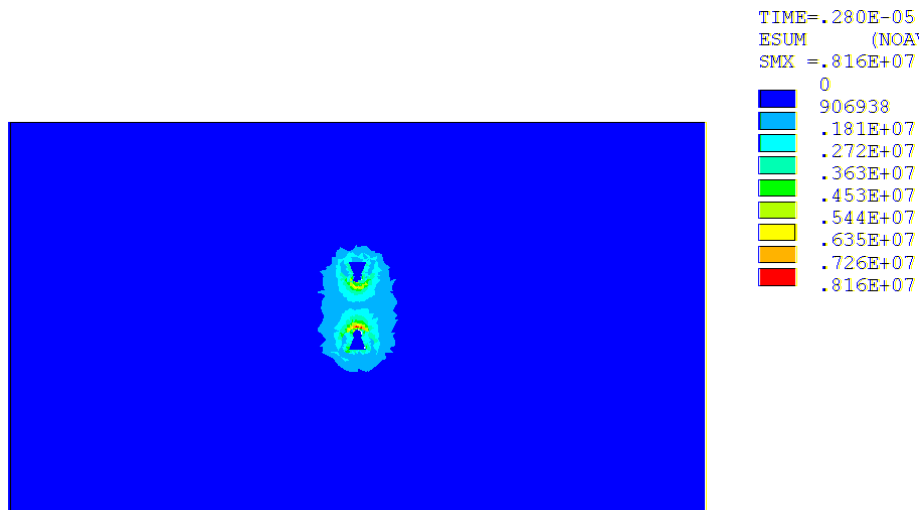


Figure 16. The module distribution of electric intensity E , $t=2.8\mu\text{s}$

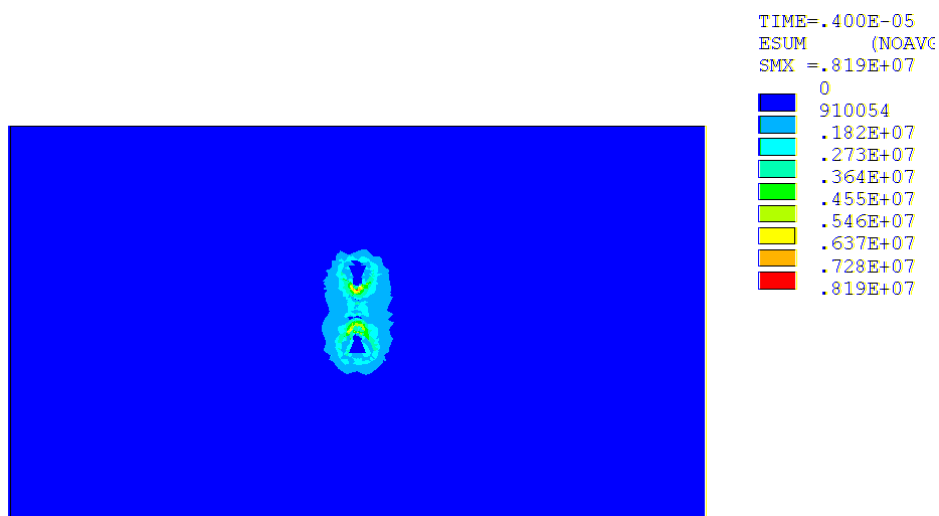


Figure 17. The module distribution of electric intensity E , $t=4.0\mu\text{s}$

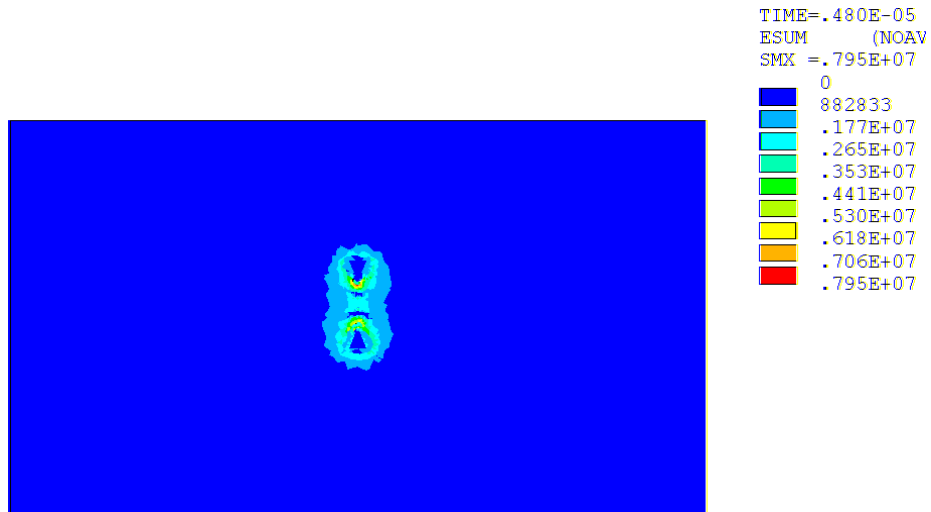


Figure 18. The module distribution of electric intensity E , $t=4.8\mu\text{s}$

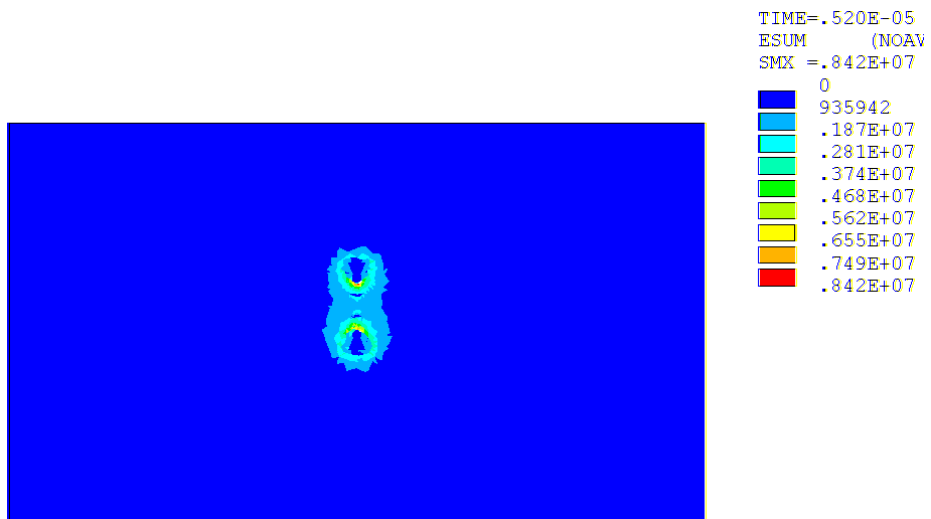


Figure 19. The module distribution of electric intensity E , $t=5.2\mu\text{s}$

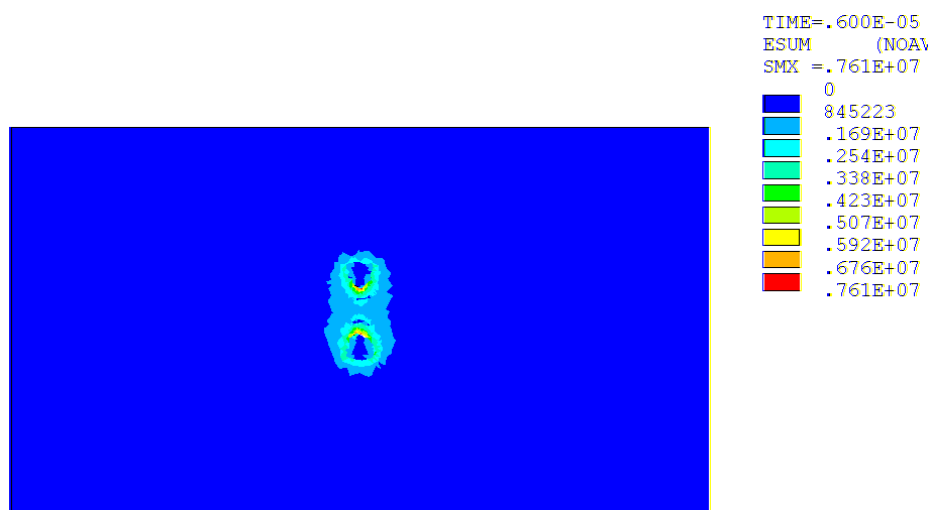


Figure 20. The module distribution of electric intensity E , $t=6.0\mu\text{s}$

4 CONCLUSION

The tests conducted by the help of a 3-D numerical model designed for the modelling of the electric discharge stochastic process proved that the quality of the assembled numerical model, uniform distribution, and boundary conditions setting are aspects of fundamental importance to the modelling procedure, Kikuchi H., 2001. As several probabilistic functions were tested, it is possible to conduct a discussion related to forms that are more suitable for faster convergence of the stochastic model.

Acknowledgements, The funding of the project was supported by the Ministry of Industry and Trade of the CR (Diagnostics of superfast objects for safety testing, FR-TI1/368), Ministry of Education, Youth and Sports of the CR, and by institutional resources from the related Research Design project of the BUT Grant Agency FEKT-S-10-13 and GACR 102/09/0314.

References

P. Fiala, 2003, *Finite Element Method Analysis of a Magnetic Field Inside a Microwave Pulsed Generator*, 2nd European Symposium on Non-Lethal Weapons, May 13-15, Ettlingen, SRN.

P. Fiala, P. Drexler, 2007, *MEASUREMENT METHODS OF PULSED POWER GENERATORS*, 4th European Symposium on Non-Lethal Weapons May 21-23, Ettlingen, SRN.

Enokizono M.; Tsutsumi H., 1994, *Finite element analysis for discharge phenomenon*, Magnetics, IEEE Transactions on , vol.30, no.5, pp.2936-2939, ISSN : 0018-9464

Kikuchi H., 2001, *Electrohydrodynamics in dusty and dirty plasmas, gravito-electrodynamics and EHD*, Kluwer academic publishers, Dordrecht/Boston/London, ISBN 0792368223, 9780792368229

Stratton J.A. , 1961, *Theory of electromagnetic field*. SNTL Praha , In Czech.

www¹, <http://www.rastko.rs/projekti/tesla/delo/10761>

www², http://books.google.cz/books?id=QclcZw7I4yMC&pg=PA112&lpg=PA112&dq=Nikola+Tesla+discharge&source=bl&ots=s1VLwDeNNX&sig=bqNGiCHEwHagK4PnIOSgWgqnbYg&hl=cs&ei=SEGoTd6TCoebOpW0scwJ&sa=X&oi=book_result&ct=result&resnum=2&ved=0CCIQ6AEwAQ#v=onepage&q=Nikola%20Tesla%20discharge&f=false

Contact address:

assoc.prof. Ing.Pavel Fiala, Ph.D.,
Ing. Michael Hanzelka, MBA

Brno university of technology, Faculty of electrical engineering and communication, Department of theoretical and experimental electrical engineering Kolejní 2906/4, 612 00 Brno, Czech Republic
fialap@feec.vutbr.cz, michael.hanzelka@daccee.eu

INCREASING THE RESISTANCE TO INTERNAL EXPLOSION OF THE STRUCTURE OF A BROWN COAL TRAY

PETR HORYL, PETR JAHN

VSB - Technical University of Ostrava, Varroc Lighting Systems s.r.o.

Abstract: This article deals with increasing the resistance of the steel structure of a brown coal tray to internal explosion. The steel tray is welded to the supporting structure of the heating plant. The paper focuses on changing the existing design to increase its resistance to internal explosion. Because internal explosion of brown coal dust takes only a few milliseconds, an explicit method was used. The explicit dynamic module from ANSYS Workbench 13 was used for the solution of this difficult nonlinear dynamic problem.

Keywords: Brown Coal Tray, Internal Explosion, Explicit Dynamic Module

1 Introduction

The subject is a concrete solution tray which is welded to the structure of the plant. The length is 11 m, width is 6 m and depth is 9.6 m, with a volume of 400 m³ of brown coal. The mass of the silo is 43,500 kg. The silo is welded on the top circuit to the supporting construction (see Image 1). The aim of computer modeling was to determine whether an internal explosion of coal dust causes this weld to break, followed by tearing of the container structure and its collapse.

The tank walls have a thickness of 10 mm and are reinforced by rolled profiles of type I, U and sheets. The tray is reinforced by a collar all around the upper and middle part welded from two I180 profiles.

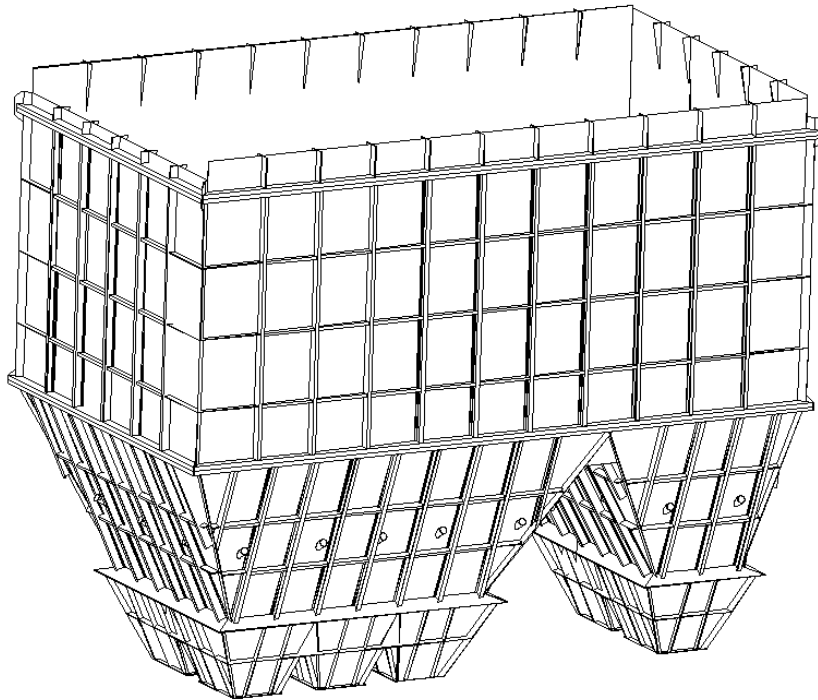


Image 12 – Tray structure

Because internal explosion of brown coal dust takes only a few milliseconds, an explicit method was used. Explicit time integration is more accurate and efficient for simulations involving large deformations, large strains and material nonlinear behavior. The explicit method is conditionally stable. There must be some limit on the maximum size of the time step. Ansys [ANSYS Explicit STR, 2009] recommends the Courant-Friedrichs-Levy condition for the size of the time step. This condition implies that the time step will be limited such that a stress wave cannot travel further than the smallest characteristic element dimension in the mesh, in a single step. The time step criterion for solution stability is

$$\Delta t \leq f \left(\frac{h}{c} \right)_{\min} \quad (1)$$

where Δt is the time increment, f is the stability time step factor (0.9 by default), h is the characteristic dimension of an element and c is the local material sound speed in an element. The element characteristic dimension, h , is calculated as follows in Table 1.

Table 1 Elements characteristic dimensions

Type of element	Characteristic dimension, h ,
Quad shell	The square root of the shell area
Tri shell	The minimum distance of any node to its opposing element edge
Beam	The length of the element

2 Loading from Eurocode 1

According to Eurocode 1 – Actions on structure (CSN EN 1991-1-7, 2007), the stack was assessed as a construction, which falls within the class consequence CC3, as when the coal-dust explodes, there can be subsequent failures. This refers to the risk to persons from the falling tank or damage to other equipment and great material damage. A crucial parameter for evaluating explosion pressure is an index K_{ST} – the deflagration index dust cloud. This is determined experimentally and gives the behavior of the explosion in a limited space. Larger deflagration index values mean internal explosions with higher pressures and shorter time waveforms. The deflagration index value K_{St} for brown coal is 18,000 $\text{kN/m}^2\cdot\text{m/s}$. For this index value we obtained from the Eurocode standard a maximum load pressure $p_{max} = 0.8 \text{ MPa}$. The highest values of dust explosion pressure are achieved within a time span of 20 ms to 50 ms.

3 Computer model

A stack model for dynamic simulation of the internal explosion was created using the drawings in the Ansys Workbench 13.0 (see Image 2).

The body model consists of areas that are reinforced by straight lines defined by the properties of objects by type and size of reinforcements. The computer model is designed from 630 parts.

For the modeling of a coal-dust explosion in a coal storage, procedures were used according to Eurocode 1 – Actions on structure (CSN EN 1991-1-7, 2007). The aim is to verify the design using nonlinear dynamic analysis in the "Explicit Dynamics" ANSYS Workbench 13.0. The worst case load condition occurs when pouring coal into the tray. The assumption is that when pouring is complete, with eight full hoppers of brown coal, the coal dust concentration will be enough to cause a blast. In this case the pressure wave reaches the largest possible area and causes the greatest damage. The pressure load acts on the inner surface reservoir. The course load is plotted in Image 3.

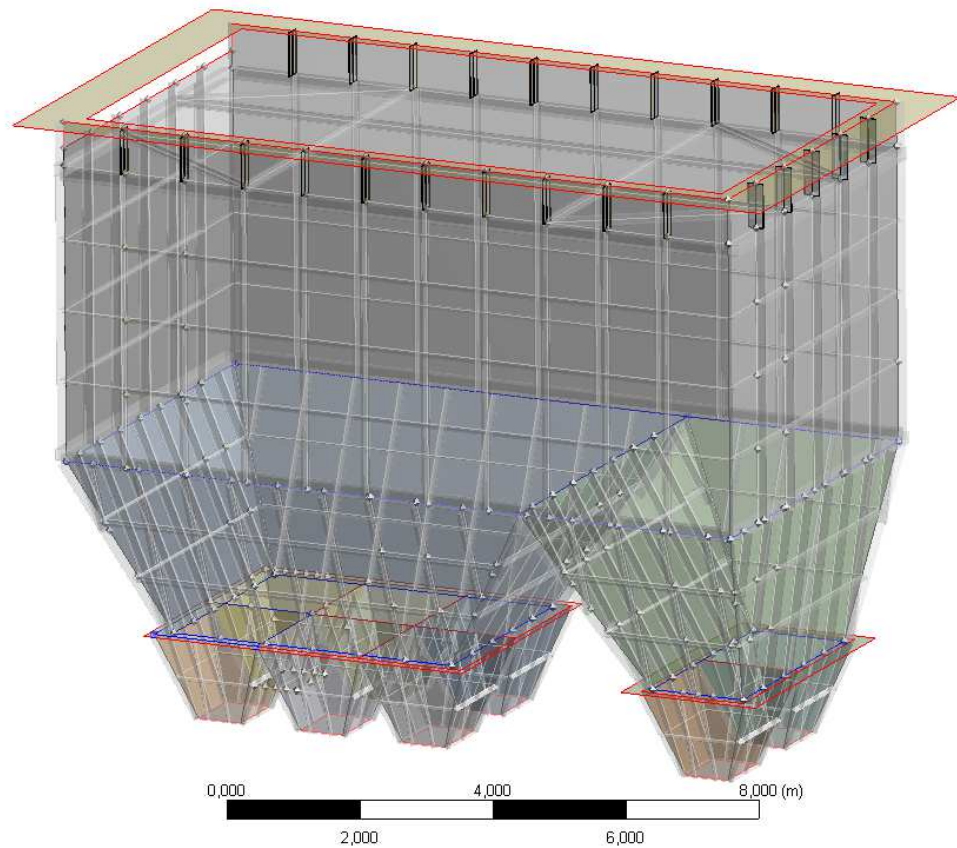


Image 2 – Computer model created in Ansys Design Modeler

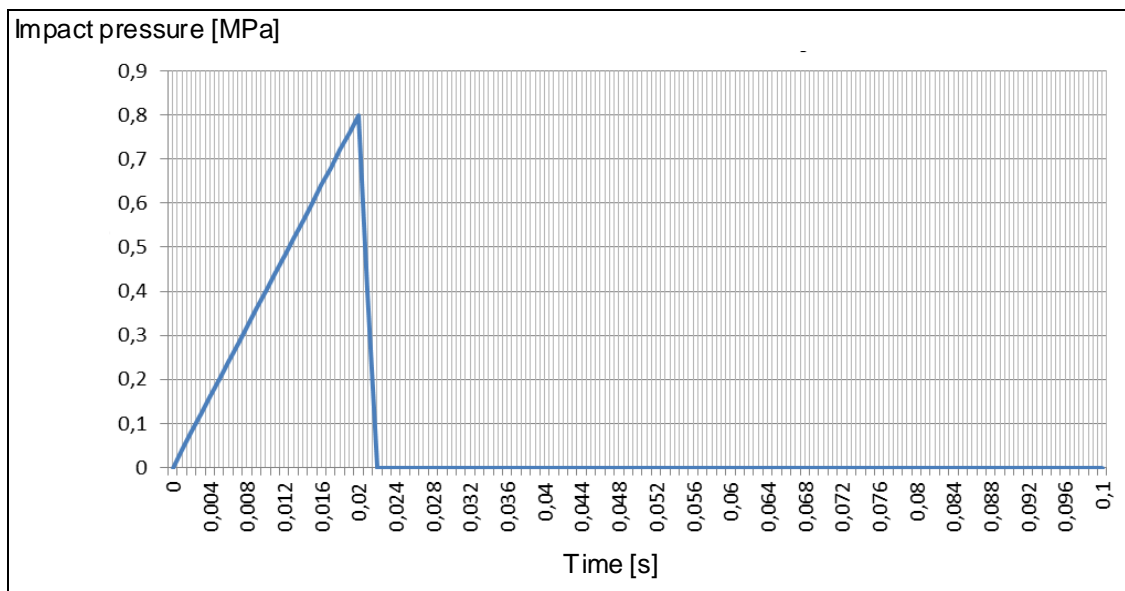


Image 3 – The course of the pressure load

3.1 Mesh

The mesh consists of the shell and the beam elements. Shell elements were used for creating the sheath. Profiles that stiffen the sheath container, beam elements are formed elements. The mesh is made up of 21,627 elements, containing 28,376 nodes. The

maximum size of the shell elements is 160 mm. The generated mesh is shown in Image 4. The mesh quality was verified by a quality metric system. The quality of the mesh elements is plotted in Image 5. The x-axis describes the quality elements and the y-axis plots the percentage of these elements. The quality of the elements is in the range from 0 to 1 and is determined by the ratio of volume to the edge length of the element. A value of 1 reflects a perfect cube or square, while a value of 0 means that the element has zero volume [Ansys Explicit, 2009]. In our case, the quality elements in all parts of the tank are very good and we can expect good results.

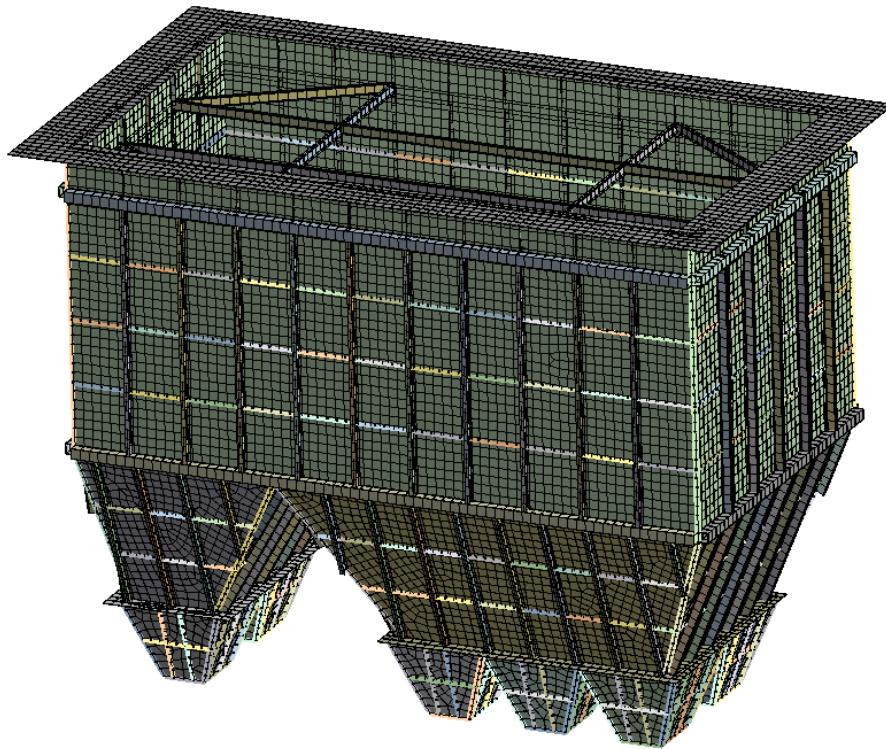


Image 4 – Silo mesh

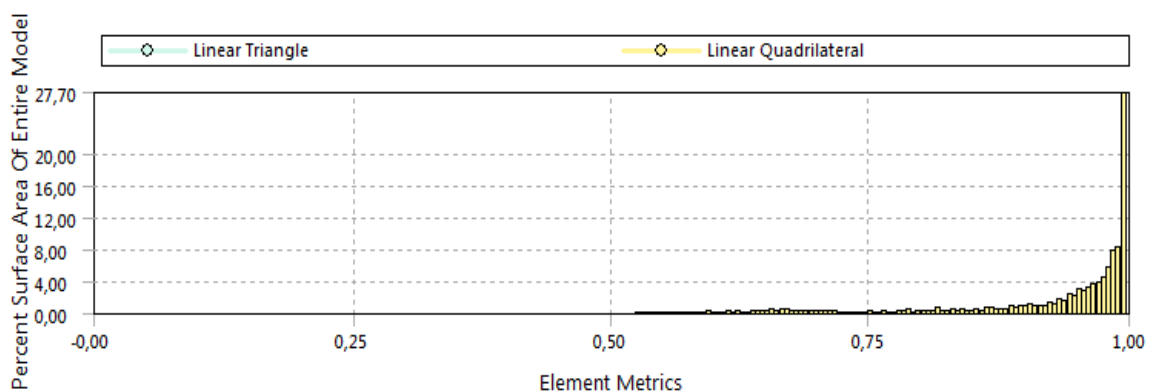


Image 5 – Mesh quality

3.2 Boundary conditions, contact

The computer model was applied to the following boundary conditions. The tray is welded to the perimeter of the structure. Therefore, the model is loaded into a special part. This simply replaced the bearing structure of the building. The welded joint has been

replaced by a "bonded - breakable" type contact [ANSYS, 2010]. So there is hard contact with the possibility of a breach. Breach of contact is limited to a maximum value of normal and shear stresses in contact elements. Our case was set to stress the ultimate strength of the material CSN 11523 to 510 MPa for the maximum normal stress, and 335 MPa for the maximum shear stress. Breach of contact occurs when these values are exceeded and this will result in the tearing of the tray from the structure. Another boundary condition is the pressure load from the blast. This load, with a maximum pressure of 0.8 MPa and the process shown in Figure 3, was applied to all the internal walls in addition to the hoppers. The boundary condition is evident from Image 7. The influence of the tray's own weight has been taken into account. This influence is not negligible, because the entire stack mass is 43,500 kg.

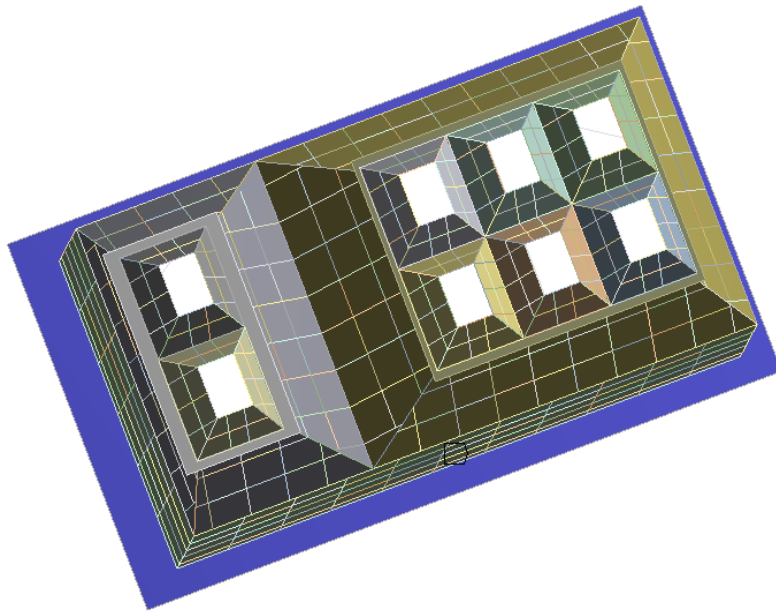


Image 6 –Fixed connection on upper part of silo jacket

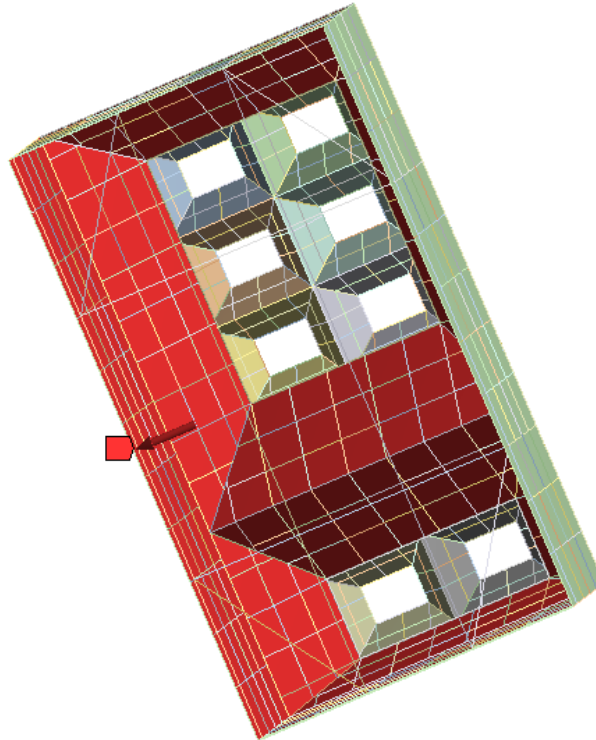


Image 7 – Pressure loading on internal walls, red areas

3.3 Material properties

All parts of the tray are made of material CSN 11 523, which is normally steel with higher carbon content. The material properties are in Table 2.

Table 2 Material properties

Material CSN	Yield stress [MPa]	Ultimate stress [MPa]	Young's modulus [GPa]	Poisson's ratio [1]
11523	355	510	200	0.3

To calculate this dynamic task we used the Johnson Cook material model [Özel, 2007]. This is a material model which describes the stress as a result of deformation, strain rate and thermal effects. The following equation expresses the stress flow.

$$\bar{\sigma} = [A + B(\bar{\epsilon})^n] \left[1 + C \ln\left(\frac{\dot{\bar{\epsilon}}}{\dot{\bar{\epsilon}}_0}\right) \right] \left[1 - \left(\frac{T - T_0}{T_m - T_0}\right)^m \right] \quad (2)$$

where parameter A is initial yield stress, B hardening constant. The equivalent plastic strain speed $\dot{\bar{\epsilon}}$ is normalized to a reference strain speed, $\dot{\bar{\epsilon}}_0$, T_0 is room temperature, T_m is melting temperature, and the temperature values are constants. While the parameter n is the hardening exponent, parameter m is the thermal softening exponent and C is the reference strain rate. The Johnson Cook model [Özel, 2007] is a numerically robust constitutive material model, which is often used in computer simulations. Table 3 shows the constants needed for the Johnson Cook model.

Table 3 Description of Johnson Cook material model [Varmint, 2012]

Initial yield stress A	250 [MPa]
Hardening constant B	712 [MPa]
Reference strain rate C	0.01 [1]
Hardening exponent, parameter n	0.196 [1]
Thermal softening exponent m	1.1164 [1]
Melting temperature Tm	1500 deg

4 Results

First, a calculation was performed on the resistance of the original tray design against an internal explosion of coal dust. It was found that the tearing supporting weld is already carrying a pressure value $p_1 = 0.6$ MPa at the time of 0.015 s, i.e. before reaching the maximum pressure value. At the moment of tear, we observed extreme values of permanent plastic deformation, as shown in Image 8. The original design is not able to withstand the full explosion, so we proceeded to make design changes.

The first change (Image 9, red lines) strengthens the walls under the weld with two new rings created from profile 2 x U180. The tray was also reinforced inside, doubling the existing internal reinforcement. In this case, there was an increase in the marginal value of the pressure to $p_2 = 0.7$ MPa.

The second change (Image 10, red lines) consisted in changing the internal stiffeners formed from profiles of type I160. For this structure, the longitudinal and transverse reinforcements were taken away and moved into the center of the tray with a spacing of 1 m. The pressure load which led to a structural collapse was now down to $p_3 = 0.58$ MPa.

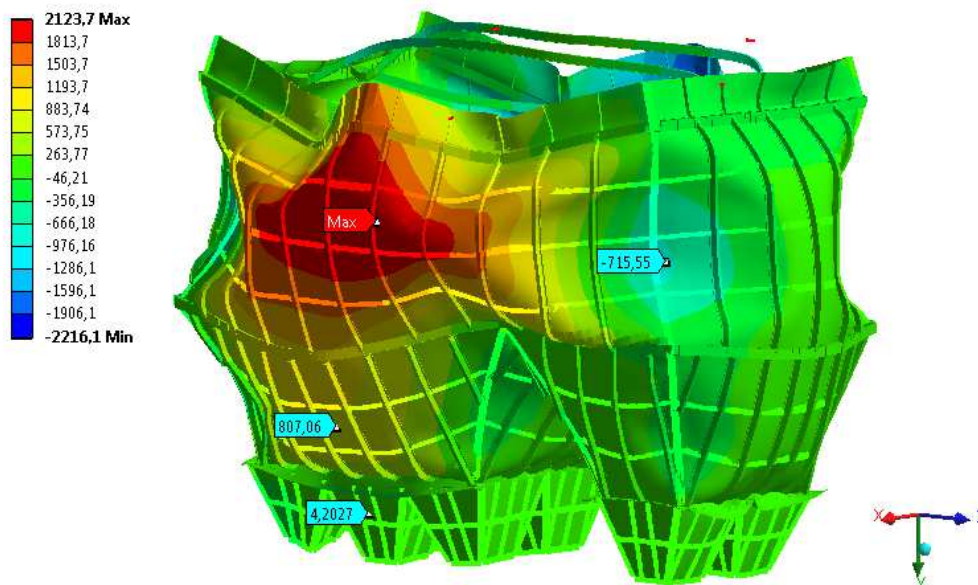


Image 8 – Permanent plastic deformation of silo jacket [mm]

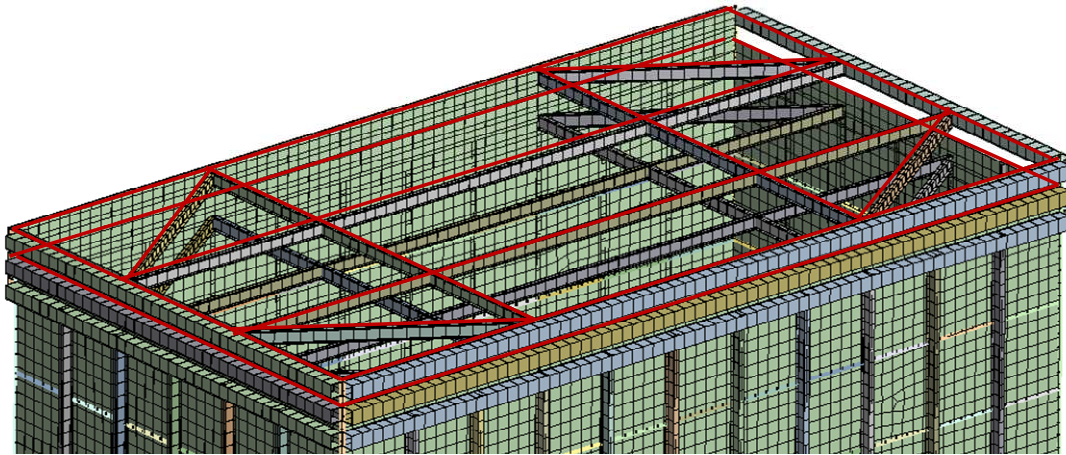


Image 9 – The first design modification, red lines

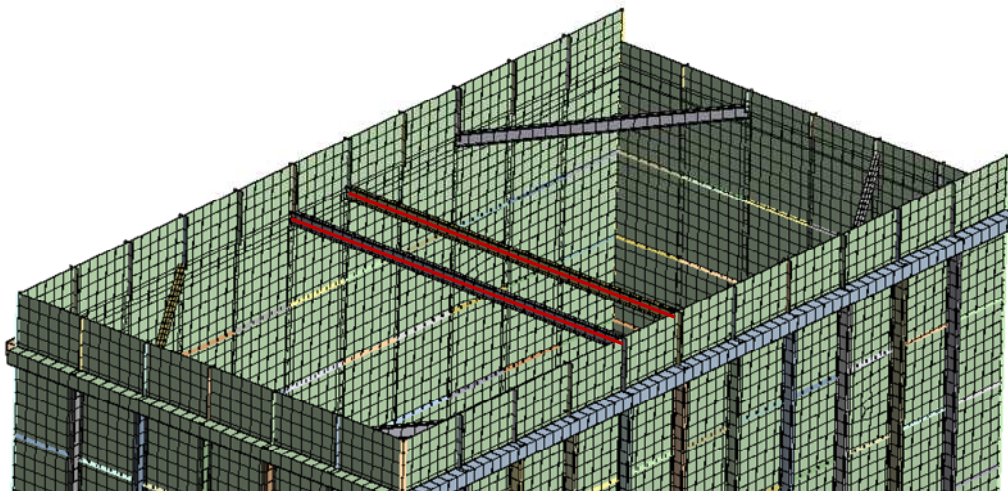


Image 10 – The second design modification, red lines

The third treatment consisted of a structural change in the wall thickness by increasing it from 10 mm to 14 mm. The value of the pressure load which led to a structural collapse fell to $p_4 = 0.62$ MPa. Calculations showed that the coal tray was not able to withstand the full value of the pressure from the blast without a full collapse. Standard Eurocode 1 in this case requires the building of a safety exhaust system with a defined cross-section and defined activation pressure. An exhaust system was designed with an area of 10.5 m^2 , with an activation pressure of 40 kN/m^2 . Based on these facts, the calculation was carried out for a control tank pressure of 50 kN/m^2 load, i.e. 0.05 MPa . The level of safety of the so-called partial load factor $\gamma_F = 50/40 = 1.25$. The results of the last calculation showed that maximum displacement during the dynamic action does not exceed the elastic limit. The maximum displacement is only 38 mm and after dynamic action this completely disappeared (see Image 11). In the supporting weld the yield stress was not exceeded at any point.

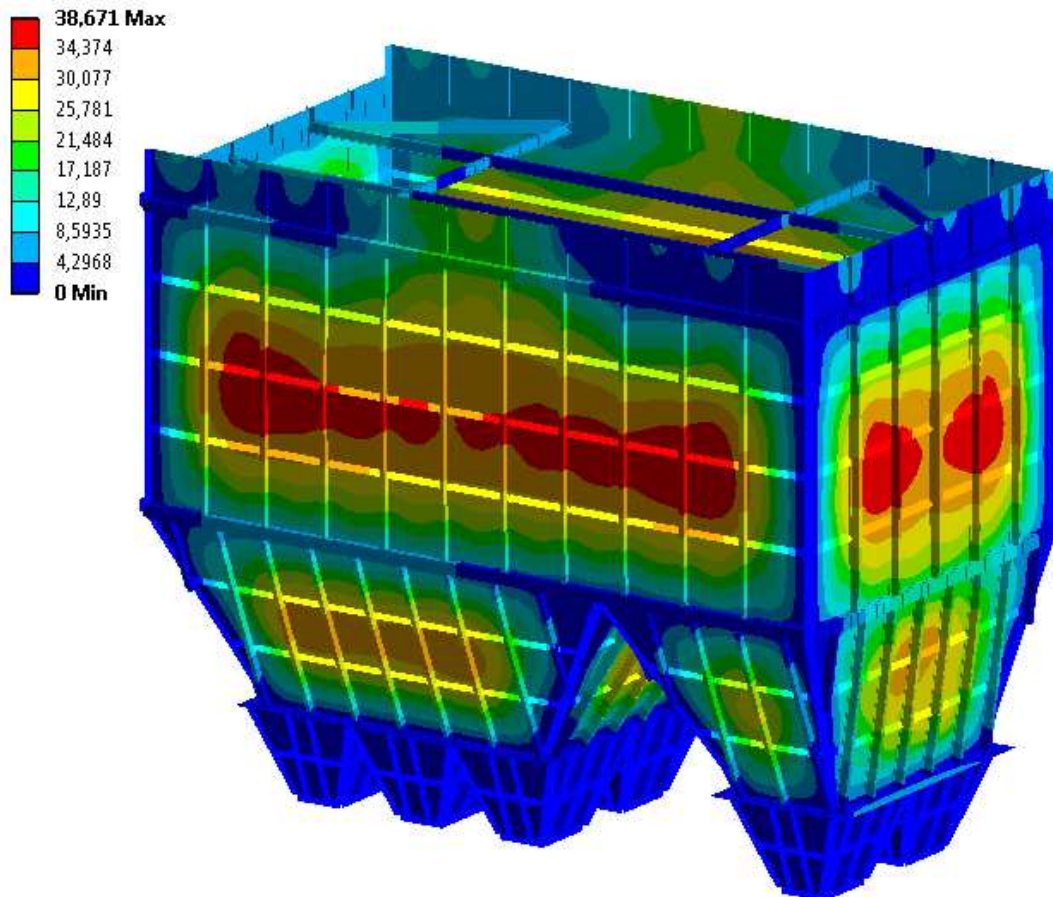


Image 11 – Maximum elastic deflection in [mm]

5 Conclusion

Calculations have shown that the structure of a brown coal tray, even after design modifications, is not able to transfer the full value of the pressure from the explosion of coal dust. A new exhaust system with a construction area of about 10.5 m^2 and the activation pressure of 40 kN/m^2 must be added. Final dynamic calculations showed that, for the maximum value of the internal pressure of the exhaust system, which is expected to be around 50 kN/m^2 , the designed tray complies. This is achieved only when the elastic deformation and stress do not exceed the maximum allowed value.

References

ANSYS Explicit STR [online]. c2009 [cit. 2009-10-01]. Available from <http://www.ansys.com/solutions/servicesandsupport/training/ansysexplicit>

ANSYS, INC. ANSYS Academic Research, Release 13.0 Help System, Theory reference. 2010

CSN EN 1991-1-7, Eurocode 1: Actions on structure - Part 1-7: General actions - Accidental actions, 2007, 64 p.

ÖZEL T, KARPAT Y., 2007 Identification of constitutive material model parameters for high-strain rate metal cutting conditions using evolutionary computational algorithms. *Materials and Manufacturing Processes* [online], vol. 22, no. 5-6 [cit. 2012-01-25]. Available from http://ie.rutgers.edu/resource/research_paper/paper_07-019.pdf. ISSN 1042-6914.

VARMINT A., 1990. Johnson-Cook Plasticity [online], last revision 10. 2. 2012 [cit. 2012-02-05]. Available from <http://www.varmintal.com/aengr.htm>

Acknowledgement

This paper has been supported by a grant from the Ministry of Education of the Czech Republic No. MSM6198910027.

Contact address:

Prof. Ing. Petr Horyl, CSc.

VSB-TU Ostrava, 17. listopadu 15, 708 33 Ostrava-Poruba

BALLISTIC RESISTANCE OF THE TRANSPORT AIRPLANE FUSELAGE TO IMPACT OF 9 MM ACTION 5 PISTOL BULLET

JURAJ HUB¹, JAN KOMENDA²

¹University of Defence, Department of Aircraft and Rocket Technologies, ²University of Defence, Department of Weapons and Ammunition

Abstract: The article presents an experimental and numerical approach to estimate ballistic limits of the pistol hollow point bullet Action 5 penetrating the target representing the transport airplane fuselage. The target containing the composite sidewall, the insulation glass wool layer and the duralumin skin plate is penetrated in two ways – directly and using forward obstacle in form of substitute biological material (ballistic gel) to achieve the conditions of firing on-board. Expansion ability of the bullet Action 5 causes a different effect on the target in case of perforation of the substitute material first. The simulation using Finite Element Method system Ansys Autodyn v.14 presents 2D model based on experimental shooting. The simulation introduces the estimation of the substitute material thickness to achieve the ballistic limit for particular parts of the target.

Keywords: Action 5, hollow point bullet, ballistic limit, aircraft fuselage, FEM

1 Introduction

Rating the ballistic resistance of airliner airframe in case of firing on-board is important to assess the behavior of the aircraft structure in order to avoid catastrophic consequences. Shooting on-board occur in case of service procedure done by armed escort, which is usually armed with a gun and expansion ammunition.

Conditions of bullet fired on-board and penetrating the plane's fuselage can be very diverse. If the standard pistol bullet strikes the fuselage wall directly at angles close to the value of 90° without any forward obstacle, a smooth penetration occurs with the surplus of energy with high velocity of the range 300 m/s to 400 m/s. Such penetration has no significant effect on the functionality of the fuselage as the pressurized vessel.

However, if the bullet penetrates another target before impacting of the fuselage, e. g. human body, which is the primary target and the fuselage is the secondary target, the effect of the bullet may be radically different with unfavorable consequences. Such a bullet is not only reduced in velocity, but also usually a large deformation occurs, so called expansion. If the loss of energy of the bullet is higher, the perforation of the fuselage is not performed or finished. The deformed bullet with higher impact energy may cause more serious damage of the outer duralumin fuselage skin in conditions close to the limit velocity in the region of low bullet velocity of 100 m/s to 200 m/s. The damage in those conditions could be more serious and can cause an irregular hole after perforating the skin with the potential for the propagation of fatigue cracks, which is not favorable. However, it is supposed, that this kind of damage is dangerous in terms of longer aircraft operation than the time needed to complete the flight.

1.4 Action 5 ammunition characteristics

Ballistic resistance analysis made in this article is related to the service cartridge Action 5. It is a cartridge of caliber 9 mm Luger with homogeneous brass bullet with front expansion cavity covered with plastic cap, see Image 1. Basic ballistic characteristics of the cartridge important for the target effecting, are shown in Table 1.



Image 13 – The cartridge Action 5 and its parts – from the left the cartridge Action 5, two times the bullet of caliber 9 mm, the cartridge case with primer, the cut view of the whole cartridge Action 5

Table 2 Ballistic characteristics of the cartridge Action 5

Weight of the bullet m_b [g]	6.1
Initial bullet velocity v_0 [m/s]	460
Initial momentum of the bullet H_0 [kg · m/s]	2.8
Initial bullet energy E_0 [J]	645
Initial specific bullet energy e_0 [MJ/m ²]	10.1/4.1*

Note: *The values of the specific energy are valid for the bullet before deformation / after standard deformation in the substitute material. The cross section area of the front part of the bullet increases due to the expansion deformation from the original undeformed value 64 mm² to the value 156 mm² corresponding to the deformation diameter of the front part 14.1 mm, that means an increase of the cross section area of the value 145 %.

1.5 Mechanism of deformation of Action 5

The mechanism of deformation of the bullet is various in different target materials. In tissues of live targets or their substitutions is the behavior of the bullet as follows. The front plastic cap is first pressed deeper into the bullet cavity after the penetration into the surface layer of the tissue or block of substitute material. This opens a cavity partially and the cavity is afterwards filled by target material. At high velocities of penetration exceeding the value 400 m/s the front part of the bullet begins to deform due to the hydrodynamic effect of the target material and increases its front radial dimension. Penetration of the fuselage directly causes pressing of the cap into the bullet cavity as well, but the bullet does not expand, as there is no hydrodynamic effect of the soft target. Conversely the bullet Action 5 may deform the front part of its body in inside direction, which prevents expansion.

The deformed bullet is shown in Image 2. A significant increase of the front area increases the level of energy transmitted into the target and thus increases the wound potential of the bullet. On the other hand, the ability of the bullet to penetrate solid obstacles decreases. Wound potential and piercing potential of the bullet are intertwined.

1.6 Article objectives and methods

One aim of the article is setting the limit velocities of undeformed and deformed bullets with respect to the interest targets that are the gel block as the primary target and the fuselage structure as the secondary target. Knowing those limits is important for understanding the mechanism of interaction between the bullet and the obstacle and also in order to assess the extent of damage of the outer aircraft surface by penetrating bullet.

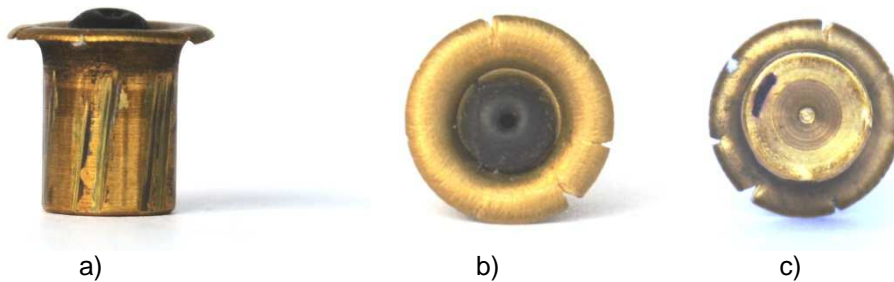


Image 2 – Deformed bullet Action 5 after standard expansion in ballistic gel: profile (a), top axial view (b) and bottom axial view (c)

Ballistic resistance of barriers with respect to bullets fired by small arms can be evaluated both theoretically and experimentally. The experimental method is firing that needs repeated shots to find desired results. Among theoretical methods of solving the interaction of bullets and obstacles is irreplaceable the Finite Element Method (FEM) simulation with possibility to change parameters and firing conditions that significantly reduces the costs compared to experiments. However, FEM simulations demands for correct representation of the behavior of investigated subject including material characteristics.

In order to achieve the objective of the article it is necessary to perform the firing experiments first and then to create a simulation model of the bullet, the gel block as the substitution of live targets and the fuselage structure based on experiments. A limit velocity of the bullet was estimated using simulation model and the corresponding thickness of the gel block. The velocity limits of the bullet can be estimated for both the complete fuselage structure assembly and for its particular parts, namely sidewall or sidewall and insulation layer.

There is possible to achieve three cases for impacting the substitution of living tissue first:

Case 1: Penetration of the fuselage structure completely at minimum residual velocity of the bullet.

Case 2: Penetration of both the inner sidewall and the insulation layer, when the bullet is stopped by the duralumin skin.

Case 3: Penetration of the inner sidewall solely and the bullet is stopped by the insulation layer.

Last two cases do not affect the integrity of the fuselage skin that could be important to prevent the leak of air pressure. However, it is supposed that the single penetration of the fuselage structure by the pistol bullet does no effect the decompression of the fuselage and risk to passengers.

2 Firing experiments

Shooting experiments were performed by the ammunition Action 5 using ballistic measure device of caliber 9 mm Luger of the length 150 mm and universal ballistic breech UZ 2002, producer Prototypa-ZM, Ltd. Brno. Two kinds of targets were used and one shot into each target was conducted at the distance 5 m from the muzzle of the measuring device, see Image 3. The velocity of the bullet v_{3m} was measured using non-contact optical gates LS-06 with the base 1 m. The process of penetration was captured by two high-speed cameras Redlake HG-100K and MotionXtra N4 in order to estimate the impact and residual velocities of the bullet. The temperature of used ammunition and gel block was 20°C and the temperature of the shooting range Prototypa, Inc., Brno, was 18°C.

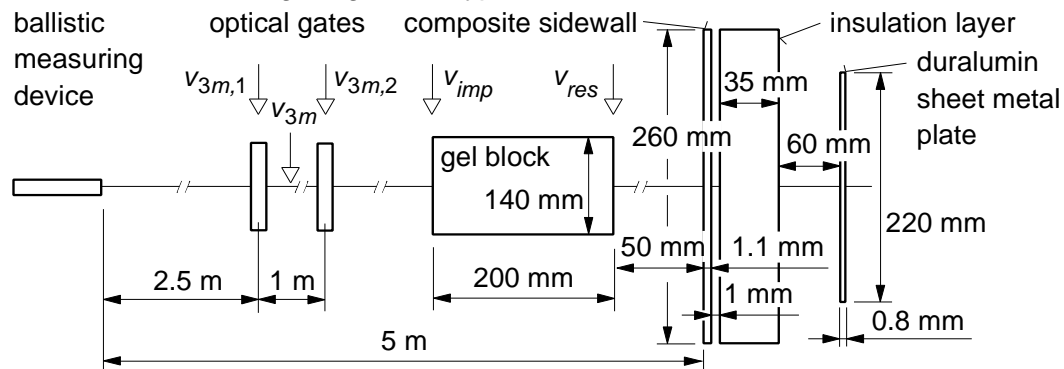


Image 3 – Scheme of experiment

2.1 Target description

The target of the first experiment was the assembly representing the commercial transport aircraft fuselage structure consisting of three parts – glass-epoxy composite sidewall of the thickness 1.2 mm, insulation glass wool layer of the thickness 35 mm and duralumin sheet metal plate of the thickness 0.8 mm. The insulation layer consists of lightweight, flexible thermal insulating glass wool blanket Microlite AA of the density 9.6 kg/m³ packed in plastic bag reinforced by fibers. The sheet metal plate used for outer skin of fuselage is of the material Al 2024T3 ALCLAD. The sheet metal plate has the rectangular dimension of 250 mm x 250 mm upon (German Police Technical Guideline, 2001). The geometry of the particular parts of fuselage structure is shown in Image 3. The process of mounting particular parts of the fuselage assembly is shown in Image 4. The experimental shooting represents firing on-board at the angle of 90° towards the front plane of the assembly, so the bullet aims out of the aircraft fuselage. The position of the fuselage assembly before shooting experiment is shown in Image 5a.

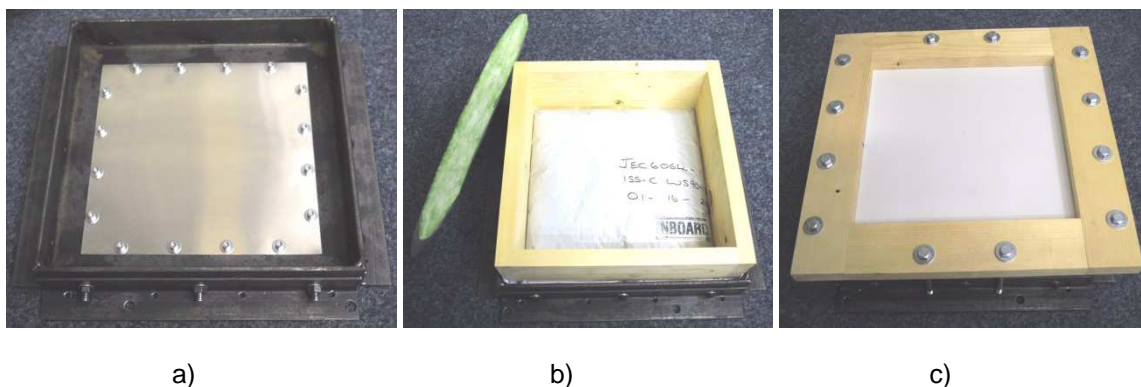


Image 4 – Scheme of mounting of fuselage structure assembly: sheet metal plate (a), insulation layer and the cut of layer (b) and composite sidewall (c)

The target of the second experiment consisted of two parts. The first part was the gel block Kraton 15% of the prismatic shape with length 200 mm and rectangle cross-section of dimensions 200 mm x 140 mm. The second part was the same assembly representing the fuselage structure used in the first experiment. The experimental shooting represents firing on-board at the angle of 90° towards the front plane of gel block first and in case of complete penetrating of the block the bullet hits the front plane of the fuselage assembly, so the bullet aims out of the aircraft fuselage as well.

The scheme of the experiment with the second target is shown in Image 5b.



a)

b)

Image 5 – Scheme of firing experiment: fuselage structure assembly (a) and fuselage structure assembly with forward gel block representing the live target hit first (b)

2.2 Experimental results

The experimental results of bullet velocities and energies of the bullet are shown in Table 2.

Table 2 Results of experimental shooting

No. of shot	$V_{3m,1}$	$V_{3m,2}$	V_{3m}	V_{imp}	V_{res}	$E_{k,imp}$	$E_{k,res}$	ΔE_k	$\Delta E_{k,rel}$
	m/s	m/s	m/s	m/s	m/s	J	J	J	%
1	442.7	442.8	442.75	436	414	580	523	57	10
2	457.8	457.9	457.85	451	92	620	26	595	96

In the first experiment the bullet penetrated the fuselage assembly as the secondary target with surplus of energy of the value $E_{k,res} = 523$ J. The character of the hollows is shown in Image 6. The penetration of the composite sidewall shown in Image 6a and 6d caused cylindrical hollow of the diameter 6.2 mm with torn fibers. It is visible at the back side of the composite sidewall a delamination process of the size approx. 35 mm x 35 mm, see Image 6d. The penetration of the insulation layer shown in Image 6b and 6e caused irregular hollow of the diameter approx. 6.9 mm with torn plastic bag and fibers and the dimension and shape of both hollows is very similar. The penetration of the duralumin sheet metal plate shown in Image 6c and 6f created a regular cylindrical hollow of the diameter 8.6 mm with relatively small plastic deformation around the hollow with teared rim. The character of

hollow proves that the bullet lacks the expansion; i. e. the deformed front part of the bullet did not exceed the caliber of the bullet.

The deformed bullet was not found after the shooting, so the exact character of the bullet expansion is not known. It is supposed, that the bullet is slightly deformed on its front part and shorten in length without the expansion as it is documented on similar experiment presented in (Hub, 2011).

In the second experiment the bullet penetrated the gel block as the primary target causing the temporary cavity in it and having reduced residual kinetic energy of the value $E_{k,res} = 26$ J. Such energy was not sufficient to penetrate even the first part of the secondary target and the bullet was bounced off the composite layer leaving behind small damage on the surface, see Image 7a. On the back side of the composite sidewall it is slightly visible delamination area of the dimension approx. 25 mm x 25 mm, see Image 7b. The shape of deformed bullet is shown in Image 7c. The bullet is expanded after penetration of the gel block, therefore the front area of the bullet is increased, see Table 1, and the bullet needs more energy to penetrate the following obstacle.

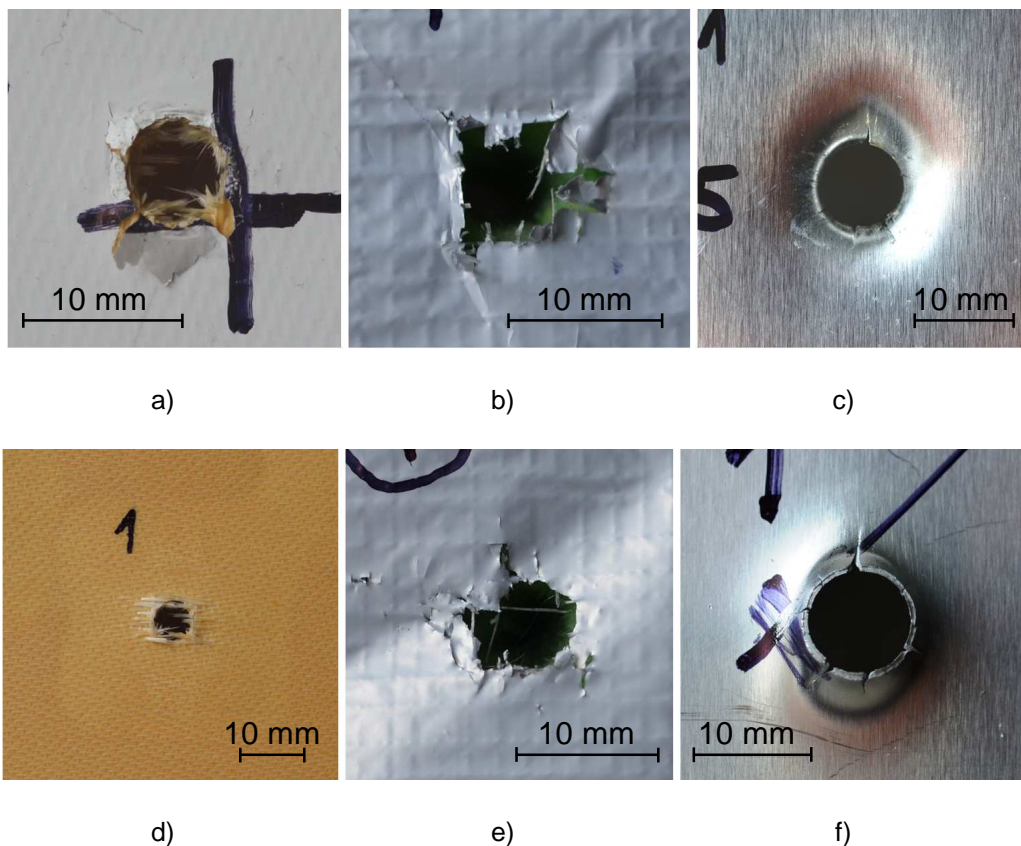


Image 6 – Results of the 1st experiment - hollows in parts of the secondary target: front side of the composite sidewall (a), front side of the insulation layer (b), front side of duralumin skin (c), back side of the composite sidewall (d), back side of the insulation layer (e), back side of the duralumin skin (f)

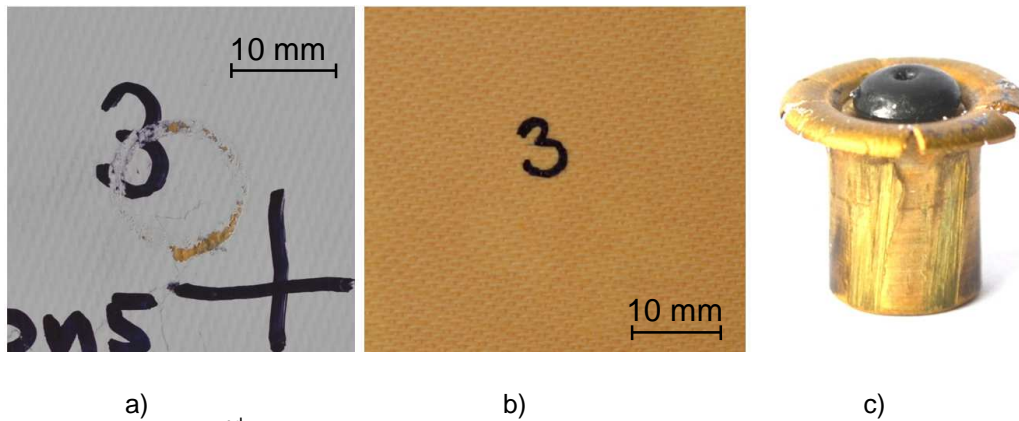


Image 7 – Results of the 2nd experiment – damaged surface of the front part of the composite sidewall (a), the back side of the composite sidewall (b) and deformed bullet (c)

The amount of energy given to the target is described through kinetic energy of the bullet. The kinetic energy of the bullet is generally described as the sum of translation and rotation energies upon equation

$$E_k = \frac{1}{2} m_b \cdot v^2 + \frac{1}{2} I_x \cdot \omega^2, \quad (1)$$

where m_b represents the weight of the bullet, v is the bullet translation velocity, I_x is inertia moment of the bullet and ω is angular velocity of the bullet caused by barrel bore of ballistic measuring device. The last part of the equation (1) is considered to be neglected and therefore the kinetic energy of the bullet corresponds to the first part of the equation (1).

The difference between impact and residual kinetic energies of the bullet ΔE_k means the energy consumed during the perforation of the gel block and the same parameter in percentual units $\Delta E_{k,rel}$ can be determined upon the equation

$$\Delta E_{k,rel} = \frac{E_{k,imp} - E_{k,res}}{E_{k,imp}} \cdot 100. \quad (2)$$

The values $\Delta E_{k,rel}$ in Table 2 show, that the bullet of the first experiment shooting the fuselage structure solely transmits just the small part of its energy into the target of the value 10 %. A different situation is with the second experiment, when the bullet hits the gel block first. In this case the bullet transmits into the gel block 96 % of its energy and therefore just the limited ability to penetrate the secondary target is left.

3 Finite Element Method simulation

The Finite Element Method simulation is presented in order to find a numerical model based on performed experiments of the bullet Action 5 penetrating the two kinds of target and using this model to find limit velocities for particular parts of the fuselage structure. Therefore an explicit nonlinear transient hydrocode Ansys Autodyn v 14.0 was used.

3.1 Simulation model

The model of the bullet and both the targets were created using 2D axial symmetry, therefore only a half parts of all components were modeled. The simulation methodology is based on (Hazell, 2009, Hub, 2011).

The geometry of the bullet is based on real dimensions and a little bit simplified in order to create a suitable mesh for the FEM analysis. The bullet uses the mesh-based Lagrangian method. The density of the bullet corresponds to the goal to meet the same total weight of the real and simulation bullets. The initial condition for the bullet is impact velocity v_{imp} equal to the experimental velocity; see Table 2. The velocity leads the bullet in perpendicular direction with respect to the sheet metal plate plane. The rotation of the bullet by barrel bore and air drag are not considered.

The fuselage structure contains three parts upon experiment – the composite sidewall, the insulation layer and the duralumin sheet metal plate. All parts have thicknesses upon experimental parts and have a rectangular shape in 2D projection that creates a disc using axial symmetry. The distance between parts follows the real geometry in aircraft structure. The periphery of all discs is clamped.

The simulation gel block is used in order to simulate the second experiment. The gel block shape does not follow the real prismatic geometry due to the axial symmetry used with FEM model. The shape of the simulation gel block is of cylindrical shape with diameter of 140 mm and length of 200 mm. The gel block uses the mesh-free particle based Smooth Particle Hydrodynamics (SPH) method and the size of particles is 1 mm.

The character and discretization of the simulation model of the bullet Action 5 and both the targets is shown in Image 8.

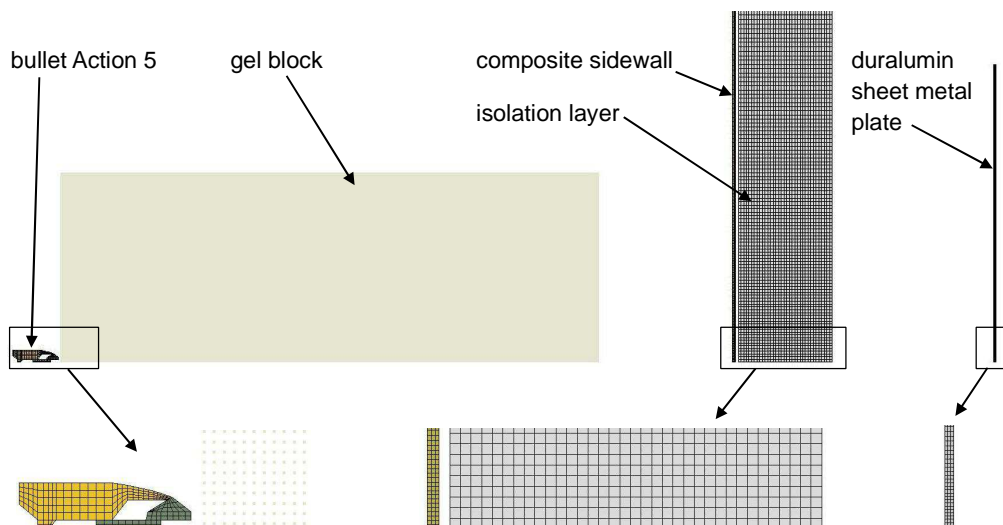


Image 8 – Character and discretization of 2D simulation model

The main parameter for validating the simulation model is residual velocity of the bullet when penetrating particular parts of target. In the case of the second experiment the next parameter is represented by the geometry of deformed bullet as well.

3.2 Material characteristics

The gel block as the primary target is represented by retrieved and modified model WATER taken from Autodyn library due to the limited published data available on the dynamic material properties of used materials. This model uses shock equation of state

relating hydrodynamic pressure with parameters $\rho = 760 \text{ kg/m}^3$, $C_0 = 1647 \text{ m} \cdot \text{s}^{-1}$ and $S_1 = 1.921$.

The fuselage structure as the secondary target consists of three parts.

The composite sidewall uses also retrieved model taken from Autodyn library GLASS-EPXY with density $\rho = 1840 \text{ kg/m}^3$. This model uses Puff equation of state covering the behavior of material from cold shocked regions to hot, highly expanded regions, with following parameters: $A_1 = 12130 \text{ MPa}$, $A_2 = 17980 \text{ MPa}$, Gruneisen coefficient 0.15, expansion coefficient 0.25 and sublimation energy 2 MJ/kg. Next the composite sidewall uses von Mises strength constitutive model premising that the yield stress has a constant value with shear modulus 4000 MPa and yield stress 143.1 MPa. The tensile pressure failure model of composite sidewall allows a maximum hydrodynamic tensile limit to be specified and has the value of -159 MPa. Also erosion is introduced in form of instantaneous geometric strain of the value 2.

The insulation layer is simplified and it is considered to be of one homogenous material without dividing between the glass wool blanket and reinforced plastic bag. Dynamic behavior of the insulation layer is described using easy linear equation of state and erosion failure model in form of instantaneous geometric strain of the value 2. Bulk modulus is considered of the value 1 kPa

A sheet metal plate made of aluminum alloy ASTM 2024-T3 is to some extent available in the Autodyn library. The equivalent designation of used material is upon ISO AlCu4Mg1, DIN AlCuMg2 and ASME SB211. The hydrodynamic shock equation of state of the alloy 2024-T3 relating hydrodynamic pressure, the local density and local specific energy is in Gruneisen form (Steinberg, 1996):

$$p = p_H + \Gamma \cdot \rho (e - e_H), \quad (3)$$

where p is hydrostatic pressure, p_H is Hugoniot pressure, $\Gamma = 2.0$ is Gruneisen Gamma, $\rho = 2780 \text{ kg/m}^3$ is density of the alloy, e is internal energy, e_H is Hugoniot energy. The pressure is based on a linear Hugoniot relation between shock velocity u_s and particle velocity u_p

$$u_s = C_0 + S_1 \cdot u_p, \quad (4)$$

where $C_0 = 5328 \text{ m/s}$ is initial sound speed and $S_1 = 1.338$ is Hugoniot slope coefficient.

The constitutive model expressing the relation between the shear stress and strain uses for the alloy 2024-T3 a Johnson-Cook model representing the strength behavior of materials subjected to large strains, high strain rates and high temperatures as it is the solving high-speed impact. The empirical Johnson-Cook model (Johnson, 1983) decouples the effect of strain, strain rate and temperature for the von Mises flow stress

$$\sigma = [A + B \cdot \varepsilon^n] [1 + C \cdot \ln \dot{\varepsilon}^*] [1 - T^{*m}], \quad (5)$$

where ε is the equivalent plastic strain, $\dot{\varepsilon}^* = \dot{\varepsilon} / \dot{\varepsilon}_0$ is the dimensionless plastic strain rate for $\dot{\varepsilon}_0 = 1.0 \text{ s}^{-1}$ and T^* is the homologous temperature. The five material constants are as follows: $A = 368.5 \text{ MPa}$ is the yield uniaxial stress, $B = 683.9 \text{ MPa}$ is the strain hardening coefficient, $n = 0.73$ is the strain hardening exponent, $C = 0.0083$ is the strain hardening coefficient and $m = 1.7$ is the thermal softening exponent. The actual values of the constitutive constant used for the material 2024-T3 are set according to (DOT, 2003, Doubrava, 2009).

The failure criterion describes the damage behavior and for the alloy 2024-T3 it is used a convenient model proposed by Johnson-Cook (Johnson, 1985). This model assumes that damage accumulates in the material element during plastic straining and that the material breaks when the damage reaches a critical value. This model is constructed in a very similar way to the Johnson-Cook strength model in that it consists of three independent terms that define the dynamic fracture strain as a function of pressure, strain rate and temperature

$$\varepsilon_f = \left[D_1 + D_2 \cdot e^{D_3 \cdot \sigma^*} \right] \left[1 + D_4 \ln|\dot{\varepsilon}^*| \right] \left[1 + D_5 T^* \right]. \quad (6)$$

The damage variable D takes values between 0 and 1. $D = 0$ corresponds to the undamaged material and $D = 1$ corresponds to the fully broken material. The evolution of D is given by the accumulated incremental effective plastic strain divided by the current strain at fracture

$$D = \sum \frac{\Delta \varepsilon}{\varepsilon_f}. \quad (7)$$

The actual values for the fracture Johnson-Cook material model of 2024-T3 alloy according (DOT, 2003, Doubrava, 2009) are following: $D_1 = 0.112$, $D_2 = 0.123$, $D_3 = 1.5$, $D_4 = 0.007$, $D_5 = 0$.

The bullet Action 5 used in simulation is described through various models.

The gilding metal jacket uses a shock equation of state with values: $\rho = 7985 \text{ kg/m}^3$, $\Gamma = 2.0$, $C_0 = 3958 \text{ m/s}$ and $S_1 = 1.497$. The constitutive model of modified COPPER model retrieved from Autodyn library uses the Piecewise Johnson-Cook model. This model is a modification of the Johnson-Cook model, where the dependence on effective plastic strain represented by the term $(A + B \cdot \varepsilon^n)$ in equation 5 is replaced by a piecewise linear function of yield stress Y versus effective plastic strain ε_p . The strain rate dependence and thermal softening term remain the same as in the Johnson-Cook model. The parameters used in gilding metal jacket simulation: $G = 68800 \text{ MPa}$, $Y_0 = 120 \text{ MPa}$, $\varepsilon_{p1} = 0.3$, $Y_1 = 450 \text{ MPa}$, $Y_2 = 450 \text{ MPa}$, $m = 1$.

The plastic cap of the bullet considers the polyurethane material POLYURETH retrieved from Autodyn library as well. This model uses the simplest shock equation of state that can be determined by assuming that the pressure is independent of the internal energy and that changes in the material density are small and reversible. Expressing the pressure as a Taylor series in the density and retaining only the linear terms leads to the linear equation of state

$$p(\rho) = K \cdot \mu, \quad (8)$$

where $K = 2000$ MPa is the bulk modulus and $\mu = \rho/\rho_0 - 1$ is the compression (Autodyn, 2006), where $\rho/\rho_0 = 1265$ kg/m³.

Strength model of the plastic cap as expressing the resistance of given material to shearing forces uses simple elastic form and failure model uses the maximum value of principal stress. The shear modulus has the value of 5 MPa.

3.3 Simulation model validation

The simulation using FEM follows the goal to reach as good correspondence as possible for two experimental and simulation penetration process parameters – the bullet velocity and the deformation character both of the bullet and the target. The results are shown in Table 3.

Table 3 Comparison of experimental and simulation velocities of the bullet

No. of shot	V_{imp}	V_{res}	$V_{res,sim}$	ΔV_{res}
	m/s	m/s	m/s	%
1	436	414	419	1
2	451	92	89	3

The expression $V_{res,sim}$ means residual velocity of the bullet obtained by simulation. The expression ΔV_{res} means the deviation of experimental and simulation results estimated as the relation between the difference of both experimental and simulation residual velocities with respect to the lower value of both residual velocities.

When comparing the experimental and simulation results, the correspondence between both velocities is very good.

The Image 9 shows the simulation results for the first shot, when the bullet penetrated the fuselage structure directly without any forward obstacle. The simulation composite sidewall is distorted in its plane and in the area of the hollow as well. Those deformations do not correspond to the real experiment due to the fact that the experimental sidewall remains in the whole plane flat. The material model of the sidewall should be corrected and needed are particular experiments done on the composite sidewall solely.

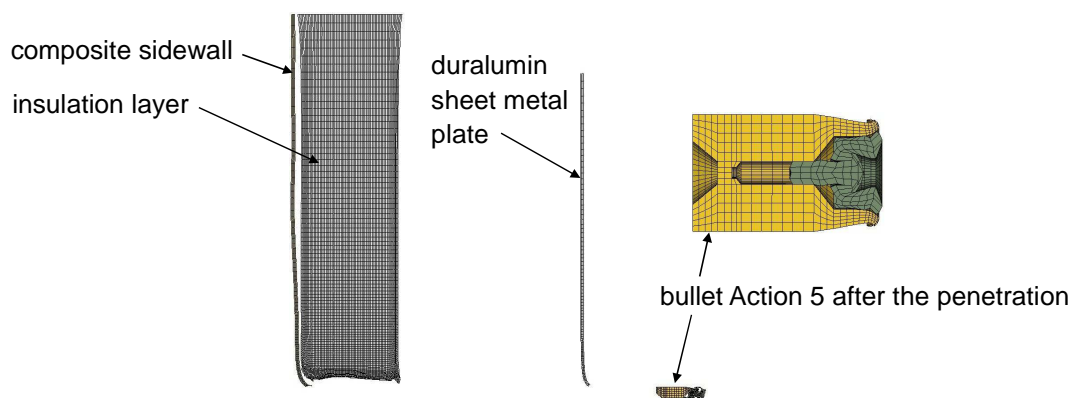


Image 9 – Character and discretization of 2D simulation model of penetrating the fuselage structure

The simulation of the insulation layer follows the general behavior of the experimental one with one exception. The bullet caused the hollow of higher diameter in the simulation insulation layer than in experiment. Also the simulation model of the insulation layer should be corrected.

The behavior of simulation sheet metal plate follows the behavior of experimental plate quite good with two exceptions. Firstly, the diameter of the hollow made by bullet is higher with simulation than with experiment. The simulation value is 9.7 mm and experimental value is 8.6 mm. And secondly, the height of the rim around the hollow has the value 3.2 mm for the simulation and the value 4.4 mm for the experiment. Those differences can be a result of making just a one shot on experiment, next by simplifying simulation model with respect to the experiment, eq. neglecting the rotation of the bullet and using 2D model that cannot meet the crack propagation on the rim of the sheet metal plate hollow.

Image 9 shows also the shape of deformed bullet. The expansion process occurs just slightly on the front part, which agrees with the presumption made in chapter 2.2. The diameter of the front part does not exceed the bullet caliber and therefore the piercing ability of the bullet remains standard. The plastic cap is pushed inside of the bullet cavity.

The shot No. 2 when the bullet penetrates the gel block first is shown in Image 10.

The interaction of the bullet and the gel block causes the deformation of the bullet in form of expansion and the deformation of the gel block in form of temporary cavity. The volume of the cavity depends on the level of bullet expansion and the bullet expansion depends on the bullet velocity. Higher velocity of the bullet causes higher expansion and larger volume of the temporary cavity (Hub, 2012). The bullet fired by standard velocity used in this experiment expresses almost the highest level of expansion and the expansion is finished in very short distance of the depth 31 mm after impacting the front face of the gel block. The expansion process changes geometrical shape of the bullet Action 5 and therefore it has a radically different effect on the secondary target. The bullet with expanded larger front area demands for higher energy to penetrate the secondary target.

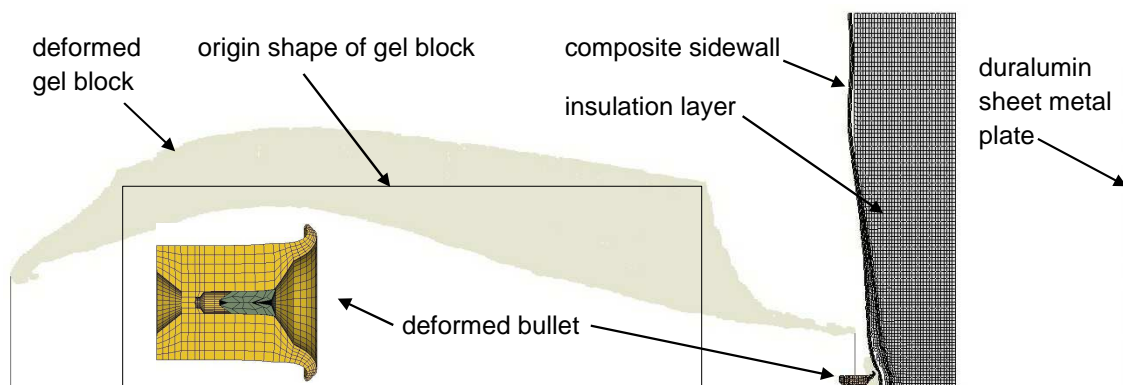


Image 10 – Character and discretization of 2D simulation model of penetrating the gel block and the fuselage structure by the bullet Action 5

The bullet penetrated the gel block with surplus of energy but not sufficient to penetrate even the first part of the secondary target – composite sidewall. The bullet was bounced back causing just plastic deformation on the sidewall surface and pressing a most of the center area of the sidewall towards the insulation layer located 1 mm behind the sidewall.

The course of the velocities of the bullet penetrating the fuselage structure is shown in Image 11a. The first downwards quasi-linear slope starting at the time approx. 0.01 ms shows the process of penetration of the composite sidewall, the velocity reduction is approx. 13 m/s and represents the most resistant part of the target upon simulation. The next slight slope starting at the time approx. 0.04 ms shows the penetration process of insulation layer, the velocity reduction is approx. 1 m/s. Finally the last nonlinear course starting at the time approx. 0.23 ms shows the penetration process of duralumin sheet metal, the velocity reduction is approx. 8 m/s. Both graphs are taken from Autodyn.

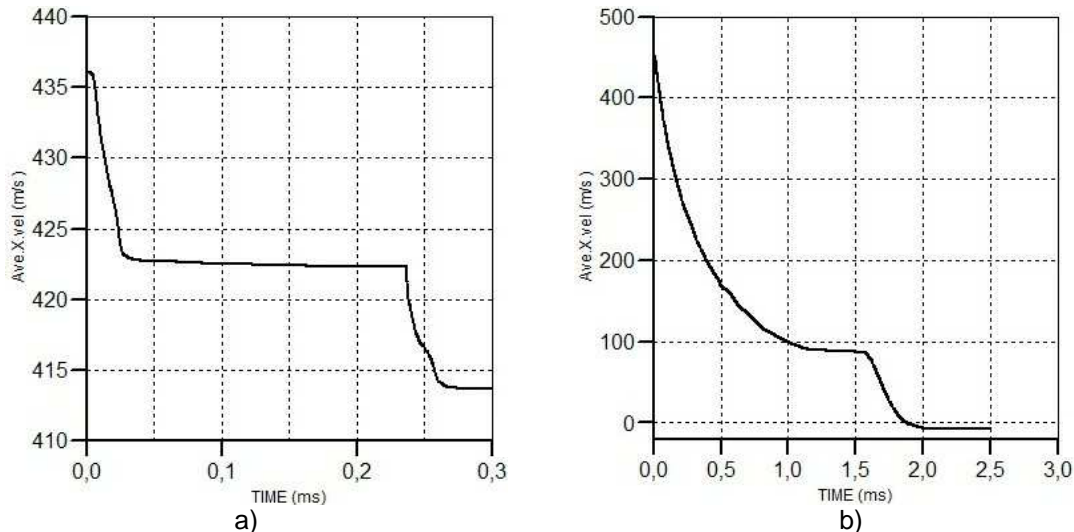


Image 11 – The course of bullet velocities: penetrating the fuselage structure solely (a) and penetrating the gel block and the fuselage structure

The course of the velocities of the bullet penetrating the gel block first and consequently the fuselage structure is shown in Image 11b. The first nonlinear downwards course shows the process of penetration of the gel block. The velocity reduction has the value 362 m/s and represents the most resistant part of all targets presented in this article. Next nonlinear downward course starting at the time approx. 1.58 ms shows the process of impact of the bullet into the first part of the fuselage structure that is composite sidewall. The energy of expanded bullet travelling at the velocity of 89 m/s is not sufficient to penetrate the sidewall and the bullet is bounced back following the experimental behavior.

The simulation of this second shot enables to compare also the shape of deformed bullet taken from experiment and simulation. The Table 4 presents the main dimensions of both bullets and Image 12 shows their graphical comparison. The parameter D means the diameter of front expanded part of the bullet; D_{min} is the minimum value, D_{max} is the maximum value and D_{avg} is the average value. The parameter L means the length of the deformed bullet; L_{cap} means the overall length of the bullet with plastic cap, L_{min} means the minimum value without considering the plastic cap, L_{max} means the maximum value without considering the plastic cap and L_{avg} means the average value without considering the plastic cap. The deviation is considered as the relation between the difference of both experimental and simulation values with respect to the lower value of both values.

Table 4 Comparing the experimental and simulation bullet dimensions

Bullet type	D_{min}	D_{max}	D_{avg}	L_{cap}	L_{min}	L_{max}	L_{avg}
	mm	mm	mm	Mm	mm	mm	mm
Experiment	14.0	14.2	14.1	13.1	12.0	12.2	12.1

Simulation	12.4			12.4			
Deviation	-	-	14 %	6 %	-	-	2 %



Image 12 – Comparison of the character of deformed bullet: experimental (a) and simulation (b)

The simulation dimensions of the bullet reflect the experimental bullet to some extent. The simulation bullet has eroded its plastic cap, see Image 10, therefore it is compared also the length of experimental bullet without its plastic cap. Such length of the bullet is in a good agreement. The diameter of the front part of the bullet has the deviation of 14 % and do not fit the real behavior completely due to the nature of 2D model that is simplified and cannot meet all aspects of real behavior, e.g. tearing process on the rim of the expanded part of the bullet that increases its diameter. Comparison of the shape and dimensions of expanded bullet will be reasonable for the 3D simulation that is supposed to be able to cover also the complexity of tearing process.

In order to validate particular parts of the fuselage structure, additional experiments were made upon the composite sidewall and insulation layer to investigate the correspondence between the experiments and simulation models of mentioned parts solely. The results of the experiment are shown in Table 5. There were used two kinds of velocities using delaboration of the cartridge in order to reduce the amount of propellant and to change the bullet velocity for better matching the correspondence. The impact velocity is equal for both the experiment and the simulation. The differences Δ are set as the difference between the residual experimental and simulation bullet velocities.

Table 5 Comparing the experimental and simulation bullet dimensions

Target type	$V_{imp,exp}$	$V_{res,exp}$	Δ_{exp}	$V_{imp,sim}$	$V_{res,sim}$	Δ_{sim}
	m/s	m/s	m/s	m/s	m/s	m/s
Composite sidewall	449	436	13	449	438	11
	465	454	11	465	452	13
	262	251	11	262	248	14
Insulation layer	456	448	8	456	455	1

	267	262	5	267	267	0
--	-----	-----	---	-----	-----	---

When comparing the differences Δ , we can see very good correspondence with composite sidewall but poor results with the insulation layer. The model for the insulation layer should be improved.

The simulation model presented here is considered to be validated and it will be used for finding the ballistic limits of the secondary target.

4 Ballistic limits estimation

The validated simulation model will be used for estimation of the ballistic limits of the fuselage structure defined in chapter 1.3 when firing the gel block first in form of three cases. Therefore the various thickness of the gel block L_B was introduced to investigate the penetration abilities of the bullet Action 5 for the firing velocity of $v_1 = v_{imp} = 451$ m/s.

The velocities on particular positions of the target are defined in Image 13.

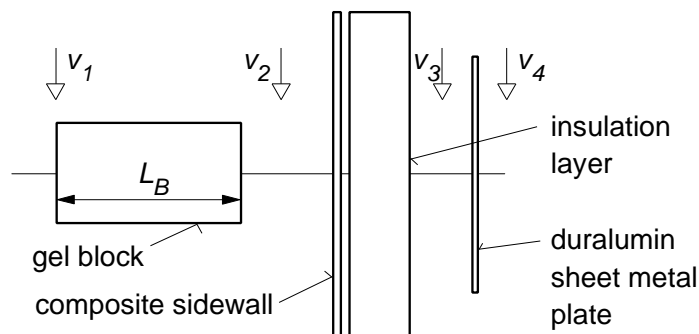


Image 13 – Definition of velocities

The results of the simulation using various gel block thickness are presented in Table 6 and graphical course of particular velocities with respect to the gel block thickness is shown in Image 14a.

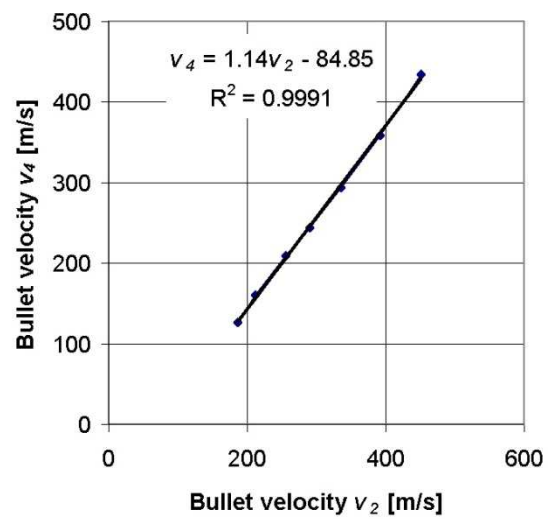
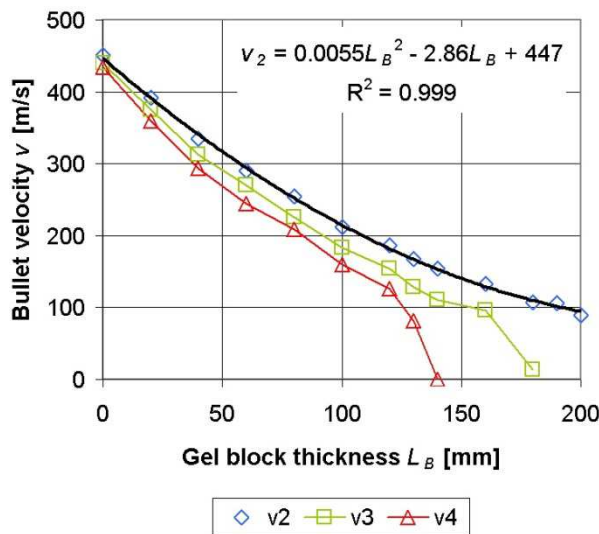
Analysis of ballistic limit cases:

Case 1: Penetration of the fuselage structure completely at minimum residual velocity of the bullet – the ballistic limit falls into the range of the thicknesses of the gel block from 130 mm to 140 mm. In the Table 5 we can see, that for the thickness of 120 mm the bullet penetrates the whole fuselage structure with residual velocity of 126 m/s. The thickness of the gel block of 140 mm caused full penetration of the sheet metal plate but in spite of this the bullet was stopped by the plate. Therefore the ballistic limit for penetrating the whole fuselage structure with minimum bullet velocity is estimated to be of the value **135 mm** for the gel block thickness.

Table 6 Simulation results of the bullet velocity in particular positions of the target

Gel thickness L_B	v_1	v_2	v_3	v_4
mm	m/s	m/s	m/s	m/s
0	451	451	440	434

20	392	375	359
40	335	312	294
60	290	270	244
80	255	225	209
100	212	183	160
120	186	154	126
130	167	128	82
140	154	111	0
160	133	96	-
180	107	13	-
190	106	-	-
200	89	-	-



a) b)
Image 14 – Course of bullet velocities versus gel block thickness (a) and relation between impact velocity of the bullet v_2 into the fuselage structure and the bullet residual v_4 velocity (b)

Case 2: Penetration of both the inner sidewall and the insulation layer and the bullet is stopped by the duralumin skin - the ballistic limit falls into the range of the thicknesses of the gel block from 140 mm to 160 mm. In the Table 5 we can see, that the thickness of the gel block of 140 mm caused full penetration of the sheet metal plate and stopping the bullet. The thickness of the gel block of 160 mm reduced the bullet velocity to the value not sufficient to penetrate the sheet metal plate although some deformation with the sheet metal plate occurred. Therefore the ballistic limit for penetrating the composite sidewall and insulation layer but stopping the bullet by the sheet metal plate is estimated to be of the value **150 mm** for the gel block thickness.

Case 3: Penetration of the inner sidewall solely and the bullet is stopped by the insulation layer – this case is difficult to achieve due to the very low resistance of the insulation layer against penetration by the bullet Action 5. Anyway, the ballistic limit falls into the range of the thicknesses of the gel block from 180 mm to 190 mm. The Table 5 shows that the thickness of the gel block of 180 mm enables for the bullet to penetrate the insulation layer with residual velocity of 13 m/s. The thickness of the gel block of 200 mm reduces the bullet velocity to the value not sufficient to penetrate the first part of the fuselage structure – composite sidewall. Therefore the ballistic limit for penetrating the composite sidewall but stopping the bullet by the insulation layer is estimated to be of the value **185 mm** for the gel block thickness.

The course of velocity v_2 impacting the fuselage structure after penetrating the gel block is fitted with polynomial approximation of the second order, see graph in Image 14a. This approximation enables to estimate the residual velocity of the bullet with respect to the gel block thickness L_B ; the thickness L_B is set in [mm], the velocities in [m/s]:

$$v_2 = 0.0055.L_B^2 - 2.86.L_B + 447 . \quad (9)$$

The graph in Image 14b shows the relation between the residual velocity leaving the fuselage structure v_4 with respect to the velocity v_2 impacting the fuselage structure for the region of gel block thickness of 0 mm to 120 mm only. In this region the bullet penetrates the both the gel block and the fuselage structure completely with surplus of energy. The value 130 mm cannot be taken into account even having the complete penetration of the bullet due to the nonlinear character of dependence of the velocity v_4 with respect to the velocity v_2 . A proposed linear approximation enables to estimate the residual velocity v_4 depending on the impact velocity v_2 in form:

$$v_4 = 1.14.v_2 - 84.85 . \quad (10)$$

Using both equations 9 and 10 is possible to estimate the residual velocity of the bullet penetrating both the gel block and fuselage structure v_4 with respect to the gel block thickness L_B . Proposed procedure is valid only for the region of gel block thickness from the value 0 mm to 120 mm.

5 Discussion

The investigated fuselage structure expresses just a little ballistic resistance upon performed FEM simulation when facing the impact of Action 5 projectile. One of the most probably impacted airplane structures is in case of firing on-board the fuselage structure as the largest are of the airplane with very poor ballistic resistance. The bullet Action 5 is able to penetrate the fuselage structure when impacting the structure directly with surplus of energy.

In case of impacting the substitute material first, the geometry of the bullet changes due to the expansion and piercing ability decreases. In spite of this, the bullet is able to penetrate the fuselage structure to large extend of the gel block thickness up to the value approx. 130 mm. Exceeding this value the bullet damages the sheet metal skin in form of incomplete penetration up to the value of 150 mm. The damage of the outer sheet metal plate should not occur exceeding the gel block thickness of 190 mm.

The bullet Action 5 proved also its expansion ability during penetration the soft target. The expansion does not progress in case of penetrating the hard target representing by the fuselage structure when firing directly.

From the point of view of damage of the outer skin of the airplane is the penetration of the expanded bullet travelling at low velocity much more dangerous than penetration by the same bullet but travelling at high velocity without expansion.

However, the most common transport airplane structure is of semimonocoque type and such structure is able to distribute the load easily to adjacent parts in case of damage. Therefore the effect of skin damage due to isolated or even the multiple complete penetration of the Action 5 bullet on airframe strength and stiffness is supposed to be negligible (Hub, 2009). The danger of damaging the inner systems by the bullet with more serious consequences remains to be occurred.

1 Conclusion

Experiments and simulations done upon the gel block and the fuselage structure targets have shown a significant difference in piercing ability of the bullet Action 5 under various target conditions. In case of firing directly to the secondary target that is fuselage structure, the bullet penetrates all parts of the fuselage structure easily with high surplus of energy. After the simulated penetration of thin and thick parts of the human body that can be represented by the arm above the elbow and thighs of the leg, penetration ability of the bullet decreases significantly partly due to the expansion of the bullet and increasing the cross section of the bullet and partly due to lower velocity of the bullet impact as a result of deceleration in the test gel block. When considering a possible damage of the fuselage skin, the least favourable situation corresponds to the firing through gel block of the thickness less than 150 mm. In this case a large damage could occur due to tear of the skin caused by low impact energy and expanded bullet, which could have negative consequences in real flight.

A numerical model has been developed upon firing experiments that simulates the penetration of the substitute material and subsequent perforation of fuselage structure used in airplane structures by bullet of mentioned projectile.

The FEM simulation results have shown:

- a good possibility to use the software Ansys Autodyn for modelling the penetration process, to consider the boundary conditions and to take an advantage of implemented material models with the possibility of modification to meet the real behaviour of the simulated objects,
- a good correlation between the experimental and simulation results in terms of comparison the residual velocities after penetration of the bullet through the both targets,
- a crucial influence of material characteristics for simulation the experimental shooting,
- a methodology for evaluating the residual velocity of the bullet penetrating both targets with respect to the gel block thickness,
- a limited ballistic resistance of investigated fuselage structure facing the impact of the projectile Action-5,
- higher relevance of the results demands for wider extent of experimental shooting especially for particular parts of the target and performing the 3D FEM simulation.

References

AUTODYN, 2006. *Autodyn Training Course. Autodyn Workbench release 11.0*

DOT/FEE/AR-03/57, 2009. *Failure modelling of titanium 6Al-4V and aluminium 2024-T3 with the Johnson-Cook material model*. Federal Aviation Administration. 24 p.

DOUBRAVA R., 2009. Simulation of rigid projectile impact on the real aircraft structure. *Czech Aerospace Proceedings*, 2009, No.2, p. 18 – 20. ISSN 1211-877X

GERMAN POLICE TECHNICAL GUIDELINE (Technische Richtlinie Patrone 9 mm x 19, Schadstoffreduziert des Unterausschusses Führungs- und Einsatzmittel), 2011. Munster: Polizeitechnisches Institut der Polizei-Führungsakademie, 63 p.

HAZELL P., 2009. Numerical simulations and experimental observations of the 5.65-mm L2A2 bullet perforating steel targets of two hardness values. *Journal of Battlefield Technology*, March 2009, Vol. 6, No. 1, p. 1 – 4. ISSN 14405113.

HUB J., KOMENDA J., RACEK F., 2011. Ballistic resistance of duralumin sheet metal plate using forward obstacle. In.: *International Conference in Military Technology Proceedings ICMT'11*, Brno, 10 – 13 May 2011. Brno : JALOVECKY R. and STEFFEK A. (ed.), p. 1683 1692. ISBN 978-80-7231-787-5.

HUB J., KOMENDA J., 2012. Analysis of Terminal-Ballistic Behaviour of Pistol Bullet Penetrating the Block of Substitute Biological Material. In.: *9th International Armament Conference on Specific aspects of armament & safety technology*, Pultusk, 25 - 28 September 2012. Warszawa : CHROMIK R., KIJEWSKI J., LECIEJEWSKI Z. (ed.), p. 344 – 360.

JOHNSON G. R., COOK W. H., 1983. A constitutive model and data for metals subjected to large strains, high strain rates and high temperatures. In.: *Proceedings 7th International Symposium on Ballistics*, The Hague, 1983, p. 541 – 547.

JOHNSON G. R., COOK W. H., 1985. Fracture characteristics of three metals subjected to various strains, strain rates, temperatures and pressures. *Engineering Fracture Mechanics*, 1985, Vol. 21, p. 31 – 48.

STEINBERG D. J., 1996. *Equation of state and strength properties of selected materials*. Lawrence Livermore National Laboratory, 1996, 69 p.

Acknowledgement

The work presented here in this paper has been supported by the Ministry of Interior of the Czech Republic (security research project VG20112015037).

Contact address:

Eng. Juraj Hub, Ph.D.*

Department of Aircraft and Rocket Technologies, University of Defence, Kounicova 65, 662 10 Brno, Czech Republic, email: juraj.hub@unob.cz, tel.: +420 973 445 189

Accoc. Prof. Eng. Jan Komenda, CSc.

Department of Weapons and Ammunition, University of Defence, Kounicova 65, 662 10 Brno, Czech Republic, email: jan.komenda@unob.cz, tel.: +420 973 445 368

MODEL OF RADIATION HEATING OF SLUSH MOULDING TECHNOLOGY

MARTIN HUŠEK

Technical university of Liberec,
Faculty of Mechatronics, Informatics and Interdisciplinary Studies

Abstract: The technology for the manufacturing of softened automotive accessories used in company Magna Exteriors & Interiors Bohemia, s.r.o is called Slush moulding. The technology is mainly suitable for the manufacturing of artificial leather, for example for the dashboards. It is a method of radiation heating of shell moulds which supplies the suitable shape, thickness and design relief to the final product. Infrared emitters are placed around the mould by the numerical model, simulating the whole process of radiation heating. For the purposes of the preparation of the model and the application of boundary conditions is IREviewBlender application suggested. The final temperatures are solved in the software ANSYS. The linkage of these information tools enables simulation of the whole process of transient heating with the application of temperature regulation.

Keywords: Slush moulding, shell mould, infrared emitter, transient heating, heat flux

1 Introduction

The company Magna Exteriors & Interiors Bohemia, s.r.o has been dealing with the Slush moulding technology used in the manufacturing of softened automotive accessories for several years. This technology is less energetically demanding and takes up much less space on the manufacturing floor in comparison with other technologies used in the same manufacturing processes.

It was clear from the very beginning that this unique technology cannot be implemented without some necessary software which enables the simulation of technological processes in the manufacturing.

The present article deals with one of these technological processes and mentions a possibility of simulation of heating of shell moulds. In this case the link between commercial software ANSYS and freeware software Blender with addition of new customised functions suitable for the preparation of the model proved to be effective.

2 Slush moulding technology and used simulation method

The base of this method of manufacturing is a shell mould. Thermoplastic powder based on PVC or PU is applied on inner surface of the shell mould. Its outer surface is heated by infrared emitters up to the temperature of approximately 220 °C. The powder melts and when the mould is cooled down by water, it becomes a compact mass representing artificial leather. The inner face of the mould has to be formed so that it gives the corresponding shape and suitable surface relief to the final product. The final leather is subjected to the strict quality control when removed from the mould. In case of the artificial leather thickness check-up, for example the airbag area is particularly watched, bound to fulfill the prescribed dimensions.

Infrared emitters allowing heating of the mould are clamped into a special structure located above the mould. The quantity of the used emitters is usually counted in tens and is defined by the size and compoundness of the surface of the mould. If a two-cavity mould is used for simultaneous manufacturing of two artificial skins for a dashboard, the number of applied emitters reached almost two hundred pieces.

The whole process of heating is carried out under the temperature regulation. There are thermocouples placed on the outer surface of the heated mould. Each thermocouple regulates one emitter or a group of emitters by two-state control. Due to the complexity of the used moulds it is not possible to achieve even temperature distribution in the range of 20 °C without any temperature regulation.

2.1 Process of design of transient heating of moulds

The process of design of heating shown in the fig. 1 is divided into two main parts. It is the virtual heating and the heating itself on a test production line or a production line. The virtual heating phase begins in IREviewBlender. With the use of the appropriate functions, the emitters are placed around a model of the mould and heat flux loading of the surface is simulated. After that the FEM analysis in ANSYS follows in order to calculate the final temperature dependant on time. In case of a positive result, the necessary data are exported, mainly the transformation matrix determining the positions of the emitters in relation to the given coordinate point for physical installation into the production line. The phase of the real heating process begins with the installation of the emitters holder in the production line by a robotic arm. Correctness of the installed heating is tested on the first samples of the artificial leather. The samples are then checked for burns or insufficiently heated patches. If the defects are small, they are corrected on the spot by redirection of a specific emitter, otherwise the design process goes back to the phase of the virtual heating. If everything is in order, the heating is released into batch production [1, 2, 3].

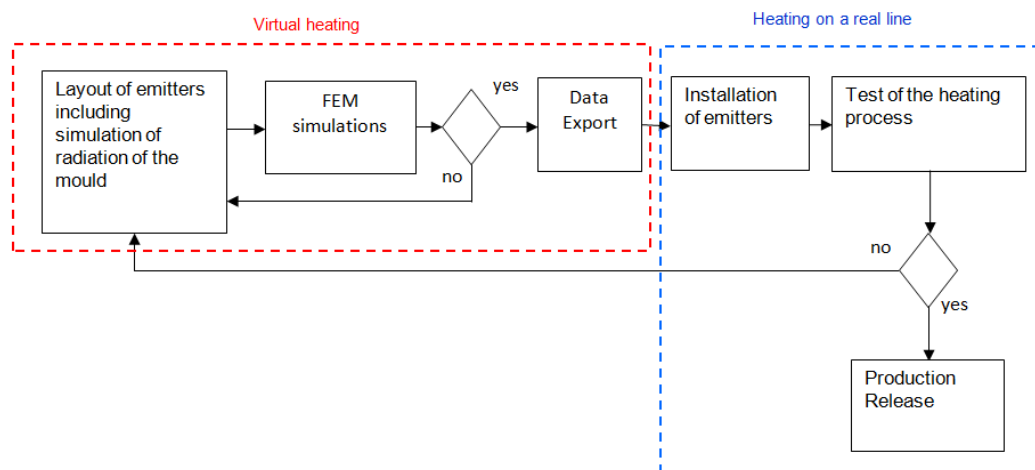


Fig. 14 – Scheme of the design process of heating

2.2 Software IREviewBlender as a pre-processor

The application can simulate heat flux loading of the mould by individual emitters or by the whole groups, see fig. 2. However, the problem of radiation is not solved by this application, but the corresponding heat flux density obtained from the database of the characteristics of different types of emitters is assigned to the individual elements of the mesh. This database was created by means of experimental measurements. Heat flux characteristics consider both the distance of an element center from an emitter and their mutual rotation. For continuous distribution of the heat flux boundary condition it is possible to interpolate the

values. The required types of emitters are selected by the user from the database of emitters, see fig. 3. The figure shows various types of emitters. There are single emitters or double emitters with or without reflectors. The most used emitters are those of 1.6 kW and 2kW.

For assembly of the model of heating in the IREviewBlender application it is possible to import some important parts for heating, e.g. the frame of the mould or the frame structure for placing the emitters. The user can thus verify the feasibility of placing the emitters in the production line and non-collision of the emitters with other objects. The user can work in several work scenes and thus compare individual variants of the emitters placing. Having finished the model preprocessing, the placing of the thermocouples and their pairing with the emitters follows. For thermal analysis in ANSYS the user does the appropriate settings and data exports [1, 2, 3].

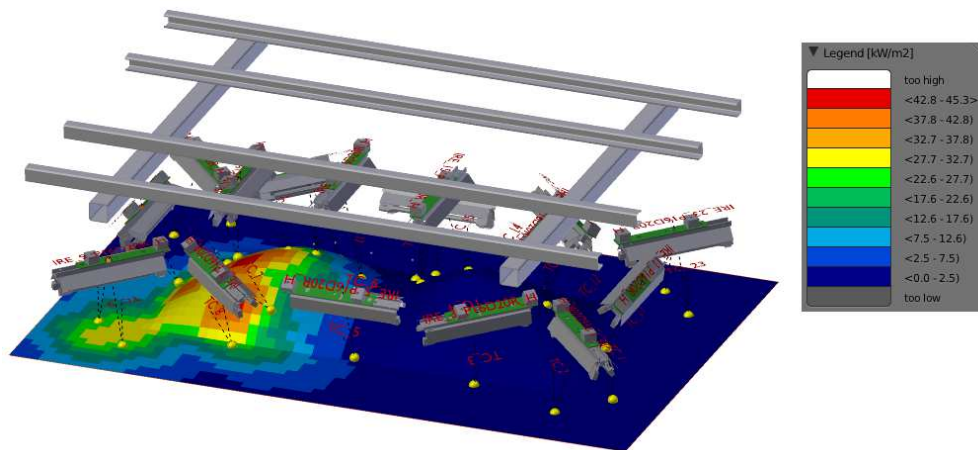


Fig. 2 - Heat flux - IREviewBlender

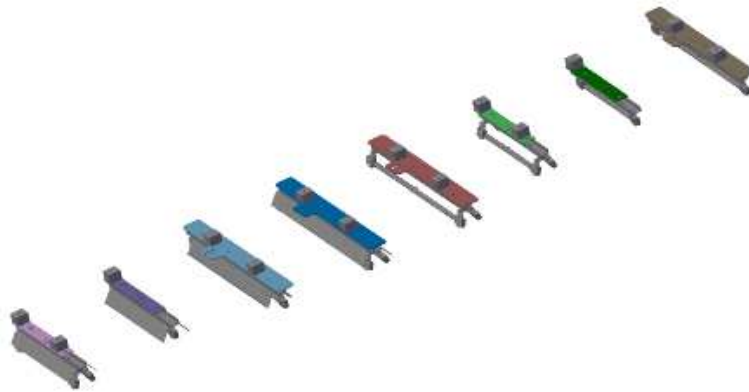


Fig. 3 - Database of emitters – IREviewBlender

2.3 Calculation of the temperature in the sw ANSYS

It is possible to calculate the final temperatures on the mould surface in the sw ANSYS by means of special exports from the sw IREviewBlender. The user has the possibility to calculate the final temperature on the basis of the heat flux density loading given by the simulation of the IREviewBlender, see fig.4, or whether he wants to solve the task by the radiation computation, see fig.5.

It is clear from the figures, that the temperature field in the first case reaches higher local maxima, as the thermal radiation is more oriented in the space under the emitter. In the second case the thermal radiation is more dispersed and reaches lower values.

The real behaviour of the radiation heating in the Slush moulding technology corresponds better to the fig.4, where the most thermal radiation is oriented into the space under the emitter. This behaviour is caused by the characteristics of the sheet metal reflector and characteristics of the reflection layer of the glass tube of the emitter.

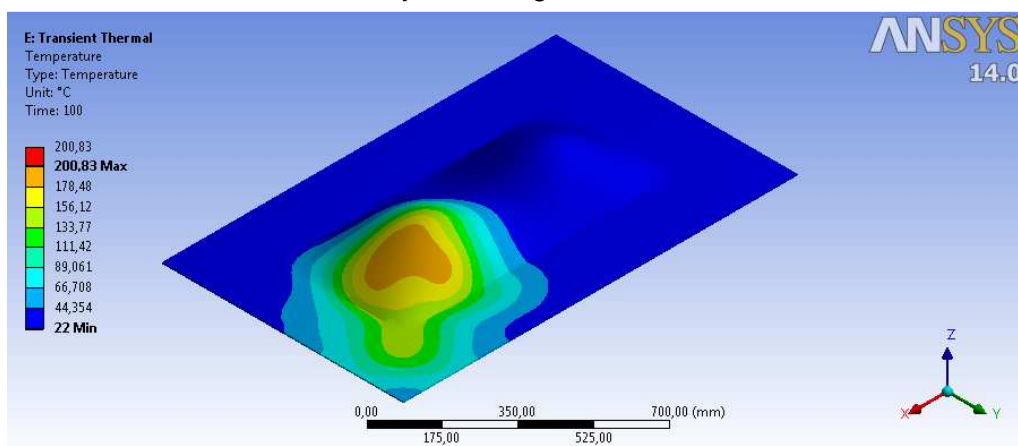


Fig. 4 - Resulting temperature, loading from IREviewBlender

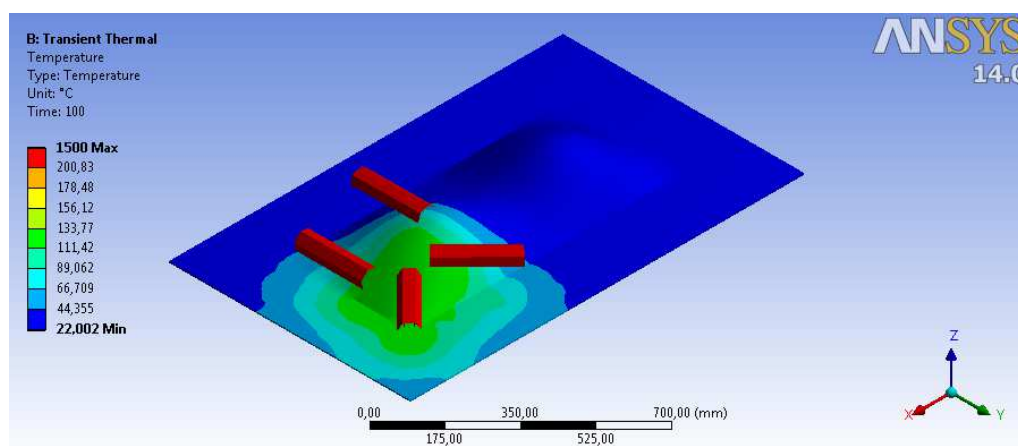


Fig. 5 – Resulting temperature, radiation computation

2.4 Possibility of simulation of regulated heating

The real heating in the line works with the temperature regulation, otherwise it would not be possible to reach uniform temperature distribution. Suitable combination of sw ANSYS and IREviewBlender allows to realize fully automatic regulated heating. For this purpose it is necessary to place thermocouples in the model. They are most often placed perpendicularly to the emitter tube or the mould edge closer to the emitter. In the model they are represented by the balls placed on the mould surface, see fig.2.

The regulation setup is executed in the application IREviewBlende where the user enters the simulation time, time steps of temperature scan, required temperature and other setup such as regulation deviations from the required temperature. Having started the simulation in the application IREviewBlender, the sw ANSYS starts in the batch mode. It waits for getting the text file with the values of the heat flux density and then computes temperatures. ANSYS then gives back to IREviewBlender the values of temperatures on the thermocouples in the textfile. On the basis of these data IREviewBlender switches on and off the emitters. It is two-step regulation where the emitter is either on or off.

The following figure 6 shows the regulated temperature behaviour on several selected thermocouples. The regulation was done around the slush temperature corresponding to the value of 220°C. Fig.7 illustrates the same heating without applied temperature regulation. This state would not be suitable for the production of the artificial leather.

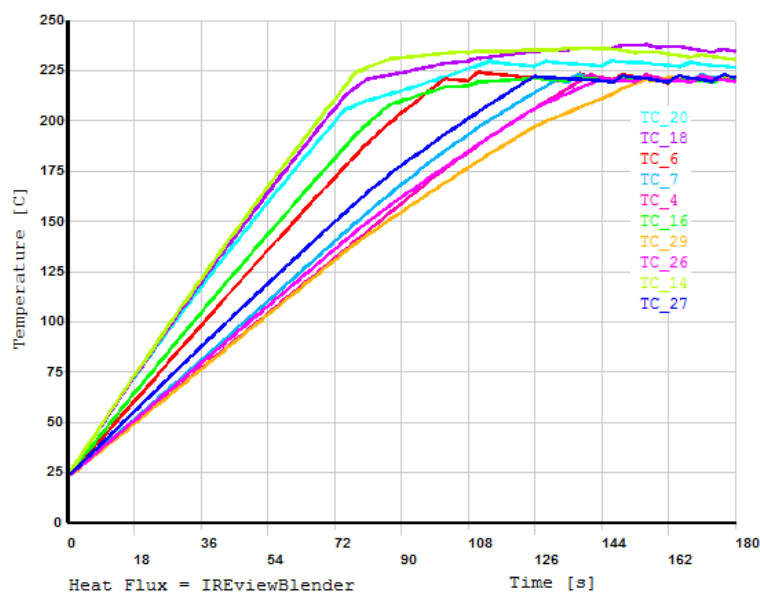


Fig. 6 - Regulated heating

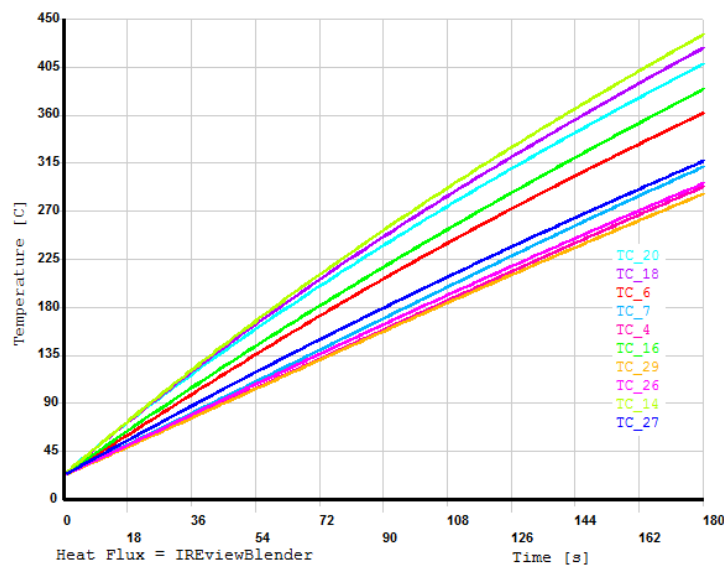


Fig. 7 – Unregulated heating

3 Conclusion

The method of simulation of the non-stationary heating of the shell moulds for production of artificial leathers presented in the present paper takes advantage of design of heating in the test and batch production lines. It is the method making use of combination of the softwares ANSYS and IREviewBlender. For simulation it is necessary to have data acquired from the experimental of production devices. They are, for example, measured power characteristics of the applied infrared emitters or of test measurements of the slush mould to get temperature dependencies at individual thermocouples. The data acquired from these measurements allow calibration of the model and specification of the boundary conditions.

The necessity of this modelling proved in a number of practical tasks solved in the company Magna Exteriors & Interiors Bohemia, s.r.o in collaboration with the company LENAM, s.r.o.

References:

- [1] Hušek M. and Potěšil A., "Software Prediction of Non-stationary Heating of Shell Moulds for Manufacture of Artificial Leathers" in *Proceedings of 18th International Conference ENGINEERING MECHANICS 2012*, Svatka - Žďár nad Sázavou, Czech Republic, 14 – 17 May 2012 (Náprstek J., Institute of Theoretical and Applied Mechanics, AS CR, Prague, 2012), pp. 120-121. ISBN 978-80-86246-39-0.
- [2] Potěšil A., "Non-stationary heating of shell moulds in the process of manufacture of artificial leathers" in *Proceedings of 17th International Conference ENGINEERING MECHANICS 2011*, Svatka - Žďár nad Sázavou, Czech Republic, 9 – 12 May 2011 (Fuis V., Ústav termomechaniky AV ČR, v. v. i. - pobočka Brno, 2011), pp. 487-490. ISBN 978-80-87012-33-8.
- [3] Potěšil A., "Experimental Measurement of Performance Characteristics of Infra-Red Emitters" in *Proceedings of 49th International Conference EAN 2011*, Znojmo, Czech

Republic, 6 – 9 June 2011 (Návrát T., Ústav mechaniky těles, mechatroniky a biomechaniky, Fakulta strojního inženýrství, Vysoké učení technické v Brně, 2011), pp. 349-356. ISBN 978-80-214-4275-7.

Acknowledgements

This project was supported by the Ministry of Education of the Czech Republic within the SGS project no. 7822/115 at the Technical University of Liberec.

Contact:

Ing. Martin Hušek, martin.husek@tul.cz

Technical university of Liberec, Faculty of Mechatronics, Informatics and Interdisciplinary Studies
Studentská 2, 461 17 Liberec

MODAL ANALYSIS OF THE ROTOR SYSTEM

TOMÁŠ JAMRÓZ, KAREL PATOČKA, VLADIMÍR DÁNIEL, TOMÁŠ HORÁČEK

Aerospace research and test establishment

Abstract: The article deals with the issue of modelling of fundamental dynamic calculations in ANSYS Workbench environment. There are shown discrepancies in the modal analysis calculation of bodies system using an unstructured grid. It is pointed out correct choice of function for the contact surface. Furthermore, the article highlights the problem of preload modal analysis. There is shown the influence of the function "Bolt Pretension" on the results of a modal analysis.

Keywords: modal analysis, rotor, preload

1 Introduction

This article deals with the issue of modelling of fundamental dynamic calculations in the ANSYS Workbench environment. Under the term basic dynamic characteristics are understood modal properties such as natural frequencies and eigenmodes of the system. These basic dynamic characteristics are obtained for rotor system of free turbine consisting of 13 parts. The reason for the identification of modal parameters is their subsequent use in the optimization of the main and distributor gear set.

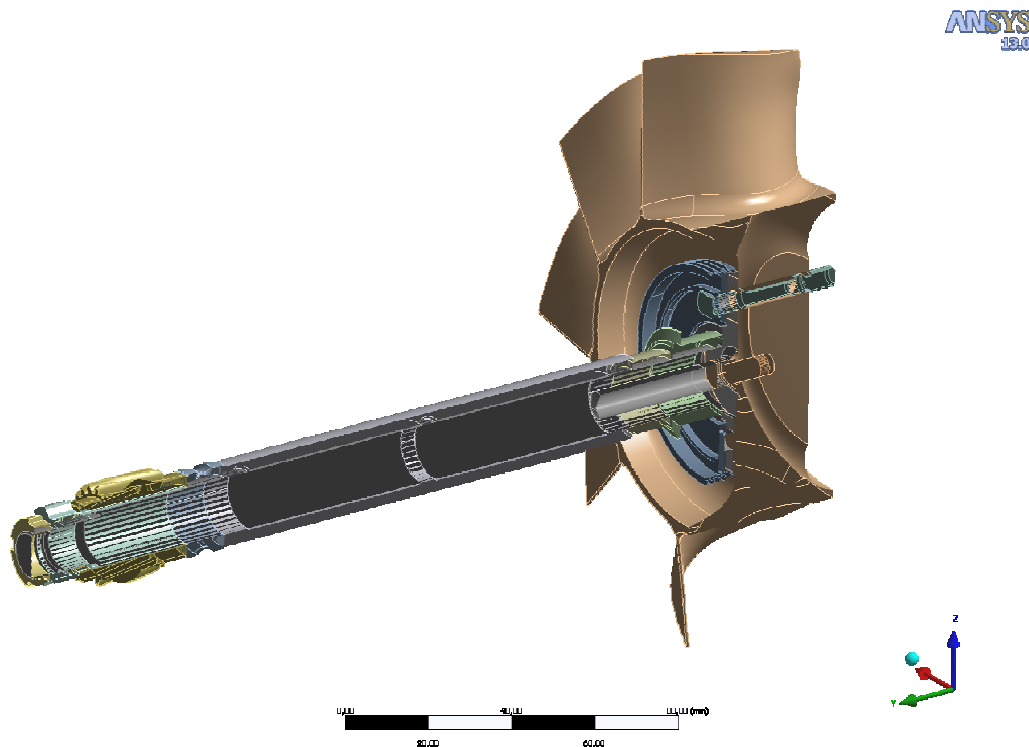


Fig. 14 Construction of rotor system

Modal properties of above mentioned rotor system were solved in the software Ansys Workbench environment. There was placed emphasis mainly on torsion modes of system whose dynamic characteristics have the greatest influence on the dynamics of gearing. Free free modal analysis of the system was calculated, thus excluding boundary conditions of rotor system. It was also taken into consideration the mounting requirements and examined the effect of rotor system preload. Preload of the rotor system was modelled using multi-bodies and contact functions instead of using one bond solid from a CAD system.

2 Modeling of preload

As mentioned in the introduction, the rotor assembly is preloaded in the axial direction of the axial force. This preload is given by torque union nut, which fixed the rotor system of the rotor shaft in the axial direction. Shift of natural frequencies of the rotor system was investigated with respect to the axial preload.

The task was solved by two successive analysis: static one followed by modal one with delegated stiffness matrix from the previous calculation. Preload of rotor shaft was solved with the help of "Bolt Pretension" function which was applied to the in the halfway cross-section of the shaft between the bearings. The results of structural analysis of rotor system with preload are shown in Fig.2. The nominal value of normal stress is 48MPa in the shaft.

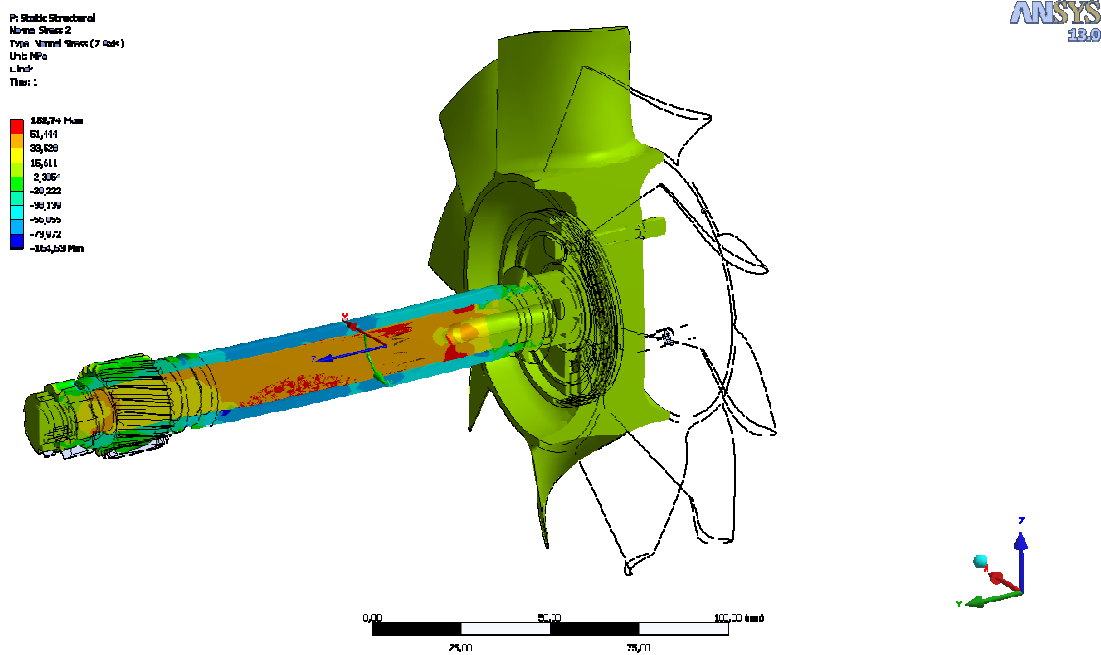


Fig. 15 Normal stress in rotor system from preload

The subsequently performed comparison between modal analyses with and without pretension proved that the preloading has a negligible effect on the natural frequencies shift with respect to torsion and bending modes. The frequency increase for these modes was very small. The only natural frequencies of axial modes were markedly affected (frequency shift was about 30%). Preload had the opposite effect for the modes (the natural frequencies were reduced).

As shown in Fig.3, the substantial decrease of the axial natural frequency values is mainly caused by the elements in a spot, where the "Bolt Pretension" function was applied to. The „Bolt Pretension“ function was applied in the form of input load.

Application of preload using either thermal boundary conditions or the “Bolt Pretension” function in the form of displacement or shifts in contacts could prevent unwanted changes of natural frequencies in the axial direction at preload modal analysis.

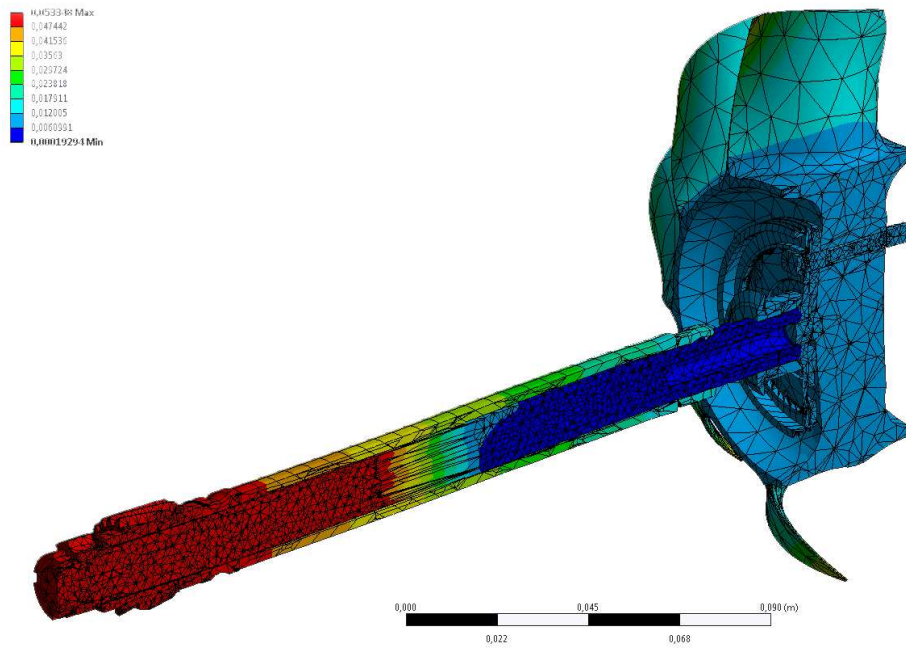


Fig. 16 Axial nature frequency

When comparing the eigenmodes of multi-body system with and without preload applied it was found that the first six rigid modes do not have zero values of natural frequencies. The frequency values are 155Hz, 155Hz and 285Hz for the rotating modes for the given rotor set.

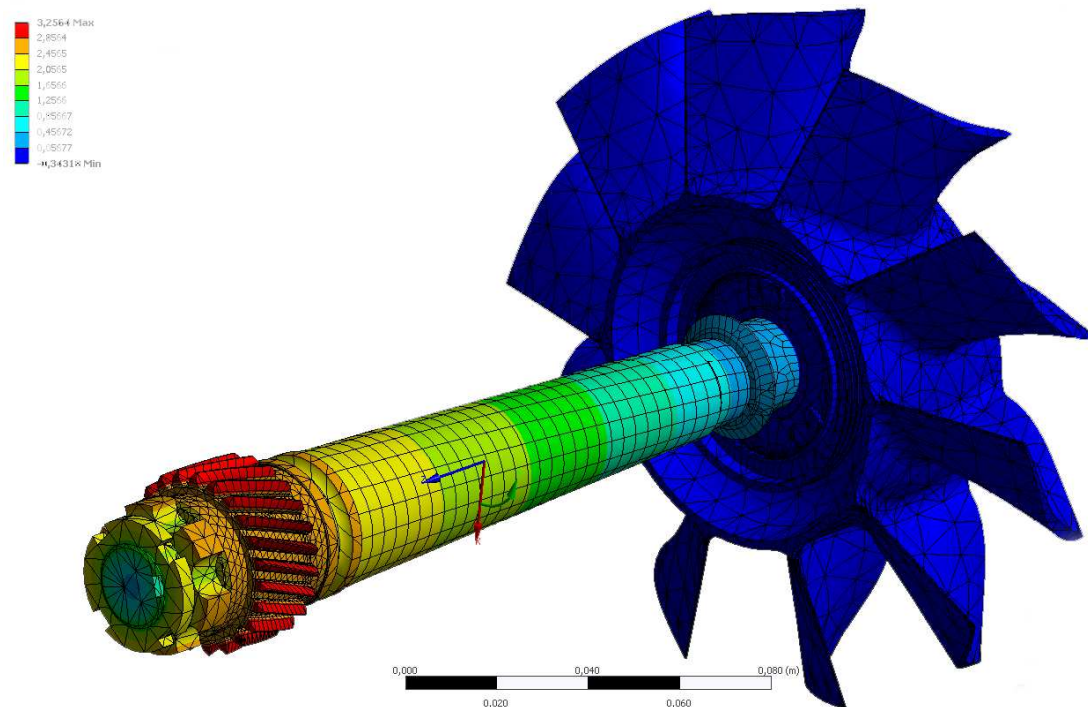


Fig. 17 The first torsion nature frequency mode

Tab. 1 Natural frequencies (number 7-10 are the bending modes, 11 is first torsion mode and 12 is the axial mode)

No.	Preload	Without preload
1	0.55776	4.26E-03
2	0.55809	6.07E-03
3	0.55812	6.28E-03
4	155	154
5	156	155
6	212	212
7	739	739
8	742	742
9	2020	2019
10	2023	2022
11	2850	2853
12	3893	5037

3 Rigid modes issues

As already mentioned in the previous chapter, Ansys Workbench environment in "standard setting" computes the non-zero rigid modes for the analysis of the system of bodies connected by contact functions with unstructured mesh.

Another finding was the discrepancy in the values of the natural frequencies for the system imported into Ansys environment as a single body and for system imported in Ansys as an assembly and afterwards connected by contact functions in Ansys/DesignModeler environment. When using the contact function "Bonded-Pure Penalty" the difference was about 5% w.r.t. single body model. The latter value also roughly corresponds to the value of the frequency shift of rigid modes. In case of the first two bending modes and torsion mode the differences were 18% and 12%, respectively.

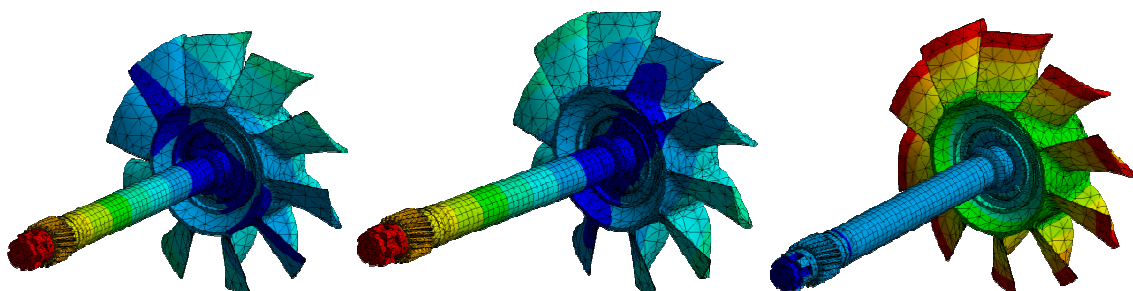


Fig. 18 The rigid rotation modes

As recommended by representatives of Ansys software, MPC method was used for contacts. Using such a contact the natural frequencies differences changed from 18% to 5% and from 15% to 2% for the first two bending modes and the first torsion mode, respectively. The frequency shift was equal about 5% for all other modes. There was also a significant decrease in the frequency values of the rotating rigid modes - from about 285Hz to about 25Hz.

Tab. 2 Comparison of natural frequencies for contact functions Pure Penalty, Augmented lagrange and MPC (number 7-10 are the bending modes, 11 is first torsion mode and 12 is the axial mode)

No.	One-body system	Multi-body system						
		Pure Penalty			Augmented lagrange		MPC	
		Frequency [Hz]	Frequency [Hz]	Shift [%]	Frequency [Hz]	Shift [%]	Frequency [Hz]	Shift [%]
1	0	0		0		0		
2	0	0		0		0		
3	0	0		0		0		
4	0	203		203		14		
5	0	205		205		24		
6	0	285		285		26		
7	755	894	18	894	18	795	5	
8	756	898	19	898	19	799	6	
9	2179	2321	6	2321	6	2284	5	
10	2182	2323	6	2323	6	2289	5	
11	3480	3850	12	3850	12	3532	1	
12	4819	5047	5	5047	5	5044	5	

4 Displacement in the gear tooth

In the introduction it was mentioned that the several dynamic variables are needed to optimize the gearbox. One of the dynamic variables is the average tangential displacement of the diametral pitch for torsion mode.

The path along the tooth could not be defined by two points for this type of gear because of helical gearing. Deviation from a straight line is small, but the resulting tangential displacement values are significantly different.

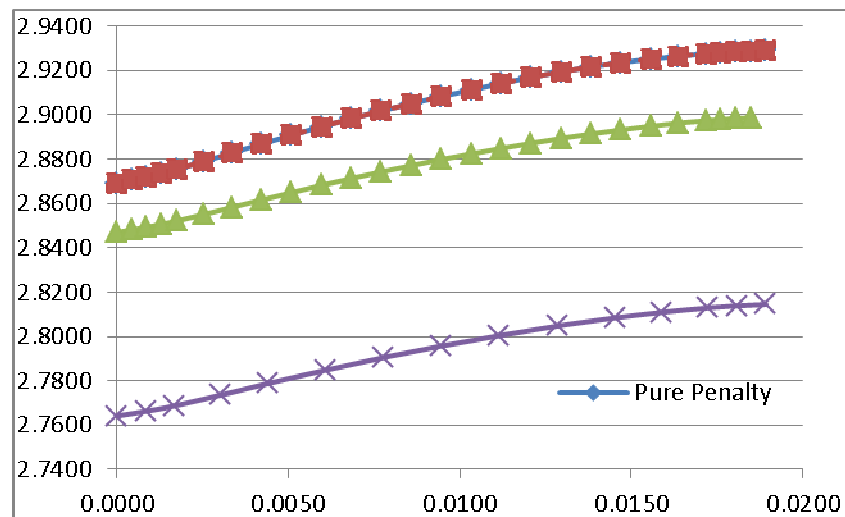


Fig. 19 Diagram of tangential displacement along the gear tooth for torsion mode

The curves showing tangential displacement values along the length of the tooth for different contact function are compared in the Fig. 19. The graph shows that the curve shape does not change for different contact functions. The curves are only shifted. In addition, the difference is negligible.

Tab. 3 Comparison of mean value of tangential displacement among contact functions

Body (Contact functions)	Mean value of tangential disp. [m]	Difference [%]
One body (no contact function)	2.7925	0.00
Multi-body („Pure Penalty“)	2.9041	3.99
Multi-body („Lagrange“)	2.9041	3.99
Multi-body(„MPC“)	2.8766	3.01

5 Conclusion

In our case the preload has no effect on the natural frequency of the torsion mode but it can affect the frequency shift of axial modes for particular contact function used. Only if "Bolt Pretension" in the form of load input is used the frequencies decrease significantly for all axial modes. This undesirable effect can be avoided by application of preload using either thermal boundary conditions or the "Bolt Pretension" function in the form of displacement or shifts in contacts.

In case of modal analysis calculation of multi-body system (where contact function have to be used), MPC contact function should be used to minimize the shift of natural frequencies and to bring the natural frequencies of rigid modes near to zero. Then the frequency deviations are also relatively small compared to one-body system. The nonzero rigid modes issue does not exist when structured mesh is used.

Acknowledgement

The work was performed with support of EC FP7 project Efficient Systems and Propulsion for Small Aircraft – ESPOSA. Project number: 284 859

Contact address:

Ing. Tomáš Jamrůz

VZLÚ

Beranových 130

19905 Praha – Letňany

jamtoz@vzlu.cz

tel: +420 225115593

ANALÝZA VRSTEVNATEJ DOSKY

NORBERT JENDŽELOVSKÝ

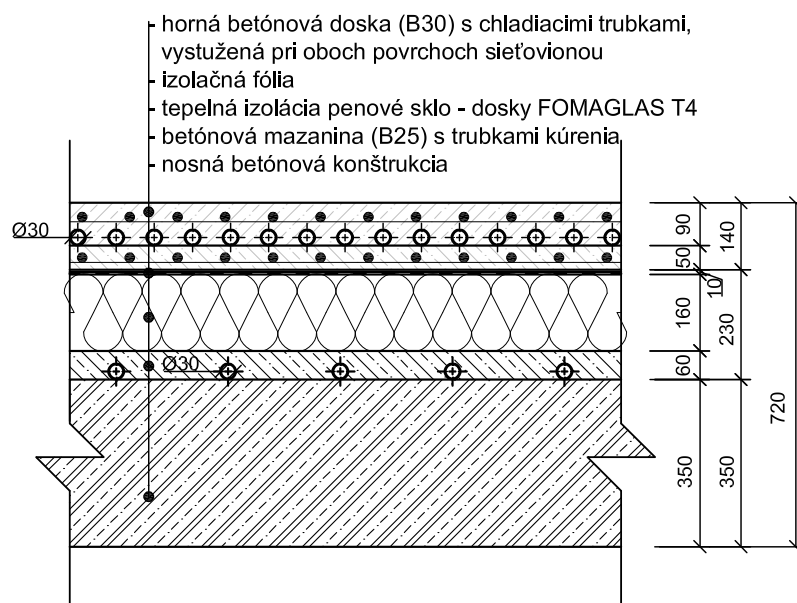
STU Bratislava, Stavebná fakulta

Abstract: This paper analyses a reinforced concrete slab. There are individual layers required for the ice area on the concrete slab (a sandwich construction). Statics and modal analysis of the construction is carried out in sequence. Eigenvalue and eigenfrequency of the slab are tested by experimental measuring. Consequently the concrete slab is analysed under a dynamic load)

Keywords: FEM, reinforced concrete slab

1 Úvod

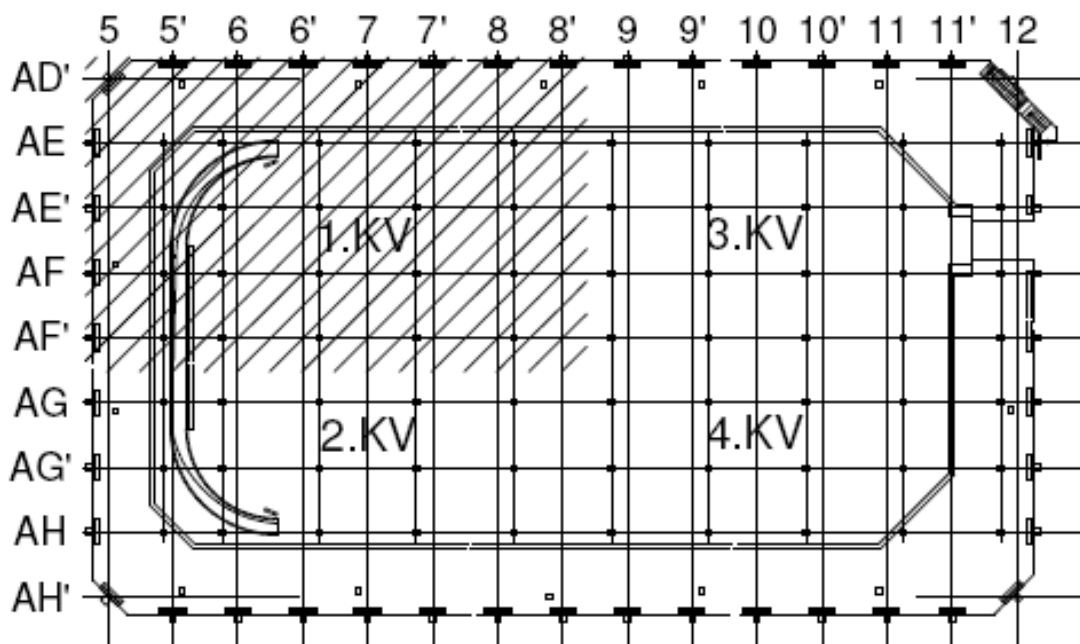
Článok prezentuje časť analýzy vrstevnatej doskovej konštrukcie. Ide o konštrukciu železobetónovej dosky, na ktorej je uložená ľadová plocha. Sendvičová doska je súčasťou konštrukcie zimného štadióna. Skúmaná konštrukcia sa po hrúbke skladá: z nosnej železobetónovej dosky hrúbky 350 mm, na nej sú uložené všetky nevyhnutné vrstvy, ktoré spolu tvoria „skladbu“ ľadovej plochy: betónová mazanina s rúrkami kúrenia, tepelná izolácia a horná betónová doska s rozvodom chladenia. Schéma a popis jednotlivých vrstiev sú uvedené na obrázku 1.



Obrázok 1 – Skladba podlahy

Vlastnosti jednotlivých betónov, ktoré boli použité v konštrukcii, sa uvažovali podľa príslušných noriem [3]. Použité penové sklo Fomaglas (typ FOMAGLAS T4) je vhodné na izoláciu ľadových plôch. Jeho fyzikálne vlastnosti sú prevzaté z výrobného listu: hustota $\rho = 120 \text{ kg/m}^3$, modul pružnosti $E = 800 \text{ MPa}$, pevnosť v tlaku $\sigma = 0,7 \text{ MPa}$.

Samostatnou dilatačnou časťou konštrukcie zimného štadióna je nosná konštrukcia ľadovej plochy. Pôdorysné rozmery analyzovanej konštrukcie sú $69,10 \times 42,60 \text{ m}$. Zvislé nosné prvky sú vytvorené železobetónovými stĺpmi $400 \times 400 \text{ mm}$ a majú výšku $3,6 \text{ m}$. Na väčšine pôdorysnej plochy sú stĺpy v modulovom rastru $7,5 \times 5,0 \text{ m}$. Po obvode sú stenové piliere hrúbky 250 mm a šírky $2,0 \text{ m}$. Rozmiestnenie nosných konštrukcií je zrejmé z obrázku 2. Na zvislých nosných prvkoch je uložená už zmienená železobetónová doska hrúbky 350 mm . Obdĺžniková doska je v rohoch skosená na dĺžke $2,7 \text{ m}$ pod uhlom 45 stupňov.



Obrázok 2 – Schéma objektu

Plocha dosky je $2\,925,5 \text{ m}^2$. Na pôdoryse dosky je v prevažnej miere uložená ľadová plocha s rozlohou $1\,750 \text{ m}^2$. Priestor za mantinelmi, kde sú umiestnené mobilné tribúny, má celkovú rozlohu $1\,175,5 \text{ m}^2$.

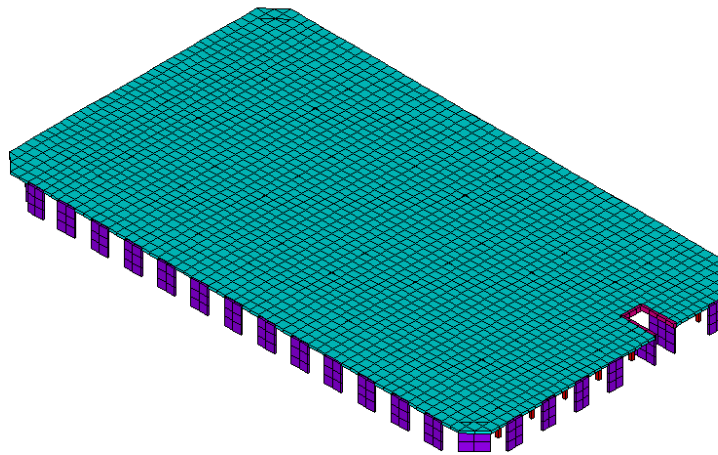
Konštrukcia sendvičovej dosky bola podrobená statickej a neskôr aj dynamickej analýze.

Statický výpočet celej konštrukcie v rámci realizačného projektu zadefinoval náhodilé zaťaženie $q = 5,0 \text{ kN/m}^2$. Konštrukcia bola na toto zaťaženie projektovaná a zrealizovaná.

Neskôr sa pristúpilo k dynamickej analýze konštrukcie vzhľadom na to, že prevádzkovateľ zimného štadióna okrem ľadovej plochy chcel na ploche robiť koncerty, diskotéky a iné spoločenské aktivity. Najväčší vplyv na dynamické namáhanie konštrukcie majú kultúrne akcie typu rockových koncertov a diskotiek, kde sa na ploche pohybuje v určitom rytme množstvo osôb.

2 Výpočtový model konštrukcie

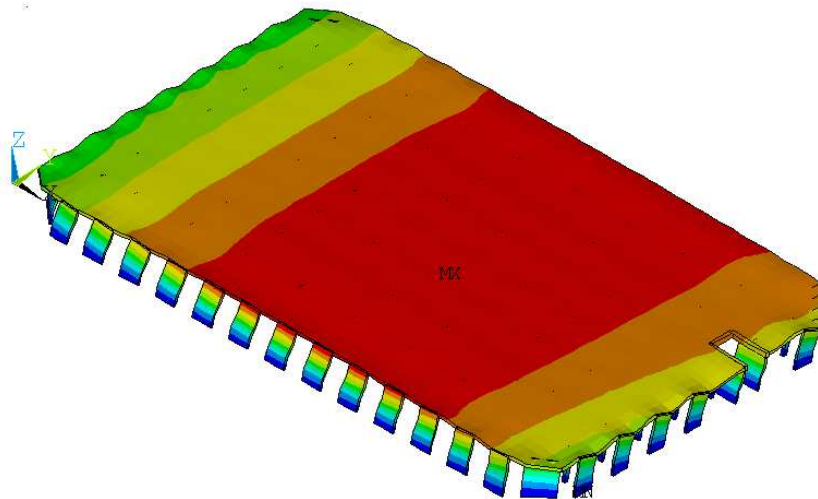
Popis konštrukcie. V programe ANSYS bol vytvorený model analyzovanej konštrukcie. Použité boli prúťové prvky na modelovanie stĺpov, ďalej plošné konečné prvky na modelovanie stien a samotnej dosky. Materiálno - fyzikálne vlastnosti boli uvažované podľa príslušných noriem (betón C25/30). Stĺpy a steny boli votknuté do základovej konštrukcie. Na obrázku 3 je pohľad na výpočtový model konštrukcie.



Obrázok 3 – Axonometrický pohľad na model konštrukcie

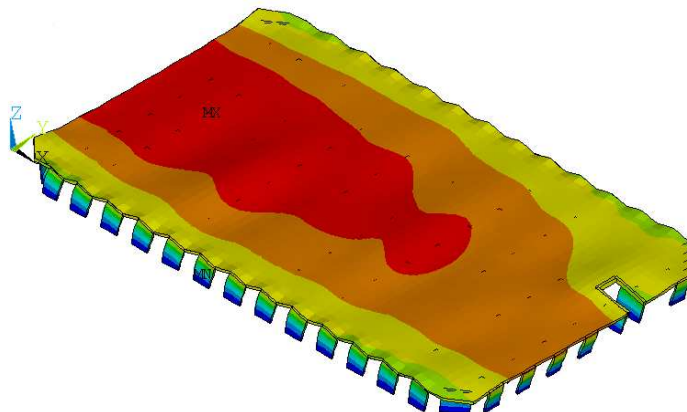
V prvej časti analýzy bolo zaťaženie jednotlivými vrstvami podlahy (mazanina, penové sklo a horná žb. doska - obr.1) modelované ako pridaná hmota k nosnej konštrukcii dosky (510 kg/m^2). Modálnou analýzou boli spočítané vlastné tvary a vlastné frekvencie konštrukcie. Riešenie rovníc pre výpočet vlastných tvarov sa uskutočnilo za pomoci iteračných postupov Lanczosovej metódy.

V nasledujúcej časti sú uvedené jednotlivé vlastné frekvencie a tvary kmitania v smeroch X, Y a Z. (os X je vodorovná os pozdĺž dlhšej strany dosky os Z je zvislá pozri obr. 4). Prvý vlastný tvar vo vodorovnom smere - v smere menšieho rozmeru konštrukcie (smer y) má hodnotu frekvencie $f_1 = 6,027 \text{ Hz}$. Tvar je na obrázku 4.



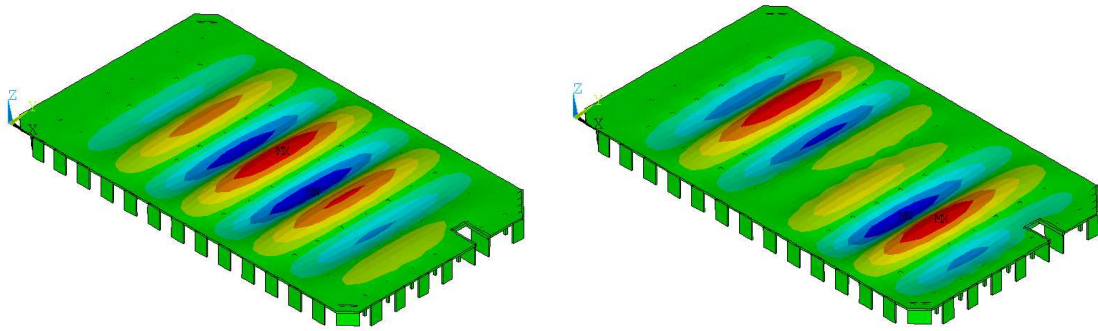
Obrázok 4 – Vlastný tvar v smere y - $f_1 = 6,027$ Hz

Druhý vlastný tvar vo vodorovnom smere - v smere väčšieho rozmeru konštrukcie (smer x) má hodnotu frekvencie $f_5 = 10,534$ Hz. Tvar je na obrázku 5.

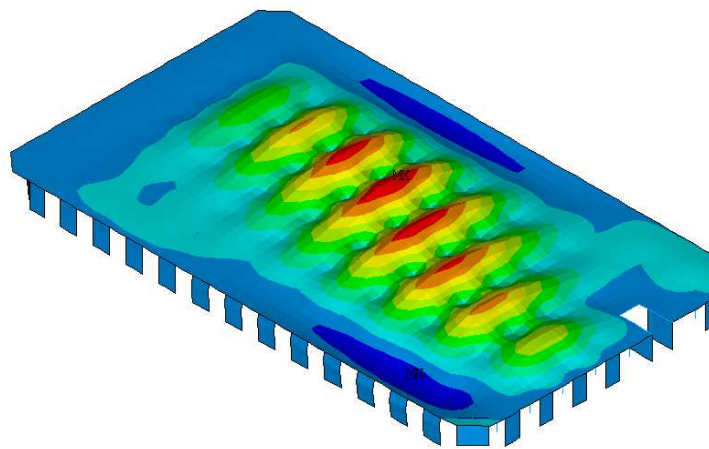


Obrázok 5 – Vlastný tvar v smere x - $f_5 = 10,534$ Hz

Pri ostatných tvaroch kmitania prevláda kmitanie vo zvislom smere, ale vždy len v určitej časti dosky (nikdy nie celej plochy). Tieto frekvencie sú z intervalu 9,524 až 13,5 Hz (viac tvarov nebolo počítaných, nakoľko nepredpokladáme dynamické zaťaženie takých vysokých frekvencií). Tvary kmitania dosky sú na nasledujúcich obrázkoch (obr. 6, 7).

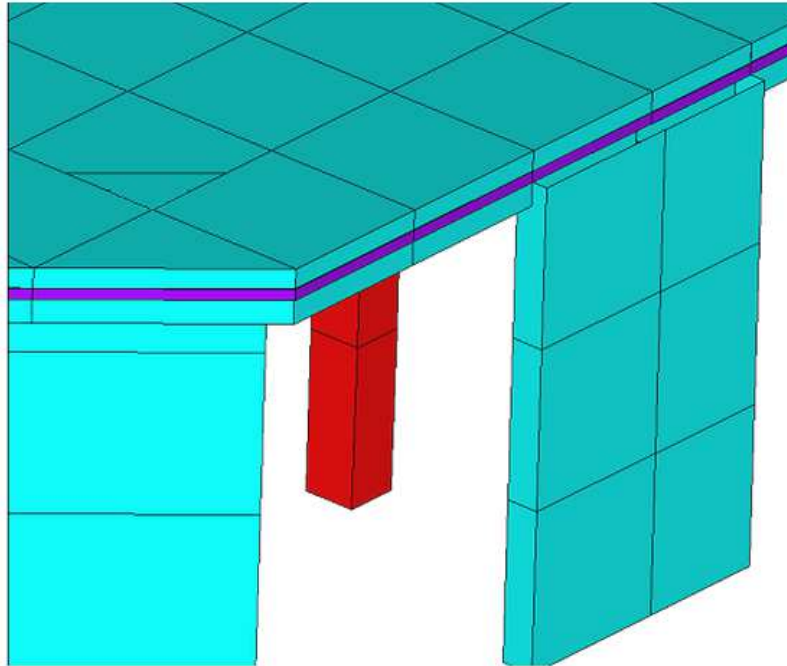


Obrázok 6 – Tvary pri frekvenciách $f_2 = 9.524$ a $f_3 = 10.105$ Hz



Obrázok 7 – Tvar pri frekvencii $f_{14} = 14.77$ Hz – kmitá najviac hmoty vo zvislom smere

V druhej časti analýzy sme sa venovali modelovaniu dosky ako sendvičovej konštrukcii. V tejto analýze sme upravili prvý model konštrukcie tak, že na nosnú betónovú dosku sme doplnili vo výpočtovom modeli izolačnú medzivrstvu z penového skla a hornú betónovú dosku. Medzivrstva má hrúbku 150mm, z výrobného listu Fomaglas T4 je prevzatý modul pružnosti $E = 800$ MPa. Detail konštrukcie je na obr. 8.



Obrázok 8 – Vrstevnatá doska

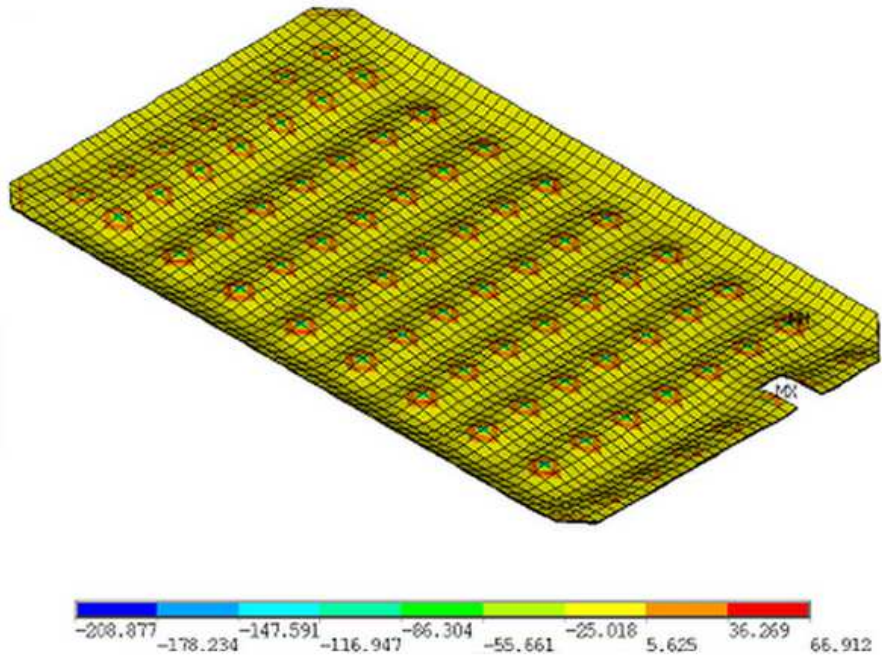
Výsledky z riešenia uvádzame nižšie, zanedbateľne sa zmenili hodnoty frekvencií. Prvé dva tvary sú vodorovné v smere y (menší rozmer) a v smere x (dlhší rozmer). V tabuľke 1 sú uvedené vlastné frekvencie z prvého a druhého modelu dosky.

Tabuľka 1 – Hodnoty frekvencií

	1.model	2.model
smer X	10.534 Hz	10.826 Hz
Smer Y	6.027 Hz	6.231 Hz
smer Z	9.524 Hz	11.658 Hz

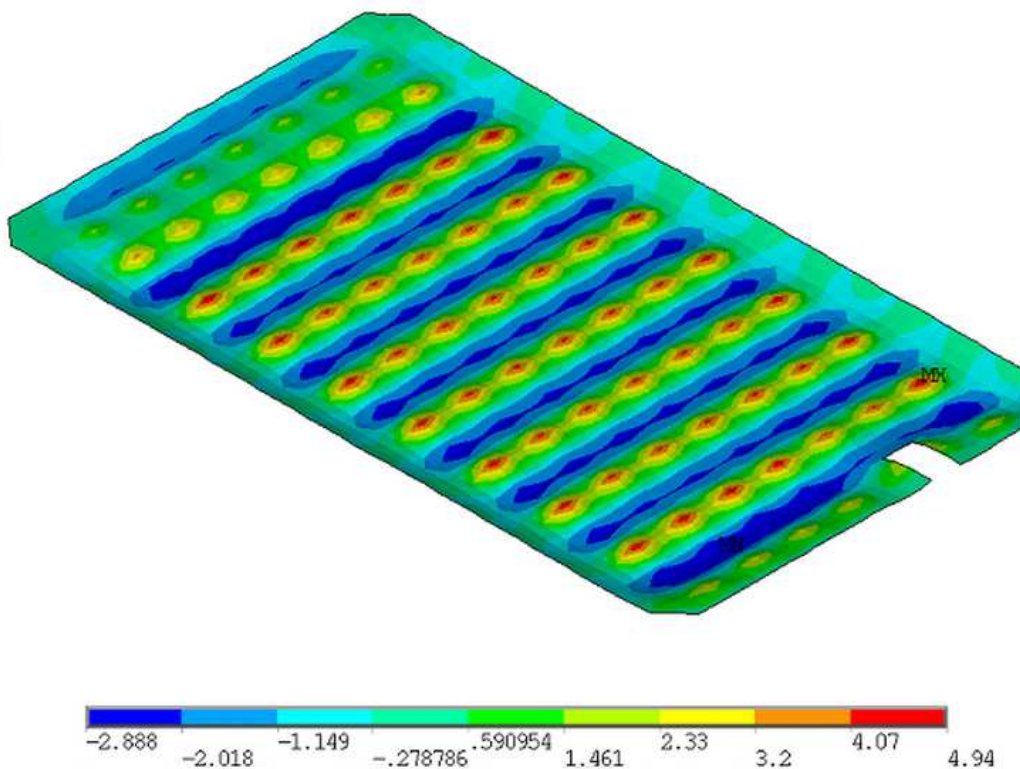
Treťou časťou, ktorá je prezentovaná v tomto príspevku, je statická analýza kontaktu tepelnej izolácie s vrchnou betónovou doskou. Pri statickom zaťažení vrstevnatej dosky bola vrchná doska zaťažená náhodilým zaťažením $q = 5 \text{ kN/m}^2$. Výsledky sú uvedené pre izolačnú medzivrstvu penového skla (obr. 9). Zvislé napätie v izolačnej vrstve je maximálne nad stĺpmi a má hodnotou 208,8 kPa, čo je menej ako $233 \text{ kPa} = 700/3$ ako uvádza výrobca pre pevnosť v tlaku izolačných dosiek Fomaglas T4.

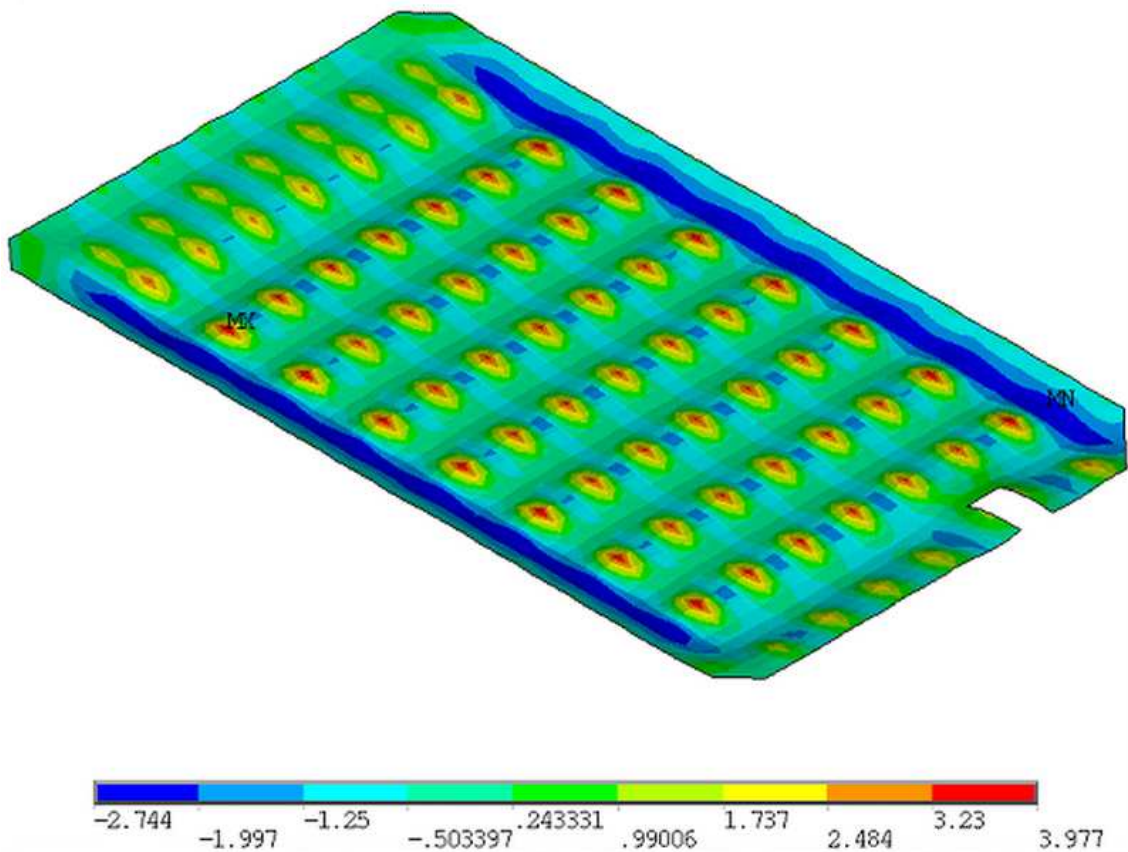
Riešenie hornej železobetónovej dosky, v ktorej je rozvod chladenia: táto doska má merné ohybové momenty uvedené na obrázku 10. Tieto momenty v oboch smeroch pri oboch povrchoch sú v intervale od -2,75 po 4,95 kNm/m. Podľa posúdenia dosky podľa únosnosti betónu nedôjde k porušeniu hornej dosky.



Obrázok 9 – Zvislé tlakové napätie (kPa) v izolačnej vrstve

Pri statickom zaťažení hodnoty merných ohybových momentov v hornej doske ukazujú, že táto je dostatočne vystužená dvojicou výstužných sietí pri dolnom aj hornom povrchu. Tepelno - izolačná vrstva taktiež vyhovela na zvislé tlakové namáhanie aj pri zohľadnení príslušných dynamických koeficientov, ktoré nadobúdajú hodnoty blízke k jednotke, t.j. dynamické efekty aj pri rezonančnom zaťažení od prípadného skákania ľudí na ploche sú malé a konštrukcia vyhovuje.

Obrázok 10 – Priebeh merných ohybových momentov m_x (kNm/m)



Obrázok 11 – Priebeh merných ohybových momentov m_y (kNm/m)

3 Záver

Numerické výsledky vlastných frekvencií boli potvrdené aj experimentálnymi meraniami. Najnižšia hodnota frekvencie je 6,03 Hz pre vodorovný tvar kmitania v kratšom vodorovnom smere konštrukcie, v druhom vodorovnom smere je hodnota frekvencie 10,5 Hz.

Podľa literatúry (Flesch 1993) aktivity tanečného charakteru sú z intervalu 1,5 až 3,5 Hz. Z uskutočnených experimentálnych výsledkov na zimnom štadióne vyplýva, že frekvencia kmitania konštrukcie vo zvislom smere je od 10 Hz vyššie.

Pohybujúce sa osoby spôsobia len také kmitanie, ktoré nerozkmitá konštrukciu ako celok ani jej jednotlivé časti.

Literatúra

- STN EN 1991-1-1 Eurokód 1. Zaťaženie konštrukcií. Časť 1-1: Všeobecné zaťaženie. Objemové hmotnosti, vlastná tiaž a úžitkové zaťaženie pozemných stavieb.
- STN EN 1991-1-1/NA Eurokód 1. Zaťaženie konštrukcií. Časť 1-1: Všeobecné zaťaženie. Objemové hmotnosti, vlastná tiaž a úžitkové zaťaženie pozemných stavieb.
- STN EN 1992-1-1 Eurokód 2. Navrhovanie betónových konštrukcií. Časť 1-1: Všeobecné pravidlá a pravidlá pre budovy.
- STN EN 1998-1 Eurokód 8. Navrhovanie konštrukcií na seizmickú odolnosť. Časť 1: Všeobecné pravidlá, seizmické zaťaženia a pravidlá pre budovy.
- FLESCHE, Rainer. Baudynamik praxisgerecht : Band 1: Berechnungsgrundlagen. Paderborn : PDC Paderborner Druck Centrum GmbH, 1993. Tab. 2.4., strana 30, s. 547. ISBN 3-7625-3010-6.
- MELCER, J. – KUCHAROVÁ, D., 2000. Dynamika stavebných konštrukcií. Žilinská univerzita.
- SOKOL, M. – TVRDÁ, K., 2011. Dynamika stavebných konštrukcií. STU Bratislava.

PodĎakovanie

Článok vznikol na základe grantu VEGA 01/0629/12

Kontaktná adresa:

STU Bratislava, Stavebná fakulta, Radlinského 11, 813 68 Bratislava
(norbert.jendzelovsky@stuba.sk)

A RSM Method for Nonlinear Analysis of Fire Resistance of Technology Support Structures in Accordance with Eurocode

JURAJ KRÁLIK

Faculty of Civil Engineering STU Bratislava

Abstract: This paper presents the methodology of the reliability analysis of the fire resistance of the steel structure of the cable way in NPP. The elastic and plastic solution of the steel structure under fire loads is discussed. The deterministic and probability analysis of the fire resistance of the steel structures are considered. The executed fire resistance analysis of the steel structures is investigated as the influence of temperature, permanent and variable loads. The Response Surface Method (RSM) for the nonlinear analysis of the fire structure reliability was used on program ANSYS. The advantages and disadvantages of the deterministic and probabilistic analysis of the fire safety are discussed.

Keywords: ANSYS, RSM, Fire, Probability, Nonlinearity, Safety, Reliability

1 Introduction

In consequence of the economic and life lost due to fire accident the new regulation was created in European countries [1, 3 and 4]. Those regulations specified :

- the escape ways by prescribing the number of emergency exits, the characteristics of the exit signs, the number of staircases and the width of the doors,
- the prevention of fire spread by referring to the concepts of "fire resistance" and "reaction to fire",
- the fire resistance of the structure in terms of ISO-fire resistance period, R30, 60, 90, or 120,
- the conditions for smoke and heat exhaust,
- the implementation of active fire fighting measures such as the number of hand extinguishers, smoke detectors and sprinklers,
- the access conditions for the fire brigade.

Each country defined its regulations generally based on its own perception of the fire safety problems [3, 4].

The objective of this paper is to describe a performance based more realistic and credible approach to the analysis of structural safety in case of fire, which takes also account of structural models, which should be as realistic as possible.

The objective of this paper is to describe a performance based more realistic and credible approach to the analysis of structural safety in case of fire, which takes also account of structural models, which should be as realistic as possible. The behavior of a structure in the fire situation may be performed either as a global structural analysis dealing with the entire structure, which should take into account the relevant failure mode under fire, the

temperature dependent material properties, or as an analysis of parts of the structure, or as a member analysis (see fig.1). In the case also the support and restraint conditions of the member, applicable at time $t=0$, may generally be assumed to remain unchanged throughout the fire exposure. According to EN1992-1-2, EN1993-1-2 and EN 1994-1-2 the assessment of structural behavior in a fire design situation shall be based on one of the following permitted design procedures:

- recognized design situations on the base of the tabulated data,
- simple calculation models for specific type of structural members,
- advanced calculation models able to deal with any kind of the structural model.

6 Safety assessment of fire resistance

Experiences from fire cases and their consequences are the main reasons for the developing of the fire safety standards [1, 2, 3, 4, 5, 7, 13, 14 and 17]. A list of codes, standards, and other legal documents being used to achieve this aim are based on the simple numerical methods. However, it is possible to solve fire resistance in another way [4]. This paper particularly shows the possibility of solution the fire resistance problem. The fire resistance of the structure could be verified by simplified or exact computational model [4, 9, 10 and 11]. This paper particularly shows the possibility of solution the fire resistance problem.

The fire resistance of the structure could be verified by simplified or exact computational model [4, 11 and 17]. From the structural behavior point of view we consider elastic or a plastic computational model. While using the elastic model, the static consideration is made of the linear elastic model and the critical intersection is tested with bending moment. Usage of the plastic model investigates the fire safety resistance of the structure until collapse. Fire safety of the structures can be solved by the deterministic or probabilistic method.

Simplified computational methods along with empirical formulations are widely used in daily design work [4]. Their main advantage is the simple formulation of critical temperature in the basis of which the stress of the structure is considered. The definition of the material properties, as well as the load condition, can be defined by deterministic or probabilistic access. In the case of deterministic access the conditions are established by the factors of load and structure resistance. In the case of probabilistic access the conditions are established by variable load factors and material properties of the structure [3, 4, 5, 6, 7, 8, 9, 10, 11, 12 and 16]. The probabilistic method describes the load and material property by histograms [4 and 11]. Fire resistance of the structure is evaluated by discrete histogram obtained from the probabilistic analysis.

7 Reliability of structures

Most problems concerning the reliability of building structures are defined today as a comparison of two stochastic values, action effects E and the resistance R , depending on the variable material and geometric characteristics of the structural element [11]. The deterministic definition of the reliability condition depend on design values of action effect E_d and resistance R_d in form

$$R_d \geq E_d \quad (1)$$

and in the case of the probabilistic approach, it has the form

$$RF = R - E \geq 0 \quad (2)$$

where RF is the reliability function, which can be expressed generally as a function of the stochastic parameters X_1, X_2 to X_n , used in the calculation of R and E .

$$RF = g(X_1, X_2, \dots, X_n) \quad (3)$$

The failure function $g(\mathbf{X})$ represents the condition (reserve) of the reliability, which can either be an explicit or implicit function of the stochastic parameters and can be single (defined on one cross-section) or complex (defined on several cross-sections, e.g., on a complex finite element model).

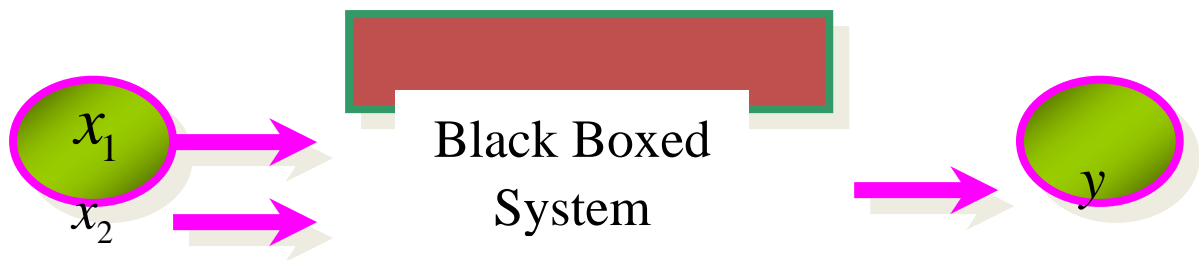
Table 1 Target values for the reliability index β_d and probability of failure p_d by Eurocode 1990

Limit state	Life time - 55 years		For 1 year	
	β_d	p_d	β_d	p_d
Structural safety	3,8	$7,23 \cdot 10^{-5}$	4,7	$1,30 \cdot 10^{-6}$
Serviceability	1,5	$6,70 \cdot 10^{-2}$	3,0	$1,35 \cdot 10^{-3}$

The most general form of the probabilistic reliability condition is given as follows:

$$p_f = P(R - E < 0) \equiv P(RF < 0) < p_d \quad (4)$$

where p_d is the so-called design ("allowed" or "acceptable") value of the probability of failure. The reliability criteria are defined in the Eurocode [3] in dependency on reliability index β , what is adequate to target level of failure probability (Table 1). In the case of the stochastic approach, various forms of analyses (statistical analysis, sensitivity analysis, probabilistic analysis) can be performed considering the probabilistic procedures, Eurocode 1990 recommends a 3-level reliability analysis. The approximation methods [11] - RSM was applied with nonlinear solution of fire response. Roux W.J. at 1998 has defined this method as follow : „Response surface method is a method for constructing global approximations to system behavior based on results calculated at various points in the design space“.



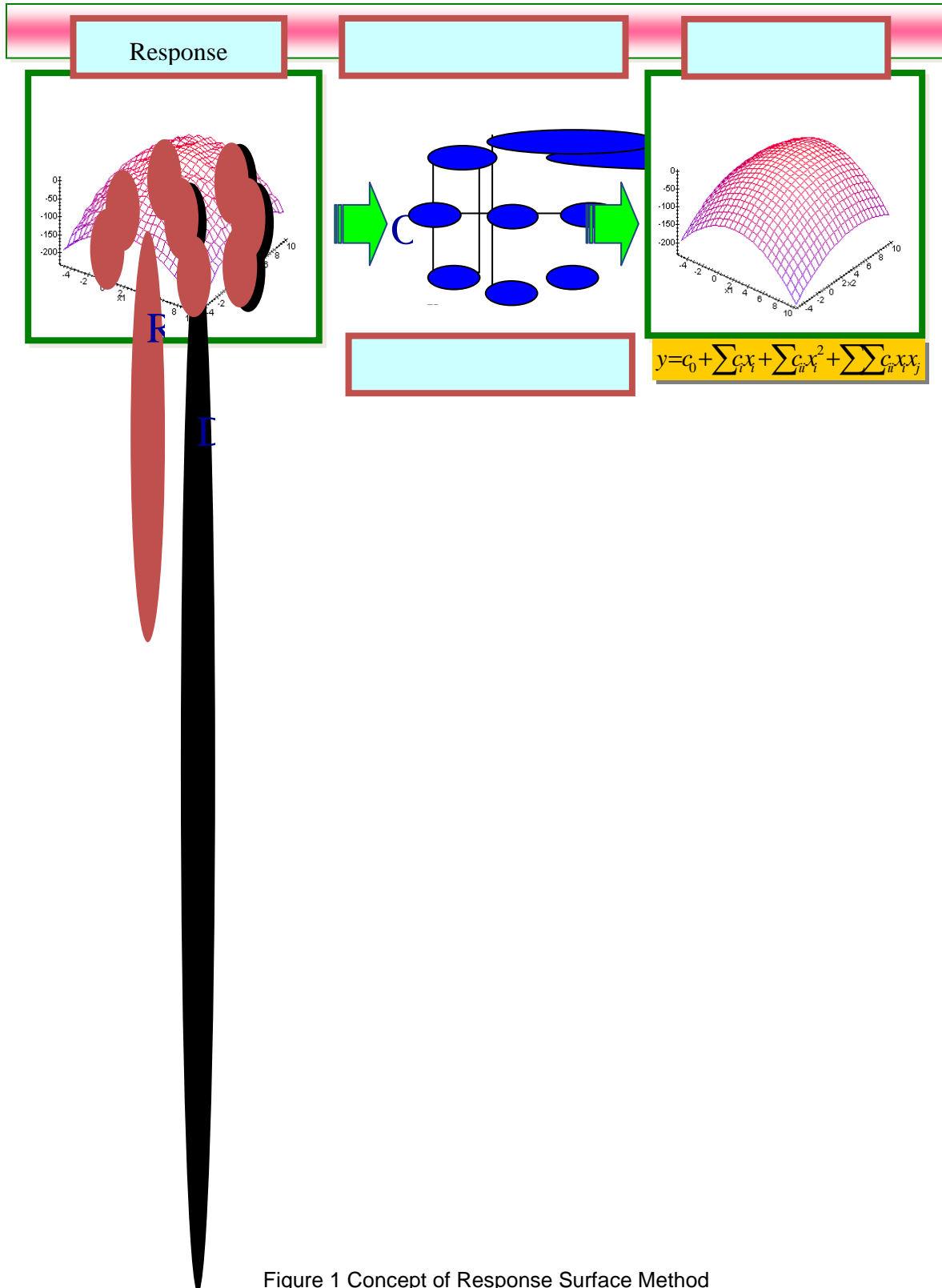


Figure 1 Concept of Response Surface Method

This method is based on the assumption that it is possible to define the dependency between the variable input and the output data through the approximation functions in the following form:

$$Y = c_0 + \sum_{i=1}^N c_i X_i + \sum_{i=1}^N c_{ii} X_i^2 + \sum_{i=1}^{N-1} \sum_{j>i}^N c_{ij} X_i X_j \tag{5}$$

where c_0 is the index of the constant member; c_i are the indices of the linear member and c_{ij} the indices of the quadratic member, which are given for predetermined schemes for the optimal distribution of the variables or for using regression analysis after calculating the response [11]. The concept of this method is described in fig.1. Approximate polynomial coefficients are given from the condition of the error minimum, usually by the "Central Composite Design Sampling" (CCD) method.

8 Fire resistance of the electrical cable way structures

On a base of the requirements of the IAEA [5], US NRC [14], Eurocodes [3, 4] and national standards [15] the fire resistance of electrical cable way structures in nuclear power plants were considered. These structures are made from the steel perforate plate placed on steel console of U8 profile and fixed on ceiling with hanger of U8 profile and steel bar. There are analyzed four type of cable troughs - RSU 60.100 OV, RSU 60.200 OV, RSU 60.300 OV, RSU 60.400 OV and the cable shaft RDV 100, 200, 300, 400 with various width (100, 200, 300 and 400mm). The modulus of support is equal 1500mm. The fire resistance of the cable way supported structures RSU without the shaft was established by experiment in the laboratory TU Braunschweig [13]. The aim of the numerical analysis was to prove the fire resistance of the cable way supported structures with the shaft RDV.



Figure 2 Experimental test of the cable way structures in TU laboratory Braunschweig [13]

The calculation model of the electrical cable way support system (fig.2) was made from the shell elements SHELL43, beam elements BEAM181 and link elements LINK8 in program ANSYS. Four models were created – RSU130, RSU230, RSU330 and RSU430 for various widths of cable troughs (100, 200, 300 and 400mm).

The consider structures are exposed to next loading inputs: permanent load (G), variable load (Q) involves the load of the electrical cables the uniform value of the temperature (T) and the characteristic value of the material properties reduced due to fire action. Those values are specified in codes and standards.

In the deterministic analysis there is the design value of effect of actions E_d and resistance R_d defined in accordance with the Eurocode (EN 1991-1-1. 2002) follow

$$E_d = \gamma_G \cdot G_k + \gamma_Q \cdot Q_k + \gamma_T \cdot T_k \quad \text{and} \quad R_d = f_{yk} / \gamma_M \quad (6)$$

where $\gamma_G, \gamma_Q, \gamma_T$ are the partial factors of actions ($\gamma_G = \gamma_Q = \gamma_T = \gamma_M = 1$), G_k, Q_k, T_k are the characteristic values of the defined actions and f_{yk} .

In the probabilistic analysis there is the value of effect of actions E defined in accordance with the JCSS code [7] (EN 1991-1-1. 2002) follow

$$E = e_{var} \cdot (g_{var} \cdot G_k + q_{var} \cdot Q_k + t_{var} \cdot T_k) \quad \text{and} \quad R = r_{var} \cdot k_{var} \cdot f_{var} \cdot f_{yk} \quad (7)$$

where $e_{var}, g_{var}, q_{var}, t_{var}, r_{var}, k_{var}, f_{var}$ are the variable functions defined in form of histogram.

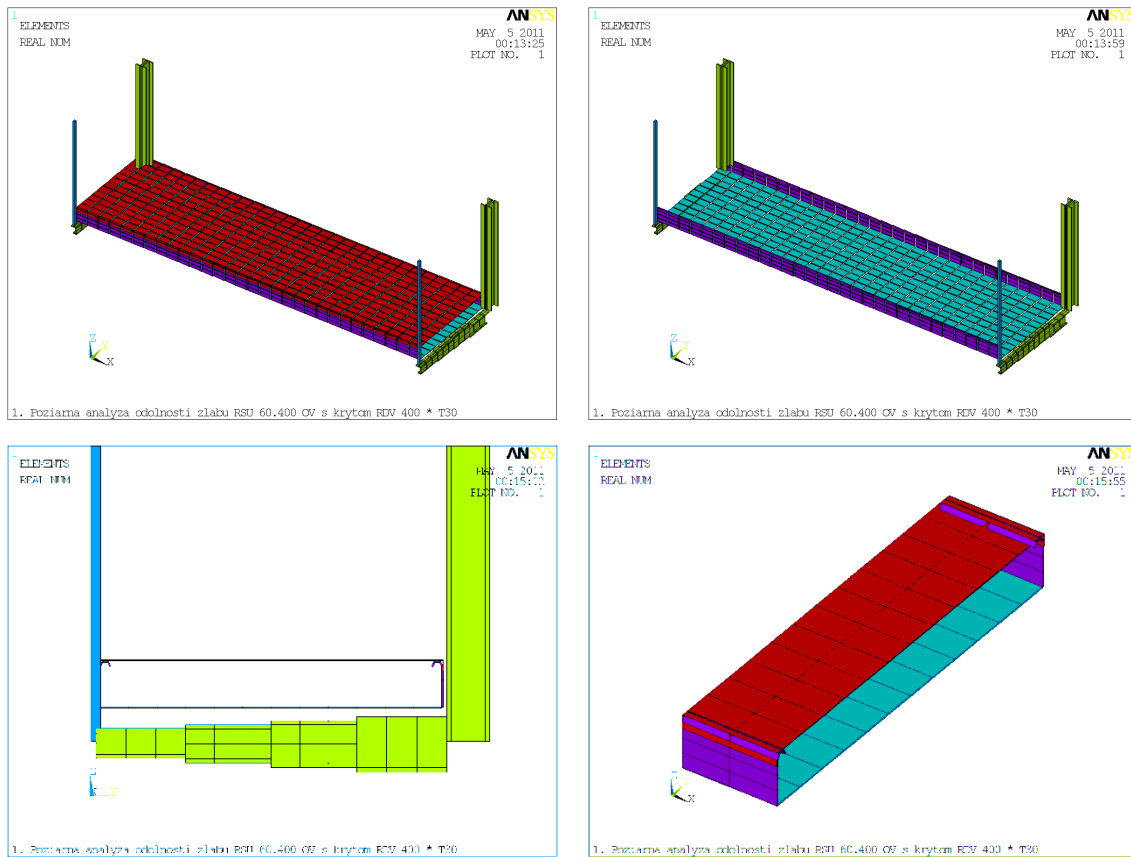


Figure 3 FEM model of cable way structure RS430 (RSU 60.400 OV and RDV400)

1 Temperature loading

The fire load depends on fire scenario and the requirements of standards [2 and 3] to the fire safety of the electrical cable ways in NPP. There are defined the temperature-time curves and reduction factors for material properties. The temperature-time curve (Fig.5) for the electrical cable ways in the NPP was defined from the experimental test in fire chamber (table 2). The standards for the NPP structures [5] require the fire resistance of the cable way equal to 30min (E30).

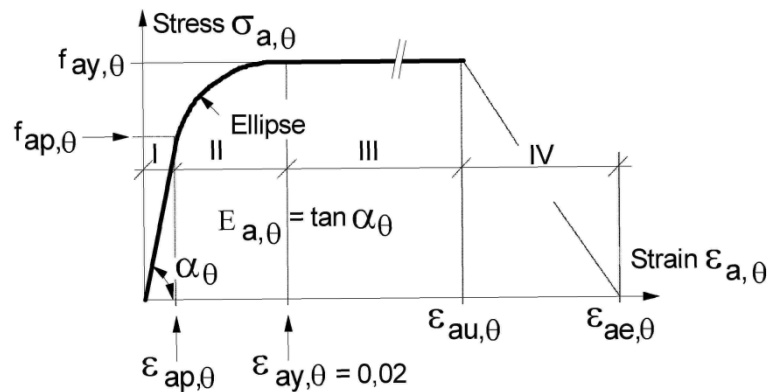


Figure 4 The stress-strain relationships for the steel by EN 1993-1-2

The critical temperature for the time 30min is defined on the base of the temperature curve. The reduced coefficients for the strength and Young modulus is obtained from the EN 1993-1-2 [2] as follow (fig.4) –

$$E30: T_1 = 841,8 \text{ } ^\circ\text{C}$$

$$E30: k_{E,\theta} = 0,081 \quad E_\theta = 16,925\text{GPa}$$

$$E30: k_{p,\theta} = 0,045 \quad f_{ap,\theta} = 10,522\text{MPa} \quad k_{y,\theta} = 0,089 \quad f_{ay,\theta} = 20,939\text{MPa}$$

Table 2 The temperature values versus time determined by experiment in fire chamber

Time t [min]	Temperature [°C]											Variation d _e [%]	Pres.[Pa] p
	Td1	Td2	Td3	Td4	Td5	Td6	Td7	Td8	Tave	Tn	To		
0	35,1	49,8	45,8	52,3	35,2	46,2	46,3	51,0	45,2	20,0	19,3	0,0	5,6
5	503,0	597,1	626,4	565,6	517,2	582,0	586,8	578,1	569,5	576,4	19,3	-13,9	13,4
10	671,9	683,4	696,0	667,2	648,4	677,0	688,3	684,4	677,1	678,4	19,4	-5,2	14,3
15	731,8	745,5	744,1	713,5	705,2	733,3	725,6	713,0	726,5	738,6	19,4	-3,6	14,1
20	738,6	740,8	757,9	745,0	738,1	746,6	749,7	762,9	747,5	781,4	19,4	-4,1	14,5
25	767,3	763,4	787,7	783,9	774,5	782,7	784,2	808,3	781,5	814,6	19,4	-3,9	17,7
30	802,5	826,5	856,5	838,6	812,3	843,6	852,5	862,0	836,8	841,8	18,8	-3,7	17,1
35	818,9	838,3	867,8	856,8	828,9	862,7	869,1	880,1	852,8	864,8	18,8	-3,1	17,4
40	855,2	876,3	900,9	875,0	866,4	906,2	918,0	911,0	888,6	884,7	19,0	-2,6	18,4
45	877,0	895,5	924,6	905,9	891,3	924,4	924,9	934,8	909,8	902,3	19,1	-2,2	17,7
50	897,6	916,1	948,0	929,4	912,6	942,9	940,3	950,1	929,6	918,1	19,4	-1,8	18,3
55	915,4	932,9	962,4	949,6	928,7	956,2	954,9	968,3	946,1	932,3	19,8	-1,5	17,5
60	934,4	948,8	970,1	958,7	946,4	972,4	967,7	968,3	958,4	945,3	19,9	-1,2	17,2
65	941,3	945,7	973,3	962,4	946,8	965,5	963,9	967,8	958,3	957,3	20,2	-1,0	15,9
70	946,5	946,6	978,4	980,4	952,5	970,2	965,0	978,7	964,8	968,4	20,6	-1,0	15,4
75	955,4	955,1	985,1	980,5	959,8	977,0	973,6	1000,0	973,3	978,7	20,7	-0,9	16,1
80	963,5	964,6	989,6	985,9	972,1	991,3	984,0	1006,0	982,1	988,4	20,9	-0,9	15,5
85	985,2	975,7	1002,0	1000,0	985,0	1001,0	996,3	1020,0	995,7	997,4	21,3	-0,9	14,8
90	999,6	990,7	1015,0	1017,0	998,3	1012,0	1005,0	1037,0	1009,3	1005,9	21,1	-0,8	15,7
91	1001,0	992,7	1016,0	1016,0	1000,0	1017,0	1012,0	1035,0	1011,2	1007,6	21,2	-0,8	14,5
92	1003,0	995,3	1017,0	1019,0	1002,0	1019,0	1012,0	1035,0	1012,8	1009,2	21,3	-0,8	15,7

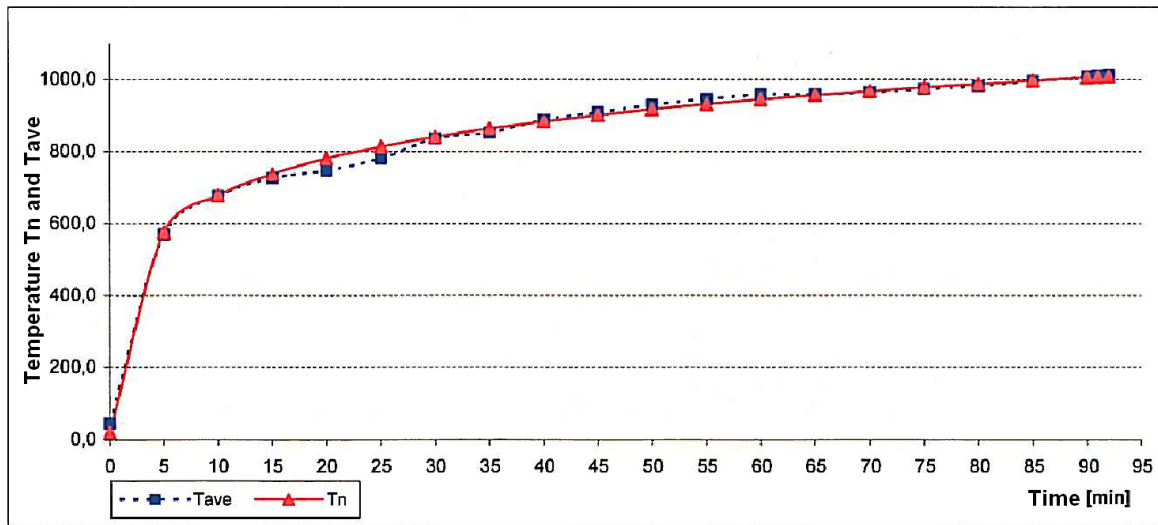


Figure 5 The thermal curve for the electrical support structures by laboratory test

9 Nonlinear material and geometric solution

The action of the high temperature due to fire effect can be analyzed using elastic or elastic-plastic solution. The elastic solution gives us the conservative results in comparison with the experimental results in the fire laboratory [17]. The elastic-plastic solution of the high temperature effect leads to more real results. The plastic deformation of the structure results in large strain. These deformations can no longer be neglected. The solution of the nonlinear (geometric and material) equations is solved on the basis of the Newton-Raphson method [11] in the increment of the displacement

$$\{du\} = [N]\{dr\}, \quad (8)$$

where $\{du\}$ is the vector of increment of displacement on element, $[N]$ is the matrix of shape functions, $\{dr\}$ is the increment of unknown nodal displacement parameters. The increment vector of large strain $\{dr\}$ is defined following

$$\{d\varepsilon\} = ([B_L] + [B_{NL}])\{dr\}, \quad (9)$$

where $[B_L]$ (resp. $[B_{NL}]$) is the vector of linear (resp. nonlinear) deformation shape.

The material equations for the incremental theory of plasticity is defined in form

$$\{d\sigma\} = [D_{ep}]\{d\varepsilon\}, \quad [D_{ep}] = [D_e] - \frac{[D_e] \left\{ \frac{\partial g(\sigma)}{\partial \{\sigma\}} \right\} \left\{ \frac{\partial g(\sigma)}{\partial \{\sigma\}} \right\}^T [D_e]}{H' + \left\{ \frac{\partial g(\sigma)}{\partial \{\sigma\}} \right\}^T [D_e] \left\{ \frac{\partial g(\sigma)}{\partial \{\sigma\}} \right\}} \quad (10)$$

where $\{d\varepsilon\}$ is the strain vector increment, $\{d\sigma\}$ is the stress vector increment, $g(\sigma)$ is the yield function, which is considered by Von Mises for the isotropic theory of plasticity in form

$$g(\sigma) = 1 - \sigma_{ef.E} / \sigma_{ay\theta.R} \geq 0, \quad \sigma_{ef} = \left(\frac{1}{2} \left[(\sigma_1 - \sigma_2)^2 + (\sigma_2 - \sigma_3)^2 + (\sigma_3 - \sigma_1)^2 \right] \right)^{\frac{1}{2}}, \quad (11)$$

where $\sigma_{ef.E}$ is the effective (equivalent) stress, $\sigma_{ay\theta.R}$ is the ultimate value of the stress depended on temperature due to fire.

On the base of the Lagrangian formulation in FEM the equilibrium equation for the i^{th} step and the increment vector of forces $\{\Delta F_o\}$ is following

$$[K_{Ti}]\{\Delta r_i\} = \{\Delta F_o\} - \{F_i^{NR}\}, \quad (12)$$

where the tangent matrix has the form

$$[K_{Ti}] = [K_{EP.i}] + [K_{G.i}], \quad (13)$$

$[K_{EP.i}]$ is the elastic-plastic stiffness matrix

$$[K_{EP.i}] = \int_{\Omega} [B_i][D_{EP.i}][B_i] d\Omega, \quad (14)$$

where $[B_i]$ is the strain-displacement matrix in terms of current geometry and the current elastic-plastic material matrix $[D_{EP.i}]$

$[K_{G.i}]$ is the geometric stiffness (stress stiffness) contribution

$$[K_{G.i}] = \int_{\Omega} [B_{G.i}][S_i][B_{G.i}] d\Omega, \quad (15)$$

where $[S_i]$ is a matrix of the current Cauchy (true) stresses $\{\sigma_i\}$ in the global Cartesian system. The Newton-Raphson restoring force vector is :

$$\{F_i^{NR}\} = \int_{\Omega} [B_i]^T \{\sigma_i\} d\Omega \quad (16)$$

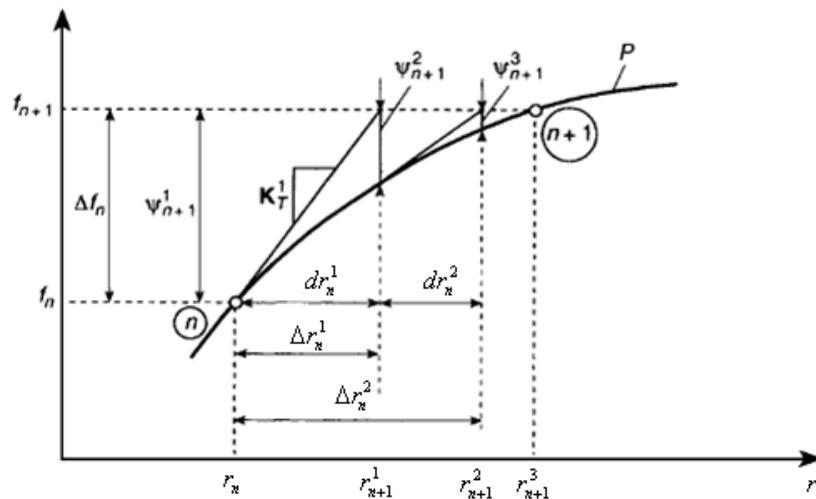


Figure 6 The Newton-Raphson method

The Newton-Raphson method is the most rapidly convergent process for solutions of problems in which only one evaluation of $\{F_i^{NR}\}$ is made in each iteration. Of course, this assumes that the initial solution is within the zone of attraction and, thus, divergence does not occur. Indeed, the Newton-Raphson method is the only process described here in which

the asymptotic rate of convergence is quadratic. The method is sometimes simply called Newton's method but it appears to have been simultaneously derived by Raphson, and the interesting history of its origins is given in [11].

10 Uncertainties of input variables

Reality is more complex than deterministic design situation, as the number of variables as well on the side of actions as on the side of resistance is often quite large.

Table 3 Probabilistic model of input parameters [6]

Name	Quantity	Charact. value	Variable paramet.	Histogram	Mean	Standard deviation	Min. value	Max. value
Material	Young's modulus	E_k	m_{var}	Lognormal	1,100	0,066	0,000	1,299
	Stress yield	f_{yk}	f_{var}	Lognormal	1,100	0,066	0,000	1,299
	Reduction factor	k_y	k_{var}	Lognormal	1,000	0,050	0,000	1,149
Load	Permanent	G_k	g_{var}	Normal	1,000	0,030	0,916	1,084
	Variable	Q_k	q_{var}	Gama T.I	0,600	0,215	0,000	1,378
	Fire- temperature	T_k	t_{var}	Gama T.I	0,822	0,246	0,000	1,684
Model	Model uncertainties	ξ_E	e_{var}	Lognormal	1,000	0,050	0,000	1,149
	Resistance uncertaint.	ξ_R	r_{var}	Lognormal	1,000	0,050	0,000	1,149

Hence the use of probabilistic procedures gets very quickly time consuming for everyday's practical engineering. The variability of input parameters are described in table 3 on the base of the literature requirements [4, 7 and 11].

11 Reliability criteria for fire resistance

Reliability of the foundation structures is analyzed in accordance of national and Eurocode standard requirements [3 and 4] for serviceability and ultimate limit state. The serviceability of structure is limited by equivalent strain and the ultimate limit state by equivalent stress in dependency on fire temperature.

The failure function of the equivalent strain and stress is defined in the form

$$g(\varepsilon) = 1 - \varepsilon_{ef.E} / \varepsilon_{ay\theta.R} \geq 0, \quad g(\sigma) = 1 - \sigma_{ef.E} / \sigma_{ay\theta.R} \geq 0 \quad (17)$$

where $\varepsilon_{ef.E}$, $\sigma_{ef.E}$ is the equivalent strain and stress of action and $\varepsilon_{ay\theta.R}$, $\sigma_{ay\theta.R}$ are the ultimate strain and stress depending on fire temperature.

1 Sensitivity analysis

Sensitivity analysis of the influence of the variable input parameters to the reliability of the structures depends on the statistical independency between input and output parameters.

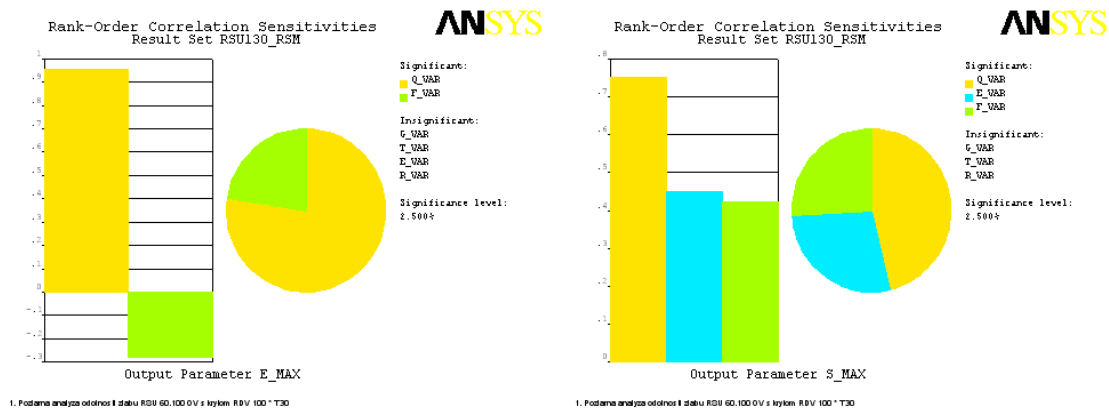


Figure 7 Sensitivity analysis of the equivalent strain and stress versus input variables

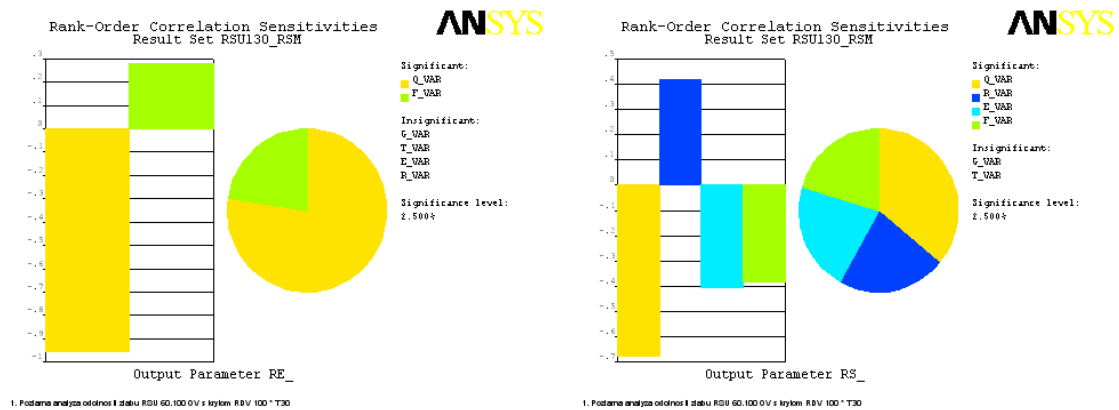


Figure 8 Sensitivity analysis of the reliability functions RE and RS versus input variables

The matrix of correlation coefficients of the input and output parameters is defined by Spearman [11].

$$r_s = \frac{\sum_{i=1}^n (R_i \bar{R})(E_i \bar{E})}{\sqrt{\sum_{i=1}^n (R_i \bar{R})^2} \sqrt{\sum_{i=1}^n (E_i \bar{E})^2}} \quad (18)$$

where R_i is rank of input parameters within the set of observations $[x_i]^T$, E_i is rank of output parameters within the set of observations $[y_i]^T$, \bar{R} , \bar{E} are average ranks of the parameters R_i and E_i respectively.

The variability of three input quantities (variable load, model and resistance uncertainties) is important to the equivalent strain and stress of cable way structures.

12 Comparison of deterministic and probabilistic analyses

The probabilistic part of the assessment is performed by the software ANSYS. The task is to consider the members of the cable way structures exposed to permanent, variable and temperature load due to fire effect (probability of fire is $P_{fire} = 0,002$).

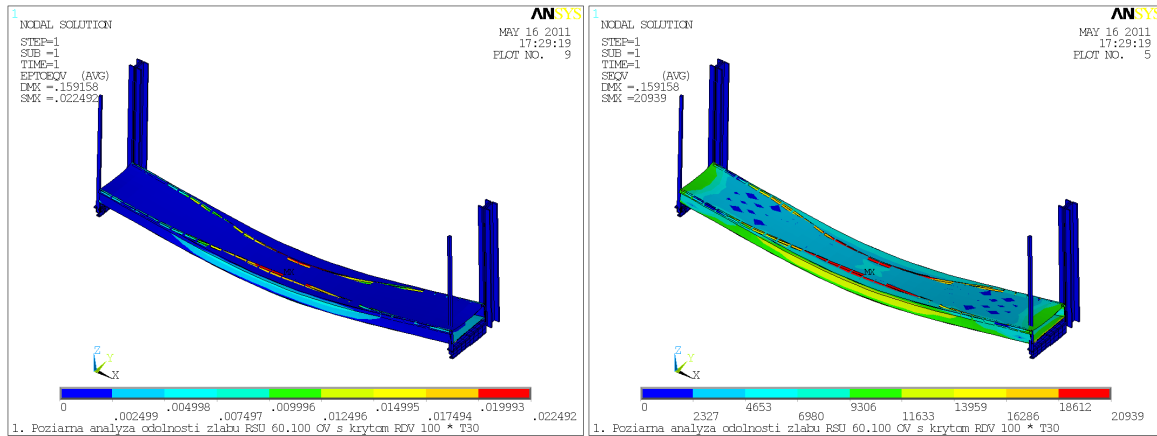


Figure 9 The equivalent strain and stress of the cable way structure

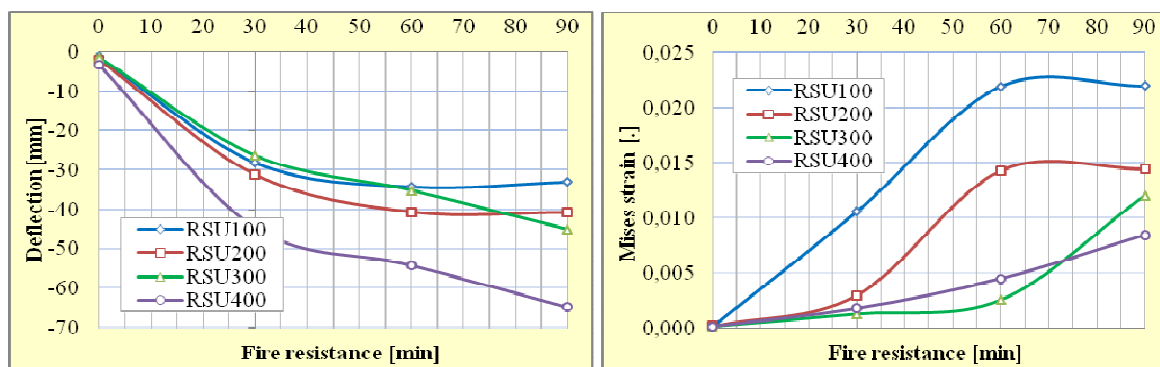


Figure 10 The deflection and Mises strain of the cable way structure – RSU 100, 200, 300 and 400

The deflection and the Mises strain of the cable way structures for various widths of cable troughs (100, 200, 300 and 400mm) and fire resistance (30, 60 and 90 min) is compared in fig.10.

Table 4 Results of probabilistic analyses of the cable way structures

Model	Equivalent strain (Von Mises)				Equivalent stress (Von Mises) [MPa]			
	Fractile 5%	Mean 50%	Fractile 95%	Failure Prob.	Fractile 5%	Mean 50%	Fractile 95%	Failure Prob.
RS130	-0,0009980	0,0014791	0,0049955	<1,0E-6	10,2530	12,4512	15,1045	1,867E-5
RS230	0,0001994	0,0008968	0,0012104	<1,0E-6	5,1410	10,9167	14,1988	<1,0E-6
RS330	0,0002112	0,0005266	0,0008183	<1,0E-6	3,6180	8,7368	13,1579	<1,0E-6
RS430	0,0006762	0,0007590	0,0008790	<1,0E-6	10,1603	11,5931	13,0782	<1,0E-6

Table 5 Results of deterministic analyses of the cable way structures

Model	Equivalent strain (Von Mises)		Equivalent stress (Von Mises)	
	Maximum action	Resistance	Maximum action	Resistance
	[.]	[%]	[MPa]	[%]

RS130	0,0077235	38,618	14,329	68,43
RS230	0,0022362	11,181	11,388	54,39
RS330	0,0009144	4,457	13,473	64,34
RS430	0,0008993	4,497	10,977	52,42

Reliability of the foundation structures is analyzed in accordance of national and Eurocode standard requirements [3 and 4] for serviceability and ultimate limit state. The serviceability of structure is limited by equivalent strain and the ultimate limit state by equivalent stress in dependency on fire temperature.

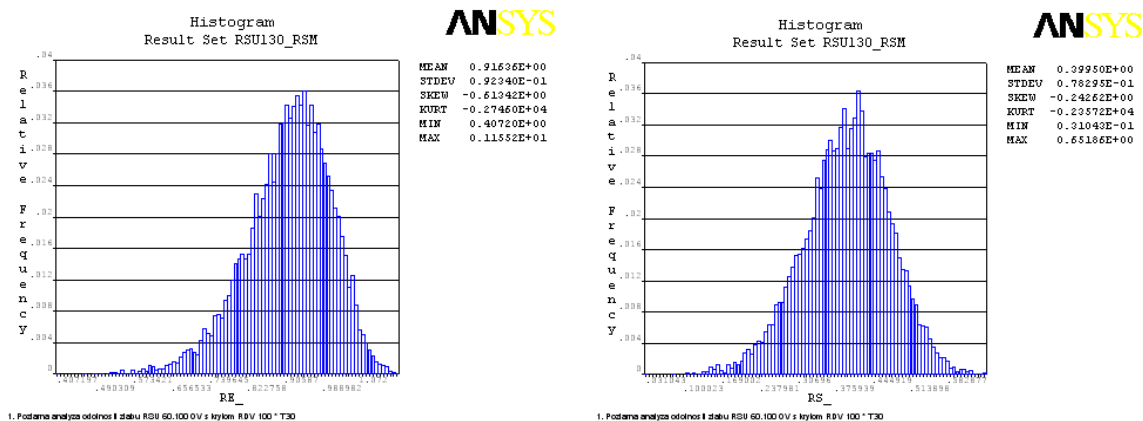


Figure 11 Histogram of the reliability functions RE and RS

The comparison of deterministic and probabilistic solution of the safety and reliability of the fire resistance of cable way structures is documented in the table 4 and 5. The histogram of reliability function $RF(\varepsilon)$ (failure function of the equivalent strain) are presented in fig.11. The differences between deterministic and probabilistic results are equal about to 2,3-45,9% (or 2,3-19,1%) for 95% equivalent strain fractile (or stress fractile) values.

13 Conclusions

This paper deals with the possibility of the deterministic and probabilistic analysis of the reliability of the cable way support structures depending on variability of the load, material and model characteristics. The analysis of the fire resistance of four types of cable way structures by deterministic as well as probabilistic calculation is shown in this paper. The fire resistance of the cable way structures are limited by the ultimate Mises strain $\varepsilon_u = 0,02$. The 49 simulations using approximate method RSM for four cases were calculated in the real time on PC (max CPU = 728sec). The nonlinear solution was running in max 191 steps. The output quantities were determined from 10^6 Monte Carlo simulations. The probabilistic method shows that the probability of the failure of all structures is less than target probability $p_d = 7,23 \cdot 10^{-5}$. However, the probabilistic calculation provides us with possibility of sensibility analysis, on the base of which the extreme load conditions on the cable way structures can be identified or also modified.

References

- [1] Barry, T., F. *Risk-Informed, Performance Based Industrial Fire Protection – An Alternative to Prescriptive Codes*. Tennessee Valley Publishing: Tennessee, USA, 2002.
- [2] BUCHANAN, A. : *Structural Design for Fire Safety*, Wiley, ISBN-10: 047189060X, 2001.
- [3] ENV 1993-1-2. *Eurocode 3: Design of steel structures. Part 1.2: General rules - Structural fire design*. CEN 2001.
- [4] *HANDBOOK 5, Implementation of Eurocodes, Design of Buildings for the fire situation*, Leonardo da Vinci pilot project Cz/02/B/F/PP-134007, CTU Prague, Luxemburg 10/2005.
- [5] IAEA, *Treatment of Internal Fires in Probabilistic Safety Assessment for Nuclear Power Plants*, IAEA Vienna, Safety Report No.10, ISBN 92-0-103298-6, 1998.
- [6] JANAS, P., KREJSA, M., KREJSA, V.: Structural Reliability Assessment Using Direct Determined Fully Probabilistic Calculation. *12th International Conference on Civil, Structural and Environmental Engineering Computing*, 2009, s. 1-20. 978-1-905088-31-7.
- [7] JCSS. *Probabilistic model code*. JCSS working materials, <http://www.jcss.ethz.ch/> 2001.
- [8] KALA, Z.: Sensitivity analysis of stability problems of steel plane frames, *Thin-Walled Structures*, 49, 5, pp.645-651 (2011). ISSN: 0263-8231. doi:10.1016/j.tws.2010.09.006.
- [9] KRÁLIK, J. VARGA, T.: Probability and Sensitivity Analysis of Fire Resistance of a Steel Frame. In proc.: *International Conference - CCCT'04*, August 14-17, 2004 - Austin, Texas, USA, Editors Chu, H. W. Savoie, M. Sanchez, B., Vol 4, Proc.85-90.pp.8.
- [10] KRÁLIK, J. VARGA, T.: Deterministic and Probability Analysis of Fire Resistance of a Steel Portal Frames with Tapered Members. In proc. *ESREL 2006, Safety and Reliability for Managing Risk*. Estoril, Portugal, 18-22 sept.2006. Balkema, CRC Press-Taylor & Francis Group, London, pp.2081-2086, ISBN 978-0-415-42315-1.
- [11] KRÁLIK, J.: *Reliability Analysis of Structures Using Stochastic Finite Element Method*, Published by STU Bratislava, 143pp. 2009.
- [12] KREJSA, M.: Application of the Direct Optimized Probabilistic Calculation. In proc. of *5th International Conference on Reliable Engineering Computing, Practical Applications and Practical Challenges REC2012*, June 13–15, 2012, Brno Czech Republic, Ed. M.Vořechovský et al, Pub. Ing. Vladislav Pokorný – LITERA, p. 241-260, ISBN 978-80-214-4507-9.
- [13] MPA iBMB, *Gültigkeit der gutachterlichen Stellungnahme Nr.7436/6716/Nau/vom 06.08.1998*, TU Braunschweig, Schreiben 4348/2005.
- [14] NUREG-1521, *Technical Review of Risk-Informed, Performance-Based Methods for Nuclear Power Plant Fire Protection Analyses*, U.S. Nuclear Regulatory Commission, Washington, DC 20555-0001, 1998.
- [15] STN 920205, *Správanie sa stavebných výrobkov a konštrukcií v požiari. Zachovanie funkčnej odolnosti elektrických káblových systémov*. SUTN Bratislava, 2010.
- [16] SUCHARDOVA, P. BERNATIK, A. SUCHARDA, O.: Risk analysis of extraordinary accident in industrial company. In *European Safety and Reliability Annual Conference: Reliability, Risk and Safety: Back to the Future, ESREL 2010*. London: CRC Press-Taylor & Francis Group, pp. 495-501. 2010, ISBN 978-0-415-60427-7.
- [17] WALD, F., SIMÕES DA SILVA, L., MOORE, D. B., LENNON, T., CHLADNÁ, M., SANTIAGO, A., BENEŠ, M. AND BORGES, L.: Experimental behaviour of a steel structure under natural fire, *Fire Safety Journal* 2006, Volume 41, Issue 7, s. 509–522.

Acknowledgement

The project was realized with the financial support of the Grant Agency of the Slovak Republic (VEGA). The project registration number is VEGA 1/1039/12.

Contact address:

Juraj Králik, prof.Ing.CSc.,

Faculty of Civil Engineering STU Bratislava, Radlinského 11, Bratislava 813 68, Slovakia,

e-mail: juraj.kralik@stuba.sk

COMPARISON OF PROBABILISTIC METHODS TO ANALYSE PROBABILITY OF STRUCTURAL FAILURE USING ANSYS

JURAJ KRÁLIK, JURAJ KRÁLIK,jr.

Faculty of Civil Engineering STU Bratislava

Abstract: This paper describes some experiences from the deterministic and probabilistic analysis of building structure reliability and safety. There are presented the methods and requirements of Eurocode EN 1990, standard ISO 2394 and JCSS. On the example of the probability analysis of the reliability of the high rise building is demonstrated the affectivity of the probability design of structures using FEM.

Keywords: ANSYS, FEM, RSM, LHS, probability, reliability, safety, high rise building

1 Introduction

Recent advances and the general accessibility of information technologies and computing techniques give rise to assumptions concerning the wider use of the probabilistic assessment of the reliability of structures through the use of simulation methods [3, 7, 9, 11, 12, 14, 15, 17, 18, 19, 20, 21 and 23]. Much attention should be paid to using the probabilistic approach in an analysis of the reliability of structures [3, 21].

Most problems concerning the reliability of building structures are defined today as a comparison of two stochastic values, loading effects E and the resistance R , depending on the variable material and geometric characteristics of the structural element. The variability of those parameters is characterized by the corresponding functions of the probability density $f_R(r)$ and $f_E(e)$. In the case of a deterministic approach to a design, the deterministic (nominal) attributes of those parameters R_d and E_d are compared.

The deterministic definition of the reliability condition has the form

$$R_d \geq E_d \quad (1)$$

and in the case of the probabilistic approach, it has the form

$$RF = R - E \geq 0 \quad (2)$$

where RF is the reliability function, which can be expressed generally as a function of the stochastic parameters X_1, X_2 to X_n , used in the calculation of R and E .

$$RF = g(X_1, X_2, \dots, X_n) \quad (3)$$

The failure function $g(\mathbf{X})$ represents the condition (reserve) of the reliability, which can either be an explicit or implicit function of the stochastic parameters and can be single (defined on one cross-section) or complex (defined on several cross-sections, e.g., on a complex finite element model).

The most general form of the probabilistic reliability condition is given as follows:

$$p_f = P(R - E < 0) \equiv P(RF < 0) < p_d \quad (4)$$

where p_d is the so-called design ("allowed" or "acceptable") value of the probability of failure.

The reliability function RF can be expressed generally as a function of the stochastic parameters X_1, X_2 to X_n , used in the calculation of R and E .

$$RF = g(X_1, X_2, \dots, X_n) \quad (5)$$

The failure function $g(\{X\})$ represents the condition (reserve) of the reliability, which can either be an explicit or implicit function of the stochastic parameters and can be single (defined on one cross-section) or complex (defined on several cross-sections, e.g., on a complex finite element model).

For a system limit state defined by $g(X_1, \dots, X_m) = 0$, where X_i are the basic variables, the failure probability is computed as the integral over the failure domain ($g(\mathbf{X}) < 0$) of the joint probability density function of \mathbf{X} . In general, the failure of any system can be expressed as a union and/or intersection of events. The failure of an ideal series (or weakest link) system (Králik, J. 2009b) may be expressed following

$$F_{sys} = F_1 \cup F_2 \cup \dots \cup F_m \quad (6)$$

in which \cup denotes the Boolean OR operator.

The probability of the failure can be defined on the base of analytical relations using the probabilistic density functions $f_R(r)$ and $f_E(e)$ and the distribution functions $\Phi_R(x)$ and $\Phi_E(x)$. Therefore the probability of the failure can be expressed as follow

$$p_f = \int_{-\infty}^{\infty} dp_f = \int_{-\infty}^{\infty} f_E(x) \Phi_R(x) dx = \int_{-\infty}^{\infty} \Phi_E(x) f_R(x) dx \quad (7)$$

Besides the probability of failure p_f the reliability index β is frequently taken as the reliability measure. The reliability index β is defined on the base of linearisation of the failure function $g(\mathbf{X})$. In the case of normal (or. lognormal) distribution function we have

$$\beta = \frac{\mu_{RF}}{\sigma_{RF}}, \quad (8)$$

where μ_{RF} and σ_{RF} are the mean value and the standard deviation of reliability function in form

$$\mu_{RF} = \mu_R - \mu_E, \quad \sigma_{RF}^2 = \sigma_R^2 + \sigma_E^2 \quad (9)$$

2 Models and methods of reliability analysis

The reliability analyses of the structures are differentiated from the point of view of design quantities as the deterministic and stochastic analyses. On the base of stochastic methodology the following analyses can be realized [11, 18]:

- Stochastic analysis – the mean values and the standard deviation of the variable quantities are calculated analytically or numerically using Monte Carlo simulation, which gives us the more accurate results than deterministic values,
- Sensitivity analysis – the dominant impact to the output quantities is calculated using the sensitivity analysis,
- Probabilistic analysis – the probability of the failure is defined in comparison with the simulated quantities.

On the base of the evaluated input quantities the methodologies can be divided following:

- Method of the allowed stresses (comparison of the maximum stresses),
- Method of the safety factor (capacity is defined by one factor),
- Method of the partial factor (action and capacity are defined by more factors).

In the present the method of the partial factor is favorable in the practice. The Eurocode [3, 6] recommends the use of three levels of the reliability analysis:

I. level - all base input quantities X_i are taken in the calculation by one (design) value. This quantity is calculated from its characteristic value and partial factors,

II. level - all base input quantities X_i are described by two statistical parameters (usually mean value and standard deviation). The probability of failure P_f (using the method FORM or SORM) can be used for comparison. The level II methods make use of certain well defined approximations and lead to results which for most structural applications can be considered sufficiently accurate.

III. level - all base input quantities X_i are calculated using the theoretical model of the probabilistic density. Value P_f is determined by calculation using simulation methods on the Monte Carlo base. Full probabilistic methods give in principle correct answers to the reliability problem as stated. Level III methods are seldom used in the calibration of design codes because of the frequent lack of statistical data.

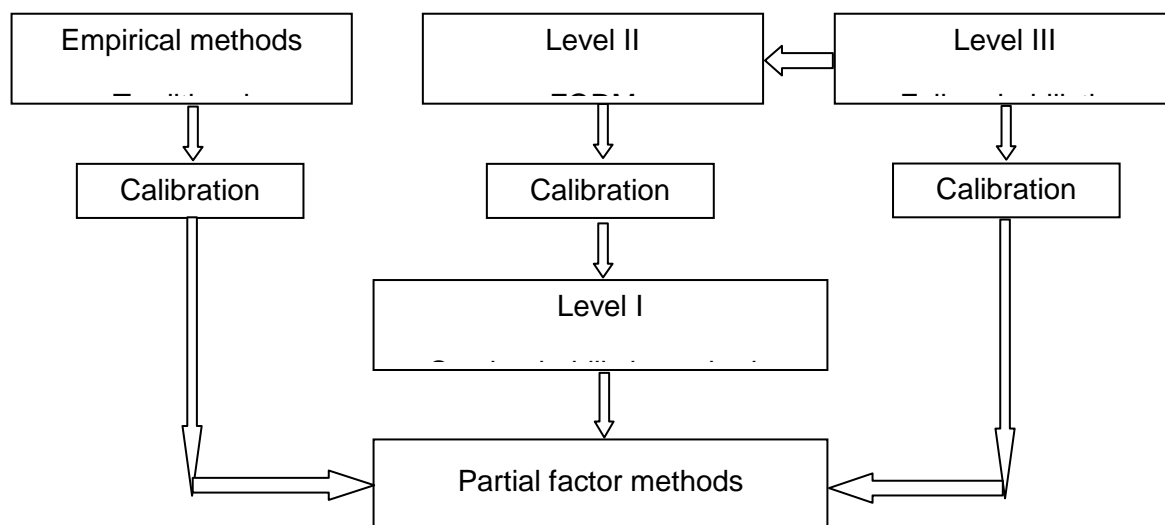


Figure 1 Overview of reliability methods by Eurocode 1990

In both the Level II and Level III methods the measure of reliability should be identified with the survival probability $P_s = (1 - P_f)$, where P_f is the failure probability for the considered failure mode and within an appropriate reference period. If the calculated failure probability is larger than a preset target value P_o , then the structure should be considered to be unsafe.

Table 1 Target probability and reliability index by Eurocode 1990 [4]

Limit state	Target reliability index β_d	
	50 years	1 year
Ultimate	3,8 ($p_f \approx 10^{-4}$)	4,7 ($p_f \approx 10^{-6}$)
Fatigue	1,5-3,8* ($p_f \approx 10^{-1} \div 10^{-4}$)	-
Serviceability	1,5 ($p_f \approx 10^{-1}$)	3,0 ($p_f \approx 10^{-3}$)

The measure of reliability in Eurocode 1990 [4] is defined by the reliability index β (Table 1). The reliability index depends on the criterion of the limited state. The standard JCSS [8] required the measure of reliability in dependency on the safety level (Table 1).

The measure of reliability depends on the lifetime of the structure and its importance (Table 2). In the case of the normal distribution of the probability failure the relation between the probability and the reliability index is defined in the form

$$p_f = \Phi(-\beta_f) \quad (10)$$

Table 2 Target probability and reliability index by JCSS [8]

Costs	Target reliability index β_d		
	Minor consequences	Moderate consequences	Large consequences
(A) Large	3,1 ($p_f \approx 10^{-3}$)	3,3 ($p_f \approx 5 \cdot 10^{-4}$)	3,7 ($p_f \approx 1 \cdot 10^{-4}$)
(B) Normal	3,7 ($p_f \approx 10^{-4}$)	4,2 ($p_f \approx 1 \cdot 10^{-5}$)	4,4 ($p_f \approx 5 \cdot 10^{-6}$)
(C) Small	4,2 ($p_f \approx 10^{-3}$)	4,4 ($p_f \approx 5 \cdot 10^{-5}$)	4,7 ($p_f \approx 1 \cdot 10^{-6}$)

When the main uncertainty comes from actions that have statistically independent maxima in each year, the values of β for a different reference period can be calculated using the following expression

$$p_n = 1 - (1 - p_1)^n \quad \text{and} \quad \Phi(\beta_n) = [\Phi(-\beta_1)]^n \quad (11)$$

where β_n is the reliability index for a reference period of n years, β_1 is the reliability index for one year.

Table 3 Indicative design working life by ENV 1990 [4]

Design working life category	Indicative design working life T_d (years)	Object
1	10	Temporary structures
2	10 to 25	Replaceable structural parts, e.g. gantry girders, bearings
3	15 to 30	Agricultural and similar structures
4	50	Building structures and other common structures
5	100 and more	Monumental building structures, bridges, and other civil engineering structures

3 Simulation methods for reliability analysis

In the case of simulation methods the failure probability is calculated from the evaluation of the statistical parameters and theoretical model of the probability distribution of the reliability function $Z = g(X)$. The failure probability is defined as the best estimation on the base of numerical simulations in the form [18]

$$p_f = \frac{1}{N} \sum_{i=1}^N I[g(X_i) \leq 0] \quad (12)$$

where N is the number of simulations, $g(\cdot)$ is the failure function, $I[\cdot]$ is the function with value 1, if the condition in the square bracket is fulfilled, otherwise is equal to 0.

Variation of the failure function can be defined by Melchers [20] in the form

$$s_{p_f}^2 = \frac{1}{(N-1)} \left\{ \frac{1}{N} \sum_{i=1}^N I^2[g(X_i) \leq 0] - \left[\frac{1}{N} \sum_{i=1}^N I[g(X_i) \leq 0] \right]^2 \right\} \quad (13)$$

The various forms of analyses (statistical analysis, sensitivity analysis, probabilistic analysis) can be performed. Most of these methods are based on the integration of Monte Carlo (MC) simulations. Three categories of methods have been presently realized:

- **Direct methods** (Importance Sampling - IS, Adaptive Sampling - AS, Direct Sampling - DS)
- **Modified methods** (Conditional, Latin Hypercube Sampling - LHS)
- **Approximation methods** (Response Surface Method - RSM)

A) The direct Monte Carlo Simulation (MCS) method is based on generation of sets of realizations of the random variables in the limit state function (with the assumed known

probability distributions) and to record the number of times the resulting limit state function is less than zero (i.e., failure). The estimate of the probability of failure (P_f) then is simply the number of failures divided by the total number of simulations (N). Clearly, the accuracy of this estimate increases as N increases, and a larger number of simulations are required to reliably estimate smaller failure probabilities. The generation of random variables is a relatively simple task (provided the random variables may be assumed independent) and requires only (1) that the relevant CDF is invertible (or in the case of normal and lognormal variants, numerical approximations exist for the inverse CDF), and (2) that a uniform random number generator is available. The generation of correlated varieties is not described here, but information may be found in the literature [11, 18].

The accuracy of this method is depended on the number of the simulations and it is defined by the variation coefficient

$$v_{p_f} = \frac{1}{\sqrt{Np_f}} \quad (14)$$

where N is the number of simulations. When the target probability of failure is $p_f = 10^{-4}$, thus the variation factor is equal to 10% for the number of simulations $N=10^6$, what is acceptable.

The failure probability for the case of a single limit state function can be extended directly to that for series and parallel systems. For example, the indicator function in Equation (12) for series system becomes

$$I\left[\bigcup_{i=1}^n g_i(x) < 0\right] = \begin{cases} 1 & \text{if } I[\cdot] \text{ is true} \\ 0 & \text{otherwise} \end{cases} \quad (15)$$

The difference in the application of importance sampling technique in this case is that the presence of numerous limit state functions complicates the choice of $h_x(x)$. A simple solution is to consider a multimodal sampling function given by

$$h_x(x) = \sum_{i=1}^N w_i h_{x_i}(x) \quad \text{where} \quad \sum_{i=1}^N w_i = 1 \quad (16)$$

and $h_{x_i}(x)$ is the sampling distribution determined based on the i^{th} limit state function and w_i is the weight, which is inversely proportional to β_i .

Advantages of the method:

- the final values of the reliability reserves can be continuously displayed in the form of a histogram or cumulative function; the simulations are independent,
- the method is easily understandable and transparent,
- the method enables the estimation of the statistical discrepancy of the estimation on a particular relevance level.

Drawbacks of the method:

- large number of simulations for small probability values,
- slow calculations of complex problems (for Finite Element Method models, the calculations are expensive and ineffective).

B) The Modified LHS method is based on the simulations of the function $g(\mathbf{X})$ so thus MC method, but the definition domain of the distribution function $\Phi(X_j)$ is divided to N intervals with the identical probability $1/N$. Characteristic values of the simulations as calculated randomly on the base of the permutation integer number $1, 2, \dots, N$. The reliability function $g(\mathbf{X})$ must be determined from the N simulation. The interval of the random simple is used one time only.

LHS method is based on the range of N values for each from K input parameters X_1, X_2, X_3 , in the next steps :

- The range of each X is divided into N non-overlapping intervals of equal marginal probability $1/N$;
- For each interval, one sample is selected randomly but taking into account the probability density in that interval; and
- The N values for X_1 are paired at random with the N values for X_2 forming N pairs of values for the pair (X_1, X_2) which are combined at random with the N values for X , to form N triplets, and so on to form a set of N K -triplets; this set is the Latin Hypercube sample.

This method gives us the best estimation of the statistical parameters of the structure in the comparison with MC method. The result of the LHS analysis is the parameter of the failure function – mean value \bar{Z} , standard deviation σ_z , skew coefficient α_z , kurtosis coefficient e_z , versus empirical cumulative distribution function.

C) Approximation methods - Response Surface Methods are based on the assumption that it is possible to define the dependency between the variable input and the output data through the approximation functions in the following form:

$$Y = c_o + \sum_{i=1}^N c_i X_i + \sum_{i=1}^N c_{ii} X_i^2 + \sum_{i=1}^{N-1} \sum_{j>i}^N c_{ij} X_i X_j \quad (17)$$

where c_o is the index of the constant member; c_i are the indices of the linear member and c_{ij} the indices of the quadratic member, which are given for predetermined schemes for the optimal distribution of the variables (Montgomery, Myers [18]) or for using regression analysis after calculating the response (Neter [18]).

Approximate polynomial coefficients are given from the condition of the error minimum, usually by the "Central Composite Design" (CCD) method or the "Box-Behnken Matrix Sampling" (BBM) method.

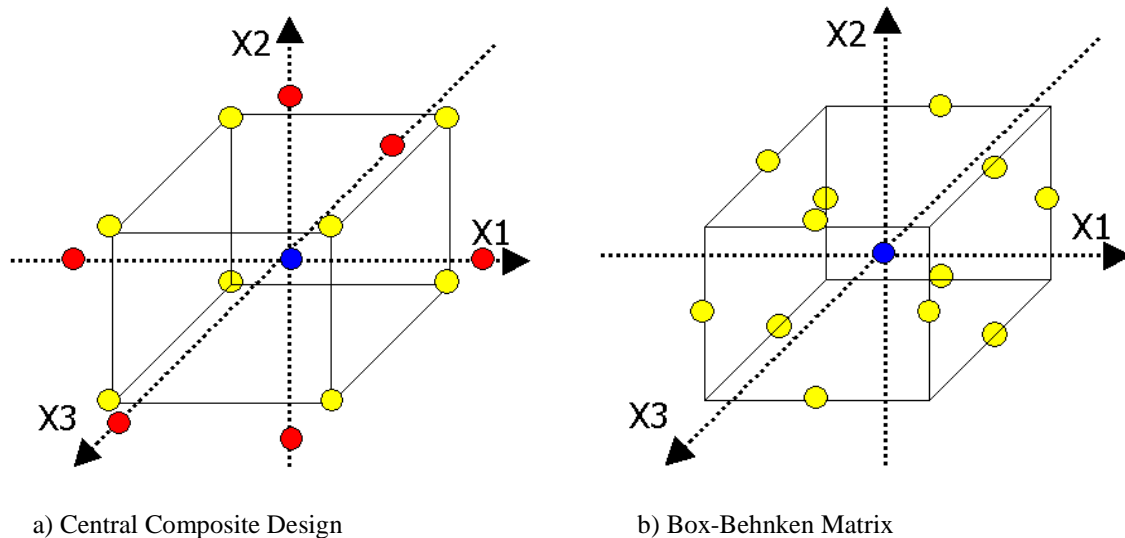


Figure 2 Distribution schemes of stochastic numbers of RSM method for three input variables

Advantages of the method:

- considerably less number of simulations than with the straight Monte Carlo method,
- it is possible to define dependencies using the "design experiments" method or regression analysis from the defined points in the case of improper approximation functions,
- particular simulations are independent from each other – parallel calculations can be used here.

Drawbacks of the method:

- the number of simulations depends on the number of variable input parameters; in the case of a large number of input parameters, the method is ineffective,
- the method is unsuitable in the case of discontinuous changes in the dependencies between the input and output values (e.g., the method is not suitable for resolving the stability of ideal elasto-plastic materials beyond the failure limit...).

Table 4 Summary of the stochastic numbers depending on the number of stochastic input variables

Number of stochastic variables	Central Composite Design			Box-Behnken Design	
	Number of quadratic function coef.	Number of factorials f	Number of stochastic numbers	Number of quadratic function coef.	Number of stochastic numbers
1	3	N/A	N/A	-	N/A
2	6	0	9	6	N/A
3	10	0	15	10	12
4	15	0	25	15	25
5	21	1	27	21	41
6	28	1	45	28	49
7	36	1	79	36	57
8	45	2	81	45	65
9	55	2	147	55	121
10	66	3	149	66	161

4 Probabilistic postprocessor in ANSYS program

For reliability analysis of the complicated structures the displacement-based FEM is favorable to use with the one from defined simulation methods. In this work the licensed program ANSYS [18] with probabilistic postprocessor was utilized for probability analysis of the reliability of NPP structures for various action effects.

The ANSYS Program belongs among the complex programs for solving potential problems. It contains a postprocessor, which enables the execution of the probabilistic analysis of structures.

In Figure 3, the procedural diagram sequence is presented from the structure of the model through the calculations, up to an evaluation of the probability of structural failure.

The postprocessor for the probabilistic design of structures enables the definition of random variables using standard distribution functions (normal, lognormal, exponential, beta, gamma, weibull, etc.), or externally (user-defined sampling) using other statistical programs like AnthILL or FReET. The probabilistic calculation procedures are based on Monte Carlo simulations (DS, LHS, user-defined sampling) and "Response Surface Analysis Methods (RSM)" (CCD, BBM, user-defined sampling).

The statistical postprocessor compiles the results numerically and graphically in the form of histograms and cumulative distributional functions. The sensibility postprocessor processes the data numerically and graphically and provides information about the sensitivity of the variables and about the correlation matrices.

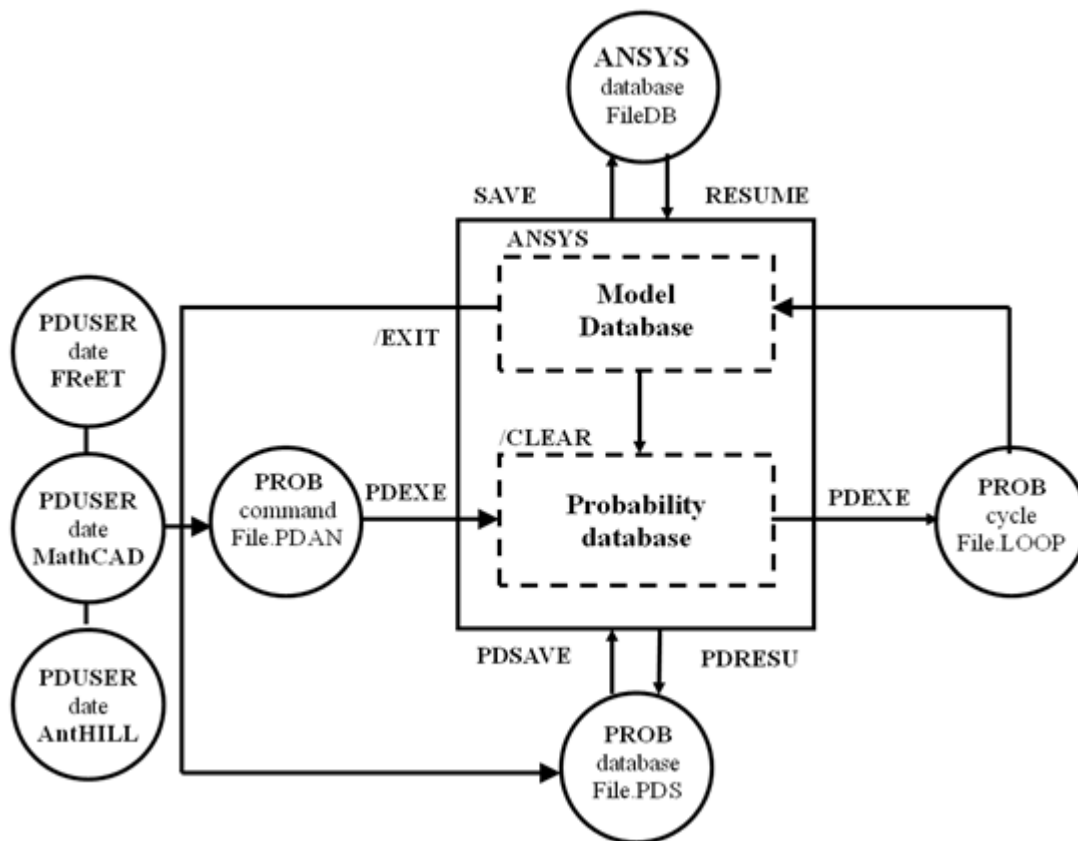


Figure 3 Procedural diagram of probabilistic calculations using the ANSYS software system

5 Probability analysis of high rise building using ANSYS

In the case of the design of high rise buildings in active seismic areas and the complicated geological conditions the uncertainties of the input data are very important from the point of view the optimal design of the structures [1, 2, 13, 14, 15 and 16]. The uncertainties of the variable loads grow by addition with the number of the floors. This effect has the importance role in the resistance of the structural elements. The locality of the Bratislava is well-known as the are with the complicated hydrogeo-logical conditions and the seismic risk level (acceleration design $a_g = \gamma \cdot a_r = 1,1 \cdot 0,41 = 0,451 \text{ms}^{-2}$). One from the important object is the building of the national slovak bank (NBS). On example of the seismic resistance of the national slovak bank building will be presented the effect of the probabilistic analysis of the seismic resistance.

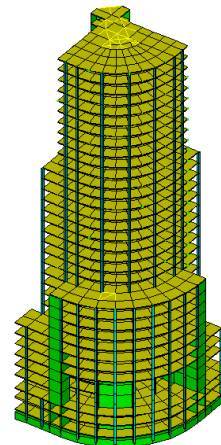


Figure 4 Calculation model of NBS

The high rise building of NBS has 32 floors and the height of 98,3m. The building is in the form of the circle quarter in plane with the radius 41,5m. This building has the 3 underground floors with the foundation level at -11,5 m. The structural walls are in the form of L in plane. The system is symmetrically about the diagonal axis. The NBS structure consists two conjugate reinforced concrete (RC) walls, RC ceiling without girder and the RC columns in space. The building is based on the RC Foundation plate of thickness 2,3m. The calculation FE model consists beam elements (BEAM44), shell elements (SHELL43) and solid elements (SOLID45) – number of elements is 5580 and nodes 3464 (Fig.4).

6 Loading and load combination

The loading and load combination in the case of the deterministic as well as the probability calculation is different due to requirements of Eurocode 1990 [4] and JCSS 2000 [8], too.

The seismic load was taken in accordance with ENV 1998 [5] as a design acceleration response spectrum for B type of soil and design acceleration $a_g = 0,451 \text{ms}^{-2}$. In the case of deterministic calculation and the ultimate limit state of the structure the load combination is considered according to ENV 1990 as follows:

D1) Permanent and variable load state

$$E_d = \gamma_G G + \gamma_Q Q_k + \gamma_w \psi_{ow} W_k \quad (18)$$

alternatively states are

$$E_d = \gamma_G G + \gamma_Q \psi_{oQ} Q_k + \gamma_w \psi_{ow} W_k \quad \text{alebo} \quad E_d = \xi \gamma_G G + \gamma_Q Q_k + \gamma_w \psi_{ow} W_k$$

D2) Seismic design situation

$$E_d = G_k + \psi_{2,Q} Q_k \pm A_{Ed} \quad (19)$$

where G_k is the characteristic value of the permanent loads, Q_k - the characteristic value of the variable loading, W_k - characteristic value of wind load, $A_{Ed} (= \gamma_1 A_{E,k})$ - the design value of the seismic loading, $A_{E,k}$ - the characteristic design value of the seismic loading, γ_1 - importance factor (of the building structure), γ_G - parciálny súčiniteľ pre stále zaťaženie, γ_Q - partial factor of variable load, $\psi_{o,w}$ ($\psi_{o,Q}$, $\psi_{2,Q}$) - combination factors ENV 1990 [4] ($\psi_{2,Q} = 0,3$).

In the case of probabilistic calculation and the ultimate limit state of the structure the load combination we take following:

P1) Permanent and variable load state

$$E = G + Q + W = g_{var} G_k + q_{var} Q_k + w_{var} W_k \quad (20)$$

P2) Seismic design situation

$$E = G + Q + A_E = g_{var} G_k + q_{var} Q_k + a_{var} A_{E,k} \quad (21)$$

where g_{var} , q_{var} , a_{var} are the variable parameters defined in the form of the histogram calibrated to the load combination in compliance with Eurocode [4].

7 Uncertainties of input variables

The uncertainties of action effects and structural resistance were considered in accordance of the Eurocode 1990 [4] and JCSS [8] using calibration methods to define the variable parameters (see tab.4). A soil stiffness variability in the vertical direction is defined by the characteristic stiffness value K_k from the geological measurement and the variable factor $k_{z,var}$. The variability of the soil stiffness in plane is defined by variable rotation of soil stiffness in the form of the rotation $k_{xx,var}$, $k_{yy,var}$. The action effects are taken with characteristic values G_k , Q_k , $A_{ED,k}$, W_k and variable factors g_{var} , q_{var} , a_{var} and w_{var} .

The random distribution of the soil stiffness under foundation plate is approximated with bilinear function on the slab plane in dependency on three parameters $k_{z,var}$, $k_{xx,var}$, $k_{yy,var}$

$$k(x, y) = \left\{ k_{z,var} + 2 \frac{(x - x_o)}{L_x} k_{yy,var} + 2 \frac{(y - y_o)}{L_y} k_{xx,var} \right\} k_{z,k} \quad (22)$$

where $k_{z,k}$ is characteristic value of soil stiffness, x_o , y_o are coordinates of foundation structure gravity centre, L_x and L_y are the plane dimensions of the slabs in directions x and y. The variability of input parameters are described in table 5 and 6.

The random distribution of the live load is approximated with bilinear function on the slab plane in dependency on three parameters q_{z_var} , q_{xx_var} , q_{yy_var}

$$q(x, y) = \left\{ q_{z_var} + 2 \frac{(x - x_o)}{L_x} q_{yy_var} + 2 \frac{(y - y_o)}{L_y} q_{xx_var} \right\}, \quad (23)$$

where q_k is characteristic value of live load ($q_k = 1 \text{ kN/m}^2$), x_o , y_o are coordinates of building slab gravity centre, L_x and L_y are the plane dimensions of the slabs in directions x and y.

Table 5 Probabilistic model of the input data

Characteristics	Soil			Loads			
	Stiffness			Perma- nent	Variable		Extrem
	Displ. Z	Rot. X	Rot. Y	Dead	Live	Wind	Earthquake
Charact. value	$k_{z,k}$	$k_{xx,k}$	$k_{yy,k}$	G_k	Q_{k1}	W_k	$A_{Ed,k}$
Variable factor	k_{z_var}	k_{xx_var}	k_{yy_var}	g_var	q_var	w_var	a_var
Histogram type	Normal	Normal	Normal	Normal	Beta(T.I)	Weibul (T.III)	Beta (T.I)
Mean value	1	1	1	1	0,57	0,37	0,67
Standard dev.	0,200	0,033	0,033	0,033	0,28	0,18	0,142
Min. value	0,451	0,851	0,853	0,569	0,858	0,021	0,419
Max. value	1,490	1,163	1,135	1,385	1,127	1,335	1,032

Table 6 Probabilistic model of the input data

Characteristics	Continuous load			Structural	Model	
	Load intensity				uncertainties	
	Vertical Z	Rot. X	Rot. Y	Modulus	Action	Resistance
Charact. value	$q_{z,k}$	$q_{xx,k}$	$q_{yy,k}$	E_k	θ_E	θ_R
Variable factor	k_{z_var}	k_{xx_var}	k_{yy_var}	e_var	F_var	Mu_var
Histogram type	Uniform	Uniform	Uniform	LogNorm	Normal	Normal
Mean value	0,5	0	0	1,0	1	1
Standard dev.	0,29	0,580	0,580	0,120	0,100	0,100
Min. value	0,0	-1	-1	0,645	0,875	0,875
Max. value	1,0	1	1	1,293	1,135	1,135

The spectrum response analysis was taken for the calculate the response from the seismic excitation in the form of the acceleration design spectrum due to Eurocode requirements of the high rise building.

The variability of the stiffness and damping characteristics of the building structure and soil lead to variability of the modal characteristic of the system. The modal analysis of the system show us that the dominant frequencies in direction X (or Y) are in the interval from 0,50Hz to 0,78Hz. This interval has the partially influency to the intensity of the seismic excitation on the slope line of the acceleration design spectrum below 2Hz.

8 Sensitivity analysis

Sensitivity analysis of the influence of the variable input parameters to the system soil-structure interaction is based on the statistical dependence of the output parameters to the input parameters. The matrix of correlation coefficients was calculated by Spearman. The sensitivity of the interstorey drift and the shear resistance on the variability of the input data is imagined on figures 4 and 5 for the model RSM2 a LHS2 in the case of the seismic excitation. The variability of the seismic load is dominant. The influency of the other parameters is different for the probabilisit analysis RSM and LHS. In the case of the RSM method the additional influency has the variability of stiffness (E_{var}) and masses (G_{var}) to maximum displacement. Otherwise the soil stiffness ($k_{z,var}$) is dominant in the method LHS. Analogously the sensitivity of the sher resistance is different in RSM and LHS method.

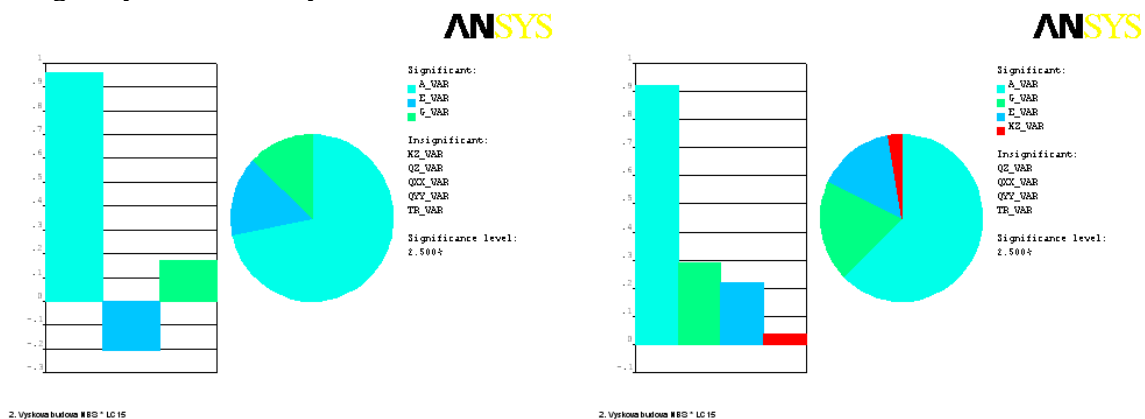


Figure 4 The results of the sensitivity analysis of D_{max} and V_{max} for model RSM2

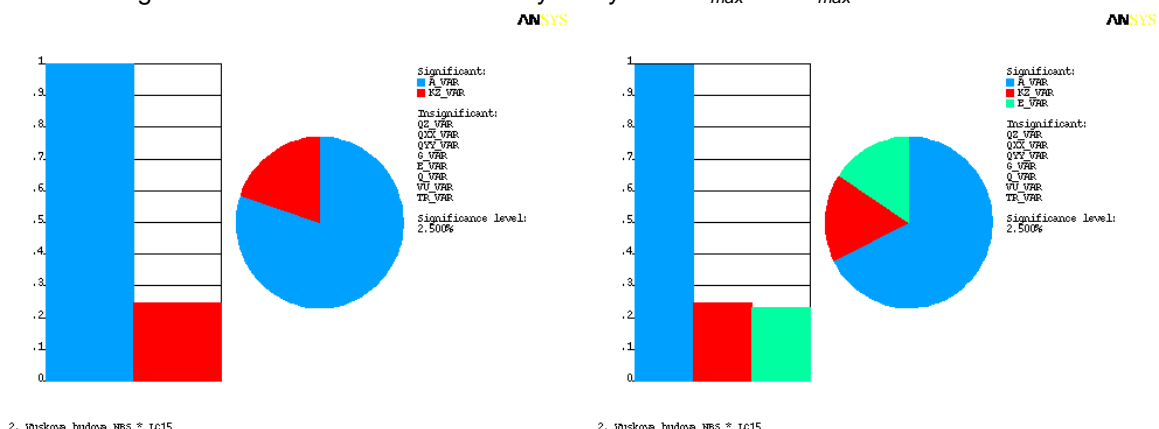


Figure 5 The results of the sensitivity analysis of D_{max} and V_{max} for model LHS2

The sensitivity analysis gives the valuable information about the influence of uncertainties of input variables (load, material, model and other) to engineer for optimal design of the structures.

1 Comparison of deterministic and probabilistic analyses

The deterministic calculation of the seismic resistance of the NBS high rise building was realized on the three models with different soil stiffness (with ratio: 0,75/1/1,5). The probabilistic analysis was considered for two methods RSM and LHS. The different number of input data was taken in three calculation models - RSM1, LHS1 (5 var.v. - $k_z, G_k, Q_k, A_k, \theta_R$), RSM2, LHS2 (8 var.v. - $k_z, k_{xx}, k_{yy}, G_k, Q_k, A_k, \theta_R, \theta_E$) and RSM3, LHS3 (10 and 11 var.v. - $k_z, k_{xx}, k_{yy}, G_k, A_k, E_k, q_{z,k}, q_{xx,k}, q_{yy,k}, \theta_R, \theta_E$). The deviation of the response data and the time calculation were considered depending on calculation methods and models.

The comparison of the deterministic and probabilistic analysis is summarized in tab.5. The mean values of the interstorey drift from the probabilistic analysis are lower than the mean values obtained from the deterministic analysis, but the maximum values of the interstorey drift histogram are higher than the maximum values obtained from the deterministic analysis. The kvantil values for 81% probability of noexcedanc (median+sigma) of the interstorey drift are near to the maximum values obtained from the deterministic analysis. The range of scatter of interstorey drift values is higher with the number of the variable input data. The results from the RSM method with 81 and 149 simulations are near the results from the LHS method with 100 simulations. The RSM method is more effective than LHS method from the point of view of the demands to the computer memory and the calculation time (see tab.7).

Table 7 Comparison of the deterministic and probabilistic analysis

Model	Extreme interstorey drift [mm]				Number of simple	Number of simulations	CPU [sec]
	Min	Mean	Max	St.dev			
Deterministic analysis							
MKP	5,72	5,73	5,74	-	-	3	147
Probabilistic analysis – RSM							
RSM1	2,14	2,19	3,92	0,83	5	27	891
RSM2	1,79	3,99	7,28	0,86	8	81	2670
RSM3	1,79	4,08	7,46	0,88	10	149	4805
Probabilistic analysis – LHS							
LHS1	2,90	4,40	7,01	0,89	5	100	3145
LHS2	2,80	4,32	6,89	0,88	8	100	4852
LHS3	2,50	4,08	6,38	0,86	11	100	4965
Probabilistic analysis – MC							
MC2	2,72	4,21	6,21	0,90	8	100	2777

The performance and demands of the probabilistic methods are compared in tab.8. From this comparison follows that the computer time grow rapidly with the number of input data up 8 quantities in the case of RSM method. The computer time for LHS method is higher in comparison with the MC method for the same number of the simulations. The maximum difference between LHS and MC method is 2,5% in values of interstorey drift if the number of simulation is the same. The value of the output quantity has changed about 15% for LHS method and 11% for MC method if the number of simulation is increased four time (see tab.8). The most effective probabilistic methods is RSM if the number of variable input data is lower as 8 simple. The effectiveness of the RSM method lies in analytical definition of the histograms. If the input data are defined in the form of the discrete histograms from the experimental test of the material and geometric characteristics of the structural element, than the MC method is the most accurate method to verify the probability of structural failure.

Table 8 Comparison of the efficiency of deterministic and probabilistic methods

Model	Extreme interstorey drift [mm]				Number of simple	Number of simulations	CPU [sec]
	Min	Mean	Max	St.dev			
Deterministic analysis							
MKP	5,72	5,73	5,74	-	-	3	147

Probabilistic analysis – RSM							
RSM2	1,79	3,99	7,28	0,86	8	81	2670
Probabilistic analysis – LHS							
LHS2a	2,80	4,32	6,89	0,88	8	100	4852
LHS2b	2,22	3,68	6,76	0,82	8	200	15243
LHS2c	2,00	3,68	5,43	0,80	8	400	30403
Probabilistic analysis – MC							
MC2a	2,72	4,21	6,21	0,90	8	100	2777
MC2b	2,16	3,59	6,21	0,85	8	200	8741
MC2c	2,08	3,75	7,55	0,83	8	400	17567

The advantage of the simulation methods is that it give us the detailed infromations about the sensitivity of the pursue output quantities in relation to the variability of input data. The simulation of the structure behaviour depending on variability input data give to engineers the possibility of the structural failure. According to these infomations it is posible to established that the probabilistic analysis of the reliability and sensitivity of the structures give us the better resource of the influnces of input data variability (action efect, impact of environs, material and geometric characteristics and structural resistance) to the behaviour of the structural elements.

9 Conclusion

This paper presented the methodology of the deterministic and probabilistic assessment to control the reliability of the large structures using finite element method. The advantages and drawbacks of various probabilistic methods to probabilistic analysis of the large structures. This analysis was realized on the example of the high rise building of NBS in Bratislava. The efectivity of the probabilistic methods MC, LHS and RSM in comparison with the deterministic methods was considered on example of the sensitivity analysis of NBS building. The sensitivity analysis of the uncertainties of the soil and structure properties and action effects using program ANSYS was considered. The most efectiv probabilistic methods is RSM if the number of variable input data is lower as 8 simple. The efectivness of the RSM method lies in analytical definition of the histograms. If the input data are defined in the form of the discrete histograms from the experimental test of the material and geometric characteristics of the structural element, than the MC method is the most accurate method to verify the probability of structural failure. The significance of the RSM method is well-known in the publications in scientific journal in the world. Application of the RSM method is determined by the analytical formulation of the histograms of the input data and the continual load effect (it is not acceptable for not continuous and buckling problems). If the input data are defined in the form of the discrete histograms, than the MC method is the most accurate method to verify the probability of structural failure.

References

- [1] CHOPRA, A.N., 2001, *Dynamics of Structures*, 2nd ed., Prentice-Hall, New York.
- [2] ČAJKA, R, MANÁSEK, P. Numerical analysis of the foundation structures with sliding joint. *Eleventh East Asia-Pacific Conference on Structural Engineering & Construction - Building a Sustainable Environment*, Taipei, Taiwan, 19. – 21.11. 2008. S. 716-717.
- [3] ELLINGWOOD, B., GALAMBOS, T.B., MACGREGOR, J.C., AND CORNELL, C.A., Development of a probability Based Load Criterion for American National Standard A58, *NBS Special Publication SP577*, National Bureau of Standards, Washington, D.C., 1980.
- [4] EN 1990, *Eurocode – Basis of structural design*. CEN Bruxelles. 2002.
- [5] Eurocode 8, *Design of structures for earthquake resistance, Part 1: General rules, seismic actions and rules for buildings*, CEN may 2000.
- [6] Hanbook 2, *Implementation of Eurocodes Reliability Backgrounds. Guide of the basis of structural reliability and risk engineering related to Eurocodes*. Development of Skills

- Facilitating Implementatio of Eurocodes. Leonardo Da Vinci Pilot Project CZ/02/B/F/PP-134007. Prague, CR, 10.2005.
- [7] JANAS, P., KREJSA, M., KREJSA, V.: Structural Reliability Assessment Using Direct Determined Fully Probabilistic Calculation. 12th *International Conference on Civil, Structural and Environmental Engineering Computing*, 2009, s. 1-20. 978-1-905088-31-7.
- [8] JCSS-OSTL/DIA/VROU-10-11-2000, *Probabilistic Model Code, Part 1, Basis of Design*, Working material, <http://www.jcss.ethz.ch/>.
- [9] HALDAR,A. & MAHADEVAN,S. 2000. *Probability, Reliability and Statistical Methods in Engineering Design*, John Wiley & Sons.,New York.
- [10] HANDRULEVA A., K. KAZAKOV, A. YANAKIEVA, Comparison of FEM computational models of shear walls with holes, In Proc.: *DCB 2010*, pp 305-310, Varna, Bulgaria, Sept. 9-11, (2010).
- [11] HOLICKÝ,M. & MARKOVÁ,J. 2005. *Base of reliability theory and risk evaluation*. ČVUT Praha, (in Czech).
- [12] KALA, Z.: Sensitivity analysis of stability problems of steel plane frames, *Thin-Walled Structures*, 49, 5, pp.645-651 (2011). ISSN: 0263-8231. doi:10.1016/j.tws. 2010.09.006.
- [13] KAZAKOV K., On the Total Dynamic Response in Time Domain of Soil-Structure Interaction Systems Using Elastodynamic Infinite Elements with Scaled Bessel Shape Functions, In *American Journal of Computational mathematics*, Vol. 2, N2, 2012, accepted on April 2012.
- [14] KRÁLIK,J.-KRÁLIK,J.JR., Probability and Sensitivity Analysis of Soil-Structure Interaction of High-Rise Buildings, *Slovak Journal of CE*, Faculty of Civil Engineering SUT in Bratislava, december, vol. 2006/3, pp.18-32.
- [15] KRÁLIK,J.-KRÁLIK,J.,JR., Deterministic and Probabilistic Assessment of Reliability Design of the High Rise Buildings. *Civil and Environmental Engineering*, ŽU Žilina, ISSN 1336-5835, 2007, Vol. 3, N.1, p.12-27.
- [16] KRÁLIK,J. KRÁLIK,J.,jr., Seismic Analysis of Reinforced Concrete Frame-Wall Systems Considering Ductility Effects in Accordance to Eurocode. *Engineering Structures*. Elsevier 2009, ISSN 0141-0296, Vol.31, Issue 12, pp. 2865 - 2872, December 2009.
- [17] KRÁLIK,J. *Safety and Reliability of Nuclear Power Buildings in Slovakia. Earthquake-Impact-Explosion*. Ed. STU Bratislava, 2009, 305 pp.
- [18] KRÁLIK,J., *Reliability Analysis of Structures Using Stochastic Finite Element Method*, Edition STU Bratislava, 2009, pp.138.
- [19] KREJSA, M., Application of the Direct Optimized Probabilistic Calculation. In proc. of 5th *International Conference on Reliable Engineering Computing, Practical Applications and Practical Challenges REC2012*, June 13–15, 2012, Brno Czech Republic, Ed. M.Vořechovský et al, Pub. Ing. Vladislav Pokorný – LITERA, p. 241-260, ISBN 978-80-214-4507-9.
- [20] MELCHERS,R.E., *Structural Reliability: Analysis and Prediction*, John Wiley & Sons, Chichester, U.K., 1999.
- [21] ROSOVSKY,D.V. Structural Reliability. Part of publ. W.Chen, *The Civil Engineering Handbook*, CRC Press, W.F.Chen Ed. 1995, Clenson University, SC.
- [22] SUCHARDOVA, P. BERNATIK, A. SUCHARDA, O. Risk analysis of extraordinary accident in industrial company. In *European Safety and Reliability Annual Conference: Reliability, Risk and Safety: Back to the Future, ESREL 2010*. London: CRC Press-Taylor & Francis Group, pp. 495-501. 2010, ISBN 978-0-415-60427-7.
- [23] ŠEJNOHA,J. NOVOTNÁ,E. Naplňování představ o pravděpodobnostním posuzování spolehlivosti systémů na základě simulace. In proc. *VII.Celostátní konference se zahraniční účastí „Spolehlivost konstrukcí“*, 5.dubna 2006, Praha, Ed. ÚTAM AV ČR, ČKAIT, ČSSI a SPS, pp.177-182.

Acknowledgement

The project was realized with the financial support of the Grant Agency of the Slovak Republic (VEGA). The project registration number is VEGA 1/1039/12.

Contact address:

Juraj Králik, prof.Ing.CSc.,

Faculty of Civil Engineering STU Bratislava, Radlinského 11, Bratislava 813 68, Slovakia,

e-mail: juraj.kralik@stuba.sk

CFD ANALYSIS OF COOLANT HOMOGENIZATION IN NUCLEAR REACTOR VVER440

EMIL MOJTO^A, VLADIMÍR KUTIŠ^A, JURAJ PAULECH^A

^AFaculty of Electrical Engineering and Information Technology, STU Bratislava, Ilkovičova 3,
Bratislava 81219, Slovakia

Abstract: The paper is focused on CFD analysis of coolant homogenization in nuclear reactor VVER 440. Investigation area start at cold inlets and finished at the entrance to fuel assemblies. Difference of temperatures at inlet nozzles of the pressure vessel is considered. Influence of these different temperatures is also evaluated in point of distribution of temperature on output part of the model that is right before the entrance to the fuel assemblies. In the model, there is considered also the flow in protective tubes for control rods.

Keywords: CFD, ANSYS CFX, reactor, coolant, turbulent model

1 Introduction

During the phase of considering safety aspects of the nuclear power plant, one of the fundamental criterions rests in determination of the thermal-hydraulic conditions in the active zone of the nuclear reactor. In reactor VVER440, there are 6 inlet parts for cold coolant water at the reactor pressure vessel. In nominal operation of reactor the difference between temperatures of coolant at these inlet parts should occur and it could be caused by several reasons. The most common reasons are: different length and segmentation of steam pipings, shut down of the one of steam generators (SG), unequal area of heat transfer surfaces of SG (Zdražil, 1980).

The paper deals with the influence of coolant mixing and homogenizing in the mixing part of reactor vessel in respect to the temperature difference at inlet parts of the reactor vessel. The inlet nozzle of fuel assembly is set up as output region of the simulation model (Kutiš, 2011). In CFD model, the flow in protective tubes for control rods is also considered. Ratio of the homogenization process is evaluated at the inlet nozzles of the fuel assemblies.

2 Geometry model of reactor

To performed CFD simulation, the geometry of reactor had to be created. Because only a part of the nuclear reactor VVER 440 is investigated by CFD, only three geometry parts were created, namely pressure vessel, reactor shaft core barrel and bottom of reactor shaft core barrel - see Image 1. In this Image, there is shown also the geometry model of assembly of all three components. All these components were created with all geometry details, but for CFD simulations, some of the details were simplified - e.g. in reactor shaft core barrel there was simplified outer shape, where surveillance channels were removed.

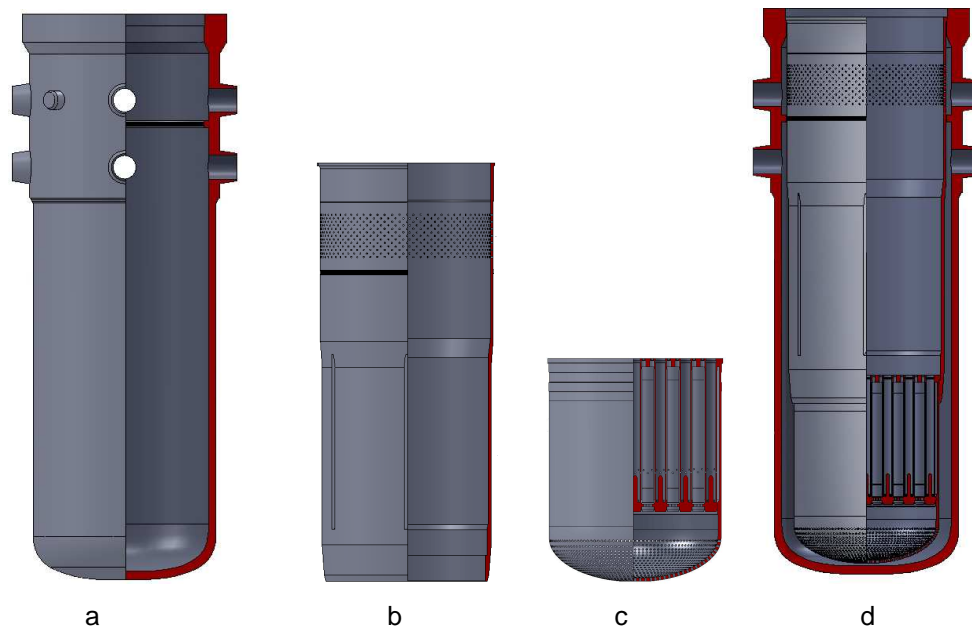


Image 1 - Geometry of model: a) pressure vessel, b) reactor shaft core barrel c) bottom of reactor shaft core barrel, d) assembly of components

3 CFD model and its discretization

After creating of geometry model of reactor negative geometry model, which represents volume of coolant, had to be created. In our simulation we also considered the flow in 37 protective tubes for control rods. The flow across 37 protective tubes can play important role (White, 1999) in distribution of velocities as well as temperatures at the output of our model that represents input nozzles of fuel assemblies. Volume of coolant was divided in 7 smaller volumes (in Image 7 each volume has different color), that were meshed separately.

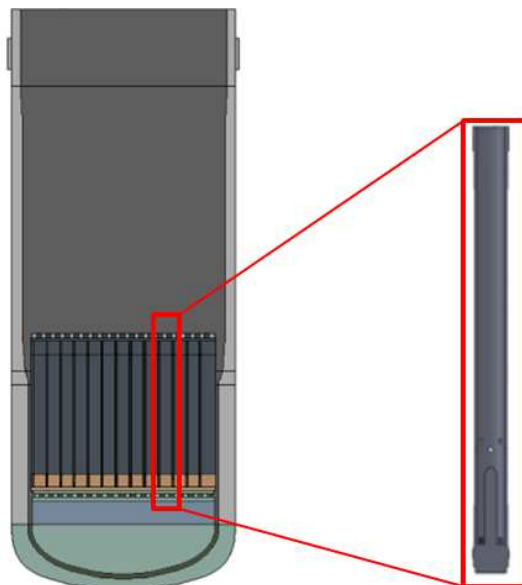


Image 2 - Geometry model of the coolant with protective tubes

ANSYS specialized mesh tool ICEM CFD was used to create structured hexahedral mesh also for complicated parts of the model, see Image 3. In common, hexahedral mesh in comparison with tetrahedral mesh provides numerically more accurate results and the number of elements is significantly smaller.

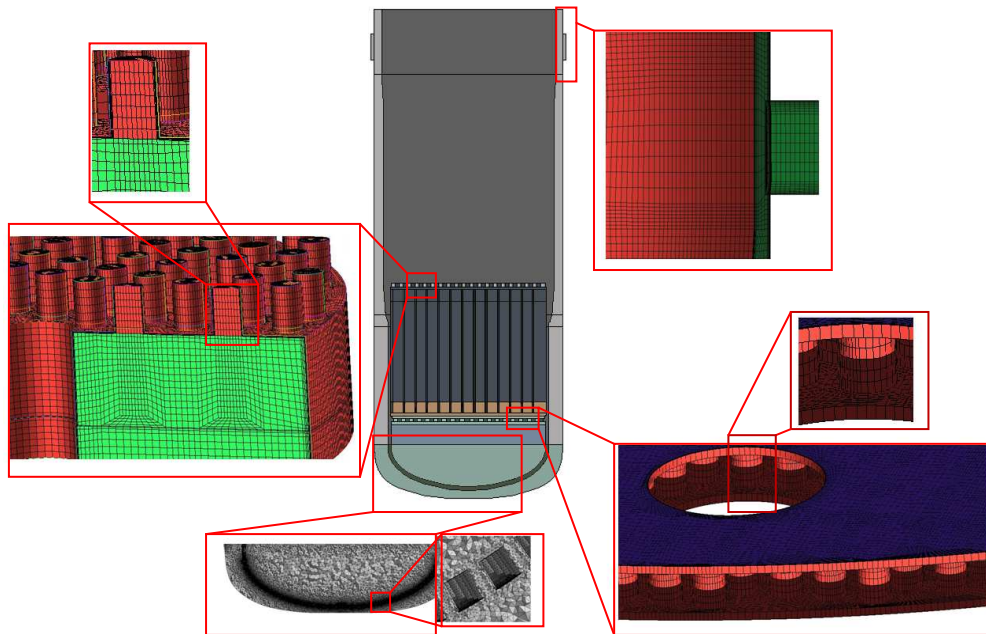


Image 3 - Geometric model of the coolant

In Image 3 we can see the details of the discretized model. The total number of elements is 51 737 086 and the number of nodes is 33 540 130. The only part which was not meshed by ICEM CFD was elliptical bottom part that is very geometrically complicated. For mesh of this part ANSYS Meshing was used and tetrahedral elements were created. Individual mesh regions were connected in ANSYS CFX using GGI connections (ANSYS, 2011).

3.1 Boundary conditions and setup of analysis

The simulation was calculated as steady-state flow of coolant in ANSYS CFX software. The temperatures at six inlet parts of the reactor pressure vessel were set according to Table 1 and Image 4. Velocity of coolant was set to value 9.2 m/s for all six inlets and this value was derived from total mass flow of coolant through the nuclear reactor pressure vessel.

Material properties of coolant (water) were set according to material model in material library IAPWS IF97. Based on our computational experiences in the previous model we chose SST turbulent model (Wilcox, 1993) for all following simulations presented in this paper. Boundary condition at the outlet region of the model was set as pressure condition with constant value 12.2 MPa.

Table 1 - Temperatures at inlet parts

Simulation	Temperature [°C]	Inlet No.
1	267,14	1
	268,73	2, 3, 4, 5, 6
2	267,14	2
	268,73	1, 3, 4, 5, 6

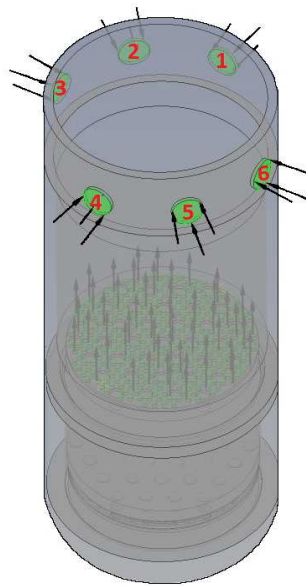


Image 4 - Boundary condition in the model

4 The results of simulations

Image 5 compares results from both simulations (setup 1 is on the left and 2 on the right side). These results show that cooler water set up on the inlet part No. 1 (“marginal inlet”) mixes only partially with the rest of coolant, the stream is crowded out from its vertical flow direction and the core temperature of the stream remains untouched.

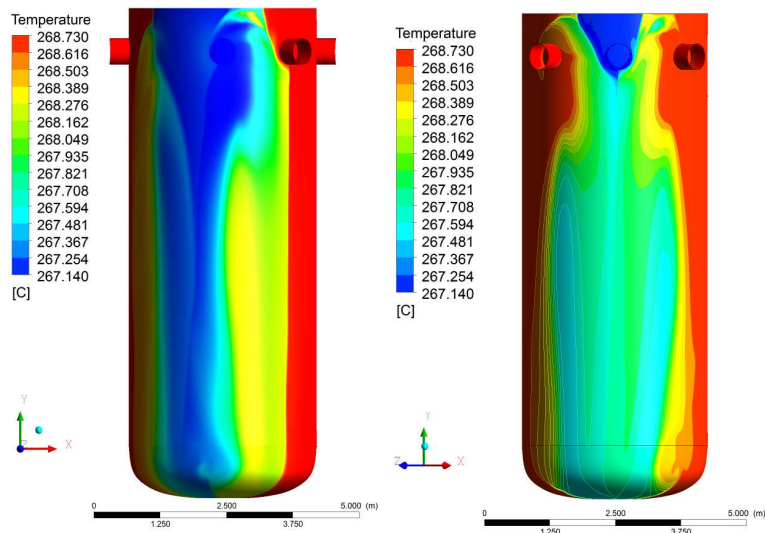


Image 5 - Mixing of coolant, front view

Setup No. 2 (cooler water on “central inlet”) shows that the influence of adjacent inlets is accentuated, mixing of coolant is more intensive and the stream direction of the flow remains vertical.

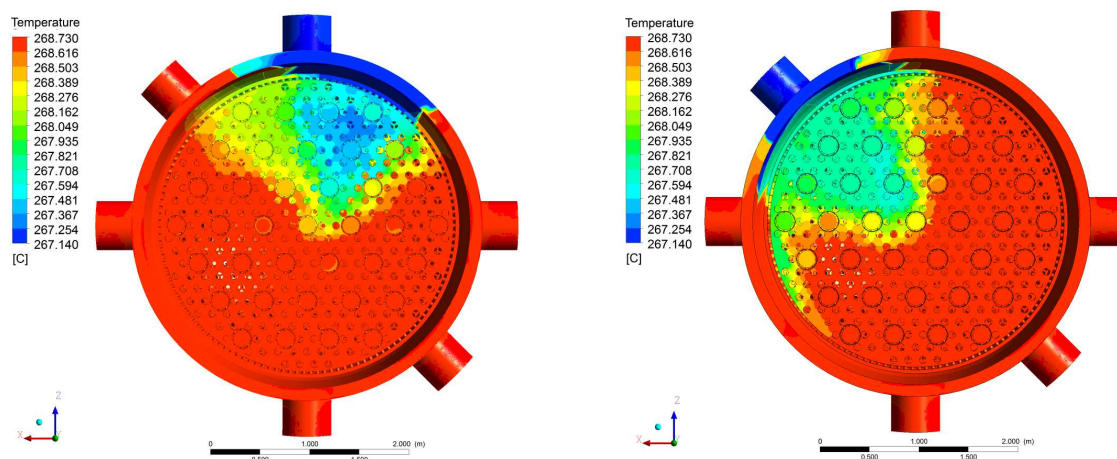


Image 6 - a) Temperature distribution, simulation No.1, b) Temperature distribution, simulation No.2

Image 6a shows the distribution of the temperature and influenced region for simulation No. 1 (top view). As was mentioned before, the stream of coolant is crowded out into the “free” region near the inlet No. 6. Image 6b shows similar situation for simulation No. 2 but cooler coolant remains in its vertical direction and the stream is significantly influenced by adjacent inlets No. 1 and 3.

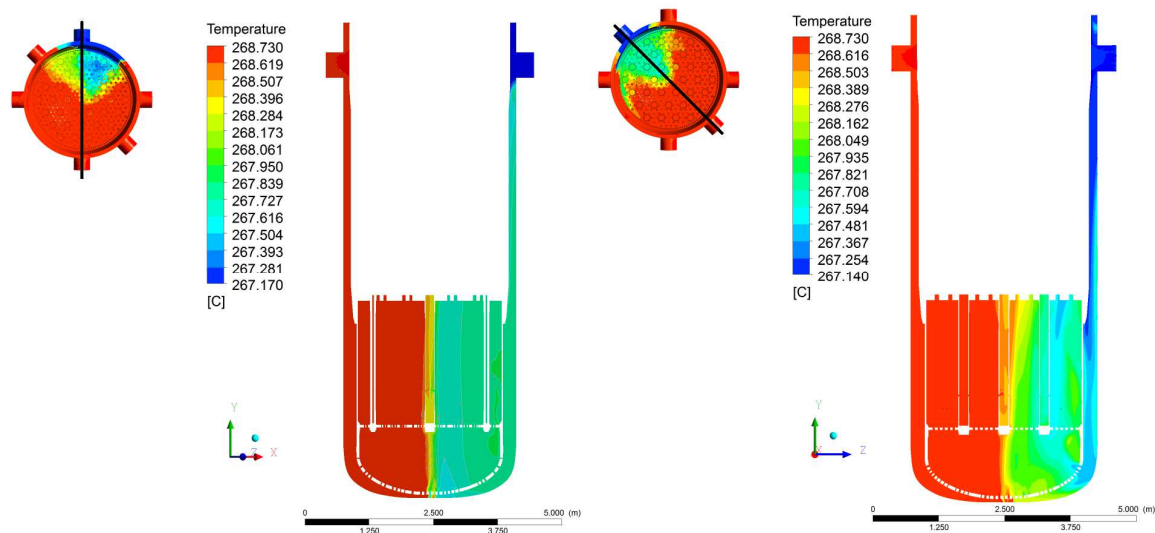


Image 7 - Mixing of coolant, cross section views

Image 7 shows flow of coolant across the reactor pressure vessel in cross section views, simulation No. 1 is on the left and simulation No. 2 on the right side. The model is cut through centre of inlets with cooler water - black line in small pictures on top left. In Image 7 there can be seen larger inhomogeneity in process of coolant mixing.

5 Conclusion

The presented paper dealt with modelling of thermal-hydraulic conditions in the nuclear reactor VVER-440 pressure vessel. Area of interest was the bottom part of reactor vessel where the coolant from six inlets is mixing together. The goal was to investigate the level of coolant temperature homogenization at the input nozzles of the fuel assemblies. Inlet temperature and the generated power in the fuel assemblies influence the outer temperature which is one of the limiting parameters in operation of the nuclear reactor. This is the reason why it is necessary to determine temperature distribution in the individual fuel assembly input nozzles.

References

- ZDRAŽIL J., BENC L., ZIGMUND J., 1980. Vplyv prevádzkových parametrov niektorých zariadení JE s VVER-440 na stacionárne tepelne-hydraulické charakteristiky aktívnej zóny. In: *Fyzikální a tepelné poměry v aktivních zónach jaderných reaktorů typu VVER-440 z hlediska bezpečnosti provozu*. Ústřední informační středisko pro jaderný program, Praha.
- KUTIŠ V., MOJTO E., PAULECH J., 2011. Modelovanie premiešavania chladiva pred vstupom do palivových kaziet JR VVER-440. In: *Elosys 2011*, Trenčín.
- WILCOX. D. C., 1993. *Turbulence Modeling for CFD*, DCW Industries, Inc.
- ANSYS, 2011. Help manual, Cinousburg.
- WHITE F. M., 1999. *Fluid Mechanics: Fourth Edition*. McGraw-Hill International, NY.

Acknowledgement

This work was supported in part by the following projects: Slovak Research and Development Agency under the contracts APVV-0450-10, Grant Agency KEGA - grant No. 015STU-4/2012.

Contact address:

doc.Ing. Vladimír Kutiš, PhD.,

Department of Applied Mechanics and Mechatronics, FEI STU Bratislava, Ilkovičova 3,
81219 Bratislava, Slovak republic

FEM ANALYSIS OF MEMS PIEZOELECTRIC PRESSURE SENSOR

VLADIMÍR KUTIŠ^A, JAROSLAV DZUBA^B, JURAJ PAULECH^A, VIKTOR KRÁLOVIČ^A,
JUSTÍN MURÍN^A, TIBOR LALINSKÝ^B

^AFaculty of Electrical Engineering and Information Technology, STU Bratislava, Ilkovičova 3, Bratislava 81219, Slovakia, ^BInstitute of Electrical Engineering, SAV, Dúbravská cesta 9, Bratislava 84104, Slovakia

Abstract: The modeling and simulation of piezoelectric MEMS pressure sensor which is AlGaIn/GaN based circular high electron mobility transistor (C-HEMT) structure is presented in the paper. The influence of the residual stress plays an important role in correct modeling of MEMS piezoelectric pressure sensor. Residual stresses which were measured by micro-Raman spectroscopy are included in the model using initial stress state of the membrane. Two different geometries of MEMS piezoelectric pressure sensor are considered - circular and ring. Piezoelectric analysis of the MEMS sensor is performed by FEM code ANSYS. 2D simplified axisymmetric FEM model, which is very effective from computational time viewpoint, is verified by full 3D FEM model. The influence of position of electrode is investigated in verified 2D simplified axisymmetric FEM model.

Keywords: FEM analysis, piezoelectric analysis, MEMS pressure sensor, residual stress

1 Introduction

Micro-Electro-Mechanical Systems (MEMS) promises drive to the next technological revolution. MEMS devices can quite replace bulky actuators and sensors with microscale devices. Pressure sensor presented in this article is based on C-HEMT structure defined on AlGaIn/GaN heterostructure. It is well known that the III-V nitrides (especially gallium nitride, GaN) propose tremendous potential for microelectronic device application due to their high mechanical and physical stability and high thermal stability (Strite, 1992). Also their excellent piezoelectric properties can be used in pressure and strain sensor applications. Compared with other commonly used piezoelectric materials, they have some important advantages such as direct compatibility with high electron mobility transistors (HEMTs), high biocompatibility, possibility to be operated at high temperatures and harsh environments. Piezoelectric polarization in the nitride layer can be changed by an external action and it means the change in the density of the two dimensional electron gas (2DEG) located at the AlGaIn/GaN interface. As a result, the HEMT conductivity can be influenced by external strain. Piezoelectric response of AlGaIn/GaN devices integrated on membrane structures also have been reported (Kang, 2004). Investigation of AlGaIn/GaN-based circular HEMT was first presented and these structures can be potentially applied in new devices for dynamic pressure and stress sensing. The process technology and piezoelectric performance analysis of C-HEMT devices were presented as well (Lalinský, Držík, 2011).

To design the piezoelectric pressure sensor with optimal properties, FEM analysis of individual design proposal need to be investigated. The goal of the presented paper is to performed piezoelectric analysis of membrane, which is initially stressed due to lattice mismatch and thermal expansion coefficient (TEC) mismatch. The influence of electrode

location is also investigated. Two different design of pressure sensor are presented, where 2D and also 3D FEM models are used.

2 Pressure sensor design

2.1 Circular and ring design of pressure sensor

Image 1 shows two different designs of presented MEMS piezoelectric pressure sensor. In both designs the working layers AlGaIn/GaN are placed on Si substrate and between substrate and GaN layer is AlN layer used as a nucleation layer that helps reduce the intrinsic stress of the structure. This AlN layer is not included in our FEM models because it is very thin.

Image 1a and 1b represent circular and ring design, respectively. In both images inner part of Si substrate is etching. Image shows also transistor electrodes – drain, gate and source. Ohmic drain and source contacts were deposited by electron beam evaporation, lift-off technique and rapid thermal annealing at high temperature and the Schottky gate electrode was deposited by the same technique but annealing at lower temperature. Only gate electrode is included in our 2D and 3D FEM models.

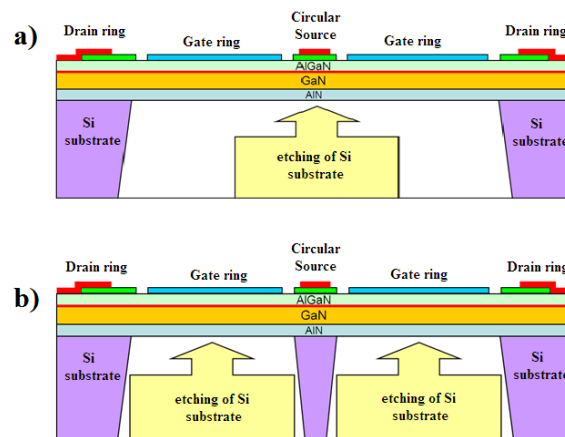


Image 15 – Design of piezoelectric MEMS pressure sensor, a) circular design, b) ring design

Image 2 shows the photos of fabricated membrane structure: (a) circular electrodes of HEMT can be seen on top surface of the membrane (blue color – membrane, lightest part - electrode), (b) membrane is created by substrate etching from backside, (c) another type of membrane – with central pillar.

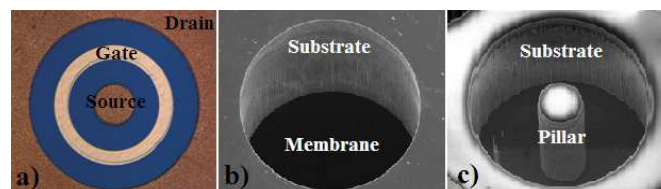


Image 2 – Membrane structure: a) top side, b) backside of circular membrane, c) backside of ring membrane

2.2 Residual stress in AlGaIn/GaN layers

The large lattice mismatch and the difference in thermal expansion coefficients between GaN and substrate leads to the formation of cracks or stress generation (Liu,

2002). The effect of the AlN buffers on the optical and crystal quality of GaN films and values of intrinsic stress on Si (Wu, 2004) and stress on other substrates (Guziewicz, 2008, Barghout, 2004) has been investigated.

To investigate residual stress in AlGaIn/GaN layers micro-Raman spectroscopy has been used. The residual biaxial stress was evaluated from the shift of GaN Raman peak by back-side mapping (from the substrate side) (Lalinský, Hudek, 2011). Image 3 shows obtained measured tensile biaxial stress distribution in ring design on AlGaIn/GaN layers. As we can see from the image, the electrode metallization plays the role in residual stress distribution. The tensile stress in AlGaIn/GaN layers is between 280 to 300MPa. Biaxial residual stress value 300MPa is taken as an initial stress state of the membrane in FEM simulation. Effect of electrode metallization on stress distribution is not taken into account in FEM model.

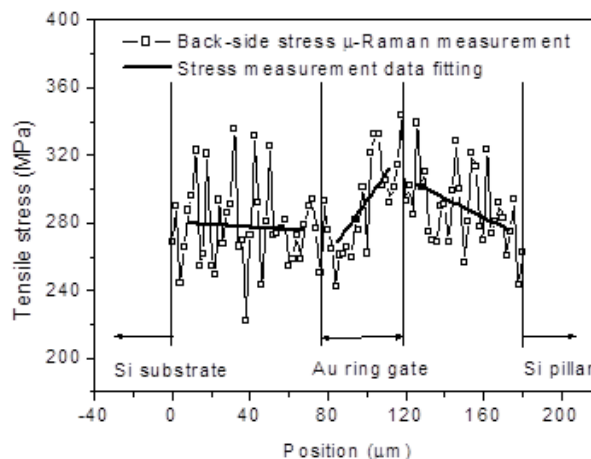


Image 3 – Distribution of the residual stress in membrane measured by μ -Raman scattering technique

3 Piezoelectric analysis of pressure sensor

3.1 Simplified geometry models

Because residual stress in AlGaIn/GaN layers is caused by two different physical phenomena, namely lattice mismatch and TEC mismatch, it is inevitable to use measured data to set initial stress conditions in FEM model. Measured residual stress represents initial stress state in AlGaIn/GaN layers and this fact is used in geometry simplification of models - Si substrate can be avoided and the influence of substrate can be represented by boundary conditions. Image 4 shows simplified geometry, where only piezoelectric layer AlGaIn and structural layer GaN is considered.

Geometry parameters of both designs are:

- outer radius: $R_2=240\mu\text{m}$
- inner radius (only ring design): $R_1=60\mu\text{m}$
- location of top electrode is defined by parameters R_{E1} and R_{E2}
- thickness of AlGaIn layer: $h_{\text{AlGaIn}}=28\text{nm}$
- thickness of GaN layer: $h_{\text{GaN}}=1.9\mu\text{m}$

3.2 Material properties of pressure sensor

Material properties, which have to be considered in piezoelectric analysis of pressure sensor, belong to three categories: mechanical, electrical and piezoelectrical. Mechanical properties have to be defined for both GaN and AlGaIn layer, but electrical and piezoelectrical properties have to be defined only for AlGaIn layer. Both layers show transversally isotropic behavior.

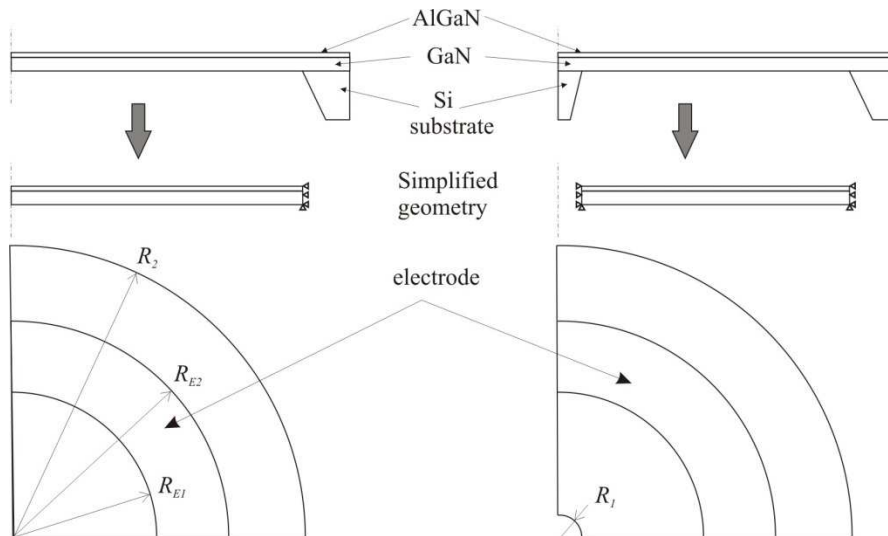


Image 4 – Simplified circular and ring geometry of pressure sensor

Constitutive law for mechanical behavior (only GaN layer) can be written in matrix form as

$$\sigma = C\varepsilon \quad (2)$$

where σ is stress vector, ε is strain vector and C is elasticity matrix and for transversally isotropic material can have form

$$C = \begin{bmatrix} c_{11} & c_{12} & c_{13} & 0 & 0 & 0 \\ & c_{11} & c_{13} & 0 & 0 & 0 \\ & & c_{33} & 0 & 0 & 0 \\ & s & & c_{44} & 0 & 0 \\ & & y & & c_{44} & 0 \\ & & & m & & c_{66} \end{bmatrix} \quad (2)$$

Constitutive law for piezoelectric behavior (only AlGaIn layer) can be written in matrix form as

$$\begin{aligned} \sigma &= C^E \varepsilon - eE \\ D &= e\varepsilon + e_p^\varepsilon E \end{aligned} \quad (3)$$

where E is vector of electric intensity, D is vector of electric displacement, e_p^ε is permittivity matrix on condition constant strain ε , C^E is elasticity matrix on condition constant electric intensity E and e is matrix of piezoelectric properties. For polarization in z (number 3 in numerical labeling) direction, elasticity matrix C^E has form (2), permittivity matrix e_p^ε has form

$$e_p^\varepsilon = \begin{bmatrix} e_{p11} & 0 & 0 \\ 0 & e_{p11} & 0 \\ 0 & 0 & e_{p11} \end{bmatrix} \quad (4)$$

and matrix of piezoelectric properties e has form

$$e = \begin{bmatrix} 0 & 0 & e_{13} \\ 0 & 0 & e_{13} \\ 0 & 0 & e_{33} \\ 0 & 0 & 0 \\ 0 & e_{15} & 0 \\ e_{15} & 0 & 0 \end{bmatrix} \quad (5)$$

Mechanical properties of AlGaIn and GaN layers are summarized in Table 1 and electric and piezoelectric properties of AlGaIn are summarized in Table 2.

Table 3 Mechanical properties of GaN and AlGaIn

Elasticity constants [GPa]	GaN	AlGaIn
c_{11}	390	395
c_{12}	145	146
c_{13}	103	104
c_{33}	405	386
c_{44}	105	110
c_{66}	123	125

Table 2 Electric and piezoelectric properties of AlGaIn

Relative permittivity	piezoelectric properties [pC/ μm^2]

[-]	
$e_{p11}=8.9$	$e_{13}=-0.51$
-	$e_{33}=0.375$
-	$e_{15}=0.67$

3.3 Analysis of ring design

Ring design of piezoelectric pressure sensor was analyzed by FEM code ANSYS (ANSYS, 2011) in order to determine optimal size of electrode. Because nonlinear analysis had to be used, the computational time is very sensitive to the number of nodes of FEM model. This was the reason why 2D analysis was chosen in the analysis, where the location of electrode was changed. To verify 2D numerical model, 3D FEM model (with simplified geometry) was also calculated. In 2D analysis, coupled field element PLANE223 and structural element PLANE183 were used. 2D axisymmetric model contained 7224 elements. Boundary conditions were set according to Image 4, the tensile residual stress 300MPa was set as initial stress state of the system and material properties were defined in accordance with Chapter 3.2. In 3D analysis, residual stress, material properties as well as boundary conditions were the same as in 2D analysis, only element types were changed, coupled field element SOLID226 and structural element SOLID186 were used. Total number of 3D elements was 12250. Both models were loaded by outer pressure 10kPa.

For verification calculation, location of top electrode was chosen as follows: $R_{E1}=70\mu\text{m}$ and $R_{E2}=230\mu\text{m}$. Obtained transversal deformations are shown in Image 5 and maximal deflection and induced charge are summarized in Table 3.

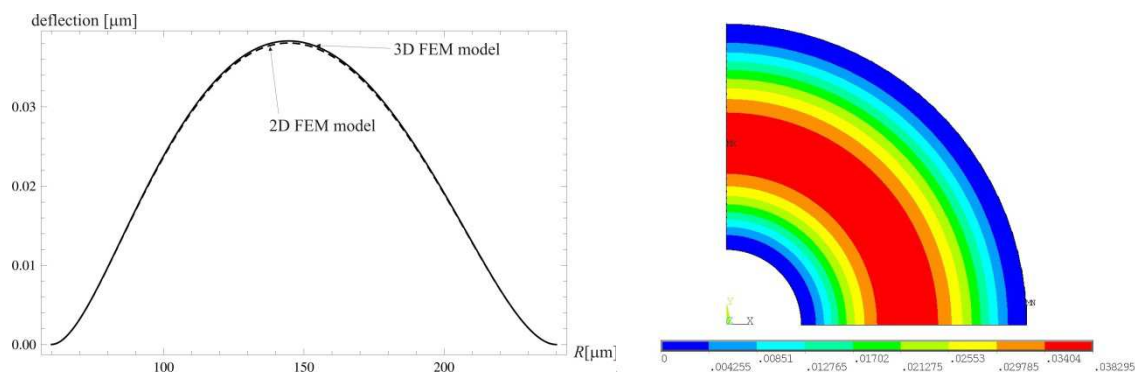


Image 5 – Verification of 2D axisymmetric model of ring design - deflection of membrane

Table 3 Comparison of 2D and 3D ring model results - deflection and induced charge

	2D model	3D model
max. deflection [μm]	0.038	0.038
induced charge [pC]	0.509	0.494

As we can see from Image 5 as well as from Table 3, obtained results for 2D FEM and 3D FEM model are almost identical, the small difference in induced charge is caused by the fact, that in 2D analysis not full piezoelectric matrix (5) as well as elasticity matrix (2) are

included in the computation. Based on the obtained results, we can claim that 2D FEM model of piezoelectric pressure sensor is verified and we can use it in next computations.

Our next step was to determine the location and size of electrode, where the induced charge is the largest in order to have the best sensor sensitivity. We chose the width of the top electrode $5\mu\text{m}$ (i.e. $R_{E2}-R_{E1}$) and in sequence we changed the central radius of electrode $R_{E21}=(R_{E2}+R_{E1})/2$. Obtained dependence of induced charge on central radius of electrode R_{E21} is shown on Image 6.

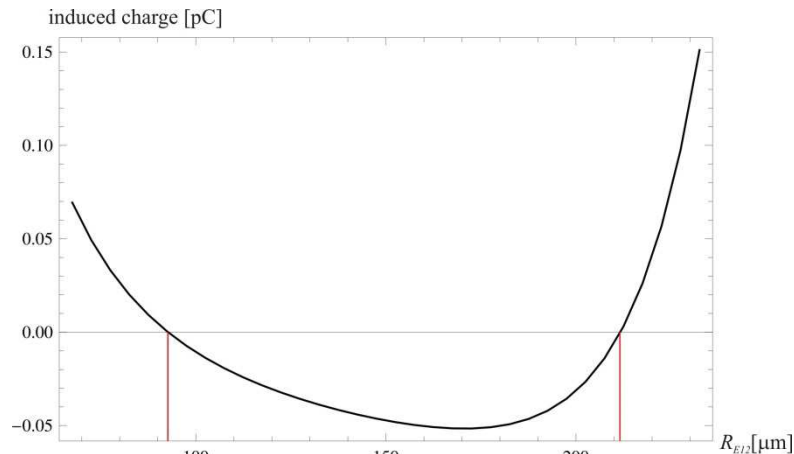


Image 6 – Dependence of induced charge on central radius of electrode R_{E21} for ring design, width of electrode is $5\mu\text{m}$

As is shown in Image 6, the sign of induced charge is changed in dependence on central radius of electrode. If the electrode cross the red lines in Image 6, the total charge would be decreasing because the sign of charge. The optimal size and location of electrode is determined by changing the sign of charge. As a result, the optimal location and size of electrode for prescribed loading and boundary conditions are determined by red lines in Image 6, i.e. $R_{E1}=95\mu\text{m}$ and $R_{E2}=210\mu\text{m}$. For these parameters of top electrode, we obtained total induced charge 0.794pC .

3.4 Analysis of circular design

In similar way, as was described above for ring design, we analyzed circular design of piezoelectric pressure sensor. Material parameters are the same as in ring design, boundary conditions were set according Image 4, residual stress was in the same level as in ring design. The model was loaded by outer pressure 10kPa .

Verification comparison is performed on the same location of electrode as was used for verification calculation in ring design. Maximal deflection and induced charge are summarized in Table 4.

Table 4 Comparison of 2D and 3D circular model results - deflection and induced charge

	2D model	3D model
max. deflection [μm]	0.214	0.216
induced charge [pC]	0.565	0.543

As we can see from Table 4, obtained results for 2D FEM and 3D FEM model are almost identical and we can consider 2D FEM model of piezoelectric pressure sensor as verified.

Similar to analysis of ring design, our goal was to set optimal location and size of the top electrode. We used the same procedure with the same width of electrode ($5\mu\text{m}$), but we started from inner electrode radius $R_{E1}=5\mu\text{m}$. Obtained dependence of induced charge on central radius of electrode R_{E2} is shown on Image 7.

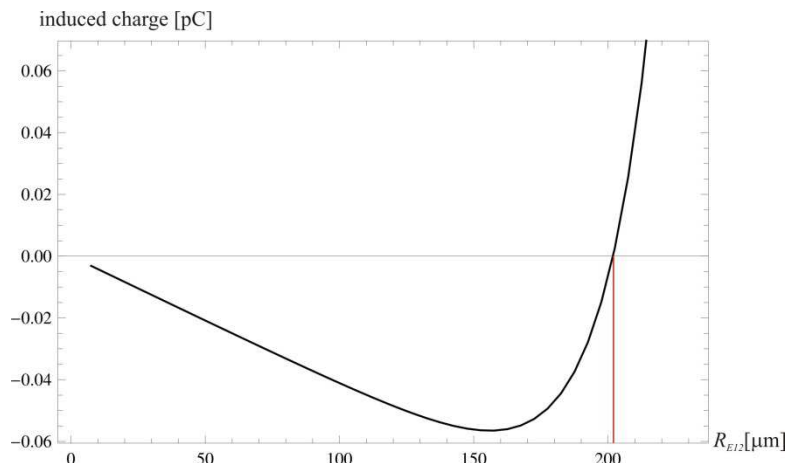


Image 7 – Dependence of induced charge on central radius of electrode R_{E2} for circular design, width of electrode is $5\mu\text{m}$

As a result for analysis of circular design of pressure sensor, the optimal location and size of electrode for prescribed loading and boundary conditions is determined by only one red line in Image 7, i.e. $R_{E2}=202\mu\text{m}$. For these parameters of top electrode, we obtained total induced charge 1.271pC .

4 Conclusion

The paper deals with piezoelectric MEMS pressure sensor, which is made as membrane AlGaIn/GaN C-HEMT structure with two different designs - circular and ring. The focus has been put on FEM piezoelectric simulations, that was performed by code ANSYS. 2D and 3D models have been performed in order to verify simpler 2D FEM model loaded by external pressure. Residual stress caused by large lattice mismatch and the difference in thermal expansion coefficients has been included into the model by prescribing the initial stress state of membrane. After verification of initially stressed 2D FEM piezoelectric model, the model has been used to investigate the influence of location and size of electrode. For both designs, optimum size and location of electrode has been derived. In our next research all these calculations will be compared with measured data, which will be performed on both designs.

References

STRITE, S., MORKOC, H., 1992. GaN, AlN, and InN: A review, *Journal of Vacuum Science and Technology*, vol. 10, p. 1237.

KANG, B.S., KIM, S., REN, F., JOHNSON, J.W., THERRIEN, R.J., RAJAGOPAL, P., ROBERTS, J.C., PINER, E.L., LINTHICUM, K.J., CHU, S.N.G., BAIK, K., GILA, B.P., ABERNATHY, C.R., PEARTON, S.J., 2004. Pressure-induced changes in the conductivity of

AlGaIn/GaN high-electron mobility-transistor membranes, *Appl. Phys. Lett.*, vol. 85, no. 14, p. 2962.

LALINSKÝ, T., DRŽÍK, M., VANKO, G., VALLO, M., KUTIŠ, V., BRUNCKO, J., HAŠČÍK, Š., JAKOVENKO, J., HUSÁK, M., 2011. Piezoelectric response of AlGaIn/GaN-based circular-HEMT structures, *Microelectrical Engineering*, vol. 88, issue 8, p. 2424.

LIU, L., EDGAR, J.H., 2002. Substrates for gallium nitride epitaxy, *Material Science and Engineering*, R 37, p. 93.

WU, M., ZHANG, B.S., CHEN, J., LIU, J.P., SHEN, X.M., ZHAO, D.G., ZHANG, J.C., WANG, J.F., LI, N., JIN, R.Q., ZHU, J.J., YANG, H., 2004. Effect of the N/Al ratio of AlN buffer on the crystal properties and stress state of GaN film grown on Si(111) substrate, *Journal of Crystal Growth*, 260, p. 331.

GUZIEWICZ, M., KAMINSKA, E., PIOTROWSKA, A., GOLASZEWSKA, K., DOMAGALA, J.Z., POISSON, M.A., LAHRECHE, H., LANGER, R., BOVE, P., 2008. Comparative study on stress in AlGaIn/GaN HEMT structures grown on 6H-SiC, Si and on composite substrate of the 6H-SiC/poly-SiC and Si/poly-SiC, *Journal of Physics: Conference Series*, 100.

BARGHOUT, K., CHAUDHURI, J., 2004. Calculation of residual thermal stress in GaN epitaxial layers grown on technologically important substrates, *Journal of Material Science*, 39, p. 5817.

LALINSKÝ, T., HUDEK, P., VANKO, G., DZUBA, J., KUTIŠ, V., SRNÁNEK, R., CHOLEVA, P., VALLO, M., DRŽÍK, M., MATAY, L., KOSTIČ, I., 2011, "Micromachined membrane structures for pressure sensors based on AlGaIn/GaN circular HEMT sensing device," published in book of abstracts, *37th International Conference on Micro and Nano Engineering MNE 2011*: Berlin.

ANSYS13.0 Help System, 2011.

Acknowledgement

This work was supported in part by the following projects: Slovak Research and Development Agency under the contracts APVV-0450-10, Grant Agency KEGA - grant No. 015STU-4/2012 and VEGA - grant No. 1/0534/12.

Contact address:

doc.Ing. Vladimír Kutiš, PhD., Department of Applied Mechanics and Mechatronics, FEI STU Bratislava, Ilkovičova 3, 81219 Bratislava, Slovak republic

AERODYNAMIC CHARACTERISTICS OF A DOUBLE SKIN FAÇADE

MILAN PALKO

SLOVAK UNIVERSITY OF TECHNOLOGY IN BRATISLAVA, Faculty of Civil Engineering,

Abstract: The article deals with determination of local aerodynamic resistance of double skin façade. To estimate aerodynamic entrances for inlet and outlet channel of the intermediate space for double skin facades. The aerodynamic entrances for the mode with convectional movement of air in the gap. The aerodynamic entrances for the mode with the influence of air. Aerodynamic and geometrical boundary conditions of the model. The example of the simulation of aerodynamic blinds for inlet channel.

Keywords: double skin façade, aerodynamic blinds, aerodynamic resistance

1 Introduction

Nowadays, computer simulation programs supported by numerical CFD (Computational Fluid Dynamics) modeling are able to deal with the air flow problems due to the fast development of the computer hardware. The CFD is the field analyzing the fluid flow using the computational models. The fluid flow can be either liquid or gas. The simulation method is currently used in the branches, such as, e.g., aircraft, ship and automobile industries. In civil engineering, the fluid flow occurs chiefly in cases of water structures. The fluid flow can also mean the air flow surrounding buildings and their segmental parts. Mainly, the two mathematic variation methods are applied at solving such tasks Finite Element Method (FEM), and Volume Element Method (VEM).

2 Material and methods

The calculation was performed as 2D task. The calculation domain is illustrated in Image 1. The model consists of approximately 28 thousand nodes and 54 thousand elements. The element FLUID 141 (Image 2) was used as the flow continuum model. That is the plane three-node element. The model for incompressible fluid with the turbulent flow was applied for the task. There are four discretion levels in each node: the velocity in direction "x", in direction "y", the pressure and the temperature.

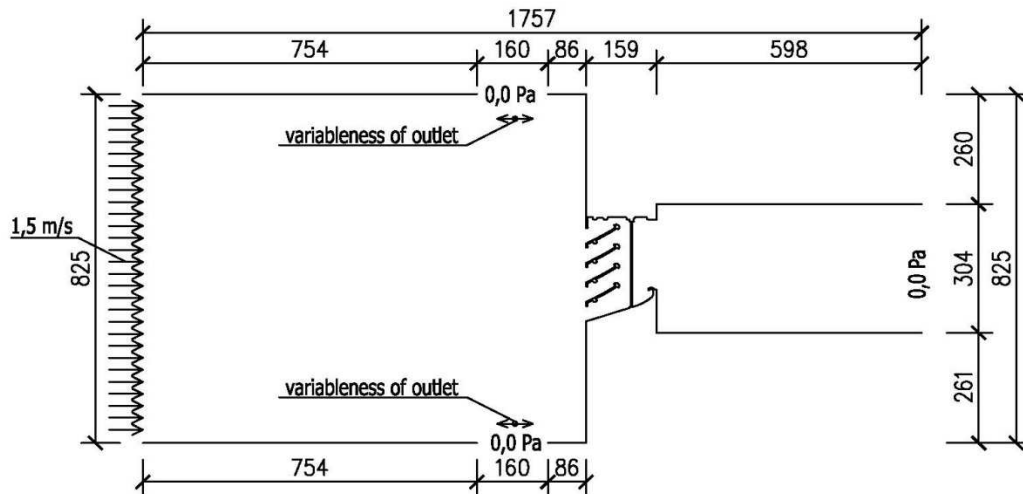


Image 16 Schema for computer simulation with support CFD for velocity 1,5 m/s

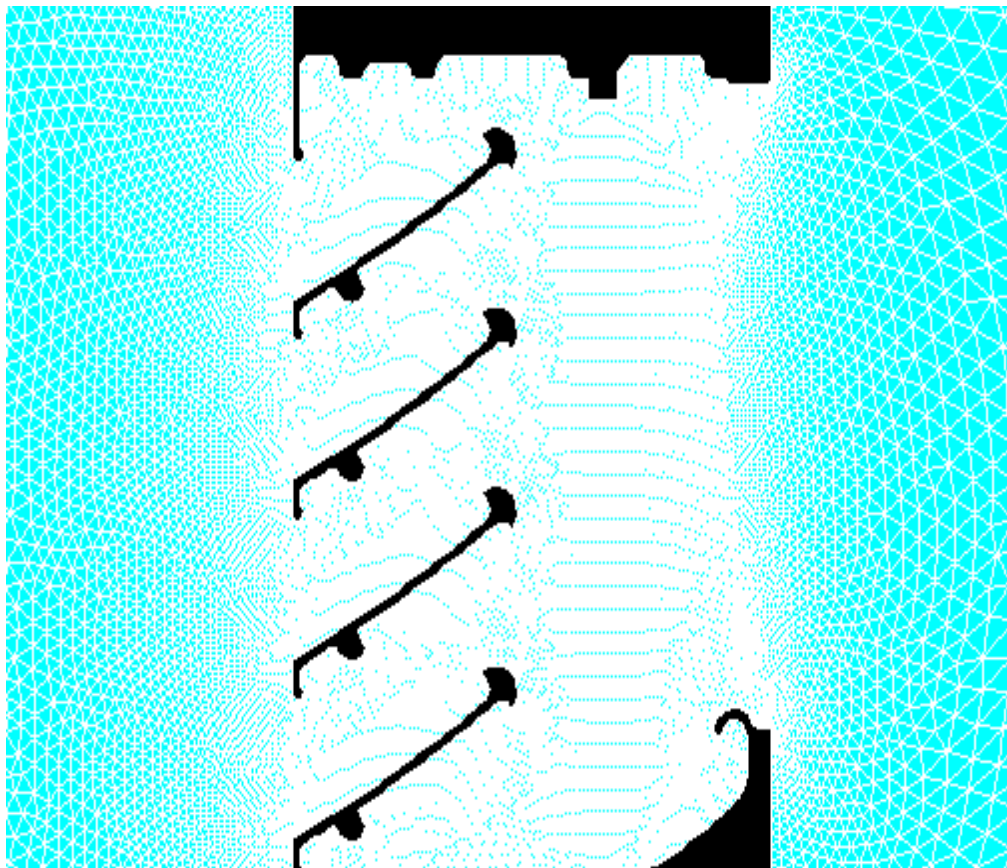


Image 17 The mash for the research region of inlet channel of double skin façade

The boundary conditions were defined on the domain model outside boundary lines and the edge lines of ventilation blinds. The load input had comprises two characters. Firstly, it was the velocity boundary condition affecting from the left side of the computational model in positive direction "x". The air velocity entering the model is 0.2, 0.4, 0.7, 1.0, 1.5 and 2.0 m/s. The application of the boundary condition has been also defined on the external surface of the ventilation blinds as well as the edge model walls. In this case, the velocity was 0 m/s. The pressure has been the second aspect of the boundary conditions. The pressure value 0 Pa has been defined in the three model places. The fluid flowing in the model has the

physical properties of incompressible air. The network density has been done following the iterative calculation and its right solution convergence (Image 1).

3 Results of velocity calculations in entry channel of double skin façade

The whole simulation of the entry channel of buffer zone of double transparent façade has been carried out during 8500 iterative cycles, within which the total error converged. The velocities of air movement in the entry channel are required for further calculation of aerodynamic coefficient of local resistance. The choice of the measuring points has been precisely made according to the experimental measurement (Image 3). The accurate values in the individual points are presented in Table 1 and Image 4.

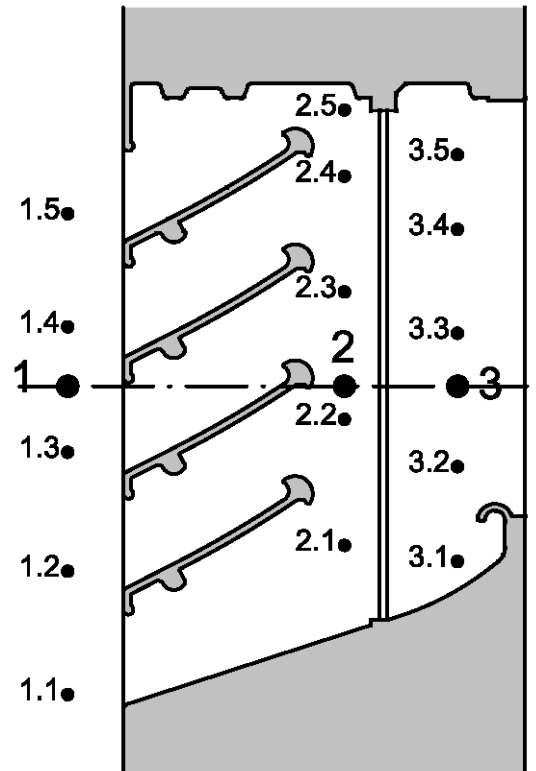


Image 18 Arrangement of detecting element for scanning velocity of air flow

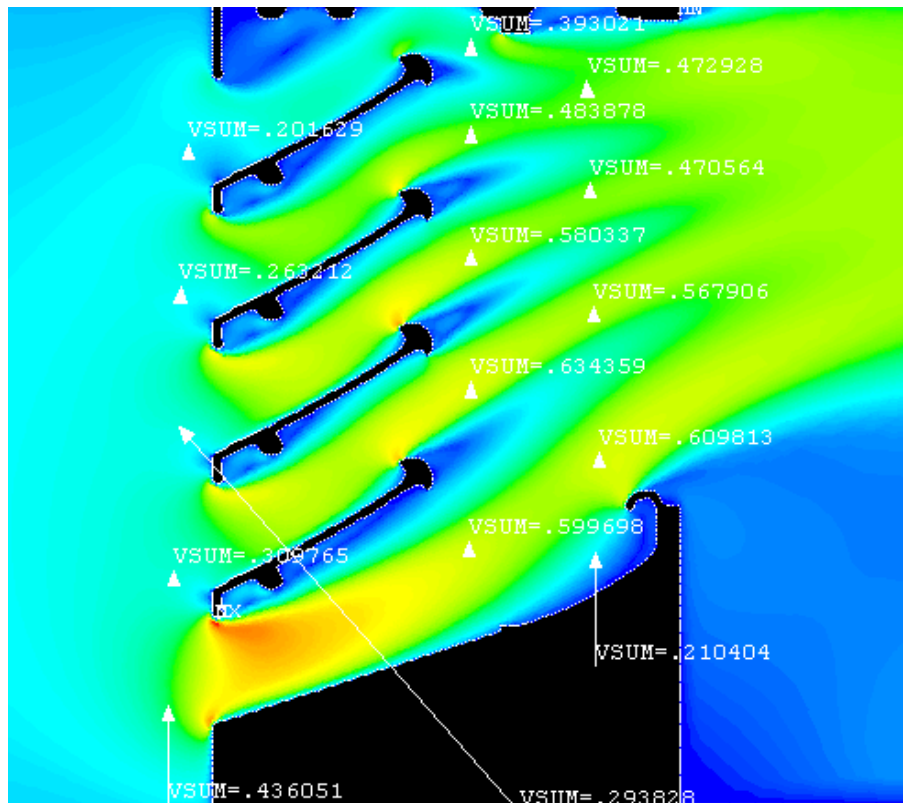


Image 19 Velocity in point according to Fig. 3(m/s)

The aerodynamic coefficient of local resistance of air flow in the entrance of the aerodynamic blind according to equation in column A and the aerodynamic coefficient of local resistance of air flow on the net of the entrance channel according to equations in column B can be determined following the mean velocities and equations in Table 2.

Table 4 Results of computer simulation on inlet channel of the intermediate space for velocity 1,5 m/s.

Measuring point	1.1	1.2	1.3	1.4	1.5	mean 1
Velocity (m/s)	0,4361	0,3098	0,2938	0,2632	0,2016	0,3009
Measuring point	2.1	2.2	2.3	2.4	2.5	mean 2
Velocity (m/s)	0,6165	0,6264	0,5803	0,4839	0,3930	0,5383
Measuring point	3.1	3.2	3.3	3.4	3.5	mean 3
Velocity (m/s)	0,2104	0,6098	0,5679	0,4706	0,4729	0,4663

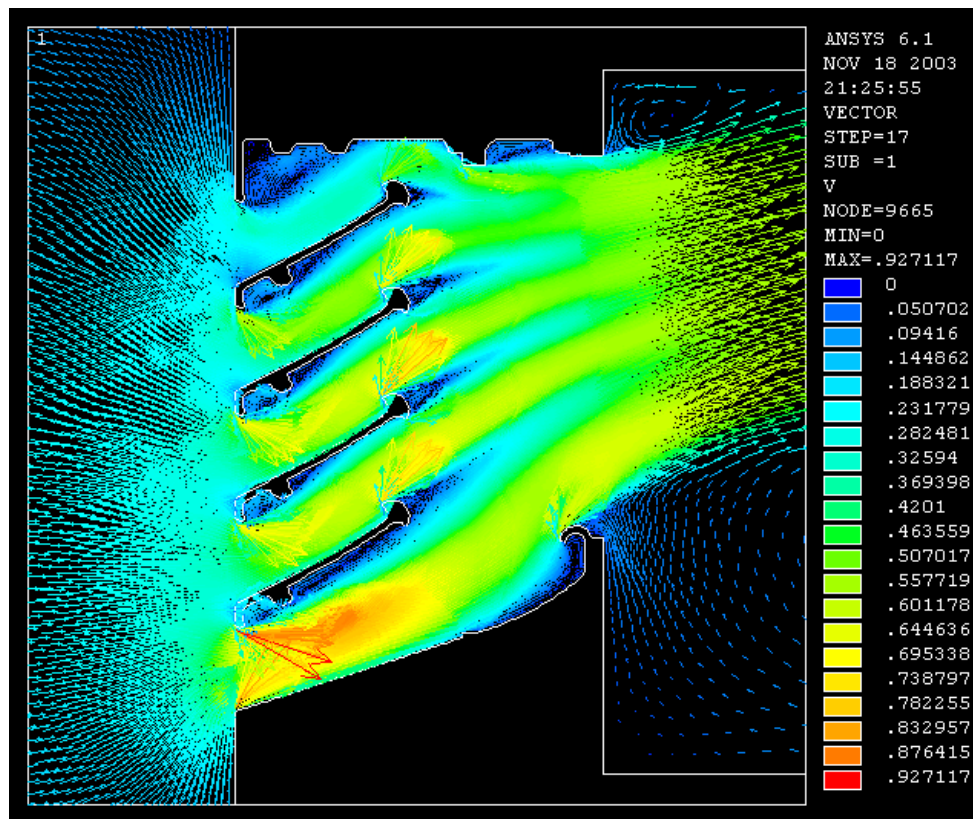


Image 20 Velocity field of vectors for velocity 1,5 m/s

4 Conclusion

Due to immense development of the computer programs and, dominantly, the operative speed, it is possible to describe numerically the issue regarding the aerodynamics of a buffer zone of a double skin façade. Comparing the results of the aerodynamic coefficients of local resistance obtained from the experimental measurements and by the computer simulation, it can be stated that they are approaching, for example:

- $\xi_{1\text{-experiment}} = 0,70$ a $\xi_{1\text{-simulation}} = 0,68$
- $\xi_{2\text{-experiment}} = 0,32$ a $0,31$ a $\xi_{2\text{-simulation}} = 0,31$ a $0,31$

Table 5 Aerodynamic coefficients of local resistance (A - On ventilation blind, B - On the net counter to insects)

Velocity v(m/s)	A		B	
	ξ_1		ξ_2	
	$\xi_1 = \frac{v_1^2 - v_2^2}{v_2^2}$	$\xi_2 = \frac{v_2^2 - v_3^2}{v_3^2}$	$\xi_2 = \frac{v_1^2 - v_3^2 + \xi_1 \cdot v_2^2}{v_3^2}$	
0,2	0,72	0,28	0,28	
0,4	0,60	0,31	0,31	
0,7	0,67	0,34	0,34	
1,0	0,7	0,32	0,32	
1,5	0,7	0,30	0,30	
2,0	0,7	0,31	0,31	
mean	0,68	0,31	0,31	

References

ANSYS, Inc.:Theory Manual.001369. Twelfth Edition. SAS IP, Inc.

Bielek, B., Bielek, M., Palko, M.:Dvojité transparentné fasády budov, 1. Diel, História, vývoj, klasifikácia a teória konštrukčnej tvorby. COREAL, Bratislava, 2002

Acknowledgement

The autors express their thanks to the project VEGA agency for financial support of the project No. 1/0281/12

Contact address:

Ing.arch. Ing.Milan Palko, PhD.

SLOVAK UNIVERSITY OF TECHNOLOGY IN BRATISLAVA, Faculty of Civil Engineering,
Department of Building Structures, Radlinského 11 813 68 Bratislava, milan_palko@stuba.sk

POSITION THE WINDOW IN THE WALL OF PASSIVE HOUSE

MILAN PALKO

SLOVAK UNIVERSITY OF TECHNOLOGY IN BRATISLAVA, Faculty of Civil Engineering,

Abstract: Windows are in terms of heat loss of the weakest element of the facade. The thermal transmittance of the window is five to eight times worse than other parts of the heat exchange surface of the building. In type buildings with the need to minimize heat loss is necessary to optimize the window geometry, material and construction with regard to the surrounding structures and environment.

Keywords: window, heat loss, passive house

1 Introduction

Window as transparent building element is a significant design and architecture, resistance to forced entry, the effect of sun, heat, wind, cold, rain, or the ability to resist mechanical loads, fire, acoustic and so on. Currently the window, as part of the heat-exchange jacket design packaging important element of the energy concept of the building (especially for passive house). When designing the location and size of glazed surfaces is important to look beyond the avoidance of heat and solar gain. It would be misleading to believe that the transparent parts of the building envelope interaction internal environment - outdoor climate affects only the size of the glazed area. An important feature of quality window is the correct solution of structural parts of the window and its incorporation into the envelope.

Passive house is building, to ensure that thermal comfort does not need conventional power supplying system. To achieve this, we must have this house heat energy demand than conventional house reduced by 90%. This density heat demand (kWh / (m².year)) is the normal modern house about 100, in an old apartment building in an average of 200, low energy house in under 50, in a passive house below 15 kWh/m².rok. Specific heat demand below 15 is an essential characteristic of the passive house and shows her calculation.

2 Material and methods

Thermal properties of windows are characterized by two variables. Heat transfer coefficient (W / m². K) and the inner surface temperature (° C). These values can be obtained by measurement or calculation. Measurement of the window construction (frieze frame and sash, glass system, glass-frame contact system) determine the declared value of the coefficient of heat transfer around windows, the boundary conditions of the internal air temperature, outside air temperature and relative humidity. For the measuring procedure is EN ISO 12567-1 - Thermal performance of windows and doors. Determination of thermal transmittance hot box method. By means of guarded hot box temperature creates a steady state to be on the basis of equation (1) characterized by a transparent product specific dimensions.

$$U_w = \frac{\Phi}{A(\theta_i - \theta_e)} \quad (3)$$

where:

- U_w is the coefficient of heat transfer window (W / (m². K)),
- Φ is the heat flow through window (W),
- A is the total window area (m²)
- θ_i, θ_e are the air temperature in indoor and outdoor (° C).

The new approach towards the quantification of thermal characteristics of opening constructions used in European standards included in the Slovak technical standards system (e.g. STN EN ISO 10077-1 Thermal characteristics of windows, doors and shutters. Calculation of heat transfer coefficient) enable designers to show the value of heat transfer coefficient for each window construction based on the values declared by an accredited company using the following equation:

$$U_w = \frac{U_f A_f + U_g A_g + \Psi_g l_g}{A_g + A_f} \quad (4)$$

where:

- U_w heat transfer coefficient of window (W / (m². K)),
- U_f heat transfer coefficient of frame and sash (W / (m². K)),
- U_g heat transfer coefficient of glazing (W / (m². K)),
- Ψ_g linear loss coefficient (W / (m. K)),
- l_g perimeter of glazing in the wing (m)
- A_f opaque parts of the area (m²)
- A_g glazed area (m²).

For windows it is relevant what kind of thermal characteristics and geometry the material used in joint glazing – casement has, as the joint influences the additional thermal flow, which has significant impact on indoor surface temperature (condensation and mould is possible), heat losses through window. U_g value (W/(m². K)) is determined for a concrete glazing system – without taking into consideration the edge influence ($U_{g,NED} \leq 1,1$ W/(m². K)). Similarly, also the U_f value (W/(m². K)) is determined for frame without glazing. Linear thermal transmittance ψ_g (W/(m . K)) expresses the impact of joint glazing – casement on frame thermal flow, that is the deformation of temperature field by additional thermal flow. ψ_g is a function of the used glazing system, frame material and spacer system. It is necessary to consider the linear thermal transmittance is not a material constant factor, but is dependant on specification of joint frame – glazing. From the above stated it follows that the frame as well as glazing systems have constant declared calculation values unlike

"characteristics" of glazing edge. The same material of spacer will have different additional thermal flow in wooden, PVC or aluminium frame depending on combination frame – glazing, and, consequently, it will have an impact on U_w value and, thus, also the energy balance. Using the glazing with improved spacer system – warm edge opposite to aluminium one, the effect of direct dependence of additional thermal flow formation is significantly pressed decrease of ψ_g value. STN EN ISO 10077-2 Thermal performance of windows, doors and shutters. Calculation of thermal transmittance. Part 2: Numerical method for frames, describes the way of determination of linear thermal transmittance also in joint of glazing as follows:

$$\Psi_g = L_o^{2D} - U_f b_f - U_g b_g \quad (5)$$

where:

Ψ_g is linear thermal transmittance (W/(m.K)),

L_o^{2D} is linear thermal coupling coefficient (W/(m.K)),

$U_f b_f$ is thermal coupling of frame (W/(m.K))

$U_g b_g$ is thermal coupling of glass (W/(m.K))

Good material characteristics of window frame and glazing system are not the only decisive factors in energy balance. From the previous chapter it is obvious that other structural elements of window construction in building envelope cannot be omitted. The following figures illustrate examples of windows of good quality used in low-energy and passive buildings.

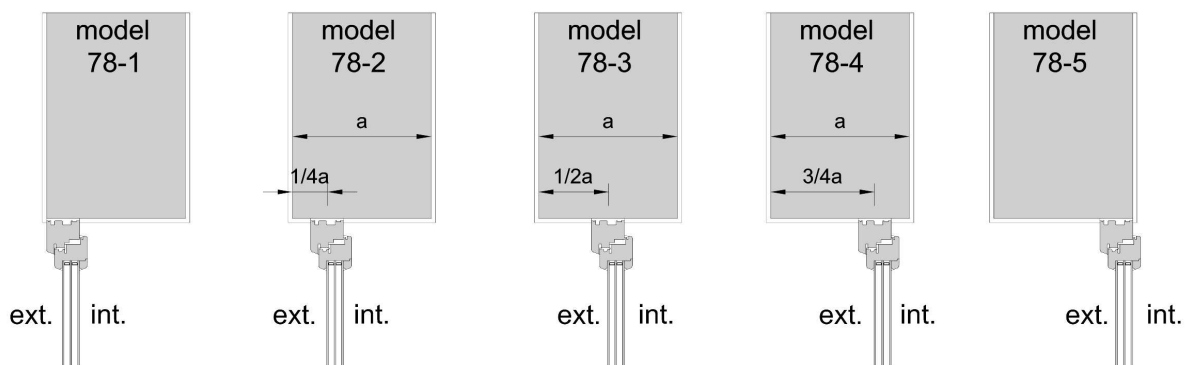
As already mentioned in properly designed passive house is necessary to place emphasis on segmental parts (such as stocking location window in the outer wall). Cladding passive houses may have variants (light wooden structure and thermal insulator, heavy and monolithic thermal insulator). Of these variants also receives the correct type of window recess in the outer wall. In this paper elaborates on the shoulder in a simplified box (homogenized) outer wall for two types of frame friezes.

Geometry window is determined by five window locations in the outer wall in relation interior and exterior. Models are two alternatives EUROPROFIL 78 mm and 92 mm (Image 1).



Image 21 EUROPROFIL 78 mm and 92 mm

Glazing has been used as thermal triple the same building and physical quantification of both systems. Position of installation of the windows are shown in Image 2



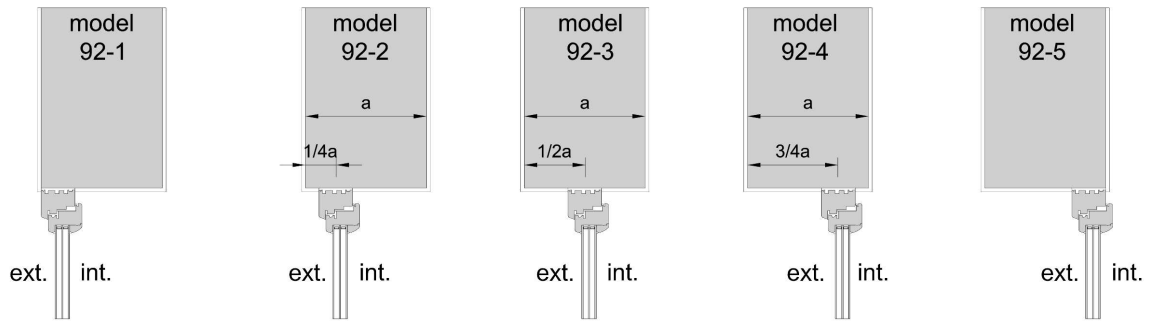


Image 22 Position of the window recess

3 Results

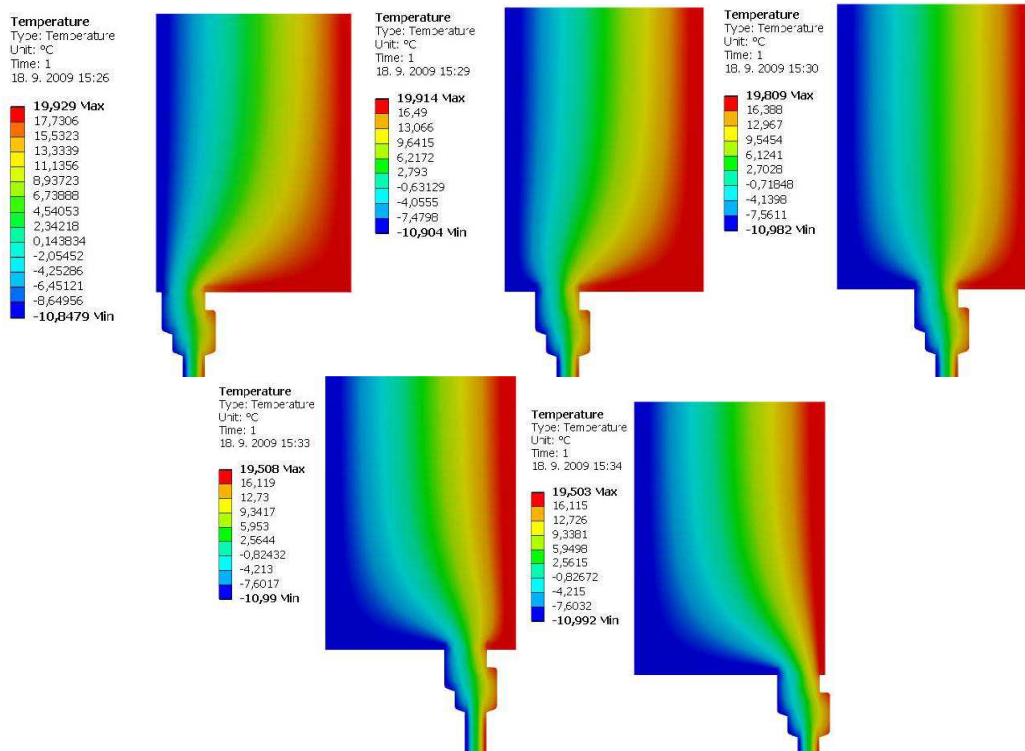


Image 23 The temperatures for the models' Euro 78 with a recess 78-1,78-2,78-3,78-4,78-5

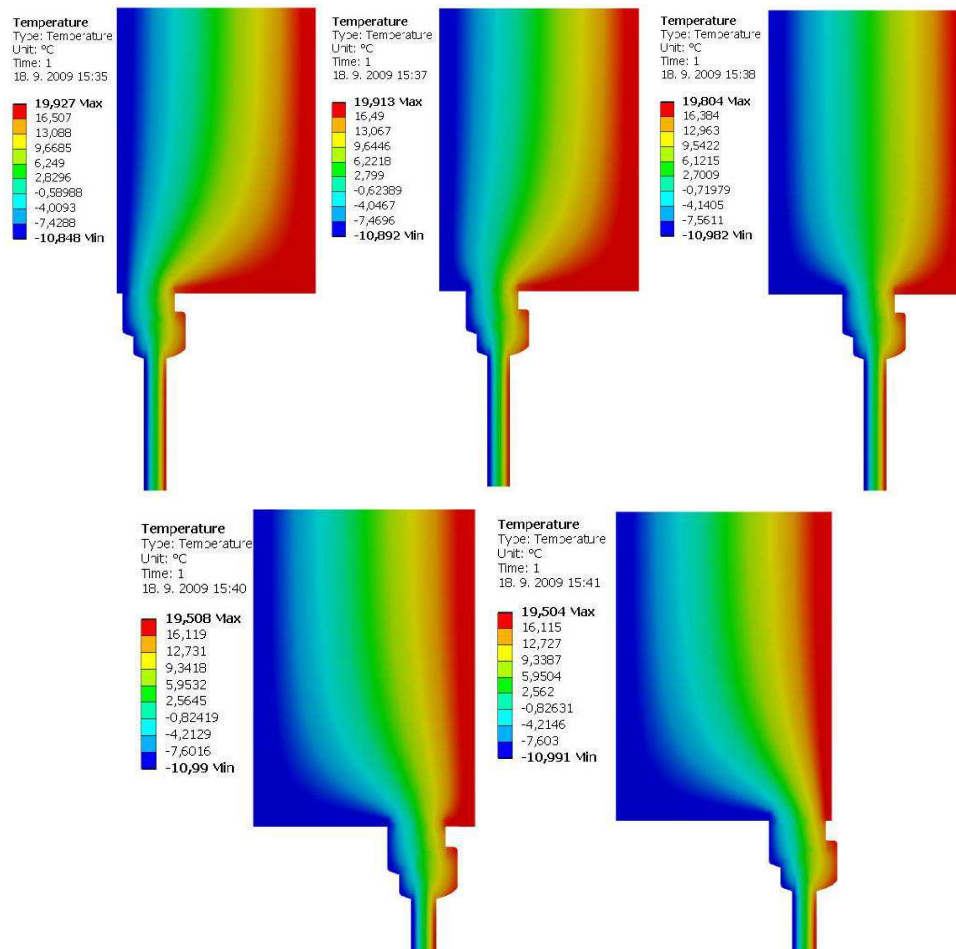


Image 24 The temperatures for the models' Euro 92 with a recess 92-1, 92-2, 92-3, 92-4, 92-5

4 Conclusion

Increased thermo-technical quantification fragment walls and window elements eliminates the problems of surface temperatures. For this reason, is limited to a stocking location in terms of minimizing heat loss. The most appropriate location of the installation of windows in terms of minimizing losses is a model 78-3 and 92-3. Given the characteristics of segments of the outer wall are very small differences, to be negligible. Can essentially rule the argument that in a simplified homogeneous wall can be fitted with a window in terms of heat loss in any place..

References

Chmúrny I.: Thermal protection of buildings. Publishers Jaga group, v.o.s., Bratislava, 2003

Acknowledgement

The authors express their thanks to the project VEGA agency for financial support of the project No. 1/0281/12

Contact address:

Ing.arch. Ing.Milan Palko, PhD.

SLOVAK UNIVERSITY OF TECHNOLOGY IN BRATISLAVA, Faculty of Civil Engineering,

Department of Building Structures, Radlinského 11 813 68 Bratislava, milan_palko@stuba.sk

WATER VAPOR IN THE FUNCTIONAL GAP OF WINDOW

MILAN PALKO

SLOVAK UNIVERSITY OF TECHNOLOGY IN BRATISLAVA, Faculty of Civil Engineering,

Abstract: The paper deals with thermal-moisture performance of a wooden window in standard external and indoor climate conditions in a gap between casement and window frame. Condensation or ice coating in the gap is the main problem of wooden windows. Thus, destructive processes on the wood surface finish causing the moisture penetration into the wood occur. The surface condensation is sufficiently covered by the requirements in currently valid standards. The condensate generation in the gap is not described neither limited by the standards nor regulations. The frequent problem occurrence in practice is to be dealt with and solved. The experimental and computing investigation was carried out using four types of MIRADOR 682, 682T, 783, 923 euro-profiles. For computing investigation the ANSYS programme was applied.

Keywords: window, condensation, water vapor

1 Introduction

The problem of moisture transmission in gaps (leakages) in building envelopes is not a newly discovered issue. The moisture penetration through leakages in building envelopes has been investigated mainly in relation to slab blocks development. The leakages due to imperfect structural design and materials applied in roof envelopes formed another area for investigation. In our country, Mrlík (1986) has dealt with research and moisture transmission in gaps of building envelopes Hauser (2005) dealt with the similar problem area: moisture transmission through gaps, mainly for wooden houses in Germany (Hauser and Kempkes 2005). While solving these problems the window structures were at a relatively low development level and had high leakage in terms of air infiltration and exfiltration. Due to these window characteristics as well as low requirements in energy efficiency field the relative humidity in buildings used to be approximately 30% (Chmúrny 2003)). By improving the thermal characteristics of building structures in relation to energy the relative air humidity has increased up to 50%, which is also given in STN 73 0540:2002. Taking into consideration the change of boundary conditions and characteristics of window structures the problem of water vapour condensation in functional gap between casement and window frame has occurred. Nowadays, Huber (2009) from IFT Rosenheim has been dealing with the problem. He analyzed the effect of the type of seal in the case of condensation in the functional joint (Huber 2009).

Thermal-moisture performance of a window in external and indoor climate conditions is a subject of our investigation. Water vapour condensation on surface of window structure is not desirable phenomena. The condensate generation in functional gap is not described neither limited by the standards nor regulations. Seriousness of the problem varies depending on the material base. Considering the wooden window structures the degradation of surface finish occur and its thermal characteristics change.

Generally, there are five condensation types occurring in different intensities:

- indoor glazing condensation,
- glazing joint condensation,
- functional gap condensation,
- external glazing condensation,
- supplementary elements condensation (shutters).

The moisture transport through gap between casement and window frame at condensation temperature is the main cause of condensation of water vapour. The transport causes:

- air pressure differences (taking water vapour),
- infiltration and exfiltration,
- diffusion of water vapour (different saturation of water vapour in exterior and indoor air).

Infiltration and exfiltration are basically permeability of window structure towards indoor or outdoor. The airflow through window structure is a function of pressure differences and window structure design and its shoulder into building structure. The phenomena causing the infiltration or exfiltration can be divided into the following groups:

- wind impact (building exterior aerodynamics),
- air temperature impact (due to gravity),
- forced ventilation (building services),
- combination of the above given phenomena.

Wind impact – if there is an obstacle on the airflow path, the airflow on windward is stopped, on both sides is accelerated and there is turbulence on leeward. The pressure on windward is, therefore, positive and on all other sides the pressure is negative (suction). The building modifies the airflow in its environment not only due to its shape, but also by surface structures, geometry of elements overhanging the façade as well as physical characteristics of its envelope and partitions (air permeability). The infiltration or exfiltration occurs due to inequality of pressure distribution on building envelope and building tightness (including indoor partitions).

Air temperature impact – at different pressure due to various air temperatures the air flows using the natural convection principle. The pressure difference values due to natural convection of warm air are from 0 to 18 Pa, depending on the thermal difference and the distance, on which the pressure difference occurs. The distance is the height between input and output apertures. Considering a multi-floor building the principle is, to a large extent, applied by staircase hall or elevator shaft. The case makes worse the air quality chiefly on upper floors, where mainly the exfiltration occurs. The polluted infiltrated air is coming from lower floors.

Forced ventilation – building services (pipes and ducts) are applied at forced ventilation. Certainly, central air conditioning is not considered (air offtake and intake), but only local venting of polluted or used air by forced ventilation (fan). The air is carried away, for example, from bathrooms, toilets and kitchens. In such cases there is a vacuum at exhaustion, which is compensated by infiltration through openings. The air intake for combustion in fireplaces is the other partly similar way (if the air intake is not provided by a pipe connected to the exterior).

Combination – all the above given reasons are relevant at infiltration or exfiltration impact. The particular factors play different roles and they can be summed up or balanced out.

Condensation of water vapour – phenomena for balancing water vapour partial pressure by interaction of molecules. The diffusing water vapours are moving from places having higher pressure to places with lower pressure. The indoor water vapour partial pressure (20°C and air humidity 50%) is calculated by:

$$p_{di} = \frac{\varphi_i \cdot p_{sat,i}}{100} = \frac{50 \cdot 2337}{100} = 1168,5 \text{ Pa} \quad (6)$$

where:

p_{di} is indoor water vapour partial pressure in Pa,

φ_i is relative humidity of indoor air in %,

$p_{sat,i}$ is saturated water vapour partial pressure of indoor air in Pa.

The outdoor water vapour partial pressure ((-11°C and air humidity 83%) is calculated as follows:

$$p_{de} = \frac{\varphi_e \cdot p_{sat,e}}{100} = \frac{83 \cdot 237}{100} = 196,7 \text{ Pa} \quad (7)$$

where:

p_{de} is outdoor water vapour partial pressure in Pa,

φ_e is relative humidity of outdoor air in %,

$p_{sat,e}$ is saturated water vapour partial pressure of outdoor air in Pa.

It follows from the above given that the pressure difference between interior and exterior is 971,8 Pa. The warmer air can contain more water vapour as the cooler one, e.g. the air with 20 °C can contain up to 17,25 g/m² of vapour, but the air with -11 °C can have only 1,96 g/m² of moisture. Interactive accumulation of infiltration or exfiltration and diffusion of water vapour leads to condensate or ice coating in winter period.

2 Material and methods

The experimental measurements were carried out in heat engineering laboratories at the Faculty of Civil Engineering. Measurement models represent real window structures. The big climatic chamber illustrated in Image 1 was used at measurements. The chamber A represents exterior climate (outdoor temperature -11°C, pressure difference between exterior and interior from 0 to 2000 Pa, heat transfer coefficient 25 W/m²K, relative humidity 50%). The chamber B represents balancing chamber for HOT-BOX and simulate the indoor climate (indoor temperature + 20°C, relative humidity 50%). The HOT-BOX is used for measurement of heat transmission using measured element simulating the indoor conditions (indoor temperature + 20°C, relative humidity 50%, heat transfer coefficient 7,7 W/m²K). Part D is a masking panel, in which the measured window structure is imbedded. In case of our measurement the HOT-BOX was not used as the conditions with infiltration or exfiltration were to be investigated.

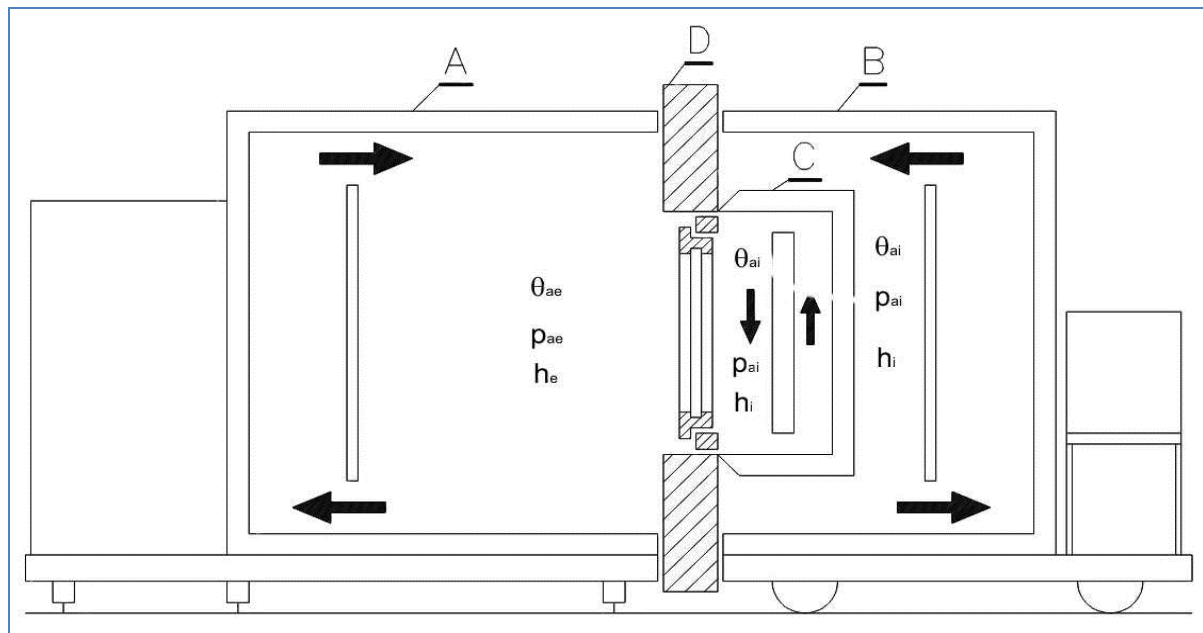


Image 25 Scheme of laboratory equipment of big climatic chamber

Thermal and humidity parameters for ambient conditions are constant for all models. The indoor air temperature is 20°C and the relative air humidity is 50 %. The outdoor air temperature is -11°C and the relative air humidity is 83%. The pressure differences are 200, 100, 75, 50, 25, 10, 5, and 0 Pa for infiltration and the similar pressure differences are also for exfiltration.

The measurements were performed on completed panel having real windows. Such panel having four windows with dimensions 540x695 mm, is illustrated in Image 2. The MIRADOR 682 with no external sealing is window No. 1, MIRADOR 682 with external sealing is window No. 2, MIRADOR 783 is window No. 3 and MIRADOR 923 is window No. 4.

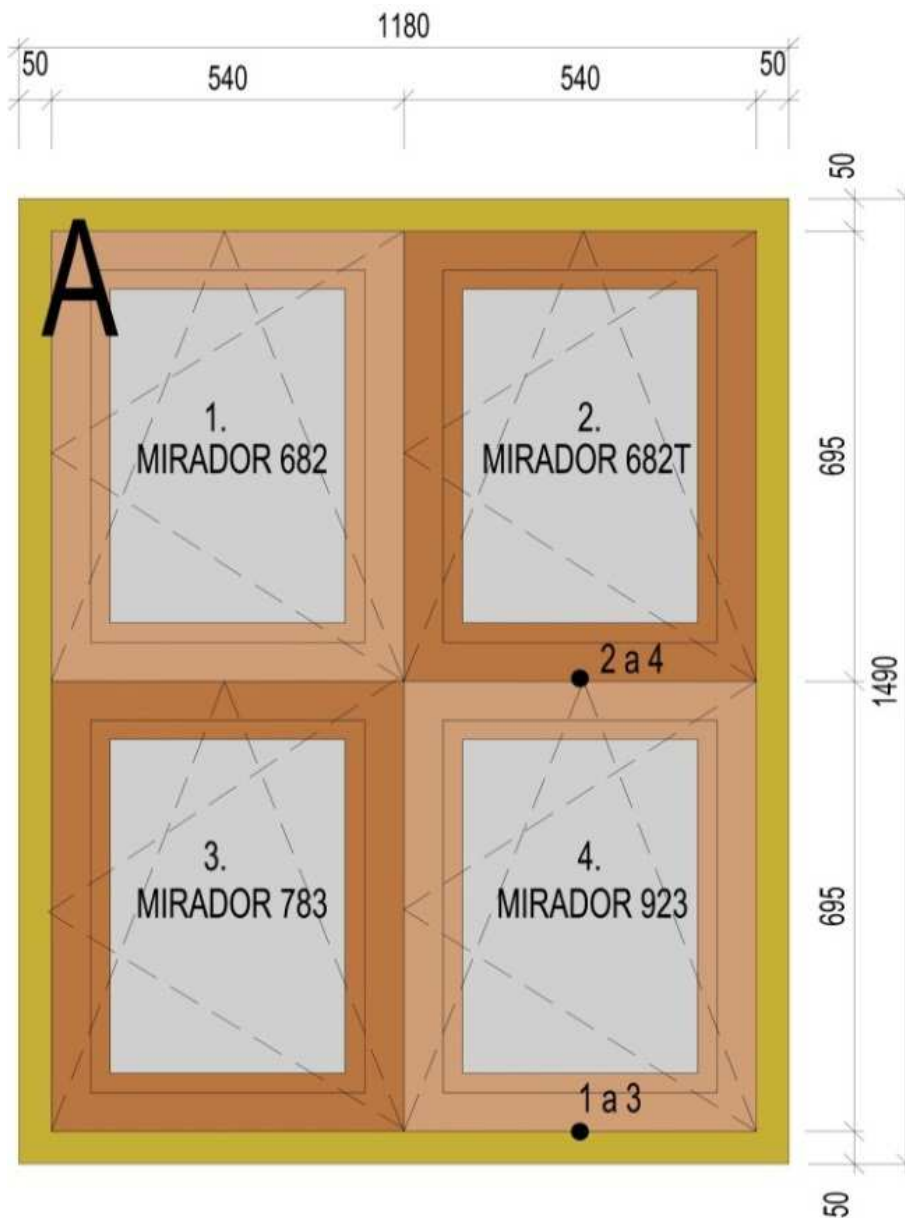


Image 26 Geometric parameters of window set ups in masking panel

Measurement sensors are divided into two groups. The first group measures the surface temperatures (PT 100). The second one measures the temperatures and relative air humidity (SHT 75). The sensors distribution is presented in Image 3. For windows No. 1, 2, 3 the temperatures and relative air humidity are measured (SHT 75). For window No. 4 the surface temperatures (PT 100), temperatures and relative air humidity are measured (SHT 75). In Image 3 for MIRADOR 923 profile the placement of SHT 75 sensors on the left side and PT 100 on the right side are shown.

Computer simulation was carried out for MIRADOR 923 profile that is used mostly at low-energy and passive building construction. The geometry of computer model is identical with the measured window. Boundary conditions and material characteristics are also compatible with the experimental model in such a way that the comparison can be done. For the calculation the ANSYS programme was used. Geometry and netting of MIRADOR 923 window computer model is given in Image 4.

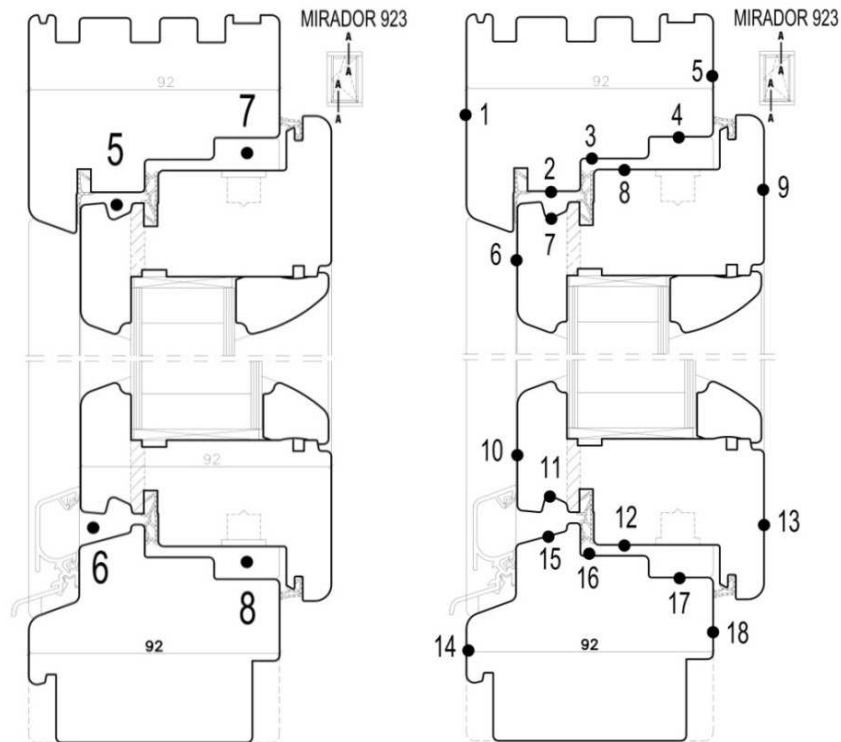


Image 27 Geometric parameters of window profiles and placement of measurement sensors

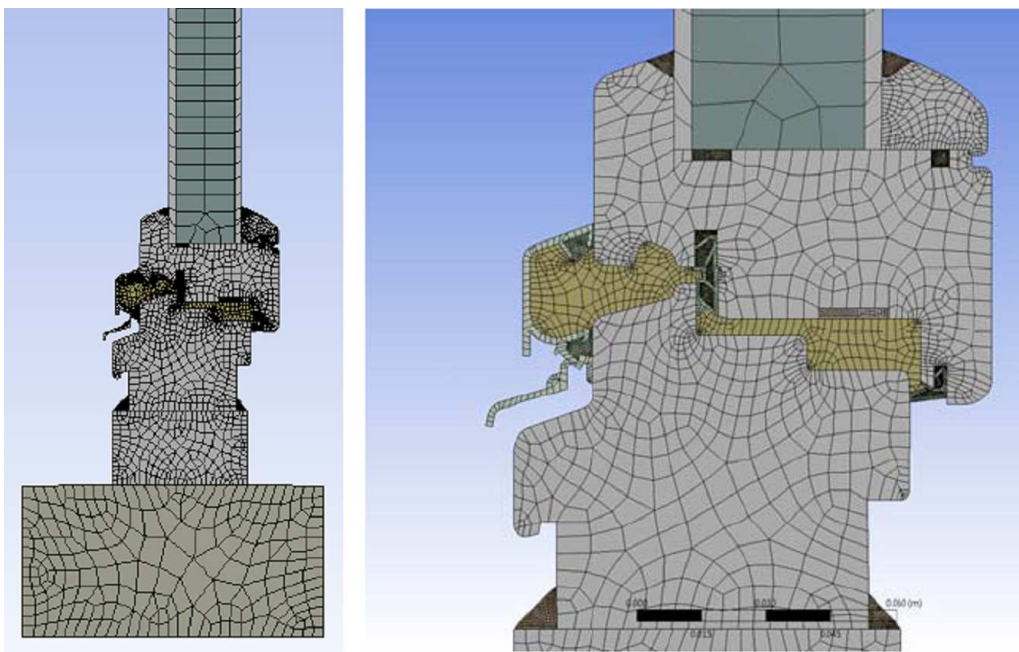


Image 28 Geometry and netting of MIRADOR 923 window computer model

3 Results and discussion

The measurement and computer models results are classified into two groups. At experimental measurements in big climatic chamber the occurrence and amount of water vapour and ice coating condensate was found out after each completed measurement phase. Their occurrence is illustrated in Image 5. The internal surface temperatures and air temperature including relative air humidity in gap measurement points (see Image 3)

belonged into the second valuation data group. The measured values are presented in graphs on Image 7 and Image 8.

Considering the fact that it is not possible to distribute the sensors in ideal positions in gap the computer model was established. The computer simulation results show more detailed temperature distribution and enable more thorough investigation of condensation possibility in required positions. The simulation results are shown in Image 6

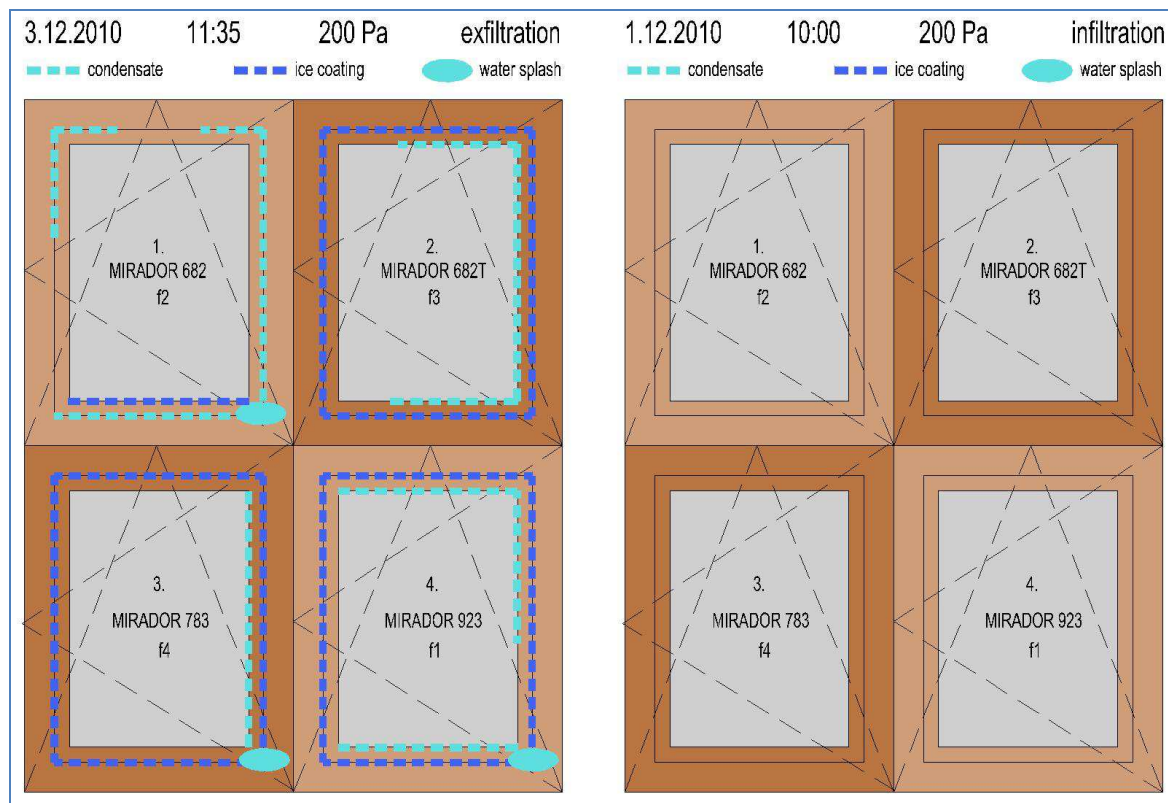


Image 29 Condensate and ice coating occurrence after exfiltration (200Pa) and infiltration (200Pa)

Table 1 presents the comparison of the results gained from experimental measurement and computer simulation. The surface temperature results in investigated gap in identical points for simulation and experiment are evaluated. It can be seen from the numerical difference in the last column that the values for both methods are comparable.

Table 2 gives the evaluation of water vapour condensation risk in the gaps and the comparison with the real condition found out in the experimental measurement on MIRADOR 923 window profile. The first column presents the pressure difference between the interior and exterior with a note whether infiltration or exfiltration is considered. The second column gives the cavity identification according to Image 3 as well as the number of sensor measuring the temperature and relative air humidity in the gap between casement and window frame. The third column defines the relative humidity value for the particular cavity. For some points two different values are given: a maximum and a minimum value.

Table 6 Comparison of measured and calculated surface temperature values for MIRADOR 923

Identification	Measured values	Simulation values	Difference
	(°C)	(°C)	(K)

θ_{s1}	-10,67	-10,379	0,29
θ_{s2}	-2,69	-2,7371	0,05
θ_{s3}	2,27	2,0896	0,18
θ_{s4}	12,77	12,67	0,10
θ_{s5}	18,37	18,371	0,00
θ_{s6}	-9,92	-9,9901	0,07
θ_{s7}	-4,39	-4,2127	0,18
θ_{s8}	7,05	6,6085	0,44
θ_{s9}	19,16	19,011	0,15
θ_{s10}	-10,00	-10,083	0,08
θ_{s11}	-6,29	-5,8594	0,43
θ_{s12}	5,69	5,4255	0,26
θ_{s13}	18,84	18,914	0,07
θ_{s14}	-10,06	-9,8648	0,20
θ_{s15}	-5,89	-5,8935	0,00
θ_{s16}	0,14	0,22193	0,08
θ_{s17}	10,36	11,695	1,34
θ_{s18}	17,03	17,305	0,28

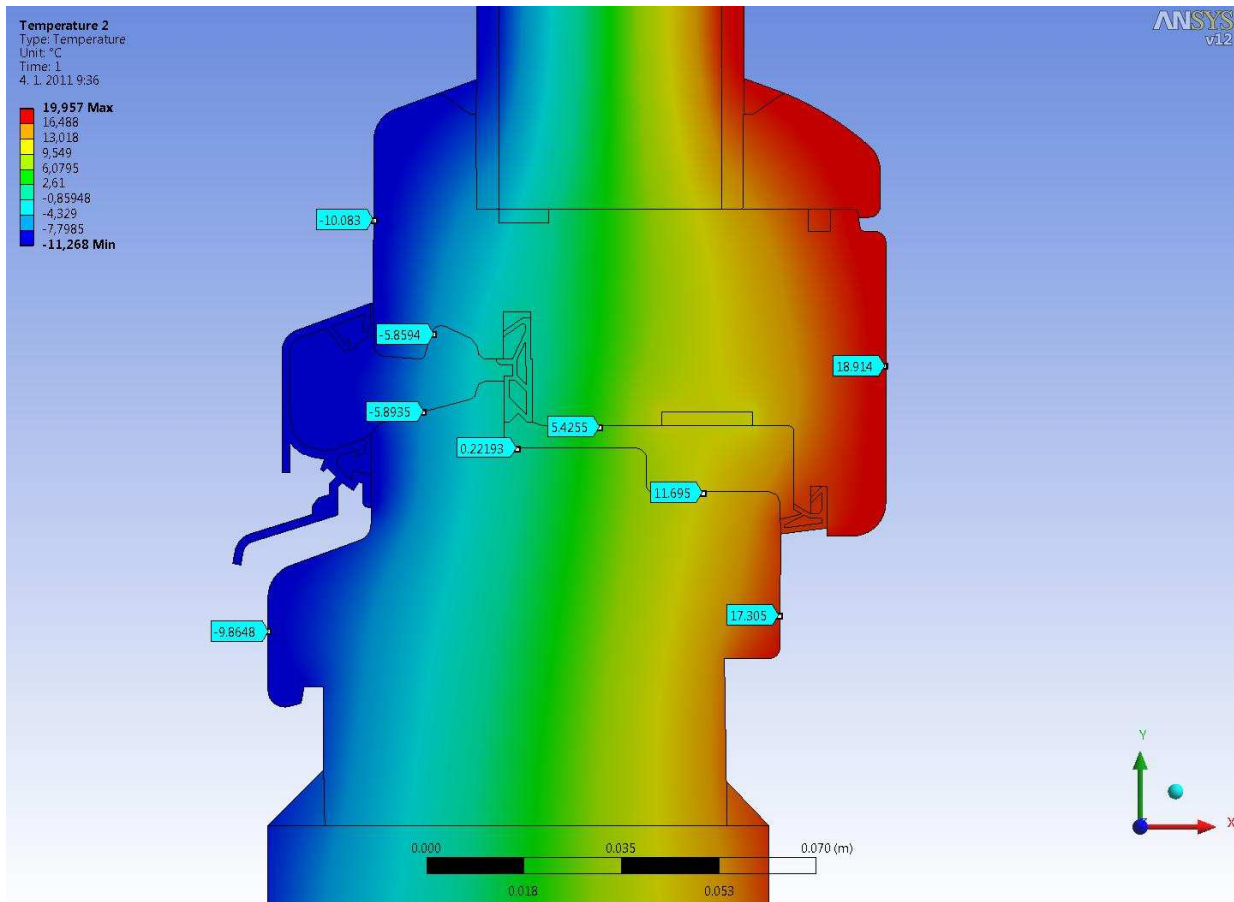


Image 30 Surface temperature fields and surface temperatures in investigated points (°C) of MIRADOR 923 window (lower part)

Table 7 Assessment of possible condensation in gap for MIRADOR 923 profile

Pressure difference	Measurement point	Φ (%)	θ (°C)	θ_{dp} (°C)	$\theta_{s,min,sim}$ (°C)	Condensation risk	Condensation experiment
0 Pa without pressure difference	5	68,50	-2,28	-6,72	-7,95	yes	yes
		68,50	-2,28	-6,72			
	6	58,70	-6,50	-12,52	-10,20	yes	yes
		56,20	-6,50	-13,00			
	7	48,80	13,18	2,65	0,34	yes	yes
		48,80	13,18	2,65			
8	51,50	11,09	1,48	-0,72	yes	yes	
	51,50	11,09	1,48				
	5	67,27	-2,76	-7,39	-7,95	yes	no
		65,24	-2,76	-7,75			

100 Pa infiltration	6	58,13	-6,44	-12,57	-10,20	no	no
		55,40	-6,44	-13,10			
	7	36,90	12,95	-1,25	0,34	no	no
		34,92	12,95	-1,91			
	8	47,17	10,98	0,16	-0,72	yes	no
		46,11	10,98	-0,13			
100 Pa exfiltration	5	77,19	-2,23	-5,29	-7,95	yes	yes
		77,19	-2,23	-5,29			
	6	61,73	-6,30	-11,77	-10,20	yes	yes
		58,71	-6,30	-12,33			
	7	51,94	13,16	3,52	0,34	yes	yes
		51,94	13,16	3,52			
	8	50,58	11,15	1,29	-0,72	yes	yes
		50,58	11,15	1,29			
75 Pa infiltration	5	67,64	-2,92	-7,49	-7,95	yes	no
		67,64	-2,92	-7,49			
	6	59,13	-6,54	-12,48	-10,20	no	no
		56,38	-6,54	-13			
	7	32,94	12,86	-2,68	0,34	yes	yes
		30,92	12,86	-3,43			
	8	50,00	10,96	0,95	-0,72	yes	yes
		50,00	10,96	0,95			
75 Pa	5	75,80	-2,10	-5,37	-7,95	yes	yes
		75,80	-2,10	-5,37			
	6	60,67	-6,40	-12,06	-10,20	no	no
		58,05	-6,40	-12,55			

exfiltration	7	51,51	13,14	3,38	0,34	yes	yes
		51,51	13,14	3,38			
	8	50,44	11,13	1,23	-0,72	yes	yes
		50,44	11,13	1,23			

In the fourth column the cavity air temperature, at which the relative air humidity is measured, is given. The fifth column defines the dew point temperature for measured temperature and relative air humidity for the cavities. The sixth column presents the lowest surface temperature of wooden wing or frame reached in the cavity. Due to the fact that it was not possible to use PT100 sensor at the position with the lowest possible assumed temperature for measurement of surface temperature, the surface temperature was subtracted from the computer model. The seventh column gives a verbal evaluation whether assumption for water vapour condensation for given air temperature, relative air humidity and the lowest surface temperature in a cavity is or is not fulfilled. In the last column in Table 2 the information on the condensate formation in case of experimental measurement for the cavities is given. The evaluations in the last two columns are mostly compatible. The incompatible ones are marked in red. These cases can be explained by error of the measurement and the mathematic modelling. In these cases the dew point temperature values and the lowest surface temperatures are quantitatively very close to each other.

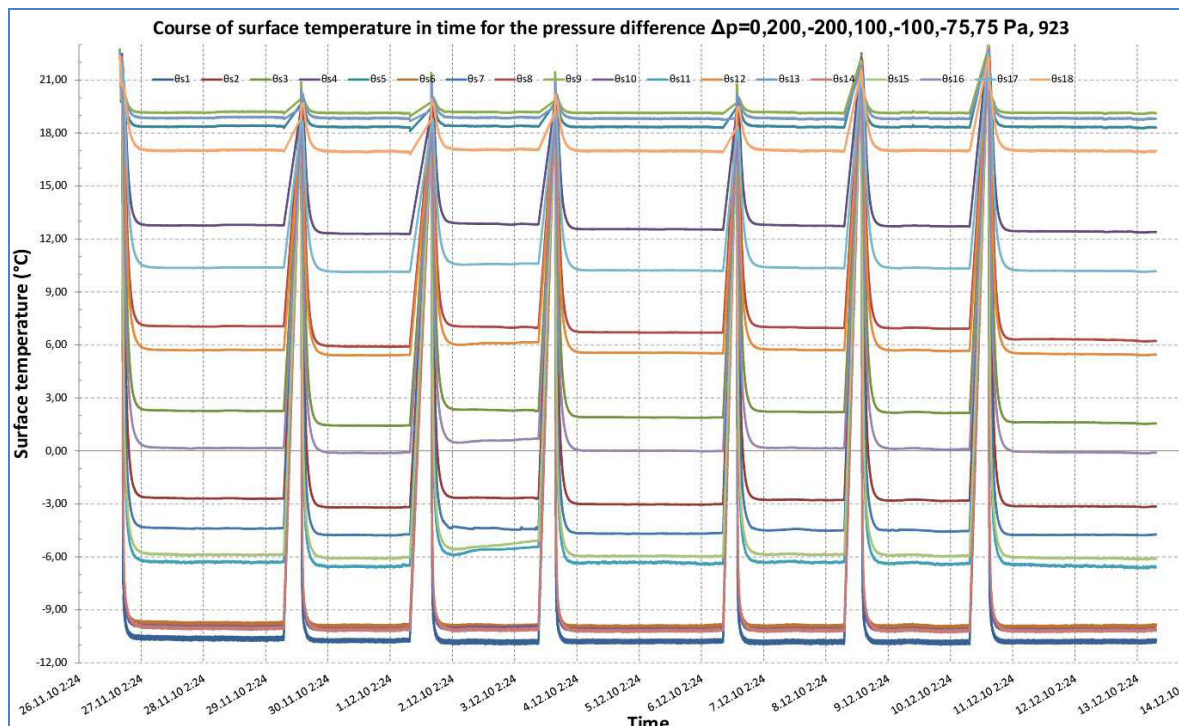


Image 31 Course of surface temperature in time for the pressure difference (MIRADOR 923)

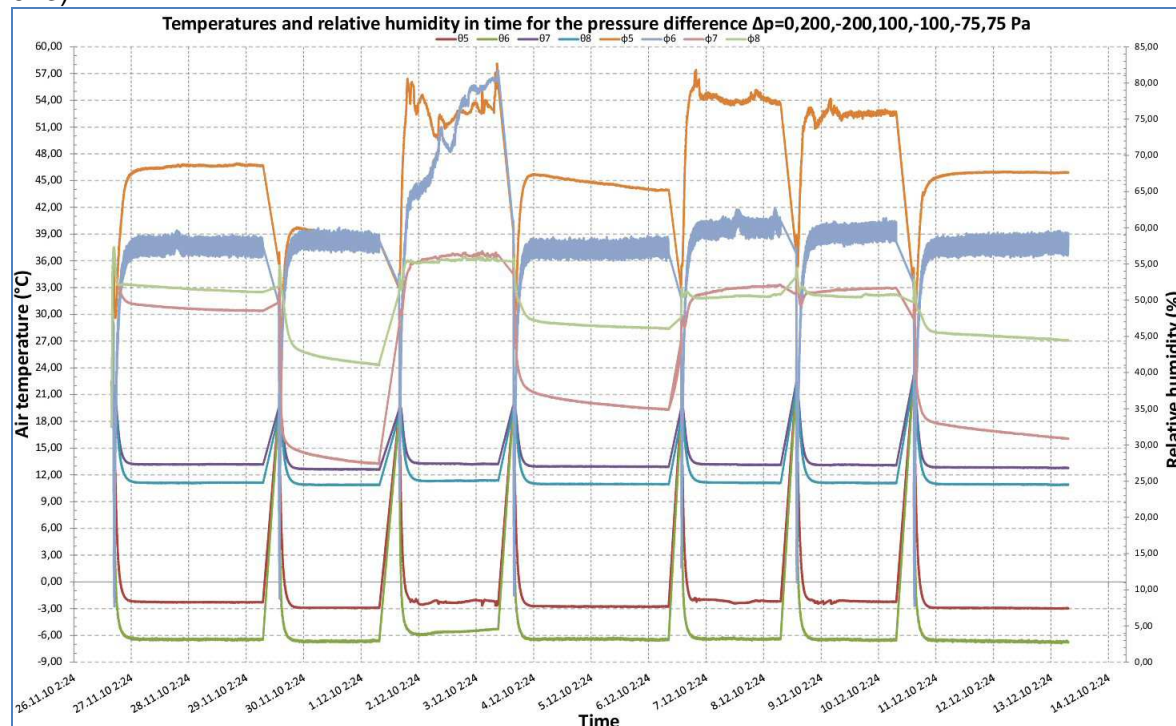


Image 32 Temperatures and relative humidity in time for the pressure difference (MIRADOR 923)

4 Conclusion

At an initial investigation stage it was known that condensation originated only in equilibrium state and at different pressure impact causing the exfiltration. However, it was found out during the measurements that the condensation also originates due to the infiltration. The condensation boundary for water vapour was being finding after the correct set up of circuit forging and, thus, also the sealing compression. After the measurements the value of differences of pressures between cool and warm chamber at which the condensate formation stops in the range 60 to 75 Pa.

The detailed computer simulation of the investigated problem is enormously demanding and the further investigation is needed. Although the mathematic algorithms for moisture transport are relatively well handled in ANSYS programme, it is not possible to continue in simulation without knowing the characteristics of used sealing materials. In order to succeed in this area it is inevitable to know the air permeability of sealing and window structure connection, diffusion constant of sealing and window frame connection. The air permeability has been already surveyed, but the diffusion constant of sealing for windows has not been investigated so far. The thermal model, which was compared with the experimental measurements in the previous chapter, has been authentically calibrated in the ANSYS programme. The total temperature distribution on the window frame was obtained by the simulation.

References

- Chmúrny I.: Thermal protection of buildings. Publishers Jaga group, v.o.s., Bratislava, 2003
 Hauser, G. – Kempkes, Ch.: Der Einfluss von windinduzierten Druckschwankungen auf das thermisch-hygrische Verhalten von durchstromten Leckagen. Kassel, 2005

Hens, H.: Building Physics – Heat, Air and Moisture. Fundamentals and Engineering Methods with Examples and Exercises. Berlin:Ernst &Sohn A Wiley Company, 2007. ISBN 978-3-433-01841-5

Palko, M.,- Ďurinová, A.: Effect of airflow on the thermal-technical properties of building envelope. In: 31. International Scientific Conference departments and institutes civil engineering conference. Čeladná, 2007

Palková, A., Palko, M. Condensation of water vapor in the window structure In: Zborník z ANSYS konference 2010, Frymburk, 2010 , ISBN: 978-80-254-8388-6

Palková,A., Palko,M.: Condensation of water vapor in the inner cavity window. In: Proceedings of the Conference ANSYS 2009, Plzeň 23.-25.9.2009,

ISBN:978-80-254-5437-4

Palková, A., Palko, M., Puškár, A. Window and water vapor condensation. In: Proceedings of the 5. international conference. Buildings and environment 2010. Brno, p.204-209, ISBN: 978-80-214-4155-2

Acknowledgement

The authors express their thanks to the project VEGA agency for financial support of the project No. 1/0281/12

Contact address:

Ing.arch. Ing.Milan Palko, PhD.

SLOVAK UNIVERSITY OF TECHNOLOGY IN BRATISLAVA, Faculty of Civil Engineering,
Department of Building Structures, Radlinského 11 813 68 Bratislava, milan_palko@stuba.sk

NUMERICKÝ MODEL TESTOVÁNÍ FIXACE SEGMENTÁLNÍHO DEFEKTU PRASEČÍHO FEMURU S 4,5 MM LCP Z CP-Ti GRADE 4

JAN PĚNČÍK¹, LUCIE URBANOVÁ², ROBERT SRNEC², PETRA FEDOROVÁ²,
ALOIS NEČAS²

¹Vysoké učení technické v Brně, Fakulta stavební, Veveří 331/95, 602 00 Brno, ²Veterinární a farmaceutická univerzita Brno, Fakulta veterinárního lékařství, Palackého 1/3, 612 42 Brno

Abstract: Z in vivo studií fixací femuru miniaturního prasete, v jehož diafýze byl vytvořen segmentální defekt, vyplývá, že je vhodnější využít pětiděrovou 4,5 mm LCP, než šestiděrovou 3,5 mm LCP [1]. K tomuto zjištění vedlo několik případů selhání fixace. Mechanické ověření získaného závěru je velice časově a materiálově náročné. Z uvedeného byla celá problematika převedena do roviny numerického modelování s využitím FEM a systému ANSYS. Numerické ověření umožnilo současně se snížením časové náročnosti odstranit i jeden z nedostatků testování, tj. možnost předefinování působící síly. Při testování by každá změna směru působící síly vyžadovala vytvoření několika vzorků kostí s defektem stabilizovaných pomocí LCP, ale také vytvoření nového upínacího zařízení. V případě použití numerických modelů toto odpadá.

Keywords: fixace defektu, porucha implantátu, femur, LCP, FEA

1 Úvod

Předlohou pro vytvoření výpočtového modelu fixace segmentálního defektu femuru byly reálné vzorky pravých femurů miniaturních prasat srovnatelného stáří (8-10 měsíců) použitých ve studii hojení segmentálního defektu levého femuru transplantací MSCs (projekt NPV II 2B06130), a jednak trojrozměrné reformáty konstrukce kost-implantát vytvořené computerovou tomografií na Oddělení zobrazovacích metod FVL VFU Brno. Femury byly vypreparovány po lege artis eutanazii miniaturních prasat. Kostí byly zbaveny okolních měkkých tkání a v jejich diafýze byl vytvořen segmentální ostektomický defekt, který byl následně přemostěn pětiděrovou titanovou 4,5 mm LCP, která byla fixována pomocí čtyř šroubů (prostřední díra nebyla vyplněna šroubem).

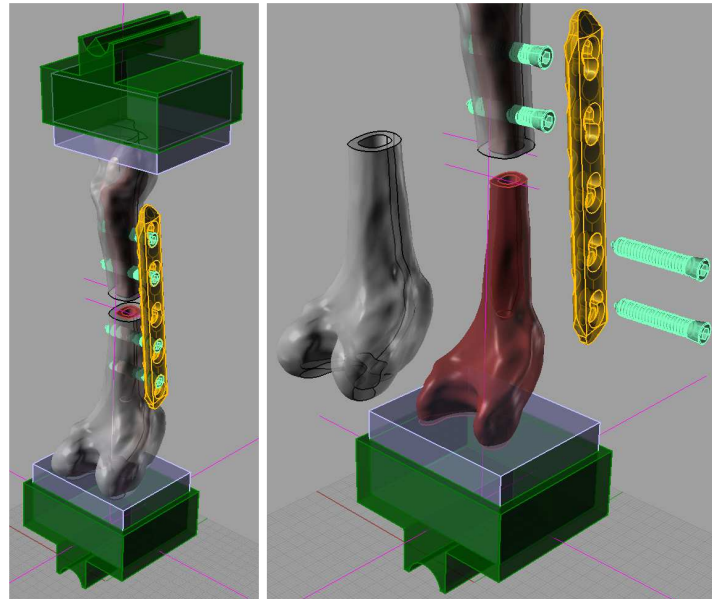
2 Výpočtový model

Definice geometrii systému fixace segmentálního defektu femuru 4,5 mm LCP byly využity výstupy dat z CT vyšetření ve formě rastrových objemových dat, digitálních obrazů tvořených maticí bodů [2]. Po provedení segmentace, vektorizace a vyhlazení tkání byl 3D geometrický vektorový model importován do 3D CAD systému Rhinoceros, kde byl pomocí NURBS ploch vytvořen uzavřený objemový 3D geometrický model kosti, včetně vnitřních anatomických struktur femuru. Model byl doplněn o titanovou pětiděrovou 4,5 mm LCP, šrouby $\varnothing 5$ mm a soustavu uchycení kosti modelující laboratorní experiment zatěžování femuru (Obr. 1). Fixace LCP byla provedena ve dvou proximálních a distálních otvorech ploténky celkově 4 ks šroubů. Střední otvor byl ponechán bez vyplnění šroubem. Při modelování NURBS ploch byl použit speciální plugin systému Rhinoceros T-Splines.

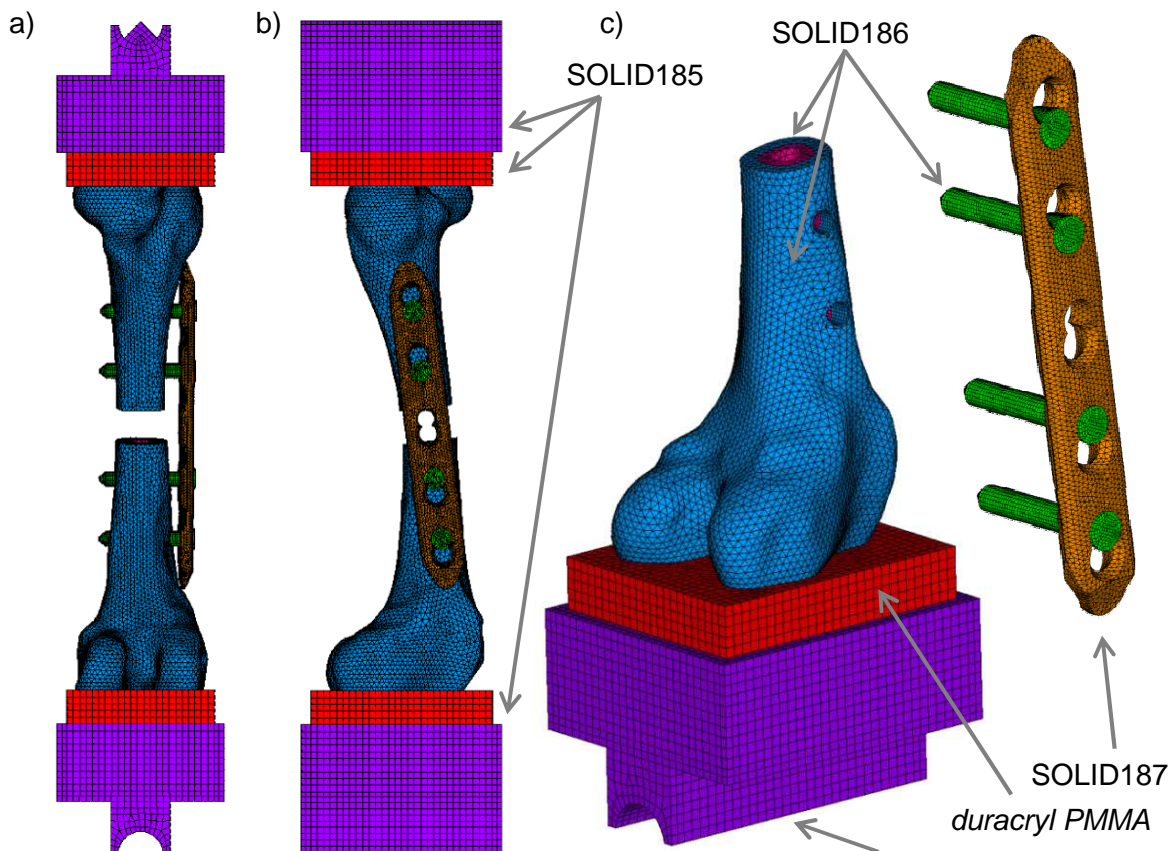
Vytvoření prostorový geometrický CAD model (Obr. 2) byl importován pomocí SAT formátu do výpočtového systému ANSYS. V tomto systému byla následně provedena úprava geometrie včetně vytvoření konečných objemů s využitím v systému nabízených logických operací.



Obrázek 1 – Reálný vzorek systému fixace segmentálního defektu femuru 4,5 mm LCP (bez soustavy uchycení kosti s duracrylem)



Obrázek 2 – 3D objemový model systému fixace segmentálního defektu femuru 4,5 mm LCP v CAD systému Rhinoceros; dělení femuru na kortikální (vnější) a sponziální (vnitřní) tkáň



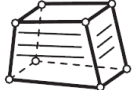


Obrázek 3 – Výpočtový konečně prvkový model systému ve výpočtovém systému ANSYS;

(a), (b) čelní a boční pohled, (c) axonometrický pohled na dolní část

S ohledem na obecnou geometrii analyzovaného systému byly při diskretizaci problému, tedy vytváření sítě konečných prvků, použity pro všechny části modelu kromě soustavy uchycení kosti kvadratické prostorové konečné prvky typu SOLID186 ve tvaru šestistěnů a jejich redukovaných tvarů (femur - kortikální i spongiózní tkáň, šrouby, PMMA) a SOLID187 ve tvaru pyramid (titanová pětiděrová 4,5 mm LCP).

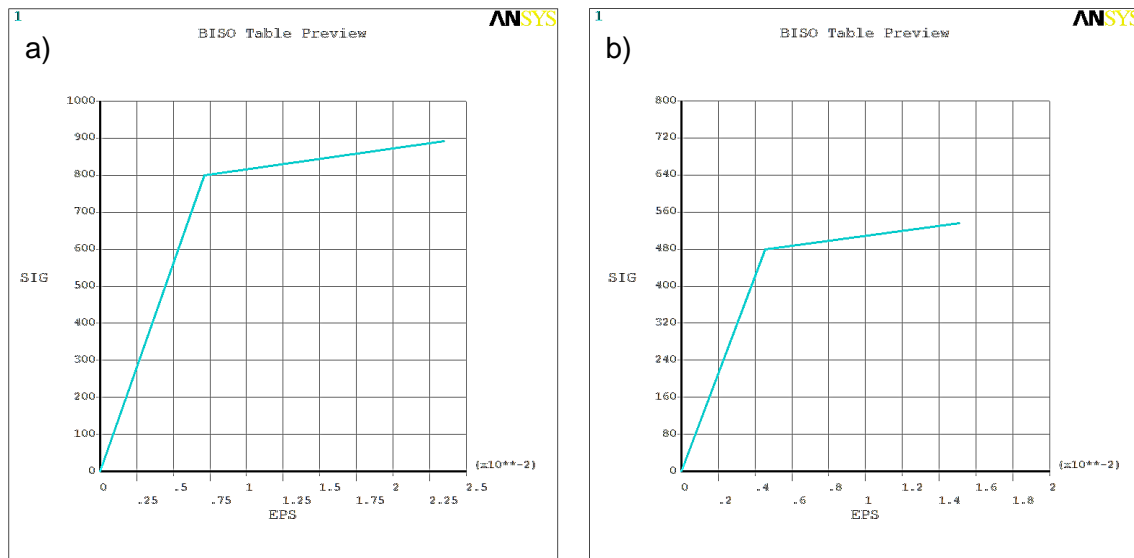
Pro soustavu uchycení kosti byly použity lineární prostorové konečné prvky typu SOLID185. Při vytváření sítě konečných prvků byla použita u objemů s jednoduchou geometrií metoda mapované sítě (soustava uchycení kosti), u obecných objemů byla použita metoda volné sítě. Pohledy na výpočtový model jsou uvedeny na Obr. 3.

Tabulka 8 Typy použitých prvků.

SOLID185	SOLID186	SOLID187
<p>SOLID185 3-D 8-Node Structural Solid 8 nodes 3-D space DOF: UX, UY, UZ</p> 	<p>SOLID186 3-D 10-Node Tetrahedral Structural Solid 10 nodes 3-D space DOF: UX, UY, UZ</p> 	<p>SOLID187 3-D 20-Node Structural Solid 20 nodes 3-D space DOF: UX, UY, UZ</p> 

Analýza chování systému tvořeného titanovou pětiděrovou 4,5 mm LCP a šrouby, byly zohledněny velké deformace, kdy byly podmínky rovnováhy sestavovány na deformované konstrukci. Při výpočtech bylo také uvažováno materiálově nelineární chování částí systému (šrouby, titanová pětiděrová 4,5 mm LCP), kdy po dosažení hodnoty napětí na mezi kluzu bylo uvažováno, že vznikají nevratné plastické deformace materiálu. Popis nelineárního chování materiálů vybraných částí systému byl proveden pomocí vhodných materiálových modelů, tj. podmínky plasticity, zákona plastického přetváření a kritéria zpevnění.

Materiálové chování šroubů, které jsou vyrobeny z materiálu Ti-6Al-7Nb a LCP vyrobeného z materiálu CP-Ti grade 4 [3] bylo modelováno použitím bilineárního pružnoplastického materiálového modelu s von Misesovou podmínkou plasticity a s izotropním kritériem zpevnění BISO (Obr. 4). K popisu použitého materiálového modelu byly použity materiálové charakteristiky uvedené v Tab. 2 převzaté z [3] a [4], kde E je počáteční modul pružnosti, E_H modul pružnosti větve zpevnění, μ Poissonův součinitel a σ_y je mez kluzu. Modul pružnosti větve zpevnění byl uvažován jako 1/20 počátečního modulu pružnosti ($E_H = E/20$).



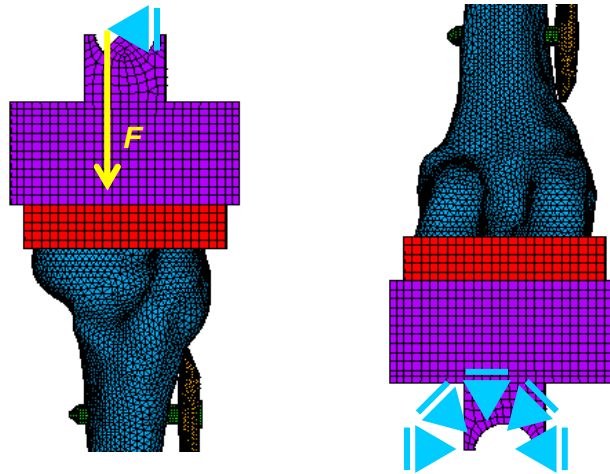
Obrázek 4 – Bilineární pružnoplastický materiálový model šroubů (a) a LCP (b).

Materiálové chování ostatních částí výpočtového modelu (soustava uchycení kosti, duractyl PMMA, kortikální a spongiózní tkáň) bylo popsáno pomocí izotropního materiálového modelu ISO, u kterého vznikají pouze vratné pružné deformace, a který byl popsán pomocí počátečního modulu pružnosti E a Poissonova součinitele μ (Tab. 2).

Tabulka 2 Materiálové charakteristiky použitých materiálových modelů.

	Model	E [MPa]	E_H [MPa]	σ_v [MPa]	μ [-]
soustava uchycení kosti – S235	ISO	210 000	-	-	0,30
duractyl PMMA - ISO	ISO	3 000	-	-	0,40
kortikální tkáň	ISO	15 230	-	-	0,30
spongiózní tkáň	ISO	225	-	-	0,30
šrouby (Ti-6Al-7Nb)	BISO	112 500	5 625	800	0,35
LCP (CP-Ti grade 4)	BISO	105 000	5 250	480	0,37

Okrajové podmínky výpočtového modelu (Obr. 5) byly na analyzovaném systému vytvořeny tak, aby modelovaly okrajové podmínky jako u reálné zátěžové zkoušky. Proto byla analyzovaná konstrukce na proximálním a distálním konci femuru opatřena bloky duracrylu, polymethylmetakrylátu (PMMA) umožňujícími její upnutí do zkušebního stroje [5], (Obr. 3). V dolní části soustavy uchycení byla uvažována cylindrická okrajová podmínka, umožňující volné pootáčení okolo osy kružnicového oblouku. Okrajová podmínka na horní části soustavy byla definována tak, aby docházelo pouze ke svislým posunům, tj. posunům paralelně s osou kosti.



Obrázek 5 – Okrajové podmínky, směr působícího zatížení.

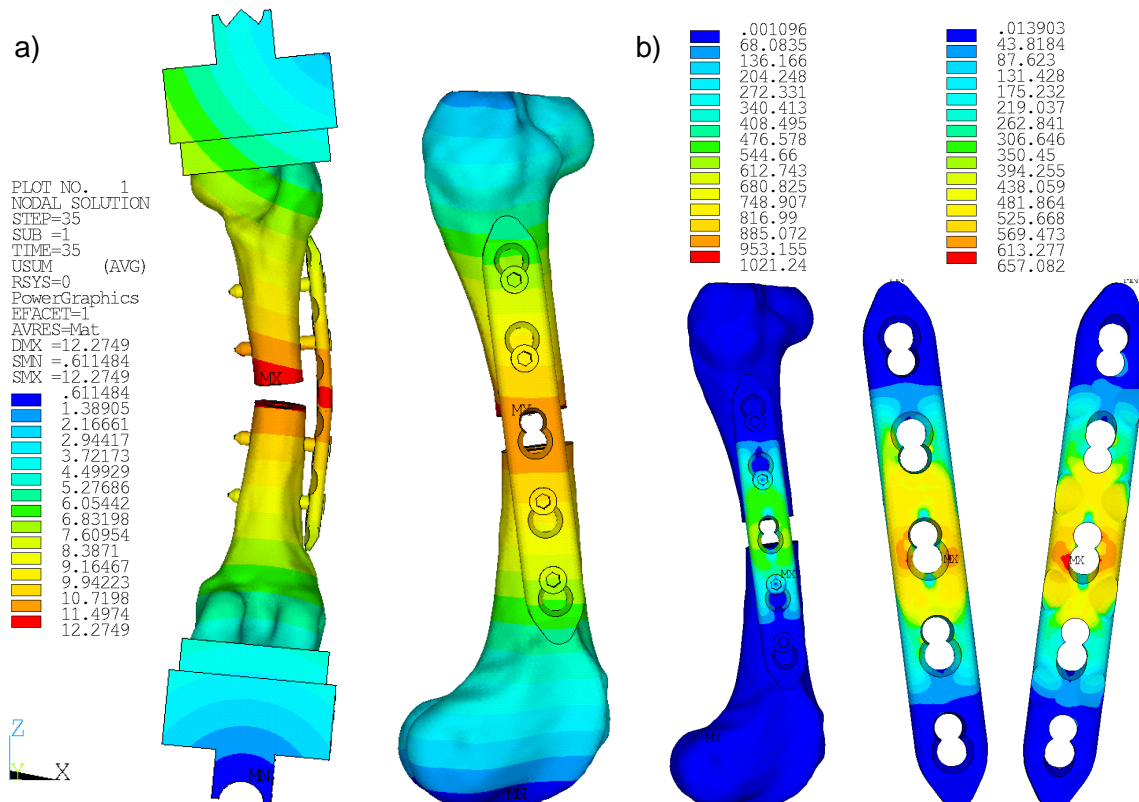
3 Postup výpočtu

Výpočtový model byl v rámci prováděných analýz zatížen silovým zatížením, tj. osamělou silou F působící na horní okraj soustavy uchycení kosti. Směr působení síly byl uvažován paralelní s osou kosti (Obr. 5). S ohledem na typ analýz, které byly geometricky a materiálově nelineární, probíhal vlastní výpočet přírůstkově v iteračním procesu. Velikost aplikovaného zatížení působícího v rámci jednoho přírůstku (zatěžovacího kroku) byl po předběžných analýzách zvoleno o velikosti 30 N.

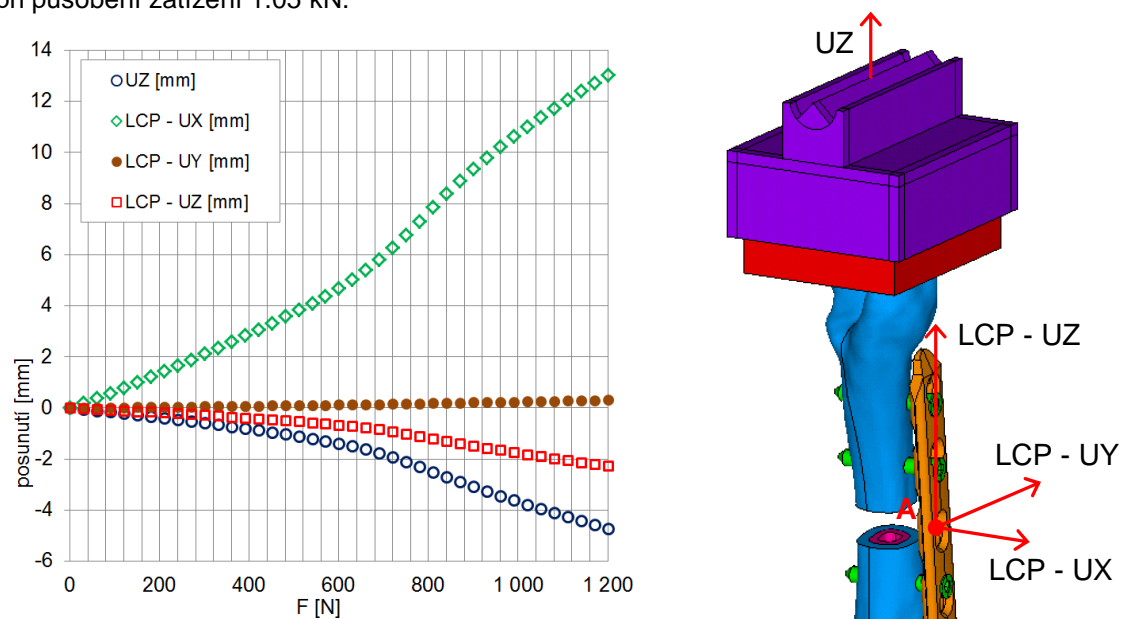
4 Výsledky

Výstupem řešení analyzovaného systému provedené výpočtovým systémem ANSYS bylo obecně pole posunutí $\{u\}$, pole deformací $\{\epsilon\}$ a pole napětí $\{\sigma\}$.

Při vyhodnocení analýz byly sledovány pro porovnání výsledků získaných mechanickým testováním a numerickou analýzou pro celý systém pole posunutí ve všech směrech (UX, UY, UZ) i celková vektorově složená posunutí (USUM). Pro dokumentaci výstupů je na Obr. 6 zobrazeno celkové vektorové posunutí USUM analyzovaného systému při působení zatížení 1.05 kN. Na Obr. 7 je grafické vyjádření závislosti svislého posunutí horní části soustavy uchycení (UZ) a svislého (LCP-UZ), příčného (LCP-UY) a podélného posunutí (LCP-UX) 4,5 mm LCP na velikosti působícího zatížení v intervalu aplikovaných přírůstků.



Obrázek 6 – Celkové vektorové posunutí USUM [mm] (a) a ekvivalentní napětí SEQV [MPa] při působení zatížení 1.05 kN.

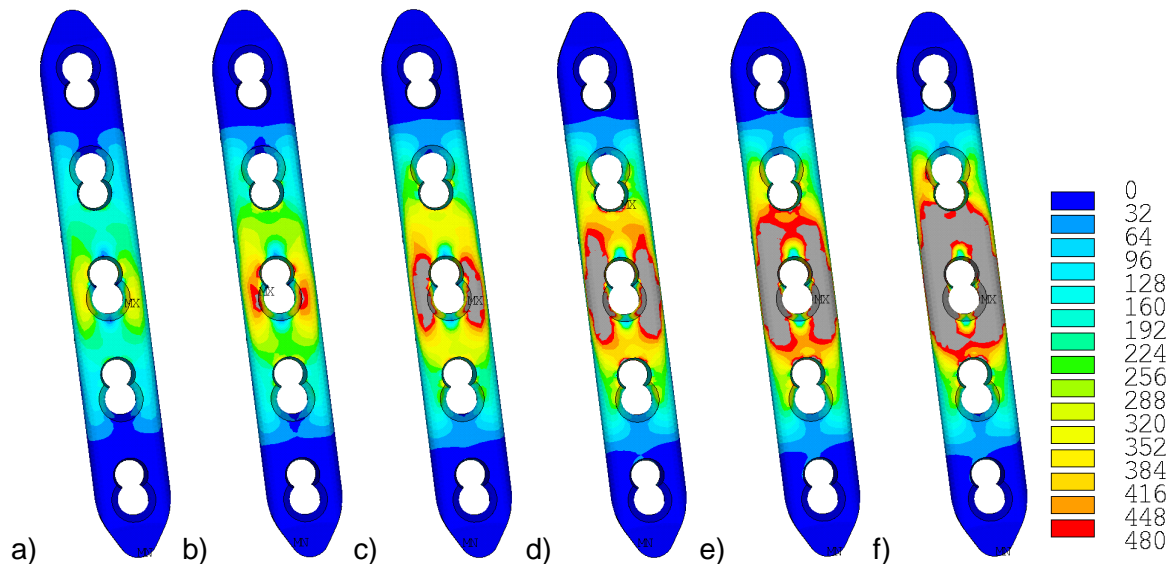


Obrázek 7 – Graf vyjadřující závislost svislého posunutí horní části soustavy uchycení UZ a podélného LCP-UX, příčného LCP-UY a svislého LCP-UZ posunutí bodu A na 4,5 mm LCP v místě volného otvoru na velikosti působícího zatížení v intervalu aplikovaných přírůstků.

Průběh postupného plastizování 4,5 mm LCP byl sledován pomocí ekvivalentního von Misesova napětí σ_{EQV} [MPa]. Proces plastizování průřezu byl též monitorován pomocí ekvivalentní von Misesovy plastické deformace ϵ_{pl} .

Pomocí matematického modelování byla vytvořena studie průběhu ekvivalentního von Misesova napětí σ_{EQV} na 4,5 mm LCP. Ze studie bylo určeno zatížení, při kterém dochází ke vzniku nevratných plastických deformací materiálu. K nevratným plastickým

deformacím, resp. překročení napětí na mezi kluzu σ_y na 4,5 mm LCP, došlo při uvažované geometrii kosti v oblasti středního otvoru 4,5 mm LCP, který nebyl vyplněn šroubem při působení 12 přírůstků zatížení, tj. při působení svislé síly o velikosti 360 N (Obr. 8). Po překročení této hodnoty zatížení dochází k postupnému plastizování průřezu 4,5 mm LCP. Z (Obr. 8) je patrné, že plastizování průřezu probíhá relativně souměrně na obě strany od středního otvoru.



Obrázek 8 – Ekvivalentní von Misesovo napětí σ_{EQV} [MPa] v 4,5 mm LCP (plastizování průřezu) při působení zatížení o velikosti 360 N (a), 480 N (b), 600 N (c), 720 N (d), 840 N (e) a 1200 N (f) zobrazené v intervalu 0 až 480 MPa. V oblastech vyznačených šedě došlo k překročení napětí na mezi kluzu σ_y .

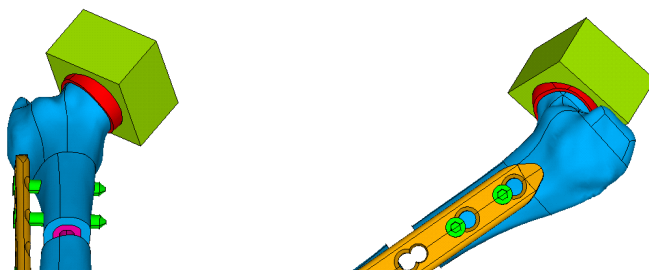
5 Zhodnocení a diskuze

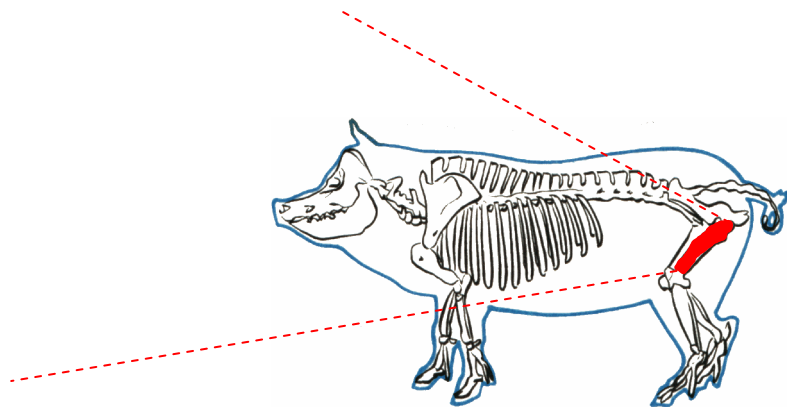
Nevýhodou mechanického testování je časová a materiálová náročnost. S materiálovou náročností je současně těsně spjata i náročnost finanční. Na každou mechanickou zkoušku je třeba použít nové fixační zařízení, ale také nový vzorek kosti. Každou změnu v nastavení působící síly je z důvodu prokazatelnosti nutné testovat na sadě několika vtorků.

Cílem představeného řešení je prezentace nahrazení mechanických testů matematickým modelováním. Nahrazení mechanického testování není zcela možné, jelikož pro výstižnost matematického modelování je nutné provést kalibraci matematického modelu pomocí mechanických testů s jednoznačně definovanými okrajovými podmínkami a působícími zatíženími.

Na verifikovaném matematickém modelu lze oproti mechanickému testování poměrně snadným způsobem měnit vstupní parametry (geometrii, okrajové podmínky, směr a velikost výslednice působící síly atp.). Současně lze oproti mechanickému testování zkombinovat působení působících sil najednou, ke kterému in vivo dochází, avšak při testování reálných vzorků tyto kombinace zatěžování jsou problematicky dosažitelné.

V prezentovaný způsob zatížení sloužil pro kalibraci a úpravu matematického modelu, který bude dále použit při analýzách namáhání systému fixace segmentálního defektu femuru 4,5 mm LCP při postavení femuru a jeho namáhání, ke kterému in vivo dochází. Upravený matematický model je zobrazen na (Obr. 9).





Obrázek 9 – Upravený matematický model uvažující in vivo postavení femuru a jeho namáhání.

Literatura

- [1] Necas, A., Proks, P., Urbanova, L., Srnec, R., Stehlik, L., Crha, M., Rauser, P., Planka, L., Amler, E., Vojtova, L., et al. (2010a). Radiographic Assessment of Implant Failures of Titanium 3.5 LCP vs. 4.5 LCP Used for Flexible Bridging Osteosynthesis of Large Segmental Femoral Diaphyseal Defects in a Miniature Pig Model. Acta Vet Brno 79, 599-U101.
- [2] Španěl, M., Kršek, P., Švub, M., Štancl, V., Šiler, O. Delaunay-Based Vector Segmentation of Volumetric Medical Images. In Proceedings of the 12th International Conference on Computer Analysis of Images and Patterns, CAIP 2007. Lecture Notes in Computer Science (IF 0,513). LNCS 4673. Berlin Heidelberg: Springer Verlag, 2007. s. 261-268. ISBN: 3-540-74271-9. ISSN: 0302-9743
- [3] Synthes Global Internet Medical Community: Product Literature [online]. 2008 [cit. 2011-11-24]. LCP Locking Compression Plate. Available from WWW: <<http://www.synthes.com/>>.
- [4] Online Material Information Resource - MatWeb [online]. 1996 [cit. 2011-11-24]. Titanium Grade 4. Available from WWW: <<http://www.matweb.com/>>.
- [5] Urbanova, L., Srnec, R., Proks, P., Stehlik, L., Florian, Z., Navrat, T., and Necas, A. (2010). Comparison of the Resistance to Bending Forces of the 4.5 LCP Plate-rod Construct and of 4.5 LCP Alone Applied to Segmental Femoral Defects in Miniature Pigs. Acta Vet Brno 79, 613-U118.

Poděkování

Příspěvek vznikl za podpory grantové agentury IGA VFU Brno (projekt 31/2011/FVL) a za podpory MŠMT ČR (projekt NPV II 2B06130). Autoři by rádi poděkovali doc. Ing. Přemyslu

Krškovi, Ph.D. a Ing. Jaroslavu Baronovi za pomoc při úpravě dat z CT a jejich exportu do systému Rhinoceros a za vytvoření 3D CAD modelu v systému Rhinoceros.

Kontaktní adresa:

Ing. Jan Pěnčík, PhD.

Vysoké učení technické, Fakulta stavební, Veveří 331/95, 602 00 Brno

PARAMETRICKÁ STUDIE PRŮBĚHU RYCHLOSTI PROUDĚNÍ V PULTOVÉ DVOUPLÁŠŤOVÉ PROVĚTRÁVANÉ STŘEŠE NA VSTUPNÍ RYCHLOSTI

TOMÁŠ BARTOŠ, JAN PĚNČÍK

Vysoké učení technické v Brně, Fakulta stavební, Veveří 331/95, 602 00 Brno

Abstract: Studium proudění a jeho modelování je zaměřeno především na návrh dvouplášťových provětrávaných střech, které jsou v českých normách doporučovány pro budovy s vlhkým provozem. Pro modelování je využit program ANSYS [1], který využívá metodu CFD. Základním problémem návrhu provětrávaných dvouplášťových střech je návrh optimální tloušťky vzduchové mezery. Z prvních modelů bylo zjištěno, že minimální výška přívaděcího otvoru je 0,3 m, při menší výšce proud vzduchu nepronikne do vzduchové mezery, ale odrazí se od atiky a stočí se nad střechu. Ze studie vyplývá, že rychlost proudění v bodě uprostřed vzduchové mezery je v drtivé většině menší, než v přívaděcích a odváděcích otvorech. V tomto bodě také rychlost poměrně kolísá, oproti bodům v otvorech, v nichž je závislost rychlosti proudění na rychlosti větru poměrně stabilnější, viz Graf.1. Maximum rychlosti ve vzduchové mezeře nastává pro rychlost $14 \text{ m}\cdot\text{s}^{-1}$, a to $12.75 \text{ m}\cdot\text{s}^{-1}$.

Keywords: dvouplášťové střechy, metoda CFD, rychlost proudění, větraná mezera

1 Úvod

Studium proudění a jeho modelování je zaměřeno na návrh dvouplášťových provětrávaných střech, které jsou v normách doporučovány pro budovy s vlhkým provozem. Pro modelování je využit program ANSYS [1], který pro analýzu využívá metodu CFD.

Základním problémem návrhu provětrávaných dvouplášťových střech je návrh optimální tloušťky vzduchové mezery. Například v české normě ČSN 73 1901:1999 „Navrhování střech - Základní ustanovení“ je uvedeno, že minimální tloušťka větrané vzduchové vrstvy, určené pro odvod vodní páry difundující do střešní konstrukce, je při sklonu střešního pláště do 5° (8.75%) minimálně 100 mm pro střechu s délkou do 10 m. Pro odvod vody technologické a zabudované do konstrukce je minimální tloušťka vrstvy 250 mm pro střechu do 10 m délky. Tyto předpoklady zahrnují vliv tepelně technických vlastností dolního pláště, atiky a horního pláště střechy. Tudiž větrání probíhá i za bezvětrí díky komínovému efektu. Plocha přívaděcích otvorů by měla odpovídat minimálně 1/400 plochy střechy, odváděcí otvory pak o 10% větší.

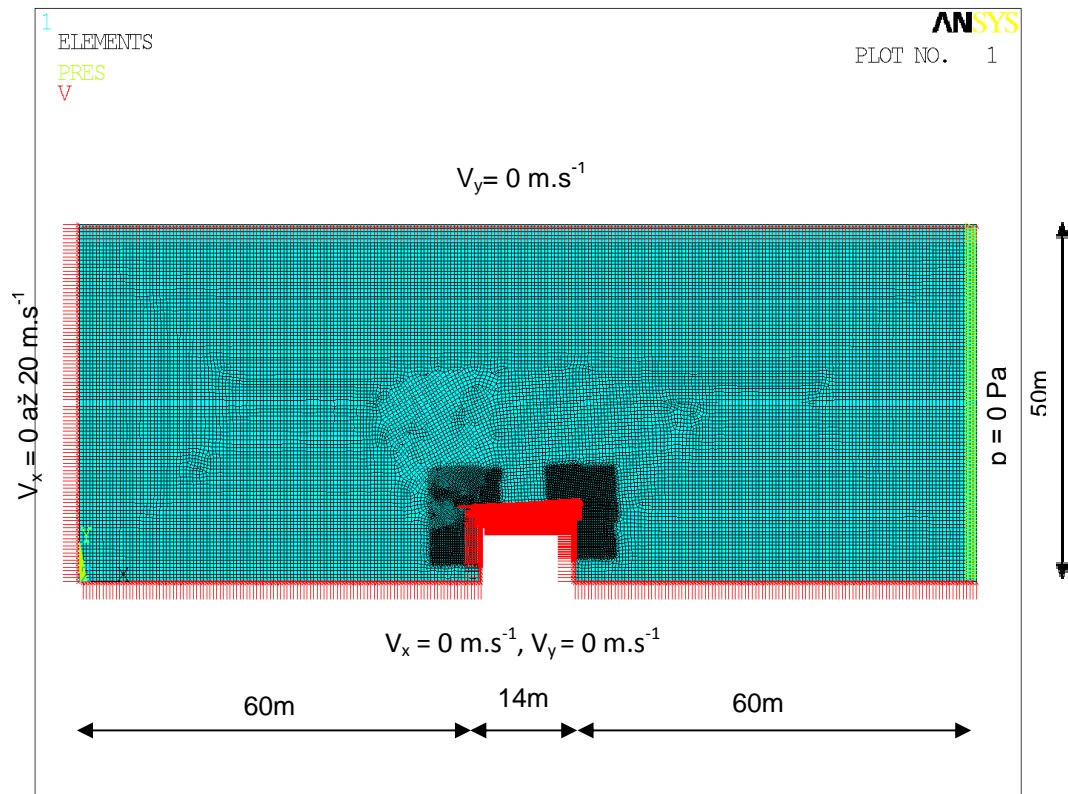
2 Výpočtový model

Pro studii závislosti rychlosti proudění vzduchu ve vzduchové mezeře dvouplášťové střechy byla zvolena pultová střecha; zkoumané body byly umístěny do přívaděcího otvoru (bod A), do středu vzduchové mezery (bod B) a do odváděcího otvoru (bod C, viz. Obr.2.). Směr proudění vzduchu probíhá v kladném směru souřadnicové osy x, a nabývá hodnot $1 \text{ m}\cdot\text{s}^{-1}$ až $20 \text{ m}\cdot\text{s}^{-1}$, tj. $3.6 \text{ km}\cdot\text{h}^{-1}$ až $72 \text{ km}\cdot\text{h}^{-1}$. Výsledný model pevné překážky (tedy zkoumaného objektu) má celkovou výšku 11.3 m a délku 16 m.

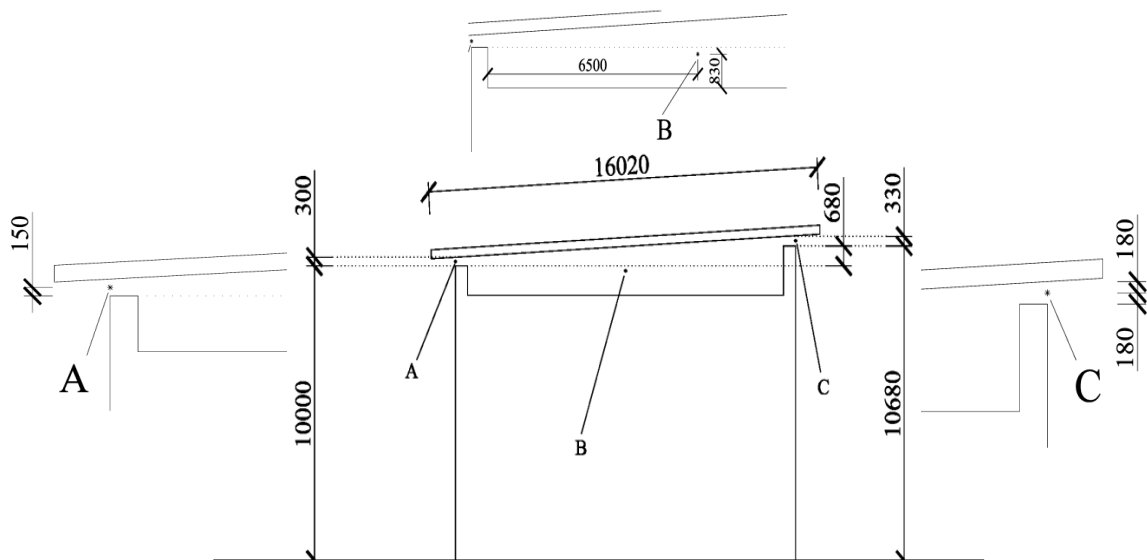
Okrajové podmínky byly zvoleny tak, že na vstupní straně (inlet) má vítr počáteční rychlost 0 až $20 \text{ m}\cdot\text{s}^{-1}$, na horní straně výpočtového modelu je nulová rychlost ve směru

souřadnicové osy y , na výstupní straně (outlet) je nulový tlak, a na spodní hraně a všech obvodových liniích překážky jsou rychlosti V_x a V_y nulové.

K popisu proudění je použit standardní $k-\epsilon$ model turbulence, při výpočtu byly uvažovány materiálové charakteristiky vzduchu: hustota $\rho=1,205 \text{ kg.m}^{-3}$, kinematická vazkost $\nu=15,0 \cdot 10^6 \text{ m}^2.\text{s}^{-1}$.



Obrázek 1 - Výpočtový model a okrajové podmínky



Obrázek 2 - Umístění bodů, ve kterých je zjišťována rychlost proudění vzduchu

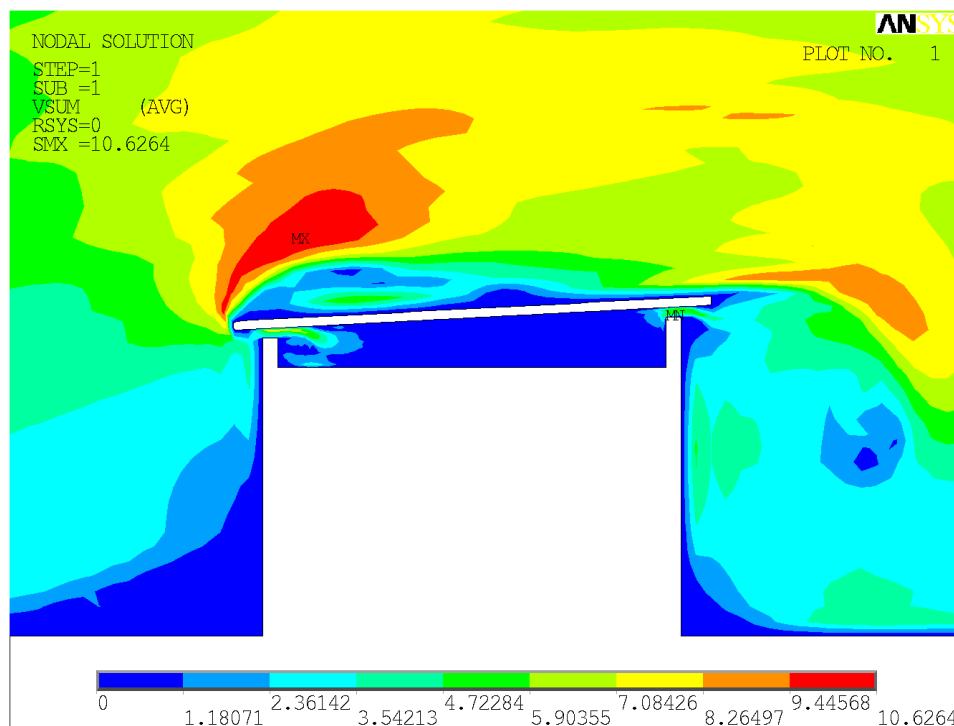
3 Postup výpočtu

První studie, zjištění minimální tloušťky vzduchové mezery, byla nejprve provedena pro výšku přiváděcího otvoru 200 mm, posléze pro 300 mm. Pro tuto studii byly zvoleny rychlosti vzduchu 5, 10, 15, 20 m.s^{-1} .

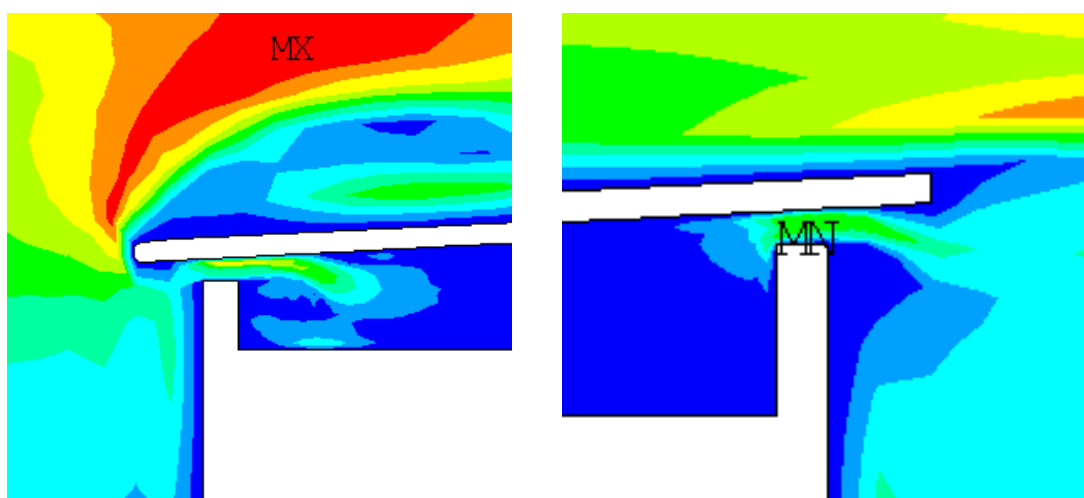
Druhá parametrická studie - analýza metodou CFD byla provedena pro rychlosti 1 až 20 $\text{m}\cdot\text{s}^{-1}$, vždy s krokem 1 $\text{m}\cdot\text{s}^{-1}$. Analýzy byly provedeny pro objekt s výškou větrané mezery 300 mm. Z každé jednotlivé analýzy byly určeny a zaznamenány tři hodnoty rychlostí (viz. Tab.1.).

4 Výsledky

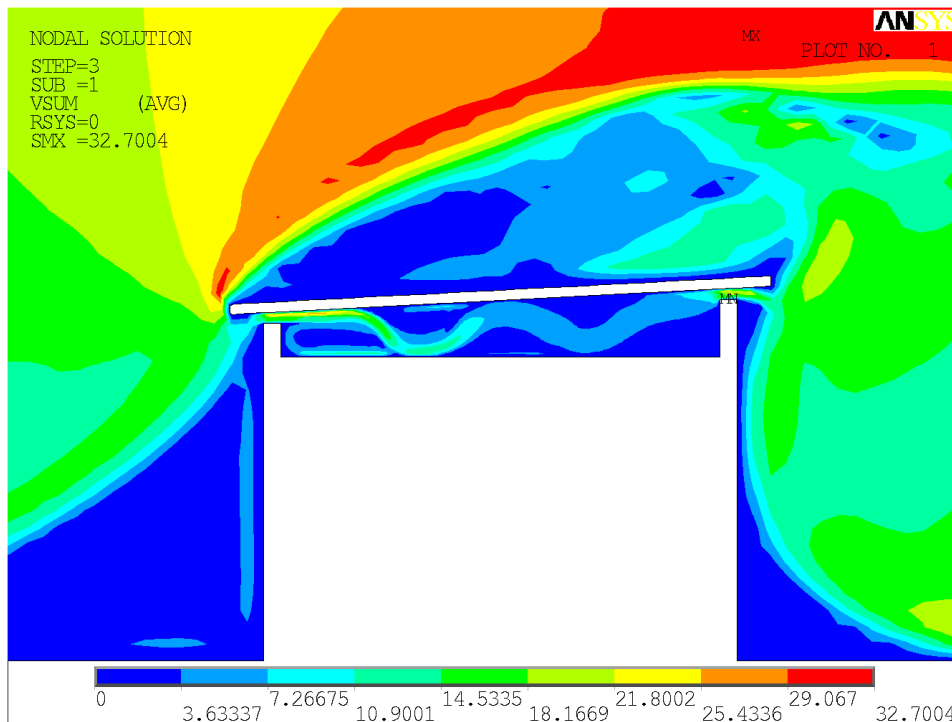
Po provedení simulací průběhu proudění byly zjištěny tři hodnoty rychlostí ve sledovaných bodech (pevně stanovených uzlech) pro každou vstupní rychlost 1 až 20 $\text{m}\cdot\text{s}^{-1}$. V tabulce jsou barevně zvýrazněny maximální a minimální hodnoty. Na obrázcích 4 až 9 je porovnán průběh rychlostí V_{sum} pro rychlosti $V_x = 5$ a 17 $\text{m}\cdot\text{s}^{-1}$. Tyto rychlosti byly vybrány z důvodu názornosti polohy maxima V_{sum} .



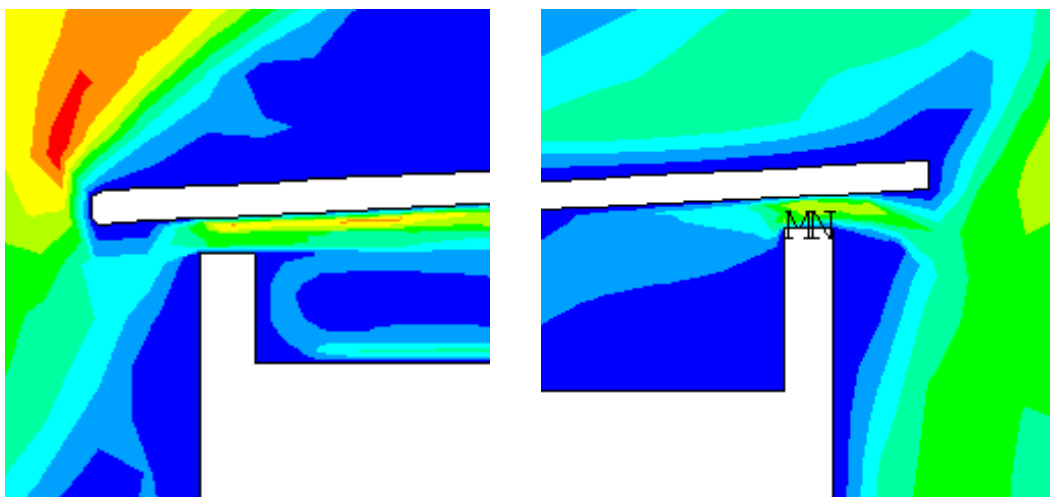
Obrázek 4 - Průběh rychlosti V_{sum} pro vstupní rychlost $V_x = 5 \text{ m}\cdot\text{s}^{-1}$



Obrázek 5 – Průběh proudění v místě přívaděcího a odváděcího otvoru (pro vstupní rychlost $V_x = 5 \text{ m}\cdot\text{s}^{-1}$)



Obrázek 6 – Průběh rychlosti V_{sum} pro vstupní rychlost $V_x = 17 \text{ m}\cdot\text{s}^{-1}$



Obrázek 7 - Průběh proudění v místě přívaděcího a odváděcího otvoru (pro vstupní rychlost $V_x = 17 \text{ m}\cdot\text{s}^{-1}$)

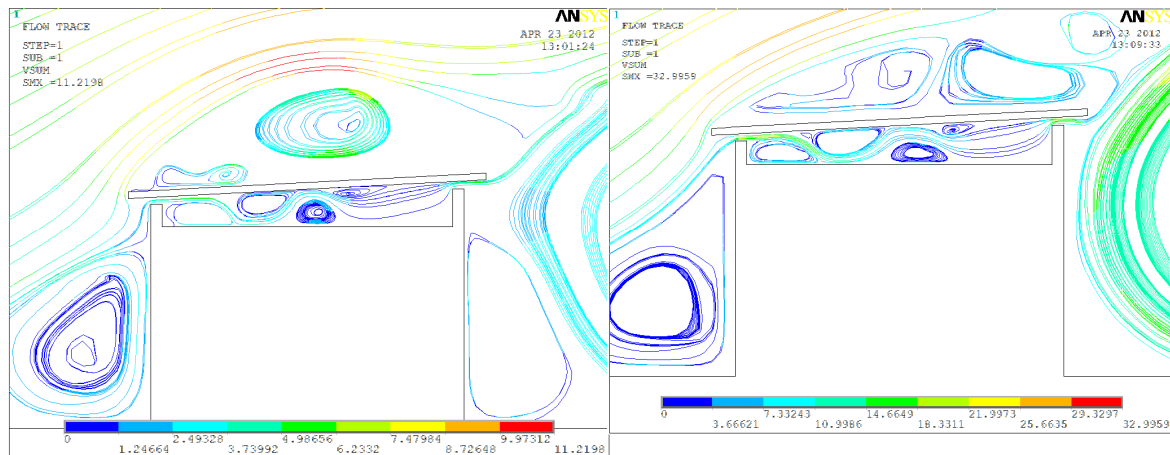
Obrázky 4 a 6 dokumentují vliv vstupní rychlosti na rozložení pole rychlostí vzduchu V_{sum} . Z obrázku 4 vyplývá, že oblast s maximální rychlostí se pohybuje nad okrajem horního pláště na straně přívaděcího otvoru, při vyšších rychlostech se maximum pohybuje směrem k odváděcímu otvoru (Obrázek 6).

5 Zhodnocení

Z prvních modelů bylo zjištěno, že minimální výška přívaděcího otvoru je 0,3 m, při menší výšce proud vzduchu způsobený větrem nepronikne do vzduchové mezery, ale odrazí se od atiky a stočí se nad střechu.

Ze studie vyplývá, že rychlost proudění v bodě uprostřed vzduchové mezery je v drtivé většině menší, než v přívaděcích a odváděcích otvorech. V tomto bodě také rychlost

poměrně kolísá, oproti bodům v otvorech, v nichž je závislost rychlosti proudění na rychlosti větru poměrně stabilnější, viz Graf 1. Maximum rychlosti ve vzduchové mezeře nastává pro rychlost $14 \text{ m}\cdot\text{s}^{-1}$, a to $12,75 \text{ m}\cdot\text{s}^{-1}$.



Obrázek 8 - Porovnání proudnic uvnitř vzduchové mezeře při $5 \text{ m}\cdot\text{s}^{-1}$ a $17 \text{ m}\cdot\text{s}^{-1}$

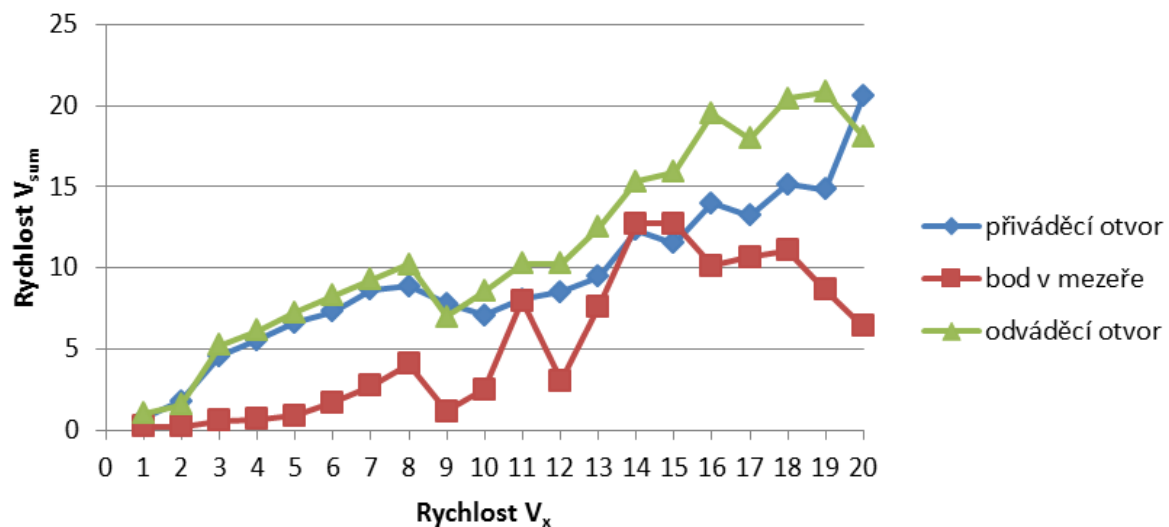
Z analýzy vyplynuly tři kombinace popsané v Tabulka 1 jako I, II, III. Nejčastěji se vyskytující je kombinace I, konkrétně v 15-ti případech. V této kombinaci nabývá rychlost maximálních hodnot v odváděcím otvoru. Minimální hodnoty rychlosti jsou pak v bodě uprostřed dutiny. Ve třech případech (II) má rychlost maximální hodnoty v přiváděcím otvoru a minimální v mezeře. Pouze ve dvou případech (III) je rychlost vzduchu v mezeře větší, než v přiváděcím otvoru.

Tabulka 1 Výsledky

rychlost $V_x [\text{m}\cdot\text{s}^{-1}]$	rychlost V_{sum}			
	přiváděcí otvor	bod v mezeře	odváděcí otvor	
1	0,75317	0,26272	1,04514	I
2	1,80195	0,26699	1,60415	II
3	4,60814	0,62467	5,27084	I
4	5,57763	0,67770	6,15392	I
5	6,66012	0,90447	7,28555	I
6	7,31886	1,71301	8,31176	I
7	8,65146	2,73901	9,29120	I
8	8,88524	4,08399	10,24299	I
9	7,81994	1,19985	7,00714	II
10	7,08890	2,54019	8,55631	I
11	8,08725	7,97315	10,25253	I
12	8,50415	3,04990	10,26602	I
13	9,47239	7,65167	12,52798	I

14	12,32121	12,75146	15,31004	III
15	11,50827	12,72782	15,90311	III
16	13,97538	10,14023	19,47644	I
17	13,22359	10,66820	17,94950	I
18	15,17159	11,07827	20,42625	I
19	14,83043	8,67031	20,85277	I
20	20,54643	6,40068	18,11052	II

Graf 1 Výsledky



Literatura

[1] ANSYS, Inc. 14.

[2] ČSN EN 1991-1-4:2007 Zatížení konstrukcí - Část 1-4 - Obecná zatížení - Zatížení větrem. Praha: ÚNM

[3] ČSN 73 1901:1999 „Navrhování střech - Základní ustanovení“

Poděkování

Příspěvek vznikl s pomocí projektu specifického výzkumu řešeného na na FAST VUT v Brně. Registrační číslo projektu je FAST-S-12-20/1650.

Kontaktní adresa:

Ing. Tomáš Bartoš

Vysoké učení technické, Fakulta stavební, Veveří 331/95, 602 00 Brno

Ing. Jan Pěňčík, PhD.

Vysoké učení technické, Fakulta stavební, Veveří 331/95, 602 00 Brno

THE NON-LINEAR STATIC ANALYSIS OF THE TEXTILE BAG

JIŘÍ PODEŠVA, ZDENĚK PORUBA, ONDŘEJ FRANTIŠEK

VŠB - Technical University of Ostrava, 17. listopadu 15, 708 33 Ostrava, Czech Republic, e-mail: jiri.podesva@vsb.cz

Abstract: The fabric material represents the anisotropic non-linear continuum. The deformation under pressure is large and represents the geometric non-linearity - large deflection. The subject of modeling is the stress state in the fabric membrane, deformation of the planar continuum and the total volume of full bag. To build the correct finite element model it is necessary to use the element coordinate system and define the different material properties in both warp and weft direction. To solve non-linearity it is necessary to use the iteration approach (Newton-Raphson). Finally the solution brings the specific problem - the first iteration problem. In the initial geometry configuration the membrane has zero stiffness and this does not allow to pass the first iteration step. The finite element model must be modified in certain way.

Keywords: The textile material, iterative solution, large deflection, planar continuum

1 Introduction

The partial differential equations of the planar continuum (see fig. 1) under in-plane tension and perpendicular pressure are:

$$\tau_x \cdot \frac{\partial^2 u}{\partial x^2} + \tau_y \cdot \frac{\partial^2 u}{\partial y^2} = p \quad (1)$$

where τ_x and τ_y are the in-plane tension forces in x and y direction, p is a perpendicular pressure and u represents the displacement under pressure.

The fabric material has no bending stiffness. The resistance against deformation results from the deformation, when the in-plane tension forces have the perpendicular component (see fig. 1).

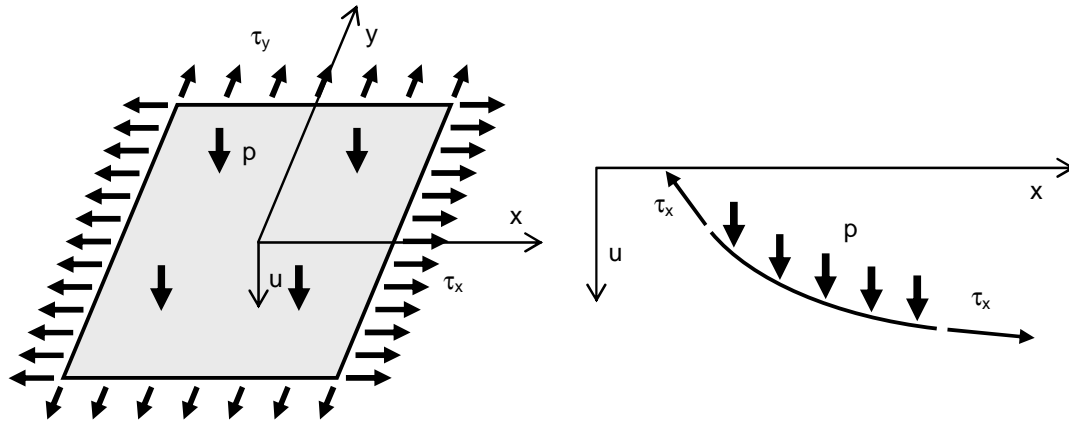


Fig. 1 – The planar continuum under 2 axis in-plane tension and perpendicular pressure

After deformation the tension forces τ_x and τ_y are not really perpendicular to the pressure. The component of the tension forces, perpendicular to the x-y plane, is in equilibrium with pressure p . This gives the mathematical description in the form of partial differential equation (1).

If the tension forces τ_x and τ_y in the x and y direction are equal ($\tau_x = \tau_y = \tau$), then the equation (1) is simplified to :

$$\frac{\partial^2 u}{\partial x^2} + \frac{\partial^2 u}{\partial y^2} = \lambda = \frac{p}{\tau} = \frac{\text{pressure}}{\text{tension}} \quad (2)$$

where the relative loading λ represents the ratio between pressure and tension. The solution of the equation (1) or (2) then depends on the area Ω , on which it is solved. In technical application the area Ω means the hole covered by the fabric (see fig. 2). The zero displacement on the hole edges are the boundary conditions.

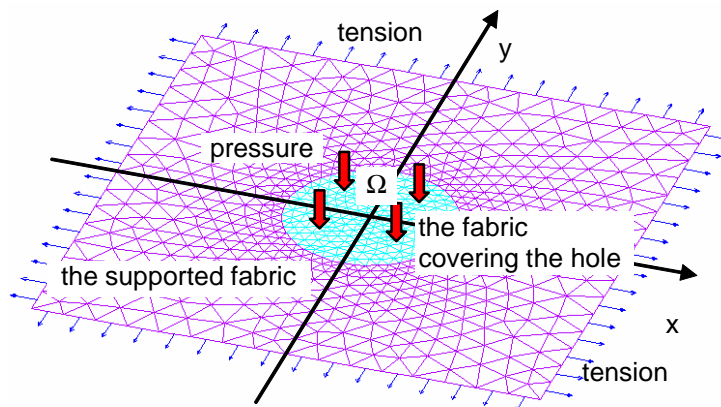


Fig. 2 – The planar continuum, discretized to the finite element mesh

For the circular area Ω of the radius R the solution of (2) is :

$$u = \frac{1}{4} \cdot \lambda \cdot (x^2 + y^2 - R^2) \quad (3)$$

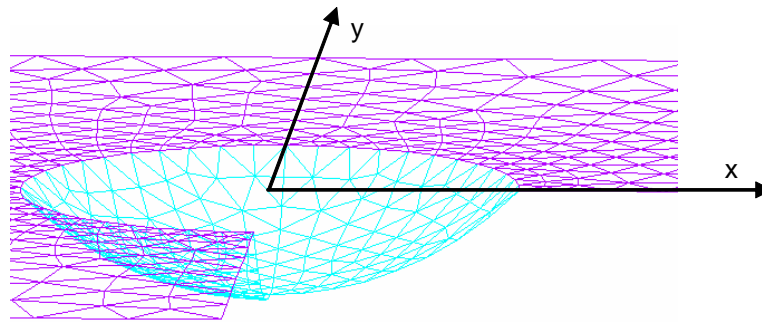


Fig. 3 – The planar continuum, the displacement solution

The results of the computer modeling (see fig. 2 and fig. 3) can be compared with the exact solution (3).

2 The Material Model

The fabric material represents the anisotropic material (Peng), characterized as the structure of perpendicular threads (see fig. 4). The threads in the direction of the long stripe of fabric are called warp, while these perpendicular to the warp threads are weft threads. The material stiffness was measured in both warp and weft direction.

The behavior under loading is not linear, but not strongly. The tension-deformation curve was linearized (see fig. 4) and the Young modulus E_x and E_y for both directions was determined.

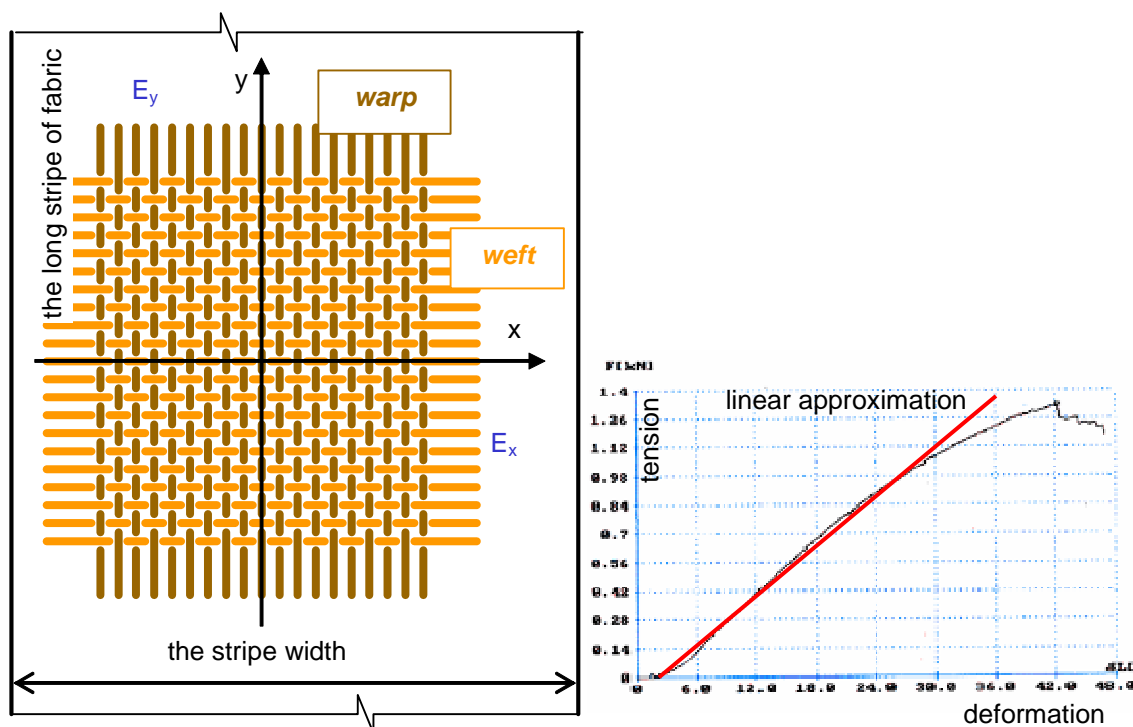


Fig. 4 – The stripe of fabric, the warp-weft structure, the tension test record

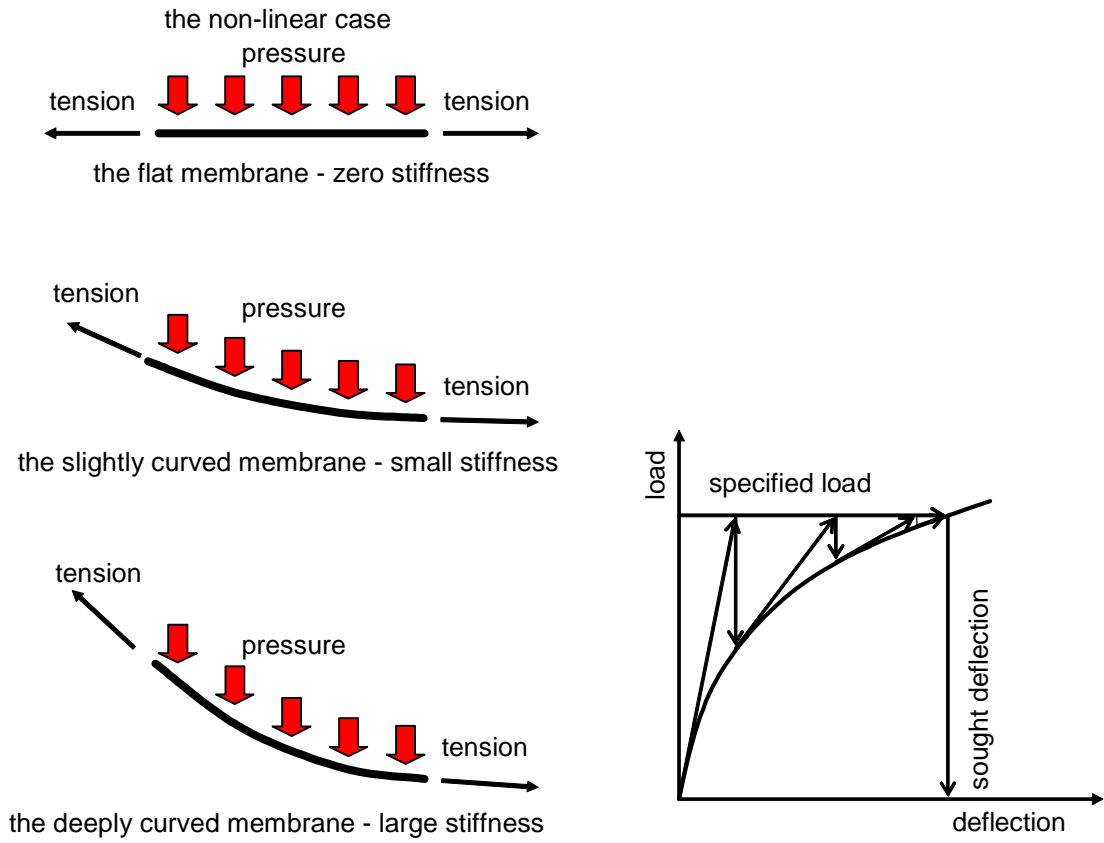


Fig. 5 – The stiffness results from deformation. The non-linear load - deflection behavior

3 The Large Deformation Approach

As written in the Introduction the resistance against pressure, the stiffness, as the ratio between loading and deformation, depends on the deformed shape. This is the typical example of so called "geometric non-linearity" (see fig. 5) (Crisfield).

The resistance against loading is given by the component of the in-plane tension in the direction of pressure.

The commercial software has the tools for the iterative solution of non-linear problems. The common approach is the Newton-Raphson method (see fig. 5). The idea is to solve the non-linear task in subsequent iterations during which the stiffness matrix is recalculated in every solution step.

But in the solution process to solve the first iteration becomes to be a problem. The described procedure fails in the case of planar membrane. If the area is initially flat, then the structure has zero stiffness in the first iteration and no first approximation can be found. The additional stiffness can be added to every node of the structure just to solve the first solution step. In that case the first iteration solution is found, what is the gate for subsequent solution. Depending on the value of the additional stiffness the first approximation can be near to or far from the final deformed shape. In subsequent solution steps this additional stiffness is not taken in account and correct final deformed shape is found.

Once, when even the first approximation of the deformed shape is found, the subsequent solution can be performed using standard non-linear algorithms.

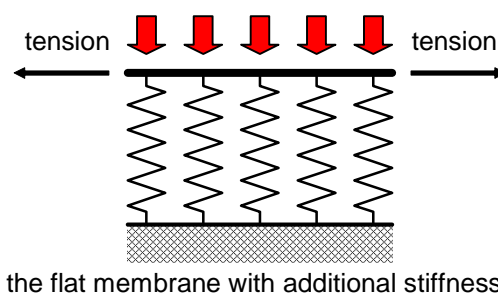


Fig. 6 – The additional stiffness for the first step

The additional stiffness can be realized through real spring elements (see fig. 6). The specific feature of the shell63 element type can be used. The element has the system switch to have or not to have bending stiffness. This switch can be turned on in first solution step and switched off in subsequent.

4 The Application

The textile material is used for flat bag (see fig. 7). The bag contains either bulk material (such as sand) or typically liquid. Under internal pressure the bag sides are deformed. For the bag design both deformation and stress state are important. It can be the subject of the computer modeling, using finite element method. The results of such modeling are deformation and stress state and, for instance, the final volume of the bag - the storage capacity.

The above described methodology was used to investigate the deformation and planar stress state of the real fabric bag. The bag is exposed to the internal hydrostatic pressure due to the weight of the enclosed liquid.

To create the finite element model the membrane triangular elements were used for the bag walls(Bijian, Eischen).



Fig. 7 – The flat fabric bag

The walls of the bag are exposed to the internal pressure, which increases downward. In case of flat bag it is rather complicated to define the pressure. The two horizontal walls are initially planar, on the same height, so it has the same pressure across the whole area. In the process of deformation the initially flat walls are warped, the bag begins to have the 3D shape and the pressure varies across the wall (see fig. 8, 9).

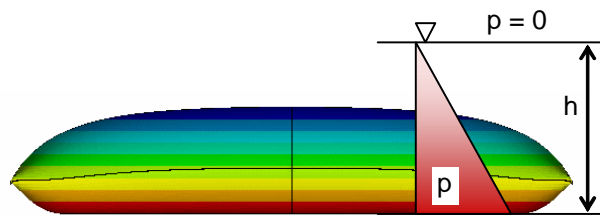
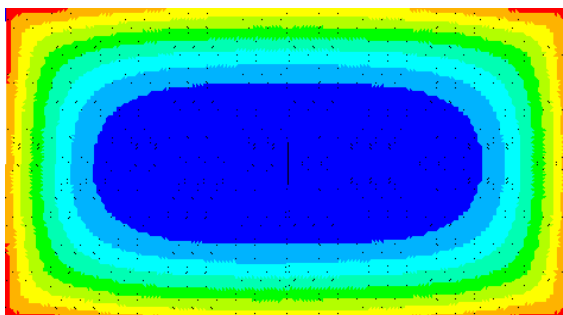


Fig. 8 – The flat fabric bag, the pressure, increasing downward

The pressure than must be redefined in each iteration cycle to be higher on element moving down and to be lower on elements moving up (see fig. 8, 9).

the lower pressure on the top fabric wall



the higher pressure on the bottom fabric wall

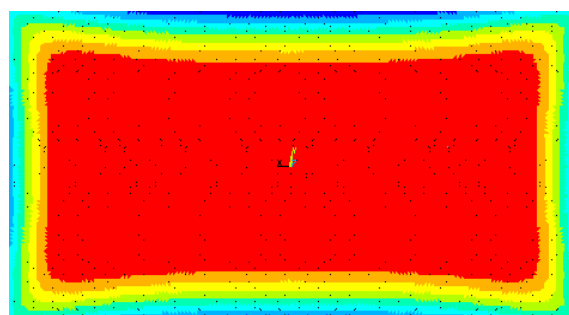


Fig. 9 – The pressure distribution across the top and bottom bag wall

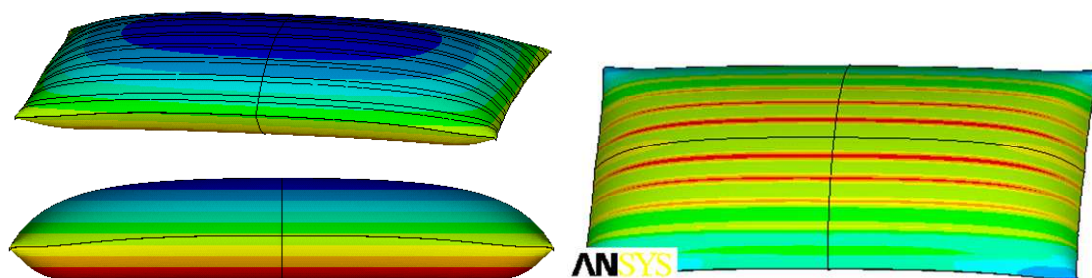


Fig. 10 – The flat bag deformation, the warp threads tension stress

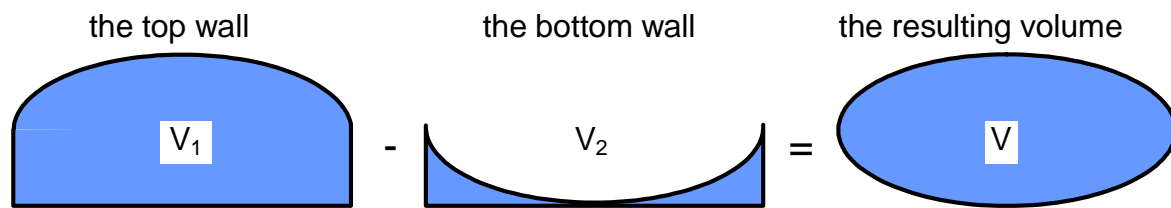


Fig. 11 – The volume calculation

The results of the solution are the deformation of the bag and the stress state (see fig. 10). To calculate the bag volume, the vertical displacement of each node must be taken into account. The total volume is calculated as the difference between height of upper wall and lower wall (see fig. 11).

1 Conclusion

The modeling of the fabric bags, the deformation and the stress state, is the case of the finite element method modeling. We use the generally defined element types, such as the shell element (the membrane element) and spring element.

The modeling brings the problems. Some of them (the geometric non-linearity) can be solved using the routines, built in the software (Newton-Raphson method). But some of them (the first step problem) are specific and the software has not the built in tools. To solve this the specific methodology was developed.

Also the post-processing has some specific features, we mean the volume calculation. To solve this the deep insight into the software is necessary and the special macros have to be developed.

References

Bijian Chen, Muthu Govindaraj. *A Physically Based Model of Fabric Drape Using Flexible Shell Theory*. Textile Research Journal, June 1995, vol. 65, no. 6 324-330, ISSN: 0040-5175.

Crisfield, M.A. *Non-linear finite element analysis of solid and structures*. John Wiley & Sons, Baffins Lane, Chichester, 1997. ISBN 0-471-92956-5.

Eischen, J.W.; Shigan Deng; Clapp, T.G. : *Finite-element modelling and control of flexible fabric parts*. Computer Graphics and Applications, IEEE, Volume: 16 Issue:5, 1996, ISSN: 0272-1716.

Peng, X.Q., Cao, J. *A continuum mechanics-based non-orthogonal constitutive model for woven composite fabrics*. Composites Part A. Applied Science and Manufacturing, Volume 36, Issue 6, June 2005, Pages 859-874, ISSN: 1359-835X.

Ansys - *Structural Nonlinearities*, User's Guide. SAS IP, Inc. 1999

Acknowledgement

The work was done with support of the MSM 6198910027 project.

Contact address :

assoc. prof. Jiří Podešva, M.Sc., Ph.D.

VŠB - Technical University of Ostrava, 17. listopadu 15, 708 33 Ostrava, Czech Republic

e-mail: jiri.podesva@vsb.cz

MODELOVANIE KONTAKTU PILOTA – ZEMNÝ MASÍV.

PREKOP ĽUBOMÍR

Stavebná fakulta STU, Katedra stavebnej mechaniky

Abstract: The paper deals with an analysis of the pile subjected to the bending and its synergy with the surrounding natural massif. The greatest emphasis is devoted to the modeling of the contact on a pile and soil. Finally some achieved results and their comparing with an analytic solution as well are presented in graphic form.

Keywords: pile, the interaction with the surrounding, modeling of a contact

1 Úvod

Pilotový základ patrí medzi najrozšírenejšie hĺbkové zakladania. V porovnaní s plošným základom sa znižuje hmotnosť základu, rozsah výkopu, vylučuje sa debnenie a veľký spätný zásyp.

Betónové piloty sa vyhotovujú z prostého betónu alebo železobetónu. Tvar piloty býva najčastejšie kruhový, štvorcový alebo mnohouholníkový. Rozmery pilot sa líšia podľa použitej technológie a sú v rozsahu od 0,3 m do 2,0 m. Druhov pilot je veľké množstvo. Vo všeobecnosti môžeme rozdeliť piloty podľa rôznych kritérií, univerzálne piloty pre všetky možné prípady neexistujú.

2 Železobetónové piloty

Pre vystužovanie pilot je dôležité ich správne pôdorysné rozmiestnenie v pilotovom základe. Piloty sa rozmiestnia tak, aby zaťaženie pilotového základu bolo čo najbližšie dostrednému zaťaženiu. Do betónového prierezu sa podľa spôsobu namáhania navrhne nosná výstuž. Pri návrhu výstuže je potrebné zvážiť aj štáduá, ktoré vzniknú počas výroby pilot a ich dopravy na miesto použitia.

Rozmiestnenie výstuže piloty v priečnom reze je v zásade symetrické. Pozdĺžna výstuž sa umiestňuje v rohoch piloty alebo pri kruhovom pôdoryse rovnomerne po obvode a volí sa s priemerom $\varnothing = 18 - 32$ mm. V prípade potreby sa dopĺňa medziľahlo umiestnenou výstužou s priemerom $\varnothing = 14 - 22$ mm. Krytie výstuže je aspoň 35 mm, v prípade pilot vŕhaných cez zeminy s agresívnou vodou sa krytie výstuže zvyšuje na 50 až 80 mm. Výstuž v špici piloty sa dopĺňa konštrukčnou výstužou. Rovnako pod hlavou piloty sa výstuž upravuje kvôli zväčšeniu tuhosti piloty pri baraní.

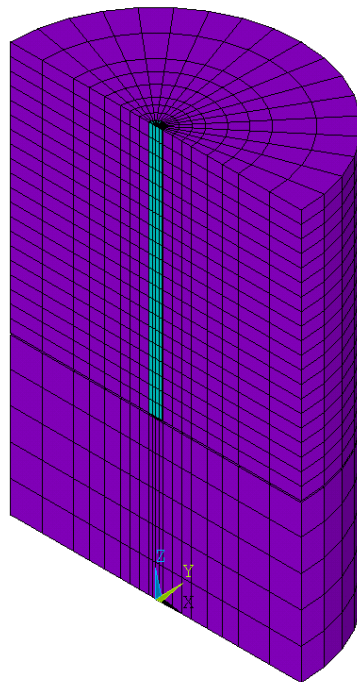
Šmyková výstuž sa navrhuje v tvare skrutkovice, prípadne v tvare uzavretých strmeňov s priemerom 5,5 až 8 mm. Výška závitú skrutkovice alebo vzdialenosť strmeňov je po výške piloty rozdielna. V spodnej a hornej časti je po 50 až 100 mm, v strednej časti piloty do 200 mm.

Monolitické piloty sa vystužujú pomocou výstužných košov, ktoré sa spúšťajú do vyrobeného otvoru. Kôš musí byť upravený tak, aby sa do otvoru mohla spustiť betónovacia rúra. Výstužné koše sa stykujú presahom.

3 Model konštrukcie

Riešená bola pilota dĺžky $l = 8,0$ m kruhového prierehového rezu s priemerom $\varnothing = 0,42$ m. Pilota bola vyrobená z materiálu, ktorého vlastnosti charakterizuje Youngov modul pružnosti $E_p = 2,1.107$ kPa. Podložie predstavuje málo únosné prostredie s modulom pružnosti $E_p = 1000$ kPa. Poissonovo číslo pre zeminu malo hodnotu $\mu = 0,35$. Pre výpočet boli použité dva zaťažovacie stavy: v prvom prípade je pilota v hlave zaťažená vodorovne pôsobiacou silou $F_x = 100$ kN, v druhom prípade je pilota v hlave zaťažená momentom $M_y = 100$ kNm.

ELEMENTS
TYPE NUM



Obrázok 1 – Model konštrukcie

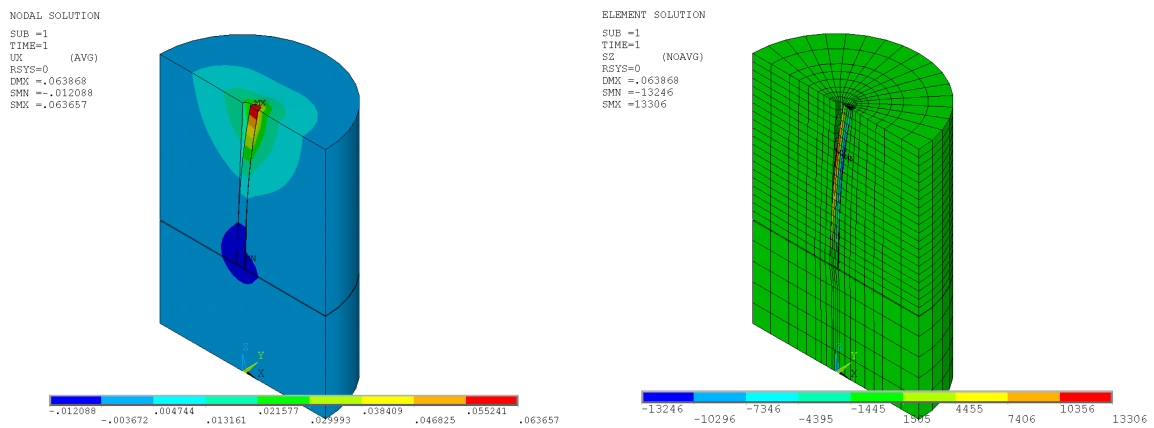
Vo výpočte boli použité rôzne spôsoby podopretia päty piloty: *voľný koniec*, *kĺbové podopretie* a *votknutie*.

Model konštrukcie bol vytvorený ako priestorový. Pilota bola modelovaná pomocou prvkov SOLID65 a okolitý zemný masív prvkami SOLID45. Z hľadiska kontaktu boli vytvorené 3 rôzne modely:

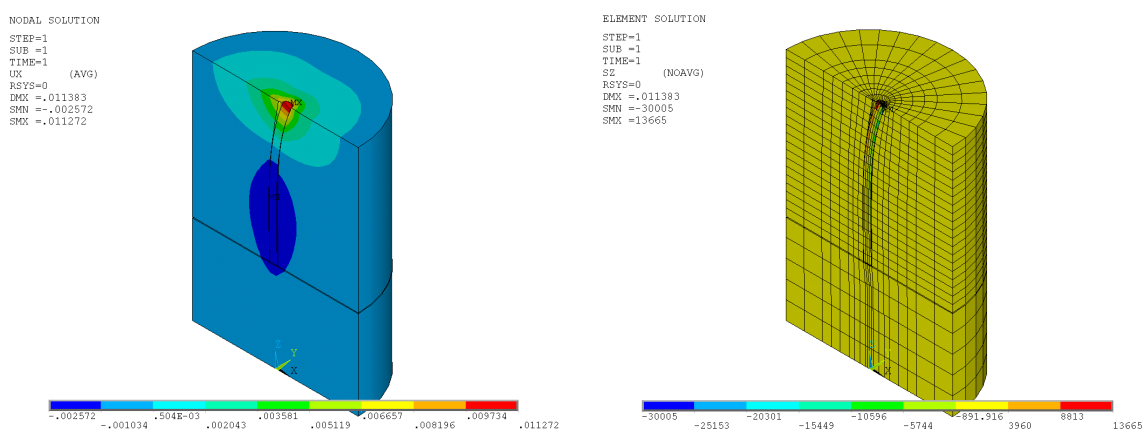
Tabuľka 1 – Popis modelov konštrukcie

Model konštr.	Typ kontaktu	Kontaktné prvky
A	bez kontaktu	–
B	bod – bod	CONTAC52
C	plocha – plocha	TARGE170 CONTA173

Na nasledujúcich obrázkoch sú pre ilustráciu uvedené výsledky priehybov a napätí pre model C, zaťaženie vodorovnou silou v hlave piloty a voľný koniec päty piloty.

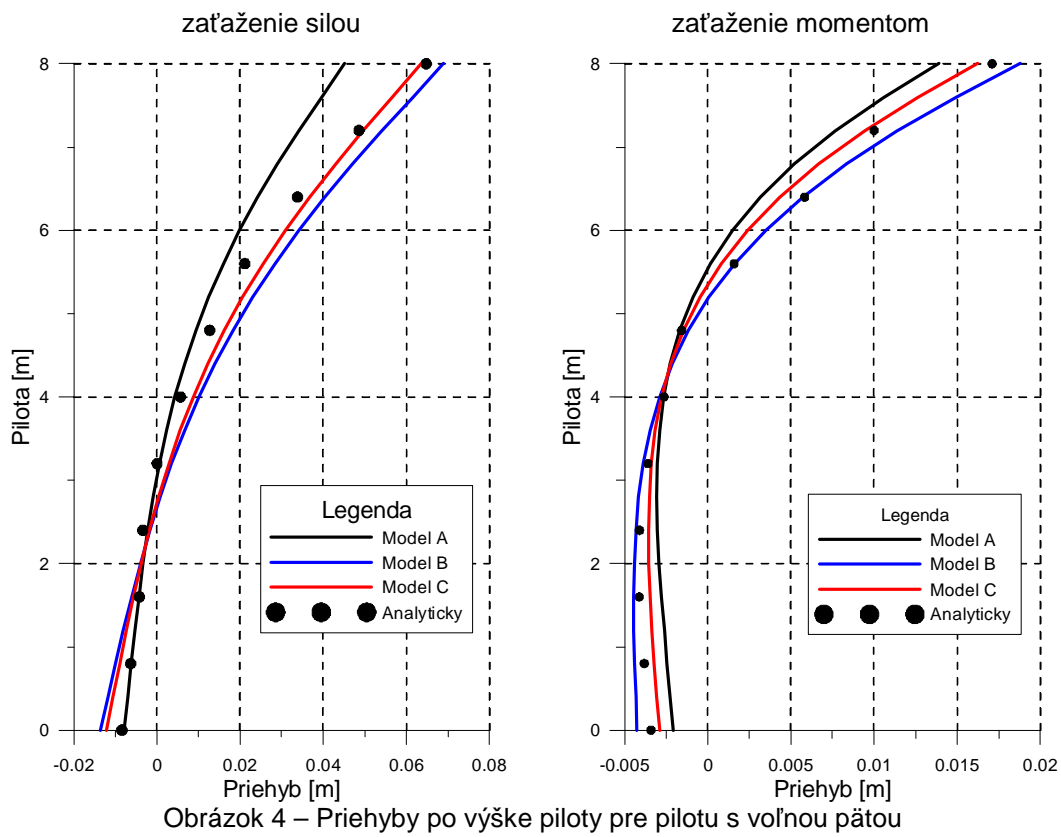


Obrázok 2 – Priebeg priehybov a napätí pri zaťažení vodorovnou silou

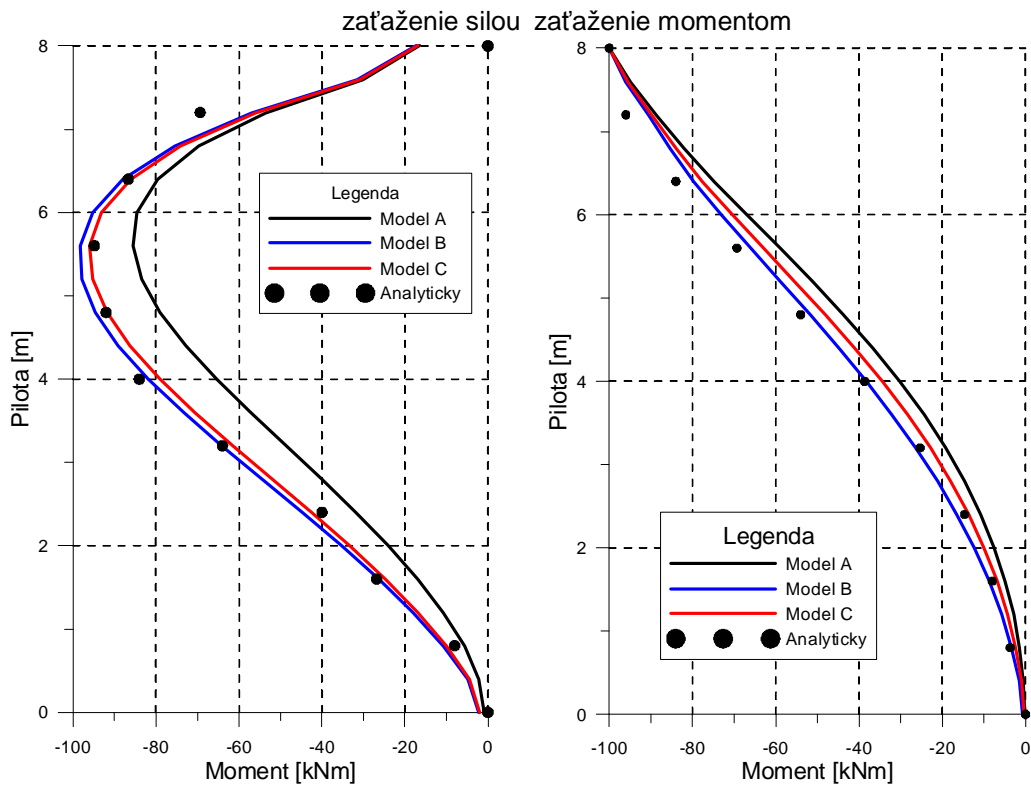


Obrázok 3 – Priebeg priehybov a napätí pri zaťažení momentom

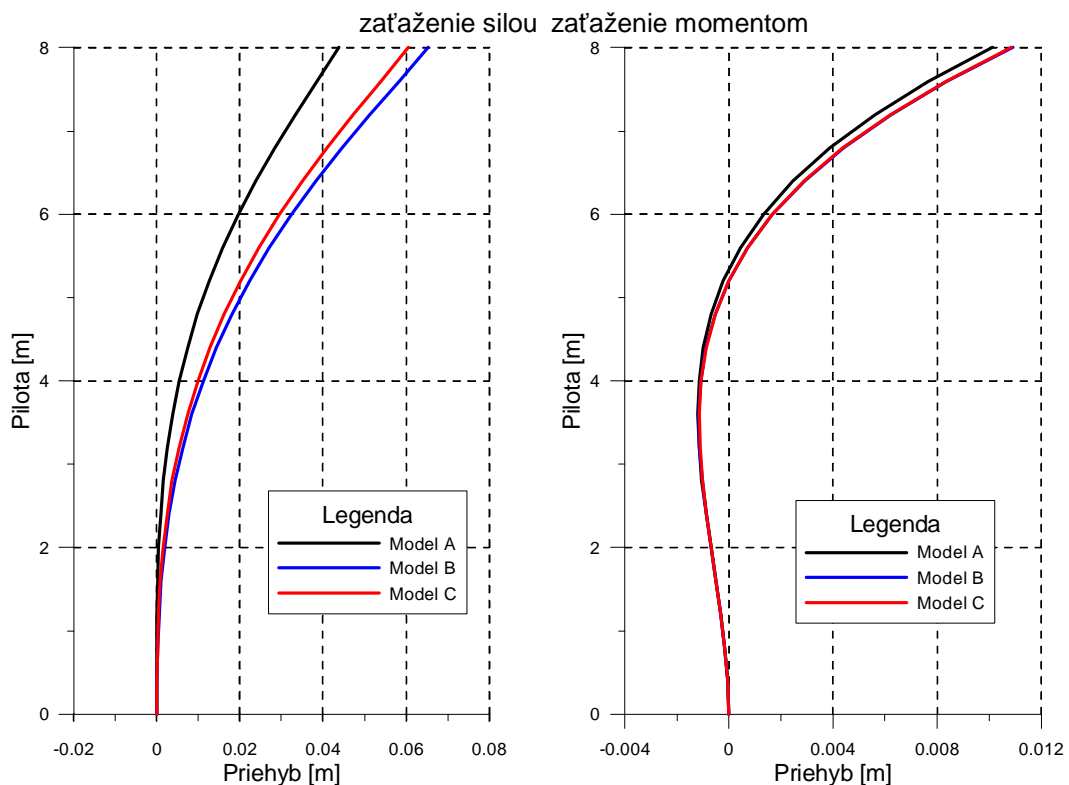
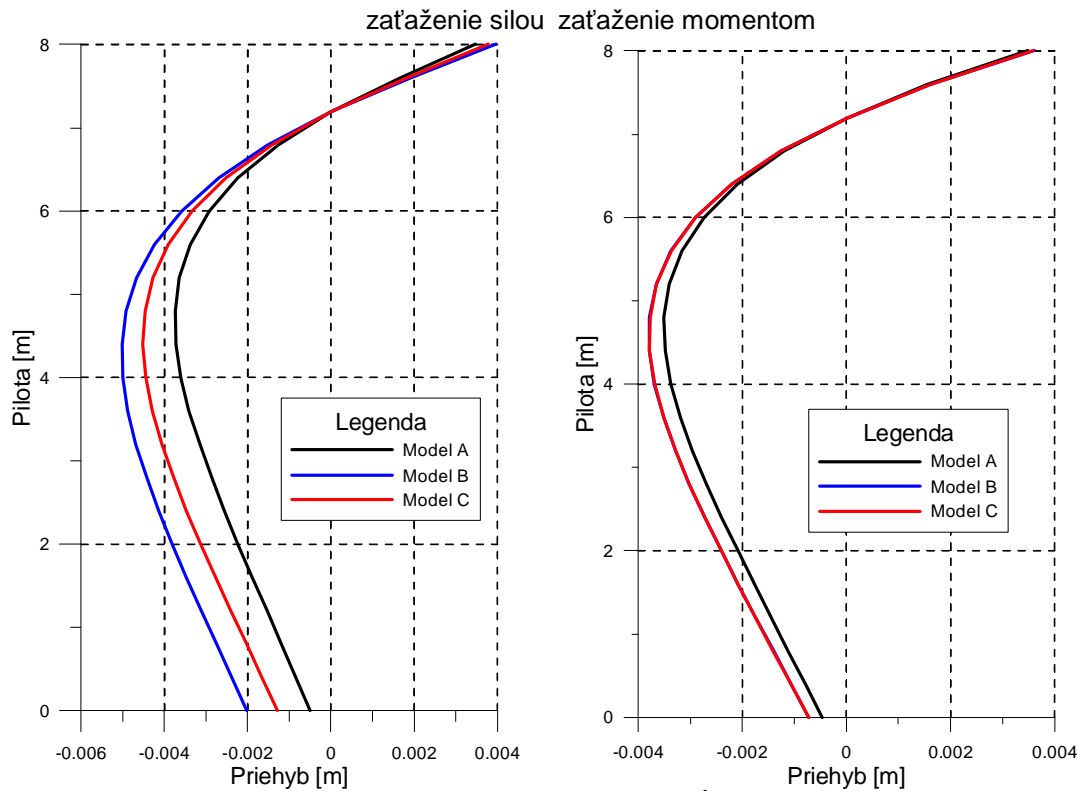
Výsledky riešenia jednotlivých zaťažovacích stavov, rôznych spôsobov podopretia a rôznych modelov kontaktu sú prezentované v nasledujúcich grafoch. V prípadoch, keď bolo k dispozícii analytické riešenie úlohy, je toto uvedené v grafických priebehoch priehybov a ohybových momentov po výške piloty.



Obrázok 4 – Priehyby po výške piloty pre pilotu s voľnou päťou



Obrázok 5 – Ohybové momenty po výške piloty pre pilotu s voľnou päťou



4 Záver

Na záver je možné konštatovať, že v prípade piloty s voľnou päťou je dosiahnutá pomerne dobrá zhoda veľkostí deformácií medzi modelmi s kontaktom (model B a model C) a analytickým riešením (pre tento prípad podopretia bolo analytické riešenie k dispozícii). Pre

ostatné dva prípady podpretia päty piloty je zrejmé, že riešenie pomocou modelovania kontaktu dosahuje oproti modelu bez kontaktu väčšie hodnoty. Pre prípad zaťaženie momentom prakticky nie sú rozdiely v prieťahoch pre modely kontaktu.

Literatúra

ANSYS ® User's Manual for Revision 12, Swanson Analysis Systems, Inc.

KOLLÁR, P., MISTRÍKOVÁ, Z.: 1985. *Spolupôsobenie ohybom namáhaných pilót s pružným polpriestorom – piloty voľné v päte*. Inžinierske stavby 01/1985, strany 29–39.

MAJDÚCH, D.: 1984. *Zásady vystužovania betónových konštrukcií*. Bratislava, Alfa, 368 strán.

PodĎakovanie

Príspevok bol vypracovaný v rámci grantovej úlohy VEGA č.1/0629/12.

Kontaktná adresa:

Ing.Ľubomír Prekop, PhD., lubomir.prekop@stuba.sk

Katedra stavebnej mechaniky, Stavebná fakulta STU, Radlinského 11, 813 68 Bratislava

A STUDY OF THE CENTRIFUGAL COMPRESSOR DISCHARGE PIPELINE CONSTRAINED OSCILLATION

KIRILL SOLODYANKIN*, JIŘÍ BĚHAL

ČKD KOMPRESORY, a.s.

Abstract: The paper presents a solution of a pipeline constrained oscillation that appeared on a natural gas compression plant. The station operator complained about a problem after installation of new higher efficiency impellers. Series of pipeline modifications were suggested for the problem solution. The structural modifications were simulated by the Finite Elements Method in ANSYS Workbench v.13.0. The numerical calculation results were compared to the each single modification and were verified by experimental measurements of the discharge pipeline shell oscillation.

Keywords: oscillation, pulsation, discharge pipeline, blade pass frequency, harmonic analysis

1 Introduction

Vibration of the mechanical systems is a well-known technical term and a widely analyzed phenomenon. Vibration problems appear in the whole range of machines with reciprocating and rotation parts movement. In addition, the mechanical vibration problem can be observed in machines which are exposed to external or internal excitation pulses. Coherent process technology influencing can be a good example of an external excitation force. The forces from unbalanced rotor parts, flowing medium turbulence or operating environment pulsation are typical internal excitation forces.

Mechanical vibrations are common for compressor machinery applications. In certain circumstances vibration complicates a safe operation. An agreement between the natural frequency of the system and an excitation frequency can lead to a resonance state of a mechanical system and cause an incident or failure.

ČKD Kompresory, a.s. is a traditional manufacturer of industrial compressors of both turbo- and reciprocating design. Three centrifugal compressors were renovated on a natural gas compression plant in 2011. Retrofit mainly covered modernization of the stator inserts and impellers with higher nominal parameters. Increased vibration of a discharge piping was reported after the first compressor proof test. Moreover, break-downs of measurement sensors, like temperature and pressure gages, were detected after the next short-time operating. Although compressor pipelines are commonly designed for particular compressor machines and not vice versa, compressor manufacturer offered a qualified technical assistance in vibration eliminating solution.

2 Vibration operating measurements

2.1 Technical parameters of the structure

With regard to the subject of retrofit, it is supposed, that higher discharge pressure pulsation can cause higher pipeline vibration. Moreover, the phenomenon of the system resonance state must be taken into account.

Compressor discharge pipeline design has following parameters:

- outer diameter 1020 mm,
- wall thickness 22 mm,
- pipeline material L415QB steel.

Centrifugal compressor has following nominal parameters:

- nominal rotation speed 3600 rpm,
- number of impeller vanes 14 pcs,
- pressure on the suction 4,85 MPa,
- pressure on the discharge 7,45 MPa,
- temperature on the suction 23 °C
- temperature on the discharge 60 °C

The centrifugal compressor is driven by a synchronous electric motor with variable speed range between 2700 rpm and 3900 rpm.

2.2 Operating measurements

Two peak frequencies of the compressor discharge pipeline shell were identified experimentally after vibration operating measurements were provided by an external company. The first pulsation peak is located near the frequency 1640 Hz. The second one is located near the frequency 2450 Hz. The amplitude-frequency response of the measurements is shown in the Diagram 1. These peak frequencies are located almost exactly in 2x and 3x blade pass frequency. The blade pass frequency (BPF) equals the product of the running rotor speed and the number of impeller vanes. This confirms the suspicion about compressor discharging pipeline shell resonance state. In other words, a clear system constrained oscillation phenomenon appears.

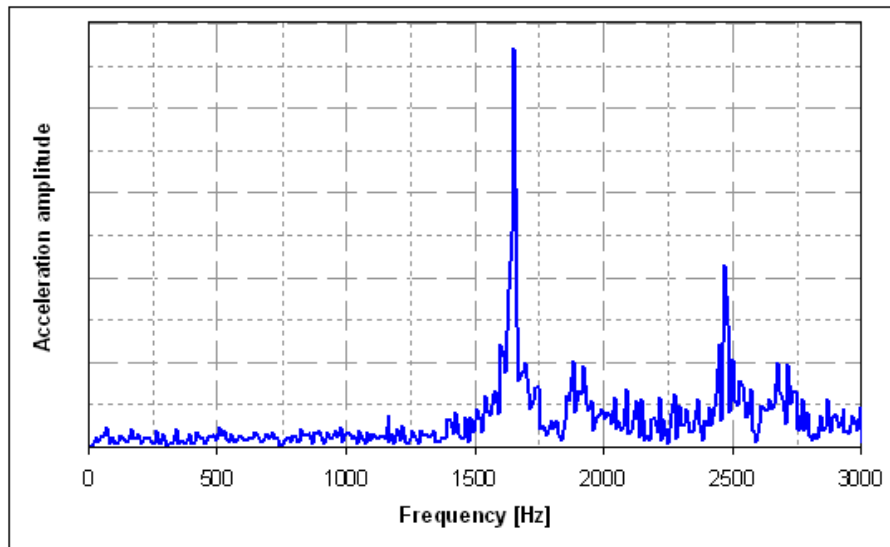


Diagram 1 - The amplitude-frequency measurement response

3 Numerical simulation of current discharge pipeline

3.1 Model for modal and harmonic analysis

Numerical simulation was done in several steps. First of all, it was necessary to confirm the peak pulsation frequency values and compressor discharge pipeline resonance state. Geometric model of the compressor set was simulated for the numerical calculations. Model consisted of compressor casing part and discharge pipeline part. Compressor casing part was derived from inner surface of the casing. The discharge pipeline was defined from compressor discharge branch to the second ell included. The model is in Image 33.

Geometry

ANSYS
2012

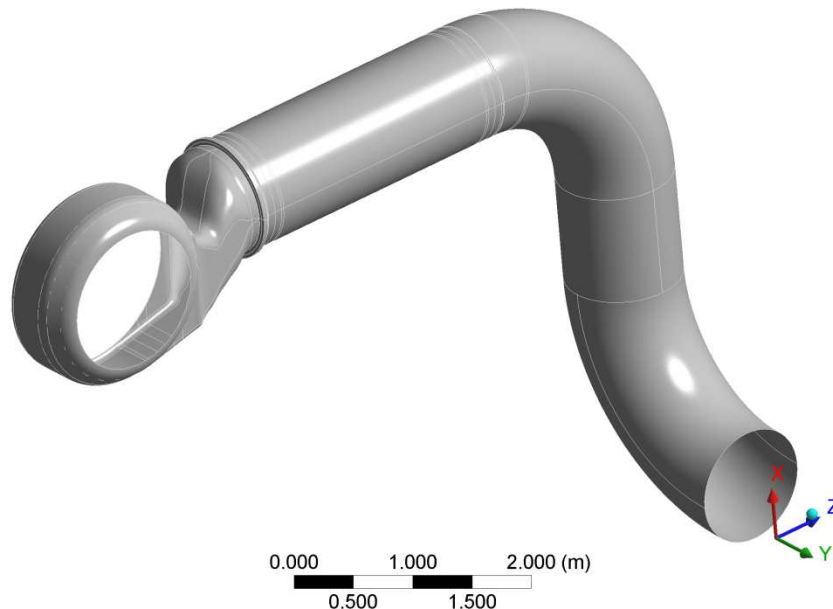


Image 33 – Geometric model for analysis

Mathematical model for modal and harmonic analysis was modelled by SHELL181 element type [1] in this step of simulation. Numerical model consisted of approximately

35 000 elements and 35 000 calculating nodes (Image 34). Compressor casing part was bound by Fixed Support on the side edges. Boundary conditions were the same for modal and harmonic analysis.

Numerical model for harmonic analysis was loaded by pressure pulsation, medium weight and deformations from omitted discharge pipeline part behind the second ell. Pressure pulsation was applied on an inner cylindrical surface of the discharge pipeline on 1 m length from compressor discharge branch. Loaded pipeline length and pressure pulsation value were determined from previous transient CFD simulation, which is not a subject of this paper. Deformations from omitted discharge pipeline were applied on the second ell cross-section. Values of directional deformations and rotation angles applied on the cross-section area were the output data from an external static analysis of discharge main and are not a subject of this paper. Constant damping ratio value was considered equal to 1%.

Mesh

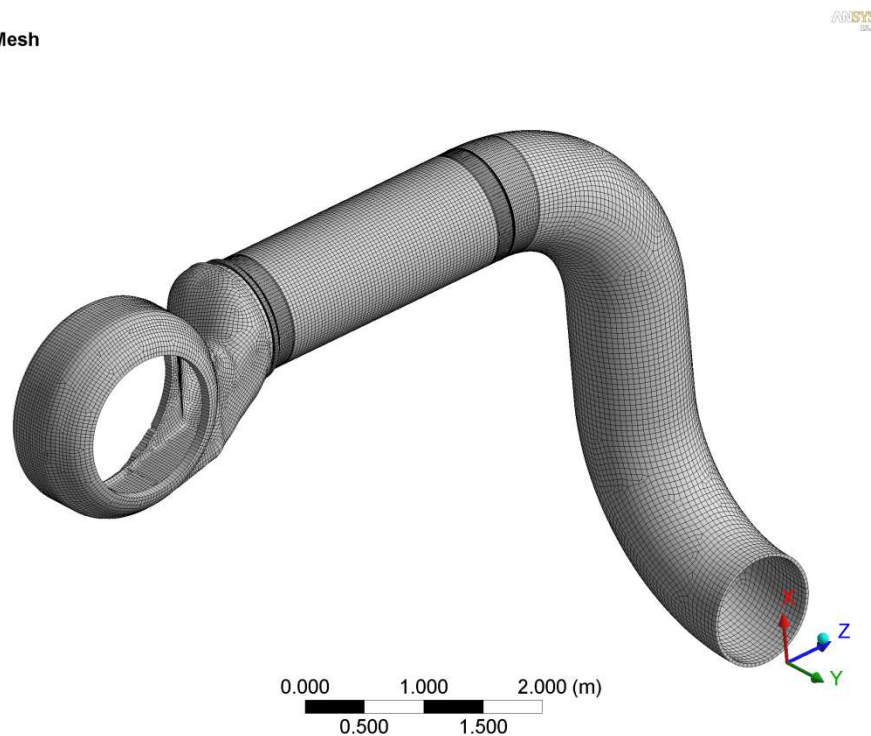


Image 34 – Numerical model with finite element mesh

3.2 Results of the current discharge pipeline harmonic analysis

Results of the modal analysis showed that a great number of shell mode piping natural frequencies is between 1500 Hz and 3000 Hz. But it doesn't mean that all of these modes can be excited. Resonance states of discharge pipeline and their shapes can be found out using the harmonic analysis. The Diagram 2 represents the harmonic response of discharge pipeline along 2.5 m length from compressor discharge branch. Analyzed length was determined with regards to temperature and pressure gages disposition on the pipeline. Harmonic amplitude-frequency response was calculated in frequency range between 0 Hz and 3000 Hz. Since exciting force value is unknown, calculated results might be used only for consequent comparison.

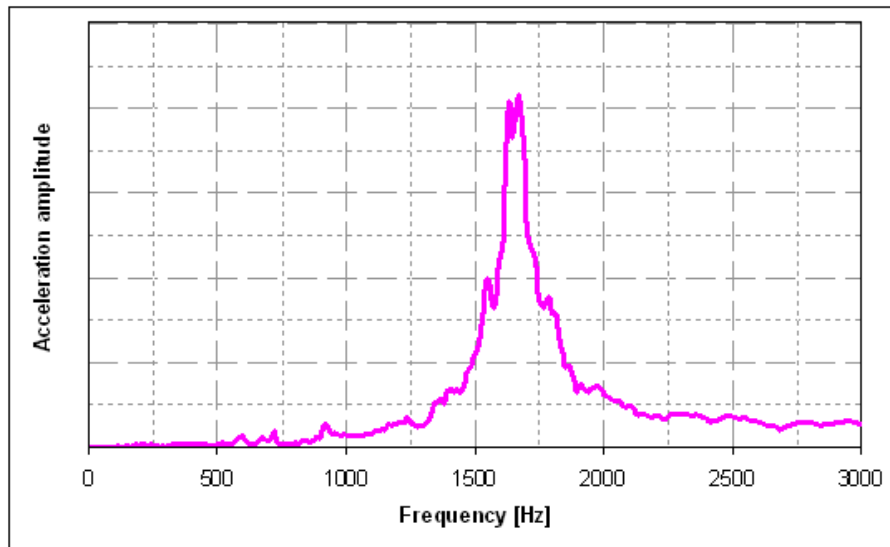


Diagram 2 – The amplitude-frequency calculated response

The first peak of frequency resonance state lies around the frequency 1630 Hz. Corresponding discharge pipeline shell shape mode is in Image 35. The second peak of frequency resonance state range was not determined in FEM simulation. It can be explained in several ways. Firstly, value of the constant damping ratio may be inappropriate. And secondly, it can be due to an unknown value and exciting force behavior. However, next adjusting of the numerical model was not carried out. It wasn't done because the maximum amplitude response at frequency around 1630 Hz is much higher than amplitude response at frequency 2450 Hz. It was supposed that damping of the first resonance response range would solve the problem of discharge pipeline constrained oscillation.

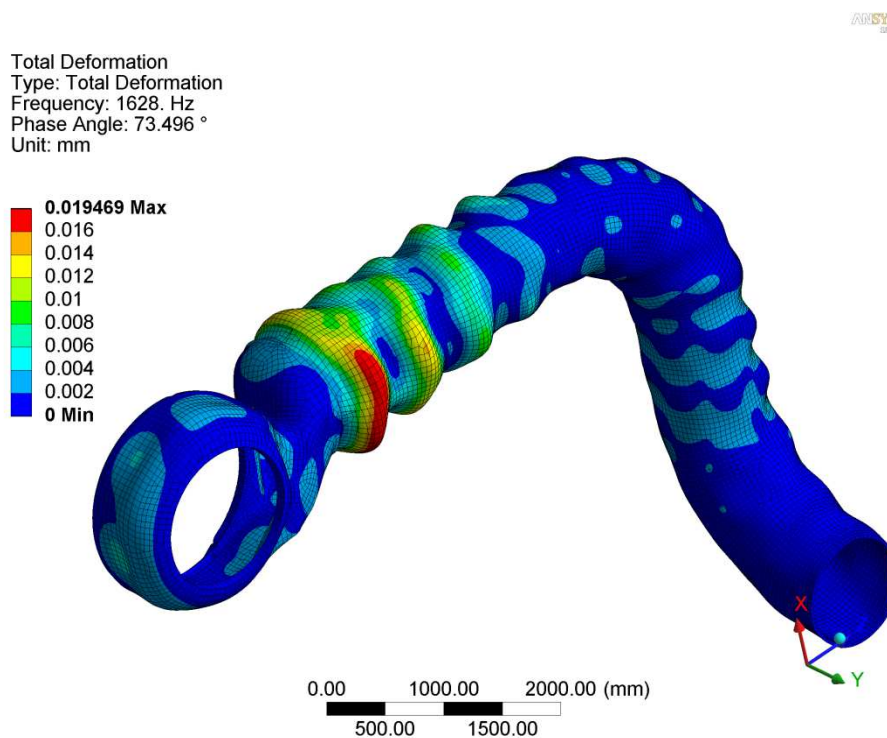


Image 35 – Mode shape of the current discharge pipeline at frequency 1630 Hz

4 Damping using an external system

4.1 External damping system design

According to operating measurements, discharge pipeline oscillation decreases significantly with the distance along pipeline. Therefore, discharge pipeline damping drafts were aimed at the first pipe section along 2.5 m length between discharge compressor branch and the first ell.

The first modification draft included damping by an external vibration absorber. Vibration absorber consisted of elastic metal cushions and supporting structure for the positioning and fixing on the discharge pipeline shell. The damping draft drawing is in Image 36. The cushions are formed from knitted wire mesh with elastic properties. Damping by cushions is caused by friction between the individual wire windings. More information about metal cushions can be found on the manufacturer's web-site [4].

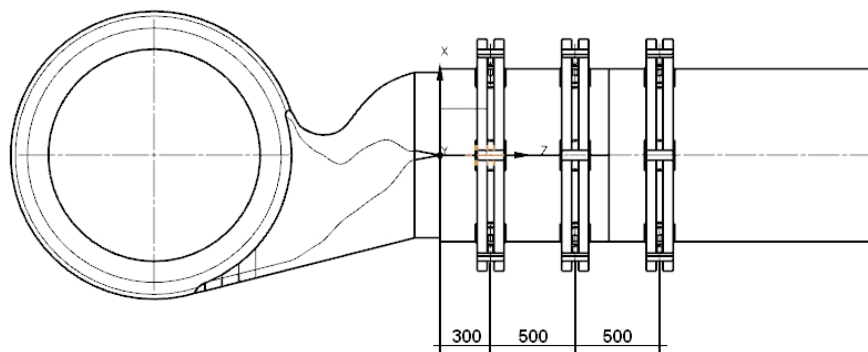


Image 36 – Vibration absorber design

4.2 Harmonic analysis of the first damping draft

Geometrical model from previous analysis was complemented by damping absorber model. Damping metal cushions were modelled by finite element COMBIN14 [1]. Stiffness and damping values were specified in compliance with manufacturer's data. Damping assisting system construction was modelled by finite element SOLID186. The mathematical model of pipeline, boundary conditions and loads remained the same as in previous analysis.

Results of the first damping draft numerical simulation showed a significant vibration damping of the first pipeline section. Oscillation amplitude decreased to 50%.

4.3 Realization and operating measurement of the first damping draft

External damping absorber was manufactured and installed on the compressor discharge pipeline. After that, the vibration operating measurement was provided. Unfortunately, vibration declination of the discharge pipeline shell was low. The Diagram 3 shows comparison between the operating measurement results for pipeline with and without external damping absorber.

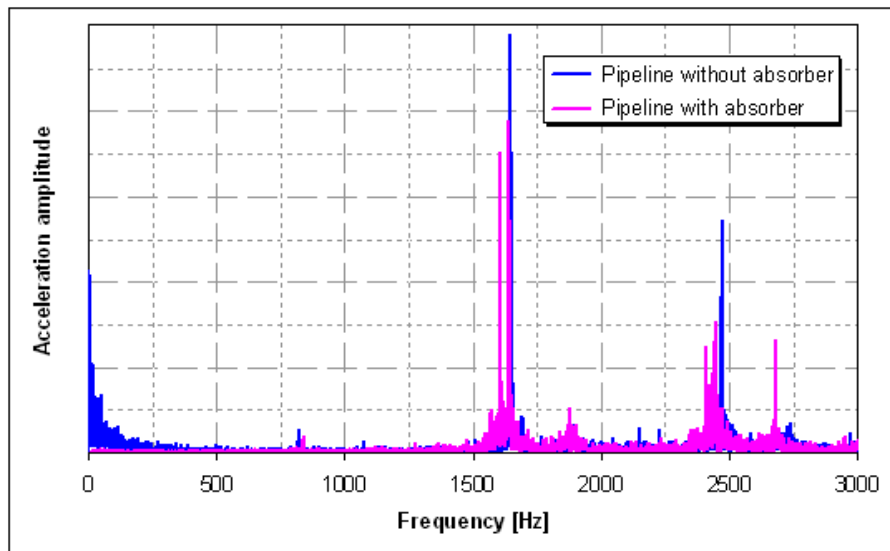


Diagram 3 – Amplitude-frequency measurement response comparison between pipeline with and without damping absorber

Mismatch of calculated and measured results can be explained by several circumstances. Firstly, metal cushions damping efficiency depends on the normal to cushion displacement magnitude. The value of the normal displacement of discharge pipeline shell is approximately $20\ \mu\text{m}$. Probably, this value is too low to develop appropriate friction between the individual wire windings. Secondly, damping absorber has six metal cushions. It is very difficult to set the same assembling conditions for each cushion during installation in practice. Possibly, the initial compression of each cushion can be different. And finally, the contact surface between metal cushions and pipeline shell was insufficient for effective oscillation damping.

5 Damping using a wall thickness increasing

5.1 Stiffness increasing design

The second vibration damping draft included stiffness increasing of the pipeline shell. The simplest way how to do this is increase the pipeline wall thickness. It was supposed that the first section pipeline with 22 mm wall thickness is replaced by another with 45 mm wall thickness. The substituting pipeline length is approximately 2.5 m long. Decreasing of the resonance state shell amplitude maximum values was expected. Additionally, it is possible to shift the resonance frequency of pipeline shell out of the resonance frequency range by stiffness changing.

5.2 Harmonic analysis of the second damping draft

Harmonic analysis of the pipeline design with increased stiffness was simulated for the efficiency and operating safety confirmation. Geometrical model of current pipeline was modified by the first section wall thickness increasing from 22 mm to 45 mm. Pipeline geometry was also complemented by detailed models of the welds between the new pipeline section and discharge compressor branch or the first ell respectively. The rest of geometrical model didn't change. Detailed welded connections were modelled by SOLID186 and are shown in the Image 37a and Image 37b. Boundary conditions and loads remained the same as in harmonic analysis of original pipeline.

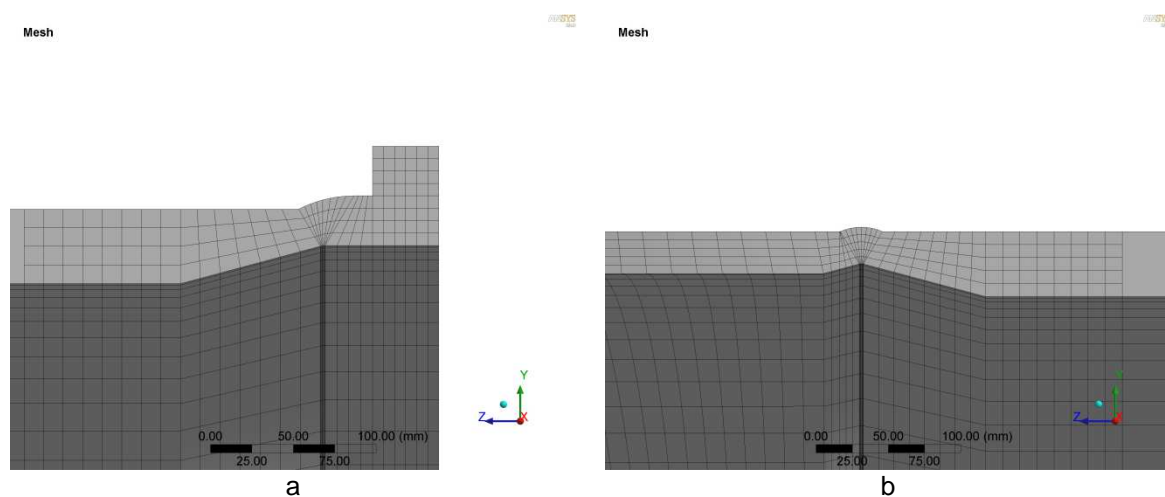


Image 37 – Welded connections on new pipeline section

a – on compressor discharge branch side

b – on first pipeline ell side

According to the analysis results, the maximum value of amplitude-frequency response decreased by 70%. The Diagram 4 shows comparison of the calculated results for original pipeline and discharge pipeline with increased stiffness. Image 38 shows the calculated shell mode shape of discharge pipeline at 1636 Hz frequency value. The mode shape of the pipeline with increased stiffness is nearly the same as for current pipeline shape form.

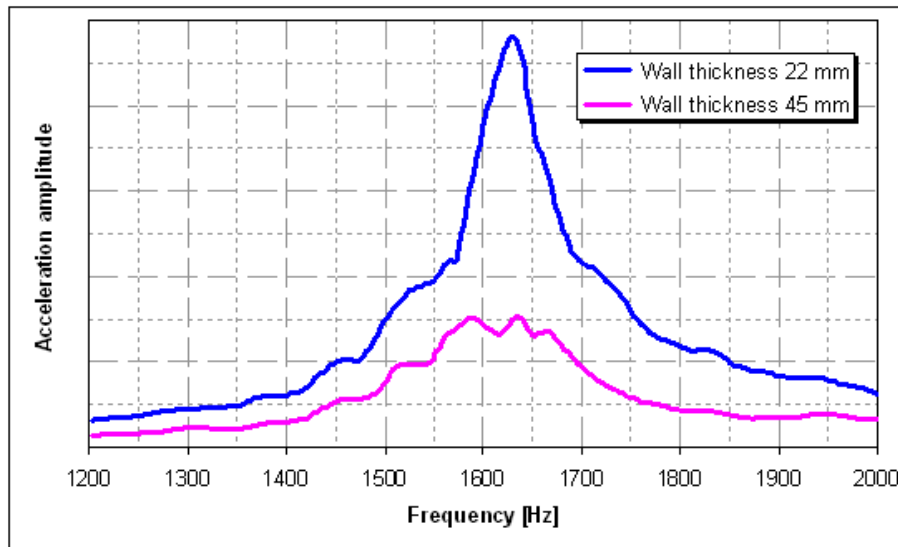


Diagram 4 – Amplitude-frequency calculated response comparison for pipeline with 22 mm and 45 mm wall thicknesses

Total Deformation
 Type: Total Deformation
 Frequency: 1636. Hz
 Phase Angle: 86.403 °
 Unit: mm

0.006207 Max
 0.0056
 0.0049
 0.0042
 0.0035
 0.0028
 0.0021
 0.0014
 0.0007
 0 Min

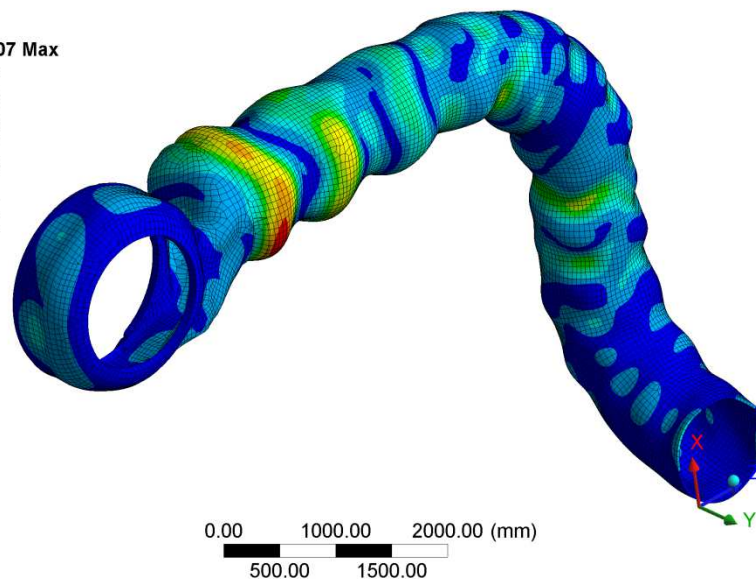


Image 38 – Mode shape of the discharge pipeline with 45 mm wall thickness at frequency 1636 Hz

The maximum equivalent stress values were calculated in discharge pipeline harmonic analysis. Their locations are on welds between the new pipeline section and discharge compressor branch or the first ell respectively. The first maximum equivalent stress value is equal to 4 MPa and is located on the welded connection between discharge compressor branch and new pipeline section. The second maximum equivalent stress value 2 MPa is on the welded connection between new pipeline section and first ell. These values are considered as amplitudes superposed on nominal stress distribution. Image 39 and Image 40 show the equivalent stress distribution from harmonic loading for both welded connections.

I: Potrubi t=45mm
 Equivalent Stress
 Type: Equivalent (von-Mises) Stress
 Unit: MPa

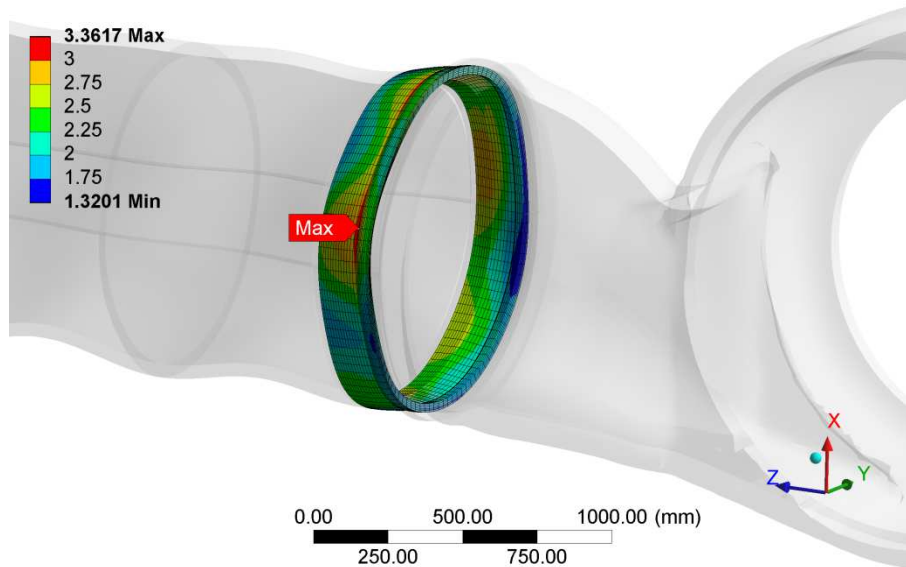


Image 39 – Equivalent stress distribution in the first welded connection

I: Potrubi t=45mm
 Equivalent Stress
 Type: Equivalent (von-Mises) Stress
 Unit: MPa

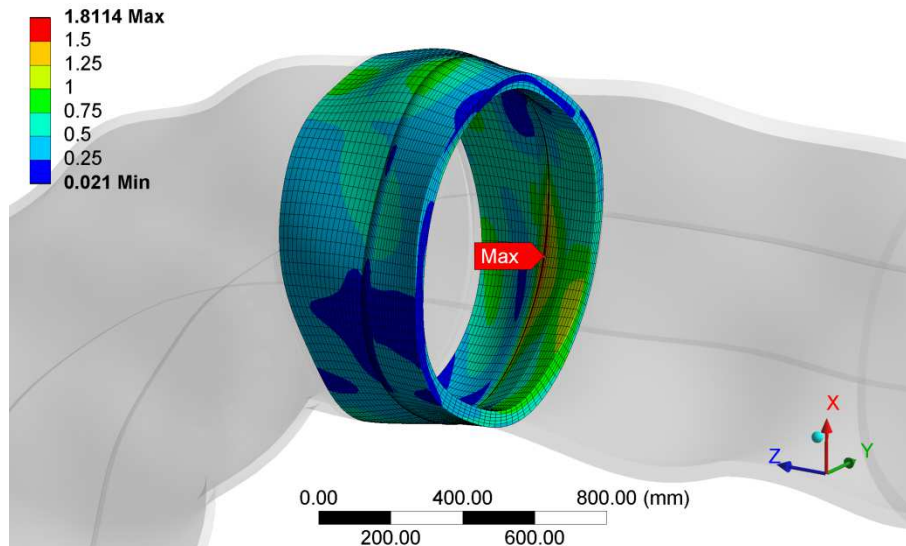


Image 40 - Equivalent stress distribution in the second welded connection

5.3 Strength analysis of the second damping draft

Strength analysis was done in order to confirm the safety of long-term operation of compressor discharge pipeline. Moreover, it was important to analyze the static stress from operation loads in new welded connections. Two critical zones with maximum equivalent stress values on the new welded connections were chosen. Image 41a and Image 41b show the stress distribution in the new welded connections from the static loading. The maximum

equivalent stress value in the first welded connection is 171 MPa, in the second welded connection is 234 MPa.

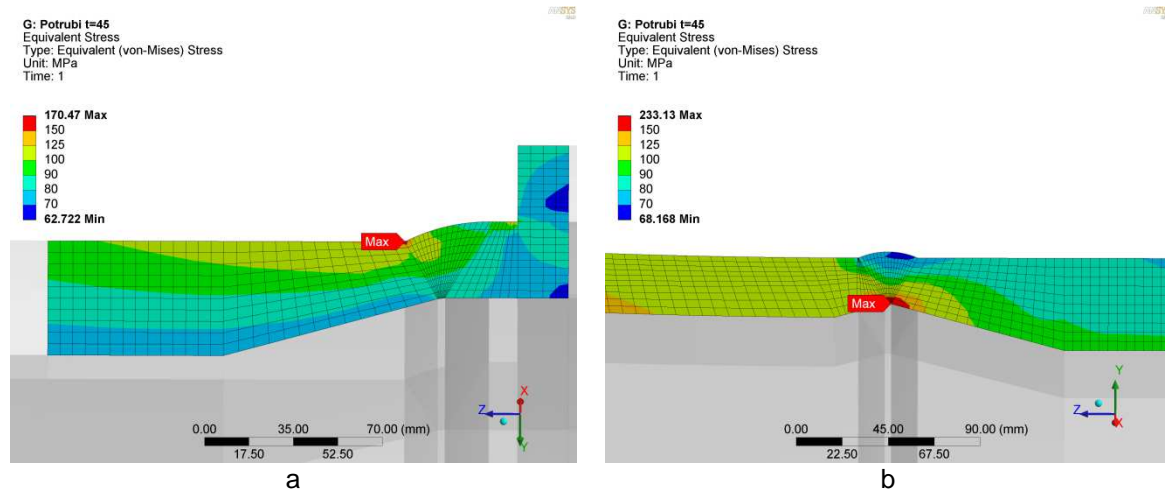


Image 41 – Equivalent stress distribution in the new pipeline section welded connections
a – on compressor discharge branch side
b – on first pipeline ell side

The stress analysis of the discharge pipeline shell was done according to the European Standard [2]. The resultant stress σ_v shall be compared with allowable stress σ_d . The standard allows using HMM stress for the analysis. The HMM stress can be calculated in accordance with equation (1), or can be taken directly from the FEM analysis.

$$\sigma_{HMM} = \sqrt{\sigma_x^2 + \sigma_y^2 + \sigma_z^2 - \sigma_x \cdot \sigma_y - \sigma_x \cdot \sigma_z - \sigma_y \cdot \sigma_z + 3 \cdot (\tau_x^2 + \tau_y^2 + \tau_z^2)} \quad (1)$$

where $\sigma_x, \sigma_y, \sigma_z$ – principal normal stresses, [MPa];

τ_x, τ_y, τ_z – principal shear stresses, [MPa].

The allowable stress σ_d is calculated in accordance with equation (2):

$$\sigma_d = 0.72 \cdot R_{t0.5} \quad (2)$$

where $R_{t0.5}$ – minimum 0.5% proof strength, [MPa].

The resultant stress σ_v is determined by the sum of stress values from static and dynamic loadings in accordance with equation (3).

$$\sigma_v = \sigma_{st} + \sigma_{dyn} \quad (3)$$

where σ_{st} – stress from static loading [MPa];

σ_{dyn} – stress from dynamic loading [MPa].

Mechanical properties of discharge pipeline material are in the Table 1. The mechanical properties are given in accordance with the European Standard [3].

Table 1 L415QB mechanical properties

ρ [kg·m ⁻³]	ν	E [MPa]	$R_{t0.5}$ [MPa]	R_m [MPa]
7 850	0.3	210 000	415	520

Resultant stresses for the first and the second critical places are:

$$\sigma_v^I = 171 + 4 = 175 \text{ [MPa]} \quad (4)$$

$$\sigma_v^{II} = 234 + 2 = 236 \text{ [MPa]} \quad (5)$$

The allowable stress is:

$$\sigma_d = 0,72 \cdot 415 = 298,8 \text{ [MPa]} \quad (6)$$

By comparing result stresses for the first and second welded connections with allowable stress the following can be received:

$$\sigma_v^I = 175 \text{ MPa} < 298,8 \text{ MPa} = \sigma_d \quad - \text{ satisfactory} \quad (7)$$

$$\sigma_v^{II} = 236 \text{ MPa} < 298,8 \text{ MPa} = \sigma_d \quad - \text{ satisfactory} \quad (8)$$

The design with increased stiffness of the compressor discharge pipeline satisfies the European Standard requirements.

6 Conclusion

The constrained oscillation of the centrifugal compressor discharge pipeline was analyzed by FEM and was compared to operating measurements. Two design improvements were offered to solve the resonance state of the compressor discharge pipeline.

The first improvement was damping by the external vibration absorber with elastic metal cushions. This draft was analyzed and experimentally validated. The first draft was rejected after the operation measurement because of low efficiency.

Damping by pipeline wall thickness increasing was the second improvement draft. It was supposed that stiffness is increased by replacing the first discharge pipeline section 2.5 m long with the new one. The new pipeline section has 45 mm wall thickness compared to the 22 mm wall thickness of original one. The second draft was analyzed by FEM and evaluated according to European Standards. Practical realization of the second improvement will have been done by the end of 2012.

Acknowledgement

This paper was supported by the Ministry of Industry and Trade of the Czech Republic within the project FR-TI2/206.

References

- [1] ANSYS 13.0 Help
- [2] EN 1594, 2009. Gas supply systems – Pipelines for maximum operating pressure over 16 bar.
- [3] EN 10208, 2009. Steel pipes for pipelines for combustible fluids.
- [4] [<http://www.stop-choc.de>]

Contact address:

Ing. Kirill Solodyankin
ČKD KOMPRESORY, a.s.
Klečákova 347
190 02 Prague 9
Czech Republic
E-mail: kirill.solodyankin@ckdkompresory.cz

PARAMETRIZACE DYNAMICKÉHO ZATÍŽENÍ OBĚŽNÝCH KOL RADIÁLNÍCH KOMPRESORŮ

OTO ŠTĚPANÍK*, KIRILL SOLODYANKIN, JIŘÍ BĚHAL

ČKD KOMPRESORY, a.s.

Abstract: The article is focused on dynamic loading of radial compressor impeller. Calculated data evaluation of common impeller types is shown in this paper. Data are parameterized and critical curves of tip speed are developed. The methodology and results will be used for elimination of impeller vibration risk in the course of design of compressor flow channel.

Keywords: Modal analysis, Impeller, Dynamic load, Vibration, Cyclic sector

1 Úvod

Maximální dovolená obvodová rychlost oběžného kola, nebo maximální dovolené provozní otáčky kola, jsou limitovány hlavně pevností materiálu kola. Zároveň je také pevnost kola ovlivněna statickým zatížením od odstředivých sil a dynamickým zatížením od nerovnoměrností tlakového pole stlačovaného media. Tento článek se primárně zabývá výpočty dynamického namáhání oběžných kol a omezením obvodové rychlosti z hlediska dynamického zatížení.

2 Řešená problematika dynamického zatížení

Nerovnoměrnosti tlakového pole vyvolávají vynucené kmitání mechanické struktury oběžného kola. Nejvíce náchylným konstrukčním prvkem na vynucené kmitání oběžného kola je oblast mezilopatkových segmentů krycího a nosného kotouče. Kmitání mezilopatkových segmentů [2] hrozí poruchou oběžného kola a odstavením stroje, případně zastavením celé technologie spojené s velkými materiálními náklady. Protože se jedná o vysokofrekvenční kmitání, primárním mechanismem porušení kola je porušení vysokocyklovou únavou.

Vzhledem k poměrně komplikovanému termodynamickému výpočtu proudění media průtočnou částí uvnitř kola, a také vzhledem k náročné nestacionární simulaci interakce mezi konstrukčními prvky oběžného kola se statorovými součástmi kompresoru, praktický není možné napočítat velikosti budících sil od nerovnoměrností tlakového pole. Z toho důvodu se posouzení dynamického zatížení oběžného kola muselo zjednodušit pouze na hodnocení vlastních tvarů a frekvencí kmitání struktury kola. Tímto způsobem hodnocení je možné se s dostatečnou přesností vyhnout rezonančním stavům konstrukce.

Pro hlubší pochopení problematiky porušení oběžného kola vlivem vysokofrekvenčního kmitání mezilopatkových segmentů je nutné se seznámit s geometrií samotného kola. Na Obr. 1 je znázorněno běžné konstrukční provedení oběžného kola radiálního kompresoru. V místech koncentrace napětí se střídavým cyklem zatížení během vynuceného kmitání hrozí iniciace a šíření únavové trhliny. Nejčastěji se únavová trhlina iniciuje v oblasti přechodových rádiusů mezi lopatkou oběžného kola a krycím nebo nosným

kotoučem z vnější strany průměru kola. Na Obr. 2 je znázorněn případ únavového porušení oběžného kola radiálního kompresoru.

Hlavním cílem řešení problematiky dynamického zatížení oběžných kol bylo dosáhnout vyhovujících dynamických vlastností celé řady oběžných kol běžně vyráběných v ČKD Kompresory, a to v celém rozsahu běžných provozních otáček kompresorů.



Obr. 1 - Model prostorového oběžného kola radiálního kompresoru.



Obr. 2 – Ilustrace výskytu ulomení mezilopatkových segmentů oběžného kola.

3 Simulace pomocí metody konečných prvků

3.1 Modální analýza

Při modální analýze jsou vlastní frekvence Ω_i a vlastní tvary kmitu u_i vypočteny z rovnice:

$$([K] - \Omega_i^2 [M])\{u_i\} = 0 \quad (8)$$

kde K je matice tuhosti soustavy a M je matice hmotnosti soustavy [6]. Při výpočtu se předpokládá:

- lineární chování materiálu,
- použití teorie malých deformací a posuvů.
- Není počítáno s tlumením soustavy a
- systém není buzen vnějším zatížením (pravá strana rovnice je rovna nule).

U vlastních tvarů u_i neznáme jejich absolutní hodnoty, ale pouze poměry jednotlivých tvarů. V programu ANSYS jsou pro modální analýzu podporovány všechny typy geometrie těles: objemová, skořepinová i prutová tělesa.

Při výpočtu byla použita metoda Block Lanczos.

3.2 Cyklická symetrie

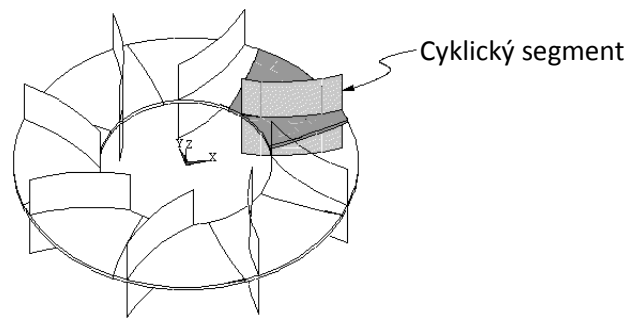
V případě rotačně periodických struktur lze využít jejich cyklické symetrie a rozdělit danou strukturu na cyklicky se opakující segmenty, Obr. 3. Tento přístup řádově snižuje počet elementů, resp. uzlů konečněprvkové sítě, a tím i nároky na výpočetní výkon a čas, při dosažení stejných výsledků jako u použití původní plné struktury.

Cyklická symetrie byla zadávána pomocí příkazů ANSYS Parametric Design Language (APDL). Hlavním příkazem, který předepisuje použití cyklické symetrie v analýze, je příkaz „CYCLIC“ [1]. U správně vytvořené sítě na plochách cyklické symetrie („Match Control“ viz. 5), není potřeba zadávat další parametry a v průběhu výpočtu bude automaticky stanoven úhel výseče segmentu a také jejich počet. U nekompatibilní sítě na plochách cyklické symetrie lze zadat cyklickou symetrii také „ručně“. Příkaz „CYCLIC“ pak obsahuje další parametry definující cyklickou symetrii struktury. Jednotlivé parametry jsou oddělovány čárkou a pořadí jejich zadávání je pevně dáno. Pořadí, v jakém se parametry definují, je následující:

- Počet cyklických segmentů
- Úhel výseče segmentu (ve stupních)
- Číslo cylindrického souřadného systému
- Název ploch cyklické symetrie segmentu
- Počet párů ploch cyklické symetrie segmentu

Pro nastavení analýzy s použitím cyklické symetrie lze použít příkaz „CYCOPT“. Při výpočtech byla používána možnost nastavení výběru vyhodnocovaných harmonických indexů pomocí příkazu „HINDEX“. Kompletní seznam všech možností nastavení je uveden v manuálu k programu ANSYS [1].

Při vyhodnocování výsledků byl použit příkaz „/CYCEXPAND“, který graficky rozvine cyklicky symetrický segment do původní plné struktury. Tento příkaz také slouží pro lepší posouzení vypočtených posuvů, napětí a přetvoření v cyklickém segmentu.

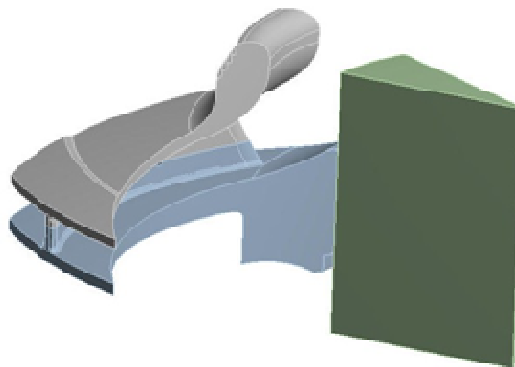


Obr. 3 - Princip tvorby cyklického segmentu [1].

3.3 Geometrický model

Geometrické modely pro výpočty byly získány na základě parametrických modelů oběžných kol. Vzhledem k tomu, že oběžné kolo obsahuje celou řadu konstrukčních parametrů, které ovlivňují velikost vlastních frekvencí (např. výstupní šířka kola, tloušťka krycího a nosného kotouče, tloušťka lopatek apod.), není prakticky možné ručně připravovat geometrii každého kola pro výpočty dynamického namáhání.

Samotný geometrický model pro výpočet dynamického zatížení představuje cyklický segment rotačně periodické struktury oběžného kola kompresoru a cyklický segment hřídele, Obr. 4, na kterém je kolo nasazeno. Doplnění geometrického modelu kola modelem hřídele je nezbytný pro zjištění zbytkové šířky kontaktu mezi nábojem kola a hřídelem během simulace roztáčení soustavy pro různé výpočetní otáčky. Zbylá šířka kontaktu hřídele s nábojem kola ovlivňuje vlastní frekvenci oběžného kola, a proto musí být do výpočtu zahrnuta.



Obr. 4 - Cyklický segment oběžného kola a hřídele.

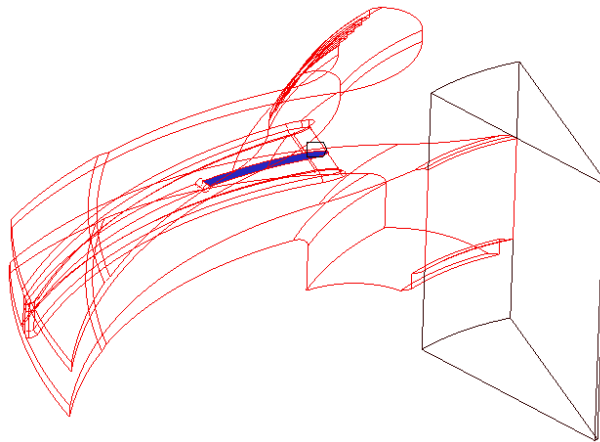
3.4 Matematický výpočetní model

Jak bylo již uvedeno výše, velikost kontaktní plochy mezi nábojem oběžného kola a hřídelí, ale také mezi nezavařenými konci lopatek se mění s velikostí provozních otáček stroje. Proto musí být nejdříve provedena statická analýza pro zjištění velikosti dotyku kontaktních ploch a také pro vyztužení struktury oběžného kola vlivem odstředivých sil. Tento předepnutý model oběžného kola pak slouží jako vstupní výpočetní model pro následnou modální analýzu.

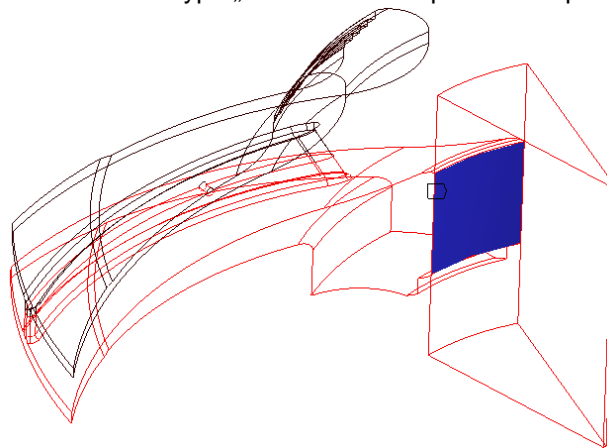
Pro statickou analýzu byl na kontaktních plochách výpočetního modelu definován třecí nelineární kontakt typu „Frictional“ s algoritmem „Augmented Lagrange“, Obr. 5 a Obr.

6. Koeficient tření byl zadán konstantou 0,12. V kontaktní ploše mezi nábojem oběžného kola a hřídelem byl navíc simulován přesah nalisování s hodnotou odpovídající technologickým předpisům ČKD Kompresory [2]. V navazující modální analýze byl nelineární typ kontaktu transformován do lineárního kontaktu typu „Bonded“ a veškeré kontaktní plochy s hodnotami kontaktního tlaku většími než 0 MPa byly slepeny. Tímto způsobem se simuloval stav oběžného kola při zatížení provozními otáčkami.

V samotné modální analýze byl proveden výpočet vlastních tvarů a frekvencí kmitání oběžného kola pro následné sestavení mezních křivek obvodových rychlostí z hlediska dynamického zatížení.



Obr. 5 - Kontakt typu „Frictional“ mezi plochami lopatky.



Obr. 6 - Kontakt typu „Frictional“ mezi nábojem kola a hřídelem.

4 Materiálové charakteristiky

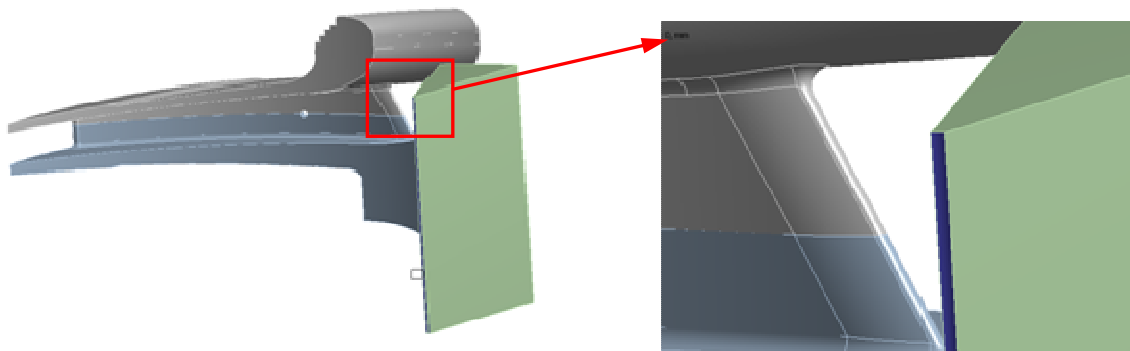
Oběžná kola se v ČKD Kompresory tradičně vyrábí z ocelových materiálů nebo z titanových slitin. Pro modální analýzu jsou dostačujícími materiálovými parametry pouze Youngův modul pružnosti v tahu E , Poissonův poměr ν a hustota materiálu ρ . Typické hodnoty těchto parametrů jsou uvedeny v Tabulce 9.

Tabulka 1 Materiálové parametry.

typ materiálu	příklad material	E [MPa]	ν [-]	ρ [kg/m ³]
ocel	X3CrNiMo13-4	$2,00 \cdot 10^5$	0,30	7700
titanová slitina	TiAl6V4	$1,14 \cdot 10^5$	0,36	4480

5 Okrajové podmínky a zatížení výpočetního modelu

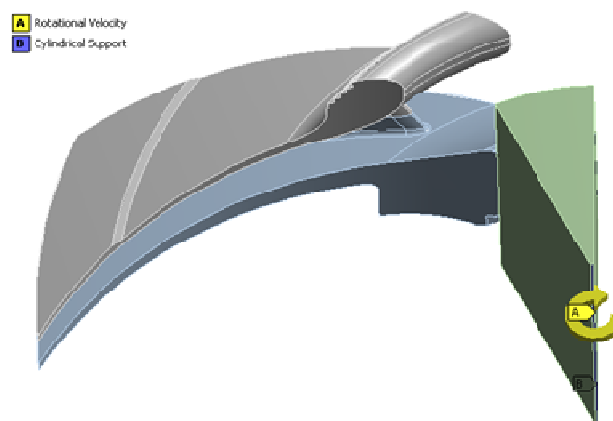
Okrajová podmínka „Cylindrical support“ byla aplikována na cylindrickou plochu hřídele, Obr. 7, která byla vytvořena pouze z důvodu modelování cyklického segmentu. Posuv plochy byl zamezen v tangenciálním, radiálním i axiálním směru.



Obr. 7 - Detail části plochy, na kterou byla aplikována okrajová podmínka.

Model byl při statické analýze zatěžován úhlovou rychlostí, Obr. 8, která byla vypočtena z obvodové rychlosti kola. Pro analýzu byly použity mezní hodnoty intervalu běžně používaných obvodových rychlostí oběžných kol v ČKD Kompresory.

V modální analýze byly vlastní tvary a frekvence počítány ve frekvenčním pásmu určeném právě z mezních hodnot obvodových rychlostí. Výsledné frekvenční pásmo se získá součinem otáčkové frekvence (odpovídající dané obvodové rychlosti) a počtem lopatek difuzoru.

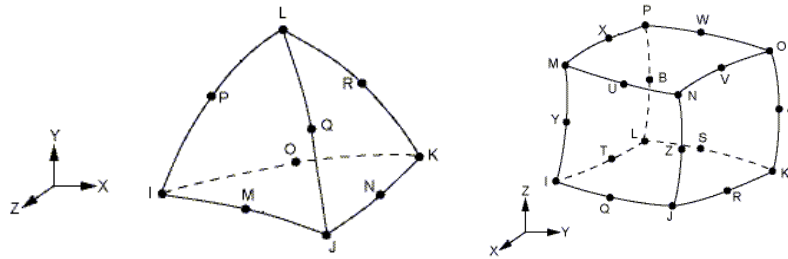


Obr. 8 - Zatížení modelu úhlovou rychlostí.

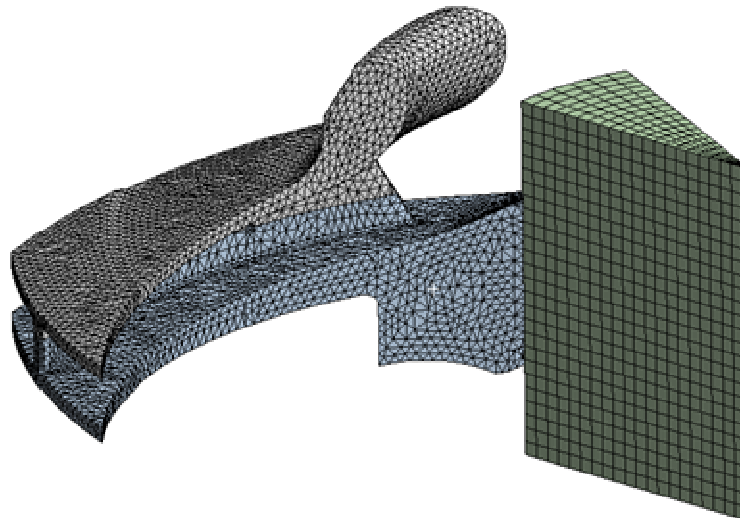
5 Výpočetní síť

Pro tvorbu sítě konečných prvků byly u kotouče použity kvadratické čtyřstěnné elementy typu SOLID187, u hřídele pak kvadratické šestistěnné elementy typu SOLID186, Obr. 9. Výpočetní síť byla relativně hrubá rovnoměrná [5], Obr. 10, s mírným zahuštěním v místech kontaktů a v přechodových rádiusech mezi lopatkou a nosným i krycím kotoučem.

Na plochy cyklické symetrie segmentu rotačně periodické struktury oběžného kola byla aplikována funkce „Match Control“. Tato funkce zajistí, že vytvořená konečněprvková síť na plochách cyklické symetrie bude shodná.



Obr. 9 - Vlevo element SOLID187, vpravo element SOLID186 [1].

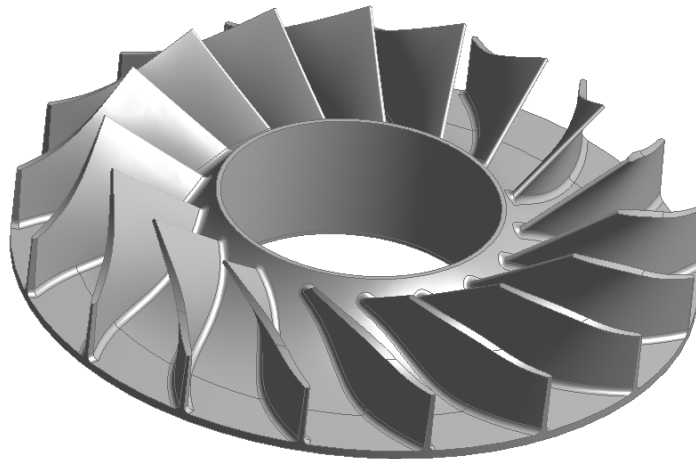


Obr. 10 - Výpočetní síť modelu.

6 Metodika hodnocení výsledků výpočtů

6.1 Oběžná kola otevřená (bez krycího kotouče)

U oběžných kol bez krycího kotouče se kontroluje první vlastní frekvence lopatky, která musí být vyšší než součin otáčkové frekvence a parametru k . Parametr k je celé číslo, jehož velikost se určuje v závislosti na hustotě proudícího plynu dle interního dokumentu [3].

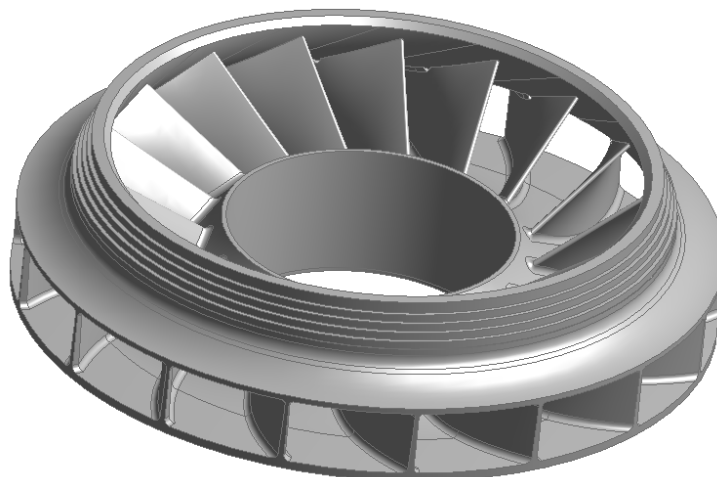


Obr. 11 - Otevřené oběžné kolo radiálního kompresoru

6.2 Oběžná kola zavřená (s krycím kotoučem)

U zavřených oběžných kol se zjišťují vlastní frekvence kmitání mezilopatkových segmentů na obvodu kola, které nesmí ležet v oblasti součinu otáčkové frekvence a počtu difuzorových lopatek.

Pro lepší názornost posouzení dynamického zatížení oběžného kola lze vlastní frekvence vyjádřit pomocí obvodových rychlostí, při kterých se mohou vybudit nebezpečné vlastní tvary kmitu odpovídající dané vlastní frekvenci.



Obr. 12 - Zavřené oběžné kolo radiálního kompresoru

6.3 Získání vlastní frekvence z výpočtu

Při výpočtu vlastních frekvencí byly použity mezní hodnoty rychlosti zatěžování a mezní hodnoty šířek kanálu. Hodnoty mezních šířek kanálu jsou rozdílné pro každou řadu

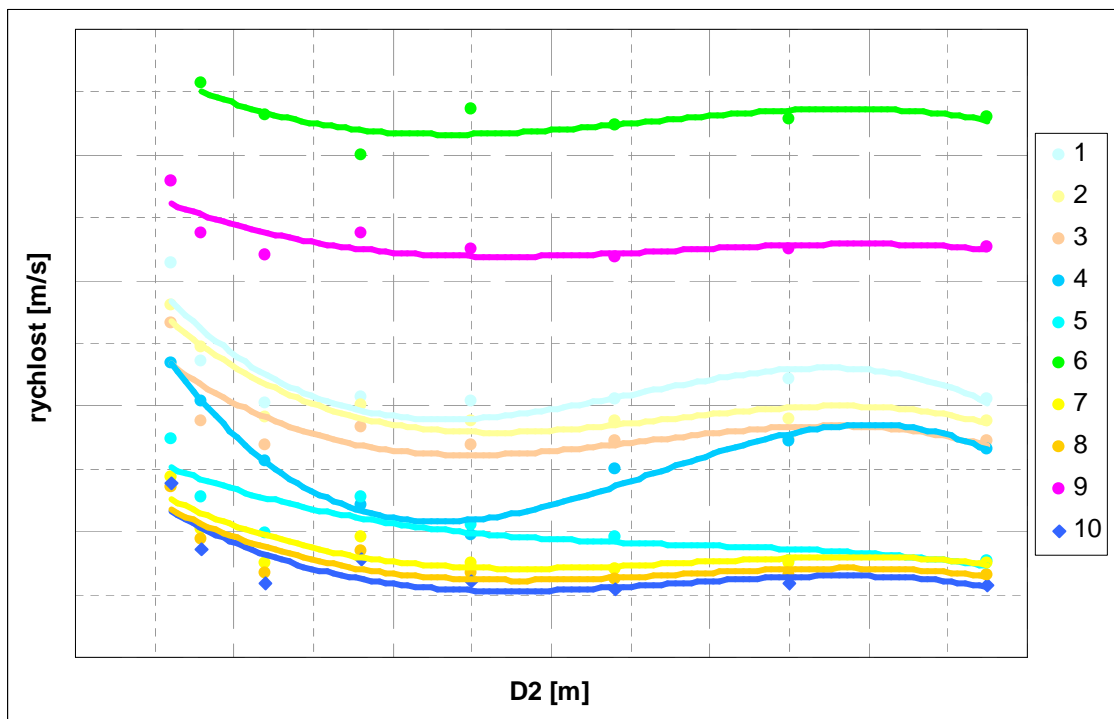
oběžných kol. K získání vlastní frekvence pro rychlost a šířku kanálu nacházející se uprostřed obou intervalů se použije lineární interpolace.

Pomocí této práce lze určit nebezpečné pásmo frekvencí, resp. rychlostí, pro libovolný průměr oběžného kola, šířku kanálu a provozní rychlost. Kontrola na dynamické zatížení se provádí pouze v případě, že oběžné kolo spadá do oblasti se zvýšeným dynamickým zatížením z hlediska vlivu hustoty stlačovaného media [7]. To platí pro kola z ocelových i titanových slitin.

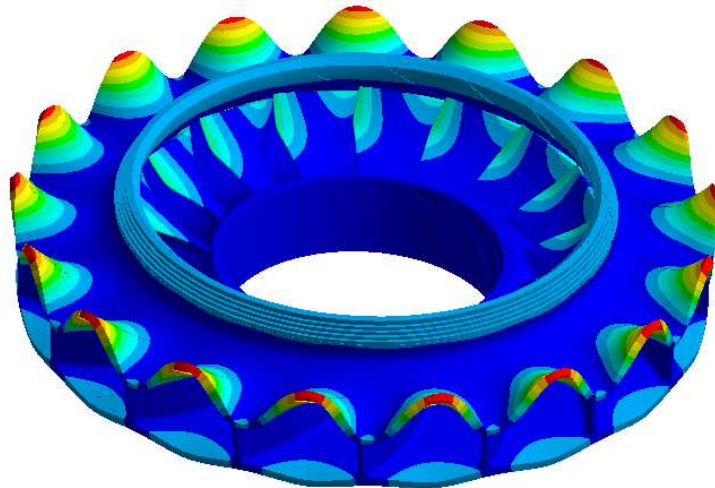
7 Souhrn výsledků výpočtu

7.1 Oběžná kola zavřená

Obr. 13Na Obr. 13 jsou zobrazeny průběhy rychlostí odpovídající nebezpečným tvarům kmitu pro typ kola s krycím kotoučem. Vyhodnoceno bylo celkem deset nebezpečných tvarů kmitu. Průběhy zobrazují případ, kdy velikost vlastních frekvencí (a tedy i jim odpovídající rychlosti) vycházejí nejmenší – nejširší kanál a nejmenší provozní rychlost.



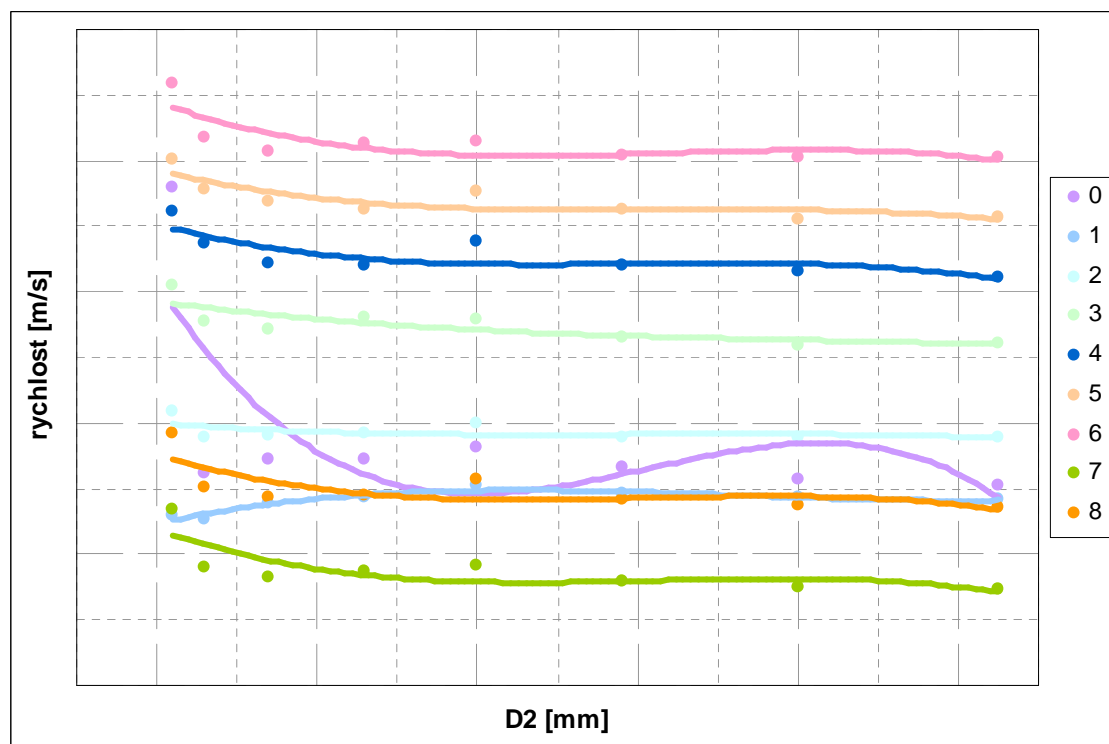
Obr. 13 - Průběh nebezpečných rychlostí v zavřeném typu kola 571.



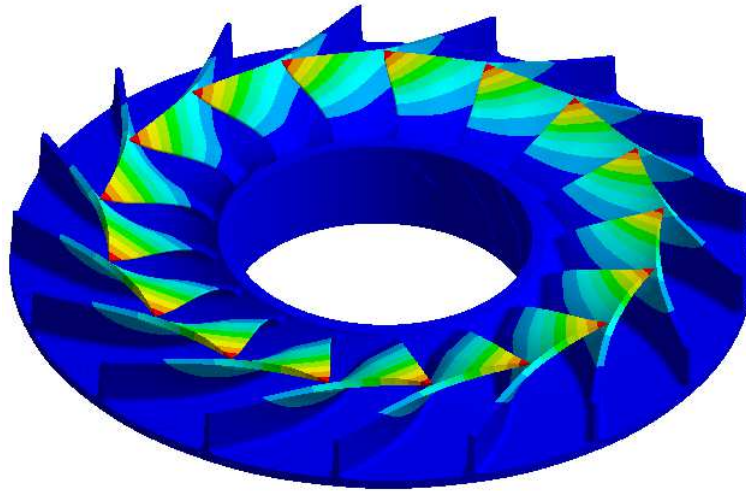
Obr. 14 - Ukázka nebezpečného tvaru kmitu mezilopatkových segmentů.

7.2 Oběžná kola otevřená

Zatímco u zavřených kol byly sledovány všechny nebezpečné tvary kmitu mezilopatkových segmentů, u otevřených kol byl sledován pouze první vlastní tvar kmitu lopatky ve všech harmonických indexech. Čísla v legendě na Obr. 15 (0 až 8) označují průběhy rychlostí odpovídající vlastním frekvencím prvního tvaru kmitu lopatky pro jednotlivé harmonické indexy.



Obr. 15 - Průběh nebezpečných rychlostí v otevřeném typu kola 571.



Obr. 16 - Ukázka nebezpečného tvaru kmitu lopatky.

8 Metodika výpočtu vlastní frekvence a jejího přepočtu na obvodovou rychlost

Vstupní parametry

- | | |
|---|---------------|
| • tabulka vypočtených frekvencí (z MKP) | f [Hz] |
| • průměr oběžného kola | D_2 [m] |
| • šířka kanálu | l_{2sk} [m] |
| • provozní rychlost | v [m/s] |

Postup výpočtu

- lineárně interpolovat frekvence v závislosti na rychlosti
- nově vyjádřené (vypočtené) frekvence lineárně interpolovat v závislosti na poměru l_{2sk}/D_2 [%]
- výslednou frekvenci

$$f = f(D_2, l_{2sk}, v) \quad (9)$$

přepočítat na rychlost pomocí vzorce

$$v = \frac{\pi \cdot D_2 \cdot f}{p}, \quad (10)$$

kde p je počet lopatek difuzoru

- určit hodnoty na hranici pásma $\pm 5\%$

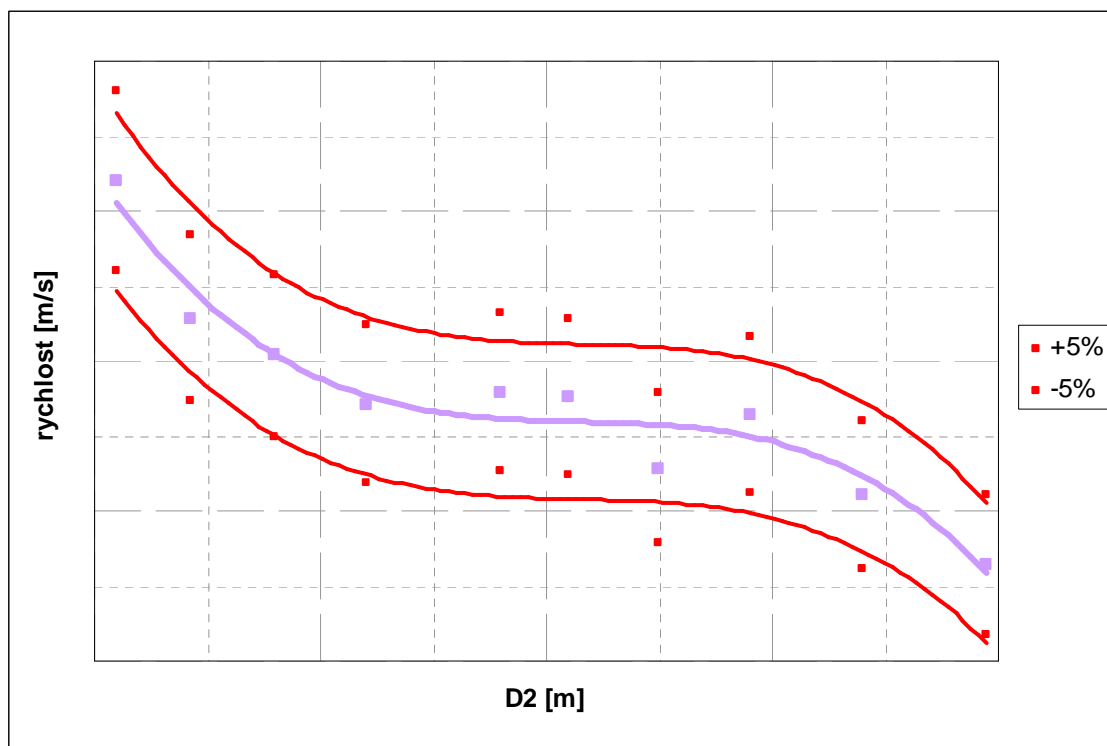
$$v_{-5\%} = 0,95 \cdot v \quad (11)$$

$$v_{+5\%} = 1,05 \cdot v \quad (12)$$

- body na hranici intervalů aproximovat polynomem 3. řádu

Výstup

Pásma rychlostí, ve kterém se mohou vybudit nebezpečné vlastní tvary kmitu mezilopátkových segmentů, Obr. 16.



Obr. 16 - Grafická interpretace tolerančního pásma kritických rychlostí

9 Závěr a diskuze

Při automatizovaném návrhu průmyslového kompresoru jsou používány softwarové aplikace. Implementované fyzikální vztahy z oblasti termodynamiky točivých strojů je pro praktické používání třeba doplnit mezními hodnotami, které je reálně fyzicky provozovat. Zohledněna by měla být i bezpečnost výrobku, který je často provozován v technologii několik desítek let.

Tradičním omezením je statická pevnost materiálu rotujícího kola. V předložené práci bylo odvozeno kritérium dynamického namáhání oběžných kol. Pro vyhodnocení byly vybrány vlastní tvary oběžného kola, kdy dochází ke kmitání mezilopatkových segmentů u kola s krycím kotoučem, a kmitání lopatky u kola bez krycího kotouče. Navrženou metodikou byly dopočítány mezní křivky pro řady typů oběžných kol z produkce ČKD. Kritické hodnoty, resp. křivky budou následně zahrnuty do návrhu průtočné části radiálního kompresoru.

Poděkování

Tento článek vznikl za finanční podpory Ministerstva průmyslu a obchodu v rámci projektu

FR-TI2/206 „Automatizace procesů technické podpory výroby kompresorů“.

Literatura

- [1] ANSYS 13.0 Help
- [2] Bartoň, P.: Kreslení výkresu hřídele. Interní směrnice ČKD Nové Energo č.TPP-023, ČKD 2011.
- [3] Bartoň, P.: Maximální dovolená odstředivací obvodová rychlost kola. Interní směrnice ČKD Nové Energo č.9-20-9050-009, ČKD 2008.
- [4] Chronin, A., V.: Kolebaniya diskov. Moskva, 1970.
- [5] Malenovský, E.: Studijní opora z předmětu Dynamika rotorových soustav [online]. VUT v Brně, Ústav mechaniky těles, mechatroniky a biomechaniky. [vid. 4.3.2012]. Dostupné z:
http://www.umt-old.fme.vutbr.cz/~pkrejci/opory/dyn_rot/index.html
- [6] Oficiální školící materiály ANSYS
- [7] Šafr, M.: Dynamické zatížení oběžných kol. Interní směrnice ČKD Nové Energo č. KKS-TK-3.1-041 Rev.1., ČKD 2011.

Kontaktní adresa:
Ing. Oto Štěpáník
ČKD KOMPRESORY, a.s.

Klečákova 347

190 02 Praha 9

E-mail: oto.stepanik@ckdkompresory.cz

ANALYSIS OF 3-D LATTICE PLATE USING FEM

MARTIN ŠTIGLIC, KATARÍNA TVRDÁ

STU BA, Slovak University of Technology, Department of Structural Mechanics

Abstract: This paper deals with design optimization, static and modal analysis of simplified space truss, which was used to cover festival square. Design optimization was used to achieve the best parameters for steel tubes. The results from two optimization methods were compared and modal analysis was performed with best parameters and gives the own shapes and own frequencies. The analysis and optimization was calculated in the software ANSYS.

Keywords: optimization, modal analysis, finite element method

1 Introduction

FEM is robust method that can be used to a wide range of engineering problems. The main idea is dividing a very complicated problem into small elements that can be solved in relation to each other. One of the most popular software based on this method is ANSYS. It offers lot of options from defining element type, material properties, real constant etc. to setting up the type of analysis. There are many types of analysis and chosen were two of them – static and modal. Advantage of ANSYS is that offers lot of modules, which are specialized to specific problems. Optimization tool is one of them and is very useful in finding the best parameters for construction. The condition is to declare optimization variables, that is, specify which parameters are design variables (DVs), which ones are state variables (SVs), and which ones is the objective function.

2 FEM model

Finite element model (Image 2) was created with some modification from real structure, which was used to cover festival square in Osaka, in 1970 (Image 1). The dimensions of space truss are 291.6 m x 108 m x 7.637 m. The whole structure has 2160 elements created from element LINK180. Each of upper chord nodes, has own load calculated from general load 2 kN/m². The construction is supported by 6 supports where each support covers six nodes with appropriate degree of freedom.



Image 1 - Space truss for the 'Symbol Zone', Festival Plaza Expo '70, Osaka, Japan

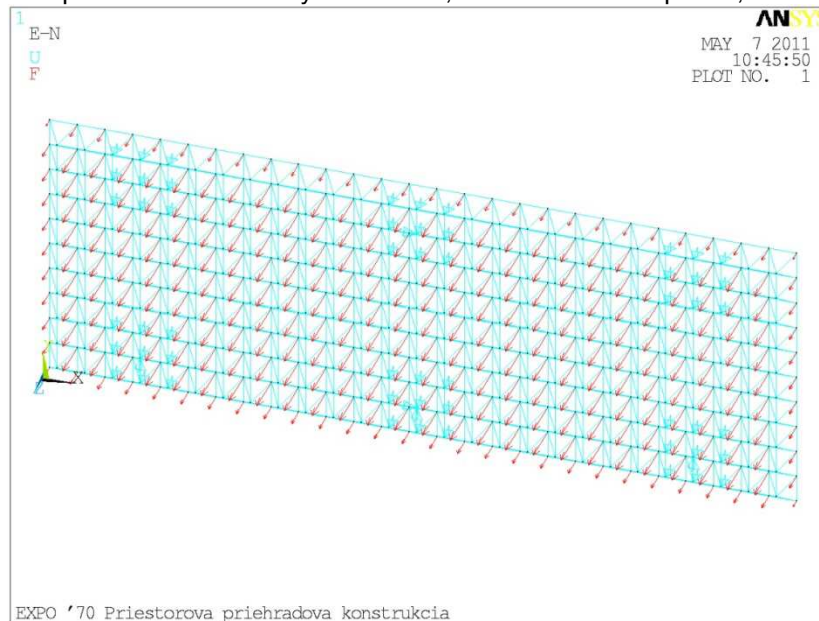


Image 2 – Space truss 3D model

3 Optimization

ANSYS offers lot of optimization method. In this case were used two of them. First one was subproblem approximation method. This is an advanced zero-order method, which uses approximations to all dependent variables (state variables and the objective function). It can be applied efficiently to a wide range of engineering problems. Next one was first order method. This method uses derivative information, that is, gradients of the dependent variables with respect to the design variables. It is highly accurate and works well for problems having dependent variables that vary widely over a large range of design space.

The goal of optimization was to find best thickness for chord and diagonal steel tubes and construction deep to obtain smallest volume. Condition was that the tensile stress could not be higher than yield strength and compressive stress could not be higher than allowed stress. So the objective function was the construction volume, design variables (Table 1) were the thicknesses and deep. State variables were tension and compression stress.

Table 1 Range for DVs

Parameter	Min. value [m]	Max. value [m]
-----------	----------------	----------------

DEEP	7,000	9,000
THICKNESS1	0,016	0,030
THICKNESS2	0,0079	0,015

In the table 2 are the best results from each optimization method. It can be seen that there are not big differences between them.

Table 2 Optimization results

		Subproblem method	First Order method
Min. normal stress	[kPa]	$-0.23382 \cdot 10^6$	$-0.23001 \cdot 10^6$
Max. normal stress	[kPa]	$0.11130 \cdot 10^6$	$0.10953 \cdot 10^6$
Thickness 1	[m]	0.0160	0.0160
Thickness 2	[m]	0.0089	0.0090
Deep	[m]	7.5562	7.6370
Volume		392.49	396.03

4 Modal analysis

Modal analysis is very useful when diagnosing structural vibrations. Results are own shapes and frequencies. They give general information about dynamic response of structure. We used best parameters from first order method to perform modal analysis. In table 3 are shown first ten own frequencies.

Table 3 Own frequencies

	Frequency [Hz]
1.	2.4272
2.	2.4811
3.	2.6672
4.	2.6859
5.	2.8383
6.	3.0522
7.	3.2694
8.	3.2697
9.	3.3199
10	3.5455

Following five images (Image 3 – Image 7) show first five own shapes. The view is set up on X-Z plane.

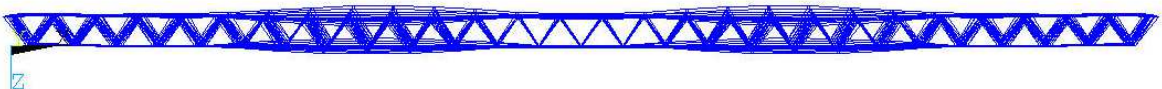


Image 3 First own shape

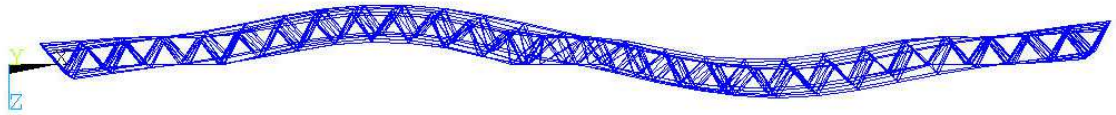


Image 4 Second own shape

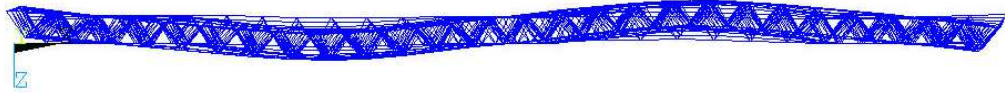


Image 5 Third own shape

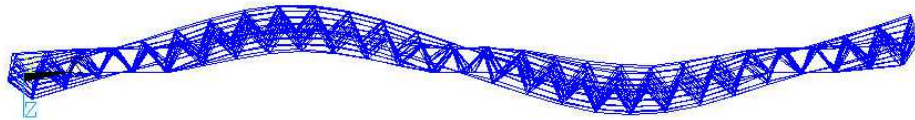


Image 6 Fourth own shape

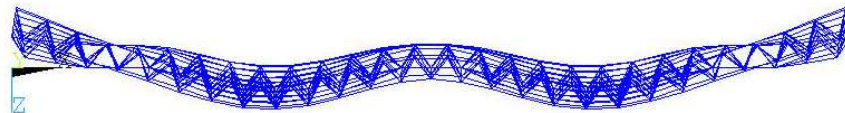


Image 7 Fifth own shape

5 Conclusion

At this time, when everybody wants to save money and build construction with minimum expense is good question, how to do it? One opportunity is to use optimization tools, which are implemented in various softwares. In this article were compared two optimization methods – subproblem and the first order method. The results were not same but very similar and results from first order method were the same values that were used for the construction. Optimization can be useful to get an overview about parameters which indicates what can be reduced, modified or eliminated from structure but the final decision is on engineer to assess whether it can be. Calculation on optimization and modal analysis sampling is concerned with a number of authors (Kormaníková 2010, Frankovský 2011).

References

ANSYS Help (ANSYS manual)

CHILTON J., 2000. Space Grid Structures. Oxford: Architectural Press, 191 s. ISBN 0-7506-3275-5

STN EN 1993-1-1:1993 : Navrhovanie ocelových konštrukcií.

FRANKOVSKÝ P., 2011. Využitie modálnej analýzy pri diagnostike vibrácií strojných zariadení. Transfer inovácií, 2011, 19, 178 -184, ISSN 1337-7094.

KORMANÍKOVÁ E., 2010. Optimization of laminate plate subjected to maximum strain criterion - 1 elektronický optický disk (CD-ROM).In: Modelování v mechanice 2010 : sborník příspěvků vědecké konference : Ostrava, P. 1-7. - ISBN 978-80-248-2234-1

Acknowledgement

The paper was supported by grant from Grant Agency of VEGA in Slovak republic No. 1/1186/12.

Contact address:

Ing. Martin Štiglic

Stavebná fakulta STU v Bratislave, Radlinského 11, 813 68 Bratislava

Ing. Katarína Tvrdá, PhD.

Stavebná fakulta STU v Bratislave, Radlinského 11, 813 68 Bratislava

A NEW SOFTWARE TOOL FOR PARALLEL COMPUTING WITH ANSYS

JINDŘICH SUŠEŇ, JAROSLAV ŠINDLER, MATĚJ SULITKA

Czech Technical University in Prague, Faculty of Mechanical Engineering, Research Center of Manufacturing Technology

Abstract: Parallel computing strategy can advantageously be employed for solving large computational problems. A typical example is an optimization problem, in which the response for each design point has to be calculated. A new scheduling manager has been developed for effective control of parallel running of large optimization problems using ANSYS solver. Three main aspects of the scheduling manager functionality are: optimized load balancing, flexibility and scriptability. The paper describes the structure of the scheduling manager and the function of all its components. Load-balancing and resource management mechanisms implemented in the software are introduced as well. Features of the system are discussed along with an example of the application of the new scheduling manager.

Keywords: Ansys, parallel computing, Python

1 Introduction

It is often needed to evaluate a large number of versions (design points) of one problem. Optimization is a typical case when the number of design points reaches hundreds or thousands and the total time required to evaluate them can be several days or weeks. It is beneficial in such a case to split the calculation among several computers and to reduce thus significantly the total computing time. This paper focuses on structural optimization with ANSYS and discusses in detail one of the possible ways to parallelize the computation.

ANSYS provides its own tool for parallel computing called RSM (Remote Solve Manager) [1], [2]. It can be run directly from Workbench, which makes it easy to use. It is relatively easy to set up and it doesn't require any additional license (so it actually doesn't cost anything). On the other hand, the RSM has some drawbacks, the most important of which are:

- No load balancing - Big jobs can make the host computer useless for other users. There is an option to run jobs in a specified time interval only. But the computer can still be overloaded and useless for work if a user connects during this time in a remote session (from home or business trip...). Moreover, the time interval can be difficult to establish in case of flexible working hours.
- No resource monitoring – There is no way of monitoring which resources are in use. If a local user decides to run his own analysis on his machine overnight, in the Ansys implemented RSM, it is not possible to specify such an intention and the RSM will send jobs to the workstation immediately anyway. Moreover, it is not possible to check which workstations are the most appropriate ones for a given job. This means that a job which could be solved quite fast on one computer in-

core can be sent to another computer with less physical memory, resulting in longer solution time.

- File transfer is slow and the RSM does not provide the opportunity of delivering just some specified parts of the solution information. The need for copying a whole project to all workstations and then copying all the results back to the computer running the RSM significantly slows down the computation. That is a problem especially in optimization tasks, where only the objective function values are of interest and a lot of jobs have to be calculated.

Another option is to use more sophisticated scheduling tools like: PBS (Portable Batch System) [3], LSF (Load Sharing Facility) [4], or Microsoft Compute Cluster. These have more options than the RSM, but they are difficult to configure and maintain. They may also cost some extra money.

The need for scripting and customizing a scheduling tool for running a large number of separate computational tasks with ANSYS, such as an optimization problem, was a motivation for developing a new software tool. Its application is, however, not limited to communicating with ANSYS only, it can cooperate with any other software.

The new scheduling manager is written in Python. Python is a modern object-oriented, interpreted programming language, which is becoming increasingly popular. Its popularity brought with it a wide range of modules, which make it relatively easy to build complicated applications.

2 Scheduling manager written in Python

This section describes the basic structure and working mechanisms of the new scheduling manager.

2.1 basic structure

The

As mentioned before, the new scheduling manager is written in Python with extensive use of open source modules, which provide lots of important functions. The most important module is Pyro. This module provides the whole communication between the computers in the network. It enables the Python processes running on different computers to exchange variables and call each other's methods. In order for Pyro to work properly, two kinds of objects are set up. The first one is passive. It doesn't do anything by itself; instead it stores methods which can be called by other objects on the same or remote computer. The second type is active. It can call methods of a passive object and exchange variables with it.

The basic structure of the scheduler can be seen in Figure 1. Roles of the individual components are as follows:

- Client – supplies work to dispatcher and collects results
- Dispatcher – stores work, results and other important information
- Worker – gets work from dispatcher and returns results
- Dispatcher controller – manages (wakes and kills) the workers.

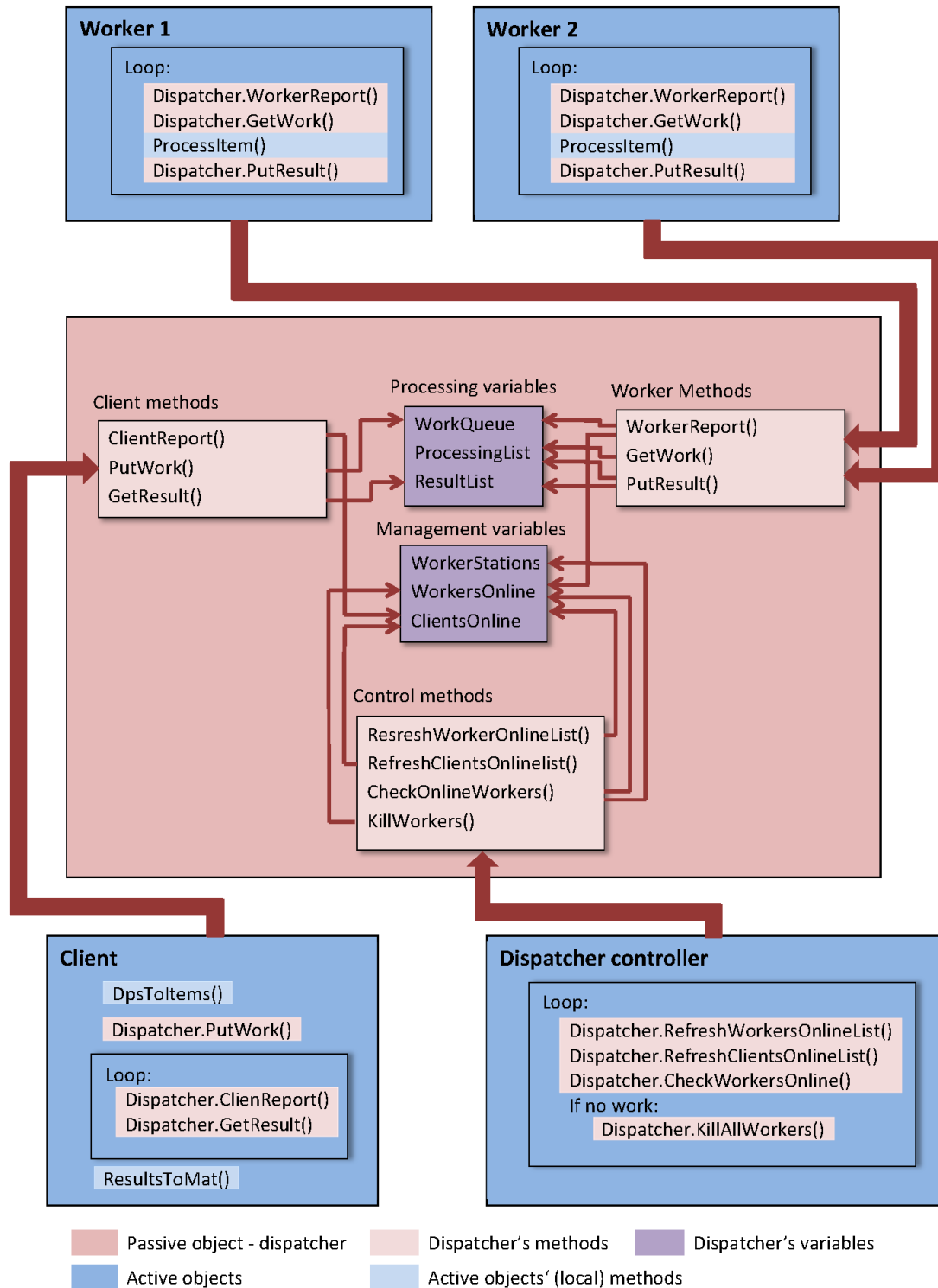


Figure 1 – Basic structure of the scheduling manager

2.2 Description of the system components

Descri

The components of the scheduling system shown in Figure 1 will be described in more detail in the following section.

-

Client

The client is an active object which transforms supplied design points into a special data structure called item. Each item stores all relevant information about its corresponding design point:

- *input* – information characterizing a given design point (values of design variables)
- *results* – values of objective functions
- *item id* – unique item identifier
- *client id* – unique client identifier used by clients to identify their items
- *ANSYS return code* – for quick identification of errors
- *problem type* – small or big, determines which workstation can process the item
- *timeout* – maximum time the computation can take
- *input script*
- *etc.*

The *input script* is of particular importance since it defines how to process the *input* and how to extract the *results*. A typical *input script* contains instructions for running Ansys in batch mode and executing some APDL script with the *input*. The *input* doesn't have to be just a vector of design variables. It can also be a whole APDL script, a model stored in a file (*.cdb, *.inp, *.dat) or anything that can be processed to get results. The flexible definition of the *input* means that the scheduler can work with any program, not just ANSYS. The only thing required to change it is a small modification of the *input script*.

Once all the inputs are converted to items, these are forwarded to the dispatcher. Consequently, a loop is run in the client, asking the dispatcher to provide the results. The loop finishes when all the items are returned back. Processed items are then exported to the output file for further use. Several clients can communicate with a dispatcher at one time. They may be running on a server or one of the workstations in the cluster as well, which makes it easy for individual users to submit their own jobs.

- Dispatcher
her

The dispatcher is a passive object which stores information about items, workers and clients. It also provides methods to exchange items with clients and workers and to kill and wake workers. When the dispatcher receives an item from a client, it stores the item in the work queue. The work queue is a special data structure which enables prioritization of items. Therefore, when a worker asks for work, it will get the item with the highest priority.

A dispatcher can be running on a server or a regular workstation. The disadvantage of running the dispatcher on a regular workstation is that it can be slowed down when the workstation processes a big item which requires a lot of physical memory. Another problem would arise when a user restarts the workstation. The dispatcher is a critical part of the system and all the items are lost when it crashes.

- Worker

The worker runs in an infinite loop in which it asks the dispatcher for work. When it gets an item, it takes the item's input script and executes it. The script produces some output and stores it as the item's results. Other information like ANSYS return code is also written to the item. The whole item is then sent back to the dispatcher where it waits for the client to pick it up.

One worker runs on each workstation in the cluster. More workers can run on a single workstation, if it is powerful enough.

- Dispatcher controller

The last component of the system is the dispatcher controller. Its role is to manage workers and clients. Just like the worker, it also runs in an infinite loop. In this loop it checks whether all workers are online. If a worker fails to report itself, it will be restarted. Workers which are busy processing an item do not have to report (they cannot because their loop is stopped). However, if a worker doesn't finish the job in a defined time (item's timeout), it will be assumed to have crashed. In such a case the worker is restarted and the item it was processing is sent back to the work queue. Another worker can thus try to process the item. If an item cannot be processed even the second time, it is marked as erroneous? and sent to the result queue.

The controller also wakes workers when the dispatcher receives work from a client. And kills them when all the work is done.

2.3 System preventing the workstation from overloading

In order for the whole system to function properly, it is important that the workstations in the cluster (workers) receive only "small" jobs when their respective users work on them. A small model would be a FEM with a small number of elements so that its solution would not affect the host performance if a user works e.g. with a text editor or a CAD system. The definition of a small item is dependent on the particular workstation, of course. Models with less than 10^5 elements can usually be classified as "small". Since it is often possible to use small models in optimization tasks (relative comparison of design points being more important than accuracy of particular results), the computers in the cluster can be used quite effectively.

The situation is more complex in case of "big" models. Such a model can only be solved if the workstation CPU is not loaded by any other application. The reason for that is obviously the impact on computer's performance. The mechanism of preventing the workstation from being overloaded when in use is based on W tasks.

First of all, a special user account has to be created by the network administrator. This worker account can have administrator privileges on all computers (in order to run Windows tasks properly) and its password can be known to the network administrator only. Afterwards two windows tasks are created on each computer. The starter-task informs the dispatcher and the worker that the workstation is not used anymore. The killer-task, on the contrary, kills all the processes running under the worker account and provides the dispatcher with the information if any other application is not running on the workstation. Consequently, the item is processed on the workstation returned to the work queue and the worker script is restarted. The killer task kills all the processes of the worker account, so it does not matter whether the worker is running ANSYS or any other program; the workstation is ready to be used. The task does not kill small jobs, of course, as they shouldn't affect the computer's performance.

Windows allows to configure tasks to run on specified events. The starter task is run every time a user locks the computer, logs off, or terminates a remote session. The killer task runs when somebody logs on, unlocks the computer or starts a remote session. This means that if somebody logs on to a computer which processes an item, all solution progress is lost and the item has to be processed on another computer from scratch. However, this system is intended for solving large numbers of relatively small jobs, so repeating the solution process of one job is not a big issue.

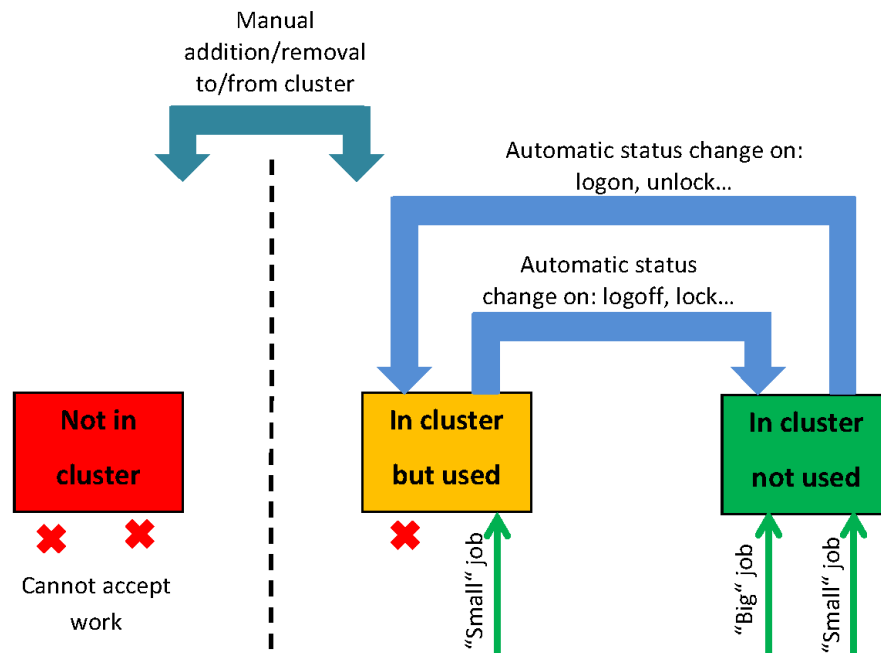


Figure 2- Possible statuses of workstations

Since the performance of available workstations as well as performance requirements of programs run on them by their users usually differ, it is often difficult to define what is a "small" job. For this reason the users have the possibility of temporarily removing their workstation from the cluster. This is done in a dialog box which tells the user whether his computer is in the cluster and which job is running (if any). Removing the workstation from the cluster and killing any running job can be easily accomplished by clicking a specific button. If a big model, not suitable for this kind of parallel computing, needs to be computed on one of the workstations (in ANSYS for instance), the workstation can be manually removed from the cluster. The model can be submitted to ANSYS using an APDL script in a batch run and the last line of the script returns the workstation to the cluster (`/SYS,'AddWsToCluster.py'`).

An automatic removal of the workstation from the cluster when a specified program is running can also be easily implemented. This can be useful especially to CAD users who need high workstation performance. An overview of the possible workstation statuses can be seen in Figure 2.

System preventing the workstation from overloading

Appropriate workstations should be added to the cluster whenever a user runs a client and submits jobs to the dispatcher. The appropriate workstation should have enough HDD space, RAM (to be able to run the particular job in-core) etc. It is also important to be able to monitor the workstations as they process items. A GUI shown in Figure 3 has been designed for these purposes.

The Worker management utility has two tabs. The first one contains functions to add and remove workstations from the cluster and to run start/kill tasks. The buttons for running the start/kill tasks are intended for debugging only as the tasks run automatically on logon/logoff etc. The "Disp. Info" button runs the information update. A special task is run on every workstation to find out its actual status, free HDD space, RAM and other information if necessary.

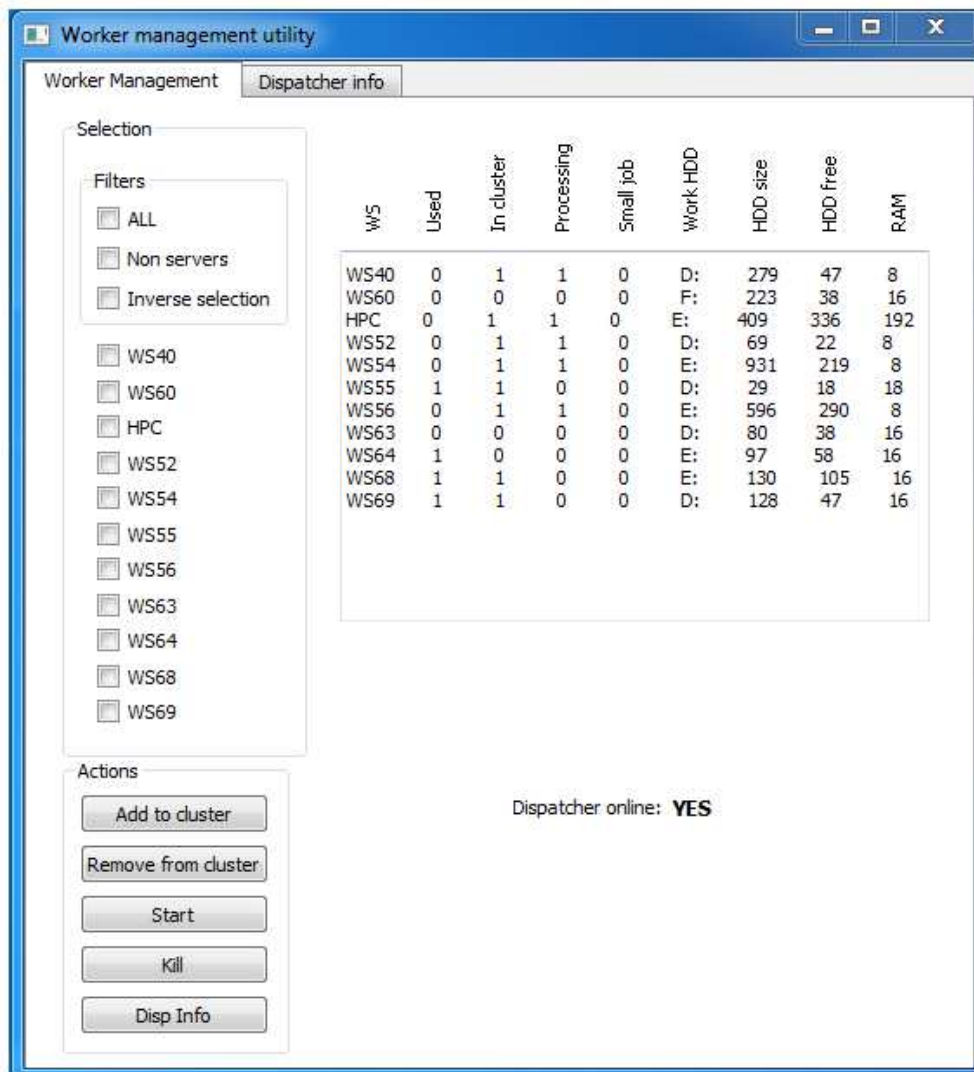


Figure 3 - Worker management utility

The second tab displays information about the dispatcher. These include for example: work queue size, result queue size, connected clients etc.

Another workstation monitoring feature is e-mailing. An e-mail is sent to the defined e-mail address on a number of events which indicate problems. These include:

- license problems - a workstation repeatedly reports a missing license
- timeouts - item computation takes longer than the defined time
- unexpected errors - anything that makes the workstation return items with errors or prevents worker script from proper running

the inner part of helmet (foam) EPS		outer part of the helmet (shell) ABS	
Young's modulus	62,73 MPa	Young's modulus	3 Gpa
density	85 kg/m ³	density	1040 kg/m ³
Poisson's	0.01	Poisson's	0.4

ratio		ratio	
maximum tensile stress	1,3 MPa	Yield stress	60 MPa
Damping coefficient	0.2	ultimate strength	70 MPa

An Example of Optimization Loop with Parallel Computing

An optimization loop with the scheduling manager can be seen in Figure 4. The optimization process is driven by Matlab script which uses optimization algorithm NSGA II. The Matlab script generates a population to be evaluated and writes it to a file. The file is read by Workbench which generates an APDL input file for each design point and submits the files to the scheduler. The scheduler then sends the results back to Matlab, thus closing the loop.

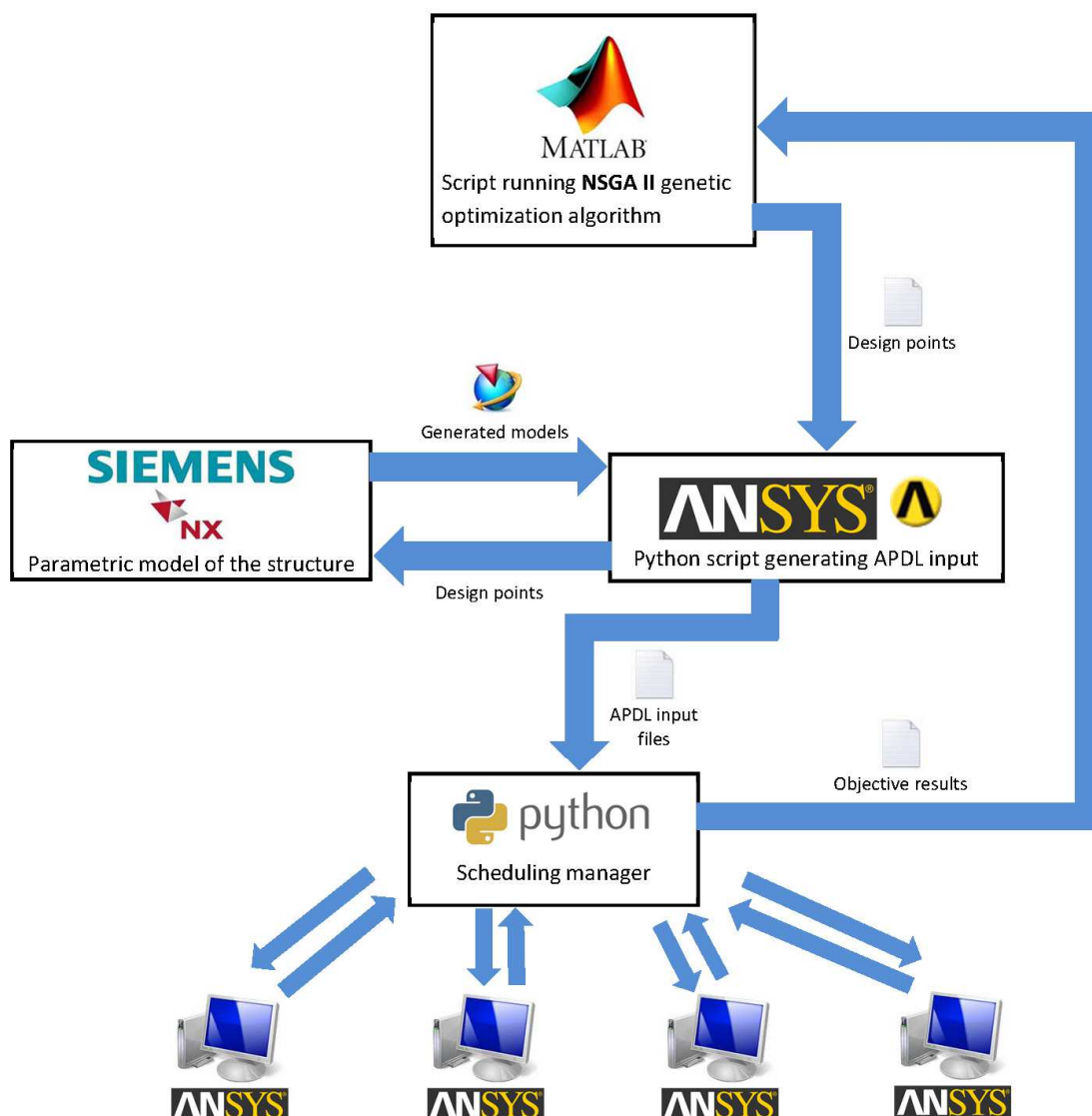


Figure 4 - Data flow in the optimization process, Ansys runs on all work stations

This setup represents one of several possibilities of using the scheduling manager. In the loop presented in Figure 4, NX as an external CAD system is employed for creating the parametric models of the structure to be optimized. Using the NX makes creating the

parametric geometrical models much easier than writing an APDL script for building the model geometry. However, a certain disadvantage is that employing an additional communication with NX slows down the model update.

An example of the solution time reduction achieved by the optimization loop presented in Figure 4, and solution times on a single computer can be seen in Figure 5. The optimization process run on a single computer was using the same way of connecting Matlab, ANSYS and NX. However, the FE solution was performed directly in ANSYS Workbench.

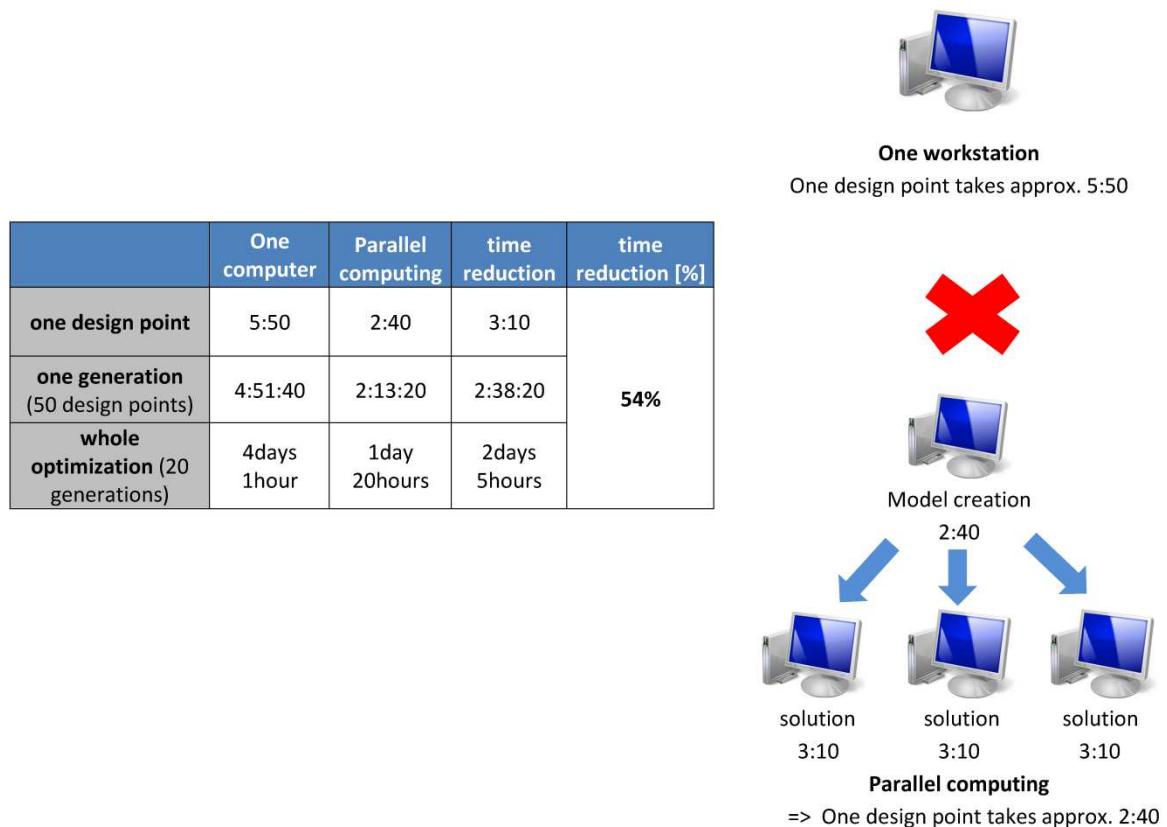


Figure 5 - Comparison of the solution times on a single computer and the solution with scheduling manager

It can be seen that the time to create the model (i.e. to update a design point in ANSYS Workbench and NX) is 2 minutes and 40 seconds. The average time to solve the generated APDL model is 3 minutes and 10 seconds. The total evaluation time of one design point is therefore 5 minutes and 50 seconds provided the update and solution is performed on a single workstation. However, splitting the procedure into creating the model on one computer and solving it using several other computers results in average evaluation time of just 2 minutes and 40 seconds.

The figure and summary table in Figure 5. show that the solution time has been reduced by 54 % using the parallel computing strategy and a new scheduling manager. This means that the whole optimization process time was reduced from four to two days.

The "bottle neck" of the presented optimization loop is the model update because it was done on the server directly. The time of solving the optimization problem could have been reduced even more if more workstations had been used for the model update. The solution would be even faster considering an APDL parametric model instead of the combination of NX and ANSYS Workbench.

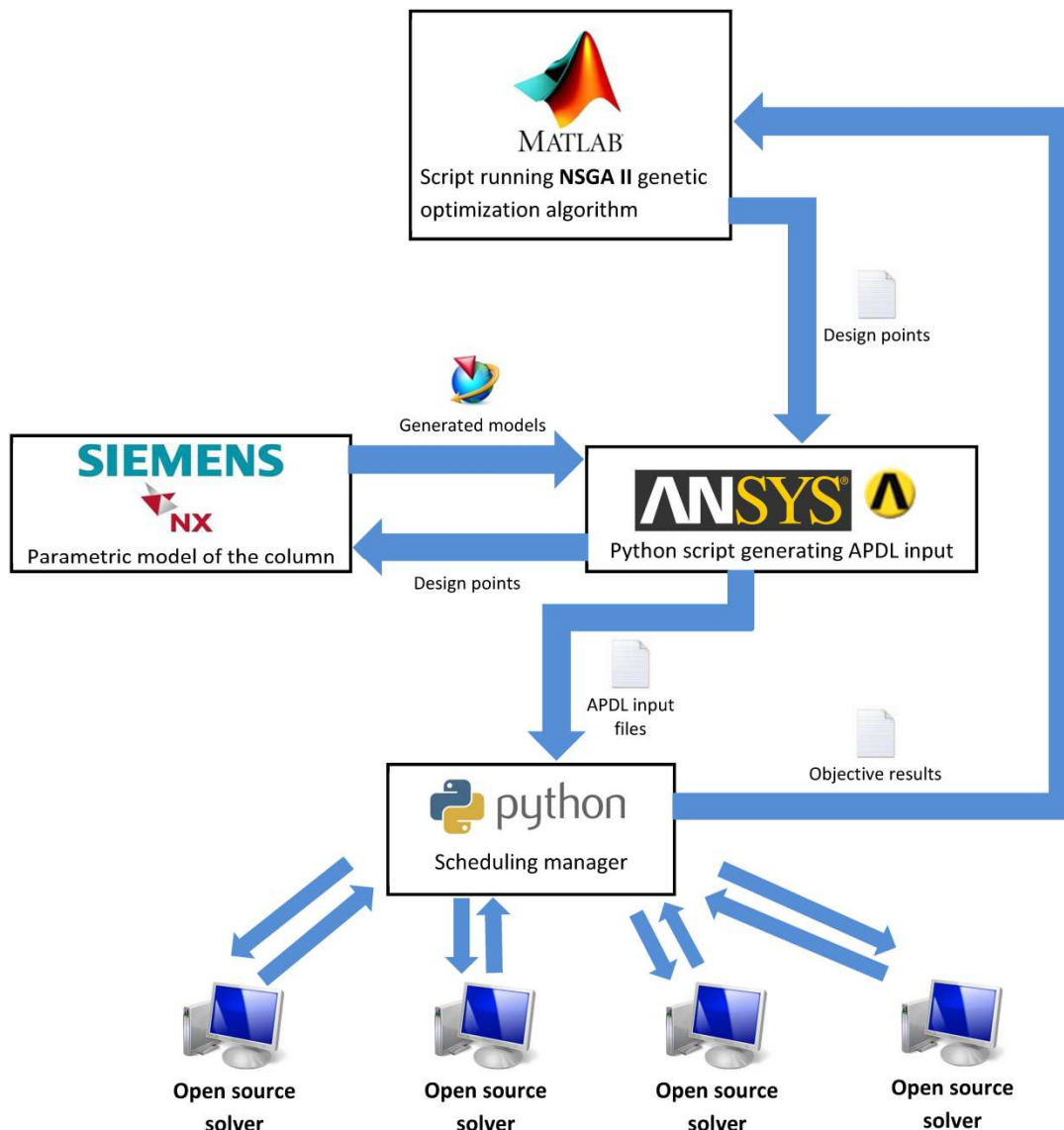


Figure 6 - Data flow in the optimization process, alternative setup with open source solvers

Another issue connected with parallel computing with ANSYS in general is the need for higher number of licenses. It is obvious that every workstation running ANSYS needs an appropriate license. The total number of required licenses can be relatively high, especially for large problems with many workstations involved. An alternative approach Figure 6 would employ Ansys only as generator of system matrices (stiffness matrix for linear static analysis, mass and stiffness matrix for modal analysis, conductivity and specific heat matrix for transient thermal etc.) and some solver to solve the problem resulting from FE discretization. Assembling system matrix is of at least order faster than solution of the system and therefore only one or a few licences of ANSYS are needed in order to keep pace of flow in the processes. Assembled system matrices are then distributed to workers where sparse solver solves the system of equations or sparse eigen solver solves for eigenvalues and eigenvectors. In case of transient analysis ODE timestepping solvers are employed. Various opensource solvers are available to use with the scheduler : MUMPS [5] is massive parrarel sparse solver, SuiteSparse [6] is another sparse solver package, PETSc [7] package interface many iterative sparse solvers with preconditioning, BLOPEX [8] or SLEPc [9] provides eigensolvers. Many other available packages are available to solve the problem.

MATLAB may be used to solve the problem as well. Many of mentioned packages also provide python interface which makes the cooperation with the scheduler easier.

3 Conclusion

The paper presents an alternative approach to parallel computing with ANSYS. The newly developed software represents a low cost alternative to RSM with improved functionality.

The new scheduling manager can avoid workstation overloading and ensure high utilization of computing performance of the workstations in the network. The amount of data transferred among computers is minimized as well as the time needed to distribute jobs and collect results. The main advantage of the new scheduling manager is high flexibility and scriptability. The high flexibility means that it is possible to use it not only for ANSYS, but for any other program or combination of the programs. This allows to use open source solvers and reduce thus number of required licenses.

The goals for future development include adaptation to computing servers. These are machines with lots of processors and a lot of physical memory. Their properties make them perfect for running several jobs simultaneously. The high amount of physical memory makes it possible to substitute hard disks with RAM disks. In this approach, a RAM disk can be converted to a virtual hard drive created in physical memory. Such a virtual hard drive provides response several times faster than a classic hard drive or SSD.

Another goal is the ability to automatically select the most suitable workstation for each job. The workstation will be selected not only based on hardware, but also on its actual free capacities. This means that no job from the scheduler would be sent to the workstation if another local analysis is run on it. And also the "weaker" workstations wouldn't receive big jobs.

References

- [1] Remote Solve Manger (RSM)
URL:< http://www1.ansys.com/customer/content/documentation/120/wb_rsm.pdf >
[cit. 23.9.2012]
- [2] Mastering the Remote Solver Manager (RSM) at R14 -20120322 1910-1
URL:
<<https://padtincevents.webex.com/mw0307l/mywebex/default.do?siteurl=padtincevents>>[cit. 23.9.2012]
- [3] PBS Works
URL:<<http://www.pbsworks.com>> [cit. 23.9.2012]
- [4] LSF introduction Guide
URL:<<http://www.vub.ac.be/BFUCC/LSF>> [cit. 23.9.2012]
- [5] MUltifrontal Massively Parallel sparse direct Solver
URL:<<http://graal.ens-lyon.fr/MUMPS/>> [cit. 23.9.2012]
- [6] Suite Sparse
URL:<<http://www.cise.ufl.edu/research/sparse/SuiteSparse/>> [cit. 23.9.2012]
- [7] Scalable Library for Eigenvalue Problem Computations
URL:<<http://www.mcs.anl.gov/petsc/>> [cit. 23.9.2012]

- [8] Block Locally Optimal Preconditioned Eigenvalue Solvers
URL:<<http://code.google.com/p/blopex/>> [cit. 23.9.2012]
- [9] Portable, Extensible Toolkit for Scientific Computation
URL:<<http://www.grycap.upv.es/slepc/>> [cit. 23.9.2012]

Acknowledgments

The results have been obtained as part of of the TE01020075 Competence Center - Manufacturing Technology project supported by the Technology Agency of the Czech Republic.

Contact address:

Ing. Jindřich Sušeň

Jaroslav Šindler

Ing., Phd. Matěj Sulitka

RCMT, Horská 3 128 00, Prague 2, Czech Republic

VÝPOČET NÍZKOCYKLOVÉ ÚNAVY JADERNÉ ARMATURY DLE NORMY NTD A.S.I. SEKCE III

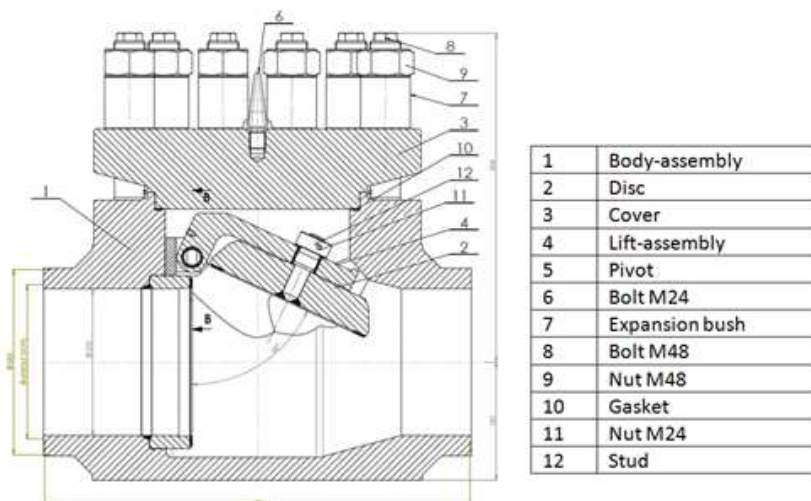
JIŘÍ TÁBORSKÝ*, LINA BRYUKHOVA
KRÁLOVOPOLSKÁ STRESS ANALYSIS GROUP, s.r.o.

Abstract: Alternative fatigue calculation according to NTD A.S.I. Section III. Comparison of different calculation approaches to fatigue assessment of the body of the valve for nuclear application. Comparison of cumulative usage factors determined using elastic and elastic-plastic material behaviour in FEM calculation.

Keywords: valve, elastic-plastic calculation, fatigue

1 Popis armatury

Jedná se o zpětnou klapku, samočinnou (bez pohonu), jednosměrnou armaturu. Talíř je otevírán hydrodynamickým účinkem protékající pracovní látky, při zastavení proudění dojde k jeho samovolnému zavření. Těleso je provedeno z výkovku, talíř a víko z plechu nebo výkovku. Materiálové provedení těchto částí je z nerezové oceli. Kontrolovaná armatura může mít více rozměrů přivařovacích konců, které jsou i s příslušným zatížením definovány v Technických podmínkách [2]. Utěsnění šroubového spoje těleso/víko je realizováno spirálovým grafitovým vinutým těsněním v hlavním silovém toku.



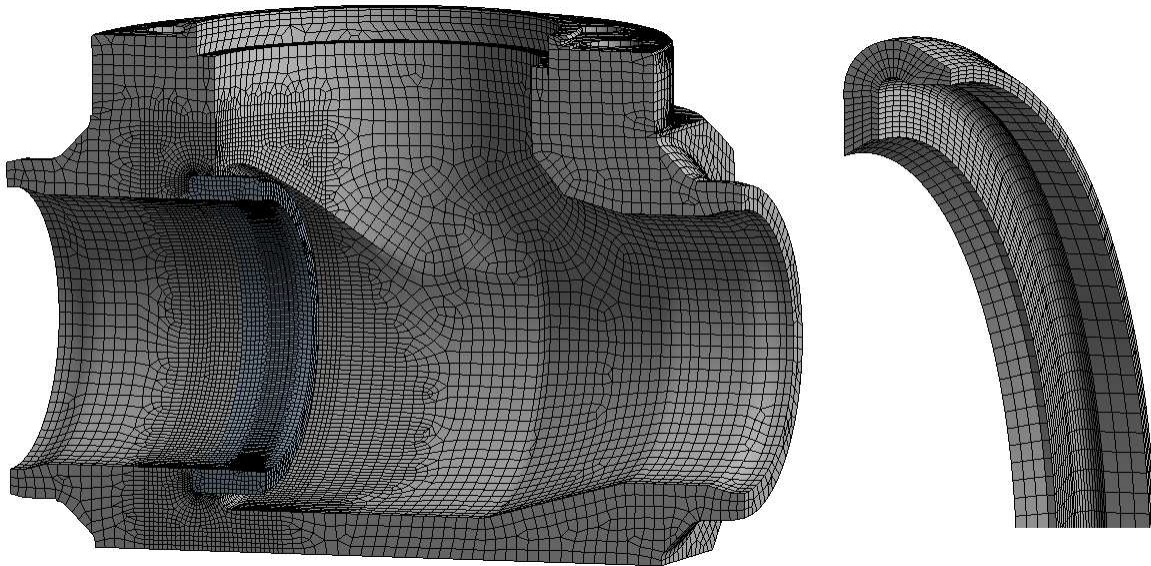
Obrázek 1 – Posuzovaná armatura

2 Výpočet únavy tělesa armatury dle normy NTD A.S.I. Sekce III

Výpočet kumulace poškození uvedený v této kapitole vychází z elastického výpočtu napjatosti MKP a následného určení amplitudy celkové (elastické a plastické) deformace pomocí Hookova zákona.

2.1 Popis modelu

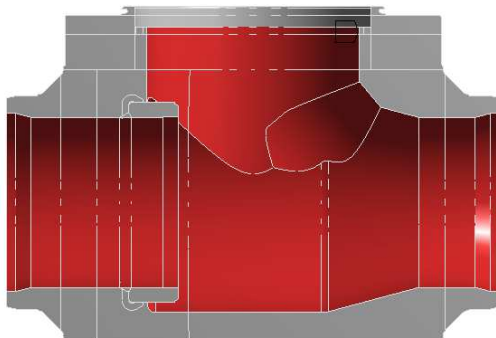
Model použitý ve výpočtu je zobrazen na Obrázku 2. Prováděná analýza se týkala jenom tělesa armatury, proto talíř, víko, šrouby a těsnění nebyly v modelu uvažovány. V místě přivaření sedla k tělesu se uvažoval kontakt typu "bonded". V místě nasazení sedla do tělesa se uvažoval kontakt typu "frictionless".



Obrázek 2 – Síť tělesa armatury. Detail sítě v oblasti zápichu.

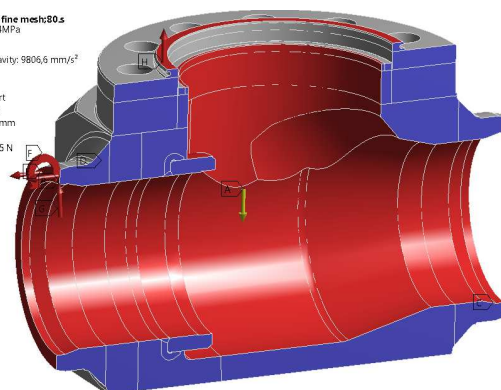
Q: 247-60C:47,4C/s
Convection
Time: 80, s

Convection: 60, °C, 1,531e-002 W/mm²·°C



R: 247-60:47,4C/s - fine mesh80.s
247-60C:47,4C/sp=34MPa
Time: 1, s

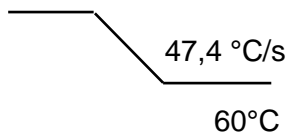
A Standard Earth Gravity: 9806,6 mm/s²
B Pressure: 34 MPa
C Displacement
D Frictionless Support
E F_pretlak: 72610 N
F Min: 1,025e+008 N·mm
G Fr: 45300 N
H Force: 1,1384e+005 N



Obrázek 3 – Teplotní OP a mechanická zatížení realizovaná na modelu

Výpočet byl proveden pro výpočtové parametry uvedené v následující tabulce. Pro jednoduchost byl uvažován pouze jeden z mnoha možných pracovních režimů dané armatury. Tento havarijní režim se vyznačuje rychlou změnu teploty média (ochlazování vnitřního prostoru armatury) a to rychlostí 47,4°C/s z 247°C na 60°C.

Tabulka 1 Výpočtové parametry havarijního pracovního režimu

Teplotní změna, rychlost změny teploty	Přetlak [MPa]	Počet opakování režimu
247°C  47,4 °C/s 60°C	3,4	N = 41 havarijních cyklů typu LOCA

Tabulka 2 Materiálové charakteristiky tělesa armatury

Materiál 08Ch18N10T			
T	[°C]	20	250
R _{p0,2} ^T	[MPa]	196	167
R _m ^T	[MPa]	491	382
E	[GPa]	205	185
α	[1/K]	16,4·10 ⁻⁶	17,2·10 ⁻⁶

2.2 Popis výpočtu únavy

Kontrola na únavu byla provedena dle normy NTD A.S.I. Sekce III [1]. Byla spočítána dílčí únavová poškození a provedla se kontrola jejich součtu, celkového únavového poškození:

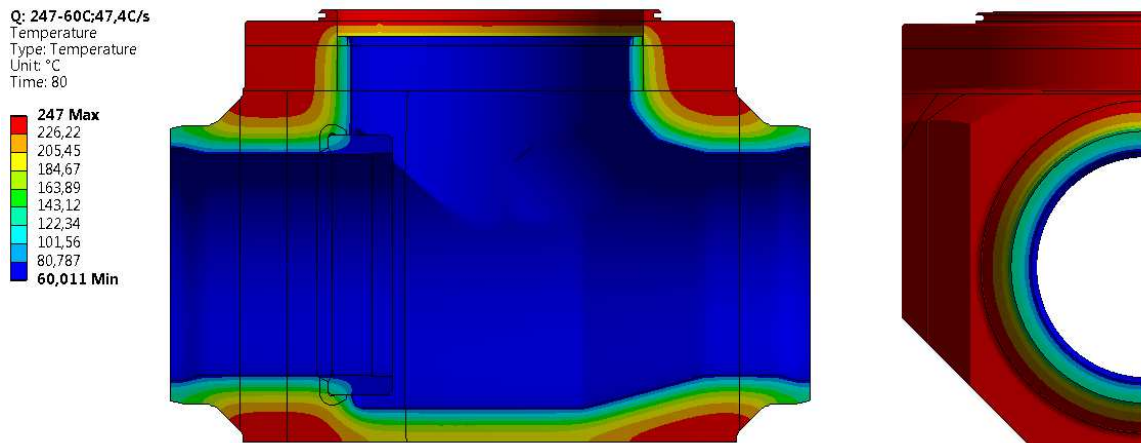
$$D = \sum_{i=1}^n \frac{N_i}{[N_i]} \leq 1,00 \quad (13)$$

kde N_i - počet cyklů i-tého typu

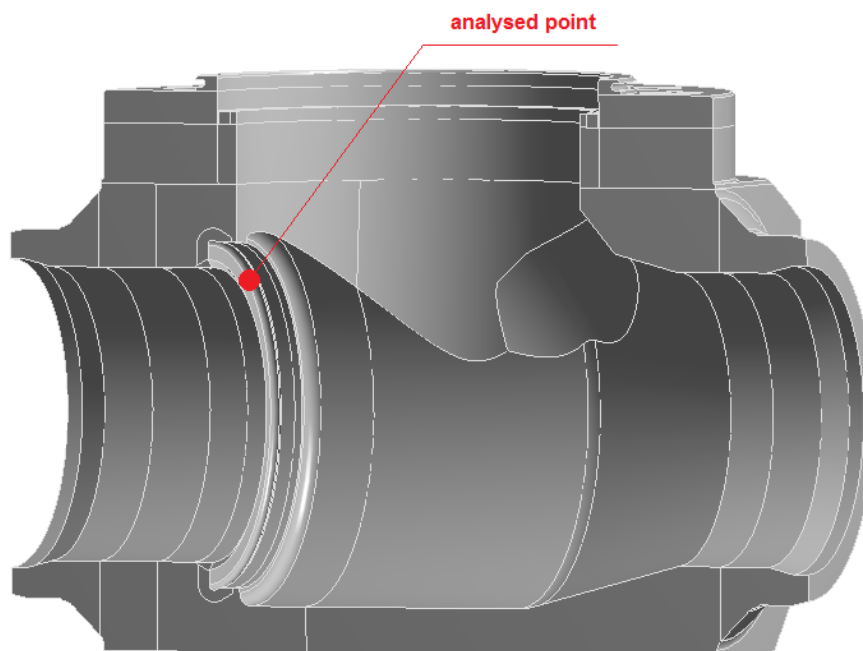
$[N_i]$ - dovolený počet cyklů i-tého typu.

2.3 Výsledky výpočtu

Vzhledem k rychlé změně teploty pracovního média armatury bylo těleso nerovnoměrně ochlazeno po tloušťce. Rozložení teplot při šoku viz Obrázek 4. Nejvyšší napětí přitom vznikala v bodě 1 (viz Obrázek 5) a to v místě zápichu pod sedlem.



Obrázek 4 – Rozložení teplot v 80 [s] teplotního šoku

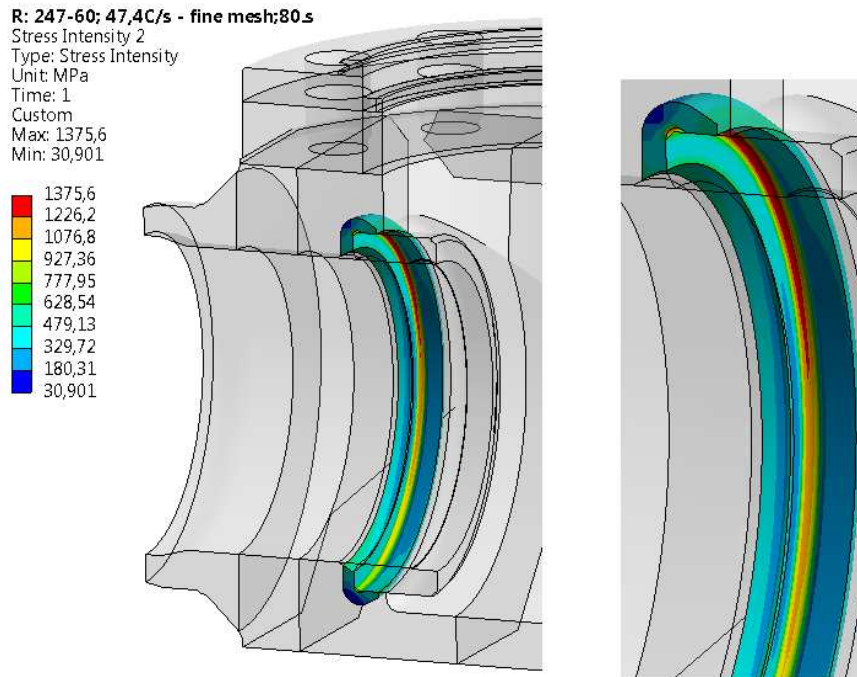


Obrázek 5 – Bod s nejvyšší hodnotou napětí

Hodnota napjatosti v bodě 1 při uvažování elastického chování materiálu je znázorněna viz Obrázek 6. Pro určení kumulace poškození (určení napjatosti v bodě 1) byl použit elastický model chování materiálu.

Tabulka 3 Složky napětí v bodě 1 v 80 [s] teplotního šoku při elastickém chování materiálu

σ_x [MPa]	σ_y [MPa]	σ_z [MPa]	τ_{xy} [MPa]	τ_{yz} [MPa]	τ_{xz} [MPa]
670,8	498,0	884,8	-65,1	-481,1	468,4



Obrázek 6 – Napětí v zápichu při uvažování elastického chování materiálu.

Tabulka 4 Kumulace poškození v bodě 1 při elastickém chování materiálu

Posuzovaný bod	Kumulace poškození D [-]	Posouzení
1	4,086 > 1	NEVYHOVUJE

Výpočtem bylo prokázáno, že výsledná kumulace poškození $D > 1$ a tedy pro elastický model chování materiálu armatura na únavu NEVYHOVUJE!

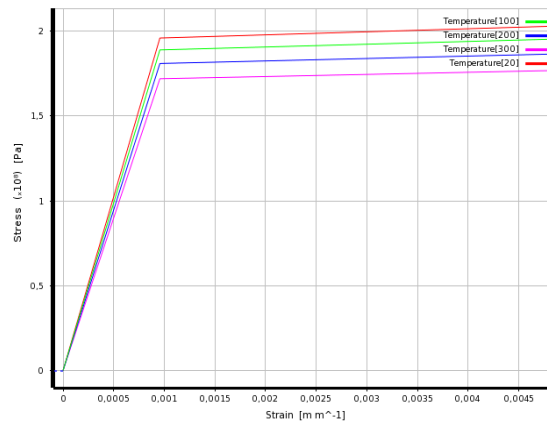
Vzhledem k tomu, že předpoklad elastického chování materiálu je příliš konzervativní, dále se provedla analýza s uvažováním elasto-plastického chování materiálu.

3 Alternativní výpočet únavy dle normy NTD A.S.I. Sekce III

Výpočet kumulace poškození uvedený v této kapitole vychází z elasto-plastického výpočtu napjatosti MKP a přímého určení amplitudy plastické deformace.

3.1 Popis modelu

Model použitý v tomto výpočtu byl shodný s kap.2, pouze se změnil materiálový model (Bilinear Isotropic Hardening) dle Obrázek 7.



Obrázek 7 – Bilineární model chování materiálu

3.2 Popis výpočtu únavy

Úpravou vzorce (10.1) z normy NTD A.S.I. Sekce III [1 (druhou část vzorce lze pro zjednodušení pro nízkocyklovou únavu zanedbat):

$$\frac{[\sigma_{aF}]}{\varphi_s} = \frac{E e_c}{(4 n_N [N_o])^m} + \frac{\sigma_{FR}}{(4 n_N [N_o])^{m_s} + \frac{1+r_\sigma}{1-r_\sigma}},$$

(14)

Použijeme-li pak vyjádření $\frac{[\sigma_{aF}]}{E} = [\varepsilon_{apl}]$ dostaneme následující vztah pro dovolenou amplitudu plastické deformace:

(15)

Z této rovnice po úpravě dostaneme dovolený počet cyklů do únavového lomu:

(16)

kde:

ε_{apl} – je skutečná amplituda plastické deformace určená z MKP (určení EPPLEQV viz Obr.8)

φ_s – je součinitel snížení únavové pevnosti svaru (pro těleso armatury je $\varphi_s = 1$)

n_N – je součinitel bezpečnosti vůči počtu cyklů (bere se roven 10).

m – je exponent křivky životnosti dle Tab.10.1

e_c – je charakteristika plasticity daná vztahem viz vzorec (10.3), kde druhá část zohledňuje předchozí plastické deformace součásti např. z předchozího zatěžování nebo z výroby (lze opět pro zjednodušení druhou část vzorce zanedbat):

$$e_c = 1,15 \log \left[\frac{100}{100 - Z_c} \right] - 0,5 \frac{(\sigma_F)_{\max} - R_{p0,2}}{E},$$

(17)

Provede se elasto-plastický výpočet MKP → určí se průběh EPPLEQV (Ekvivalent Plastic Strain = rozkmit plastické deformace) pro jednotlivé zatěžovací stavy. Amplituda plastické deformace je pak poloviční.

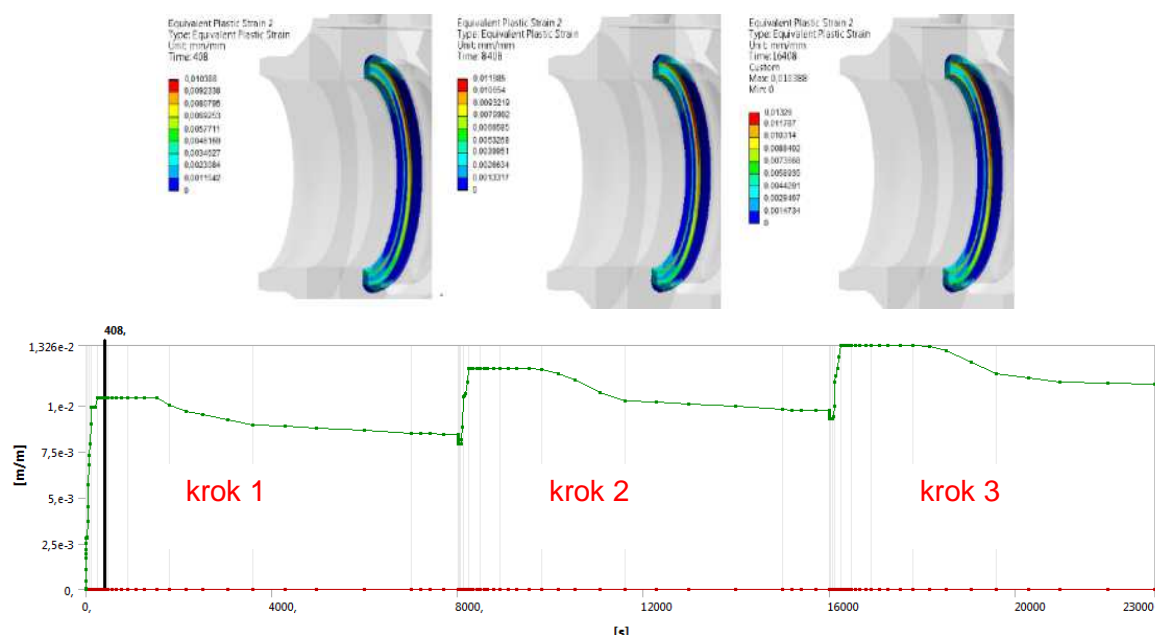
Určí se $[N_i]$ pro všechny amplitudy plastické deformace.

$$D = \sum \frac{N_i}{[N_i]}$$

Vyčíslí se kumulace poškození:

3.3 Výsledky výpočtu

Provedl se kumulovaný výpočet tří po sobě následujících “studených” šoků (viz Tab.1) jehož výsledkem bylo určení rozkmitu plastické deformace mezi jednotlivými kroky. Mezi jednotlivými kroky následoval pomalý ohřev na výchozí teplotu 247°C při zachování „paměti“ materiálu.



Obrázek 8 – Průběh EPPLEQV během n = 3 zatěžovacích kroků

Tabulka 5 Výsledky elasto-plastického výpočtu

Krok	Rozkmit plastické deformace EPPLEQV	Amplituda plastické deformace ϵ_{apl}	Dovolený počet cyklů $[N_i]$
1-2	0,010388	0,005194	60
2-3	0,00356	0,001780	514

Výsledná kumulace poškození pro elasto-plastický model chování materiálu pak bude daná součtem poměrů jednotlivých dovolených počtů cyklů pro jednotlivé zatěžovací kroky:

$$D = \sum_i^{n-1} \frac{1}{[N_i]} \quad \text{v našem případě bude platit:} \quad D = \frac{1}{[N_1]} + \frac{N-1}{[N_2]}$$

kde n - počet zatěžovacích kroků

N - požadovaný počet cyklů ($N = 41$)

$[N_i]$ - dovolený počet cyklů i-tého typu.

Tabulka 6 Kumulace poškození v bodě 1 při elasto-plastickém chování materiálu

Posuzovaný bod	Kumulace poškození D [-]	Posouzení
1	0,0945 < 1	VYHOVUJE

Výpočtem bylo prokázáno, že výsledná kumulace poškození $D < 1$ a tedy pro elasto-plastický model chování materiálu armatura na únavu VYHOVUJE!

4 Závěr

Výpočet kumulace poškození při uvažování elastického chování materiálu může v řadě případů vést k příliš konzervativním výsledkům. Výhodou výpočtu a posouzení stavu čistě elastické napjatosti je nižší časová náročnost výpočtu. Výpočet kumulace poškození za pomoci přímého určování amplitudy plastické deformace je značně časově náročnější, přináší však výsledky bližší skutečnému chování materiálu.

Literatura

[1] ASOCIACE STROJNÍCH INŽENÝRŮ, 2007. *Normativně technická dokumentace A.S.I. Hodnocení pevnosti zařízení a potrubí jaderných elektráren typu VVER Sekce III*. Praha, Brno.

[2] FEDERÁLNÍ SLUŽBA PRO EKOLOGICKÝ, TECHNOLOGICKÝ A JADERNÝ DOZOR, 2005. *Potrubní armatury pro jaderné elektrárny. Všeobecné technické podmínky*. Moskva: 92 p.

Kontaktní adresa:
Ing. Jiří Tábořský
KRÁLOVOPOLSKÁ STRESS ANALYSIS GROUP, s.r.o.
Okružní 19a, 638 00 Brno

COMPARATIVE ANALYSIS OF DIFFERENT APPROACHS TO MODEL TRABECULAR AND COMPACT BONE IN LONG BONES

PETR VOSYNEK, DAVID NEČAS, TOMÁŠ NÁVRAT

Abstract: The contribution presents the context of the need to address biomechanical problems in human society. Some hip joint dysfunctions are solved by replacing the bone contact surfaces with implants (TEP, hip resurfacing, Proxima DePuy). With the aid of computer modeling, we can predict the behavior of implants in the human body with a certain degree of simplification. Especially the model of material plays big role in these simulations. Our comparative analysis is aimed on the different approach to simulate the material used in finite element model additionally with experimental verification. We used computer tomography to get the material data from tested bone. Because of the experimental device prototype and easier manipulation (also less biohazard) we used dried bone. Measured response variables were strain on the bone surface.

Keywords: hip joint, FEM, experiment, comparative analysis.

1 Introduction

The need for biomechanical problems is obvious from the well-known phenomena such as extending the active life of the human population, increasing numbers of trauma and unilaterally oriented way of life leading to unbalanced mental and physical activity. For solving the biomechanical problems we can use experimental and computational modeling.

In this paper we consider a finite element simulation made parallel with experimental loading of the femur. The whole analysis is aimed on the different approach to simulate the material used in finite element model. The comparative output from solution is surface strain of the femoral neck. The neck itself is the most critical usually for older patients when inappropriate loading will occur or could be also result of osteoporosis.

Based on biomechanics problem we need appropriate simulation of material used in computational model. Our analysis covers the gap between using the rough level – linear, homogenous, elastic and isotropic model of material used for two volumes of bone (compact and trabecular) and fine level – using the same model but in each element different material constant (E) based on computer tomography. The best level is to involve the geometry of trabeculas but for the most application it is still impossible to use that.

2 Materials and methods

2.1 Experimental modeling

The physiological loading analysis assumes free body diagram of the femur bone. The significant interactions are between the proximal femoral head and the pelvic acetabulum, than the trochanteric protrusion of the femur and ischium muscle group. In the opposite side (distal side of femur) we could consider the transposed contact force acting on the lower surface of the foot to the knee (image 1). Where we use the following description:

g - gravitational acceleration; F_S – force reaction from sitting system of muscles, F_J - force acting from the acetabulum socket, F_P – given force from the pad, M_P - the moment as result of shifting the force F_P horizontally, distance x .

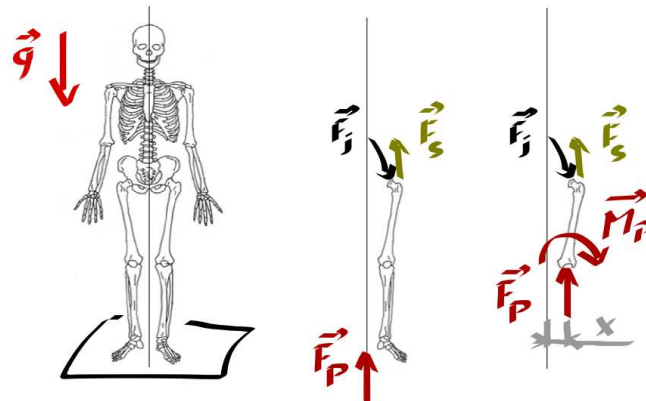


Image 42 – Free body diagram of the femur bone

Realization of 3D supports is shown in the picture. Possible moves for the establishment of the device are shown on image 2. Description of the supports:

-Spherical support: the femoral head fits into the load system socket. Required load is applied by downward movement of the socket, which is done by rotating the load screw. Alignment of the socket against to the femoral head is corresponding to the physiological condition of the hip - anteverse 15° , 45° inclination (Čihák, 2001).

-Link support. The proximal part of the bone is anchored by steel wires. The other ends of the wires are mounted in loading system, which allows us to set the preload of each wire.

-Sliding support allows us to control the rotation of the distal end of the bone by adjustable screws in directions R_x , R_y , while R_z is fixed. Furthermore, it allows free displacement in the x-axis, the other are fixed. With these degrees of freedom will be the end of the distal femur loaded by force and force couple. The design includes force sensors so that each sensor transmits only axial load.

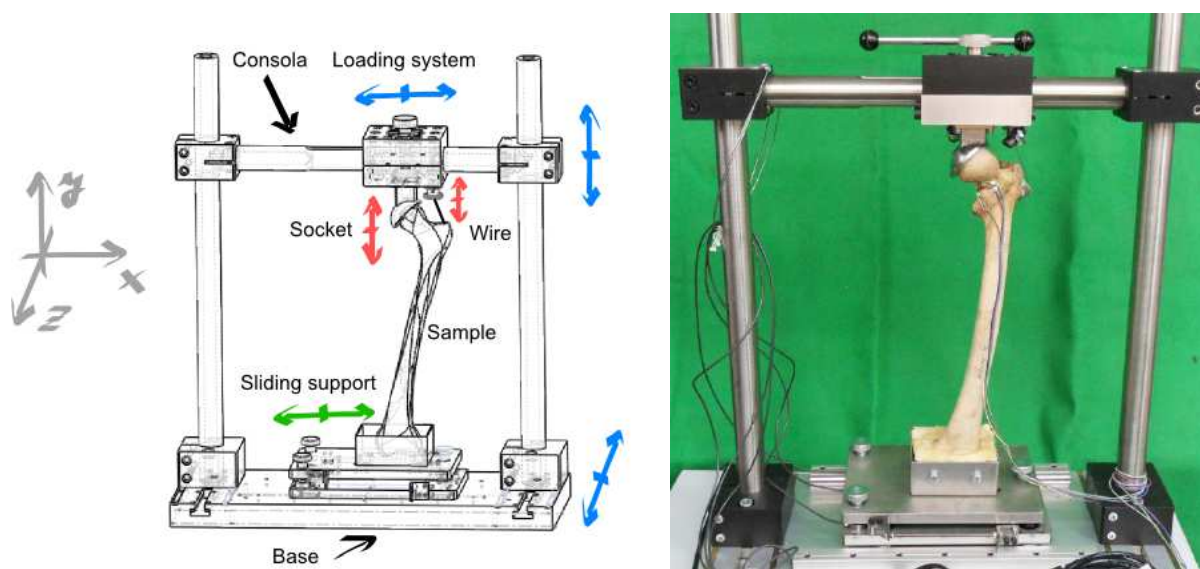


Image 43 – Description of the loading device and its real finish

Measuring chain is consist of three force sensors (HBM C9B/1 kN), strain rossete (HBM RY11-3/120 ohm), signal evaluation complete module (National Instruments - NI 9237, chasis NI cDAQ 9174) and signal processing (NI LabVIEW Signal Expres software).

2.2. Computational modeling

The computational model consists of different types of model. First is the model of geometry. Because the bone itself has complicated geometry it could not be drawn by the classic way compared with classical machine part. We choose the following way: build the volumetric model from 2D outer lines of many cross sections given from computer tomography (CT). Usually we can distinguish between compact and trabecular bone. We used Amira (its free module) software for segmentation the CT slices - image 3, and Catia for creation the volumetric model.

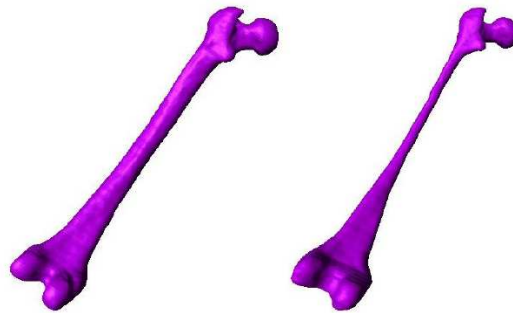


Image 44 – Surface model of bone in Amira software (left: compact bone, right: trabecular bone)

The basic model of geometry has to be modified for further usage in ANSYS Workbench simulations. Modifications were done directly in ANSYS Workbench Design modeler and they are: simplifying the number of surfaces on the bone (virtual topology), preparing the geometry for part connection, dividing (cutting) the bone body into several volumes and finally for adding and alignment the geometry of loading device – see image 4.

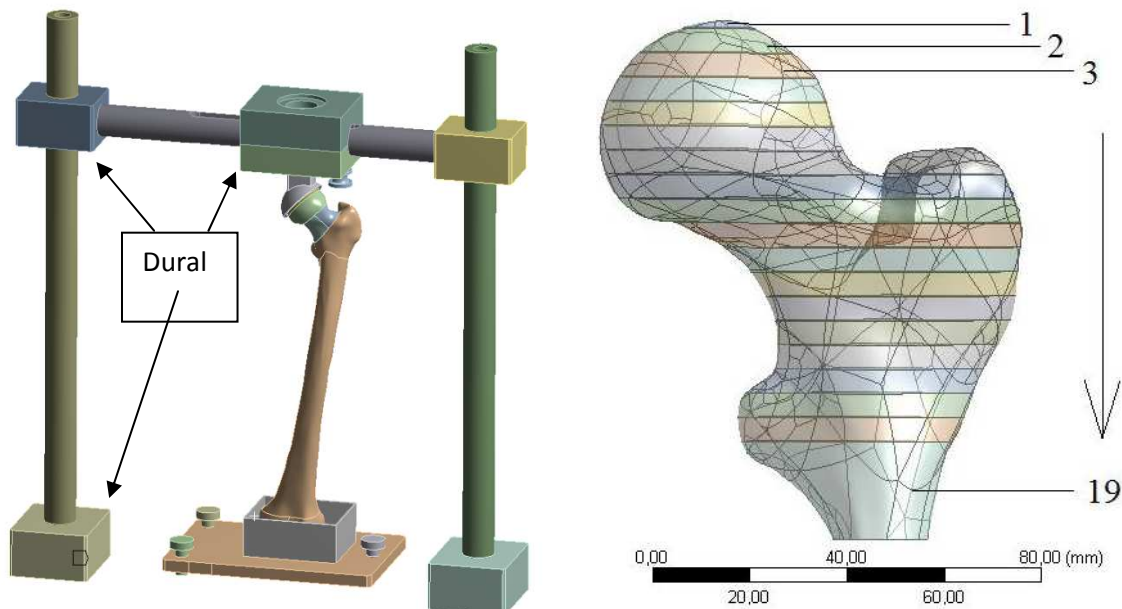


Image 45 – From left to right: model of geometry, dividing the trabecular bone in proximal femur

Second is the model of material. We used linear, homogenous, elastic and isotropic continuum. So we need two characteristic, Young modulus and Poisson ratio (for whole analysis in each model we use $\mu = 0.3$). For trabecular bone we used several equations to

transfer the pixel degree of shade thru Hounsfield unit to Young modulus of elasticity. And then apply these data to subdivision of trabecular and cortical bone. Equation 1 is for variant B, equation 2 is for variant C and so on.

$$E = -38,644 + 1,3665 \cdot CT^{\#} \quad (\text{Ciarelli, 1991}) \quad (18)$$

$$E = 1949 \cdot \rho_{app}^{2.5} \quad (\text{Cody, 2000}) \quad (19)$$

$$E = 1912 \cdot \rho_{dry}^{1.13} \quad (\text{Keyak, 1994}) \quad (20)$$

$$E = -34,7 + 3230 \cdot \rho_{QCT} \quad (\text{Kopperdahl, 2002}) \quad (21)$$

Different variants were done and they are summarized in table 1 and 2. Variant A has a uniform material data in compact bone and in trabecular bone.

Table 10 Material data for variant A

Bone	Young modulus of elasticity [MPa]
Compact	170 000
Trabecular	750

Table 11 Material data for trabecular bone of variant B, C, D and E

Slice number	Young modulus of elasticity [MPa]			
	Variant B	Variant C	Variant D	Variant E
1	1 054	2 718	1 188	3 894
2	942	2 129	1 065	3 498
3	984	2 340	1 111	3 646
4	933	2 083	1 054	3 465
5	861	1 754	976	3 210
6	774	1 400	882	2 902
7	754	1 326	861	2 832
8	738	1 267	843	2 774
9	739	1 273	845	2 780
10	721	1 206	825	2 713
11	752	1 319	858	2 825
12	782	1 431	890	2 931

13	785	1 441	893	2 940
14	833	1 637	946	3 112
15	695	1 119	797	2 622
16	596	819	693	2 272
17	463	499	555	1 798
18	303	234	395	1 233
19	184	109	281	811

The second type of bone – compact bone, was divided into six parts with different values of Young modulus based on CT data with use of equation 4. These data are the same in variant B, C, D and E.

$$E = (10^{7.81} \cdot HU^{0.74}) / 10^6 \text{ [MPa]} \text{ (Snyder, 1991)} \quad (22)$$

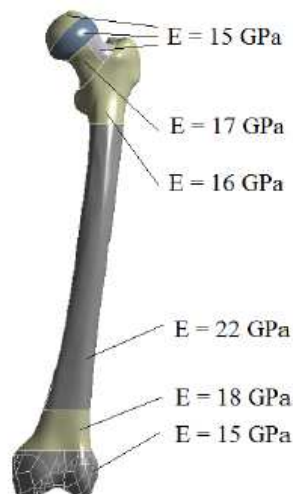


Image 46 – Material data for compact bone of variant B, C, D and E

In the model two muscles are present. They are simulating musculus gluteus muscles group and they are added by command line between trochanter major and locking screw device on loading system (image 2). Young modulus of the muscles is $E = 100 \text{ GPa}$. There is also interaction between femoral head and socket which was simulated by nonlinear contact with friction coefficient $f=0.1$.

Finally there have to be defined last characteristic for structural steel ($E = 210 \text{ GPa}$) and for aluminum alloy – dural ($E = 70 \text{ GPa}$).

Finite element mesh was generated with following types of element: SOLID 187, CONTA 174, TARGE 170 and for muscles LINK 10. Element and nodes quantity is summarized in table 1.

Table 12 Elements and nodes quantity

Nodes	209 910
Elements	135 158

To complete the computational model boundary conditions has to be added. Three forces are involved with magnitudes – image 6: $F_A = F_B = 317 \text{ N}$, $F_C = 200 \text{ N}$. The forces were evaluated from static equilibrium. Supports are plotted in image 7 where displacement in z axes are equal to zero (red colour flag B).

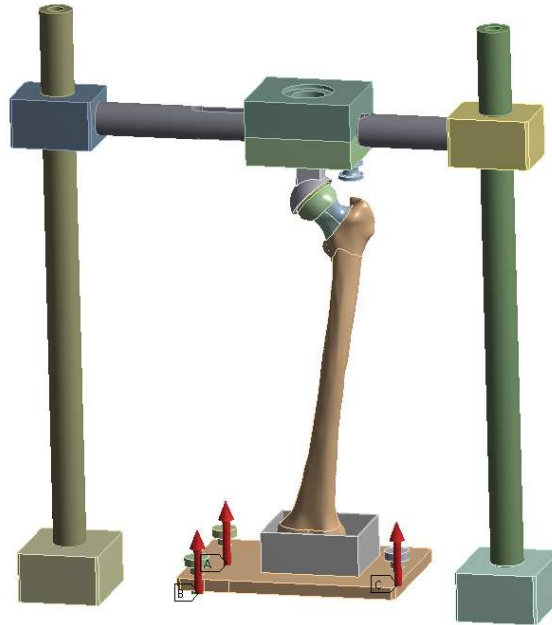


Image 47 – Boundary conditions: forces

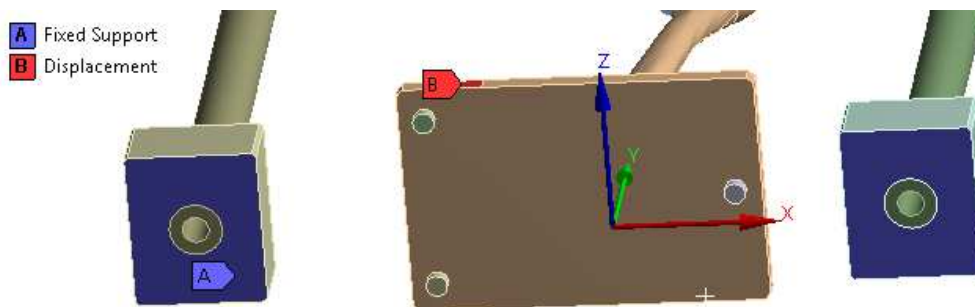


Image 48 – Boundary conditions: displacement

3 Results

First of all total deformation was shown to ensure the right formulation of the boundary conditions image 8 and table 4. Following variables was strain in the neck area were the comparison could be done – strain rosette placement, image 9 and table 5.

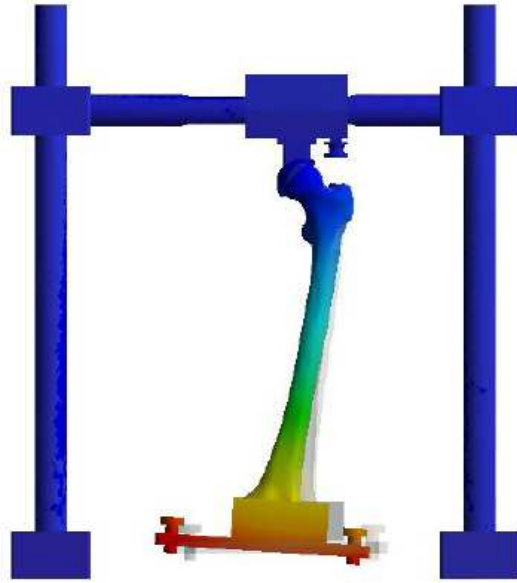


Image 49 – Total deformation

Table 13 Total deformation in variants

	Variant A	Variant B	Variant C	Variant D	Variant E
Total deformation [mm]	31.9	29.2	28.5	29.1	27.9

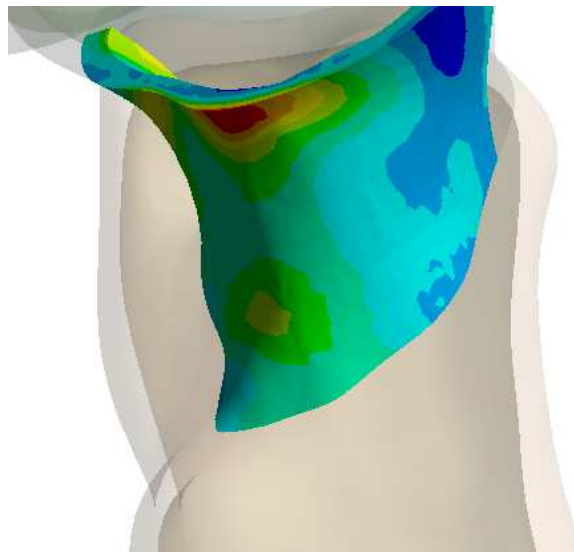


Image 50 – Distribution of Equivalent strain (von-Mises) on bottom side

Table 14 Equivalent strain (von-Mises) in variants

	Variant A	Variant B	Variant C	Variant D	Variant E
$\epsilon_{ekv} [\mu m \cdot m^{-1}]$					
FEM	590	505	395	483	308
$\epsilon_{ekv} [\mu m \cdot m^{-1}]$	416				

experiment					
Error	42%	21%	5%	16%	26%

4 Conclusion

The paper presents the results of work in the field of biomechanical problems related to the hip joint. The work is focused on the comparison analysis between variants of computational model with validation by experimental modeling. The tight bone (femur) was loaded by forces equivalent to steady standing on single lower extremity (limb). Results can be organized into the following points of conclusion:

- Computational model was created based on the computer tomography data. Comput
- Experimental validation was performed on loading device. Experi
- Up to now evaluation of the discrete outputs were done. Mean values of the material data – Young modulus, and mean values of strain output. The Variant A shows that modeling the compact bone and trabecular bone by distinguishing between two Young modulus is not quite precise (42% error) compared to other quite simple method which is dividing the bones into several more parts with different Young modulus (5% to 26% error).

Further view on this problem will be the probabilistic computation and evaluation of the outputs variables.

References

- CIARELLI M., et all., 1991. Evaluation of orthogonal mechanical properties and density of human trabecular bone from the major metaphyseal regions with materials testing and computed tomography. *Journal of Orthopedic Research*, volume 9, number 5, pages 674-682.
- CODY D., et all., 2000. Short Term In Vivo Precision of Proximal Femoral Finite Element Modeling. *Annals of Biomedical Engineering.*, volume 28, number 4, pages 408-414.
- ČIHÁK R., 2001. *Anatomie 1*. Praha: Grada publishing a.s., 497. ISBN 80-7169-970-5
- KEYAK J., LEE I., SKINNER H., 1994. Correlations between orthogonal mechanical properties and density of trabecular bone: Use of different densitometric measures. *Journal of Biomedical Materials Research*, volume 28, number 11, pages 1329-1336.
- KOPPERDAHL D., MORGAN E., KEAVENY T., 2002. Quantitative computed tomography estimates of the mechanical properties of human vertebral trabecular bone. *Journal of Orthopedic Research*, volume 20, number 4, pages 801-805. ISSN 0736-0266

SNYDER S., SCHNEIDER E., 1991. Estimation of mechanical properties of cortical bone by computed tomography. *Journal of Orthopedic Research*, volume 9, number 3, pages 422-431. ISSN 0736-0266

Acknowledgement

The present work has been supported by European Regional Development Fund in the framework of the research project NETME Centre under the Operational Programme Research and Development for Innovation. Reg. Nr. CZ.1.05/2.1.00/01.0002, id code: ED0002/01/01, project name: NETME Centre – New Technologies for Mechanical Engineering)

Contact address:

Ing. Petr Vosynek; Institute of Solid Mechanics, Mechatronics and Biomechanics, Faculty of Mechanical Engineering, University of Brno; Technická 2896/2,619 69, Brno, Czech Republic; vosynek@fme.vutbr.cz

Ing. David Nečas; Institute of Solid Mechanics, Mechatronics and Biomechanics, Faculty of Mechanical Engineering, University of Brno; Technická 2896/2,619 69, Brno, Czech Republic; y107449@stud.fme.vutbr.cz

Ing. Tomáš Návrát, Ph.D.; Institute of Solid Mechanics, Mechatronics and Biomechanics, Faculty of Mechanical Engineering, University of Brno; Technická 2896/2,619 69, Brno, Czech Republic; navrat@fme.vutbr.cz

ANALÝZA SMYKOVÉHO PORUŠENÍ ŽELEZOBETONOVÉ STĚNY

LUBOMÍR JURÁŠEK¹, PETR HRADIL¹, PETR VYMLÁTIL²

¹Fakulta stavební VUT v Brně, ²Designtec s.r.o.

Abstract: This paper proposes 3D computational FE model of the shear wall test including the concrete slab with the test device. Finite Element Analysis software ANSYS with material model for concrete from material library multiPlas was used for this highly nonlinear problem. Simulation results are compared to measured data.

Keywords: shear wall test, nonlinear concrete model, ANSYS, multiPlas

1 Úvod

Smykové namáhání rovinných železobetonových prvků nastává u řady stavebních konstrukcí. Typickým příkladem jsou komorové nebo dvoutrémové průřezy používané v mostním stavitelství. U těchto průřezů je deska mostovky namáhána deskostěnovými vnitřními silami, tedy kombinací smyku a ohybu. Není jasné, do jaké míry vzdoruje element porušený ohybem stěnovým účinkům a jaká je jeho výsledná smyková tuhost. Zkoumání tohoto problému bylo předmětem práce (Martinec, 2003). Zde je popsáno navržené zkušební zařízení pro provádění smykových zkoušek stěnových elementů a jsou zdokumentovány výsledky provedených měření na elementech porušených i neporušených ohybem.

Příspěvek popisuje numerickou simulaci smykové zkoušky neporušeného stěnového elementu. Pro výpočet byl v programu ANSYS sestaven prostorový výpočtový model zkušebního zařízení a železobetonového elementu. Pro popis nelineárního chování betonu byl použit materiálový model z knihovny elasto-plastických materiálových modelů multiPlas. Výsledky simulací jsou porovnány s naměřenými hodnotami.

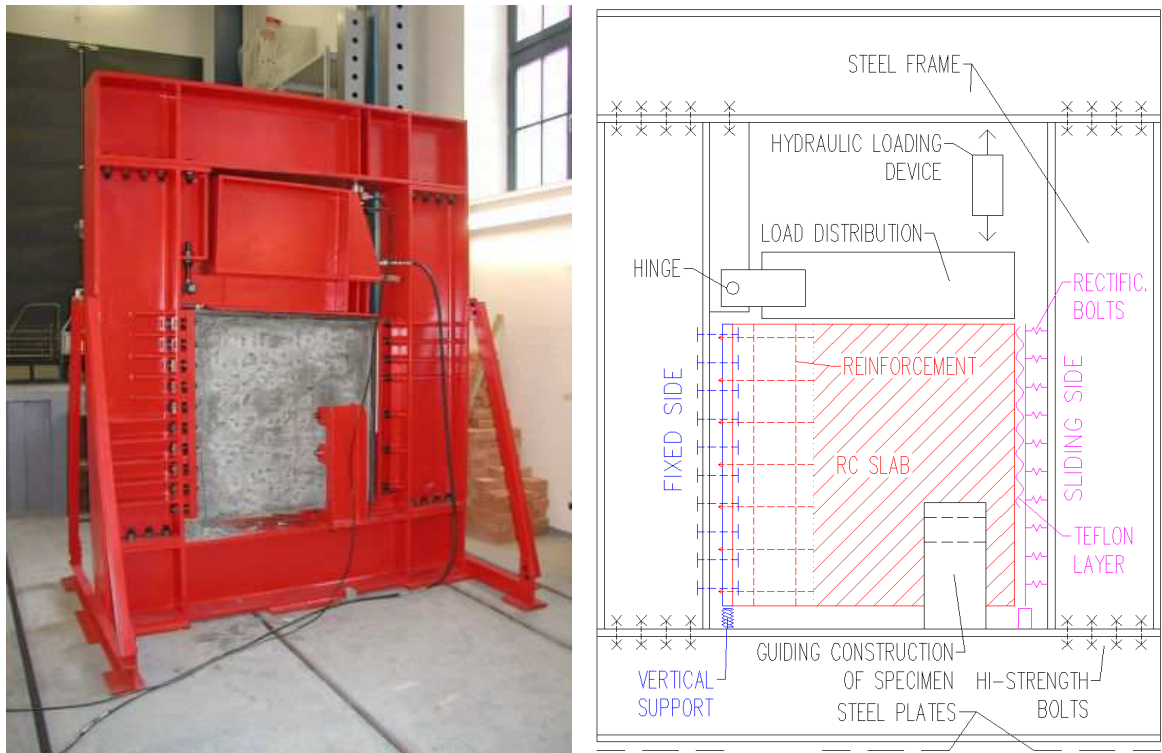
2 Testovací zařízení, zkušební element a průběh smykové zkoušky

Navržené zkušební zařízení je tvořeno masivním tuhým ocelovým rámem, který simuluje podobné podmínky jako při umístění zkušebního vzorku v konstrukci, viz Obr. 17. Zkušebním vzorkem je železobetonová stěna o rozměrech 1000 mm x 1000 mm x 80 mm. Stěna je vyztužena kari sítí při obou površích. V rámci zkušebního programu byla stanovena smyková únosnost železobetonových prvků porušených ohybovými trhlinami i bez trhlin.

Hlavním prvkem zkušebního zařízení je uzavřený ocelový rám, tvořený HEB profily. Rámové rohy jsou spojeny vysokopevnostními šrouby. Ocelový rám je uložen na roznášecích ocelových deskách a je vertikálně stabilizován.

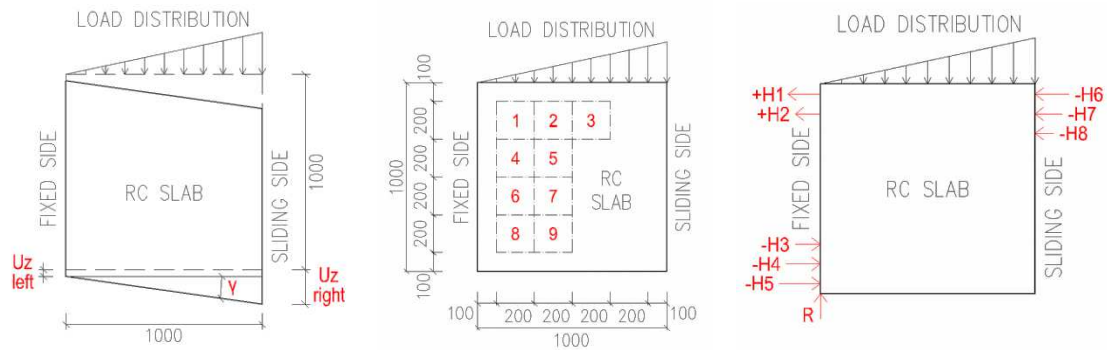
Levá strana zkušebního vzorku je připojena k rámu tak, aby byl zajištěn přenos horizontálních sil. To je zajištěno přilepením ocelové desky k betonovému povrchu a zakotvením přesahující výztuže. Ocelová deska je po výšce připojena k rámu pomocí prvků, které přenáší pouze horizontální síly. Celková vertikální síla je přenášena z dolní části desky do rámu. Pravá strana vzorku je vůči rámu uložena kluzně. Zde je použita teflonová vrstva minimalizující vertikální tření, která je vsazena do ocelové desky připojené rektifikačními šrouby k rámu.

Zatížení vyvolává hydraulický rozpěrný lis, který vnáší zatížení do horní části rámu a přes roznášecí rameno do zkušební vzorku. Zatěžování probíhalo v několika zatěžovacích a odlehčovacích cyklech.



Obr. 17 - Fotografie a schéma zkušebního zařízení

Z experimentů byly vyhodnoceny dvě skupiny dat – údaje o zkosení stěnového elementu a o silových účincích elementu na zkušební zařízení. Na Obr. 18 (vlevo) jsou zobrazeny body pro měření svislých posunutí elementu, která byla použita pro výpočet celkového zkosení. Tato svislá posunutí jsou měřena jako změna výšky dolních rohů stěnového elementu a proto celkové zkosení zahrnuje nejen zkosení vlastního elementu ale i rotaci elementu způsobenou deformací ocelového rámu zkušebního zařízení. Dále bylo měřeno zkosení monitorovaných oblastí, rozměru 0.2 m x 0.2 m, definovaných na povrchu stěnového elementu, viz Obr. 18 (uprostřed). Tato zkosení jsou vyhodnocována ze změn délek vertikály, horizontály a diagonály na každé monitorované oblasti a proto vyjadřují smyková přetvoření bez vlivu deformací rámu. Účinky stěnového elementu na ocelový rám byly měřeny pomocí siloměrů a jsou reprezentovány horizontálními silami H1, H2, ..., H8 a vertikální silou R (celková síla přenesená ze zkušební elementu do rámu), viz Obr. 18 (vpravo).



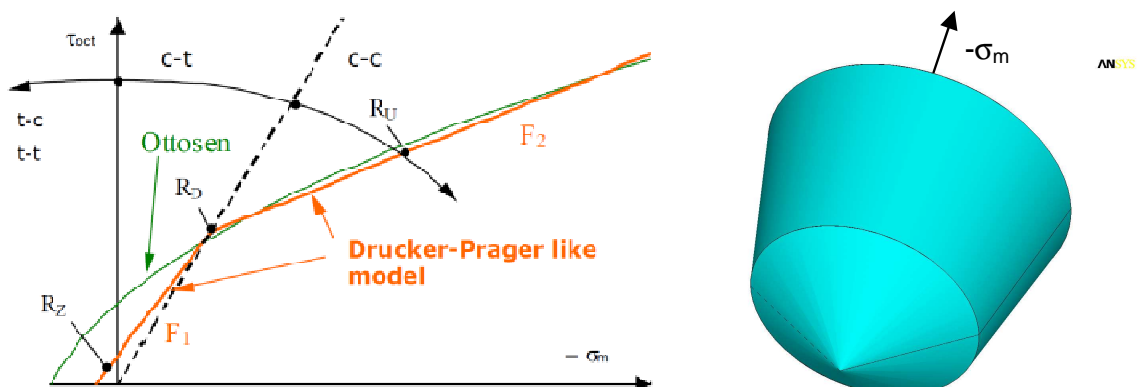
Obr. 18 – Smyková deformace (zkosení) stěnového elementu (vlevo), schéma monitorovaných oblastí na povrchu stěnového elementu (uprostřed), silové účinky elementu na rám (vpravo)

3 Nelineární model betonu

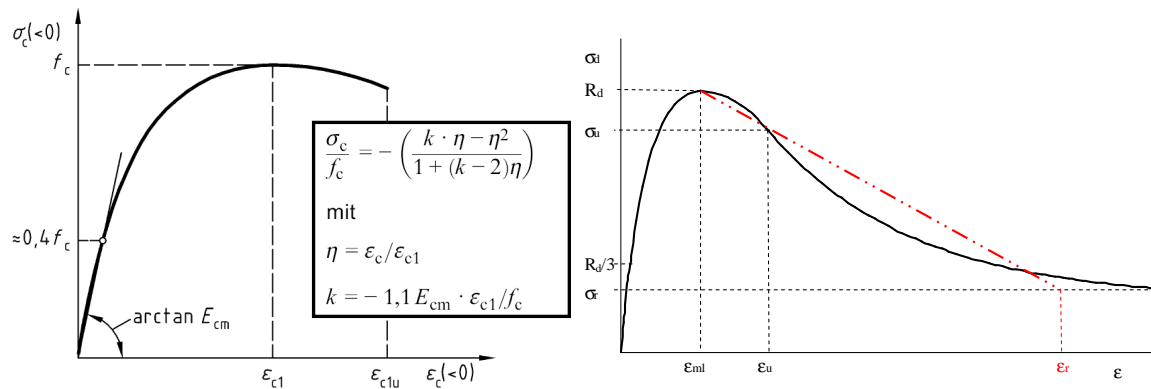
Pro modelování nelineárního chování betonu byl použit model z materiálové knihovny multiPlas. Tato knihovna je rozšířením programu ANSYS a zaměřuje se na materiálové modely používané ve stavebnictví (beton, zdivo, dřevo) a geotechnice (isotropní a anisotropní Mohr-Coulombův a Drucker-Pragerův model). Tyto elasto-plastické modely jsou založeny na podmínce plasticity s asociativním nebo neasociativním zákonem tečení. Pro FEM-analýzy v programu ANSYS má multiPlas efektivní a robustní algoritmus pro materiálové modely s jednou plochou plasticity (single surface) i více plochami plasticity (multi surface). To je často využíváno u modelů, které zahrnují isotropní i anisotropní podmínky plasticity. Knihovna je vyvíjena německou firmou DYNARDO GmbH (multiPlas - User's manual, 2011).

Pro modelování železobetonové desky byl použit modifikovaný elasto-plastický materiálový model. Podmínka plasticity se skládá ze dvou kritérií, kterými lze realisticky popsat pevnost betonu v tlaku, tahu i smyku. Podmínka plasticity je zobrazena na Obr. 19.

Model chování betonu v tahu je založen na nelineární lomové mechanice v kombinaci s metodou šířky pásu trhlin a konceptem rozetřených trhlin. Změkčení v tahu je definováno exponenciální funkcí a lomovou energií, viz Obr. 20. Funkce změkčení je stanovena individuálně pro každý konečný prvek, aby byl zachován vztah pro šířku otevření trhliny a zajištěna nezávislost na síti konečných prvků. Při popisu chování betonu v jednoosém tlaku model uvažuje nelineární závislost mezi napětím a přetvořením se změkčením podle Obr. 20 (vlevo).



Obr. 19 – Modifikovaná Drucker-Prager podmínka plasticity v oktaedrické rovině (vlevo) a v prostoru (vpravo)



Obr. 20 – Nelineární model betonu – pracovní diagram betonu v tlaku (vlevo) a v tahu (vpravo)

4 Výpočtový model a výsledky simulace

Pro simulaci smykové zatěžovací zkoušky byl vytvořen prostorový konečně prvkový model stěnového elementu a zkušebního zařízení, který korektně popisuje nelineární chování železobetonového prvku a tuhost zkušebního zařízení včetně jejich vzájemné interakce. Pro výpočet byla využita konfigurace stěnového elementu neporušeného ohybovými trhlinami.

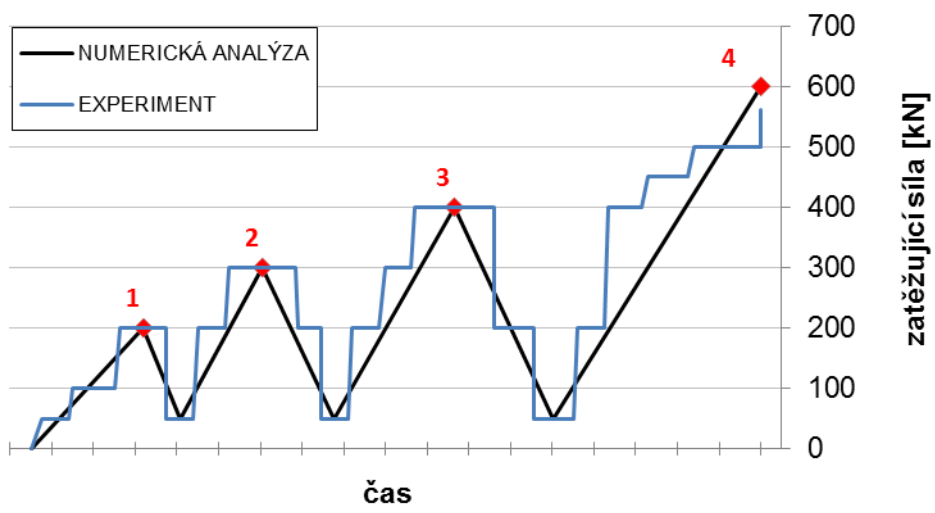
Prostorová geometrie stěnového elementu je tvořena prvky typu SOLID45 s nelineárním materiálovým modelem betonu, viz kap. 3. Výztuž železobetonové stěny je idealizována prvky typu LINK8 s multilineárním elasto-plastickým materiálovým model oceli.

Ocelový rám tvořený HEB profily je diskretizován prostorovými prvky SOLSH190. V rozích rámu jsou modelovány vysokopevnostní šrouby pomocí prvků LINK8 s předpětím. Na styčných plochách HEB profilů jsou modelovány kontaktní prvky přenášející pouze tlak. Rám je uložen na podkladních ocelových podložkách, na jejichž styku je definován kontakt.

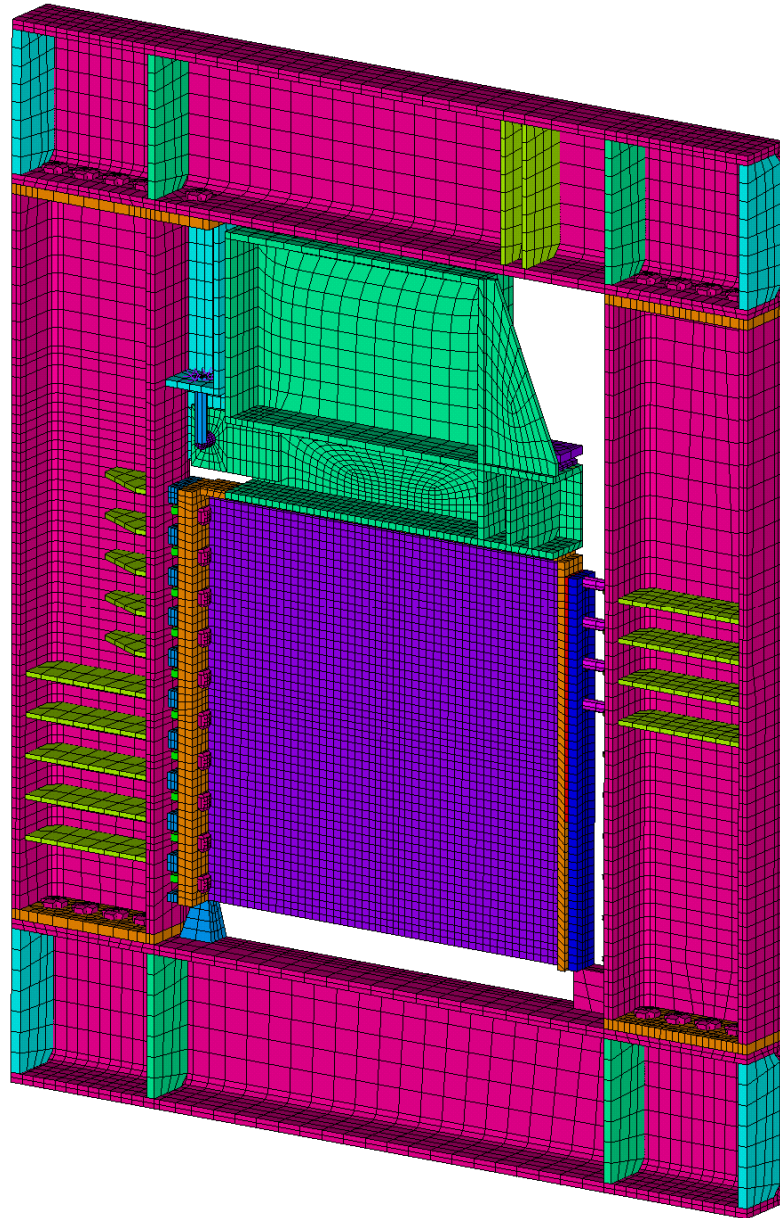
Na levé straně (pevné uchycení) je ke zkušebnímu prvku připojena ocelová roznášecí deska. Spojení této desky s ocelovým rámem je modelováno prutovými prvky LINK8, které přenáší pouze horizontální síly. Vertikální síla z roznášecí desky je přenášena přes tuhou vazbu do spodní části ocelového rámu. Kluzné uložení na pravé straně je modelováno prvky SOLSH190, které tvoří ocelové deska a vrstvu teflonového pásu. Mezi elementy ocelové desky a teflonového pásu je definován nelineární kontakt bez tření. Materiálový model teflonové vrstvy je popsán elasto-plastickým pracovním diagramem. Připojení tohoto kluzného uložení k rámu je modelováno prutovými prvky, které přenáší pouze tlak.

Rameno pro roznos zatížení je diskretizováno prvky SOLSH190. Kloubové uložení ramene je modelováno prutovým prvkem BEAM4 a lineárními vazebními rovnicemi.

Při provádění zkušebního testu bylo aplikováno cyklické zatížení se stanovenou délkou časového kroku při každém přitížení či odtížení. Vzhledem k tomu, že numerický výpočet nezahrnuje reologické jevy, byl skutečný průběh cyklického zatěžování zjednodušen, viz Obr. 21. Zatížení je zadáno silami na roznášecí rameno a horní část rámu, tak jak na konstrukci působí rozpěrný lis.

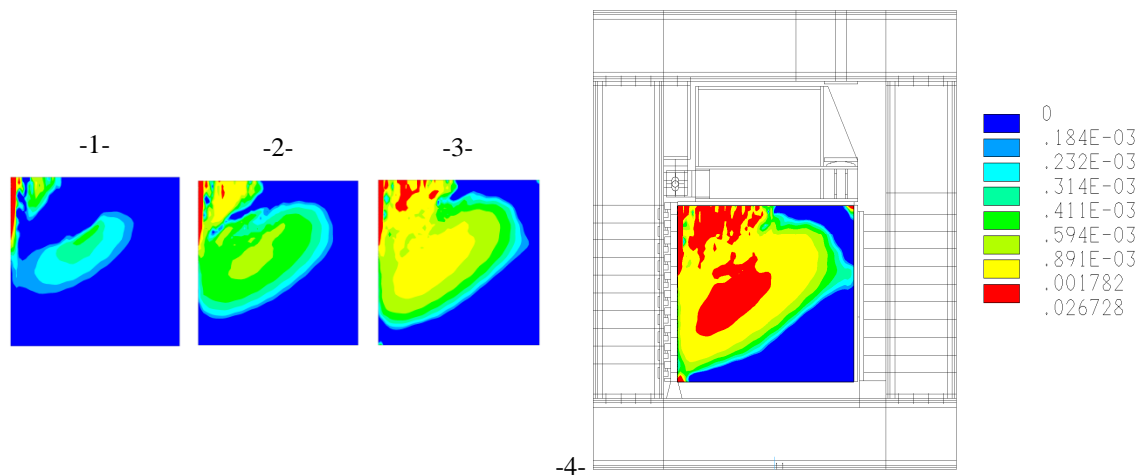


Obr. 21 – Schéma cyklického zatížení

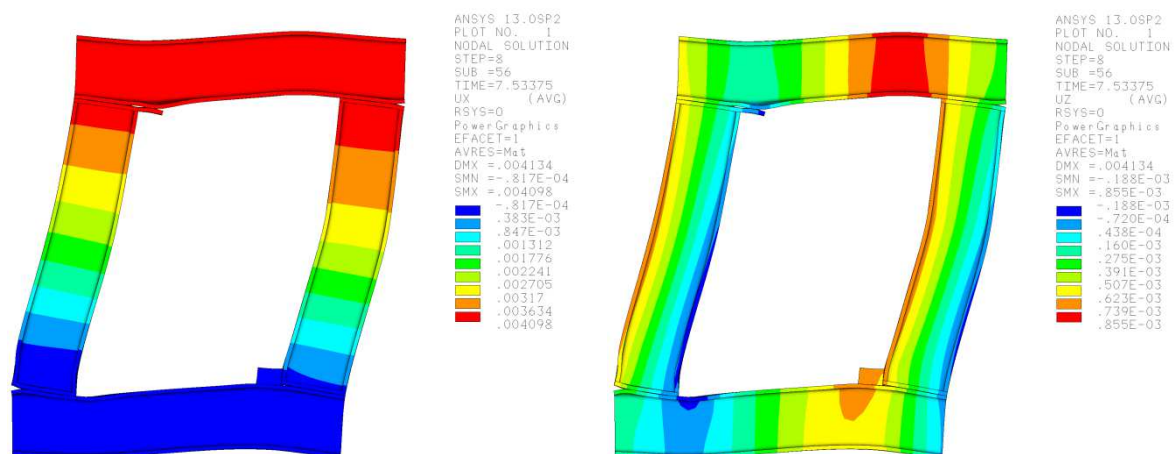


Obr. 22 – Konečně prvkový model zkušebního zařízení

Použitý prostorový výpočtový model poskytuje detailní informace o chování zkoušeného vzorku i zkušebního zařízení. Na Obr. 22 jsou zobrazena maximální hlavní plastická přetvoření stěnového elementu v jednotlivých zatěžovacích krocích. Posunutí rámu ve vodorovném a svislém směru jsou zobrazeny na Obr. 24.

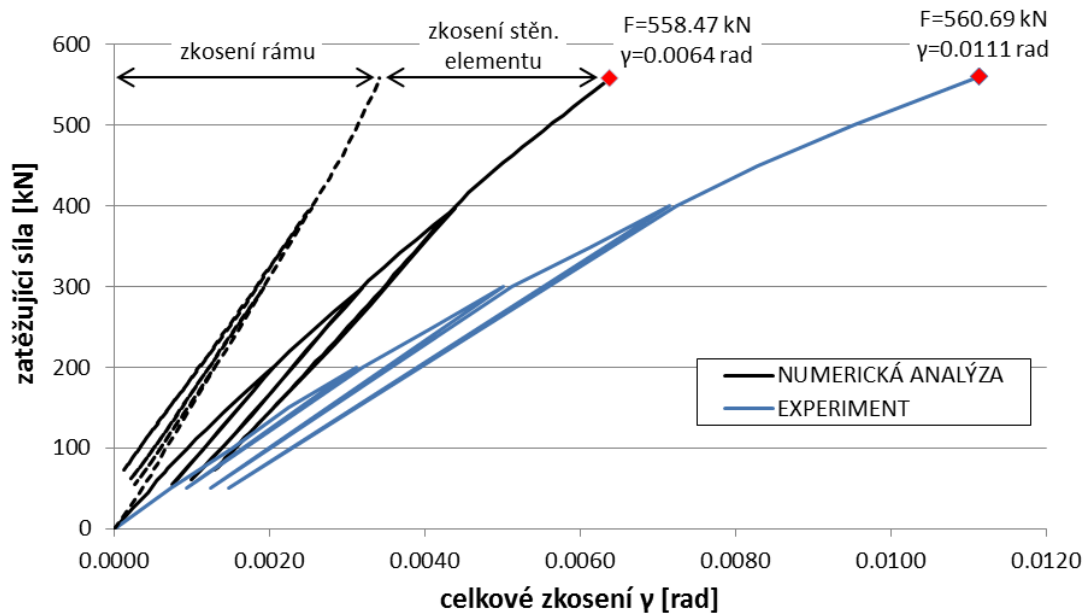


Obr. 23 – Maximální hlavní plastická přetvoření stěnového elementu

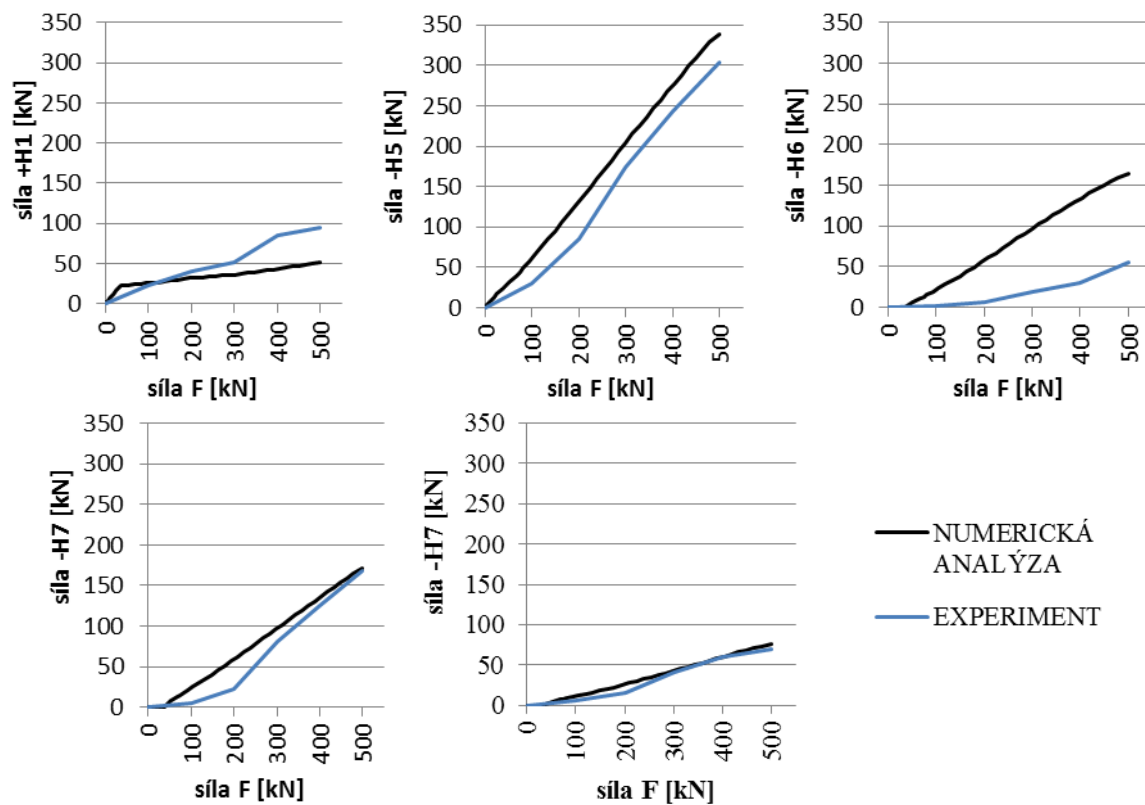
Obr. 24 – Horizontální posunutí ocelového rámu (vlevo), vertikální posunutí (vpravo)
[zvětšeno 100x]

5 Porovnání výsledků s experimentem

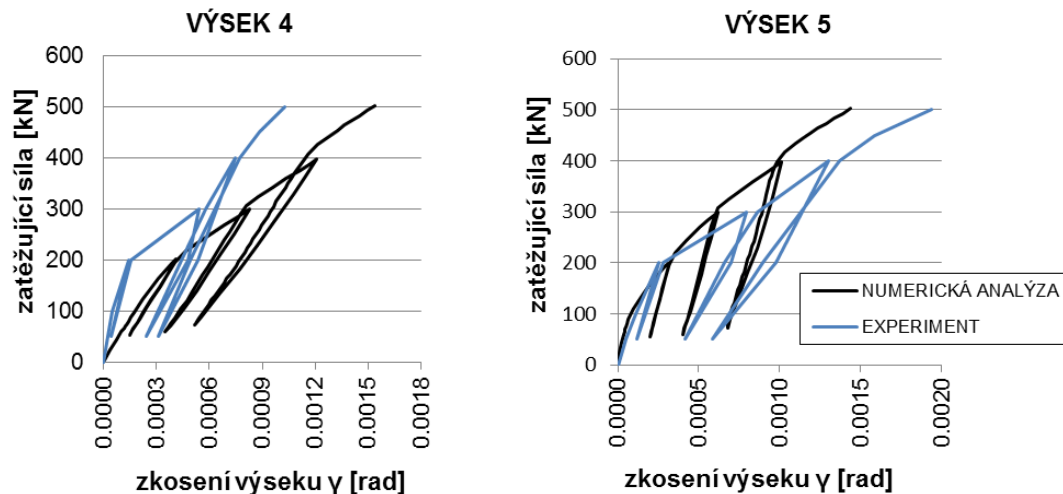
Výsledky získané z numerické simulace vykazují velmi dobrou shodu s experimentálně měřenými daty. Maximální vypočtená síla přenesená vzorkem (558 kN) odpovídá naměřené hodnotě (561 kN). Vypočtený průběh celkového zkosení elementu v závislosti na zatěžovací síle je porovnám s měřením na Obr. 25. Vypočtené zkosení je nižší u experimentu. To může souviset s rozdíly ve vypočtených a naměřených horizontálních silách mezi zkušebním vzorkem a rámem, zejména síla H6 (viz. Obr. 26) může výrazně ovlivnit celkové zkosení stěnového elementu. Odchyly mezi naměřenými a vypočtenými silami je možné přisoudit nestejněmu nastavení rektifikačních šroubů. Výpočet prokázal také výrazný vliv tuhosti rámu na velikost celkového zkosení. Z Obr. 25 je zřejmé, že se rotace elementu způsobená deformací zkušebního zařízení podílí na celkovém zkosení z více jak 50%. Dobrou shodu s měřením vykazují zkosení měřičských výšek na Obr. 27.



Obr. 25 – Závislost zatěžující síly na celkovém zkosení stěnového elementu



Obr. 26 – Záznamy okrajových horizontálních sil v závislosti na zatížení



Obr. 27 – Závislost zatěžující síly na zkosení měříčského výseku č.4 (vlevo) a č.5 (vpravo)

6 Závěr

Prezentované výsledky numerických výpočtů prokázaly dobrou shodu s měřením. Příspěvek prokazuje význam detailních matematických modelů u náročných a složitých experimentů a to zejména v případě, kdy se jedná o netypický prototyp zkušebního zařízení. Využití výpočtové podpory při provádění složitých experimentů je opodstatněné již během přípravné fáze. Numerické simulace predikují, zda zkušební zařízení vyvolá ve zkušebním prvku požadovaný stav napjatosti a deformace.

Literatura

JURÁŠEK, Lubomír. Nelineární analýza železobetonových stěn. Brno, 2012. Diplomová práce. VUT Brno. Vedoucí práce Ing. Petr Hradil, Ph.D.

MARTINEC, Stanislav. Chování železobetonových prvků namáhaných smykem. Brno, 2003. Disertační práce. VUT Brno. Vedoucí práce doc. Ing. Jaroslav Navrátil, CSc.

WENDRINSKI, Jacek. Nelineární a plastická analýza vyztužených betonových konstrukcí a detailu. Brno, 2009. Disertační práce. VUT Brno.

ANSYS, Theory Release 13.1, ANSYS Inc., 2010

multiPlas, User's manual Rev. 10 Release 4.1.0 for ANSYS 13, Dynardo, Weimar, Germany

Poděkování

Tento výsledek byl získán za finančního přispění projektu P104/11/0703 „Použití progresivních materiálů u cyklicky namáhaných konstrukcí s využitím výsledků získaných v rámci projektu MSM0021630519 Progresivní spolehlivé a trvanlivé nosné stavební konstrukce.

Kontaktní adresa:

Ing. Lubomír Jurášek

Vysoké učení technické v Brně - Fakulta stavební, Veveří 331/95, 602 00 Brno,
tel.: +420 541 141 111, e-mail: jurasek.l@fce.vutbr.cz

Ing. Petr Hradil, Ph.D.

Vysoké učení technické v Brně - Fakulta stavební, Veveří 331/95, 602 00 Brno,
tel.: +420 541 147 366, e-mail: hradil.p@fce.vutbr.cz

Ing. Petr Vymlátíl, Ph.D.

Designtec s.r.o., Žižkova 59, 616 00 Brno, tel.:+420 777 568 356, e-mail: vymlatil.p@designtec.cz

Title: 20th SVSFEM ANSYS Users' Group Meeting and Conference 2012

Date and place of the event: 17th – 19th of October 2012, Hotel Jana in Přerov, Czech Republic

Publisher: SVS FEM spol. s r.o., SVS FEM s.r.o., Škrochova 3886/42, 615 00 Brno-Židenice

Editor: doc. Ing. Petr Koňas, Ph.D.

Pages: 320

Edition: 1.

Year: 2012, Přerov, Czech Republic

ISBN: 978-80-905040-0-4

The ANSYS logo is displayed in a stylized, bold font with a metallic or 3D effect, set against a dark background.The SVS FEM logo features the text 'SVS FEM' in a bold, sans-serif font, with 'Your partner in computing' written in a smaller font below it. The logo is set against a yellow and white background.

SVS FEM s.r.o.
www.svsfem.cz
info@svsfem.cz
+420 543 254 554

SVS FEM s.r.o. je česká firma, která se od roku 1991 specializuje na výpočty metodou konečných prvků (FEM). V současné době má tým s více než desátkou analytiků - specialistů na problematiku FEM. Za dobu své existence řešila více než 400 různých FEM projektů jak pro tuzemské tak i zahraniční zákazníky. V současné době patří mezi špičková pracoviště v tuzemsku i v zahraničí v oblasti simulací velmi rychlých dynamických jevů a spolupracuje na několika mezinárodních projektech v oblasti vojenství. Od roku 1992 firma působí jako ANSYS Channel Partner pro Českou Republiku a Slovensko. V této oblasti celou dobu velmi úzce spolupracuje s partnerskou firmou CAD FEM GmbH. Od roku 2004 je držitelem certifikátu ISO 9001:2009, což zásadním způsobem přispívá ke zvyšování kvality prováděných služeb.

ANSYS and any and all ANSYS, Inc. brand, product, service and feature names, logos and slogans are registered trademarks or trademarks of ANSYS, Inc. or its subsidiaries in the United States or other countries. All other brand, product, service and feature names or trademarks are the property of their respective owners.